Homogenization of periodic and quasi-periodic architectural media towards generalized continua

Seyed Ehsan Alavi

THÈSE

Pour obtenir le grade de:

DOCTEUR DE L'UNIVERSITÉ DE LORRAINE

Mention: Mécanique des Matériaux

École doctorale: C2MP

Présentée par:

Seyed Ehsan ALAVI

Intitulée :

Homogénéisation de milieux architecturés périodiques et quasi-périodiques vers des milieux continus généralisés

Préparée au LEM3 et à l'École Polytechnique de Téhéran

Thèse soutenue à:

Nancy, le 17/12/2021

Devant le jury composé de:

Fodil Meraghni	Pr., LEM3, ENSAM, Metz	Président
Luigi Gambarotta	Pr., DICCA, Université de Gênes	Rapporteur
Amir Zadpoor	Pr., TU Delft, Pays-Bas	Rapporteur
Florence Dinzart	MCF HDR, LEM3, Université de Lorraine	Examinateur
Claude Boutin	Pr., ENTPE, Université de Lyon	Examinateur
Abdolhamid Akbarzadeh	Pr. Associé, Université McGill, Montréal	Examinateur
Jean-François Ganghoffer	Pr., LEM3, Université de Lorraine	Directeur de thèse
Mojtaba Sadighi	Pr., École Polytechnique de Téhéran	Co-directeur de thèse

Acknowledgments

This thesis is the result of my study at laboratory LEM3 of Université de Lorraine and the mechanical engineering department of Tehran polytechnic.

I want to express my tremendous appreciation and thanks to my thesis director Jean-François Ganghoffer and co-director, Mojtaba Sadighi.

Jean-François, from the beginning of our scientific collaboration, you gave me as much overall support as possible. You always respected all the aspects relating to my life and my decisions, and you were available whenever I needed to discuss. Your optimism and kindness were always giving me the desire to move forward. Also, your attempts to lower the stress and pressure of work with a sense of humor were appreciated. Your great scientific qualities, listening skills, and calm personality allowed me to grow, learn pleasantly, and change my life path to the new one. Thank you, Jean-François, for all of your support.

Mojtaba, I started the beginning of my thesis at Tehran Polytechnic with you. You have always trusted me in this way and given me full autonomy during my thesis. You provided me with the opportunity to continue my study. Your responsible personality is appreciated. You allowed me to extend my skills in cooperation with many researchers and work in a multi-disciplinary environment starting from Tehran Polytechnic. Many thanks to you both for supervising me during these years of my Ph.D. study at Université de Lorraine and for giving me a taste for research.

I would also like to thank professors Hamid Akbarzadeh, Artan Sinoimeri, and Hilal Reda, who helped me with my thesis. Thank you a lot Hamid; collaborating with you taught me many things that I will always be proud of it.

Many thanks to all my friends, which without them, these years of the thesis would not have been so easy. I will not make a list because I am afraid to forget someone by mistake. I need to truly thank two friends of mine, Mohana Afsharian and Ehsan Jamshidpour, for all the moments we shared and their support and help, especially during the last three months of my thesis.

Also, I would like to express an immeasurable amount of gratitude to my parents and my brothers for their unconditional and endless love and support throughout my life.

Finally, I wanted to thank the love of my life, Maryam, but words can not describe the inexhaustible affection and support provided by her to finish this work. This long road would have been impossible without you and your comprehensive support.

Ehsan

"To My Dear Love Maryam"

Contents

Contents vi

List of figures xii

List of tables xiv

1 General introduction 1

1.1 Architected materials as a new paradigm in material science . . . 1

1.2 Effective models for architected media . . . 4

1.3 A survey of homogenization methods in linear elasticity . . . 4

1.4 Discrete homogenization as a reduced modeling approach . . . 6

1.5 Enriched constitutive models for heterogeneous materials . . . 7

1.5.1 Phenomenological versus micromechanical formulations of enriched constitutive laws 8

1.6 Limitations of the existing homogenization methods . . . 10

1.6.1 Computational methods of higher order homogenized properties . . . 11

1.6.2 Emergence of new degrees of freedom by upscaling . . . 11

1.6.3 Edge and Size effects for lattice materials . . . 11

1.6.4 Lack of strict periodicity: quasi-periodic homogenization . . . 13

1.7 Analyzed scientific issues and methodology . . . 15

1.8 Thesis outline . . . 16

I Continuous homogenization towards generalized effective continua and applications to architected materials and composites

2 Homogenization towards chiral Cosserat continua and applications to enhanced Timoshenko beam theories 19

2.1 Introduction . . . 20

2.2 General methodology for the homogenization of generalized continua . . . 21

2.3 Elaboration of the kinematic and static variables of the effective Cosserat continuum . . . 23

2.4 Effective moduli of the Cosserat medium . . . 26

2.4.1 Determination of the homogeneous part of the microscopic displacement . . . 27

2.4.2 Variational principle for Cosserat homogenization and determination of the fluctuation . . . 28

2.4.3 Computation of the micropolar properties of lattice . . . 29

2.5 Identification of a chiral Cosserat model for tetrachiral and anti-tetrachiral lattices 30
2.5.1 Validation of the computed effective moduli 31
2.5.2 Sensitivity of the effective tetrachiral unit cell moduli to its microstructural parameters 36
2.5.3 Composite unit cell 38
2.5.4 Analysis of unit cell size effects 39
2.5.5 Homogeneous micropolar BVP 42
2.6 Construction of an enriched Timoshenko beam theory with chirality and non-centrosymmetric effects 43
2.6.1 Enhanced Timoshenko beam theory 46
2.6.2 Response of the enhanced Timoshenko beam under combined applied normal load N, shear force V and bending moment M 47
2.6.3 Macrobeams incorporating tetrachiral unit cells 50
2.7 Conclusion 52

3 Construction of micromorphic continua by homogenization, based on variational principles 53

3.1 Introduction 54
3.2 Construction of the balance equations for the effective micromorphic continuum 57
3.2.1 Balance equations for the micromorphic continuum 57
3.2.2 Expression of the virtual power of internal forces 59
3.3 Determination of the homogeneous part of the total microscopic displacement 60
3.3.1 Evaluation of the microscopic displacement from the macroscopic energy 61
3.3.2 Averaged classical and micromorphic kinematic variables 63
3.3.3 Determination of the microscopic stress based on complementary energy and Hill lemma 64
3.3.4 Determination of the complete homogeneous part of the microscopic displacement field from macroscopic complementary energy 66
3.3.5 Determination of the complete homogeneous part of the microscopic displacement field for Cosserat and second gradient theories 67
3.4 Variational principle for the determination of the fluctuating part of the displacement . . 68
3.5 Evaluation of the effective micromorphic moduli 70
3.6 Computation of the micromorphic properties of lattice structures and composite materials 71
3.6.1 Homogeneous micromorphic BVP 71
3.6.2 Micromorphic deformation modes and energetic contribution of the displacement fluctuation 75
3.6.3 Effect of inclusion volume fraction and contrast of fiber and matrix Young's modulus 80

3.6.4 Analysis of unit cell size effects . . . 81
3.7 Discussion . . . 84
3.7.1 Classification of generalized continua . . . 86
3.8 Conclusion . . . 88

II Beyond continuous homogenization: phenomenological beam models and discrete homogenization of architected materials towards Cosserat media

4 Development of size-dependent consistent couple stress theory of Timoshenko beams 91
4.1 Introduction . . . 92
4.2 Consistent Couple Stress Theory (C-CST) . . . 95
4.2.1 Timoshenko Beam with size-dependency effect . . . 96
4.2.2 Exact Solution . . . 100
4.2.3 Two Primary Variable consistent couple stress Timoshenko Beam . . . 103
4.2.4 Ritz approximation for the consistent couple stress Timoshenko beam . . . 106
4.3 Case studies . . . 108
4.3.1 Verification of C-CST and comparison with other size-dependent beam theories . . . 108
4.3.2 Fully clamped cantilever beam . . . 109
4.3.3 Inflexurable couple stress theory $l \to \infty$ . . . 111
4.3.4 Free-free beam . . . 112
4.3.5 Partially clamped cantilever beam . . . 114
4.3.6 Material dependency of the domain of validity of C-CST . . . 116
4.4 Relevance of the C-CST based on a dimensionless length . . . 117
4.5 Conclusion . . . 118

5 Continualization method towards homogenized Cosserat media and size effects in architected macro-beams under bending 121
5.1 Introduction . . . 122
5.2 Homogenization of lattice materials towards generalized continua . . . 124
5.3 Two-node Timoshenko beam element . . . 126
5.3.1 The effective length of the beam . . . 127
5.3.2 Discrete expression of the beam energy . . . 128
5.3.3 Summary of Cosserat continuum formulation . . . 128
5.4 Continualization towards generalized continua . . . 130
5.4.1 Homogenization of generic hexagonal honeycomb to a Cosserat effective medium . . . 131
5.5 Homogenization of lattice materials towards generalized continua . . . 136
5.5.1 Periodic boundary conditions . . . 137

5.5.2 Applying PBCs in the FE method . . . 137
5.5.3 Micropolar deformation modes . . . 139
5.6 Numerical results . . . 139
5.6.1 Validation and sensitivity analysis of the effective moduli . . . 140
5.6.2 Window analysis size effect . . . 142
5.6.3 Extended Timoshenko beam theory . . . 142
5.7 Discussion . . . 152
5.8 Conclusion . . . 153

III Continuous homogenization methods for quasi-periodic media and case of conformal transformations of the geometry

6 Homogenization of quasi-periodic heterogeneous materials and applications to functionally graded materials 157
6.1 Introduction . . . 158
6.2 General properties of quasi-periodic homogenization . . . 159
6.2.1 Preliminary steps . . . 159
6.2.2 A reminder of asymptotic homogenization of periodic media . . . 160
6.3 Quasi-periodic homogenization . . . 162
6.3.1 Preliminary steps . . . 162
6.3.2 Evaluation of the tensor of quasi-periodic effective moduli based on the unit cell BVP 167
6.3.3 Evaluation of the effective quasi-periodic moduli based on energy and Hill lemma . 170
6.3.4 Evaluation of the tensor of quasi-periodic moduli based on the effective homogeneous medium . . . 171
6.3.5 Specific case: mapping with homogeneous microscale volumetric part . . . 171
6.3.6 More specific case of a microscopically homogeneous design transformation . . . 173
6.4 Smoothness conditions of quasi-periodic mappings . . . 174
6.5 Strain gradient models of quasi-periodic microstructures . . . 176
6.6 Conclusion . . . 179

7 Homogenization of quasi-periodic conformal architectured materials 181
7.1 Introduction . . . 182
7.2 Design of quasi-periodic domains by conformal transformations . . . 183
7.2.1 General properties of conformal mappings and smoothness conditions . . . 184
7.2.2 Kinematic compatibility of conformal transformations . . . 186
7.2.3 General form of conformal transformations . . . 187
7.3 Homogenization of quasi-periodic conformal isotropic microstructures . . . 188
7.3.1 Microscopic periodic and quasi-periodic boundary value problems . . . 189

7.3.2 Determination of the tensor of quasi-periodic moduli 192
7.3.3 Numerical illustration: case of a conformally mapped tetrachiral microstructure . . 192
7.4 Unit cell microcurvature effect on effective properties 194
7.4.1 Sensitivity of the apparent compressibility modulus to number of unit cells 196
7.5 Conclusion 198

General conclusion and perspectives **201**

Résumé étendu en français **205**

References **232**

A Evaluation of the effective micropolar moduli **233**

B Effective engineering material parameters **235**
B.1 Tetrachiral lattice 235
B.2 Anti-tetrachiral lattice 236

C Boundary constraint equations and corresponding classical rigidity components **237**

D Proof of Whitaker averaging theorem **238**

E Derivation of the two balance laws of the effective micromorphic medium **240**

F Determination of the microscopic displacement field for the effective micromorphic continuum **242**

G Computation of the higher-order moments of area and expression of strain components in 2D **246**

H extended macrohomogeneity lemma for the micromorphic continuum **248**

I Index computations to the effective micromorphic moduli **252**

J Exact C-CST shape functions **254**

K Stiffness matrix of the C-CST Ritz approximate solution **257**

L Continualization Method for repetitive periodic lattices **259**
L.1 Direct translational bases 259
L.1.1 Direct translational vector 260
L.1.2 Position vector 260
L.1.3 Direct lattice 260
L.1.4 Periodic transformation matrices 260

L.2 Stiffness system of the unit cell 262
L.3 Homogenization process to derive the macroscopic stiffness of periodic lattice materials . . 262
L.3.1 Microscopic nodal deformations in terms of the macroscopic strain field 263
L.3.2 Homogenized macroscopic stiffness of lattice materials 263

M Extended macrohomogeneity lemma for the micropolar continuum 264

N A reminder of differential geometry in curvilinear coordinates 267

List of figures

1.1 3D Ashby performance diagram of engineering materials showing the relation between strength, modulus, and density for different classes of materials [1]. 2

1.2 Examples of cellular materials: (A) closed cell foam, (B) open cell foam, (C) regular cellular material (body cubic centered BCC unit cell) [2]. 3

1.3 2D architectures with controlled Poisson's ratio: (a, b) Hexagonal, star-shaped re-entrant, (c, d) rectangular, semi-entrant, (e, f, g) diamond, kagome, triangular-saped, chiral lattices (chiral diamond (h), tetrachiral (i), hexachiral (j)) [3]. 3

1.4 Highly oscillating functions [4]. Fast oscillations occur within the repetitive unit cell whereas slow variations of the average occur at the macroscale 5

1.5 (a) The material domain architectured with periodic hexagonal unit cells, (d) the homogeneous substitution medium. The initial geometry can be modeled as: (b) a continuum body or, (c) using a reduced model with a discrete set of degrees of freedom. . 7

1.6 Classification of generalized continua into higher order and higher-grade media [5]. 9

1.7 (top) Complete lattice , (bottom) Cut edge lattice. 13

1.8 Quasi-periodic composites with quasi-periodic microstructure: (a) varying inclusion size, (b) inclusion spacing, (c) inclusion material, All quasi-periodic domains can be mapped to the same periodic unit cell of a parent periodic composite [6]. 13

1.9 Quasi-periodic microstructures generated by conformal mappings of periodic ones.(left): Periodic hexagonal unit cell - (middle): Periodic domain – (right): Quasi-periodic domain. 14

2.1 (left) Composite periodic unit cell Y made of two elastic materials,(right) The homogeneous substitution medium (right) with domain V($\boldsymbol{x}$) centered around point $\boldsymbol{x}$. 22

2.2 Schematic diagram for the computation of the effective micropolar moduli. 30

2.3 (left) Non-centrosymmetric anti-tetrachiral unit cell, (right) Non-centrosymmetric tetrachiral unit cell. 31

2.4 Schematic boundary faces of the unit cell. 33

2.5 Non-centrosymmetric 3D model of: (a) tetrachiral unit cell, (b) anti-tetrachiral unit cell. . 33

2.6 Non-classical deformation modes: (a) Tetrachiral: $\Phi_{,x_1}$, (b) Tetrachiral: $\Phi_{,x_2}$, (c) Anti-tetrachiral: $\Phi_{,x_1}$, (d) Anti-tetrachiral: $\Phi_{,x_2}$. 35

2.7 (a) Centrosymmetric tetrachiral lattice, (b) Non-centrosymmetric tetrachiral lattice. . . . 36

2.8 Variation of the effective rigidity coefficients versus: (a, b) the slenderness ratio η, (c, d) the ring radius R. 37

2.9 Chiral coefficient C_4, coupling terms D_1 and D_3 in function of the position of the center of the ring with respect to the center of gravity of the square unit cell of unit size. 37
2.10 Variation of the effective rigidity coefficients versus volume fraction: (a) C_1, (b) C_3, (c) γ_1, (d) D_1 and C_4. 38
2.11 Non-centrosymmetric fibrous composite unit cell. 39
2.12 Variation of the effective moduli with the inclusion volume fraction. 40
2.13 Windows of analysis including an increasing number of repetitions of the irreducible unit cells. 40
2.14 Distribution of the m_{13} under the kinematic loading $\Phi_{,x} = 1$. 40
2.15 Variation of the effective moduli versus the number of irreducible unit cells, N: (a) Cauchy effective moduli $C_{1,2,4}$, (b) Micropolar effective modulus γ_1. 41
2.16 Deformed shape of the $3by3$ repetition of the tetrachiral unit cell under bending mode: (a) $\Phi_{,x}$, (b) $\Phi_{,y}$. 41
2.17 (a) Full periodic network and (b) Homogenized representation of a tetra-chiral plate consisting of 12×15 unit cells. 43
2.18 Load-displacement responses of the tetrachiral plate, under axial loading normalized with respect to $F_0 = 1$. 44
2.19 (a) Normalized displacement profile u_2 along the horizontal centerline of the plate, (b) Normalized displacement profile u_1 along the vertical centerline of the plate at prescribed displacement $U = 0.06l$. 44
2.20 Tetrachiral lattice structure and homogenized plate at prescribed displacement $U = 0.06l$: (a) Normalized horizontal displacement contour u_1, (b) Normalized vertical displacement contour u_2. 45
2.21 Deformation of a Timoshenko beam. 46
2.22 Schematic representation of the deformation mechanism: (a) undeformed shape, (b) common engineering material, (c) material with an inner normal to shear strain coupling. 48
2.23 Microstructured beam made of 50×8 non-centrosymmetric tetrachiral unit cells, under axial loading at the right end and clamped boundary condition at the left end. 49
2.24 Deformed shape of the beam with plotted distribution of the: (a) axial displacement, (b) vertical displacement. 49
2.25 Macrobeam made of tetrachiral unit cells under: (a) uniform axial stress, (b) pure bending moment 51
2.26 Deformed shape of the macro beam under: (a) uniform axial stress, (b) pure bending moment 51

3.1 Schematic diagram of the proposed methodology for micromorphic homogenization. . . . 56
3.2 (left) Composite unit, (right) the homogenized effective medium. 57
3.3 Composite unit cell with two constituents labelled (1) and (2). 58

3.4 Schematic diagram for the computation of the effective micromorphic moduli. 72
3.5 Centro-symmetric tetrachiral unit cell. 74
3.6 a) Full periodic network and b) homogenized representation of a tetra-chiral plate consisting of 12x15 unit cells. 74
3.7 Load-displacement responses of the tetra-chiral plate, under axial loading normalized with respect to $F_0 = 1$. 75
3.8 (a) Normalized displacement profiles u_2 along the horizontal center line of the plate, (b) Normalized displacement profiles u_1 along the vertical center line of the plate at prescribed displacement $U = 0.06l$. 76
3.9 (a) Normalized horizontal displacement contour u_1, (b) Normalized vertical displacement contour u_2 of the tetrachiral lattice structure and homogenized plate at prescribed displacement $U = 0.06l$. 76
3.10 Non-centrosymmetric fibrous composite unit cell. 77
3.11 Microscopic total deformation modes induced by the imposed: (a)E_{11}, (b)E_{22}, (c)E_{12}, (d)K_{112}, K_{121}, (e)K_{221}, K_{212}, (f) e_{11}, e_{22}, e_{12}, e_{21}, K_{111}, K_{122}, K_{211}, K_{222}. 78
3.12 Microscopic fluctuation deformation modes induced by the imposed micromorphic components: (a) e_{11}, (b) e_{22}, (c) e_{12}, (d) e_{21}, (e) K_{111}, (f) K_{222}, (g) K_{122}, (h) K_{211}. . . . 79
3.13 Non-centrosymmetric unit cell with indicated inclusion centerline. 79
3.14 Distribution of the fluctuating displacement under the following kinematic loadings: $E_{11} = 1$, (b) $K_{112} = 1$. 80
3.15 Variation of the effective moduli with the inclusion volume fraction. 82
3.16 Variation of the effective moduli with the ratio of inclusion to matrix Young's modulus. . 82
3.17 Unit cells including an increasing number of repetitions of the irreducible unit cell. 82
3.18 Variation of the effective moduli versus the number of irreducible unit cells, N. 83
3.19 Classification of micromorphic effective medium and its degenerate media arising from Table 3.4. 88

4.1 Timoshenko beam element coordinates and displacements 96
4.2 An infinitesimal element of the beam and applied forces and moments. 97
4.3 Beam element subjected to concentrated bending moments at the ends with general boundary conditions. 100
4.4 Comparison of dimensionless deflection of a fully clamped cantilever beam under a concentrated shear force. 109
4.5 Cantilever beam under a shear force at the tip 109
4.6 Tip deflection of a Fully clamped cantilever beam under a concentrated shear force: (a) tip deflection, (b) tip rotation. 111

4.7 Fully clamped cantilever beam under a concentrated shear force: (a) deflection at $L =$ 0.001 m, (b) rotation at $L = 0.001$ m. 112
4.8 Effect of the length scale parameter of a fully clamped cantilever beam under a concentrated shear force: (a) on the deflection, (b) on the microcurvature. $L = 0.001$ m 112
4.9 (a) Pure bending of a free-free beam with length L, (b) Pure bending of a fully clamped cantilever beam with length $L/2$. 113
4.10 Free-free beam under pure bending: (a) tip deflection, (b) rotation. 114
4.11 Partially clamped cantilever beam under a concentrated shear force: (a) tip deflection, (b) rotation. 115
4.12 Partially clamped cantilever beam with $L = 0.001$ m under a concentrated shear force: (a) deflection, (b) rotation. 116
4.13 Concentrated shear force at the free end of: (a) a fully/partially clamped cantilever beam, (b) a free-free beam. 117
4.14 Variations of the deflection percentage error versus the dimensionless length for: (a) an Epoxy beam with different boundary conditions, (b) a partially clamped cantilever beam made of different materials. 118

5.1 (left)Lattice material domain made of hexagon unit cell, (right) The homogeneous substitution medium (right) with domain $V(\boldsymbol{x})$ centered around point $\boldsymbol{x}$. 124
5.2 Schematic representation of periodic (a) Hexagonal ($\theta > 0$), (b) Re-entrant ($\theta < 0$), (c) Pantograph ($h = 0$), and (d) Rectangular $\theta = 0$ honeycombs; unit cell boundaries are indicated with dashed lines for each microarchitecture. 125
5.3 Beam element coordinates and displacements. 126
5.4 Effective lengths for the general periodic unit cell. 127
5.5 Contours of (a)$\mathrm{E}^*_{x_1}$, (b)ρ^*_f, versus θ and t/L; solid lines use L and h, and dotted lines use L_{eff} and h_{eff}. 128
5.6 (a) Generic Honeycomb lattice material, (b) periodicity vectors of unit cell, (c) unit cell with dependency groups of nodes, and (d) unit cell nodal DOFs. 131
5.7 Hexagon unit cell with faces (F^i), edges (E^i) and vertices (V^i) and their numbering. . . . 138
5.8 Schematic representation of different modes related to the effective Cauchy and Cosserat moduli for a hexagonal honeycomb $\theta = 30$. 139
5.9 Contours of the (a) $\mathrm{E}^*_{x_1}$, (b) $\mathrm{E}^*_{x_2}$, (c) $\nu^*_{x_2x_1}$, (d) $\nu^*_{x_1x_2}$, (e) $\mathrm{G}^*_{x_1x_2}$, (f) B^*_{123}, (g) R^*_{13}, (h) $l^*_{x_1}$, (i) $l^*_{x_2}$, (j) ρ^*_f versus θ and t/L; solid lines are results from continualization and dotted lines FE results. 141
5.10 Window of analysis comprising a unit cell with the side length: (a) ‘a’, (b) ‘2a’, (c) ‘3a’, (d) ‘4a’. 143

5.11 Variation of the effective moduli versus the window size number 'n':(a) Cauchy effective moduli (b) Micropolar effective modulus. 143
5.12 An infinitesimal element of the beam and applied forces and moments. 144
5.13 Architected Macro beam made of honeycomb unit cells with its geometrical descriptors. h^{UC} is the total height of the unit cell shown in the magnified part. 145
5.14 Variation of the Constant 'C' with the unit cell angular variable θ. 146
5.15 Representation of the homogenized area and height for (a) complete lattice, (b) cut edge lattice. 147
5.16 Variation of the normalized Cosserat bending moduli versus normalized height of the macro beam for a hexagonal unit cell of Table 5.5, based on fully resolved FE computations. . . 147
5.17 Architected macro beam comprising: (a) honeycomb unit cells and (b) the equivalent homogenized macro beam, under uniaxial (top view) and pure bending loads (bottom view).148
5.18 Contribution of the Cauchy and Cosserat bending moments in the pure bending response of the macro beam. 150
5.19 Vertical displacement contour of a cantilever (top) Hexagon lattice beam with 335×10 unit cells, (bottom) Homogeneous beam, under pure bending moment $M_{x_3} = 100$ N.mm. . 151

6.1 (a) Illustration of the transformation introduced in the present approach, defined by a mapping $\boldsymbol{\varphi}$ between the perfectly periodic domain $\tilde{\omega}$ (b) A quasi-periodic domain, (c) aiming at studying more complex special domains. 159
6.2 (left) Composite periodic unit cell of made of two elastic materials, (right)The homogeneous substitution medium. The inner material could be an inclusion or void in case of an architected material. Non-connected constituents can be envisaged. 163

7.1 (top and bottom left views) Initial periodic domain tessellated with regular hexagonal and hexachiral unit cells, (top and bottom right views) quasi-periodic circular macrodomain resulting from the conformal transformation of the periodic microstructures. 183
7.2 (left) Schematic representation of periodic material, (right top row) definition of micropoints within the physical and zoomed non-dimensional unit cells of the periodic, (right bottom row) quasi-periodic domains; The small parameter η is defined as the ratio of a unit cell size to a characteristic macroscopic dimension of the macrodomain. 189
7.3 Conformal mapping of a (left) tetrachiral periodic unit cell to a (right) quasi-periodic domain.193
7.4 Predicted tensile quasi-periodic rigidity versus the number of the unit cells in the circumferential direction. 194
7.5 Spatial variation of the tensile quasi-periodic modulus along a radius of the quasi-periodic domain for the case of the converged number of unit cells in the circumferential direction (moving from the external edge inwards). 195

7.6 Evaluation of the macroscopic and mesoscopic (unit cell based) mechanical properties based on a mapping to a periodic parent domain. The macroscopic moduli express as surface integrals over the external domain boundary due to vanishing internal surface contributions.197
7.7 Conformal mapping of a (left) hexachiral periodic unit cell to a (right) quasi-periodic domain.198
7.8 Variation of the quasi-periodic compressibility modulus versus the number of radial unit cells of the hexachiral lattice computed by FE simulations and theory, for varying number of angular unit cells. Here, k=50. 198
R.1 Diagramme de performance d'Ashby en 3D des matériaux utilisés en ingénierie montrant la relation entre la résistance, le module et la densité pour différentes classes de matériaux [1].206
R.2 Exemples de matériaux cellulaires : (A) mousse à cellules fermées, (B) mousse à cellules ouvertes, (C) matériau cellulaire ordinaire (cellule unitaire BCC à corps cubique centré) [2].206
R.3 Architectures 2D avec un coefficient de Poisson contrôlé : (a, b) Hexagonale, étoile rentrante, (c, d) rectangulaire, semi-entrante, (e, f, g) diamant, kagome, triangulaire, treillis chiraux (diamant chiral (h), tétrachiral (i), hexachiral (j)) [3]. 207
R.4 Evaluation of the macroscopic and mesoscopic (unit cell based) mechanical properties based on a mapping to a periodic parent domain. The macroscopic moduli express as surface integrals over the external domain boundary due to vanishing internal surface contributions.216

H.1 Composite unit cell and the associated periodicity vectors Y_1,Y_2 in a 2D situation. 248

L.1 A generic unit cell with its periodic displacement boundary conditions. 261
L.2 Generic unit cell with its periodic equilibrium boundary conditions. 261

M.1 Hexagon unit cell and the associated periodicity vectors Y_1,Y_2,Y_3 in a 2D situation. . . . 264

List of tables

2.1 Values of the geometrical and mechanical parameters of the tetrachiral and anti-tetrachiral lattices. . . . 32
2.2 Boundary constraint equations and corresponding classical rigidity components. . . . 35
2.3 Mechanical properties of the Fiber and Matrix within the composite unit cell of Fig. 2.11 [7]. 38
2.4 Comparison between the macroscopic and microscopic energies and contribution of the fluctuation energy to the total deformation energy. . . . 42
2.5 Values of the geometrical and mechanical parameters of the tetrachiral lattice. . . . 50
2.6 Effective Cauchy compliance components and Cosserat effective moduli. . . . 51

3.1 Values of the geometrical and mechanical parameters of the tetrachiral lattice. . . . 73
3.2 Mechanical properties of Fiber and Matrix. . . . 77
3.3 Elastic and Shear Moduli for various Materials [7]. . . . 81
3.4 Micromorphic's degenerated generalized continua and their kinematic variables. . . . 87

4.1 Constitutive law and assumptions of classical and couple stress continuum theories. . . . 94
4.2 Error of the tip deflection: fully clamped cantilever beam under a concentrated shear force at free end. . . . 111
4.3 Error of the tip deflection: fully clamped cantilever beam under pure bending at free end. 114
4.4 Error of the tip deflection: partially clamped cantilever beam under a concentrated shear force at free end. . . . 115
4.5 Elastic and Shear Moduli for various Materials [7]. . . . 117

5.1 Dependency relations of the unit cell nodes. . . . 132
5.2 Closed-from expressions for effective properties of general hexagonal lattices. . . . 135
5.3 Boundary constraint equations for faces, edges, and vertices. . . . 138
5.4 Kinematic loadings corresponding to the Cauchy and Cosserat rigidity components. . . . 138
5.5 Values of the geometrical and mechanical parameters of the hexagonal lattice. . . . 142
5.6 Effect of the absolute unit cell size in a macro beams comprising 440×13 unit cells, with a ratio $L^b/H^b = 20$. Error is the difference between the macro beam measured values of $\mathrm{E}^*_{x_1}$ and $l^*_{x_1}$, and those calculated by unit cell homogenization approach. . . . 148
5.7 Effect of the unit cell geometrical parameters in the response of the macro beam; Cauchy and Cosserat represent their percentage contributions, respectively. . . . 149

5.8 Effective Cauchy compliance components and Cosserat effective moduli. Error is the difference between the macro beam measured values of $\mathrm{E}^*_{x_1}$ and $l^*_{x_1}$, and those calculated by unit cell homogenization approach; Cauchy and Cosserat represent their percentage contributions, respectively. 150

5.9 Effective Cauchy compliance components and Cosserat effective moduli for a macro beam with cut edges unit cells. Error is the difference between the macro beam measured values of $\mathrm{E}^*_{x_1}$ and $l^*_{x_1}$, and those calculated by unit cell homogenization approach; Cauchy and Cosserat represent their percentage contributions, respectively. 151

6.1 Summary of the formulated quasi-periodic homogenization theories 172

Chapter 1

General introduction

1.1 Architected materials as a new paradigm in material science

The history of humanity is marked with the discovery of new materials and manufacturing techniques having tangible societal impacts, as witnessed by the prehistory of humankind, witnessing successive periods in its evolution, coined 'stone age', 'bronze age', and 'steel age'. In the recent period (late twentieth century), major technological breakthroughs like additive manufacturing techniques and manipulation of matter at the same scale of atoms have opened up the possibility to design and fabricate new classes of materials with unprecedented mechanical, and beyond, multiphysical properties. The search of engineers in the field of materials science to improve materials properties in order to meet the challenging demands of the industry has moved to a new paradigm, in which the inner material's architecture appears as a new degree of freedom (DOF in short) (beyond chemical composition) in material design to control and improve the material properties. The wording architected materials appeared in the literature in a review paper by [8] to link the methods of topology optimization used to design light, highly performing, and elegant (like the Eiffel tower) materials with structural engineering. As it is defined, an architectured (the wording architected is also of use in the literature) material combines several simpler base materials in a synergetic way - and sometimes with a hierarchy of imbricated scales, like the Eiffel tower, as mentioned in [9–11]. This topology organization has the consequence that new performances not reachable by any of the individual constituents emerge to reach given requirements set by the designer. The large variability of possible geometries of topologies of the elementary building blocks defining the inner architecture of the material offers a tremendous richness of the materials design space. Materials performances condensed into the visual Ashby diagrams, as illustrated in Fig. R.1 for modulus, strength, and density in a 3D representation.

Architected materials designed for engineering applications most often are characterized by a unit cell, defined as the elementary 'brick' of matter from which the entire structure is fabricated using the convenient (from the point of view of fabrication, but also of modeling) notion of periodicity; few

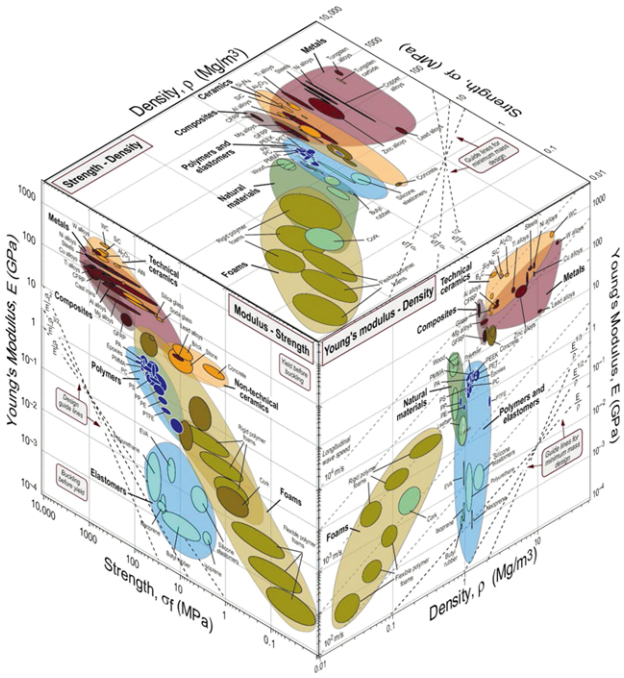

Figure 1.1 3D Ashby performance diagram of engineering materials showing the relation between strength, modulus, and density for different classes of materials [1].

examples of cellular materials with such a regular architecture are shown in Fig. R.2. Although the actual microstructure is not precisely periodic, its representation as a periodic medium is often a good approximation.

The architecture of the material can be realized from the atomic or molecular level up to the structural (macroscopic) dimensions. It is nowadays common practice to integrate materials design in structural mechanics from the outset. Despite its powerfulness, this methodology borrows essentially from heuristics and relies on the experience and intuition of the designer; it, however, lacks a more rigorous rationale methodology for defining suitable (even optimal) topologies for a given application or set of mechanical requirements. The wording *metamaterials* has been created to designate a new class of materials amongst architected materials emerging in the last decades, endowed with mechanical static or dynamic attributes not commonly encountered in natural materials that have deserved the specific coinage metamaterials [3]. The term denotes the ability to adjust the effective material properties (at the unit cell level of an effective substitution continuum) by modifying its inner topology rather than changing the chemical composition to modify the base material properties.

This technological advancement has become feasible mainly due to the rapid development and advances in additive manufacturing techniques. Amongst the mechanical properties, Poisson's ratio plays a privileged role as it is sometimes considered a metric of material properties. *Auxetic materials* with a negative Poisson's ratio have exceptional static and dynamical properties, like high resistance to shock and impact, mitigation of vibrations and sound waves. A portfolio of periodic architected materials with positive or negative (auxetics) Poisson's ratio is shown in Fig. R.3.

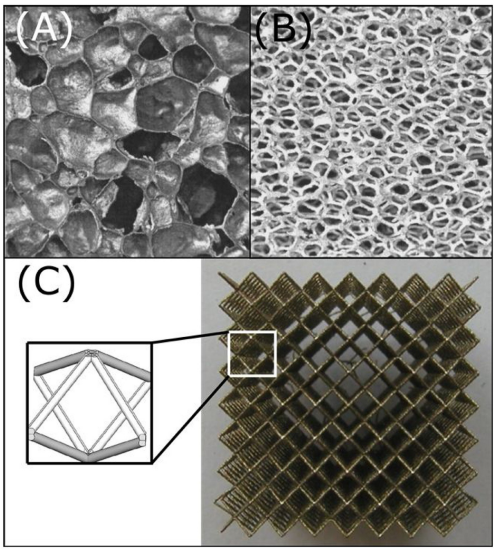

Figure 1.2 Examples of cellular materials: (A) closed cell foam, (B) open cell foam, (C) regular cellular material (body cubic centered BCC unit cell) [2].

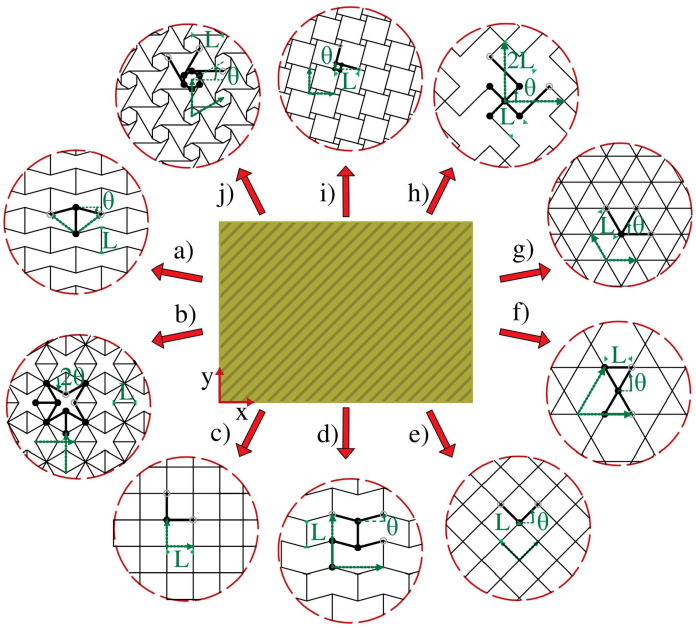

Figure 1.3 2D architectures with controlled Poisson's ratio: (a, b) Hexagonal, star-shaped re-entrant, (c, d) rectangular, semi-entrant, (e, f, g) diamond, kagome, triangular-saped, chiral lattices (chiral diamond (h), tetrachiral (i), hexachiral (j)) [3].

1.2 Effective models for architected media

In order to evaluate the benefit of designing complex topologies of architected materials, material scientists and engineers in search of optimized performances must rely on mathematical models, modeling tools, and computational methods to evaluate the effective properties at the unit cell level (or apparent properties at structural level) and relate them to the inner architecture and properties of the different base materials within the unit cell.

The prediction of the overall mechanical response of microstructured materials like *architected materials* and *cellular materials* cannot be achieved by performing direct numerical simulations, whereby all microstructural details are fully resolved using a sufficiently fine mesh resolution. However, such numerical analyses usually have a substantial computational cost, making them unfeasible for typical engineering problems. Moreover, the experimental determination of the mechanical properties of such structures is delicate since the overall anisotropy has to be accounted for. In addition, the lack of a clear scale separation may require using *enriched continuum* theories that include many more constitutive parameters than Cauchy elasticity theory. For these reasons, it is more convenient to perform *homogenization* towards effective microstructure models in a first step that can be used to perform computations at the macrostructural level.

Composites and architectured materials are typical classes of materials widely used in engineering due to their high mechanical performances (like strength, energy absorption capacity, thermal and acoustic insulation properties) at low weight in a wide diversity of applications. Their excellent properties are mainly due to the possibility of adjusting the architecture and microstructural properties of the underlying microstructure to reach targeted properties at the mesoscopic or macroscopic scales. The full exploitation of the potential of these materials requires a clear understanding and prediction of their mechanical response at the level of a unit cell, incorporating the available microstructural information. The development of predictive micromechanical schemes to understand the impact of the existing microstructure on the mechanical response at both mesoscopic and macroscopic levels is essential to bridge the scales and relate the equivalent properties to both the geometrical properties and mechanical parameters of the structure.

1.3 A survey of homogenization methods in linear elasticity

Homogenization theory has become, over the last decades, a fundamental tool to analyze the overall behavior of highly heterogeneous media such as composites, in which several associate constituents usually have a strong contrast of their properties. Numerous methods of homogenization rely on the determination of a representative volume element (RVE in short), which implicitly assumes that the structure of the RVE is found almost everywhere in the structure: it is, in fact, a disguised pseudo-periodicity. Periodic homogenization plays a privileged role as a theory to account for the overall homogenized behavior.

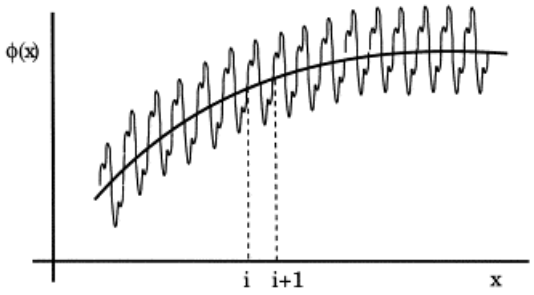

Figure 1.4 Highly oscillating functions [4]. Fast oscillations occur within the repetitive unit cell whereas slow variations of the average occur at the macroscale

Moreover, this hypothesis makes it possible to obtain exact mathematical results of the homogenized behavior. Historically, Sanchez-Palencia [12] was the first to develop these techniques based mainly on multi-scale asymptotic developments. The mathematician J. L. Lions and his collaborators [13] developed these techniques from a more mathematical point of view. Nevertheless, in periodic homogenization, most of the most fruitful ideas, close to applications, must be attached to the name of L. Tartar. This contribution on the subject traces the history of homogenization and perfectly situates the significant contribution of its author in this field.

Homogenization is a mathematical theory to study partial differential equations (PDEs in short) with rapidly oscillating coefficients at the microscale of the individual phases of heterogeneous composites, which are replaced at the macrolevel with PDEs having slow-varying coefficients (Fig. 1.4); it aims at relating the physical behavior of heterogeneous material - and especially composites - at the macroscopic level from the behavior occurring at the microscopic level.

The *mathematical theory of homogenization* witnessed a rapid expansion from the sixties, with the pioneering contributions of Marchenko and Khruslov [14] devoted to non-periodical structured domains with fine-grained boundaries. In the 1970s, homogenization became a specific research area in applied mathematics [13]; [15]; [16]; [17], and several methods were introduced, like the method of asymptotic expansion, G-convergence, H-convergence, Γ-convergence, two-scale convergence, with applications in composite materials [18, 19] or in finding the macroscopic limit of microscopic systems.

The *asymptotic expansion method* was historically developed by both engineers and mechanical researchers [20] to treat problems of PDE with rapidly varying coefficients [12, 13, 21–23]. The G-convergence introduced by Spagnolo [24] for second-order elliptic and parabolic operators is an operator-like convergence for self-adjoint BVPs involving periodic or non-periodic coefficients; it was extended by Tartar and Murat [25–27] to non-symmetric boundary value problems (BVPs in short) under the coinage H-convergence. Note that the periodicity assumption is not required for both G and H convergence theories. The Γ-convergence introduced by Giorgi [28] as an analog of G-convergence for the convergence properties of functional. The two-scales convergence was introduced by Nguetseng [29] – see also Allaire [30] for an extension - for the analysis of BVPs with fast varying coefficients, and moreover extended to stochastic two-scale convergence in [29, 31–34]. The alternative unfolding method was

developed to homogenize periodic composites [35,36]. The method of oscillating functions, mainly applied to multi-layer composites, leads to analytic expressions of the homogeneous behavior [37], and it was extended to strain gradient homogenization of linear elastic materials with individual constituents obeying a strain gradient behavior [38]. We refer the reader to general references in the field of mathematical homogenization, providing an excellent overview and details of these methods [12, 17, 29, 30, 39–49].

The specific case of *periodic microstructures* is of particular interest due to the progress of engineering and manufacturing in composites having a regular microstructure. It was initiated in the works of [12,49]; more recently, several authors analyzed the influence of higher-order terms in the asymptotic expansions of the fields on the macroscopic behavior of linear elastic composites, see [50–53],.

Experimental or multiscale analyses can be carried out to achieve the structural material properties at an effective substitution medium level. However, performing fully resolved simulations may be quite computationally expensive, mainly when relying on full-scale FE models [54]. Multiscale homogenization methods can efficiently link the heterogeneous material properties and effective continuum-based properties [55, 56]. Such methods stem essentially from asymptotic expansion techniques to analyze the mechanical response at the level of the repetitive unit cell, which is representative of the entire lattice [57].

1.4 Discrete homogenization as a reduced modeling approach

A distinction can be made between the *continuous homogenization methods* traditionally employed for composite materials and the so-called *discrete homogenization* that employs reduced, discrete type models for the structural elements defining the unit cell as either a collection of bars or beams. The difference between continuous and discrete homogenization lies in the spatial representation of the initial geometry, either as a continuous collection of material points in 2D or 3D, as a reduced representation having only a finite number of spatial descriptors. Fig. 1.5 shows homogenization of architectured media using continuous or discrete modelling. both representations aim to reach a continuous substitutions medium.

Discrete homogenization is adequate for low-density lattice materials and architected materials since their inner structural elements can be naturally modeled as beams or rods at an affordable computational cost compared to continuous homogenization schemes.

These discrete modeling approaches have the advantage of considering a finite number of DOFs at the microscale and can sometimes provide closed-form expressions for the effective moduli [3, 58]. The mechanics of lattice materials encompasses static aspects related to stiffness and strength [59] and dynamic features like dispersive wave propagation [52, 60] that can be captured through equivalent continuum models.

Amongst the class of *discrete homogenization methods*, the so-called *continualization methods* introduced in [61] deserved some special interest in the literature since then. *Continualization methods of periodic lattices*, developed to compute the static and dynamic effective properties at a continuum

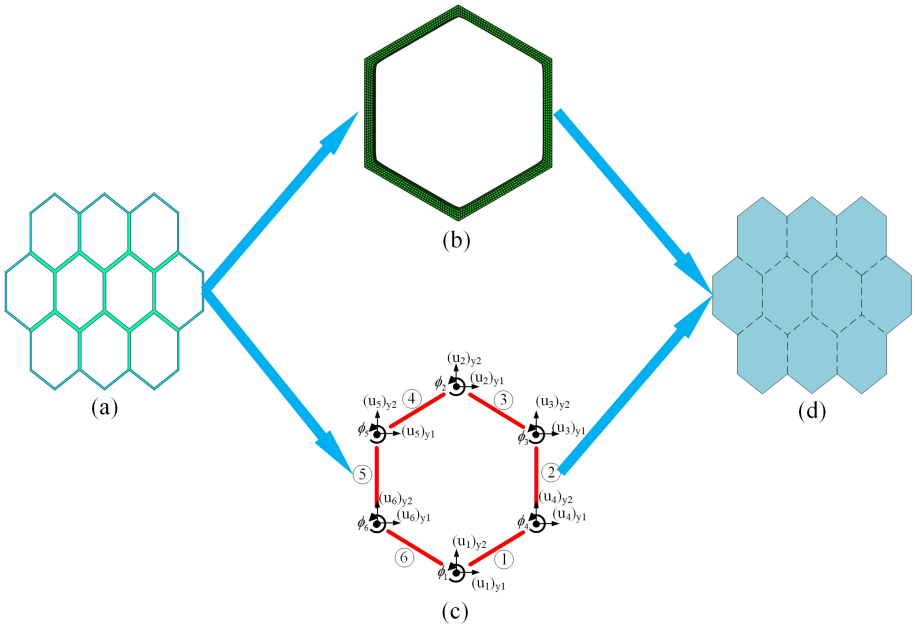

Figure 1.5 (a) The material domain architectured with periodic hexagonal unit cells, (d) the homogeneous substitution medium. The initial geometry can be modeled as: (b) a continuum body or, (c) using a reduced model with a discrete set of degrees of freedom.

level [62], rely on the idea of replacing the discrete equations of motion with continuum type differential equations. These methods are based on the following two main steps: (i) replacing the discrete kinematic DOFs by field variables having a continuous variation in space and time, and (ii) expressing the microscopic DOFs within neighboring unit cells using a Taylor series expansion versus the selected continuous DOFs. The methodology is described in more detail in [63]. A Lagrangian formulation of the equations of motion may be adopted at the microlevel as an alternative to the local strong form description of the lattice statics or dynamics. Continualization methods relying on a Lagrangian formulation of the lattice mechanics via truncated Taylor series expansion emerged in the literature about twenty years ago [64–66]. Truncating the Taylor series to a first-order leads to an effective Cauchy continuum, the simplest reachable effective medium.

1.5 Enriched constitutive models for heterogeneous materials

Classical continuum mechanics relies on the sole first gradient of the displacement field for measuring the deformations of the body, and all higher-order displacement gradients are neglected. Such a kinematic framework turns out not to be rich enough to describe a variety of important mechanical and physical phenomena [67]. Significantly, the classical continuum mechanics prove to be intrinsically size-independent, whereas non-local behaviors may arise due to the discrete nature of materials at a sufficiently small scale, as reported in [68]. First-order Cauchy-based theories are valid under a strict condition of scale separation, but they fail for small structural sizes since the sizes of the micro and

macro structures become comparable (like in MEMS). As a particular case, when the wavelength of the loading becomes comparable to the size of the underlying microstructure, or when localization of the deformation within narrow bands occurs caused by strain softening. The width of these bands depends on microstructural length scales like voids of grains spacing, the size and distance between internal defects. since classical continuum theories are devoid of internal length scales, they cannot describe such localization phenomena adequately. Moreover, finite element (FE in short) simulations usually exhibit a spurious mesh dependency and are thus unable to resolve the width of the localization bands correctly.

1.5.1 Phenomenological versus micromechanical formulations of enriched constitutive laws

The writing and identification of enriched constitutive models for microstructured solid materials can follow two different approaches, namely, a *phenomenological approach* and a *micromechanically inspired strategy*.

Phenomenology relies on a single-scale description of the material, wherein a constitutive law is postulated at the macrolevel, and its coefficients are identified from either experiments or simulations. Enriched constitutive models defined this way include new parameters like internal lengths (Cauchy mechanics is devoid of such internal lengths). The need for enriched constitutive law may arise due to the lack of representativeness (in a statistical sense) of the chosen volume element so that individual carriers of the microstructure will be excited and averaging can not be done, or due to topological effects generating internal deformation modes not captured by a first gradient elastic theory. By moving to the micro or even nanoscale, surface effects neglected in Cauchy elasticity become dominant over volumetric ones so that new behaviors emerge at these scales.

The drawback of this method is its lack of predictive nature since the identification procedure needs to be repeated for each new material or new loading conditions. The material is viewed as a kind of 'black box' at each point, and the constitutive law includes adjustable parameters reflecting its response for specific loading conditions. Going into more details into the microstructural origin of these new phenomena not covered by Cauchy mechanics is the object of micromechanics.

In contrast, *micromechanical approaches* provide a more refined class of methods to identify material's constitutive laws since they directly start from a microscopic scale description and aim to incorporate the microstructural information into the constitutive law by some upscaling method. Due to this, they have a predictive capability regarding the topology, mechanical (or physical) properties of the individual constituents, and the nature of the applied loading. Micromechanical models quantitatively aim to understand the impact of microstructural parameters of geometrical or mechanical nature within composite materials on macro-scale characteristics witness significant developments due to the need for efficient predictive computational methods of their performances in both the static and dynamic regimes. In the case of periodic composites, the construction of equivalent substitution media at the intermediate

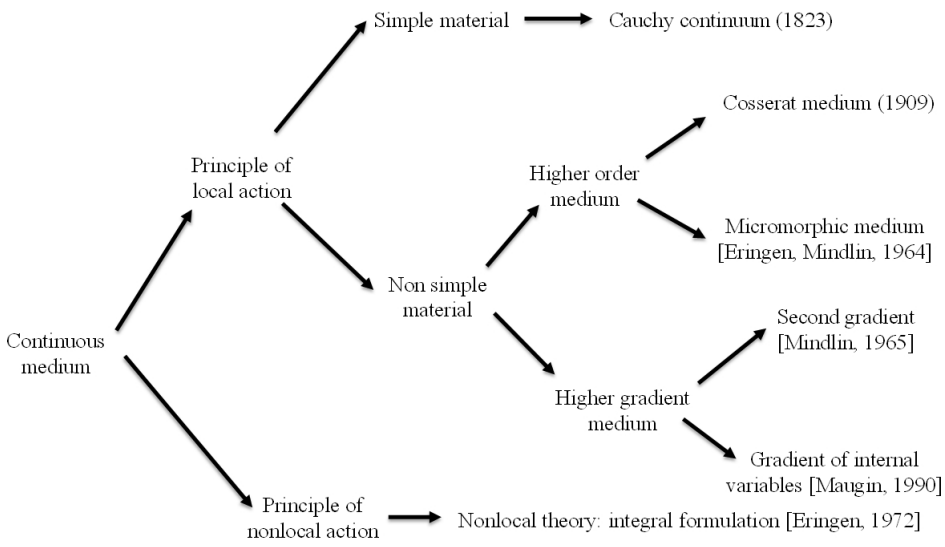

Figure 1.6 Classification of generalized continua into higher order and higher-grade media [5].

scale of a repetitive unit cell is a classical approach in the literature, providing a good compromise between accuracy and numerical efficiency because of performing structural computations. Thereby, the effective properties computed from suitable homogenization schemes reflect the influence of the composite constituents' geometrical and mechanical microstructural parameters. It is well recognized that classical homogenization relies on a precise scale separation assumption, bearing the name Hill-Mandel macro-homogeneity condition [69–71].

Enriched continuum theories are required in such situations to capture the effect of spatially rapid fluctuations at the mesoscopic and macroscopic levels. Homogenization towards generalized continua aims to remedy these limitations and extend the range of validity of the continuum approach beyond the strict assumption of the scale separation [72, 73]. Enhanced continuum formulations involve a relaxation of the local action hypothesis and introduce spatial interactions and internal material-dependent length scales to account for the influence of neighboring points in the formulation of constitutive equations. The generalization of the classical definition of a continuum can follow two different strategies, based on the classification in two main groups, namely higher-order and higher-gradient continua, pictured in Fig. 1.6. *Higher-order continua* incorporate additional degrees of freedom, like the *Cosserat medium* promoted by the Cosserat brothers [74] and the *micromorphic medium* [72, 73, 75].

In *Cosserat elasticity* [74], local rotations are added as degrees of freedom. The *micropolar theory* assumes that interactions between material points through a surface element occur with a force vector and a moment vector. This theory establishes the 'force-stress' tensor and the 'couple-stress' tensor, respectively, as force per unit area and moment per unit area. The balance of momentum shows that the stress tensor in the micropolar media is no longer symmetrical as in the classical theory due to the unbalance of the local moments generated by the underlying microstructure. The non-symmetric stress tensor can be decomposed into symmetric and skew-symmetric parts; the symmetric part causes the

deformation of the macro-element, and its skew-symmetric part contributes to the rigid rotation of the microstructure concerning the material. A more specific Cosserat theory is the *couple-stress theory*, with the coincidence of the microrotation and macrorotation [76]. A vast list of references to Cosserat and couple stress elasticity models is available in review articles [77–80].

Whereas, in higher-grade continua, higher gradients of the primary kinematic variable (displacement, strain) or internal variables (like damage, plasticity) are included as additional variables in the formulation [50, 51, 53, 81–84]. Amongst the possible a priori choices of the effective substitution medium mentioned previously (Cosserat, micromorphic, strain-gradient, etc), the strain gradient elastic continuum introduced in Mindlin [72] and Mindlin and Eshel [85] offer several advantages as underlined in [86], since it is rich enough to represent emergent properties without having recourse to the micromorphic medium that has many more inherent parameters [87] and such a model can be constructed using asymptotic homogenization [51, 88–90]. A large body of works has been devoted to strain gradient homogenization in the literature for more than 40 years [84, 88, 90–98], for both composites with periodic or random microstructures [99], auxetic architectured materials [100] or random fibrous media [101].

Following Boutin [51] and Smyshlyaev and Cherednichenko [53], who further proved the convergence of the asymptotic expansion of the solution, Tran et al. [90] proposed a more systematic method to identify the strain gradient elastic moduli, also relying on asymptotic expansions of the fields. The most advanced generalized continuum theory is the micromorphic theory, advanced by [72, 73, 75, 102–105], constitutes the most general enriched model incorporating a full second-order microdeformation tensor attached to each material point. Some authors [94, 102, 105] extended micropolar frameworks by considering a full second-rank non-symmetric tensor as an additional variable to capture the underlying microstructural deformation mechanisms. It encompasses both higher gradient and higher-order continuum theories, obtained as degenerated formulations by imposing constraints on the microdeformation [104, 106, 107], see [107, 108] for a review and a comprehensive classification of these theories. Micromorphic continua have found successful applications to describe the behavior of composite materials [109, 110], architectured materials with chirality [111], elastomeric metamaterials [112], porous media [113], and also phenomena like material growth [114], anisotropic ductile damage [115], crystal plasticity [116, 117], non-affine elastic reorientation of fibers in soft fibrous reinforced materials [118], wave propagation [119, 120], or pattern transformation of mechanical metamaterials [112, 121, 122].

1.6 Limitations of the existing homogenization methods

Despite the success of generalized continuum models to capture the salient specific features of microstructures prone to such effects, they still face some limitations in their capability to predict the supposedly intrinsic mechanical properties of microstructures accurately.

1.6.1 Computational methods of higher order homogenized properties

Pure asymptotic expansion methods [51, 53] are sometimes combined with a fast Fourier transform method to compute the effective mechanical properties [90, 123]. Two popular methods employed in the context of second-order homogenization of heterogeneous microstructures to capture its higher-order effects are asymptotic expansion methods and more heuristic approaches based on the application of enriched kinematic boundary conditions of polynomial types [99,101] aiming to capture the search higher-order effective continuum. A pretty common strategy following this last method is the recourse to quadratic boundary conditions applied over the unit cell, as proposed in [81, 92–94, 124–127]. Despite its appealing simplicity as a natural extension of the classical homogenization (with classical uniform kinematic boundary conditions) [128, 129], this method, however, suffers from two significant flaws, since the effective strain gradient moduli remain non-zero for homogeneous materials or under conditions of scale separation [105], thus conflicting with the local Cauchy type response of the individual constituents. Moreover, they do not vanish in conditions of perfect scale separation or for a purely homogeneous material [105]. Furthermore, the effective strain gradient moduli are not convergent with the RVE size [81, 123]. Corrections to these spurious effects were recently proposed [81, 86]. The last authors added a body force field to the quadratic boundary conditions and corrected the localization tensor.

1.6.2 Emergence of new degrees of freedom by upscaling

Cosserat models have been derived from an asymptotic homogenization of the microscopic BVP of Cosserat elasticity in [105,130,131] and micromorphic substitution models for a mixture of micromorphic continua established in Forest [104]. The definition of a hierarchy of characteristic lengths allows classification and ranking of the derived effective medium, which can be Cauchy, micropolar, microstrain, or full micromorphic type according to the considered scheme of hypothesis. The difficulty of the emergence of a higher-order effective medium like Cosserat or micromorphic effective continuum arises when the medium is of Cauchy type at the microscopic level of the individual constituents since the effective constitutive law at the macro level shall involve new micromorphic degrees of freedom that are not present at the microscale. The construction of higher-order generalized continua by upscaling the microstructure behavior is one challenging issue we plan to tackle in the thesis.

1.6.3 Edge and Size effects for lattice materials

The significant effect of reducing the external sample size to the order of the *characteristic length scale* of the material's microstructure (or even below) on material effective properties – up to strength and resistance to failure – manifests itself via the activation of new deformation mechanisms of the underlying microstructure and arising surface and or interface effects in the submicronic range (at the nanometric scale). Most materials exhibit such size effects due to a too-small volume element for averaging towards a classical continuum to make sense so that individual carriers of the microstructure become individually

excited and new behaviors emerge. These size effects affect a wide range of mechanical attributes, from static mechanical properties (elastic and plastic properties) to dynamical properties condensed into the wave dispersion diagrams (partial full-band gaps may appear). Reducing the size may lead to more robust materials (like monocrystalline materials, ceramics, composites) or weaker materials (nanocrystalline metals). The design of architected materials at the nanoscale enables decoupling of co-dependent properties like strength and weight via the control of the inner architectured, thereby leaving the designer with the capacity to push the performance envelope of existing materials.

At a more macroscopic scale, some experimental results on the cellular solids revealed the size effect due to the relative size of the specimen to the unit cell size [132–134]. It is nevertheless known that classical Cauchy type effective models are not able to capture effects resulting from these microstructural length scales of materials [72, 135–139]. Size effects in lattice materials are usually classified into two main types. The first effect is due to the edge of the macrodomain, which is crossed by a truncated cell located close to the surface of the specimen [134, 140]. Depending on the specific arrangement of the lattice close to the boundary, hardening or softening effects can be appeared [139]. The second size effect, called the micropolar effect, reflects the inability of a classical continuum theory to describe some macroscopic properties like the flexural rigidity when the size of the unit cell of the lattice material is not small enough compared to the structural sample size [137]. These drawbacks of classical homogenization methods can be bypassed by recoursing to enriched effective continua like generalized continua that include higher gradients of the fields like displacement or strain [139] and additional degrees of freedom like rotation. In this last class of approaches, a micro deformation (in micromorphic theories) or microrotation (in micropolar theories) is incorporated as a different kinematic descriptor into the model. The homogenized continuum in the context of micropolar can be either derived from the discrete asymptotic homogenization of lattice materials in the linear [58] and nonlinear [141, 142] regimes, or the continuous higher order homogenization [137]. Gradient-enriched theories of architected materials emerged following this methodology [95,135,143,144] to model their static elastic response. The enhanced continualization method considers a Taylor series expansion of the discrete DOFs so that higher gradients of the continuous kinematic variables will emerge at the macroscale effective higher-order continuum. Effective nonlocal media have been formulated for lattice materials based on an enhanced continualization method [62].

Edge effects arise from truncation of the unit cell edges (these stress-free cut edges do not contribute to the overall mechanical response) crossing the external domain boundary (Fig. 1.7).

Some authors [139, 145] introduce softening effects associated with a negative higher-order rigidity to account for edge effects (a negative higher-order stiffness corrects Cauchy contribution to the overall beam response). Experimental results with bending tests [133] show a significant increase of the bending rigidity when the beam thickness is reduced, the departure from the conventional bending solution arising below a thickness of 80 µm. This effect is attributed in [133] to the decisive importance of strain gradient effects for the selected beam dimensions. This short literature overview reveals differences in both the

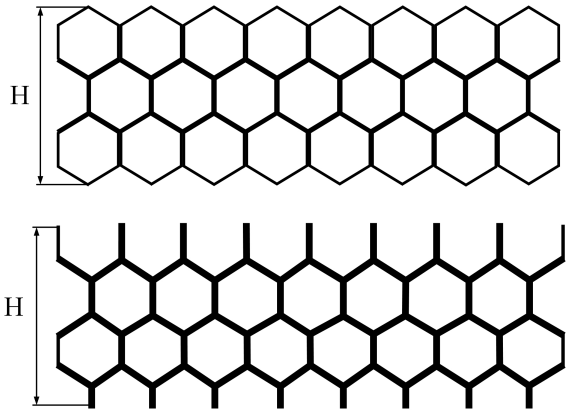

Figure 1.7 (top) Complete lattice , (bottom) Cut edge lattice.

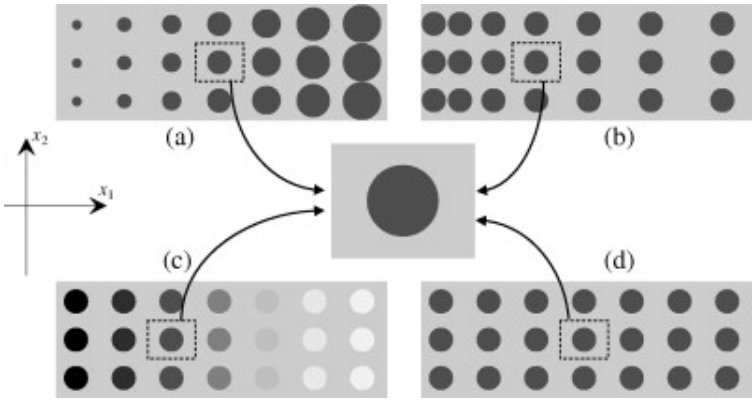

Figure 1.8 Quasi-periodic composites with quasi-periodic microstructure: (a) varying inclusion size, (b) inclusion spacing, (c) inclusion material, All quasi-periodic domains can be mapped to the same periodic unit cell of a parent periodic composite [6].

source, or such arising effects, and the conclusions reached by the panel of authors, sometimes with opposite interpretations.

1.6.4 Lack of strict periodicity: quasi-periodic homogenization

In contrast to periodic composite materials, quasi-periodic composites have a unit cell that does no repeat exactly periodically throughout the structure but it gradually changes along one or several periodicity directions, called grading directions. This feature has given rise to the class of functionally graded materials (FGM in short), characterized by a spatial variation of the geometry (and sometimes of the material properties) of the underlying microstructure within the unit cell, as illustrated in Fig. 1.9 for the case of conformal transformations, and in Fig. 1.8 for inclusion-based composites.

The spatial variation may occur in a single direction (like in the case of stratified materials) discretely or continuously. Engineering applications of FGMs involving thermal or mechanical properties with targeted spatial gradients are, for instance, thermal barrier coatings or contact surfaces [146]. Classical homogenization methods become inapplicable to FGM in situations where the grading is too fast

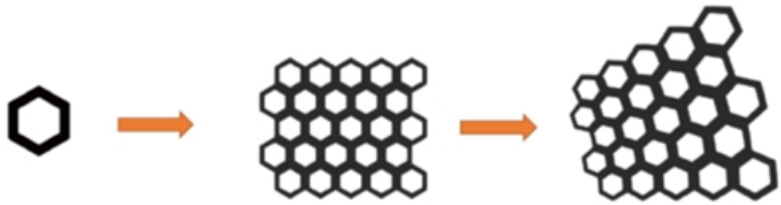

Figure 1.9 Quasi-periodic microstructures generated by conformal mappings of periodic ones.(left): Periodic hexagonal unit cell - (middle): Periodic domain – (right): Quasi-periodic domain.

compared to the size of heterogeneities present within the composite, prohibiting the definition of a statistically homogeneous RVE. In that case, the grading of the geometry cannot be neglected at the micro-level, and any RVE is graded at the microscopic level. When the composite has a smoothly varying in space unit cell, the grading within neighboring unit cells can be neglected, so a given unit cell does not perceive those neighboring ones have a different microstructure. This feature has the consequence that the homogenized behavior can be considered locally without accounting for differences in the microgeometry of successive unit cells. The grading is only accounted for at the macro level because the homogenized material properties vary from one unit cell to another one in the considered macrodomain. One can, in such situations, model the initially heterogeneous structure as a graded macroscopic material based on a field of homogenized properties experiencing a (slow) variation at the macroscale. For instance, layered materials with a graded microstructure may be approximated by an equivalent FGM with continuously varying properties at the macroscale [146–148], replacing the unit cell with a homogeneous material of Cauchy type (the behavior remains purely local in space) with macroscopically varying properties (but ignoring the variation of microstructure at the microlevel).

In opposite and more complex situations of too fast grading across the unit cells, the variation of unit cell geometry has to be considered at the microscale. Thus one expects that higher-order terms will appear when performing the asymptotic homogenization. Due to this microscopic variability, the overall effective behavior of the composite may cease to be purely local, and nonlocal mechanical behaviors may appear in proportion to the rate of grading. As mentioned in [6], classical homogenization methods become inapplicable to FGM since the minimum size of the RVE is larger than the size of statistically homogeneous RVE, thus requiring to take into account the grading within the RVE, which is also graded. Minimal effort has been devoted in the literature to the homogenization of quasi-periodic media, especially considering the higher-order terms in asymptotic expansion methods. First-order homogenization of quasi-periodic structures has been studied in [149]. In the field of dynamics, [150, 151] performed a non-periodic homogenization of the wave equation for seismic applications, obtaining, however, an incomplete higher-order solution. In [152], the authors develop a second gradient model for composites experiencing a gradation of their material properties but devoid of variation of its geometry. The authors combine asymptotic expansions up to second order with a variational approach to derive the higher-order macroscopic energy, assuming that the properties within the unit cell also depend on the position of the

cell within the composite. The resulting energy depends on the strain gradient as a new kinematic variable and a characteristic microstructure parameter gradient. In contrast to most homogenization methods for FGM, which account for the grading only at the macrolevel by replacing the effective homogeneous properties by a field of material properties varying at the macroscale, the work of [6] also accounts for the grading at the micro-level through the development of a second gradient effective constitutive law.

1.7 Analyzed scientific issues and methodology

The elaboration of enriched constitutive models of solids with a microstructure – and significantly architected media – requires tackling several scientific issues mentioned above. In response to these scientific issues, we bring in this thesis the following novel aspects:

- A novel homogenization methodology based on variational principles is proposed for evaluating effective size-independent moduli of heterogeneous materials in the small strains range; in essence, a general homogenization strategy for heterogeneous materials towards enriched media is developed.
- In substance, a unified variational formulation articulated with the extended Hill lemma is formulated for the determination of the effective classical and higher gradient moduli.
- A constructive proof of Hill macrohomogeneity condition for higher-order and higher grade continua is formulated, highlighting the new emergent kinematic and static measures.
- The coupling moduli of strain gradient, Chiral Cosserat, and micromorphic substitution continua are computed for non-centrosymmetric microstructures.
- The correction factors of size effects and translation of the unit cell are computed, resulting in higher order moduli that are intrinsic to the microstructure.
- A novel discrete homogenization method of periodic lattice materials is proposed to efficiently handle the computation of intrinsic higher-order properties at a repetitive unit cell level.
- The size and edge effects arising for domains tessellated with a finite number of unit cells are analyzed with a new look to set new size-independent apparent elastic moduli in the framework of Cosserat mechanics.
- A new homogenization framework of quasi-periodic microstructures is established, with particular consideration of conformal transformations.

1.8 Thesis outline

The manuscript is organized into three main parts as follows. Architected materials can be modeled in two ways, either borrowing from a continuum viewpoint or using reduced models – based on beam elements, which provide an efficient alternative description from the computation point of view.

Part I of the thesis is devoted to the continuous homogenization of periodic architected materials and composites, considering the Cosserat chiral mechanics and micromorphic continua frameworks successively. A general classification of the family of generalized continua is proposed as an outcome of the developed homogenization scheme for the micromorphic continuum. Homogenization towards Cosserat and micromorphic substitution media deserve the developments of **chapter 2 and 3** successively.

Part II of the document Deals with reduced models of architected materials, considering successively phenomenological couple stress models of beams in **chapter 4** and discrete periodic homogenization of architected materials towards Cosserat effective media in **chapter 5**. Moreover, the issues of edge and size effects of truncated unit cells tessellating a macrodomain are considered in **chapter 5**.

Part III of the thesis deals with quasi-periodic homogenization; a general theory is proposed in **chapter 6** to handle non-affine transformations of the initial periodic geometry and determine the modified effective properties over the transformed quasi-periodic domain. The important case of conformal transformations of periodic designs deserves the developments of **chapter 7**.

The main novel aspects of the research activities and a list of planned developments at modeling, computational and experimental levels are summarized in **conclusion** part .

Part I

Continuous homogenization towards generalized effective continua and applications to architected materials and composites

Chapter 2

Homogenization towards chiral Cosserat continua and applications to enhanced Timoshenko beam theories

Summary

A homogenization methodology for constructing effective Cosserat substitution media for heterogeneous materials is proposed, combining a variational principle in linear elasticity with the extended Hill-Mandel lemma accounting for the introduced generalized kinematics. The proposed method is general and can be applied to a broad class of architected materials and composites prone to such micropolar effects. The microscopic displacement field of the initially heterogeneous continuum splits into a homogeneous part polynomial in the generalized kinematic measures and a fluctuation involving localization operators. The tensors of effective micropolar moduli are formulated as integrals over a representative unit cell utilizing the displacement localizators, solution of classical, and higher-order unit cell problems. The proposed method has the chief advantage of delivering size-independent higher-order effective moduli. Based on the developed homogenization method, the effective micropolar moduli of the tetrachiral /anti-tetrachiral lattices and composites made of a tetrachiral lattice reinforcement are computed. This proposed model is implemented to elaborate an enhanced Timoshenko microstructured beam model exhibiting couplings between different deformation modes induced by the response of its underlying tetrachiral microstructure.

2.1 Introduction

In recent decades, a new class of artificial materials emerged with mechanical attributes not encountered in natural materials that received the wording metamaterials [153]. This name indicates the ability to control artificial materials properties by adjusting and optimizing the appropriate design of their inner topology, rather than by changing the chemical composition or properties of the base material [154, 155]. Such advancement has become feasible through the rapid development of additive manufacturing techniques [156–158]. A primary cell is used as the repetitive material unit, replacing atoms in conventional materials [159]. A wide range of unit-cell based materials has been designed so far, a specific class of importance being named «auxetic» metamaterials, which are artificial materials with a negative Poisson's ratio [160–162] or showing unusual couplings between different deformation modes - tension, shear, or bending - in the presence of chiral effects [3]. Different types of approaches for modeling the behavior of architected materials have been developed over the past decade: phenomenological ones postulating an effective enriched type continuum model [163] - these last authors proposing a micropolar model of tetrachiral lattices - micropolar models of hexachiral structures [164], analytical or computational homogenization techniques [100, 163, 165].

A chiral Cosserat solid has three new elastic constants and the six considered for an isotropic micropolar solid [166]. Chirality means handedness, meaning that an object having this property cannot be superimposed to its mirror image [167]. Chirality - chiral structures exhibit an inherent lack of symmetry for their mirror lattice image [168] - has been used as a mechanism for the retrieval of auxetic material behaviors, with hexachiral lattices to approach the negative Poisson's theoretical limit (-1) predicted for isotropic materials [169]. Chiral structures are encountered in both artificial and natural materials, including right and left-handed seashells, DNA, chiral carbon nanotube, twisted leaves, chiral structures like cables, amongst others [170–172]. Chiral structures with zero or almost zero Poisson's ratio, positive values have been reported, typical examples of the kind being chiral-diamond and tetrachiral lattices [100, 173]. Chiral materials and structures require adequate constitutive equations, including handedness, to describe their distinct and characteristic features. In the context of continuum mechanics, the chiral behavior is described by generalized continuum models, like micropolar elasticity theory [74, 102, 174] or chiral elasticity chosen for its ability to describe the coupling between local rotation, bending, and volumetric deformations. Thereby, chiral elasticity manifests many unusual behaviors, like negative Poisson's ratio (auxetic), significant volumetric changes, and the coupling between different deformation modes not encountered for classical materials. A review of the recently developed models is exposed in [175] and references therein.

Bacigalupo and Gambarotta [100] developed Cosserat type, and strain gradient homogenized models as two alternative strategies for centrosymmetric tetrachiral and hexachiral microstructures. Relying on a model of the kinematics of the ligaments and rings, they led to the expression of the average energy and thus to a constitutive model for the effective micropolar continuum. The constitutive model for the

hexachiral lattice obtained by the last authors is identical to that obtained in [176]. The predictions of micropolar and strain gradient models are mutually consistent, but they disagree with experimental results and the predictions of [168] model.

The chapter's main objective is to set up a novel homogenization method towards chiral Cosserat continua delivering size-independent higher-order effective moduli, including the additional coupling moduli between tension and bending. Novel aspects presented in this chapter are the following:

- A unified formulation of the minimum principle of potential energy in linear elasticity combined with an extension of Hill-Mandel macrohomogeneity condition is formulated for the determination of the effective classical and higher-order moduli of chiral Cosserat media.
- The microscopic displacement field is decomposed additively into a homogeneous polynomial part, in terms of the introduced generalized kinematics, and a fluctuating part obtained from classical and a higher-order unit cell BVPs.
- Effective size-independent moduli for the effective micropolar continua are computed numerically for architected materials prone to both chiral and centrosymmetric effects in the small strains range.
- The effective moduli are computed for periodic composites made of a tetrachiral or anti-tetrachiral lattice as a reinforcement.
- An enriched Timoshenko microstructured beam theory is constructed, Relying on the developed higher-order homogenization method, including new couplings due to the chiral and non-centrosymmetric effects.

A few words regarding the employed notations are in order. The physical space is embedded with the Euclidean space and vectors and higher-order tensors are implicitly decomposed into an orthonormal basis of the underlying vector space. Vectors and higher-order tensors are denoted by boldface symbols. The gradient of a scalar or tensor field with respect to the position is denoted with the nabla operator and the position as a subscript, viz $\nabla_x \mathbf{E}(\mathbf{x})$, represents the gradient of the tensor field $\mathbf{E}(\mathbf{x})$ with respect to $\mathbf{x}$. The transpose of a tensor is written with a superscript notation, for instance $\mathbf{B}^T$. The gradient of a tensor field $\mathbf{A}(\mathbf{y})$ is denoted $\mathbf{A}(\mathbf{y}) \otimes \nabla_y$ ($\otimes$ represents the tensor product), and its divergence is obtained as the trace of the gradient, denoted $\mathbf{A}(\mathbf{y}).\nabla_y$. The dot product therein represents the internal product in the space of Cartesian tensors. The vector product of two arbitrary vectors $\mathbf{U}, \mathbf{V}$ is denoted as $(\mathbf{U} \times \mathbf{V})$, with components $(\mathbf{U} \times \mathbf{V})_i = \epsilon_{ijk} U_j V_k$. The vector product of a second-order tensor and a vector is the second-order tensor defined as $(A \times v)_{ij} = \epsilon_{jmk} A_{im} v_k$.

2.2 General methodology for the homogenization of generalized continua

Three distinct scales for composites with periodic microstructures can be identified: the scale of the microstructure for which the microscopic position is denoted by the label 'y', the macroscopic structural

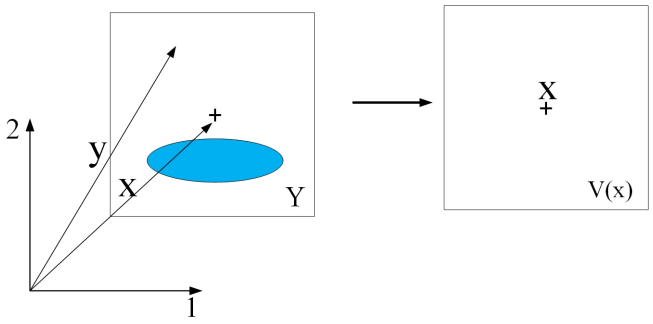

Figure 2.1 (left) Composite periodic unit cell Y made of two elastic materials,(right) The homogeneous substitution medium (right) with domain V($\boldsymbol{x}$) centered around point $\boldsymbol{x}$.

scale, and the intermediate scale called the mesoscopic level (or scale). By contrast with the microscopic position, the macroscopic position variable is denoted by the label 'x', and an implicit dependency upon the macroscopic position holds for the macroscopic kinematic variables to be elaborated later on contribution. Here and in the sequel, vectors $\boldsymbol{y}$ and $\boldsymbol{x}$ denote the microscopic and macroscopic spatial positions of material points concerning a fixed Cartesian basis, respectively. In the present context of periodic homogenization, the microstructure is identified within a representative unit cell, which generates the entire composite domain by periodic translation. The unit cell domain consists of at least two phases or constituents with specific mechanical properties; in the context of composite materials (Fig. 2.1), the reinforcement has higher properties in comparison to its surrounding matrix, with the extreme case of architected materials chosen as an illustration in this work, for which the contrast of properties is infinite.

The center of area of the unit cell, point $\boldsymbol{x}$ on Fig. 2.1, is defined implicitly by the integral relation adopting a fixed Cartesian basis

$$\frac{1}{|Y|}\int_{Y}(\boldsymbol{y}-\boldsymbol{x})dV_y=\boldsymbol{0} \tag{2.1}$$

In Eq. 2.1, integration is performed over all micropoints labeled with the position vector $\boldsymbol{y}$ within the RVE; relation 2.1 has the significance that the relative position ($\mathbf{y}$ - $\mathbf{x}$) of the micropoints has zero average over the unit cell. Note that the definition given in Eq. 2.1 is simplified when the origin of coordinates is selected at the center of area of the RVE and it further guarantees the objectivity of the virtual power of internal forces [126]. This will be our choice here and in the sequel so that the relative position vector simply coincides with the microscopic position.

In order to set the stage, the displacement vector is decomposed additively into a homogeneous part $\boldsymbol{u}^{\mathrm{hom}}(\boldsymbol{y})$ affine in the macrostrain kinematic variables of the Cosserat continuum and a periodic fluctuation denoted $\tilde{\boldsymbol{u}}(\boldsymbol{y})\in H^1_{per}(Y)$, the Sobolev space of Y-periodic displacements, viz it holds

$$\boldsymbol{u}=\boldsymbol{u}^{\mathrm{hom}}(\boldsymbol{y})+\tilde{\boldsymbol{u}}(\boldsymbol{y}) \tag{2.2}$$

The homogeneous displacement describes the response of a (fictive) effective continuum that would behave exactly as the selected homogeneous Cosserat substitution medium, so that the added fluctuation $\tilde{\boldsymbol{u}}(\boldsymbol{y})$ in

Eq. 2.2 corrects the deviation of the microscopic displacement of the initial heterogeneous medium from that of a homogeneous Cosserat substitution medium.

The determination of the homogeneous displacement, representative of both classical and Cosserat effects, is the first step of the proposed higher-order homogenization method. We will proceed in a two steps method as follows: i) evaluation of the microscopic homogeneous displacement $\boldsymbol{u}^{\text{hom}}(\boldsymbol{y})$ in Eq. 2.2, and subsequently ii) the computation of the fluctuating displacement, vector $\tilde{\boldsymbol{u}}(\boldsymbol{y})$ in the same Eq. 2.2 relying on a variational formulation, before evaluating the effective classical and micropolar moduli.

2.3 Elaboration of the kinematic and static variables of the effective Cosserat continuum

At the microscopic scale, the material obeys a first gradient linear elastic constitutive law given in a static situation by

$$\boldsymbol{\sigma} \cdot \nabla_y + \boldsymbol{f} = \boldsymbol{0} \;\; in\; V \tag{2.3}$$

$$\boldsymbol{\sigma} \cdot \boldsymbol{n} = \boldsymbol{t} \quad on\; \partial V \tag{2.4}$$

$$\boldsymbol{\sigma} = \boldsymbol{C} : \boldsymbol{\varepsilon} \tag{2.5}$$

with $\boldsymbol{\sigma} = \boldsymbol{\sigma}^T$ the symmetrical Cauchy stress, $\boldsymbol{f}$ the body force vector, $\boldsymbol{n}$ the unit external normal, $\boldsymbol{t}$ the traction vector, and $\boldsymbol{C}$ the fourth-order rigidity tensor. The Cauchy's strain tensor $\boldsymbol{\varepsilon}$, is defined in a small strains framework in component format as

$$\varepsilon_{ij} = \frac{1}{2}\left(u_{i,j} + u_{j,i}\right) \tag{2.6}$$

The macroscopic equilibrium equation is obtained by integrating the balance equation 2.3 over the unit cell domain Y with the bracket notation, and use of Gauss divergence theorem and considering the Whitaker averaging theorem for continuous interfaces, viz the relation $< \nabla_y \boldsymbol{\sigma} >_y = \nabla_x < \boldsymbol{\sigma} >_y$ [177,178], as follows:

$$\langle \boldsymbol{\sigma} \rangle_Y \cdot \nabla_x + \langle \boldsymbol{f} \rangle_Y = 0 \tag{2.7}$$

$< \bullet >_Y$ is generally known as the phase average and is defined explicitly as

$$< \bullet >_Y = \frac{1}{|Y|} \int_Y \bullet dV_y \tag{2.8}$$

The second microbalance equation results by taking the vector product of Cauchy stress equilibrium in Eq. 2.3 by the microscopic position vector $\boldsymbol{y}$, resulting in the relation

$$\epsilon_{ijk} y_j \sigma_{kl,l} + \epsilon_{ijk} y_j f_k = 0 \tag{2.9}$$

where ϵ_{ijk} is the Levi-Civita permutation symbol. Integrating Eq. 2.9 over the volume unit cell and defining the couple stress tensor as the second-order tensor $\mu_{ij} := \epsilon_{ilk} y_l \sigma_{kj}$, and the internal body couple

forces $f_i^{\phi} := \epsilon_{ijk} y_j f_k$ along with the recourse to the divergence theorem leads to the following balance law in an integral format

$$\int_Y \left(\frac{\partial \mu_{ij}}{\partial y_j} + f_i^{\phi} \right) dV = 0 \tag{2.10}$$

The second macroscopic equilibrium equation is obtained using Gauss divergence theorem and taking the average of Eq. 2.10 over the domain Y and considering further Withaker's averaging theorem in the case of coherent continuous interfaces (the displacement and traction vectors are continuous across the interface between the constituents), namely the relation $< \nabla_y \boldsymbol{\mu} >_y = \nabla_x < \boldsymbol{\mu} >_y$ [177, 178] as follows:

$$\langle \boldsymbol{\mu} \rangle_Y \cdot \nabla_x + \left\langle \mathrm{f}^{\phi} \right\rangle_Y = 0 \tag{2.11}$$

The previous relation means from a physical point of view that the average of the microscopic couple stress tensor over the unit cell elaborated from Cauchy stress is balanced by the body couple emanating from the density of body couples $f^{\phi} := \boldsymbol{y} \times \boldsymbol{f}$. Multiplying Eqs. 2.7 and 2.11 by virtual velocity and rate of rotation, variables $\boldsymbol{v}$ and φ , respectively and integrating over the macroscopic homogeneous volume $V(\boldsymbol{x})$ depicted in Fig. 2.1, leads to the total virtual power of internal forces. After a few straightforward manipulations, the two following relations are obtained:

$$-\int_{V(x)} \langle \boldsymbol{\sigma} \rangle_Y : \nabla_x \boldsymbol{v} dV + \int_{V(x)} \langle \boldsymbol{f} \rangle_Y \cdot \boldsymbol{v} dV + \int_{\partial V(x)} \langle \boldsymbol{\sigma} \rangle_Y \cdot \boldsymbol{v} ds = 0 \tag{2.12}$$

$$\int_{V(x)} \langle \boldsymbol{\mu} \rangle_Y : \nabla_x \phi dV + \int_{V(x)} \left\langle \mathrm{f}^{\phi} \right\rangle_Y \cdot \phi dV + \int_{\partial V(x)} \langle \boldsymbol{\mu} \rangle_Y \cdot \phi ds = 0 \tag{2.13}$$

Eqs. 2.12 and 2.13 can be divided into four contributions, P_c^i, P_m^i, P_c^e, and P_m^e, wherein the indices i, e, m, and c stand for the powers of internal, external, Cauchy and micropolar type forces, respectively:

$$\begin{aligned} P_c^i &= -\int_{V(x)} \langle \boldsymbol{\sigma} \rangle_Y : \nabla_x \boldsymbol{v} dV; & P_m^i &= -\int_{V(x)} \langle \boldsymbol{\mu} \rangle_Y : \nabla_x \phi dV \\ P_c^e &= \int_{V(x)} \langle \boldsymbol{f} \rangle_Y \cdot \boldsymbol{v} dV + \int_{\partial V(x)} \langle \boldsymbol{\sigma} \rangle_Y \cdot \boldsymbol{v} ds; & P_m^e &= \int_{V(x)} \left\langle \mathrm{f}^{\phi} \right\rangle_Y \cdot \phi dV + \int_{\partial V(x)} \langle \boldsymbol{\mu} \rangle_Y \cdot \phi ds \end{aligned} \tag{2.14}$$

The virtual power of the effective continuum at the macroscopic level is the sum of the internal power of the Cauchy medium and the micropolar internal power:

$$\delta W_M = -(P_c^i + P_m^i) = \frac{1}{|V(x)|} \left\{ \int_{V(x)} \langle \boldsymbol{\sigma} \rangle_Y : \nabla_x \boldsymbol{v} dV + \int_{V(x)} \langle \boldsymbol{\mu} \rangle_Y : \nabla_x \phi dV \right\} \equiv \delta \left(\frac{1}{|Y|} \int_Y \frac{1}{2} \boldsymbol{\sigma} : \boldsymbol{\varepsilon} dV_y \right) \tag{2.15}$$

The fields $\boldsymbol{v}$ and φ can be viewed as virtual variations of micro deformation field, $\boldsymbol{u}$ and micro rotation field, ϕ successively. The last relation in Eq. 2.13 is the extended Hill macrohomogeneity condition expressing the identity (here in virtual power form) of the macroscopic energy with the volume average of the microscopic energy density, the scalar quantity $\frac{1}{2} \boldsymbol{\sigma} : \boldsymbol{\varepsilon}$.

Let further define two macroscopic kinematic variables, $\boldsymbol{E}(\boldsymbol{x})$ and $\mathbf{K}$(x), namely the second-order micropolar strain and the macro curvature tensors respectively as,

$$\boldsymbol{E}(\boldsymbol{x}) := \nabla_x \boldsymbol{U} - \boldsymbol{\epsilon} \cdot \boldsymbol{\Phi}(\boldsymbol{x}) \tag{2.16}$$

$$\mathbf{K}(\boldsymbol{x}) := \nabla_x \boldsymbol{\Phi}(\boldsymbol{x}) \tag{2.17}$$

with $\boldsymbol{\Phi}(\boldsymbol{x})$ the macrorotation vector, considering small rotations and curvatures. In Eq. 2.17, the averaged kinematic tensors are defined by the following set of relations:

$$\begin{aligned}
&\boldsymbol{U}(\boldsymbol{x}) := \tfrac{1}{|Y|}\int_Y \boldsymbol{u}(\boldsymbol{y})dV_y \\
&\boldsymbol{E}^{sym}(\boldsymbol{x}) := \tfrac{1}{2}\left(\boldsymbol{E}(\boldsymbol{x}) + \boldsymbol{E}^T(\boldsymbol{x})\right) = \tfrac{1}{|Y|}\int_Y \boldsymbol{\varepsilon}(\boldsymbol{y})dV_y = \left(\tfrac{1}{|Y|}\int_Y \boldsymbol{u}(\boldsymbol{y}) \otimes \nabla_y dV_y\right)^{sym} \\
&\boldsymbol{\Phi}(\boldsymbol{x}) := \tfrac{1}{|Y|}\int_Y \phi(\boldsymbol{y})dV_y \rightarrow \boldsymbol{\epsilon}\cdot\boldsymbol{\Phi}(\boldsymbol{x}) := \tfrac{6}{l^2|Y|}\int_Y \boldsymbol{u}(\boldsymbol{y}) \otimes (\boldsymbol{y}-\boldsymbol{x})\, dV_y \\
&\boldsymbol{E}^{Tskew}(\boldsymbol{x}) = skw(\boldsymbol{U}\otimes\nabla_x)^{skew} - \boldsymbol{\epsilon}\cdot\boldsymbol{\Phi}(\boldsymbol{x}) = \tfrac{1}{|Y|}\int_Y ((\boldsymbol{u}(\boldsymbol{y})\otimes\nabla_y)^{skw} + \tfrac{6}{l^2}\boldsymbol{u}(\boldsymbol{y})\otimes(\boldsymbol{y}-\boldsymbol{x}))dV_y \\
&\rightarrow \boldsymbol{E} = \boldsymbol{E}^{sym} + \boldsymbol{E}^{Tskew} \\
&\mathbf{K}(\boldsymbol{x}) := \boldsymbol{\Phi}(\boldsymbol{x}) \otimes \nabla_x
\end{aligned} \tag{2.18}$$

where $\boldsymbol{E}^{skew,T}$ is the second-order skew-symmetric strain tensor. Tensor $\mathbf{K}(\boldsymbol{x})$ in the last relation designates the curvature tensor, defined as the macroscopic gradient of the microrotation vector $\boldsymbol{\Phi}(\boldsymbol{x})$. The skew-symmetric part of the macro strain can be expressed as follows

$$\begin{aligned}
&\boldsymbol{\omega} = \frac{1}{2}\left((\boldsymbol{U}\otimes\nabla_x) - (\boldsymbol{U}\otimes\nabla_x)^T\right) \\
&\varpi = \boldsymbol{\epsilon} : \boldsymbol{\omega} \\
&\mathbf{E}^{skew} = \varpi - 2\boldsymbol{\Phi}
\end{aligned} \tag{2.19}$$

where $\mathbf{E}^{skew}$ is the pseudo-vector dual to the antisymmetric tensor $\mathbf{E}^{skew,T}$ (similarly, vector ϖ is dual to the skew-symmetric tensor $\boldsymbol{\omega}$) . The macroscopic kinematic tensors are obtained from the minimization of the quadratic difference between the microscopic displacement field and its quadratic homogeneous approximation, as detailed in [84]. The vector form of $\mathbf{E}^{skew}$ is used in the subsequent computations.

The macroscopic constitutive law relating the macroscopic stress tensors versus their microscopic counterparts will be used to derive the homogenized part of the microscopic displacement; therefore, appropriate averaging rules must be determined. The fundamental assumption underlying the homogenization towards a Cosserat continuum is the principle of the equivalence of the macroscopic and microscopic strain energy densities: the macroscopic energy density of the Cosserat substitution medium is identified to the volume average of the microscopic energy density. This relation is commonly called Hill-Mandel macrohomogeneity condition [69–71, 179, 180], writing in the static and isothermal case,

$$W_M = \langle w_\mu(\varepsilon)\rangle_Y \tag{2.20}$$

Substituting expressions 2.16, 2.17 and 2.19 into Eq. 2.15 and accounting for the macrohomogeneity of the fields within the macrodomain $V(\boldsymbol{x})$, leads to the variation of the macroscopic energy density of the effective micropolar continuum, function $W_M\left(\boldsymbol{E}^{sym}, \boldsymbol{E}^{skew}, \mathbf{K}\right)$:

$$\begin{aligned}
\delta W_M &= \frac{1}{V(x)}\int_{V(x)} \left(\boldsymbol{\Sigma} : (\delta\boldsymbol{E} + \epsilon\cdot\delta\boldsymbol{\Phi}) + \boldsymbol{M} : \delta\mathbf{K}\right) dV_x \\
&= \frac{1}{V(x)}\int_{V(x)} \left(\boldsymbol{\Sigma}^{sym} : \delta\boldsymbol{E}^{sym} + \boldsymbol{\Sigma}^{skew}\cdot\delta\boldsymbol{E}^{skew} + \boldsymbol{M} : \delta\mathbf{K}\right) dV_x
\end{aligned} \tag{2.21}$$

wherein the macroscopic stress, and the couple stress tensors are elaborated as follows:

$$\begin{aligned}
&\boldsymbol{\Sigma} = \boldsymbol{\Sigma}^{sym} + \boldsymbol{\Sigma}^{Tskew} \\
&\frac{1}{2}\left(\boldsymbol{\Sigma}(\boldsymbol{x}) + \boldsymbol{\Sigma}^{T}(\boldsymbol{x})\right) = \boldsymbol{\Sigma}^{sym}(\boldsymbol{x}) := \frac{1}{|Y|}\int\limits_{Y} \boldsymbol{\sigma}(\boldsymbol{y}) dV_y \\
&\boldsymbol{\Sigma}^{skew}(\boldsymbol{x}).\boldsymbol{N}(\boldsymbol{x}) := \int\limits_{\partial Y} \boldsymbol{n}\cdot(\boldsymbol{y}\times\boldsymbol{\sigma}(\boldsymbol{y}))\, ds = \int\limits_{\partial Y} \boldsymbol{n}\cdot\boldsymbol{\epsilon}\cdot\boldsymbol{y}\otimes\boldsymbol{\sigma}(\boldsymbol{y}) ds \\
&\qquad\qquad = \int\limits_{Y} div_y\left(\boldsymbol{y}\times\boldsymbol{\sigma}(\boldsymbol{y})\right) dv \equiv div_x\left\langle \boldsymbol{y}\times\boldsymbol{\sigma}(\boldsymbol{y})\right\rangle \Rightarrow \boldsymbol{\Sigma}^{skew} := \int\limits_{Y} div_y\left(\boldsymbol{\epsilon}\cdot\boldsymbol{y}\cdot\boldsymbol{\sigma}(\boldsymbol{y})\right) dv \\
&\boldsymbol{\Sigma}^{Tskew} = -\boldsymbol{\epsilon}\cdot\boldsymbol{\Sigma}^{skew} \\
&\boldsymbol{\mu}(\boldsymbol{y}) := \boldsymbol{y}\times\boldsymbol{\sigma}(\boldsymbol{y}) \Leftrightarrow \mu_{ij} := \epsilon_{imk}\sigma_{jm}y_k \rightarrow \boldsymbol{M}(\boldsymbol{x}) := \frac{1}{|Y|}\int\limits_{Y}\boldsymbol{\mu}(\boldsymbol{y}) dV_y
\end{aligned} \tag{2.22}$$

Here, $\boldsymbol{\Sigma}^{skew}$ is the dual pseudo-vector to the second-order skew-symmetric tensor $\boldsymbol{\Sigma}^{Tskew}$. The stress measures then follow from Eq. 2.13 as the partial derivatives of the strain energy density:

$$\boldsymbol{\Sigma}^{sym} = \frac{\partial W_M}{\partial \mathbf{E}^{sym}}; \quad \boldsymbol{\Sigma}^{skew} = \frac{\partial W_M}{\partial \mathbf{E}^{skew}}; \quad \boldsymbol{M} = \frac{\partial W_M}{\partial \mathbf{K}} \tag{2.23}$$

which leads to the following expressions:

$$\frac{\partial W_M}{\partial \mathrm{E}^{sym}_{ij}} = \Sigma^{sym}_{ij} = \langle\sigma_{ij}\rangle_Y \tag{2.24}$$

$$\frac{\partial W_M}{\partial \mathrm{E}^{skew}_{i}} = \Sigma^{skew}_{i} = \left\langle\left(\epsilon_{ijk}y_j\sigma_{kl}\right)_{,l}\right\rangle_Y \tag{2.25}$$

$$\frac{\partial W_M}{\partial \mathrm{K}_{ij}} = M_{ij} = \langle\epsilon_{ikl}y_l\sigma_{kj}\rangle_Y \tag{2.26}$$

After straightforward calculations, the macroscopic definition of the strain energy density, Eq. 2.21, leads to the following well-known micropolar balance equations.

$$\int\limits_{Y}\sigma_{ij,j}dV + \int\limits_{Y} f_i dV = 0 \Rightarrow \frac{\partial \Sigma_{ij}}{\partial x_j} + F_i = 0 \tag{2.27}$$

$$\int\limits_{Y}\mu_{ij,j}dV + \int\limits_{Y}\epsilon_{ijk}\sigma_{kj}dV + \int\limits_{Y} f^{\phi}_i dV = 0 \Rightarrow \frac{\partial M_{ij}}{\partial x_j} + \epsilon_{ijk}\Sigma_{kj} + F^{\phi}_i = 0 \tag{2.28}$$

wherein F_i and F^{ϕ}_i are the components of the macro body force and body couple, defined as the following volume averages:

$$F_i := \frac{1}{|Y|}\int\limits_{Y} f_i dV_y, \mathrm{F}^{\phi}_i := \frac{1}{|Y|}\int\limits_{Y} f^{\phi}_i dV_y$$

2.4 Effective moduli of the Cosserat medium

The determination of the effective moduli of the Cosserat substitution medium follows a two steps procedure. First, the homogeneous part of the microscopic displacement in Eq. 2.2 is determined, and the fluctuating part correcting for it in Eq. 2.2 is next obtained from a variational principle.

2.4.1 Determination of the homogeneous part of the microscopic displacement

From the expressions of the static variables in Eqs. 2.24 - 2.26, the homogenous part of the displacement introduced in Eq. 2.2 are related to the macroscopic kinematic variables $\mathbf{E}^{sym}(\boldsymbol{x})$, $\mathbf{E}^{skew}(\boldsymbol{x})$, and $\mathbf{K}(\boldsymbol{x})$ can be evaluated as the sum of the following three contributions. Firstly, from Eq. 2.2, given that at the micro level the micro stress and strain energy densities are connected by the relation $\sigma_{ij} = \frac{\partial W_\mu(\varepsilon_{ij})}{\partial \varepsilon_{ij}}$, it follows the subset of relations valid for arbitrary stress components therein:

$$\Sigma_{ij}^{sym} = \langle \sigma_{ij} \rangle_Y = \left\langle \sigma_{kl} \frac{\partial \varepsilon_{kl}}{\partial \mathrm{E}_{ij}^{sym}} \right\rangle_Y \rightarrow \int_Y \sigma_{kl} \left(\frac{\partial \varepsilon_{kl}}{\partial \mathrm{E}_{ij}^{sym}} - \mathrm{I}_{ijkl} \right) dV_y = 0, \quad \forall \sigma_{kl} \tag{2.29}$$

wherein I_{ijkl} is the fourth-order identity tensor. Consideration of the arbitrariness of the stress tensor in Eq. 2.29 leads to the expression of the microscopic strain versus the macroscopic strain

$$\frac{\partial \varepsilon_{kl}}{\partial \mathrm{E}_{ij}^{sym}} - \mathrm{I}_{ijkl} = 0 \rightarrow \varepsilon_{kl} = \mathrm{I}_{ijkl} \mathrm{E}_{ij}^{sym} \rightarrow \varepsilon_{kl} = \mathrm{E}_{kl}^{sym} \tag{2.30}$$

Substituting the definition of Cauchy strain versus displacement into Eq. 2.30 leads to

$$\frac{\partial u_k^{\mathrm{hom}}}{\partial y_l} = \mathrm{E}_{kl}^{sym} \rightarrow u_k^{\mathrm{hom}}(\boldsymbol{y}) = y_l \mathrm{E}_{kl}^{sym} \tag{2.31}$$

up to a macroscopic rigid body translation, however not written here. The second part of the micropolar deformation field is calculated by forming a BVP by considering Eq. 2.25, the dependency of the microscopic displacement versus the antisymmetric strain vector $\mathbf{E}^{skew}(\boldsymbol{x})$ is obtained as:

$$\Sigma_i^{skew} = \left\langle \left(\epsilon_{ijk} y_j \sigma_{kl} \right)_{,l} \right\rangle_Y = \langle \epsilon_{ilk} \sigma_{kl} \rangle_Y + \langle \epsilon_{ijk} y_j \sigma_{kl,l} \rangle_Y = \left\langle \sigma_{kl} \frac{\partial \varepsilon_{kl}}{\partial \mathrm{E}_i^{skew}} \right\rangle_Y \tag{2.32}$$

Since at the micro-level Cauchy stress is symmetrical, the term $\langle \epsilon_{ilk} \sigma_{kl} \rangle_Y$ vanishes, which leads to the following expression of the skew-symmetric part of the macro stress tensor

$$\Sigma_i{}^{skew} := \langle \epsilon_{ijk} y_j \sigma_{kl,l} \rangle_Y = \left\langle \sigma_{kl} \frac{\partial \varepsilon_{kl}}{\partial \mathrm{E}_i^{skew}} \right\rangle_Y \tag{2.33}$$

Eq. 2.33 can be reformulated as

$$\int_Y \left(-\epsilon_{ijk} y_j \sigma_{kl,l} + \sigma_{kl} \frac{\partial \varepsilon_{kl}}{\partial \mathrm{E}_i^{skew}} \right) = 0 \tag{2.34}$$

Integrating by part, one can rewrite Eq. 2.34 as

$$\int_Y \left(\epsilon_{ijk} y_j \sigma_{kl,l} + \sigma_{kl,l} \frac{\partial u_k}{\partial \mathrm{E}_i^{skew}} \right) dV_y - \int_{\partial Y} n_l \sigma_{kl} \frac{\partial u_k}{\partial \mathrm{E}_i^{skew}} ds_y = 0 \tag{2.35}$$

Isolating the volume integral in the BVP 2.35 leads to the local relation

$$\int_Y \left(\epsilon_{ijk} y_j \sigma_{kl,l} + \sigma_{kl,l} \frac{\partial u_k}{\partial \mathrm{E}_i^{skew}} \right) dV_y = 0 \rightarrow \epsilon_{ijk} y_j \sigma_{kl,l} + \sigma_{kl,l} \frac{\partial u_k}{\partial \mathrm{E}_i^{skew}} = 0, \quad \forall \sigma_{kl,l} \tag{2.36}$$

Solving previous relation leads to the following expression of the deformation field related to $\mathbf{E}^{skew}(\boldsymbol{x})$

$$\epsilon_{ijk} y_j + \frac{\partial u_k}{\partial \mathrm{E}_i^{skew}} = 0 \rightarrow u_k^{\mathrm{hom}} = -\epsilon_{ijk} y_j \mathrm{E}_i^{skew} \tag{2.37}$$

The third contribution of the displacement field is determined using Eq. 2.26 and repeating the same arguments as above:

$$M_{ij} = \langle \epsilon_{inm} y_n \sigma_{mj} \rangle_Y = \left\langle \sigma_{kl} \frac{\partial \varepsilon_{kl}}{\partial \mathrm{K}_{ij}} \right\rangle_Y \rightarrow \int_Y \sigma_{kl} \left(\frac{\partial \varepsilon_{kl}}{\partial \mathrm{K}_{ij}} - \epsilon_{inm} y_n \mathrm{I}_{mjkl} \right) dV_y = 0, \quad \forall \sigma_{kl} \tag{2.38}$$

which leads to the dependency of the microscopic deformation upon the micropolar gradient:

$$\frac{\partial \varepsilon_{kl}}{\partial \mathrm{K}_{ij}} - \epsilon_{inm} y_n \mathrm{I}_{mjkl} = 0 \rightarrow \varepsilon_{kl} = \epsilon_{inm} y_n \mathrm{I}_{mjkl} \mathrm{K}_{ij} \rightarrow \varepsilon_{kl} = \epsilon_{ink} y_n \mathrm{K}_{il} \tag{2.39}$$

Substituting the definition of Cauchy strain into Eq. 2.39, then leads to

$$\frac{\partial u_k^{\mathrm{hom}}}{\partial y_l} = \epsilon_{ink} y_n \mathrm{K}_{il} \tag{2.40}$$

According to Eq. 2.31, Eq. 2.37 and Eq. 2.40, one can conclude that the homogeneous part of the displacement expresses as the following quadratic function of the microscopic position

$$\boldsymbol{u}^{\mathrm{hom}}(\boldsymbol{y}, \boldsymbol{x}) = \boldsymbol{U}^0 + \boldsymbol{E}^{\mathrm{sym}}(\boldsymbol{x}) \cdot \boldsymbol{y} - \boldsymbol{\epsilon} \cdot \boldsymbol{E}^{\mathrm{skew}}(\boldsymbol{x}) \cdot \boldsymbol{y} + \boldsymbol{\epsilon} \cdot \mathbf{K} : (\boldsymbol{y} \otimes \boldsymbol{y}) \tag{2.41}$$

in which $\boldsymbol{U}^0(\boldsymbol{x})$ is a rigid body motion. Note that in the situation that body forces experience variations within the RVE, the microscopic displacement would include additional dependencies in both the body force components and the skew-symmetrical macroscopic strain components.

2.4.2 Variational principle for Cosserat homogenization and determination of the fluctuation

In general, one may adopt the generic expansion of the homogeneous part of the microscopic displacement, Eq. 2.41, and substitute it into the total displacement vector expressed in Eq. 2.2 as:

$$\boldsymbol{u}(\boldsymbol{y}, \boldsymbol{x}) = \boldsymbol{u}^{\mathrm{hom}}(\boldsymbol{x}, \boldsymbol{y}) + \tilde{\boldsymbol{u}}(\boldsymbol{y}) = (\mathbf{I}_4 \cdot \boldsymbol{y}) : \mathbf{E}^{sym}(\boldsymbol{x}) - (\boldsymbol{\epsilon} \cdot \boldsymbol{y}) \cdot \mathbf{E}^{skew}(\boldsymbol{x}) + (\boldsymbol{\epsilon} \cdot \boldsymbol{y} \otimes \boldsymbol{y}) : \mathbf{K}(\boldsymbol{x}) + \tilde{\boldsymbol{u}}(\boldsymbol{y}) \tag{2.42}$$

The quadratic displacement evaluated in Eq. 2.42 defines the basis for the computation of the effective Cosserat moduli, following the variational formulation for generalized continua established in section 2.2. An extended minimization principle over all periodic fluctuations holds so that one can write using Hill extended macrohomogeneity condition combined with the principle of minimum potential energy in the absence of body forces:

$$\begin{aligned} W_M\left(\boldsymbol{E}^{sym}, \mathbf{E}^{skew}, \boldsymbol{K}\right) &= \underset{\tilde{\boldsymbol{u}} \in H^1_{per}(Y)}{Min} \left\{ \int_Y \frac{1}{2} \left(\boldsymbol{u}^{\mathrm{hom}} \otimes \nabla_y + \tilde{\boldsymbol{u}}(\boldsymbol{y}) \otimes \nabla_y \right) : \boldsymbol{C}(\boldsymbol{y}) : \left(\boldsymbol{u}^{\mathrm{hom}} \otimes \nabla_y + \tilde{\boldsymbol{u}}(\boldsymbol{y}) \otimes \nabla_y \right) dV_y \right\} \\ &= \underset{\tilde{\boldsymbol{u}} \in H^1_{per}(Y)}{Min} \left\{ \begin{array}{l} \int_Y \frac{1}{2} C(\boldsymbol{y}) : \left(\boldsymbol{I}_4 : \mathbf{E}^{sym}(\boldsymbol{x}) - \epsilon \cdot \mathbf{E}^{skew}(\boldsymbol{x}) + \epsilon \cdot \boldsymbol{y} \otimes \mathbf{I}_2 : \mathbf{K}(\boldsymbol{x}) + \tilde{\boldsymbol{u}}(\boldsymbol{y}) \otimes \nabla_y \right) : \\ \left(\boldsymbol{I}_4 : \mathbf{E}^{sym}(\boldsymbol{x}) - \epsilon \cdot \mathbf{E}^{skew}(\boldsymbol{x}) + \epsilon \cdot \boldsymbol{y} \otimes \mathbf{I}_2 : \mathbf{K}(\boldsymbol{x}) + \tilde{\boldsymbol{u}}(\boldsymbol{y}) \otimes \nabla_y \right) dV_y \end{array} \right\} \end{aligned} \tag{2.43}$$

The stationarity condition of the functions on the right-hand side of Eq. 2.43 delivers as a necessary condition a BVP to be satisfied by the optimal fluctuation associated with the actual displacement field (in the absence of body forces):

$$\left| \begin{array}{l} -div_y \left\{ C(\boldsymbol{y}) : \left(\mathbf{E}^{sym}(\boldsymbol{x}) - \boldsymbol{\epsilon} \cdot \mathbf{E}^{skew}(\boldsymbol{x}) + \boldsymbol{\epsilon} \cdot \boldsymbol{y} \cdot \mathbf{K}(\boldsymbol{x}) + \tilde{\boldsymbol{u}}(\boldsymbol{y}) \otimes \nabla_y \right) \right\} = \mathbf{0} \\ \tilde{\boldsymbol{u}}(\boldsymbol{y}) \mathrm{Y} - \text{periodic} \end{array} \right. \tag{2.44}$$

The linearity of the solution of BVP 2.44 versus the prescribed kinematic macroscopic loading, tensors $\mathbf{E}^{sym}(\boldsymbol{x})$, $\mathbf{E}^{skew}(\boldsymbol{x})$, $\mathbf{K}(\boldsymbol{x})$, ensures the existence of three localization tensor for the gradient, rotation and curvature loadings, successively the third, the second, and third-order tensors $\boldsymbol{H}^{E^{sym}}(\boldsymbol{y})$, $\boldsymbol{H}^{\mathrm{E}^{skew}}(\boldsymbol{y})$, $\boldsymbol{H}^{K}(\boldsymbol{y})$, such that the fluctuation writes

$$\tilde{\boldsymbol{u}}(\boldsymbol{y}) = \boldsymbol{H}^{E^{sym}}(\boldsymbol{y}) : \boldsymbol{E}^{sym}(\boldsymbol{x}) + \boldsymbol{H}^{E^{skew}}(\boldsymbol{y}) \cdot \mathbf{E}^{skew}(\boldsymbol{x}) + \boldsymbol{H}^{K}(\boldsymbol{y}) : \boldsymbol{K}(\boldsymbol{x}) \tag{2.45}$$

Substituting the expression of the fluctuation, Eq. 2.45, into the displacement field in Eq. 2.42 results in

$$\boldsymbol{u}(\boldsymbol{y},\boldsymbol{x}) = \left((\mathbf{I}_4 \cdot \boldsymbol{y}) + \boldsymbol{H}^{E^{sym}}(\boldsymbol{y})\right) : \mathbf{E}^{sym}(\boldsymbol{x}) + \left(-(\boldsymbol{\epsilon} \cdot \boldsymbol{y}) + \boldsymbol{H}^{E^{skew}}(\boldsymbol{y})\right) \cdot \mathbf{E}^{skew}(\boldsymbol{x}) + \left((\boldsymbol{\epsilon} \cdot (\boldsymbol{y} \otimes \boldsymbol{y})) + \boldsymbol{H}^{K}(\boldsymbol{y})\right) : \mathbf{K}(\boldsymbol{x}) \tag{2.46}$$

Defining the microstrain as the symmetric part of the displacement gradient leads to

$$\boldsymbol{\varepsilon}(\boldsymbol{y},\boldsymbol{x}) = \boldsymbol{u} \otimes^{s} \nabla_y \equiv \mathbf{A}^{\mathrm{E}^{sym}}(\boldsymbol{y}) : \mathbf{E}^{sym}(\boldsymbol{x}) + \mathbf{A}^{E^{skew}}(\boldsymbol{y}) \cdot \boldsymbol{E}^{skew}(\boldsymbol{x}) + \mathbf{A}^{\mathrm{K}}(\boldsymbol{y}) : \mathbf{K}(\boldsymbol{x}) \tag{2.47}$$

wherein $\mathbf{A}^{\mathrm{E}^{sym}}(\boldsymbol{y})$, $\mathbf{A}^{E^{skew}}(\boldsymbol{y})$, and $\mathbf{A}^{\mathrm{K}}(\boldsymbol{y})$ represent the localization tensors relating the microstrains to the macroscopic kinematic variables, viz.

$$\begin{aligned} \mathbf{A}^{\mathrm{E}^{sym}}(\boldsymbol{y}) &= \boldsymbol{I}_4 + \boldsymbol{H}^{E^{sym}}(\boldsymbol{y}) \otimes \nabla_y \\ \mathbf{A}^{E^{skew}}(\boldsymbol{y}) &= -\epsilon + \boldsymbol{H}^{E^{skew}}(\boldsymbol{y}) \otimes \nabla_y \\ \mathbf{A}^{\mathrm{K}}(\boldsymbol{y}) &= \boldsymbol{\epsilon} \cdot \boldsymbol{y} \otimes \mathbf{I}_2 + \boldsymbol{H}^{\mathrm{K}}(\boldsymbol{y}) \otimes \nabla_y \end{aligned} \tag{2.48}$$

Inserting Eq. 2.48 into the BVP of Eq. 2.44 then leads to a new BVP for the micropolar strain localization tensor

$$\left| \begin{array}{l} -div_y \left\{ \boldsymbol{C}(\boldsymbol{y}) : \left[\mathbf{A}^{E^{sym}}(\boldsymbol{y}) : \boldsymbol{E}^{sym}(\boldsymbol{x}) + \mathbf{A}^{E^{skew}}(\boldsymbol{y}) \cdot \boldsymbol{E}^{skew}(\boldsymbol{x}) + \mathbf{A}^{\mathrm{K}}(\boldsymbol{y}) : \boldsymbol{K}(\boldsymbol{x}) \right] \right\} = \mathbf{0} \\ \tilde{\boldsymbol{u}}(\boldsymbol{y}) \mathrm{Y} - \text{periodic} \end{array} \right. \tag{2.49}$$

From a numerical point of view, the two localization tensors are obtained following a sequential scheme: the first gradient localization tensor $\boldsymbol{H}^{E^{sym}}(\boldsymbol{y})$ is obtained by solving the first order unit cell BVP, Eq. 2.49 for nil higher-order kinematic measures $\boldsymbol{E}^{skew} = \boldsymbol{K} = \mathbf{0}$, and the Cosserat curvature localization tensor $\boldsymbol{H}^{K}(\boldsymbol{y})$ is obtained in a second step by solving the second unit cell BVP 2.49. For the choice $\boldsymbol{E}^{sym} = \boldsymbol{K} = \mathbf{0}$, the localization tensor $\boldsymbol{H}^{E^{skew}}(\boldsymbol{y})$ is obtained by solving BVP 2.49, which reflects the antisymmetric part of the macroscopic stress tensor.

2.4.3 Computation of the micropolar properties of lattice

More details about the strategy to compute the localization tensors and effective moduli are given in Appendix A. The unit cell BVPs for the determination of the displacement localization operators are solved with the general open-source code FreeFEM++, as explained synthetically in Fig. 2.2.

Bacigalupo and Gambarotta [100] the chiral lattices as a beam-lattices modeled as a two-dimensional micro-polar continuum (thus restricting to slender ligaments), whereas we employ a complete continuum modeling. Liu et al. [176] derives a 2D micropolar constitutive model for the triangular chiral lattice,

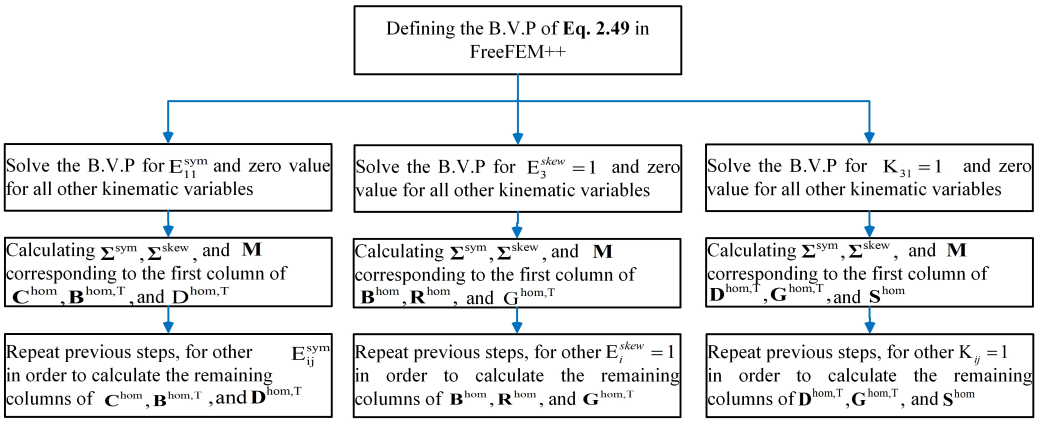

Figure 2.2 Schematic diagram for the computation of the effective micropolar moduli.

based on a Taylor series expansion of the discrete lattice degrees of freedom and the expression of the lattice Hamiltonian. Accordingly, although the homogenization method developed by these authors leads to closed-form effective moduli versus the microstructural lattice parameters, their method is specific to the studied lattices. Contrary to this, our homogenization theory is not specific to the tetrachiral or hexachiral lattice, but it can deliver the entire set of effective micropolar moduli of any centrosymmetric noncentrosymmetric periodic microstructure showing chirality effects.

In the following section, the developed homogenization method will be used to identify a chiral Cosserat constitutive law for architectured materials prone to the coupling between different deformation modes exhibited by the general constitutive law A.3.

2.5 Identification of a chiral Cosserat model for tetrachiral and anti-tetrachiral lattices

In the absence of body forces, $\boldsymbol{\Sigma}^{skew}$ vanishes due to Eq. 2.33, and A.5 receives the following form:

$$\begin{aligned} \boldsymbol{\Sigma}^{sym} &:= \frac{\partial W_M(\boldsymbol{E}^{sym}, \mathbf{E}^{skew}, \boldsymbol{K})}{\partial \boldsymbol{E}^{sym}} \equiv \boldsymbol{C}^{\text{hom}} : \boldsymbol{E}^{sym} + \boldsymbol{D}^{\text{hom}} : \boldsymbol{K}; \\ \boldsymbol{M} &:= \frac{\partial W_M(\boldsymbol{E}^{sym}, \mathbf{E}^{skew}, \boldsymbol{K})}{\partial \boldsymbol{K}} \equiv \boldsymbol{D}^{\text{hom},T} : \boldsymbol{E}^{sym} + \boldsymbol{S}^{\text{hom}} : \boldsymbol{K} \end{aligned} \tag{2.50}$$

The constitutive law of the non-centrosymmetric 2D chiral lattice (Fig. 2.3) can be arranged in matrix format as:

$$\begin{pmatrix} \Sigma_{11}^{sym} \\ \Sigma_{22}^{sym} \\ \Sigma_{12}^{sym} \\ \Sigma_{21}^{sym} \\ M_{13} \\ M_{23} \end{pmatrix} = \begin{pmatrix} \mathrm{C}_1 & \mathrm{C}_2 & -\mathrm{C}_4 & -\mathrm{C}_4 & -\mathrm{D}_1 & -\mathrm{D}_2 \\ \mathrm{C}_2 & \mathrm{C}_1 & \mathrm{C}_4 & \mathrm{C}_4 & \mathrm{D}_2 & \mathrm{D}_1 \\ -\mathrm{C}_4 & \mathrm{C}_4 & \mathrm{C}_3 & \mathrm{C}_3 & \mathrm{D}_3 & \mathrm{D}_3 \\ -\mathrm{C}_4 & \mathrm{C}_4 & \mathrm{C}_3 & \mathrm{C}_3 & \mathrm{D}_3 & \mathrm{D}_3 \\ -\mathrm{D}_1 & \mathrm{D}_2 & \mathrm{D}_3 & \mathrm{D}_3 & \gamma_1 & \gamma_2 \\ -\mathrm{D}_2 & \mathrm{D}_1 & \mathrm{D}_3 & \mathrm{D}_3 & \gamma_2 & \gamma_1 \end{pmatrix} \begin{pmatrix} E_{11}^{sym} \\ E_{22}^{sym} \\ E_{12}^{sym} \\ E_{21}^{sym} \\ \Phi_{,x_1} \\ \Phi_{,x_2} \end{pmatrix} \tag{2.51}$$

Relation 2.51 contains three classical Cauchy elastic constants $\mathrm{C}_{1,2,3}$ and the parameter C_4 characterizing

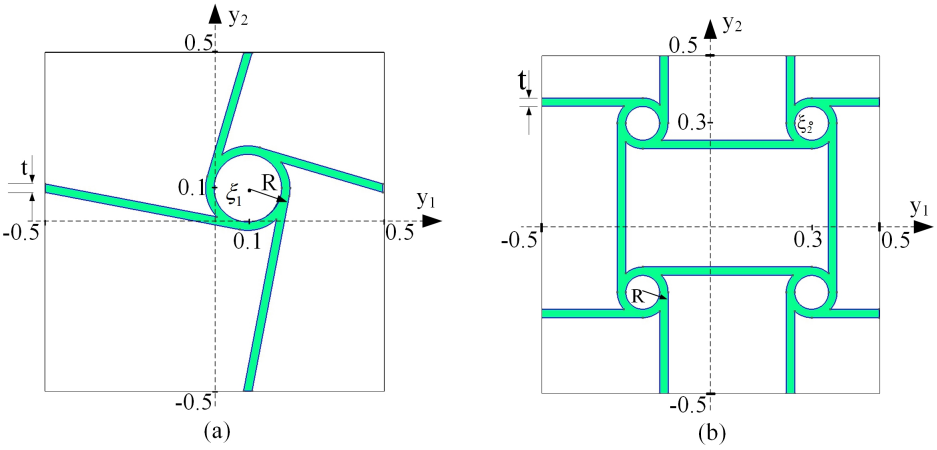

Figure 2.3 (left) Non-centrosymmetric anti-tetrachiral unit cell, (right) Non-centrosymmetric tetrachiral unit cell.

the chiral effect between the normal stress and the shear strain E_{12}^{sym}. Two new parameters $D_{1,2}$ characterize the coupling between normal stress and rotation gradients $\Phi_{,x_1}, \Phi_{,x_2}$. Similarly, the parameter D_3 characterize the coupling between shear stress and the rotation gradients $\Phi_{,x_1}, \Phi_{,x_2}$. The micropolar coefficients relating the bending moment M_{13} (resp. M_{23}) and the curvature $\Phi_{,x_1}$ (resp. $\Phi_{,x_2}$) are denoted as $\gamma_{1,2}$.

For tetrachiral lattices the coefficients $D_{1,2,3}$ are only activated for non-centrosymmetric microstructures, whereas they vanish in the centrosymmetric case. In all of the cases for anti-tetrachiral lattice the coefficients C_4, D_3, and γ_2 are zero.

Considering the plane strain condition, and according to the 2D Cauchy stiffness matrix $\boldsymbol{C}^{\text{hom}}$ the effective behavior of the tetrachiral lattices and the anti-tetrachiral lattices can be considered as a monoclinic elastic solid and orthotropic elastic solid, respectively. The effective engineering material parameters of the tetrachiral and anti-tetrachiral lattices are evaluated in B.1.

The homogenization method exposed in the previous section for chiral Cosserat mechanics is applied to determine the material constants in Eq. 2.51. We checked numerically that the obtained effective chiral Cosserat moduli are size-independent (they take the same values when repeating the unit cell), so they are intrinsic to the microstructure. Thereby, the proposed homogenization method does not exhibit the spurious size-dependency of the existing literature schemes dealing with homogenization towards generalized continua. Corrections to these spurious effects have been recently proposed for the strain gradient effective continuum [81, 82]. The last authors added a body force field to the quadratic boundary conditions and a correction of the localization tensor.

2.5.1 Validation of the computed effective moduli

As a specific case, the numerical calculation of the effective moduli in relation 2.51 are shown in relations 2.52 and 2.52 for the following geometry of the tetrachiral and anti-tetrachiral lattices, respectively

(Fig. 2.3). The following values of geometrical and mechanical parameters indicated in Table 2.1; R, t, ξ, and b are the outer radius of the central ring, the thickness of the ligaments, the location of the center of the ring, and the out-of-plane lattice thickness (considered only in the 3D FE simulation), respectively.

Table 2.1 Values of the geometrical and mechanical parameters of the tetrachiral and anti-tetrachiral lattices.

Elastic modulus (MPa)	Poisson's ratio	R (mm)	t (mm)	ξ_1 (mm)	ξ_2 (mm)	b (mm)
1400	0.3	0.25	0.05	(0.1,0.1)	(0.3,0.3)	0.2

$$\begin{pmatrix} \Sigma_{11}^{sym} \\ \Sigma_{22}^{sym} \\ \Sigma_{12}^{sym} \\ \Sigma_{21}^{sym} \\ M_{13} \\ M_{23} \end{pmatrix} = \begin{pmatrix} 9.01 & -6.12 & -4.37 & -4.37 & -1.15 & -0.8 \\ & 9.01 & 4.37 & 4.37 & 0.8 & 1.15 \\ & & 2.8 & 2.8 & 0.58 & 0.58 \\ & & & 2.8 & 0.58 & 0.58 \\ & sym & & & 0.41 & 0.23 \\ & & & & & 0.41 \end{pmatrix} \begin{pmatrix} E_{11}^{sym} \\ E_{22}^{sym} \\ E_{12}^{sym} \\ E_{21}^{sym} \\ \Phi_{,x_1} \\ \Phi_{,x_2} \end{pmatrix} \tag{2.52}$$

$$\begin{pmatrix} \Sigma_{11}^{sym} \\ \Sigma_{22}^{sym} \\ \Sigma_{12}^{sym} \\ \Sigma_{21}^{sym} \\ M_{13} \\ M_{23} \end{pmatrix} = \begin{pmatrix} 8.6 & -8.2 & 0 & 0 & -0.86 & -0.82 \\ -8.2 & 8.6 & 0 & 0 & 0.82 & 0.86 \\ & & 0.134 & 0.134 & 0 & 0 \\ & & & 0.134 & 0 & 0 \\ & sym & & & 0.328 & 0 \\ & & & & & 0.328 \end{pmatrix} \begin{pmatrix} E_{11}^{sym} \\ E_{22}^{sym} \\ E_{12}^{sym} \\ E_{21}^{sym} \\ \Phi_{,x_1} \\ \Phi_{,x_2} \end{pmatrix} \tag{2.53}$$

2.5.1.1 Application of periodic Boundary conditions (PBCs in short) to capture effective moduli

PBCs are applied to the cubic unit cell of Fig. 2.4 to establish the material's bulk response without any edge effect. This boundary condition will ensure that the deformed shape of the unit cell on external surfaces remains periodic.

The periodicity conditions on the boundary ∂V are [181]:

$$u_i = \bar{\varepsilon}_{ik} + \hat{u}_i \tag{2.54}$$

where $\hat{u}_i$ is the periodic fluctuating part of the displacement, and $\bar{\varepsilon}_{ik}$ is the average strain. Eq. 2.54 contains the unknown fluctuating part of the displacement (the method applies for both periodic and non-periodic microstructures), thus taking the difference of the displacement over two opposite pairs of DOFs on the unit cell boundary entails the following relative boundary conditions on the opposite boundary surfaces of the unit cell

$$u_i^{j+} - u_i^{j-} = \bar{\varepsilon}_{ik} \left(y_k^{j+} - y_k^{j-} \right) = \bar{\varepsilon}_{ik} \Delta y_k^j \tag{2.55}$$

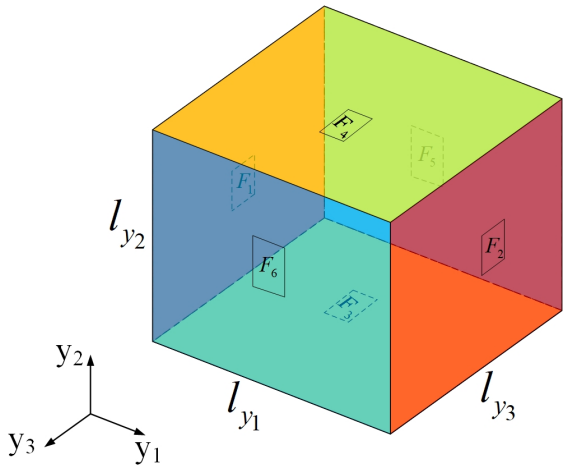

Figure 2.4 Schematic boundary faces of the unit cell.

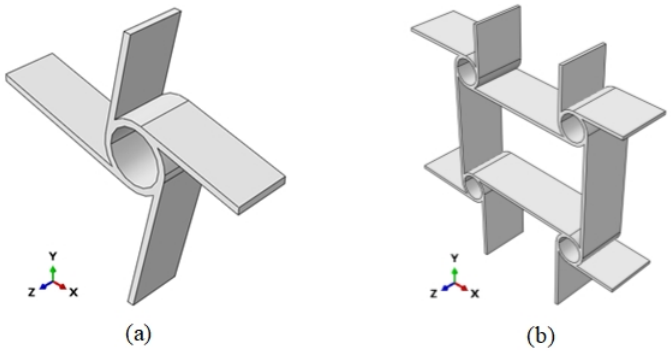

Figure 2.5 Non-centrosymmetric 3D model of: (a) tetrachiral unit cell, (b) anti-tetrachiral unit cell.

where indices $j+$ and $j-$ denote the positive and negative y_j directions, respectively. It can be seen from Eq. 2.55 that although the difference of the displacements on the two opposite boundary surfaces is determined, the individual displacement component is a function of the coordinates, and a plane does not necessarily remain planar after deformation. In order to validate the previous 2D plane strain micropolar constitutive law, the 3D FE computations are performed for the same geometries. Calculating the complete 3D rigidity matrix components requires 21 elementary tests, namely, six tests to evaluate the tensile and shear components and fifteen tests for computing the coupling terms between tension and shear. The energy equivalence principle is used in the form of the extended Hill macrohomogeneity condition stated in Eq. 2.13, here used in an actual (non-virtual) form. The required PBCs for evaluating each classical rigidity component are listed in Appendix C.

The following non-centrosymmetric unit cells are simulated with the general-purpose ABAQUS FE code using a 3D model for the tetrachiral and anti-tetrachiral unit cells, adopting geometrical and mechanical properties indicated in Table 2.1. The standard element of type C3D20 with 19000 elements have been used for these analyses. Applying the PBCs of Appendix C on the unit cells shown in Fig. 2.5 leads to the following rigidity matrix:

$$\boldsymbol{\Sigma} = \boldsymbol{C} : \boldsymbol{E} \tag{2.56}$$

For the present example of Fig. 2.5 with parameters indicated in Table 2.1, the values of the effective 3D Cauchy moduli for tetrachiral and anti-tetrachiral unit cells are computed in Eq. 2.57 and Eq. 2.58, respectively:

$$\begin{Bmatrix} \Sigma_{11} \\ \Sigma_{22} \\ \Sigma_{33} \\ \Sigma_{13} \\ \Sigma_{23} \\ \Sigma_{12} \end{Bmatrix} = \begin{bmatrix} 9.4335 & -4.8977 & 0.52 & 0 & 0 & -4.578 \\ & 9.4335 & 0.51 & 0 & 0 & 4.578 \\ & & 134.3 & 0 & 0 & 0 \\ & & & 20.86 & 0 & 0 \\ & Sym & & & 20.86 & 0 \\ & & & & & 1.39 \end{bmatrix} \begin{Bmatrix} E_{11} \\ E_{22} \\ E_{33} \\ 2E_{13} \\ 2E_{23} \\ 2E_{12} \end{Bmatrix} \tag{2.57}$$

$$\begin{Bmatrix} \Sigma_{11} \\ \Sigma_{22} \\ \Sigma_{33} \\ \Sigma_{13} \\ \Sigma_{23} \\ \Sigma_{12} \end{Bmatrix} = \begin{bmatrix} 8.944 & -8.364 & 0.52 & 0 & 0 & 0 \\ & 8.944 & 0.51 & 0 & 0 & 0 \\ & & 145 & 0 & 0 & 0 \\ & & & 23.98 & 0 & 0 \\ & Sym & & & 23.98 & 0 \\ & & & & & 0.066 \end{bmatrix} \begin{Bmatrix} E_{11} \\ E_{22} \\ E_{33} \\ 2E_{13} \\ 2E_{23} \\ 2E_{12} \end{Bmatrix} \tag{2.58}$$

The effective 2D micropolar rigidity matrix indicated in Eqs. 2.52 and 2.53 can be compared respectively with the effective 3D Cauchy rigidity matrix of Eqs. 2.57 and 2.58 considering the in-plane x-y coefficients. The moduli C_1, C_2, C_3, $-C_4$, and C_4 in Eq. 2.51, correspond to the set of rigidity coefficients C_{11}, C_{12}, C_{66}, C_{16}, and C_{26}, respectively. Comparing the corresponding rigidity matrix coefficients of the 3D computation with the 2D rigidity matrix predicted by the proposed homogenization method shows a very good agreement, with a maximum relative difference of about 4.75%.

To validate the non-classical components of the rigidity matrix of Eq.(51), related to the curvature components $\Phi_{,\mathrm{x}_1}$ and $\Phi_{,\mathrm{x}_2}$, the PBCs listed in Table 2.2 are applied over the unit cell boundaries.
These boundary conditions should be written in terms of translational degrees of freedom. It has been concluded that in the absence of the body forces $\mathrm{E}^{\mathrm{skew}} = 0$; substituting this result in the last relation in Eq. 2.19 leads to the following expression of the rotation vector versus deformation field:

$$\Phi_i = \epsilon_{ijk} \left(u_{j,k} - u_{k,j} \right) \tag{2.59}$$

Substituting Eq. 2.59 into the last relation of Eq. 2.18, and considering the 2D case gives the relations:

$$\begin{aligned} \Phi_{3,1} &= \mathrm{K}_{31} = 2u_{1,21} - 2u_{2,11} \\ \Phi_{3,2} &= \mathrm{K}_{32} = 2u_{1,22} - 2u_{2,12} \end{aligned} \tag{2.60}$$

According to Eq. 2.51, to calculate modulus γ_1, constant values of $\Phi_{,x_1}$ or $\Phi_{,x_2}$ should be applied over the unit cell boundaries. To this end, Eq. 2.60 leads to:

$$\begin{aligned} \Phi_{3,1} = cte \quad &\rightarrow \quad u_1 = -y_1 y_2 \Phi_{3,1}; \qquad u_2 = y_1^2 \Phi_{3,1} \\ \Phi_{3,2} = cte \quad &\rightarrow \quad u_1 = -y_2^2 \Phi_{3,2}; \qquad u_2 = y_1 y_2 \Phi_{3,2} \end{aligned} \tag{2.61}$$

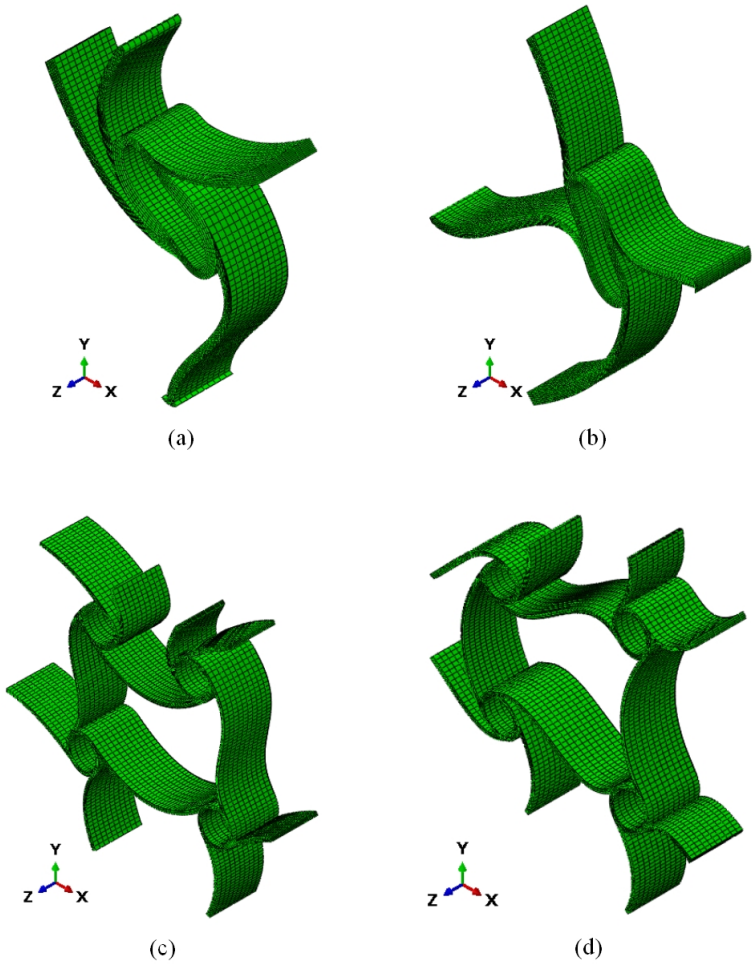

Figure 2.6 Non-classical deformation modes: (a) Tetrachiral: $\Phi_{,x_1}$, (b) Tetrachiral: $\Phi_{,x_2}$, (c) Anti-tetrachiral: $\Phi_{,x_1}$, (d) Anti-tetrachiral: $\Phi_{,x_2}$.

It should be noted that for calculating coefficient γ_2, the two microcurvatures $\Phi_{,x_1}$ and $\Phi_{,x_2}$ should be applied simultaneously over the unit cell boundaries.

Table 2.2 Boundary constraint equations and corresponding classical rigidity components.

Applied value	Rigidity Components	PBCs ($\Phi_{,x_1},\ \Phi_{,x_2} = 1$)
$\Phi_{,x_1}$	$\gamma_1 = \frac{2U^{cell}}{V^{cell}}$	${u_{y_1}}^{F2} - {u_{y_1}}^{F1} + l_{y_1}y_2\Phi_{,x_1} = 0, \quad {u_{y_1}}^{F4} - {u_{y_1}}^{F3} + l_{y_2}y_1\Phi_{,x_1} = 0$
$\Phi_{,x_2}$	$\gamma_1 = \frac{2U^{cell}}{V^{cell}}$	${u_{y_2}}^{F2} - {u_{y_2}}^{F1} - l_{y_1}y_2\Phi_{,x_2} = 0, \quad {u_{y_2}}^{F4} - {u_{y_2}}^{F3} - l_{y_2}y_1\Phi_{,x_2} = 0$

Considering the non-centrosymmetric unit cells in Fig. 2.5 for the set of parameters listed in Table 2.1, and applying the abovementioned boundary conditions in Table 2.2 results in values of γ_1 equal to 0.422 and 0.341, and γ_2 equal to 0.237 and 0 for tetrachiral and anti-tetrachiral lattices, respectively. Comparing these values with the predictions of the micropolar model shows a quite good agreement, with a relative error of about 4%. The non-classical modes of deformation related to the microcurvatures $\Phi_{,x_1}$ and $\Phi_{,x_2}$, are depicted in Fig. 2.6. Although the unit cells of the tetrachiral and anti-tetrachiral lattices are non-centrosymmetric, their periodic repetition over the entire lattice generates a centrosymmetric structure.

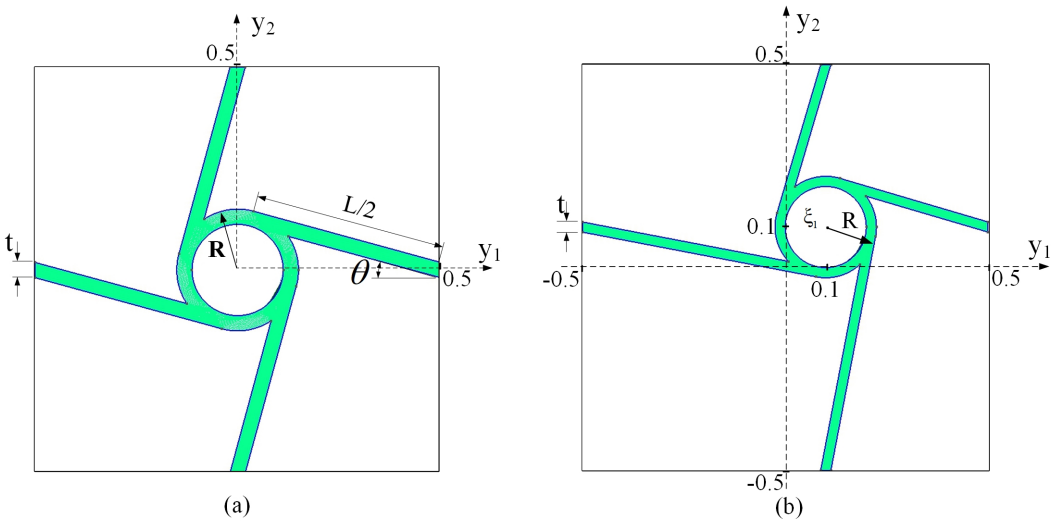

Figure 2.7 (a) Centrosymmetric tetrachiral lattice, (b) Non-centrosymmetric tetrachiral lattice.

Convergence to a nil value of the coupling coefficients between Cauchy and micropolar elasticity has been checked, resulting in non-centrosymmetry being an artifact not reflecting an intrinsic non-centrosymmetry of the pattern within the unit cell.

The effective mechanical properties of centrosymmetric and non-centrosymmetric structures as a function of their geometrical characteristics are analyzed in the next part.

2.5.2 Sensitivity of the effective tetrachiral unit cell moduli to its microstructural parameters

In order to provide perception for the mechanical behavior of the chiral lattice, two particularly classical elastic constants C_1 and C_3, the chiral coefficient C_4, and the micropolar terms γ_1 are depicted in Fig. 2.8 versus the slenderness ratio $\eta = t/L$, defined as the ratio of strut thickness to its length and the ring radius R. It is observed in Fig. 2.8 that a non-regular behavior of the rigidity matrix coefficients appears when varying the radius of the ring. The chiral coefficient C_4 decreases with the slenderness ratio and the ring radius R, as shown in Fig. 2.8. Moreover, the slenderness ratio has a strong influence on the values of the effective Cauchy moduli and chiral coefficient C_4; this influence has a recurring feature, as it holds for all effective moduli. This example indicates that geometrical properties contribute enormously to the rigidity matrix in terms of their sensitivity to the mechanical properties of the individual lattices constituents. Results in Fig. 2.8 show a strong influence of the slenderness ratio on the tensile rigidity coefficient C_1 and a sensitive effect on both chiral coefficient C_4 and micropolar constant γ_1. On the contrary, the micropolar coefficient γ_1 is not sensitive to variations of the ring radius and slenderness ratio.

A non-centrosymmetric tetrachiral lattice, obtained by shifting the center of the ring with respect to the center of the unit cell, is analyzed; mainly, the effect of the coupling coefficients $D_{1,2,3}$ for different

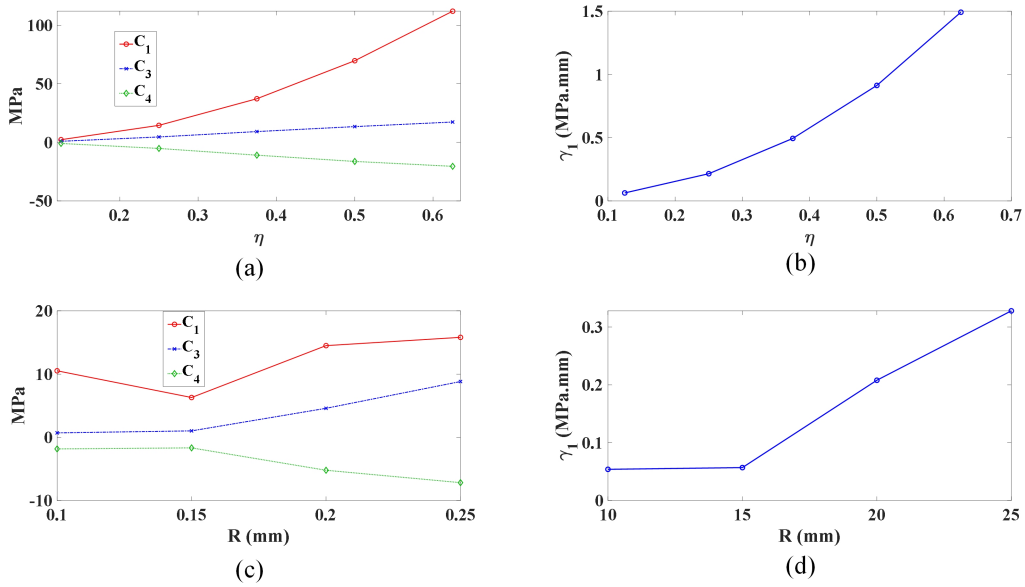

Figure 2.8 Variation of the effective rigidity coefficients versus: (a, b) the slenderness ratio η, (c, d) the ring radius R.

structures are investigated. The center of the square and circle for the tetrachiral structure is on the origin of the coordinate, as indicated in Fig. 2.7(a), resulting in a centrosymmetric structure. The coordinate for each point in Fig. 2.9 defined by the vector (x_1, x_2) represents the location of the center of the unit cell from the centrosymmetric structure (for which the center is the vector $(0, 0)$). Fig. 2.9 shows a high sensitivity of the chiral coefficients and coupling terms to the relative position of the ring center for non-centrosymmetric unit cell designs, with however a less marked influence of this geometrical parameter on coupling coefficient D_3.

In order to provide a comparison for the mechanical behavior of the tetrachiral and anti-tetrachiral lattices, two particularly classical elastic constants C_1 and C_3, the chiral coefficient C_4 the coupling coefficient D_1 and the micropolar term γ_1 are depicted in Fig. 2.10 versus the volume fraction, defined

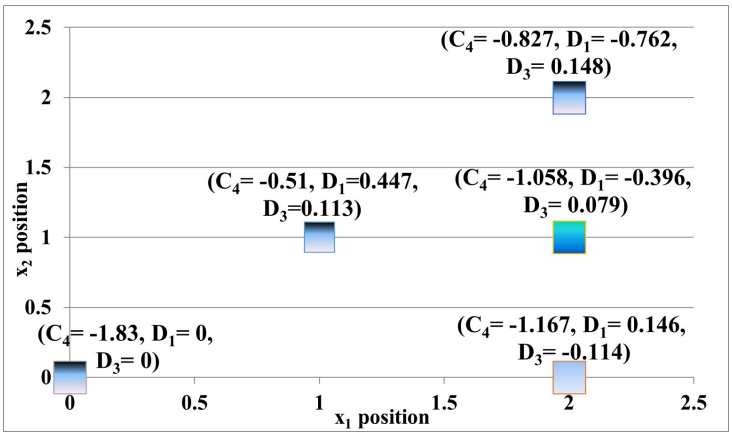

Figure 2.9 Chiral coefficient C_4, coupling terms D_1 and D_3 in function of the position of the center of the ring with respect to the center of gravity of the square unit cell of unit size.

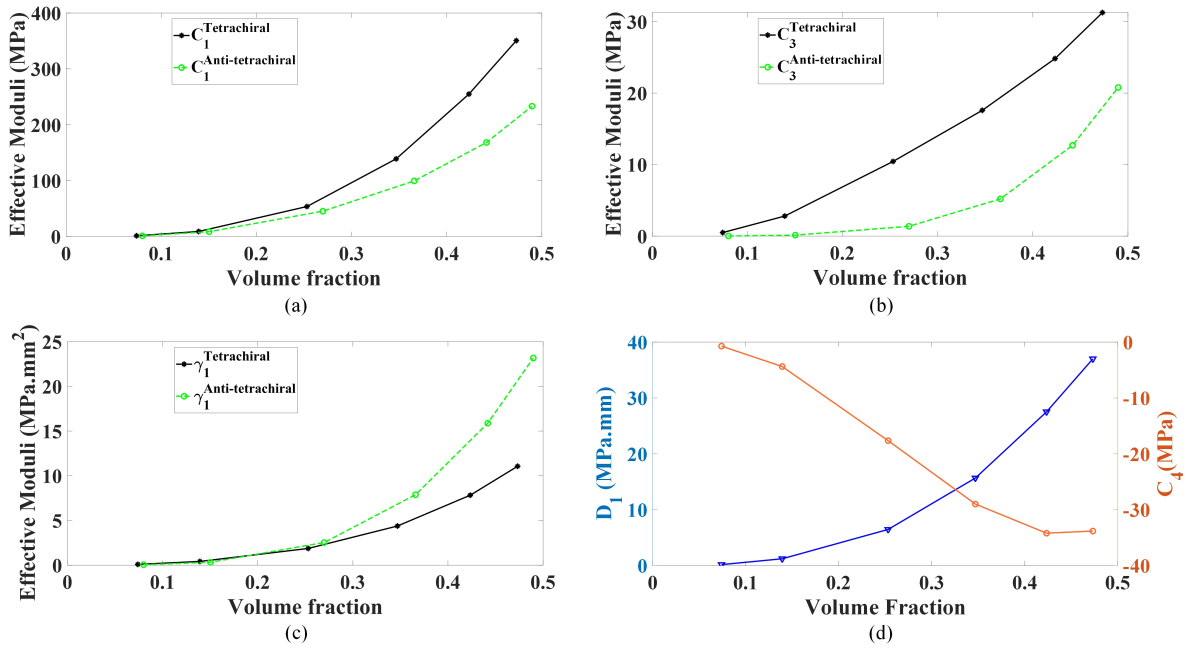

Figure 2.10 Variation of the effective rigidity coefficients versus volume fraction: (a) C_1, (b) C_3, (c) γ_1, (d) D_1 and C_4.

as the ratio of occupied volume with material to the volume of unit cell outer boundaries. It is observed in Fig. 2.10 that regular Cauchy effective coefficients rise with an increase in the volume fraction, and in the same volume fraction tetrachiral has stiffer behavior compared with anti-tetrachiral lattice. The micropolar coefficient γ_1 increases with rising in the volume fraction (V_f) and for $V_f \geq 0.25$ take the higher values for anti-tetrachiral. The chiral coefficient C_4, which only exists for the tetrachiral lattice, decreases rapidly with the volume fraction and in $V_f \approx 0.42$ start to increase to the smaller absolute values. Results in Fig. 2.10 show a strong influence of the volume fraction on the coupling rigidity coefficient D_1.

2.5.3 Composite unit cell

The 3D non-centrosymmetric composite unit cell depicted in Fig. 2.11 is considered; the unit cell is assumed to have a much larger thickness in the y_3 direction compared to its plane dimensions so that a plane strain model is adopted. The center of the inclusion with a tetrachiral shape is located at point $(y_1, y_2) = (0.1, 0.1)$, resulting in a non-centrosymmetric unit cell. The properties of the composite constituents, a carbon reinforcement within an epoxy matrix, are indicated in Table 2.3.

Table 2.3 Mechanical properties of the Fiber and Matrix within the composite unit cell of Fig. 2.11 [7].

	Fiber (Carbon)	Matrix (Epoxy)
Elastic modulus (MPa)	228000	1400
Poisson's ratio	0.26	0.3

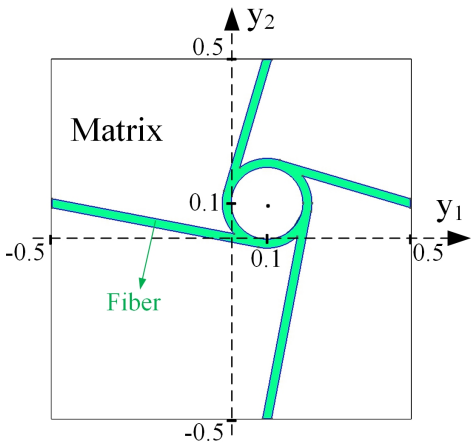

Figure 2.11 Non-centrosymmetric fibrous composite unit cell.

Fig. 2.12 shows the variation of the effective moduli components versus the inclusion's volume fraction. Fig. 2.12(b) shows that by reducing the volume fraction of the inclusion, the coupling components D_1 and D_3 tend to zero, by the fact that for a homogeneous material, the coupling moduli have to vanish.

2.5.4 Analysis of unit cell size effects

In order to perform the size independency analysis, a 2D centrosymmetric composite with the tetrachiral inclusions is considered, as pictured in Fig. 2.13. The lattices are aligned in the third out-of-plane direction and are periodically distributed in the (y_1, y_2) plane. The elastic coefficients are given in Table 2.1 and the geometrical parameters are selected as R = 0.2 mm and t = 0.075 mm related to the outer radius and thickness, respectively. In Fig. 2.13, three windows of analysis containing N = 1 , 4, 9 irreducible cells are shown to investigate the possible effects of unit cell size on the effective mechanical properties of the lattice structure. The distribution of the micro Cosserat component m_{13} in y_2 direction is evaluated, resulting from the components $\Phi_{,x}$ of the micropolar deformation. To this end, the window of analysis is subjected to the applied kinematic loading $\Phi_{,x} = 1$; the variation of m_{13} is computed along the vertical line crossing the centers of the inclusion (the dashed line in Fig. 2.13, and the results are shown in Fig. 2.14. For all of the repetitions, m_{13} takes the same values over the boundaries, and the average values are equal for all of the figured repetitions. For $2by2$ and $3by3$ repetitions, some fluctuations on m_{13} curve can be observed which are related to the interface between the inclusion and void phases. As indicated in Fig. 2.15(a), the effective Cauchy coefficients are invariant to the number of unit cells shown in Fig. 2.13. Moreover, Fig. 2.15(b) shows the fast convergence of the micropolar moduli, which results in the size-independency of the represented homogenization method. Note nevertheless that more than a single unit cell is needed to reach the intrinsic higher-order moduli.

The deformed shapes due to the two bending modes, $\Phi_{,x}$ and $\Phi_{,\mathrm{y}}$ are shown for the $3by3$ repetition of the unit cell in Fig. 2.16. To investigate the accuracy of modeling of the lattice structures by a micropolar continuum, the relative contribution of the fluctuation energy to the total macroscopic energy for the

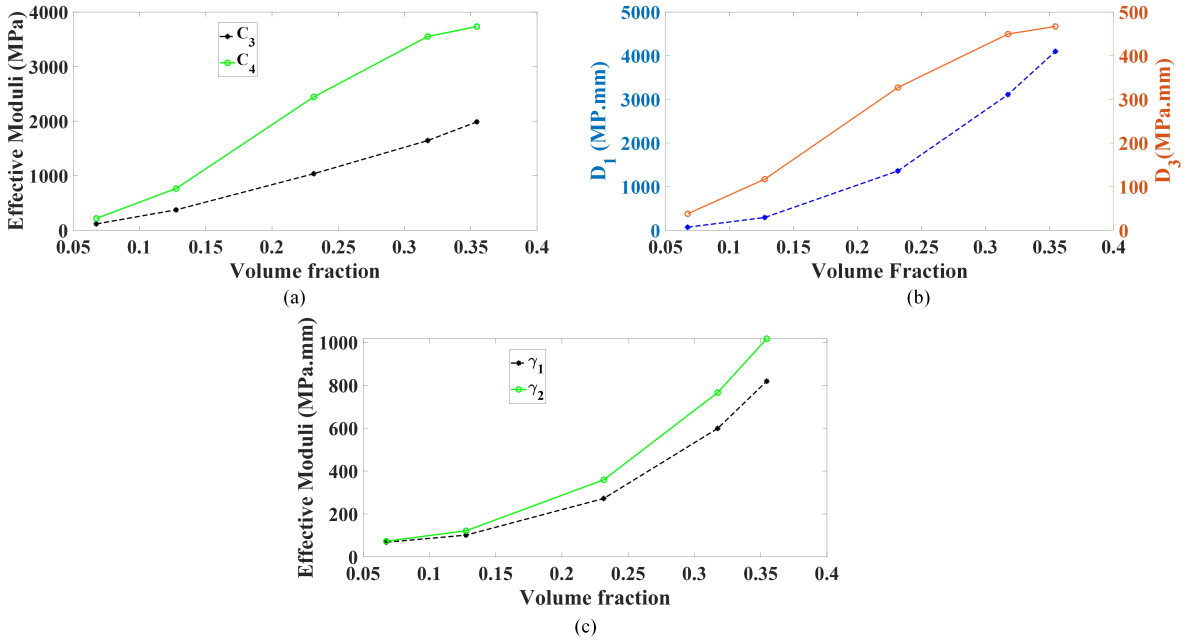

Figure 2.12 Variation of the effective moduli with the inclusion volume fraction.

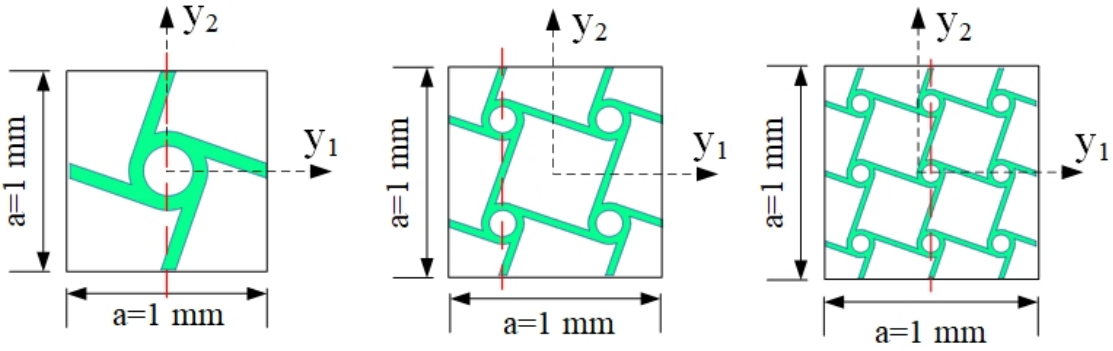

Figure 2.13 Windows of analysis including an increasing number of repetitions of the irreducible unit cells.

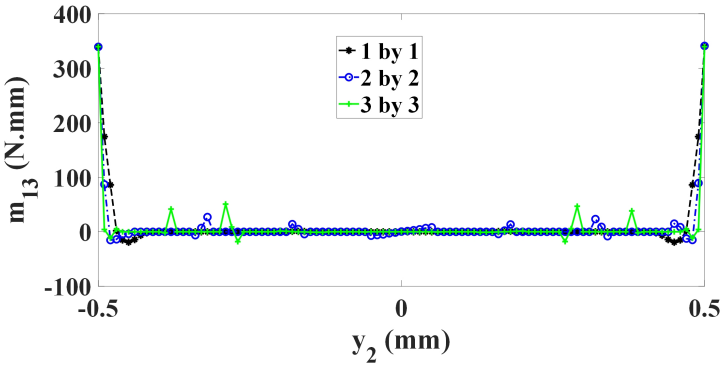

Figure 2.14 Distribution of the m_{13} under the kinematic loading $\Phi_{,x} = 1$.

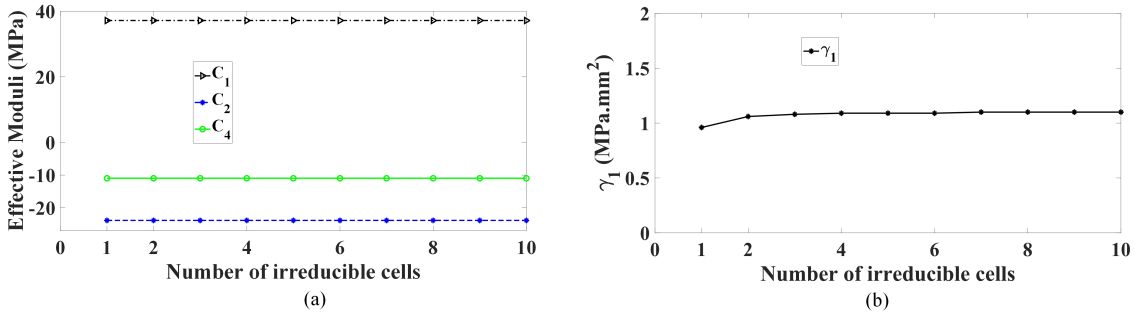

Figure 2.15 Variation of the effective moduli versus the number of irreducible unit cells, N: (a) Cauchy effective moduli $C_{1,2,4}$, (b) Micropolar effective modulus γ_1.

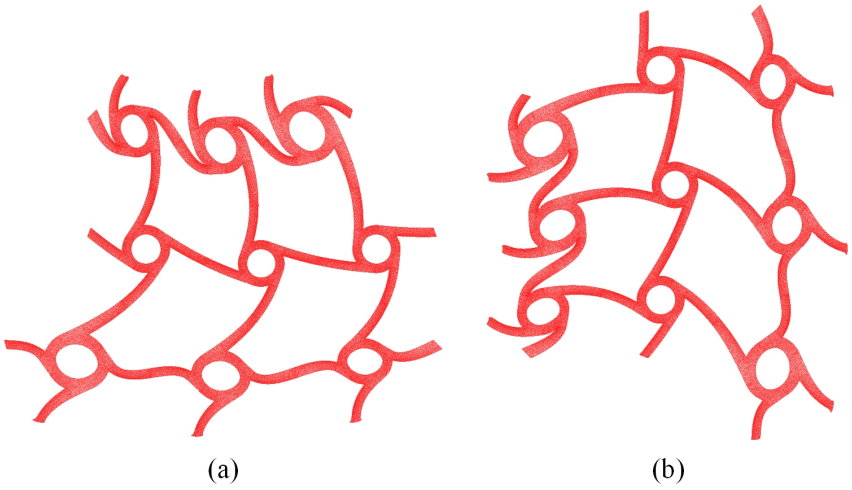

Figure 2.16 Deformed shape of the $3by3$ repetition of the tetrachiral unit cell under bending mode: (a) $\Phi_{,x}$, (b) $\Phi_{,y}$.

successive components of the Cauchy strain and micropolar kinematic measures are evaluated. Table 2.4 shows the macroscopic, microscopic, and fluctuation energies for the tetrachiral unit cell of Fig. 2.3; these energetic terms are successively defined as

$$W_{Macro} = \boldsymbol{\Sigma}^{sym} : \mathbf{E}^{sym} + \boldsymbol{\Sigma}^{skew} \cdot \mathbf{E}^{skew} + \boldsymbol{M} : \mathbf{K}$$
$$W_{micro} = \left\langle \underset{\sim}{\boldsymbol{\sigma}} : \underline{\underline{\boldsymbol{\xi}}}(\underline{\mathbf{u}}^{\hom} + \underline{\tilde{\mathbf{u}}}) \right\rangle_Y$$
$$W_{fluctuation} = \left\langle \underset{\sim}{\boldsymbol{\sigma}} : \underline{\underline{\boldsymbol{\xi}}}(\underline{\tilde{\mathbf{u}}}) \right\rangle_Y$$

Table 2.4 Comparison between the macroscopic and microscopic energies and contribution of the fluctuation energy to the total deformation energy(energy unit is N/m^2).

Applied component	Macroscopic Energy	Total microscopic energy	Fluctuation Energy	Contribution of the fluctuation (%)
E_{11}	18.5904	18.4975	-0.09287	0.502
E_{22}	18.5896	18.4895	-0.1001	0.5
E_{12}	4.5937	4.5801	-0.0068	0.148
$\Phi_{,x}$	0.240672	0.228777	-0.01189	5.197
$\Phi_{,y}$	0.24067	0.228776	-0.01189	5.197

Overall, the maximum energy of the fluctuation is about 0.5% for the Cauchy deformation modes. For the micropolar mode, the fluctuating part of the energy is about 5%, showing that the adopted micropolar effective continuum is representative of the initially heterogeneous microstructure with reasonable accuracy in the mechanical response.

2.5.5 Homogeneous micropolar BVP

Multiplying Eqs. 2.27 and 2.28 by virtual displacement and rotation, variables $\boldsymbol{v}$ and φ, respectively and integrating over the macroscopic homogeneous volume V(x) depicted in Fig. 2.1, leads to the following relations.

$$-\int_{V(x)} \boldsymbol{\Sigma} : \nabla\nu \, dV(x) + \int_{\partial V(x)} \boldsymbol{\Sigma} \cdot \nu \, dS(x) = 0 \tag{2.62}$$
$$-\int_{V(x)} \boldsymbol{M} : \nabla\varphi \, dV(x) + \int_{\partial V(x)} \boldsymbol{M} \cdot \varphi \, dS(x) + \int_{V(x)} \boldsymbol{\epsilon} : \boldsymbol{\Sigma}^{skew} \cdot \varphi \, dV(x) = 0 \tag{2.63}$$

Substituting the micropolar constitutive law, Eq. A.5 into 2.63 and subtracting Eq. 2.62 from Eq. 2.63 leads to the following Homogeneous micropolar BVP

$$\int_{V(x)} \left(\mathbf{E}^{sym}(\nu) + \mathbf{E}^{skew}(\nu) \right) : \left(\boldsymbol{\Sigma}^{sym} + \boldsymbol{\Sigma}^{skew} \right) dV(x) + \int_{V(x)} \Phi(\varphi) \cdot \boldsymbol{\epsilon} : \boldsymbol{\Sigma}^{skew} \, dV(x)$$
$$-\int_{V(x)} \mathrm{K}(\varphi) : \left(\boldsymbol{D}^{\hom,T} : \mathbf{E}^{sym}(u) + \boldsymbol{G}^{\hom,T} : \mathbf{E}^{skew}(u) + \boldsymbol{S}^{\hom} : \mathrm{K}(\phi) \right) dV(x) - \int_{\partial V(x)} \boldsymbol{\Sigma} \cdot \nu \, dS(x) + \int_{\partial V(x)} \boldsymbol{M} \cdot \varphi \, dS(x) = 0$$

2.5.5.1 Axial loading of the lattice structured plate

In this section, the benchmark example of the tetrachiral lattices is considered in a plane strain condition to underline the correctness and accuracy of the proposed micropolar model. The lattice structure shown

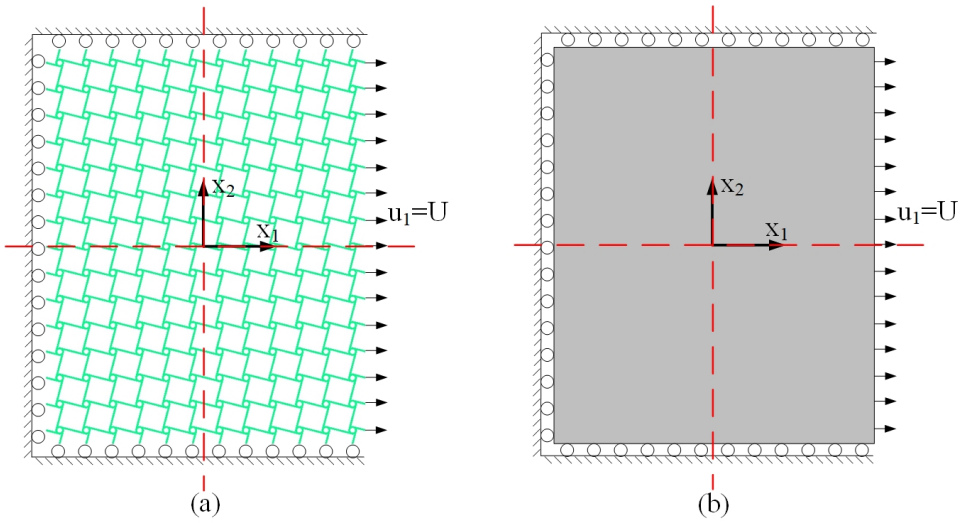

Figure 2.17 (a) Full periodic network and (b) Homogenized representation of a tetra-chiral plate consisting of 12×15 unit cells.

in Fig. 2.17 is considered, comprising a sufficient number of 12×15 tetrachiral unit cells, such that edge effects can be minimized in the central part of the network. Roller boundary conditions are imposed at the left, bottom, and top surfaces, and a uniform displacement U is prescribed along the right surface. A simple uniaxial loading case is considered to illustrate the capability of the proposed homogenization approach in capturing the coupling effect between rotational and stretching mechanisms. The material parameters of the isotropic base material are chosen to compare the current micropolar model predictions with micromorphic results of [111]: the elastic modulus is E = 200 GPa, and Poisson's ratio is $\nu = 0.3$. The reaction forces along the x_1 direction is plotted in Fig. 2.18 for both the homogeneous micropolar plate and the whole periodic lattice. The homogenized micropolar model can predict the force-displacement responses of the lattice structure with a maximum error of about 11%. To confirm the local predictive capability of the presented micropolar model, vertical and horizontal displacements on the dashed red lines in Fig. 2.17 are compared with Biswas's micromorphic results [111]. Fig. 2.19 shows that the proposed micropolar model coincides with the results of the Biswas, and it can accurately predict the response of the plate for the regions that are far enough from the boundaries. The displacement contours u_1 and u_2 for the homogenized plate and tetrachiral lattice structure are shown in Fig. 2.20, illustrating that the homogenous micropolar plate reproduces the local displacement pattern shown over the entire lattice.

2.6 Construction of an enriched Timoshenko beam theory with chirality and non-centrosymmetric effects

To demonstrate the unconventional mechanical response of non-centrosymmetric chiral metamaterials at the structural level, the mechanical response of a cantilever beam made from the previously incorporated non-centrosymmetric tetrachiral metamaterial unit cells is analyzed in detail. To that scope, an extended

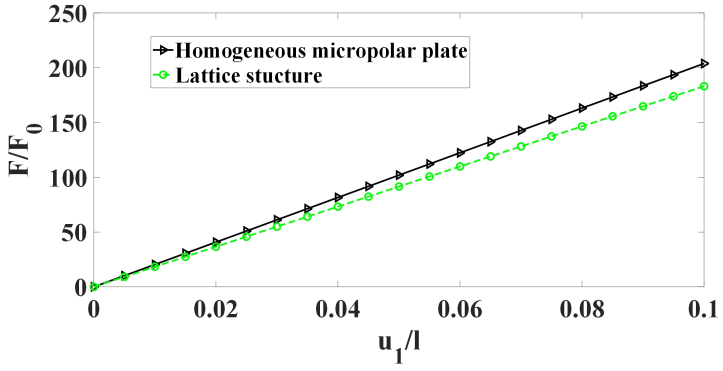

Figure 2.18 Load-displacement responses of the tetrachiral plate, under axial loading normalized with respect to $F_0 = 1$.

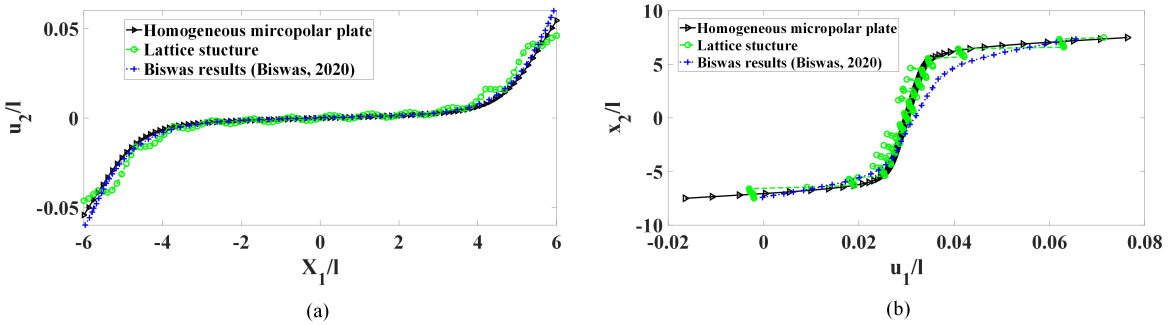

Figure 2.19 (a) Normalized displacement profile u_2 along the horizontal centerline of the plate, (b) Normalized displacement profile u_1 along the vertical centerline of the plate at prescribed displacement $U = 0.06l$.

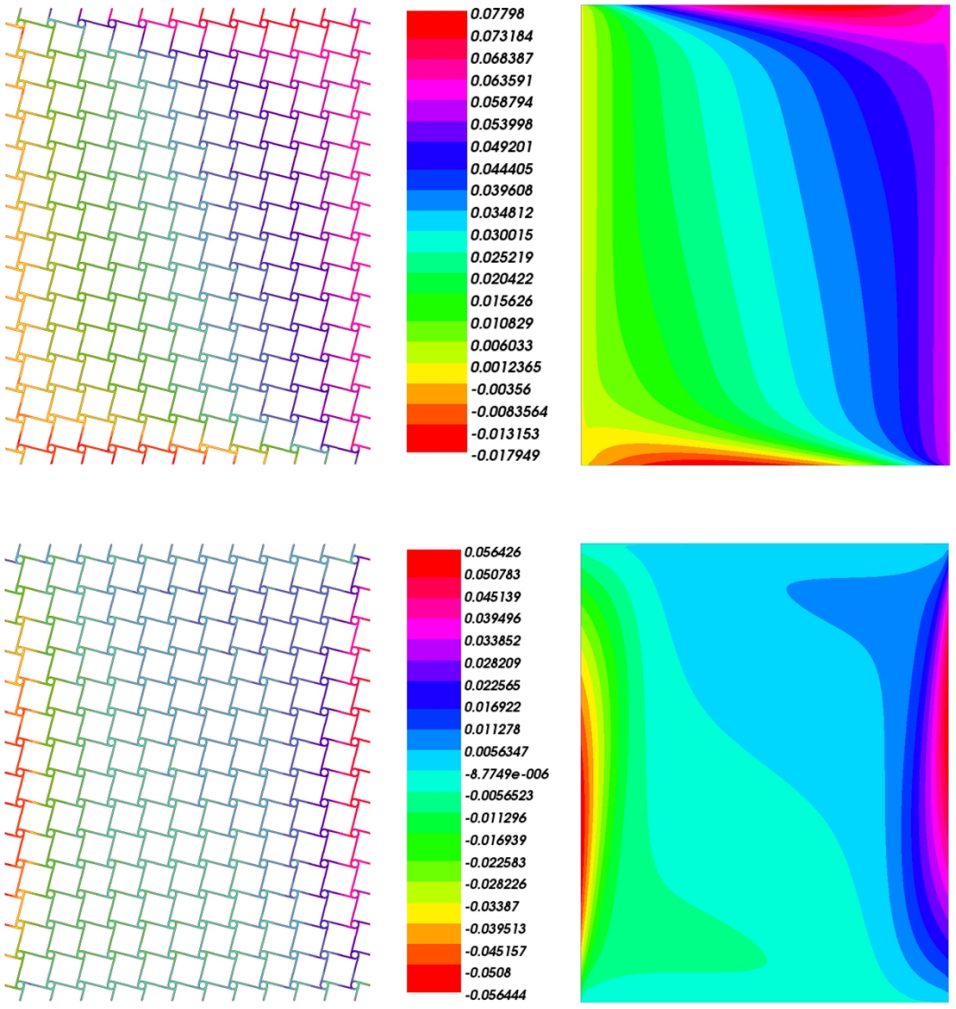

Figure 2.20 Tetrachiral lattice structure and homogenized plate at prescribed displacement $U = 0.06l$: (a) Normalized horizontal displacement contour u_1, (b) Normalized vertical displacement contour u_2.

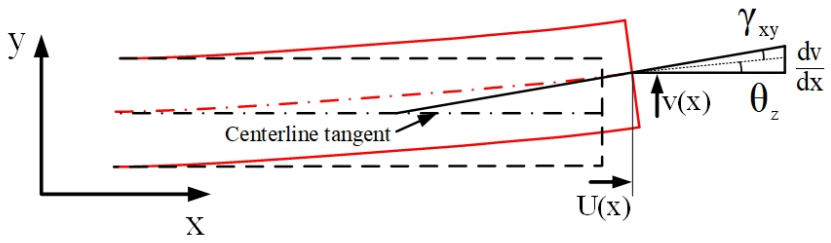

Figure 2.21 Deformation of a Timoshenko beam.

Timoshenko beam theory considers the coupling between tension, shear, and bending induced by the specific chiral behavior at the unit cell level is developed.

2.6.1 Enhanced Timoshenko beam theory

For the two-dimensional, small strain case, with no axial twist moment development and zero out-of-plane deformations ($\theta_y = 0$), the motion of the centerline of a standard Timoshenko beam is described through the axial displacement $u(x)$, the vertical deflection $v\,(x)$, and the angular variable θ, as depicted in Fig. 2.21. The displacement fields of the Timoshenko beam with Cartesian coordinates (x, y) writes as:

$$\begin{aligned} u_x\,(x,y) &= u\,(x) - y\theta_z(x) \\ v\,(x,y) &= v(x) \end{aligned} \tag{2.64}$$

where θ_z in Eq. 2.64 denotes the rotation of beam cross-section around the z-axis (Fig. 2.21). According to the previously defined kinematics, the normal strain field component is elaborated as:

$$\varepsilon_{xx} = \frac{\partial u(x,y)}{\partial x} = \frac{\partial}{\partial x}\left(u(x) - y\theta_z(x)\right) = u'(x) - y\theta_z'(x) \tag{2.65}$$

and the shear strain component, as follows:

$$2\varepsilon_{xy} = \frac{\partial u(x,y)}{\partial y} + \frac{\partial v(x,y)}{\partial x} = \underbrace{-\theta_z + v'(x)}_{=\gamma_{xy}} \tag{2.66}$$

One shall note here that for the Bernoulli beams, the neutral axis remains normal to the beam cross-section after deformation, so it holds $\gamma_{xy} = 0$. After inserting the expression of the deformation from Eqs. 2.65 and 2.66 into the stress-strain constitutive law relation the strain to the stress involving the homogenized compliance matrix $\boldsymbol{S}$ (the inverse of the rigidity matrix obtained in Eq. 2.51 for a fully non-centrosymmetric chiral structure), we obtain:

$$\begin{aligned} S_{11}\sigma_{11} + S_{12}\sigma_{22} + S_{13}\sigma_{12} + S_{14}\sigma_{21} + S_{15}m_{13} + S_{16}m_{23} &= u'(x) - y\theta_z(x) \\ S_{31}\sigma_{11} + S_{32}\sigma_{22} + S_{33}\sigma_{12} + S_{34}\sigma_{21} + S_{35}m_{13} + S_{36}m_{23} &= \underbrace{-\theta_z + v'(x)}_{=\gamma_{xy}} \\ S_{51}\sigma_{11} + S_{52}\sigma_{22} + S_{53}\sigma_{12} + S_{54}\sigma_{21} + S_{55}m_{13} + S_{56}m_{23} &= \theta_z'(x) \end{aligned} \tag{2.67}$$

Next, integrating both the left and right-hand sides of Eq. 2.67 over the cross-sectional area A annihilates all terms in the 'y' direction (for a 1D beam). By introducing the generalized forces $N\,(x) = \int \sigma_{xx} dA$

(axial force), $V(x) = \int \sigma_{xy} dA$ (shear force), and $M_z(x) = \int m_{13} dA$ (bending moment), the resulting normal and shear force equilibrium equations then reads:

$$\begin{aligned} &S_{11}N + S_{13}V + S_{15}M_z = u'(x)A - \theta_z(x) \underbrace{\int_A y dA}_{=0} = u'(x)A \\ &S_{31}N(x) + S_{33}V(x) + S_{35}M_z = \left[-\theta_z + v'(x)\right] A \\ &S_{51}N(x) + S_{53}V(x) + S_{55}M_z = \theta_z'(x)A \end{aligned} \tag{2.68}$$

The final expressions of the generalized axial and shear forces, and bending moments are then obtained after substituting the compliances by the corresponding moduli, A.5, as follows:

$$\begin{aligned} N(x) &= \underbrace{\left(\frac{S_{35.}}{S_{11}S_{35.} - S_{15}S_{31}}\right)}_{E_{11}^*} Au'(x) + V \underbrace{\left(\frac{(S_{15}S_{33} - S_{13}S_{35})}{S_{11}S_{35.} - S_{15}S_{31}}\right)}_{\alpha} - \underbrace{\left(\frac{S_{15}}{S_{11}S_{35.} - S_{15}S_{31}}\right)}_{G_{12}^*} A\left(-\theta_z + v'(x)\right) \\ N(x) &= \underbrace{\left(\frac{S_{33}}{S_{11}S_{33} - S_{13}S_{31}}\right)}_{E_{11}^{\oplus}} Au'(x) + M \underbrace{\left(\frac{E_{11}(S_{13}S_{35.} - S_{15}S_{33})}{(S_{11}S_{33} - S_{13}S_{31})}\right)}_{\beta} - \underbrace{\left(\frac{S_{13}}{S_{11}S_{33} - S_{13}S_{31}}\right)}_{G_{12}^{\oplus}} A\left(-\theta_z + v'(x)\right) \\ &S_{51}N(x) + S_{53}V(x) + S_{55}M_z = \theta_z'(x)A \end{aligned} \tag{2.69}$$

The developed enhanced Timoshenko beam theory differs from the classical Timoshenko beam model by the coefficients $E_{11}^*, G_{12}^*, E_{11}^{\oplus}, G_{12}^{\oplus}$ defined in Eq. 2.69, having the following meaning:

- $\left(E_{11}^*, E_{11}^{\oplus}\right)$: The modified Young's modulus in direction 1 due to the coupling between stresses and the shear deformation and the gradient of rotation (S_{31}, S_{51}, S_{35}). Neglecting these coefficients we return to the classical Young's modulus E_{11}.
- $\left(G_{12}^*, G_{12}^{\oplus}\right)$: The coupling coefficients between the normal force N and the shear deformation $(-\theta_z + v'(x))$; for a classical material, this effect is neglected (Fig. 2.22).
- (α, β): the coupling coefficients between the normal force N, the shear force, and bending moment, respectively.

In the case of statically determinate systems, the generalized forces are known from equilibrium and the functions $u(x)$, $v(x)$, and $\theta_z(x)$ are readily obtained by solving Eq. 2.69.

In Eq. 2.69 under any applied external load (N, V, or M), the angular slope of the beam is given by:

$$A\,\theta_z(x) = \int_0^x \left(S_{51}N(u) + S_{53}V(u) + S_{55}M_z(u)\right) du \tag{2.70}$$

Eq. 2.70 shows the dependency of the expression of the angular slope of the beam, function $\theta_z(x)$ on the position x and the normal force N, which is not the case for a classical Timoshenko beam.

2.6.2 Response of the enhanced Timoshenko beam under combined applied normal load N, shear force V and bending moment M

As an application of the developed enriched Timoshenko beam theory a 1D beam incorporating four hundred non-centrosymmetric tetrachiral unit cells subjected to a normal force N is considered (Fig. 2.22).

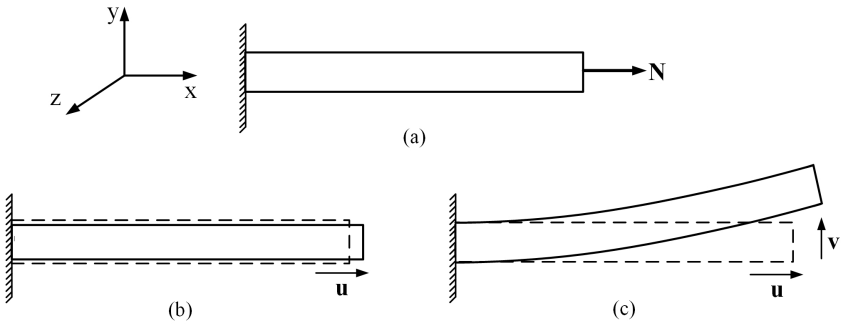

Figure 2.22 Schematic representation of the deformation mechanism: (a) undeformed shape, (b) common engineering material, (c) material with an inner normal to shear strain coupling.

For the non-centrosymmetric tetrachiral unit cell the effective moduli are evaluated from Eq. 2.69 as:

$$\begin{aligned} &E_{11} = 2.44\,MPa \qquad G_{12} = 7.55\,MPa \qquad \alpha = 0.41 \\ &E_{11}^{*} = 2.45\,MPa \qquad G_{12}^{*} = 6.3\,MPa \qquad \beta = 0.618 \\ &E_{11}^{\oplus} = 2.44MPA \qquad G_{12}^{\oplus} = 0.034\,MPa \qquad S_{15} = 0.231\,MPa.mm \end{aligned}$$

For the classical Timoshenko behavior, the beam undergoes an axial deformation $\varepsilon_{xx} = \mathrm{u_x^{'}} = \mathrm{N/AE}_{xx}$, uniform across the beam. The chiral effect and the coupling terms in Eq. 2.69 result in a new unconventional beam behavior. Applying a normal effort result in a normal and shear strain given by their derivatives as follows:

$$\begin{aligned} u'(x) &= \frac{N\left(G_{12}^{\oplus} - G_{12}^{*}\right)}{A\left(E_{11}^{*}G_{12}^{\oplus} - E_{11}^{\oplus}G_{12}^{*}\right)} = 2.44\frac{N}{A} \\ v'(x) &= \frac{N\left(S_{15}\,x\left(E_{11}^{*}G_{12}^{\oplus} - E_{11}^{\oplus}G_{12}^{*}\right) - E_{11}^{*} + E_{11}^{\oplus}\right)}{A\left(E_{11}^{*}G_{12}^{\oplus} - E_{11}^{\oplus}G_{12}^{*}\right)} \\ &= \frac{N}{A}\left(S_{15}\,x + \frac{\left(-E_{11}^{*} + E_{11}^{\oplus}\right)}{\left(E_{11}^{*}G_{12}^{\oplus} - E_{11}^{\oplus}G_{12}^{*}\right)}\right) = 0.231x\frac{N}{A} + 0.00194\frac{N}{A}x \end{aligned} \tag{2.71}$$

Accordingly, the maximum shear strain at the extremity of the beam generated by the normal stress ($\mathrm{N/A} = 0.001\mathrm{N/mm^2}$) is computed which have a magnitude of 0.1155 pointing upwards, in a counter-clockwise rotational direction, thus opposite to the generated bending deformation, and a horizontal deformation with axial strain around 0.0244. In order to verify our beam model, a beam including 50×8 unit cells of the tetrachiral lattice shown in Fig. 7(a) is simulated using the FE software ABAQUS. The beam shown in Fig. 2.23 has a clamped boundary condition at the left end, and uniform axial stress of 0.001 $\mathrm{N/mm^2}$ is applied at the right end. Fig. 2.24 shows the deformed shape of the beam under the abovementioned loading.

For the same macrobeam shown in Fig. 2.23 subjected to the normal load N, the maximum horizontal axial displacement and the vertical displacements are computed as 0.0264 mm, and 0.119 mm (Fig. 2.24(a),(b)), respectively. Vertical displacement values predicted by Eq. 2.71 exhibit a very good

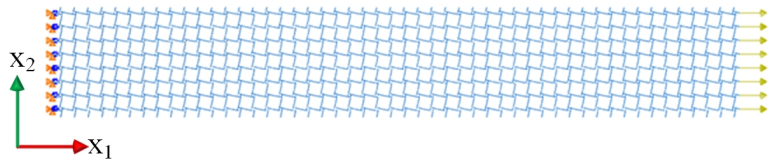

Figure 2.23 Microstructured beam made of 50×8 non-centrosymmetric tetrachiral unit cells, under axial loading at the right end and clamped boundary condition at the left end.

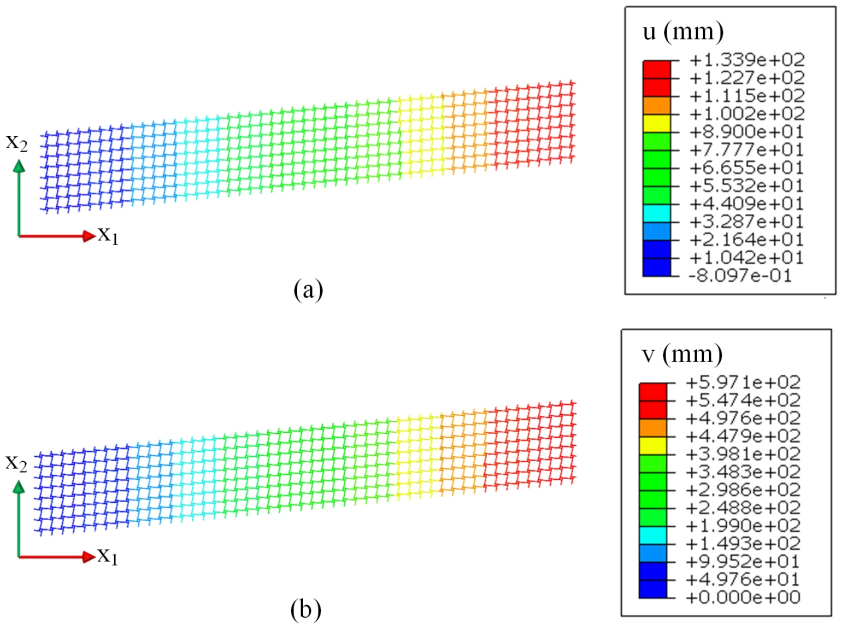

Figure 2.24 Deformed shape of the beam with plotted distribution of the: (a) axial displacement, (b) vertical displacement.

agreement with the FE result, with a relative error of 3%, which shows the excellent predictability of Eq. 2.71. One shall note here that without the coupling term S_{15}, the shear deformation is negligible under the applied load N. In the case of an applied shear force V, the normal and shear deformations are given successively by:

$$\begin{aligned} u'(x) &= \frac{V\,x\left(G_{12}^{*}\beta - G_{12}^{\oplus}\alpha\right)}{A\left(E_{11}^{*}G_{12}^{\oplus} - E_{11}^{\oplus}G_{12}^{*}\right)} \\ v'(x) &= \frac{V\left(\left(S_{53}\,x + S_{55}\,\frac{x^2}{2}\right)\left(E_{11}^{*}G_{12}^{\oplus} - E_{11}^{\oplus}G_{12}^{*}\right) + E_{11}^{*}\beta\,x - E_{11}^{\oplus}\alpha\,x\right)}{A\left(E_{11}^{*}G_{12}^{\oplus} - E_{11}^{\oplus}G_{12}^{*}\right)} \end{aligned} \tag{2.72}$$

In the case of an applied bending moment M, the normal and shear deformations are successively given by:

$$\begin{aligned} u'(x) &= -\frac{G_{12}^{*}\beta M}{A\left(E_{11}^{*}G_{12}^{\oplus} - E_{11}^{\oplus}G_{12}^{*}\right)} \\ v'(x) &= \frac{M\left(S_{55}x\left(E_{11}^{*}G_{12}^{\oplus} - E_{11}^{\oplus}G_{12}^{*}\right) + E_{11}^{*}\beta\right)}{A\left(E_{11}^{*}G_{12}^{\oplus} - E_{11}^{\oplus}G_{12}^{*}\right)} \end{aligned} \tag{2.73}$$

In Eqs. 2.71, 2.72, and 2.73, an explicit form of the normal and shear deformation in the function of the applied external loads N, V, and M are presented. In the case of a combined applied load on the beam, the solution of Eq. 2.69 exhibits both normal and shear strains and a curvature $\theta_z'(x)$.

2.6.3 Macrobeams incorporating tetrachiral unit cells

In this section, an example of macrobeams incorporating tetrachiral lattices is considered to underline the accuracy of the proposed micropolar model for different sizes of the macrostructures. The macrostructure shown in Fig. 2.25 is considered, comprising tetrachiral unit cells of Table 2.6, in order to investigate the macrobeam response comparing to the homogenized values calculated by the PBCs imposed over the unit cell. The geometrical and mechanical parameters of the building unit cell are presented in Table 2.5, and the total length and height of the beam are denoted by L and H, respectively. The left boundary of the macro beam is just free to move along the vertical direction, and they are fixed at the one point of the left boundary. Two different types of loading, uniform axial stress and a pure bending moment, are prescribed along the right surface to illustrate the capability of the proposed homogenization method in capturing the Cauchy and Cosserat effective moduli respectively.

Table 2.5 Values of the geometrical and mechanical parameters of the tetrachiral micro structure.

Elastic modulus (MPa)	Poisson's ratio	R (mm)	t (mm)	ξ_1 (mm)	b (mm)
1400	0.3	0.15	0.05	(0,0)	0.2

Applying the PBCs over the tetraciral unit cell of Table 2.5 gives the effective Cauchy compliance components and the effective Cosserat components as:

$$\mathrm{S}_{11}^{\mathrm{hom}} = 2.69\mathrm{MPa}; \qquad \mathrm{S}_{14}^{\mathrm{hom}} = 9.97\mathrm{MPa}; \qquad \gamma_1^{\mathrm{hom}} = 0.0527\mathrm{N}$$

Considering the deformations of the beams shown in Fig. 2.26, one can compute the S_{11}, S_{14}, and γ_1

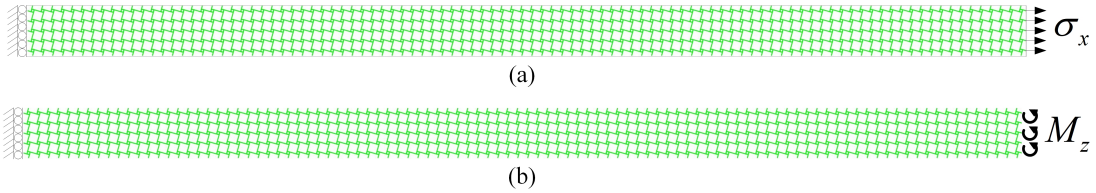

Figure 2.25 Macrobeam made of tetrachiral unit cells under: (a) uniform axial stress, (b) pure bending moment

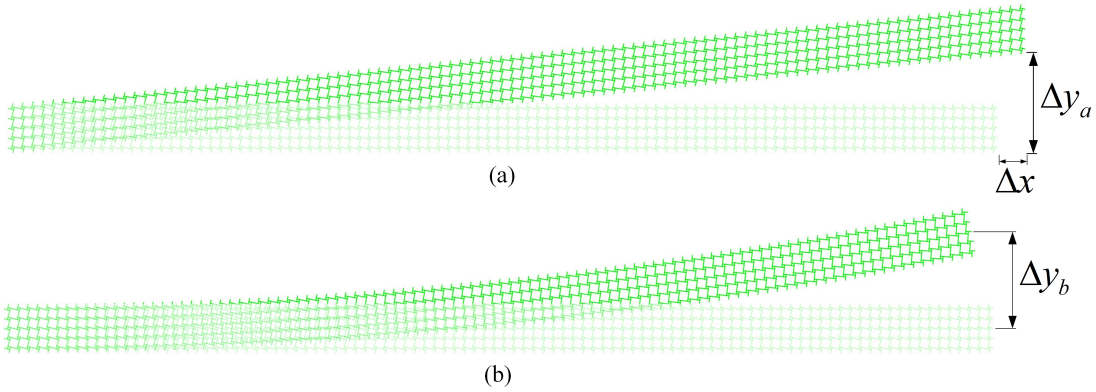

Figure 2.26 Deformed shape of the macro beam under: (a) uniform axial stress, (b) pure bending moment

using the following formulations:

$$\mathrm{S}_{11} = \frac{\Delta x}{L\sigma_{xx}}; \quad \mathrm{S}_{14} = \frac{\Delta y_a}{L\sigma_{xx}}; \quad M^{\phi} = \int_A \frac{\gamma_1}{h^{UC}} h dA \Rightarrow \gamma_1 = \frac{2\left(\frac{\mathrm{M_z L^2}}{2\Delta_{\mathrm{y_b}}} - \frac{\mathrm{I}}{\mathrm{S}_{11}}\right)}{\mathrm{H}^2} \tag{2.74}$$

with M^{ϕ} the moment due to the Cosserat modulus and h^{UC} the unit cell height, here chosen to be unity.

Table 2.6 Effective Cauchy compliance components and Cosserat effective moduli.

Macro beam	S_{11} ($^{\mathrm{mm}^2}/_{\mathrm{N}}$)	Error of S_{11} (%)	S_{14} ($^{\mathrm{mm}^2}/_{\mathrm{N}}$)	Error of S_{14} (%)	γ_1 (N)	Error of γ_1 (%)
60×3	2.65809	1.19	9.3171	6.55	-0.00038	100.7
100×5	2.66908	0.78	9.4960	4.76	0.00793	84.95
200×10	2.67779	0.45	9.6060	3.65	0.02020	61.67
300×15	2.67833	0.43	9.6259	3.45	0.03124	40.72
400×20	2.67898	0.41	9.6402	3.31	0.04115	21.92
500×25	2.67942	0.39	9.6514	3.2	0.05013	4.88

Results in Table 2.6 show that the accuracy of unit cell based homogenized moduli on predicting the beam effective properties increases with the number of unit cells in height (there are enough unit cells in length) up to a stage where edge effects become negligible. The sole Cauchy bending prediction is not sufficient to capture the bending response of the macrobeam since the classical bending modulus needs to be complemented by the Cosserat bending modulus.

2.7 Conclusion

A general homogenization method for computing the effective elastic moduli of heterogeneous materials of Cosserat continua type is proposed, combining a variational principle with the extended Hill-Mandel macrohomogeneity accounting for the introduced generalized kinematics. The microscopic displacement field of the heterogeneous continuum splits into a homogeneous part polynomial in the generalized kinematic measures of the Cosserat effective continuum and fluctuation that corrects for the discrepancy between the assumed effective homogeneous generalized medium and the actual heterogeneous microstructure. The developed method leads to a closed-form expression of the tensors of effective moduli from the knowledge of the displacement localizators and the solution of the classical and higher-order unit cell problems. The proposed method has the chief advantage of providing a size-independency of the higher-order effective moduli, and it incorporates the fluctuation of the microscopic displacement that corrects for the polynomial homogeneous part. Its extension to capture the observed nonlinear response of architectured materials prone to geometrical nonlinearities is planned in future developments.

As an illustration, effective micropolar continua moduli have been computed for tetrachiral and anti-tetrachiral architectured materials and composites made of these reinforcements prone to chiral micropolar effects. Macroscopic beams architected with tetrachiral unit cells have been shown to obey an enhanced Timoshenko beam model constructed from the homogenized constitutive laws at the unit cell level. The response of the macrobeam under pure bending proves to be size-independent provided edge effects in vertical directions have been eliminated; the provided analysis shows moreover that Cauchy mechanics is not sufficient to capture the bending response of the macrobeam.

The proposed methodology will be extended in future developments to a broader range of microstructures of architected materials prone to higher-order effects. Its extension to capture the observed nonlinear response of architectured materials prone to geometrical nonlinearities is planed in future developments.

Chapter 3

Construction of micromorphic continua by homogenization, based on variational principles

Summary

This chapter revisits higher-order homogenization schemes towards micromorphic media based on variational principles and extends the Hill macrohomogeneity condition. Starting from the microscopic Cauchy balance equations, the local balance equations of the micromorphic continuum are formulated, highlighting the micromorphic stress measures. Relying on both energy and complementary energy expressions combined with Hill lemma, the complete homogeneous microscopic displacement field representing the effective micromorphic continuum is obtained as a quartic expansion of the macroscopic micromorphic kinematic variables. This procedure leads to a higher-grade micromorphic theory, with the relative stress and hyperstress tensors, including second-order and third-order polynomials of the relative position within the unit cell. A fluctuating part completes the microscopic displacement evaluated from a variational principle and is characterized by three BVPs over the unit cell. Numerical applications are made for inclusion-based composite materials. The obtained results highlight that the higher-order moduli converge very quickly with unit cell size due to considering correction factors based on the higher-order moments of area.

3.1 Introduction

The micromorphic theory has been advanced by [72, 73, 75, 103–105, 182] constitutes the most general enriched model incorporating a full second-order microdeformation tensor attached to each material point. From a computational point of view, Jänicke et al. [183, 184] implemented a homogenization scheme incorporating a full micromorphic continuum for cellular materials to capture size-dependent boundary layer effects.

Despite the great success of micromorphic theories in modeling microstructured materials, micromorphic homogenization raises specific difficulties compared to higher-gradient and higher-order theories, considering both theoretical and numerical aspects. The evaluation of the non-classical properties requires the prescription of higher-order polynomial kinematic constraints on the unit cell boundary [179, 180] and extending Hill's macrohomogeneity condition, like [126] and [185] for the strain gradient continuum.

A critical review of the non-homogeneous boundary conditions adopted in generalized computational homogenization can be found in [105]. One difficulty in prescribing the minimum kinematic loading conditions onto the unit cell is the transformation of the volume averages defining the micromorphic kinematic and static variables into corresponding surface integrals, as mentioned in recent contributions to the field [113, 186, 187]. To circumvent this difficulty, Jänicke and Steeb [184] proposed minimal loading conditions to impose the macroscopic kinematic variables onto the unit cell in terms of average volume constraints. Hütter [187] proposed incorporating nonstandard body forces that translate to the macroscale as generalized micromorphic stresses. Forest provided explicit integral expressions for the relations between microscopic and macroscopic kinematic quantities [5, 188]. However, the introduced generalized deformation measures could not be fully converted as surface integrals over the unit cell boundary. Polynomial expressions of the microscopic displacement field have been proposed and identified following different strategies and attempts made to characterize the other fluctuations that complete the homogeneous polynomial part of the micro displacement, as exposed in [5, 183, 189]. Nevertheless, none of them was able to formulate a BVP at the microscale. Eringen derived the governing balance equations for the micromorphic continuum at the macroscale using a spatial averaging procedure [182, 190]; however, these last works did not relate macroscopic to microscopic kinematic quantities, and they did not formulate a BVP at the microscale.

In this chapter, a homogenization strategy for heterogeneous materials towards effective micromorphic media is developed, and the effective kinematic and static micromorphic variables are constructed in terms of the microscopic fields. The homogeneous displacement and stress fields imposed over the unit cell are determined from variational principles, and they are completed by fluctuating fields. In substance, the novel aspects presented in this chapter are the following:

- The construction of micromorphic effective media of third-order by homogenization methods relying on variational principles for the computation of the fluctuating microscopic fields;

- The recourse to a general systematic method in order to find the homogeneous part of the microscopic displacement ensuring completeness of its polynomial expansion;
- The extension and proof of Hill macrohomogeneity condition towards micromorphic continua;
- The elaboration of the kinematics and statics of the micromorphic continuum based on closed-form averaging relations for the microscopic fields over the unit cell;
- Incorporating the expression of the effective higher-order moduli of the higher-order geometric moments of the unit cell leads to nearly size-independent moduli.

The outline of this chapter is as follows: In Section 3.2, starting from the microscopic balance laws, the balance of linear momentum for the micromorphic continua is derived. The microscopic displacement corresponding to the homogeneous part of the total displacement for the effective micromorphic continuum is determined based on the expressions of the energy and complementary energy densities articulated with Hill's extended macrohomogeneity condition, as exposed in section 3.3. The remaining fluctuating part of the microscopic displacement is evaluated from a variational principle detailed in section 3.4. The effective micromorphic moduli are evaluated versus the displacement localization functions characterized by unit cell BVPs in section 3.5. Numerical examples for inclusion-based composites are provided in section 3.6, and a discussion of the proposed methodology and results are presented in Section 3.7. Section 3.8 concludes with a summary of the main results and a few perspectives for future work.

The methodology of the proposed micromorphic homogenization method leading to the computation of the effective micromorphic moduli is provided synthetically in Fig. 3.1.

A few words regarding the employed notations are in order. The physical space is embedded with the Euclidean space and vectors and higher-order tensors are implicitly decomposed into an orthonormal basis of the underlying vector space. Vectors and tensors are denoted by boldface symbols along with proper underlining notation, in order to show more explicitly their rank. The gradient of a scalar or tensor field with respect to the position is denoted with the nabla operator and the position as a subscript, viz. $\nabla_x \underset{\sim}{\boldsymbol{E}}(\boldsymbol{x})$ represents the gradient of the second-order tensor field $\underset{\sim}{\boldsymbol{E}}(\boldsymbol{x})$ w.r.to $\underline{\boldsymbol{x}}$. The transpose of a tensor is written with a superscript notation, for instance $\underset{\sim}{\boldsymbol{B}}^T$ is the transpose of second-order tensor $\underset{\sim}{\boldsymbol{B}}$. The gradient of a third-order tensor field $\underline{\underline{\boldsymbol{A}}}(\mathbf{y})$ is denoted $\underline{\underline{\boldsymbol{A}}}(\boldsymbol{y}) \otimes \nabla_y$, (with $\otimes$ the tensor product) and its divergence is obtained as the trace of the gradient, $\underline{\underline{\boldsymbol{A}}}(\boldsymbol{y}).\nabla_y$. The symmetrized dyadic product is denoted with $\otimes^s$. The dot product therein represents the internal product in the space of Cartesian tensors. The simple, double, and triple contractions of tensors are written as $\cdot$, :, and $\therefore$, respectively. The vector product of two vectors or tensors $\underline{\boldsymbol{U}}, \underline{\boldsymbol{V}}$ is denoted $\underline{\boldsymbol{U}} \times \underline{\boldsymbol{V}}$.

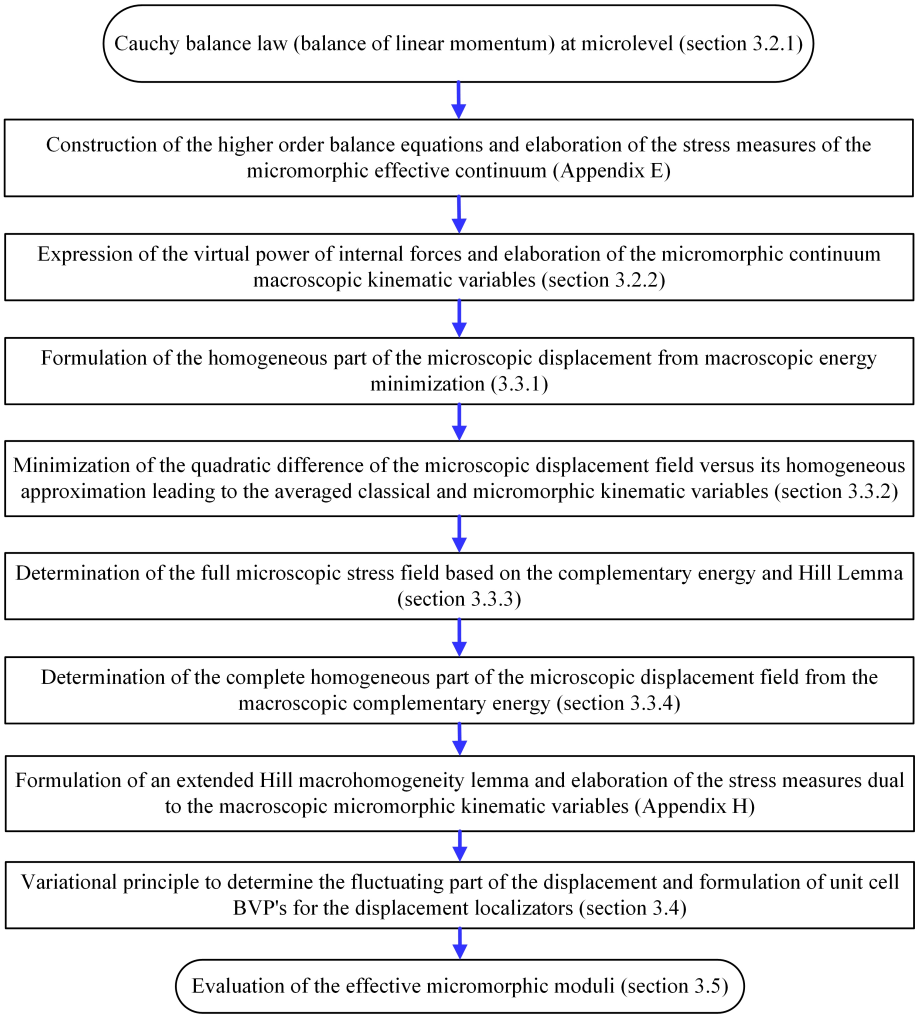

Figure 3.1 Schematic diagram of the proposed methodology for micromorphic homogenization.

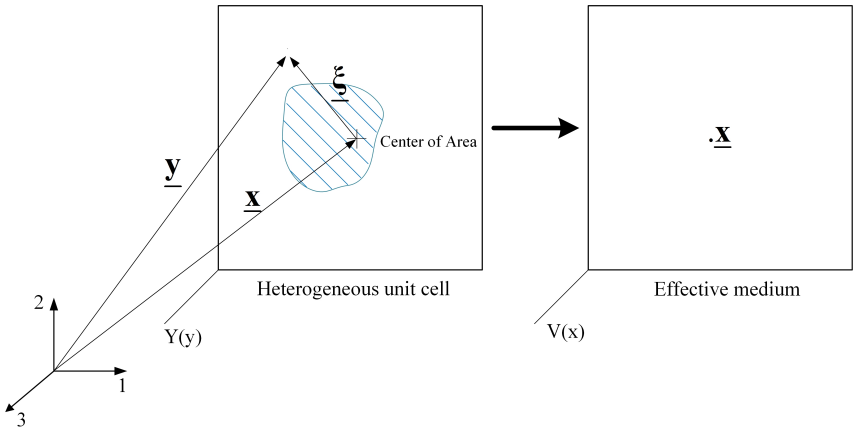

Figure 3.2 (left) Composite unit, (right) the homogenized effective medium.

3.2 Construction of the balance equations for the effective micromorphic continuum

By definition, a continuum with microstructure is a continuum in which at least two length scales $\underline{\boldsymbol{x}}$ and $\underline{\boldsymbol{y}}$ are present, named here and in the sequel macroscopic and microscopic scales, respectively. For a periodic medium, the mechanical response can be analyzed over a representative unit cell identified, as pictured in Fig. 3.2, which shows a two-phase heterogeneous material with domain Y at the microscale. The goal of the subsequent developments is to find the effective mechanical response of the micromorphic medium over the homogeneous substitution medium $V(\boldsymbol{x})$ centered around the center of the area of domain Y, point $\underline{\boldsymbol{x}}$. According to Fig. 3.2, the relative position $\underline{\boldsymbol{\xi}}$ is denoted as

$$\underline{\boldsymbol{\xi}} = \underline{\boldsymbol{y}} - \underline{\boldsymbol{x}} \rightarrow \int_Y \underline{\boldsymbol{\xi}} dV_y = \mathbf{0} \tag{3.1}$$

The volume average therein is defined for any field $\psi\left(\underline{\boldsymbol{y}}\right)$ as the following integral $<\psi>_y = \frac{1}{|Y|}\int_Y \psi dV_y$. At the microscopic level, the constituents of the heterogeneous material are assumed to obey Hooke's law in the framework of first gradient Cauchy elasticity theory.

3.2.1 Balance equations for the micromorphic continuum

Balance equations for the micromorphic continuum

$$\underset{\sim}{\boldsymbol{\sigma}} \cdot \nabla_y + \underline{\boldsymbol{b}} = \mathbf{0} \;\; in\; Y \tag{3.2}$$

$$\underset{\sim}{\boldsymbol{\sigma}} \cdot \underline{\boldsymbol{n}} = \underline{\boldsymbol{t}} \quad on\; \partial Y \tag{3.3}$$

$$\underset{\sim}{\boldsymbol{\sigma}} = \underset{\approx}{\mathbb{C}} : \underset{\sim}{\boldsymbol{\varepsilon}} \tag{3.4}$$

with $\underset{\sim}{\boldsymbol{\sigma}} = \underset{\sim}{\boldsymbol{\sigma}}^T$ the symmetrical Cauchy stress (symmetry being a consequence of the balance of angular momentum), $\underline{\boldsymbol{b}}$ the body force vector, $\underline{\boldsymbol{n}}$ the unit-length exterior normal vector, $\underline{\boldsymbol{t}}$ the traction vector,

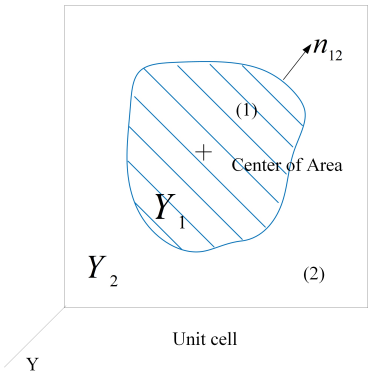

Figure 3.3 Composite unit cell with two constituents labelled (1) and (2).

and $\underset{\approx}{\mathbf{C}}$ the fourth-order microscopic rigidity tensor. The symmetry of Cauchy stress tensor results from the balance of angular momentum which holds at the microlevel. The small strains formalism is used throughout the chapter so that the linearized strain tensor is the symmetrical part of the displacement gradient

$$\underset{\approx}{\boldsymbol{\varepsilon}} := \underline{\boldsymbol{u}} \otimes^{S} \nabla_y \tag{3.5}$$

In order to relate volume averages of microscopic gradients in terms of macroscopic gradients of their averages to be able to write the micro-macro kinematic and static relations, Withaker averaging theorem is needed, a proof of which is exposed in Appendix D. Here the traditional form of the averaging theorem [177]; [178] is applied on a two-phase heterogeneous material, with an assumed continuity of displacement and traction at the interface between constituents within the identified unit cell (Fig. 3.3). In order to construct the balance equations of the effective micromorphic continuum highlighting the macroscopic stress measures, the tensor product of the microscopic balance of linear momentum with the relative microscopic position is taken to establish the first higher-order balance law of the micromorphic continuum; the second higher-order balance law is established by taking the average of Eq. 3.2 and using Withaker averaging theorem from Appendix D. The technical developments leading to these two balance laws are detailed in Appendix E.

The final form of the resulting two macroscopic equilibrium equations of the micromorphic continuum is obtained with compact notation as

$$\underset{\approx}{\boldsymbol{\Sigma}} \cdot \nabla_x - \underset{\approx}{\boldsymbol{s}} \cdot \nabla_x + \underline{\mathbf{B}} = 0 \tag{3.6}$$

$$\underline{\underline{\mathbf{S}}} \cdot \nabla_x - \underset{\approx}{\boldsymbol{\Sigma}} + \underset{\approx}{\boldsymbol{s}} + \underset{\sim}{\mathbf{B}}^{\chi} = 0 \tag{3.7}$$

wherein the following higher-order micromorphic stress tensors and body forces are introduced:

$$\begin{vmatrix} \underline{\underline{\mathbf{S}}} := < \underline{\boldsymbol{\xi}} \otimes \underset{\approx}{\boldsymbol{\sigma}} >_Y ; & \underset{\approx}{\boldsymbol{s}} := < \underline{\boldsymbol{\xi}} \otimes (\underset{\approx}{\boldsymbol{\sigma}} \cdot \nabla_y) >_Y ; & \underset{\approx}{\boldsymbol{\Sigma}} := < \underline{\boldsymbol{\xi}} \otimes \underset{\approx}{\boldsymbol{\sigma}} >_{\partial Y} ; \\ \underline{\mathbf{B}} = \left\langle \underline{\mathbf{b}} \right\rangle_Y ; & \underset{\sim}{\mathbf{B}}^{\chi} = \left\langle \underline{\boldsymbol{\xi}} \otimes \underline{\mathbf{b}} \right\rangle_Y \end{vmatrix} \tag{3.8}$$

In Eq. 3.8, $\underline{\underline{\mathbf{S}}}$, $\underset{\approx}{\boldsymbol{s}}$, $\underline{\mathbf{B}}$, and $\underset{\sim}{\mathbf{B}}^{\chi}$ are the hyperstress tensor, relative stress tensor, the volume average of body force, and of higher-order body forces over the unit cell, respectively. The second-order tensor $\underset{\approx}{\boldsymbol{\Sigma}}$

elaborated in Eq. 3.8 as a surface integral is the macroscopic external stress over the unit cell boundary. These stress measures of the micromorphic continuum will be completed by additional terms in subsequent elaborations of this chapter.

3.2.2 Expression of the virtual power of internal forces

From the two balance equations E.13 and E.2, one defines the total virtual power of internal forces by multiplying these balance laws by $\underset{\sim}{\boldsymbol{y}}^{\chi}$ and $\underset{\sim}{\boldsymbol{y}}$ respectively, the virtual rate of microdeformation and virtual classical velocity. Integrating the resulting expressions over the macroscopic homogeneous volume $V(\boldsymbol{x})$, and after a few straightforward manipulations, the two following relations are obtained

$$\begin{aligned}&\left\{-\int_{V(x)} <\underline{\underline{\boldsymbol{\xi}}}\otimes\underset{\sim}{\boldsymbol{\sigma}}>_Y \therefore \nabla_x\underset{\sim}{\boldsymbol{y}}^{\chi}dV_x + \int_{V(x)} <\underline{\underline{\boldsymbol{\xi}}}\otimes(\underset{\sim}{\boldsymbol{\sigma}}\cdot\nabla_y)>_Y : \underset{\sim}{\boldsymbol{y}}^{\chi}dV_x\right\} + \\ &\left\{\int_{V(x)} <\underline{\underline{\boldsymbol{\xi}}}\otimes\underline{\boldsymbol{b}}>_Y : \underset{\sim}{\boldsymbol{y}}^{\chi}dV_x - \int_{V(x)} <\underline{\underline{\boldsymbol{\xi}}}\otimes\underset{\sim}{\boldsymbol{\sigma}}>_{\partial Y} : \underset{\sim}{\boldsymbol{y}}^{\chi}dV_x + \int_{\partial V(x)} \underline{\underline{\mathbf{N}}}\cdot <\underline{\underline{\boldsymbol{\xi}}}\otimes\underset{\sim}{\boldsymbol{\sigma}}>_Y : \underset{\sim}{\boldsymbol{y}}^{\chi}ds_x\right\} = 0\end{aligned} \tag{3.9}$$

and

$$\begin{aligned}&\left\{\int_{\partial V(x)} \underline{\underline{\mathbf{N}}}\cdot\left(<\underline{\underline{\boldsymbol{\xi}}}\otimes\underset{\sim}{\boldsymbol{\sigma}}>_{\partial Y} - <\underline{\underline{\boldsymbol{\xi}}}\otimes(\underset{\sim}{\boldsymbol{\sigma}}\cdot\nabla_y)>_Y\right)ds_x + \int_{V(x)} <\underline{\boldsymbol{b}}>_Y\cdot\underline{\boldsymbol{v}}dV_x + \int_{V(x)} <\underline{\underline{\boldsymbol{\xi}}}\otimes(\underset{\sim}{\boldsymbol{\sigma}}\cdot\nabla_y)>_Y : \nabla_x\underline{\boldsymbol{v}}dV_x\right\} + \\ &\left\{-\int_{V(x)} <\underline{\underline{\boldsymbol{\xi}}}\otimes\underset{\sim}{\boldsymbol{\sigma}}>_{\partial Y} : \nabla_x\underline{\boldsymbol{v}}dV_x\right\} = 0\end{aligned} \tag{3.10}$$

In Eq. 3.9 and Eq. 3.10, four following contributions P_c^i, P_m^i, P_c^e, and P_m^e can identified wherein the indices i, e, m, and c stand for the power of internal, external, micromorphic, and Cauchy types forces, respectively:

$$\begin{aligned}P_c^i &= -\int_{V(x)} <\underline{\underline{\boldsymbol{\xi}}}\otimes\underset{\sim}{\boldsymbol{\sigma}}>_{\partial Y} : \nabla_x\underline{\boldsymbol{v}}dV_x \\ P_m^i &= -\int_{V(x)} <\underline{\underline{\boldsymbol{\xi}}}\otimes\underset{\sim}{\boldsymbol{\sigma}}>_Y \therefore \nabla_x\underset{\sim}{\boldsymbol{y}}^{\chi}dV_x + \int_{V(x)} <\underline{\underline{\boldsymbol{\xi}}}\otimes(\underset{\sim}{\boldsymbol{\sigma}}\cdot\nabla_y)>_Y : \underset{\sim}{\boldsymbol{y}}^{\chi}dV_x \\ P_c^e &= \int_{\partial V(x)} \underline{\underline{\mathbf{N}}}\cdot\left(<\underline{\underline{\boldsymbol{\xi}}}\otimes\underset{\sim}{\boldsymbol{\sigma}}>_{\partial Y} - <\underline{\underline{\boldsymbol{\xi}}}\otimes(\underset{\sim}{\boldsymbol{\sigma}}\cdot\nabla_y)>_Y\right)\cdot\underline{\boldsymbol{v}}ds_x + \int_{V(x)} <\underline{\boldsymbol{b}}>_Y\cdot\underline{\boldsymbol{v}}dV_x \\ &\quad + \int_{V(x)} <\underline{\underline{\boldsymbol{\xi}}}\otimes(\underset{\sim}{\boldsymbol{\sigma}}\cdot\nabla_y)>_Y : \nabla_x\underline{\boldsymbol{v}}dV_x \\ P_m^e &= \int_{V(x)} <\underline{\underline{\boldsymbol{\xi}}}\otimes\underline{\boldsymbol{b}}>_Y : \underset{\sim}{\boldsymbol{y}}^{\chi}dV_x - \int_{V(x)} <\underline{\underline{\boldsymbol{\xi}}}\otimes\underset{\sim}{\boldsymbol{\sigma}}>_{\partial Y} : \underset{\sim}{\boldsymbol{y}}^{\chi}dV_x + \int_{\partial V(x)} \underline{\underline{\mathbf{N}}}\cdot <\underline{\underline{\boldsymbol{\xi}}}\otimes\underset{\sim}{\boldsymbol{\sigma}}>_Y : \underset{\sim}{\boldsymbol{y}}^{\chi}ds_x\end{aligned} \tag{3.11}$$

The virtual internal power of the micromorphic continuum at the macroscopic level is the sum of the internal power of the Cauchy medium and of the micromorphic internal power:

$$\begin{aligned}\delta W_M = -(P_c^i + P_m^i) &= \int_{V(x)} <\underline{\underline{\boldsymbol{\xi}}}\otimes\underset{\sim}{\boldsymbol{\sigma}}>_{\partial Y} : \nabla_x\underline{\boldsymbol{v}}dV_x + \int_{V(x)} <\underline{\underline{\boldsymbol{\xi}}}\otimes\underset{\sim}{\boldsymbol{\sigma}}>_Y \therefore \nabla_x\underset{\sim}{\boldsymbol{y}}^{\chi}dV_x \\ &\quad - \int_{V(x)} <\underline{\underline{\boldsymbol{\xi}}}\otimes(\underset{\sim}{\boldsymbol{\sigma}}\cdot\nabla_y)>_Y : \underset{\sim}{\boldsymbol{y}}^{\chi}dV_x\end{aligned} \tag{3.12}$$

The classical displacement field $\underline{\mathbf{u}}$ is associated with the external actions $\left(\underline{\mathbf{b}},\ \underline{\mathbf{t}}\right)$ of the classical Cauchy continuum, while for each microdeformation $\underset{\sim}{\boldsymbol{\chi}}$ there is a micro body force $\underline{\underline{\mathbf{b}}}^{\chi} = \underline{\underline{\boldsymbol{\xi}}}\otimes\underline{\mathbf{b}}$, and a surface micro traction $\underline{\underline{\mathbf{t}}}^{\chi} = \underline{\underline{\boldsymbol{\xi}}}\otimes\underline{\mathbf{t}}$, both being second-order tensors. The fields $\underline{\boldsymbol{v}}$ and $\underset{\sim}{\boldsymbol{y}}^{\chi}$ (respectively a vector and a second-order tensor) are defined as virtual variations of $\underline{\mathbf{u}}$ and $\underset{\sim}{\boldsymbol{\chi}}$. Let further define two macroscopic

kinematic variables, $\underset{\sim}{\mathbf{E}}(\boldsymbol{x})$ and $\underset{\sim}{\mathbf{K}}(\boldsymbol{x})$, the classical strain and the microdeformation gradient tensors, respectively as:

$$\underset{\sim}{\mathbf{E}}(\boldsymbol{x}) := \nabla_x \underline{\mathbf{U}} \tag{3.13}$$

$$\underset{\sim}{\mathbf{K}}(\mathrm{x}): = \nabla_x \underset{\sim}{\boldsymbol{\chi}} \tag{3.14}$$

where the displacement vector $\underline{\mathbf{U}}$ describes the macroscopic deformation.

Substituting expressions 3.13 and 3.14 into Eq. 3.12 then leads to

$$\delta W_M = \underset{\sim}{\boldsymbol{\Sigma}} : \delta \underset{\sim}{\mathbf{E}} - \underset{\sim}{\mathbf{s}} : \delta \underset{\sim}{\boldsymbol{\chi}} + \underline{\underline{\mathbf{S}}} \therefore \delta \underset{\sim}{\mathbf{K}} \tag{3.15}$$

Furthermore, it holds according to Eq. E.1 the macro Cauchy stress elaborated as the difference

$$\bar{\underset{\sim}{\boldsymbol{\sigma}}} = \underset{\sim}{\boldsymbol{\Sigma}} - \underset{\sim}{\mathbf{s}} \tag{3.16}$$

One can obtain the following alternative relation by inserting Eq. 3.16 into Eq. 3.15:

$$\delta W_M = \bar{\underset{\sim}{\boldsymbol{\sigma}}} : \delta \underset{\sim}{\mathbf{E}} + \underset{\sim}{\mathbf{s}} : \delta \underset{\sim}{\mathbf{e}} + \underline{\underline{\mathbf{S}}} \therefore \delta \underset{\sim}{\mathbf{K}} \tag{3.17}$$

wherein the relative strain is introduced as,

$$\underset{\sim}{\mathbf{e}} := \left(\underset{\sim}{\mathbf{E}} - \underset{\sim}{\boldsymbol{\chi}} \right) \tag{3.18}$$

Determining the homogeneous part of the total microscopic displacement of the micromorphic continuum is the object of the next section.

3.3 Determination of the homogeneous part of the total microscopic displacement

As done classically in homogenization theories [94]; [105] and [186] towards generalized continua, the microscopic displacement is decomposed additively into a homogeneous part $\mathbf{u}^{\mathrm{hom}}(\boldsymbol{y})$ for the heterogeneous medium identified to an exact micromorphic continuum and a periodic fluctuation denoted $\tilde{\mathbf{u}}(\boldsymbol{y})$, that belongs to the Sobolev space of Y-periodic displacements $H^1_{per}(Y)$, so that it holds

$$\underline{\mathbf{u}} = \underline{\mathbf{u}}^{\mathrm{hom}}(\boldsymbol{\xi}) + \tilde{\underline{\boldsymbol{u}}}(\boldsymbol{\xi}) \tag{3.19}$$

The fluctuation $\tilde{\underline{\mathbf{u}}}(\boldsymbol{\xi})$ corrects the deviation of the microscopic displacement from the homogeneous displacement.

The macroscopic constitutive law relating the macroscopic stress tensors versus their microscopic counterparts will be used to derive the homogenized part of the microscopic displacement; therefore, appropriate averaging rules must be determined. The fundamental assumption underlying the homogenization towards a micromorphic continuum is the principle of the equivalence of the macroscopic and microscopic strain energy densities: the macroscopic energy density of the micromorphic substitution

medium is identified to the volume average of the microscopic energy density. This relation is commonly called Hill-Mandel macrohomogeneity condition [179]; [70]; [69]; [180] and [71], writing for the static and isothermal case,

$$W_M =< w_\mu \left(\underset{\sim}{\boldsymbol{\xi}} \right) >_Y \tag{3.20}$$

The strain energy density in Eq. 3.17 is assumed to depend on the following kinematic variables that pertain to the effective micromorphic continuum:

$$W_M = W_M \left(\underset{\sim}{\mathbf{E}},\ \underset{\sim}{\mathbf{e}},\ \underset{\approx}{\mathbf{K}} \right) \tag{3.21}$$

From Eq. 3.17, and due to the macrohomogeneity of the fields within the macrodomain $V(\underline{\mathbf{x}})$, the variation of the strain energy becomes:

$$\delta W_M = \frac{1}{|V(\boldsymbol{x})|} \int_{V(x)} \left(\bar{\underset{\sim}{\boldsymbol{\sigma}}} : \delta \underset{\sim}{\mathbf{E}} + \underset{\sim}{\mathbf{s}} : \delta \underset{\sim}{\mathbf{e}} + \underset{\approx}{\mathbf{S}} \therefore \delta \underset{\approx}{\mathbf{K}} \right) dV_x \tag{3.22}$$

Eq. 3.22 is the basis for the evaluation of the homogeneous part of the microscopic displacement, as detailed in the next section.

3.3.1 Evaluation of the microscopic displacement from the macroscopic energy

The macroscopic stress measures then follow as the partial derivatives of the strain energy density:

$$\bar{\underset{\sim}{\boldsymbol{\sigma}}} = \frac{\partial W_M}{\partial \underset{\sim}{\mathbf{E}}}; \quad \underset{\sim}{\mathbf{s}} = \frac{\partial W_M}{\partial \underset{\sim}{\mathbf{e}}}; \quad \underset{\approx}{\mathbf{S}} = \frac{\partial W_M}{\partial \underset{\approx}{\mathbf{K}}} \tag{3.23}$$

Given that at micro level the micro stress and strain energy density are connected by the relation $\sigma_{ij} = \frac{\partial W_\mu(\boldsymbol{\varepsilon})}{\partial \varepsilon_{ij}}$, Eq. 3.23 leads to the following three sets of relations:

$$\frac{\partial W_M}{\partial \mathrm{E}_{ij}} = \bar{\sigma}_{ij} = \langle \sigma_{ij} \rangle_Y = \left\langle \sigma_{kl} \frac{\partial \varepsilon_{kl}}{\partial \mathrm{E}_{ij}} \right\rangle_Y \tag{3.24}$$

$$\frac{\partial W_M}{\partial e_{ij}} = s_{ij} = \langle \xi_i \sigma_{jk,k} \rangle_Y = \left\langle \sigma_{pq} \frac{\partial \varepsilon_{pq}}{\partial e_{ij}} \right\rangle_Y \tag{3.25}$$

$$\frac{\partial W_M}{\partial \mathrm{K}_{ijk}} = S_{ijk} = \langle \xi_i \sigma_{jk} \rangle_Y = \left\langle \sigma_{pq} \frac{\partial \varepsilon_{pq}}{\partial \mathrm{K}_{ijk}} \right\rangle_Y \tag{3.26}$$

From the expression of Eqs. 3.24-3.26 along with Eq. 3.23, the homogenous part of the displacement related to the macroscopic kinematic variables $\mathbf{E}(\boldsymbol{x})$, $\underset{\sim}{\mathbf{e}}(\boldsymbol{x})$, and $\underset{\approx}{\mathbf{K}}(\mathbf{x})$ can be evaluated as the sum of the following three contributions:

Firstly, from Eq. 3.24, it follows the subset of integral relations valid for arbitrary stress components therein:

$$\bar{\sigma}_{ij} = \langle \sigma_{ij} \rangle_Y = \left\langle \sigma_{kl} \frac{\partial \varepsilon_{kl}}{\partial \mathrm{E}_{ij}} \right\rangle_Y \rightarrow \int_Y \sigma_{kl} \left(\frac{\partial \varepsilon_{kl}}{\partial \mathrm{E}_{ij}} - \mathrm{I}_{ijkl} \right) dV_y = 0, \quad \forall \sigma_{kl} \tag{3.27}$$

which leads to the expression of the microscopic strain versus the macroscopic strain

$$\frac{\partial \varepsilon^{\mathrm{I}}_{kl}}{\partial \mathrm{E}_{ij}} - \mathrm{I}_{ijkl} = 0 \rightarrow \varepsilon^{\mathrm{I}}_{kl} = \mathrm{I}_{ijkl} \mathrm{E}_{ij} \rightarrow \varepsilon^{\mathrm{I}}_{kl} = \mathrm{E}_{kl} \tag{3.28}$$

Substituting the definition of Cauchy strain, Eq. 3.5 into Eq. 3.28 leads to

$$\frac{\partial u_k^{\mathrm{I}}}{\partial \xi_l} = \mathrm{E}_{kl} \rightarrow u_k^{\mathrm{I}}(y) = \xi_l \mathrm{E}_{kl} \tag{3.29}$$

up to a macroscopic rigid body translation, however not written here.

The second part of the microscopic deformation field can be calculated by forming a BVP by considering Eq. 3.25, and solving it to find the dependency of the microscopic displacement versus the relative strain $\underset{\sim}{\mathbf{e}}(\boldsymbol{x})$:

$$\langle \xi_i \sigma_{jk,k} \rangle_Y = \left\langle \sigma_{pq} \frac{\partial \varepsilon_{pq}}{\partial e_{ij}} \right\rangle_Y \tag{3.30}$$

Eq. 3.30 can be reformulated as

$$\int_Y \left(-\xi_i \sigma_{jk,k} + \sigma_{pq} \frac{\partial \varepsilon_{pq}}{\partial e_{ij}} \right) = 0 \tag{3.31}$$

Integrating by part, one can rewrite Eq. 3.31 as

$$\int_Y \left(\xi_i \sigma_{jk,k} + \sigma_{pq,q} \frac{\partial u_p}{\partial e_{ij}} \right) dV_y - \int_{\partial Y} n_q \sigma_{pq} \frac{\partial u_p}{\partial e_{ij}} ds_y = 0 \tag{3.32}$$

Isolating the volume integral in the BVP 3.32 leads to the following local relation,

$$\int_Y \left(\xi_i \sigma_{jk,k} + \sigma_{pq,q} \frac{\partial u_p}{\partial e_{ij}} \right) dV_y = 0 \rightarrow \xi_i \sigma_{pq,q} \delta_{pj} + \sigma_{pq,q} \frac{\partial u_p}{\partial e_{ij}} = 0, \quad \forall \sigma_{pq,q} \tag{3.33}$$

Solving previous relation leads to the following expression of the deformation field related to the relative strain $\underset{\sim}{\mathbf{e}}(\mathbf{x})$

$$\frac{\partial u_p^{\mathrm{II}}}{\partial e_{ij}} = -\xi_i \delta_{pj} \Rightarrow u_p^{\mathrm{II}}(\xi) = -\xi_i e_{ip} \rightarrow \varepsilon_{pq}^{\mathrm{II}} = -e_{qp} \tag{3.34}$$

Substituting Eq. 3.34 into the boundary condition of Eq. 3.32 (the boundary term) and considering Eq. 3.3 results in the relation

$$\int_{\partial Y} \xi_i t_j ds_y = \int_{\partial Y} \underline{\boldsymbol{\xi}} \otimes \underline{\boldsymbol{t}} ds_y = \underset{\sim}{0} \tag{3.35}$$

The boundary condition 3.35 need to be satisfied. To this end, the balance equation 3.2 is multiplied by $\underline{\boldsymbol{\xi}}$ and integrated over the unit cell volume Y, which results in

$$\int_Y \underline{\boldsymbol{\xi}} \otimes \underline{\mathbf{b}} dV_y + \int_{\partial Y} \underline{\boldsymbol{\xi}} \otimes \underline{\mathbf{t}} ds_y = \underset{\sim}{0} \tag{3.36}$$

Assuming the dependency $\underline{\mathbf{b}} = \underline{\mathbf{b}}(\mathbf{x})$ and $\underline{\boldsymbol{\xi}} = \underline{\boldsymbol{y}}$ - $\underline{\mathbf{x}}$ which $\underline{\mathbf{x}}$ is the geometrical center of the unit cell. the first term in Eq. 3.36 vanishes, which ensures the satisfaction of boundary condition 3.35.

The third part of the displacement field can be constructed using Eq. 3.26 as

$$S_{ijk} = \langle \xi_i \sigma_{jk} \rangle_Y = \left\langle \sigma_{pq} \frac{\partial \varepsilon_{pq}}{\partial \mathrm{K}_{ijk}} \right\rangle_Y \rightarrow \int_Y \sigma_{pq} \left(\frac{\partial \varepsilon_{pq}}{\partial \mathrm{K}_{ijk}} - \xi_i \mathrm{I}_{jkpq} \right) dV_y = 0, \quad \forall \sigma_{pq} \tag{3.37}$$

which leads to the identification of the dependency of the microscopic deformation upon the micromorphic gradient:

$$\frac{\partial \varepsilon_{pq}^{\mathrm{III}}}{\partial \mathrm{K}_{ijk}} - \xi_i \mathrm{I}_{jkpq} = 0 \rightarrow \varepsilon_{pq}^{\mathrm{III}} = \xi_i \mathrm{I}_{jkpq} \mathrm{K}_{ijk} \rightarrow \varepsilon_{pq}^{\mathrm{III}} = \xi_i \mathrm{K}_{ipq} \tag{3.38}$$

Substituting the definition of Cauchy strain, Eq. 3.5 into Eq. 3.38, then leads to

$$\frac{\partial u_p^{\mathrm{III}}}{\partial \xi_q} = \xi_i \mathrm{K}_{ipq} \tag{3.39}$$

According to Eq. 3.29, Eq. 3.33 and Eq. 3.39, one can conclude that the homogeneous part of the displacement expresses as the following quadratic function of the microscopic position

$$\underline{\mathbf{u}}^{\mathrm{hom}}(\boldsymbol{\xi}, \mathbf{x}) = \underline{\mathbf{U}}(\mathbf{x}) + \underset{\sim}{\boldsymbol{\chi}}(\mathbf{x}) \cdot \underline{\boldsymbol{\xi}} + \frac{1}{2} \underline{\underline{\mathbf{K}}}(\mathbf{x}) : \left(\underline{\boldsymbol{\xi}} \otimes \underline{\boldsymbol{\xi}} - \underset{\sim}{\mathbf{G}} \right) \tag{3.40}$$

wherein the tensor of quadratic moments is introduced as

$$\underset{\sim}{\mathbf{G}} = \frac{1}{|\mathrm{Y}|} \int_Y \underline{\boldsymbol{\xi}} \otimes \underline{\boldsymbol{\xi}} dV_y \tag{3.41}$$

3.3.2 Averaged classical and micromorphic kinematic variables

As a next step, the macroscopic variables $\underset{\sim}{\boldsymbol{\chi}}$, $\underline{\underline{\mathbf{K}}}$, $\underline{\mathbf{U}}$ will be defined from the condition that the difference between the homogeneous displacement $\underline{\mathbf{u}}^{\mathrm{hom}}$ and the exact microscopic displacement field $\underline{\mathbf{u}}(\boldsymbol{\xi})$ should be minimized in an average sense over the volume element Y, so according to the condition [105]

$$\underset{\left(\underset{\sim}{\boldsymbol{\chi}}, \underline{\underline{\mathbf{K}}}, \underline{\mathbf{U}} \right)}{Min} \left\langle \left| \underline{\mathbf{u}}(\boldsymbol{\xi}) - \underline{\mathbf{U}}(\mathbf{x}) - \underset{\sim}{\boldsymbol{\chi}}(\mathbf{x}) \cdot \underline{\boldsymbol{\xi}} - \frac{1}{2} \underline{\underline{\mathbf{K}}}(\mathbf{x}) : \left(\underline{\boldsymbol{\xi}} \otimes \underline{\boldsymbol{\xi}} - \underset{\sim}{\mathbf{G}} \right) \right|^2 \right\rangle_Y \tag{3.42}$$

This minimization problem has the following solution, relating the average kinematic variables to the microscopic displacement:

$$\underline{\mathbf{U}}(\boldsymbol{x}) = \left\langle \underline{\mathbf{u}}(\boldsymbol{\xi}) \right\rangle_Y \tag{3.43}$$

$$\underset{\sim}{\boldsymbol{\chi}}(\boldsymbol{x}) = \frac{1}{|\mathrm{Y}|} \left(\int_Y \underline{\mathbf{u}} \otimes \underline{\boldsymbol{\xi}} \, dV_y \right) \cdot \underset{\sim}{\mathbf{G}}^{-1} \tag{3.44}$$

$$\underline{\underline{\mathbf{K}}}(\boldsymbol{x}) = \frac{2}{|\mathrm{Y}|} \left[\int_Y \underline{\mathbf{u}} \otimes \underline{\boldsymbol{\xi}} \otimes \underline{\boldsymbol{\xi}} \, dV_y - \int_Y \underline{\mathbf{u}} \, dV_y \otimes \underset{\sim}{\mathbf{G}} \right] : \left[\underset{\sim}{\mathbf{G}}_4 - \underset{\sim}{\mathbf{G}} \otimes \underset{\sim}{\mathbf{G}} \right]^{-1} \tag{3.45}$$

where $\underset{\sim}{\mathrm{G}}_4$ is the quartic moment of area (normalized by the area) evaluated in the Appendix G. To complete the homogenous part of the displacement field, one has to find the correct polynomial order of the displacement field. To this end, using the abovementioned macroscopic variables and the expression of the complementary energy, the exact order of the stress field will be evaluated, leading in turn to the exact polynomial expansion of the displacement function.

3.3.2.1 Degeneration of the micromorphic to the second gradient and Cosserat theories

In Cosserat and second gradient theories the macroscopic variables are $\underline{\mathbf{E}}$, $\underline{\boldsymbol{\Phi}}$, $\underline{\underline{\mathbf{K}}}$, $\underline{\mathbf{U}}$ and $\underline{\mathbf{E}}$, $\underline{\underline{\mathbf{K}}}$, $\underline{\mathbf{U}}$, respectively. We replace the kinematic tensors $\underset{\sim}{\boldsymbol{\chi}}(\mathbf{x}), \underline{\underline{\mathbf{K}}}(\mathbf{x})$ in Eq.(42) by $\boldsymbol{\epsilon} \cdot \Phi(\mathbf{x})$ and $\boldsymbol{\epsilon} \cdot \underline{\underline{\mathbf{K}}}^{(c)}(\mathbf{x})$ for the micropolar effective medium and by $\underline{\mathbf{E}}(\mathbf{x})$ and by $\underline{\underline{\mathbf{K}}}^{(2nd)}(\mathbf{x})$ for the strain gradient effective continuum. Using the same minimization problem as above leads to following relation between the average kinematic

variables and the microscopic displacement:

$$\textit{Cosserat (micropolar)}\begin{cases}\underline{\mathbf{U}}\left(\boldsymbol{x}\right)=\left\langle \underline{\mathbf{u}}\left(\boldsymbol{\xi}\right)\right\rangle_{Y} & (3.46)\\ \boldsymbol{\epsilon}\cdot\boldsymbol{\Phi}\left(\mathbf{x}\right)=\dfrac{1}{|\mathrm{Y}|}\left(\displaystyle\int_{Y}\underline{\mathbf{u}}\otimes\underline{\boldsymbol{\xi}}\,dV_{y}\right)\cdot\underset{\sim}{\mathrm{G}}^{-1} & (3.47)\\ \boldsymbol{\epsilon}\cdot\underset{\sim}{\mathbf{K}}^{(c)}\left(\boldsymbol{x}\right)=\dfrac{2}{|\mathrm{Y}|}\left[\displaystyle\int_{Y}\underline{\mathbf{u}}\otimes\underline{\boldsymbol{\xi}}\otimes\underline{\boldsymbol{\xi}}\,dV_{y}-\int_{Y}\underline{\mathbf{u}}\,dV_{y}\otimes\underset{\sim}{\mathbf{G}}\right]:\left[\underset{\approx}{\mathrm{G}}_{4}-\underset{\sim}{\mathrm{G}}\otimes\underset{\sim}{\mathrm{G}}\right]^{-1} & (3.48)\end{cases}$$

$$\textit{Second gradient}\begin{cases}\underline{\mathbf{U}}\left(\mathbf{x}\right)=\left\langle \underline{\mathbf{u}}\left(\boldsymbol{\xi}\right)\right\rangle_{Y} & (3.49)\\ \underline{\mathbf{E}}\left(\mathbf{x}\right)=\dfrac{1}{|\mathrm{Y}|}\left(\displaystyle\int_{Y}\underline{\mathbf{u}}\otimes\underline{\boldsymbol{\xi}}\,dV_{y}\right)\cdot\underset{\sim}{\mathbf{G}}^{-1} & (3.50)\\ \underset{\approx}{\mathbf{K}}^{(2nd)}\left(\mathbf{x}\right)=\dfrac{2}{|\mathrm{Y}|}\left[\displaystyle\int_{Y}\underline{\boldsymbol{u}}\otimes\underline{\boldsymbol{\xi}}\otimes\underline{\boldsymbol{\xi}}\,dV_{y}-\int_{Y}\underline{\mathbf{u}}\,dV_{y}\otimes\underset{\sim}{\mathbf{G}}\right]:\left[\underset{\approx}{G}_{4}-\underset{\sim}{G}\otimes\underset{\sim}{G}\right]^{-1} & (3.51)\end{cases}$$

where $\underset{\approx}{\mathbf{K}}^{(2nd)}\left(\mathbf{x}\right)$, $\underline{\boldsymbol{\Phi}}\left(\mathbf{x}\right)$, $\underset{\sim}{\mathbf{K}}^{(c)}\left(\mathbf{x}\right)$, and ϵ are the second gradient tensor, macro rotation tensor, macro curvature tensor, and permutation symbol, respectively; these kinematic tensors are defined as follows:

$$\textit{Cosserat (micropolar)}\begin{cases}\underline{\mathbf{E}}\left(\mathbf{x}\right)=\nabla_{x}\underline{\mathbf{U}}-\underline{\underline{\boldsymbol{\epsilon}}}\cdot\underline{\Phi}\left(\mathbf{x}\right) & (3.52)\\ \underset{\sim}{\mathbf{K}}^{(c)}\left(\mathbf{x}\right)=\nabla_{x}\underline{\Phi} & (3.53)\end{cases}$$

$$\textit{Second gradient}\begin{cases}\underline{\mathbf{E}}\left(\mathbf{x}\right)=\nabla_{x}\underline{\mathbf{U}} & (3.54)\\ \underset{\approx}{\mathbf{K}}^{(2nd)}\left(\mathbf{x}\right)=\nabla_{x}\underset{\approx}{\mathrm{E}} & (3.55)\end{cases}$$

3.3.3 Determination of the microscopic stress based on complementary energy and Hill lemma

The macroscopic strain energy density can be written using Euler's homogeneity theorem for quadratic functions of its argument as

$$2W_{M}\left(\boldsymbol{\chi},\ \mathbf{K}\right)=\frac{\partial W_{M}}{\partial\underset{\sim}{\boldsymbol{\chi}}}:\underset{\sim}{\boldsymbol{\chi}}+\frac{\partial W_{M}}{\partial\underset{\approx}{\mathbf{K}}}\therefore\underline{\underline{\mathbf{K}}}=\bar{\boldsymbol{\sigma}}:\underset{\sim}{\boldsymbol{\chi}}+\underline{\underline{\mathbf{S}}}\therefore\underline{\underline{\mathbf{K}}} \tag{3.56}$$

Assuming that $W_{M}\left(\boldsymbol{\chi},\ \mathbf{K}\right)$ is a differentiable and convex function with respect to its arguments $\underset{\sim}{\boldsymbol{\chi}}$ and $\underset{\approx}{\mathbf{K}}$, a one-to-one correspondence between $\left(\underset{\sim}{\boldsymbol{\chi}},\ \underset{\approx}{\mathbf{K}}\right)$ and $\left(\bar{\boldsymbol{\sigma}},\ \underline{\underline{\mathbf{S}}}\right)$ can be established, leading to the complementary energy density $W_{M}^{C}\left(\bar{\boldsymbol{\sigma}},\ \boldsymbol{S}\right)$, elaborated by the following Legendre transform of $W_{M}\left(\boldsymbol{\chi},\ \mathbf{K}\right)$:

$$W_{M}^{C}\left(\bar{\boldsymbol{\sigma}},\ \boldsymbol{S}\right):=\underset{\boldsymbol{x}\in\left(\underset{\sim}{\boldsymbol{\chi}},\ \underset{\approx}{\mathbf{K}}\right)}{Sup}\left[\frac{\partial W_{M}\left(\boldsymbol{\chi},\ \mathbf{K}\right)}{\partial\mathbf{x}}.\underline{\boldsymbol{x}}-W_{M}\left(\boldsymbol{\chi},\ \mathbf{K}\right)\right] \tag{3.57}$$

Expression 3.57 leads to the constitutive law in inverse form

$$\underset{\sim}{\boldsymbol{\chi}}=\frac{\partial W_{M}^{C}\left(\bar{\boldsymbol{\sigma}},\ \boldsymbol{S}\right)}{\partial\bar{\boldsymbol{\sigma}}},\qquad\underset{\approx}{\mathbf{K}}=\frac{\partial W_{M}^{C}\left(\bar{\boldsymbol{\sigma}},\ \mathbf{S}\right)}{\partial\mathbf{S}} \tag{3.58}$$

Similar to the above statement, the micro complementary energy is elaborated as

$$W_{\mu}^{C}\boldsymbol{\sigma}:=\underset{\left(\underline{\boldsymbol{\varepsilon}}\right)}{Sup}\left[\frac{\partial W_{\mu}\left(\boldsymbol{\varepsilon}\right)}{\partial\underline{\boldsymbol{\varepsilon}}}.\underline{\boldsymbol{\varepsilon}}-W_{\mu}\left(\boldsymbol{\varepsilon}\right)\right] \tag{3.59}$$

Expression 3.59 leads to the constitutive law in inverse form

$$\underset{\sim}{\boldsymbol{\xi}} = \frac{\partial W_{\mu}^{C}(\boldsymbol{\sigma})}{\partial \boldsymbol{\sigma}} \tag{3.60}$$

Given that at the micro level the micro strain and complementary energy density are related by Eq. 3.60, Eq. 3.58 leads to the following expressions

$$\chi_{ij} = \left\langle \varepsilon_{pq} \frac{\partial \sigma_{pq}}{\partial \bar{\sigma}_{ij}} \right\rangle_{Y}, \qquad \mathrm{K}_{ijk} = \left\langle \varepsilon_{pq} \frac{\partial \sigma_{pq}}{\partial S_{ijk}} \right\rangle_{Y} \tag{3.61}$$

Substituting the expression of tensor form Eq. 3.44 into Eq. 3.61 results in the following integral relation:

$$\int_{Y} \left(\delta\varepsilon_{pq} \frac{\partial \sigma_{pq}}{\partial \bar{\sigma}_{ij}} - \delta u_i \xi_k {G_{kj}}^{-1} \right) dV_y = 0 \tag{3.62}$$

Integrating by part Eq. 3.62 and using the micro strain definition, $\varepsilon_{pq} = (u_{p,q})^{s}$, and the symmetry of Cauchy stress tensor one obtains the following integral relation:

$$\int_{Y} \left(\delta u_p \frac{\partial}{\partial \xi_q} \left(\frac{\partial \sigma_{pq}}{\partial \bar{\sigma}_{ij}} \right) + \delta_{ip} \delta u_p \xi_k {G_{kj}}^{-1} \right) dV_y = 0, \quad \forall \delta u_p \tag{3.63}$$

Solving the BVP 3.63 for the microscopic stress $\underset{\sim}{\boldsymbol{\sigma}}$ leads to

$$\frac{\partial \sigma_{pq}}{\partial \bar{\sigma}_{ij}} = -{G_{jk}}^{-1} \xi_k \xi_q \delta_{ip} + T_{pqij}(x) \rightarrow \sigma_{pq}(\boldsymbol{\xi}, \bar{\boldsymbol{\sigma}}) = -\bar{\sigma}_{pj} {G_{jk}}^{-1} \xi_k \xi_q + T_{pqlm} \bar{\sigma}_{lm} \tag{3.64}$$

where T_{pqij} is an integration constant. According to the expression of the microscopic stress $\underset{\sim}{\boldsymbol{\sigma}}$ in Eq. 3.64, it can be concluded that $\underset{\sim}{\boldsymbol{\xi}}$ is quadratic in $\underline{\boldsymbol{\xi}}$ and therefore $\underline{\mathbf{u}}(\boldsymbol{\xi})$ is cubic in $\underline{\boldsymbol{\xi}}$. Similarly, substituting Eq. 3.45 into Eq. 3.61, and integrating by part results in

$$\begin{aligned} &\int_{Y} \left(\delta u_p \frac{\partial}{\partial \xi_q} \left(\frac{\partial \sigma_{pq}}{\partial S_{ijk}} \right) + 2\delta_{ip} \delta u_p \xi_l \xi_m \left[(G_4)_{lmjk} - G_{lm} G_{jk} \right]^{-1} \right. \\ &\left. -2\delta_{ip} \delta u_p G_{lm} \left[(G_4)_{lmjk} - G_{lm} G_{jk} \right]^{-1} \right) dV_y = 0, \quad \forall \delta u_p \end{aligned} \tag{3.65}$$

Solving the BVP 3.65 for $\underset{\sim}{\boldsymbol{\sigma}}$ leads to

$$\sigma_{pq}(\boldsymbol{\xi}, \boldsymbol{S}) = -2S_{pjk} \xi_l \xi_m \xi_q \left[(G_4)_{lmjk} - G_{lm} G_{jk} \right]^{-1} + 2S_{pjk} \xi_q G_{lm} \left[(G_4)_{lmjk} - G_{lm} G_{jk} \right]^{-1} + R_{pqijk} S_{ijk} \tag{3.66}$$

where R_{pqijk} is the integrating constant. Looking at Eq. 3.65, one can conclude that $\underset{\sim}{\boldsymbol{\xi}}$ has linear and cubic terms in $\underline{\boldsymbol{\xi}}$ and therefore $\underline{\mathbf{u}}(\boldsymbol{\xi})$ has a quadratic and 4^{th} order terms in $\underline{\boldsymbol{\xi}}$.

Due to the linearity of the microscopic fields versus the macroscopic variables over the unit cell, one can apply summation over the partial stresses in Eq. 3.64 and Eq. 3.66, which leads to the following expression of the microscopic stress field:

$$\begin{aligned} &\sigma_{pq}(\boldsymbol{\xi}, \bar{\boldsymbol{\sigma}}, \boldsymbol{S}) = -2S_{pjk} \xi_l \xi_m \xi_q \left[(G_4)_{lmjk} - G_{lm} G_{jk} \right]^{-1} + 2S_{pjk} \xi_q G_{lm} \left[(G_4)_{lmjk} - G_{lm} G_{jk} \right]^{-1} \\ &-\bar{\sigma}_{pj} {G_{jk}}^{-1} \xi_k \xi_q + T_{pqlm} \bar{\sigma}_{lm} + R_{pqijk} S_{ijk} \end{aligned} \tag{3.67}$$

3.3.4 Determination of the complete homogeneous part of the microscopic displacement field from macroscopic complementary energy

One can infer from the previously obtained expression of the microscopic stress field, Eq. 3.67, cubic in the microscopic relative position that the induced displacement field will express as a quartic polynomial expansion of the relative position, as follows:

$$u_i^{\mathrm{hom}}(\boldsymbol{\xi},\boldsymbol{x}) = A_i(\boldsymbol{x}) + B_{ij}(\boldsymbol{x})\,\xi_j + \frac{1}{2}C_{ijk}(\boldsymbol{x})\,\xi_j\xi_k + \frac{1}{3}D_{ijkl}(\boldsymbol{x})\,\xi_j\xi_k\xi_l + \frac{1}{4}E_{ijklm}(\boldsymbol{x})\,\xi_j\xi_k\xi_l\xi_m \tag{3.68}$$

The displacement field 3.67 completes the quadratic expansion obtained previously in Eq. 3.40; it accordingly involves five unknown coefficients, the determination of which is exposed in Appendix F. The final expression of the homogenous part of the microscopic displacement versus the macroscopic strain and strain gradient tensors corresponding to the homogeneous exact displacement field representative of a pure micromorphic continuum receives the following expression

$$\begin{aligned}\underline{\mathbf{u}}^{\mathrm{hom}}(\boldsymbol{\xi},\mathbf{x}) = {}& \underset{\sim}{\mathbf{E}}(\mathbf{x})\cdot\underline{\boldsymbol{\xi}} - \underset{\sim}{\mathbf{e}}(\mathbf{x})\cdot\underset{\sim}{\boldsymbol{\Gamma}}\cdot\underline{\boldsymbol{\xi}} + \underset{\sim}{\mathbf{e}}(\mathbf{x})\cdot\underset{\approx}{\boldsymbol{\Upsilon}}\therefore\left(\underline{\boldsymbol{\xi}}\otimes\underline{\boldsymbol{\xi}}\otimes\underline{\boldsymbol{\xi}}\right) + \frac{1}{2}\underline{\underline{\mathbf{K}}}:\left(\underline{\boldsymbol{\xi}}\otimes\underline{\boldsymbol{\xi}}\right)\\ & - \frac{1}{4}\left(\mathrm{P}^{-1}\underline{\underline{\mathbf{K}}}:\underline{\underline{\mathbf{G}}}\right)\otimes\underset{\approx}{\boldsymbol{\Lambda}}::\underset{\approx}{\underline{\underline{\boldsymbol{\Omega}}}}:\left(\underline{\boldsymbol{\xi}}\otimes\underline{\boldsymbol{\xi}}\right) + \frac{1}{4}\left(\mathrm{P}^{-1}\underline{\underline{\mathbf{K}}}:\underline{\underline{\mathbf{G}}}\right)\otimes\underset{\approx}{\boldsymbol{\Lambda}}::\left(\underline{\boldsymbol{\xi}}\otimes\underline{\boldsymbol{\xi}}\otimes\underline{\boldsymbol{\xi}}\otimes\underline{\boldsymbol{\xi}}\right)\end{aligned} \tag{3.69}$$

The homogenous part of the micro strain is obtained from the micro displacement in Eq. 3.68 as

$$\begin{aligned}\varepsilon_{ij}^{\mathrm{hom}}(\boldsymbol{\xi},\boldsymbol{x}) = {}& B_{ij}(\boldsymbol{x}) + \frac{1}{2}C_{ikl}(\boldsymbol{x})\left(\xi_k(\mathrm{I}_2)_{lj} + \xi_l(\mathrm{I}_2)_{kj}\right) + \frac{1}{3}D_{ilkm}(\boldsymbol{x})\left(\xi_k\xi_l(\mathrm{I}_2)_{mj} + \xi_k\xi_m(\mathrm{I}_2)_{lj} + \xi_l\xi_m(\mathrm{I}_2)_{lj}\right)\\ & + \frac{1}{4}E_{irlmn}(\boldsymbol{x})\left(\xi_r\xi_l\xi_m(\mathrm{I}_2)_{nj} + \xi_r\xi_l\xi_n(\mathrm{I}_2)_{mj} + \xi_r\xi_m\xi_n(\mathrm{I}_2)_{lj} + \xi_l\xi_m\xi_n(\mathrm{I}_2)_{rj}\right)\end{aligned} \tag{3.70}$$

Inserting the expression of coefficients $\underline{\underline{\mathbf{B}}}$, $\underset{\sim}{\boldsymbol{C}}$, $\underset{\approx}{\mathbf{D}}$, and $\underline{\underline{\underline{\mathbf{E}}}}$ versus the macroscopic variables into Eq. 3.70 results in the following cubic polynomial expression of the microscopic homogeneous strain

$$\begin{aligned}\boldsymbol{\varepsilon}_{ij}^{\mathrm{hom}} = {}& \mathrm{E}_{ij} - e_{iq}\Gamma_{qj} + e_{iq}\Upsilon_{qklm}\left(\xi_k\xi_l(\mathrm{I}_2)_{mj} + \xi_k\xi_m(\mathrm{I}_2)_{lj} + \xi_l\xi_m(\mathrm{I}_2)_{kj}\right)\\ & + \frac{1}{2}\mathrm{K}_{ikl}\left(\xi_k(\mathrm{I}_2)_{lj} + \xi_l(\mathrm{I}_2)_{kj}\right) - \frac{1}{4}\left(\mathrm{P}^{-1}\mathrm{K}_{ist}G_{st}\right)\Lambda_{rlmn}\Omega_{rlmnpq}\left(\xi_p(\mathrm{I}_2)_{qj} + \xi_q(\mathrm{I}_2)_{pj}\right)\\ & + \frac{1}{4}\left(\mathrm{P}^{-1}\mathrm{K}_{ist}G_{st}\right)\Lambda_{rlmn}\left(\xi_r\xi_l\xi_m(\mathrm{I}_2)_{nj} + \xi_r\xi_l\xi_n(\mathrm{I}_2)_{mj} + \xi_r\xi_m\xi_n(\mathrm{I}_2)_{lj} + \xi_l\xi_m\xi_n(\mathrm{I}_2)_{rj}\right)\end{aligned} \tag{3.71}$$

The displacement and strain fields are evaluated in Appendix G, for a 2D square unit cell with a side length of 'a'. Previous relation 3.69 writes in tensor format as

$$\underline{\mathbf{u}}^{\mathrm{hom}} = \underline{\underline{\mathbf{a}}}(\boldsymbol{\xi}) : \underset{\sim}{\mathbf{E}}(\mathbf{x}) + \underline{\underline{\mathbf{b}}}(\boldsymbol{\xi}) : \underset{\sim}{\mathbf{e}}(\mathbf{x}) + \underset{\approx}{\underline{\underline{\mathbf{c}}}}(\boldsymbol{\xi}) \therefore \underline{\underline{\mathbf{K}}}(\mathbf{x}) \tag{3.72}$$

with the following expressions of the coefficients therein:

$$\begin{aligned}\underline{\underline{\mathbf{a}}}(\boldsymbol{\xi}) &= \left(\underset{\approx}{\mathbf{I}}\right)_4\cdot\underline{\boldsymbol{\xi}}\\ \underline{\underline{\mathbf{b}}}(\boldsymbol{\xi}) &= \left(\underset{\approx}{\mathbf{I}}\right)_4\cdot\left[\underset{\approx}{\boldsymbol{\Upsilon}}\therefore\left(\underline{\boldsymbol{\xi}}\otimes\underline{\boldsymbol{\xi}}\otimes\underline{\boldsymbol{\xi}}\right) - \underset{\sim}{\boldsymbol{\Gamma}}\cdot\underline{\boldsymbol{\xi}}\right]\\ \underset{\approx}{\underline{\underline{\mathbf{c}}}}(\boldsymbol{\xi}) &= \left(\underset{\approx}{\mathbf{I}}\right)_6 : \left[\frac{1}{2}\left(\underline{\boldsymbol{\xi}}\otimes\underline{\boldsymbol{\xi}}\right) - \frac{1}{4}\left(\mathrm{P}^{-1}\underline{\underline{\mathbf{G}}}\right)\otimes\underset{\approx}{\boldsymbol{\Lambda}}::\underset{\approx}{\underline{\underline{\boldsymbol{\Omega}}}}:\left(\underline{\boldsymbol{\xi}}\otimes\underline{\boldsymbol{\xi}}\right) + \frac{1}{4}\left(\mathrm{P}^{-1}\underline{\underline{\mathbf{G}}}\right)\otimes\underset{\approx}{\boldsymbol{\Lambda}}::\left(\underline{\boldsymbol{\xi}}\otimes\underline{\boldsymbol{\xi}}\otimes\underline{\boldsymbol{\xi}}\otimes\underline{\boldsymbol{\xi}}\right)\right]\end{aligned} \tag{3.73}$$

The determination of the homogeneous part of the displacement is the basis for formulating an extended Hill macrohomogeneity lemma that holds for the micromorphic effective continuum, proven in

Appendix H. It traduces the identity of the average microscopic energy with the energy of the postulated micromorphic continuum obtained as Eqs. H.22, H.23, and H.24:

$$\begin{aligned}
\int_Y \underset{\sim}{\boldsymbol{\sigma}} : (\underset{\sim}{\boldsymbol{\omega}} \otimes \nabla_y) dV_y = & \sum_{i=1,2} \left(\left(\underset{\sim}{\mathbf{E}}(\mathbf{x}) \cdot \underset{\sim}{\boldsymbol{Y}}^i \right) \otimes \underset{\sim}{\boldsymbol{N}}^i \right) : \frac{1}{|Y|} \sum_{j=1,2} \left(\int_{\partial Y} \left(\underset{\sim}{\boldsymbol{\sigma}} \cdot \underset{\sim}{\mathbf{n}} \right) ds_y \otimes \underset{\sim}{\boldsymbol{Y}}^j \right) \\
& + \sum_{i=1,2} \left(\left(\underset{\sim}{\mathbf{e}}(\mathbf{x}) \cdot \underset{\approx}{\Upsilon} \cdot \underset{\sim}{\boldsymbol{Y}}^i \right) \otimes \underset{\sim}{\mathbf{N}}^i \right) :: \frac{3}{|Y|} \sum_{j=1,2} \frac{1}{3} \left(\int_{\partial Y} \left(\underset{\sim}{\boldsymbol{\sigma}} \cdot \underset{\sim}{\mathbf{n}} \right) ds_y \otimes \underset{\sim}{\boldsymbol{Y}}^j \otimes \underset{\sim}{\boldsymbol{Y}}^j \otimes \underset{\sim}{\boldsymbol{Y}}^j \right) \\
& - \sum_{i=1,2} \left(\left(\underset{\sim}{\mathbf{e}}(\mathbf{x}) \cdot \underset{\sim}{\boldsymbol{\Gamma}} \cdot \underset{\sim}{\boldsymbol{Y}}^i \right) \otimes \underset{\sim}{\mathbf{N}}^i \right) : \frac{1}{|Y|} \sum_{j=1,2} \left(\int_{\partial Y} \left(\underset{\sim}{\boldsymbol{\sigma}} \cdot \underset{\sim}{\mathbf{n}} \right) ds_y \otimes \underset{\sim}{\boldsymbol{Y}}^j \right) \\
& \sum_{i=1,2} \left(\left(\underset{\approx}{\mathrm{K}}(\mathbf{x}) \cdot \underset{\sim}{\boldsymbol{Y}}^i \right) \otimes \underset{\sim}{\mathbf{N}}^i \right) \therefore \frac{2}{|Y|} \sum_{j=1,2} \frac{1}{2} \left(\int_{\partial Y} \left(\underset{\sim}{\boldsymbol{\sigma}} \cdot \underset{\sim}{\mathbf{n}} \right) ds_y \otimes \underset{\sim}{\boldsymbol{Y}}^j \otimes \underset{\sim}{\boldsymbol{Y}}^j \right) \\
& - \mathrm{P}^{-1} \sum_{i=1,2} \left(\left(\underset{\approx}{\mathrm{K}}(\mathbf{x}) : \underset{\sim}{\mathbf{G}} \otimes \underset{\approx}{\boldsymbol{\Lambda}} :: \underset{\approx\approx}{\boldsymbol{\Omega}} \cdot \underset{\sim}{\boldsymbol{Y}}^i \right) \otimes \underset{\sim}{\mathbf{N}}^i \right) \therefore \frac{2}{|Y|} \sum_{j=1,2} \frac{1}{2} \left(\int_{\partial Y} \left(\underset{\sim}{\boldsymbol{\sigma}} \cdot \underset{\sim}{\mathbf{n}} \right) ds_y \otimes \underset{\sim}{\boldsymbol{Y}}^j \right) \\
& + P^{-1} \sum_{i=1,2} \left(\left(\underset{\approx}{\mathrm{K}}(\mathbf{x}) : \underset{\sim}{\mathbf{G}} \otimes \underset{\approx}{\boldsymbol{\Lambda}} \cdot \underset{\sim}{\boldsymbol{Y}}^i \right) \otimes \underset{\sim}{\mathbf{N}}^i \right) :: \frac{4}{|Y|} \sum_{j=1,2} \frac{1}{4} \left(\int_{\partial Y} \left(\underset{\sim}{\boldsymbol{\sigma}} \cdot \underset{\sim}{\mathbf{n}} \right) ds_y \otimes \underset{\sim}{\boldsymbol{Y}}^j \otimes \underset{\sim}{\boldsymbol{Y}}^j \otimes \underset{\sim}{\boldsymbol{Y}}^j \otimes \underset{\sim}{\boldsymbol{Y}}^j \right) \\
& = \langle \underset{\sim}{\boldsymbol{\sigma}} \rangle_Y : \underset{\sim}{\mathbf{E}}(\mathbf{x}) + \left[3 \left\langle \underset{\sim}{\boldsymbol{\xi}} \otimes \underset{\sim}{\boldsymbol{\xi}} \otimes \underset{\sim}{\boldsymbol{\sigma}} \right\rangle_Y \therefore \underset{\approx}{\Upsilon} - \langle \underset{\sim}{\boldsymbol{\sigma}} \rangle_Y \cdot \underset{\sim}{\boldsymbol{\Gamma}} \right] : \underset{\sim}{\mathbf{e}}(\mathbf{x}) \\
& + \left[2 \left\langle \underset{\sim}{\boldsymbol{\xi}} \otimes \underset{\sim}{\boldsymbol{\sigma}} \right\rangle_Y - 2\mathrm{P}^{-1} \underset{\sim}{\mathbf{G}} \otimes \underset{\approx}{\boldsymbol{\Lambda}} :: \left(\underset{\approx\approx}{\boldsymbol{\Omega}} : \left\langle \underset{\sim}{\boldsymbol{\xi}} \otimes \underset{\sim}{\boldsymbol{\sigma}} \right\rangle_Y + 2 \left\langle \underset{\sim}{\boldsymbol{\xi}} \otimes \underset{\sim}{\boldsymbol{\xi}} \otimes \underset{\sim}{\boldsymbol{\xi}} \otimes \underset{\sim}{\boldsymbol{\sigma}} \right\rangle_Y \right) \right] \therefore \underset{\approx}{\mathrm{K}}(\mathbf{x})
\end{aligned} \tag{3.74}$$

The previous relation constitutes Hill macrohomogeneity condition for the strain gradient effective continuum, highlighting in the last expression the stress measures conjugated to the macroscopic kinematic variables, tensors $\underset{\sim}{\mathbf{e}}(\mathbf{x})$, $\underset{\approx}{\mathbf{K}}(\mathbf{x})$, namely the relative stress and hyperstress expressing as

$$\underset{\sim}{\mathbf{s}} := 3 \left\langle \underset{\sim}{\boldsymbol{\xi}} \otimes \underset{\sim}{\boldsymbol{\xi}} \otimes \underset{\sim}{\boldsymbol{\sigma}} \right\rangle_Y \therefore \underset{\approx}{\Upsilon} - \langle \underset{\sim}{\boldsymbol{\sigma}} \rangle_Y \cdot \underset{\sim}{\boldsymbol{\Gamma}} \tag{3.75}$$

$$\underset{\approx}{\mathbf{S}} := 2 \left\langle \underset{\sim}{\boldsymbol{\xi}} \otimes \underset{\sim}{\boldsymbol{\sigma}} \right\rangle_Y - 2\mathrm{P}^{-1} \underset{\sim}{\mathbf{G}} \otimes \underset{\approx}{\boldsymbol{\Lambda}} :: \left(\underset{\approx\approx}{\boldsymbol{\Omega}} : \left\langle \underset{\sim}{\boldsymbol{\xi}} \otimes \underset{\sim}{\boldsymbol{\sigma}} \right\rangle_Y + 2 \left\langle \underset{\sim}{\boldsymbol{\xi}} \otimes \underset{\sim}{\boldsymbol{\xi}} \otimes \underset{\sim}{\boldsymbol{\xi}} \otimes \underset{\sim}{\boldsymbol{\sigma}} \right\rangle_Y \right) \tag{3.76}$$

We have obtained at this final stage the complete quartic expression of the displacement field, Eqs. 3.75 and 3.76; this leads to the new expression of the relative stress and hyperstress tensors. It is important to note that the obtained expression of the relative stress does not depend on the body forces; this is further shown in the proposed derivation of the extended Hill macrohomogeneity condition developed in Appendix H (we assume nil body forces in the microscopic BVP).

3.3.5 Determination of the complete homogeneous part of the microscopic displacement field for Cosserat and second gradient theories

The displacement field 3.68 contains five unknowns that can be determined using the procedure explained in Appendix C. In order to find the homogenous part of the displacement field of Cosserat theory, the set of equations 3.46-3.48, 3.52-3.53 and for second gradient theory, the set of equations 3.49-3.51, 3.54, and 3.55 must be used instead of the expressions F.1-F.5, leading to the following expressions for the homogenous microscopic displacement fields of the micropolar and second gradient, respectively:

$$\begin{aligned}
\underset{\sim}{\mathbf{u}}^{\text{micropolar, hom}}(\boldsymbol{\xi}, \mathbf{x}) = & \underset{\sim}{\mathbf{E}}(\mathbf{x}) \cdot \underset{\sim}{\boldsymbol{\xi}} - \underset{\sim}{\mathbf{E}}(\mathbf{x}) \cdot \underset{\sim}{\boldsymbol{\Gamma}} \cdot \underset{\sim}{\boldsymbol{\xi}} + \underset{\sim}{\boldsymbol{\epsilon}} \cdot \underset{\sim}{\Phi}(\mathbf{x}) \cdot \underset{\sim}{\boldsymbol{\xi}} + \underset{\approx}{\mathbf{E}}(\mathbf{x}) \cdot \underset{\approx}{\Upsilon} \therefore \left(\underset{\sim}{\boldsymbol{\xi}} \otimes \underset{\sim}{\boldsymbol{\xi}} \otimes \underset{\sim}{\boldsymbol{\xi}} \right) + \frac{1}{2} \underset{\sim}{\boldsymbol{\epsilon}} \cdot \underset{\approx}{\mathbf{K}} : \left(\underset{\sim}{\boldsymbol{\xi}} \otimes \underset{\sim}{\boldsymbol{\xi}} \right) \\
& - \frac{1}{4} \left(\mathrm{P}^{-1} \underset{\sim}{\boldsymbol{\epsilon}} \cdot \underset{\approx}{\mathbf{K}} : \underset{\sim}{\mathbf{G}} \right) \otimes \underset{\approx}{\boldsymbol{\Lambda}} :: \underset{\approx\approx}{\boldsymbol{\Omega}} : \left(\underset{\sim}{\boldsymbol{\xi}} \otimes \underset{\sim}{\boldsymbol{\xi}} \right) + \frac{1}{4} \left(\mathrm{P}^{-1} \underset{\sim}{\boldsymbol{\epsilon}} \cdot \underset{\approx}{\mathbf{K}} : \underset{\sim}{\mathbf{G}} \right) \otimes \underset{\approx}{\boldsymbol{\Lambda}} :: \left(\underset{\sim}{\boldsymbol{\xi}} \otimes \underset{\sim}{\boldsymbol{\xi}} \otimes \underset{\sim}{\boldsymbol{\xi}} \otimes \underset{\sim}{\boldsymbol{\xi}} \right)
\end{aligned} \tag{3.77}$$

$$\underline{\mathbf{u}}^{\text{secondgrad, hom}}(\boldsymbol{\xi},\mathbf{x}) = \underset{\sim}{\mathbf{E}}(\mathbf{x})\cdot\underline{\boldsymbol{\xi}} + \frac{1}{2}\underset{\sim}{\mathbf{K}} : \left(\underline{\boldsymbol{\xi}}\otimes\underline{\boldsymbol{\xi}}\right) \tag{3.78}$$

The full kinematics of the micromorphic continuum and its two degenerated media (micropolar and strain gradient) is expressed in the set of equations F.22.

3.4 Variational principle for the determination of the fluctuating part of the displacement

In general, one may adopt the generic expansion of the homogeneous part of the microscopic displacement, Eq. 3.72 and substitute it into the total displacement, the vector in Eq. 3.19:

$$\underline{\mathbf{u}}(\boldsymbol{\xi},\mathbf{x}) = \underline{\underline{\mathbf{a}}}(\boldsymbol{\xi}) : \underset{\sim}{\mathbf{E}}(\mathbf{x}) + \underline{\underline{\mathbf{b}}}(\boldsymbol{\xi}) : \underset{\sim}{\mathbf{e}}(\mathbf{x}) + \underset{\approx}{\mathbf{c}}(\boldsymbol{\xi}) \therefore \underline{\underline{\mathbf{K}}}(\mathbf{x}) + \underline{\tilde{\mathbf{u}}}(\boldsymbol{\xi}) \tag{3.79}$$

with $\underline{\underline{\mathbf{a}}}(\boldsymbol{\xi})$, $\underline{\underline{\mathbf{b}}}(\boldsymbol{\xi})$, and $\underset{\approx}{\mathbf{c}}(\boldsymbol{\xi})$ therein third-order, third-order, and fourth-order tensors (expressed in Eq. 3.73), respectively. The homogeneous part of the displacement has been obtained from the extended Hill lemma and expressing the three conjugated stress measures as per their definition introduced in section 3.2. The fluctuating part of the displacement corrects for the existing discrepancies between the (postulated) homogeneous effective micromorphic continuum and the real displacement field of the heterogeneous media.

An extended minimization principle over all periodic fluctuations holds, so that one can write

$$\begin{aligned} W_M\left(\underset{\sim}{\mathbf{E}},\ \underset{\sim}{\mathbf{e}},\ \underline{\underline{\mathbf{K}}}\right) &= \underset{\underline{\tilde{\mathbf{u}}}\in H^1_{per}(Y)}{Min}\left\{\int_Y \frac{1}{2}\left(\underline{\mathbf{u}}^{\text{hom}}\otimes\nabla_\xi + \underline{\tilde{\mathbf{u}}}(\boldsymbol{\xi})\otimes\nabla_\xi\right) : \underset{\approx}{\mathbf{C}}(\boldsymbol{\xi}) : \left(\underline{\mathbf{u}}^{\text{hom}}\otimes\nabla_\xi + \underline{\tilde{\mathbf{u}}}(\boldsymbol{\xi})\otimes\nabla_\xi\right) dV_y\right\} \\ &= \underset{\underline{\tilde{\mathbf{u}}}\in H^1_{per}(Y)}{Min}\left\{\begin{array}{l}\displaystyle\int_Y \frac{1}{2}\underset{\approx}{\mathbf{C}}(\boldsymbol{\xi}) : \left(\underline{\underline{\mathbf{a}}}(\boldsymbol{\xi})\otimes\nabla_\xi : \underset{\sim}{\mathbf{E}}(\mathbf{x}) + \underline{\underline{\mathbf{b}}}(\boldsymbol{\xi})\otimes\nabla_\xi : \underset{\sim}{\mathbf{e}}(\mathbf{x}) + \underset{\approx}{\mathbf{c}}(\boldsymbol{\xi})\otimes\nabla_\xi \therefore \underline{\underline{\mathbf{K}}}(\mathbf{x}) + \underline{\tilde{\mathbf{u}}}(\boldsymbol{\xi})\otimes\nabla_\xi\right) \\ : \left(\underline{\underline{\mathbf{a}}}(\boldsymbol{\xi})\otimes\nabla_\xi : \underset{\sim}{\mathbf{E}}(\mathbf{x}) + \underline{\underline{\mathbf{b}}}(\boldsymbol{\xi})\otimes\nabla_\xi : \underset{\sim}{\mathbf{e}}(\mathbf{x}) + \underset{\approx}{\mathbf{c}}(\boldsymbol{\xi})\otimes\nabla_\xi \therefore \underline{\underline{\mathbf{K}}}(\mathbf{x}) + \underline{\tilde{\mathbf{u}}}(\boldsymbol{\xi})\otimes\nabla_\xi\right) dV_y\end{array}\right\} \end{aligned} \tag{3.80}$$

The stationarity condition of the functional on the right-hand side of Eq. 3.80 delivers as a necessary condition a BVP to be satisfied by the optimal fluctuation associated to the real displacement field (in the absence of body forces):

$$\left|\begin{array}{l} -div_\xi\left\{\underset{\approx}{\mathbf{C}}(\boldsymbol{\xi}) : \left(\underline{\underline{\mathbf{a}}}(\boldsymbol{\xi})\otimes\nabla_\xi : \underset{\sim}{\mathbf{E}}(x) + \underline{\underline{\mathbf{b}}}(\boldsymbol{\xi})\otimes\nabla_\xi : \underset{\sim}{\mathbf{e}}(\mathbf{x}) + \underset{\approx}{\mathbf{c}}(\boldsymbol{\xi})\otimes\nabla_\xi \therefore \underline{\underline{\mathbf{K}}}(\mathbf{x}) + \underline{\tilde{\mathbf{u}}}(\boldsymbol{\xi})\otimes\nabla_\xi\right)\right\} = \mathbf{0} \\ \underline{\tilde{\mathbf{u}}}(\boldsymbol{\xi}) \text{ Y - periodic} \end{array}\right. \tag{3.81}$$

The linearity of the solution of the previous BVP versus the prescribed kinematic macroscopic loading, tensors $\underset{\sim}{\mathbf{E}}$, $\underset{\sim}{\mathbf{e}}$, $\underline{\underline{\mathbf{K}}}$, ensures the existence of three displacement localization functions, successively the two third-order tensor and the fourth-order tensor $\underline{\underline{\mathbf{H}}}^E(\boldsymbol{\xi})$, $\underline{\underline{\mathbf{H}}}^e(\boldsymbol{\xi})$, $\underset{\approx}{\mathbf{H}}^K(\boldsymbol{\xi})$ such that the displacement fluctuation decomposes as

$$\underline{\tilde{\mathbf{u}}}(\boldsymbol{\xi},\mathbf{x}) = \underline{\underline{\mathbf{H}}}^E(\boldsymbol{\xi}) : \underset{\sim}{\mathbf{E}}(\mathbf{x}) + \underline{\underline{\mathbf{H}}}^e(\boldsymbol{\xi}) : \underset{\sim}{\mathbf{e}}(\mathbf{x}) + \underset{\approx}{\mathbf{H}}^K(\boldsymbol{\xi}) \therefore \underline{\underline{\mathbf{K}}}(\mathbf{x}) \tag{3.82}$$

Substituting the expression of the fluctuation, Eq. 3.82, into the displacement field, Eq. 3.79, results in

$$\underline{\mathbf{u}}(\boldsymbol{\xi},\mathbf{x}) = \left(\underline{\underline{\mathbf{a}}}(\boldsymbol{\xi}) + \underline{\underline{\mathbf{H}}}^E(\boldsymbol{\xi})\right) : \underset{\sim}{\mathbf{E}}(\mathbf{x}) + \left(\underline{\underline{\mathbf{b}}}(\boldsymbol{\xi}) + \underline{\underline{\mathbf{H}}}^e(\boldsymbol{\xi})\right) : \underset{\sim}{\mathbf{e}}(\mathbf{x}) + \left(\underset{\approx}{\mathbf{c}}(\boldsymbol{\xi}) + \underset{\approx}{\mathbf{H}}^K(\boldsymbol{\xi})\right) \therefore \underline{\underline{\mathbf{K}}}(\mathbf{x}) \tag{3.83}$$

Defining the microstrain as the symmetric part of the displacement gradient leads to

$$\underset{\sim}{\varepsilon}(\boldsymbol{\xi},\boldsymbol{x}) = \underline{\boldsymbol{u}} \otimes^{s} \nabla_{\xi} \equiv \underset{\approx}{\mathbf{A}}^{\mathrm{E}}(\boldsymbol{\xi}) : \underset{\sim}{\mathbf{E}}(\boldsymbol{x}) + \underset{\approx}{\mathbf{A}}^{e}(\boldsymbol{\xi}) : \underset{\sim}{\boldsymbol{e}}(\boldsymbol{x}) + \underset{\approx}{\underline{\mathbf{A}}}^{\mathrm{K}}(\boldsymbol{\xi}) \therefore \underset{\sim}{\mathbf{K}}(\boldsymbol{x}) \tag{3.84}$$

wherein $\underset{\approx}{\mathbf{A}}^{\mathrm{E}}(\boldsymbol{\xi})$, $\underset{\approx}{\mathbf{A}}^{e}(\boldsymbol{\xi})$ and $\underset{\approx}{\underline{\mathbf{A}}}^{\mathrm{K}}(\boldsymbol{\xi})$ represent the localization tensors relating the microstrains to the macroscopic kinematic variables, viz.

$$\begin{aligned}
\underset{\approx}{\mathbf{A}}^{\mathrm{E}}(\boldsymbol{\xi}) &= \underline{\boldsymbol{a}}(\boldsymbol{\xi}) \otimes \nabla_{\xi} + \underset{\sim}{\boldsymbol{H}}^{E}(\boldsymbol{\xi}) \otimes \nabla_{\xi} \\
\underset{\approx}{\mathbf{A}}^{e}(\boldsymbol{\xi}) &= \underline{\boldsymbol{b}}(\boldsymbol{\xi}) \otimes \nabla_{\xi} + \underset{\sim}{\boldsymbol{H}}^{e}(\boldsymbol{\xi}) \otimes \nabla_{\xi} \\
\underset{\approx}{\underline{\mathbf{A}}}^{\mathrm{K}}(\boldsymbol{\xi}) &= \underset{\approx}{\boldsymbol{c}}(\boldsymbol{\xi}) \otimes \nabla_{\xi} + \underset{\approx}{\boldsymbol{H}}^{K}(\boldsymbol{\xi}) \otimes \nabla_{\xi}
\end{aligned} \tag{3.85}$$

Inserting Eq. 3.85 into the BVP of Eq. 3.81 leads to a new BVP for the micromorphic strain localizator

$$\left| \begin{aligned}
&-div_{\xi} \left\{ \underset{\approx}{\boldsymbol{C}}(\boldsymbol{\xi}) : \left[\underset{\approx}{\mathbf{A}}^{\mathrm{E}}(\boldsymbol{\xi}) : \underset{\sim}{\boldsymbol{E}}(\boldsymbol{x}) + \underset{\approx}{\mathbf{A}}^{e}(\boldsymbol{\xi}) : \underset{\sim}{\boldsymbol{e}}(\boldsymbol{x}) + \underset{\approx}{\underline{\mathbf{A}}}^{\mathrm{K}}(\boldsymbol{\xi}) \therefore \underset{\sim}{\boldsymbol{K}}(\boldsymbol{x}) \right] \right\} = \mathbf{0} \\
&\underline{\tilde{\boldsymbol{u}}}(\boldsymbol{\xi}) \text{ Y - periodic}
\end{aligned} \right. \tag{3.86}$$

From a numerical point of view, the determination of the expression of the effective moduli and three localization functions is exposed in the following subsection.

The first gradient localization function $\underset{\sim}{\boldsymbol{H}}^{E}(\boldsymbol{\xi})$ is obtained by solving the unit cell BVP, Eq. 3.86, in the framework of Cauchy homogenization, viz.

$$\begin{aligned}
&-div_{\xi} \left\{ \underset{\approx}{\boldsymbol{C}}(\boldsymbol{\xi}) : \left[\underset{\approx}{\mathbf{A}}^{\mathrm{E}}(\boldsymbol{\xi}) : \underset{\sim}{\boldsymbol{E}}(\boldsymbol{x}) \right] \right\} = 0, \quad \forall \underset{\sim}{\boldsymbol{E}}(\boldsymbol{x}) \\
&\rightarrow -div_{\xi} \left\{ \underset{\approx}{\boldsymbol{C}}(\boldsymbol{\xi}) : \underset{\approx}{\mathbf{A}}^{\mathrm{E}}(\boldsymbol{\xi}) \right\} = 0
\end{aligned} \tag{3.87}$$

The localization function $\underset{\sim}{\boldsymbol{H}}^{E}(\boldsymbol{\xi})$ is obtained by solving the BVP 3.87 with periodicity boundary conditions. The relative strain localization function $\underset{\sim}{\boldsymbol{H}}^{e}(\boldsymbol{\xi})$ is derived by truncating the unit cell BVP, Eq. 3.86, up to the second term,

$$\begin{aligned}
&-div_{\xi} \left\{ \underset{\approx}{\boldsymbol{C}}(\boldsymbol{\xi}) : \left[\underset{\approx}{\mathbf{A}}^{e}(\boldsymbol{\xi}) : \underset{\sim}{\boldsymbol{e}}(\boldsymbol{x}) \right] \right\} = 0, \quad \forall \underset{\sim}{\boldsymbol{e}}(\boldsymbol{x}) \\
&\rightarrow -div_{\xi} \left\{ \underset{\approx}{\boldsymbol{C}}(\boldsymbol{\xi}) : \underset{\approx}{\mathbf{A}}^{e}(\boldsymbol{\xi}) \right\} = 0
\end{aligned} \tag{3.88}$$

In the last step, the micromorphic displacement localization function $\underset{\approx}{\boldsymbol{H}}^{K}(\boldsymbol{\xi})$ is obtained by solving the third unit cell BVP, Eq. 3.86, in a similar way as for the two other parts:

$$\begin{aligned}
&-div_{\xi} \left\{ \underset{\approx}{\boldsymbol{C}}(\boldsymbol{\xi}) : \left[\underset{\approx}{\underline{\mathbf{A}}}^{\mathrm{K}}(\boldsymbol{\xi}) \therefore \underset{\sim}{\boldsymbol{K}}(\boldsymbol{x}) \right] \right\} = 0, \quad \forall \underset{\sim}{\boldsymbol{K}}(\boldsymbol{x}) \\
&\rightarrow -div_{\xi} \left\{ \underset{\approx}{\boldsymbol{C}}(\boldsymbol{\xi}) : \underset{\approx}{\underline{\mathbf{A}}}^{\mathrm{K}}(\boldsymbol{\xi}) \right\} = 0
\end{aligned} \tag{3.89}$$

The next section is devoted to the determination of the expression of the effective micromorphic moduli, based on the displacement localization functions computed there above.

3.5 Evaluation of the effective micromorphic moduli

A more symmetrical expression of effective micromorphic moduli can be obtained as follows: Since the functional defined on the right-hand side of Eq. 3.80 is regular in the macroscopic kinematic variables $\underset{\sim}{\boldsymbol{E}}(\boldsymbol{x})$, $\underset{\sim}{\boldsymbol{e}}(\boldsymbol{x})$, and $\underset{\sim}{\underline{\boldsymbol{K}}}(\boldsymbol{x})$ imposed over the unit cell, playing the role of parameters. Since the integrand in Eq. 3.80 is a bounded expression, partial derivative and integration can be exchanged, so that the stress measures in Eq. 3.23 express as

$$
\begin{aligned}
\bar{\underset{\sim}{\boldsymbol{\sigma}}} &:= \frac{\partial W_M(\underset{\sim}{\mathbf{E}},\, \underset{\sim}{\mathbf{e}},\, \underset{\sim}{\underline{\mathbf{K}}})}{\partial \underset{\sim}{\mathbf{E}}} = \underset{\underset{\sim}{\boldsymbol{u}} \in H^1_{per}(Y)}{Min} \frac{\partial}{\partial \underset{\sim}{\mathbf{E}}} \left\{ \int_Y \frac{1}{2} \underset{\approx}{\boldsymbol{C}}(\boldsymbol{\xi}) : \left(\underset{\approx}{\mathbf{A}}^{\mathrm{E}}(\boldsymbol{\xi}) : \underset{\sim}{\mathbf{E}}(\boldsymbol{x}) + \underset{\approx}{\mathbf{A}}^{e}(\boldsymbol{\xi}) : \underset{\sim}{\mathbf{e}}(\boldsymbol{x}) + \underset{\approx}{\underline{\mathbf{A}}}^{\mathrm{K}}(\boldsymbol{\xi}) \therefore \underset{\sim}{\underline{\mathbf{K}}}(\boldsymbol{x}) \right) \right. \\
&\qquad \left. : \left(\underset{\approx}{\mathbf{A}}^{\mathrm{E}}(\boldsymbol{\xi}) : \underset{\sim}{\mathbf{E}}(\boldsymbol{x}) + \underset{\approx}{\mathbf{A}}^{e}(\boldsymbol{\xi}) : \underset{\sim}{\mathbf{e}}(\boldsymbol{x}) + \underset{\approx}{\underline{\mathbf{A}}}^{\mathrm{K}}(\boldsymbol{\xi}) \therefore \underset{\sim}{\underline{\mathbf{K}}}(\boldsymbol{x}) \right) dV_y \right\} \\
\underset{\sim}{\boldsymbol{s}} &:= \frac{\partial W_M(\underset{\sim}{\mathbf{E}},\, \underset{\sim}{\mathbf{e}},\, \underset{\sim}{\underline{\mathbf{K}}})}{\partial \underset{\sim}{\mathbf{e}}} = \underset{\underset{\sim}{\boldsymbol{u}} \in H^1_{per}(Y)}{Min} \frac{\partial}{\partial \underset{\sim}{\mathbf{e}}} \left\{ \int_Y \frac{1}{2} \underset{\approx}{\boldsymbol{C}}(\boldsymbol{\xi}) : \left(\underset{\approx}{\mathbf{A}}^{\mathrm{E}}(\boldsymbol{\xi}) : \underset{\sim}{\mathbf{E}}(\boldsymbol{x}) + \underset{\approx}{\mathbf{A}}^{e}(\boldsymbol{\xi}) : \underset{\sim}{\mathbf{e}}(\boldsymbol{x}) + \underset{\approx}{\underline{\mathbf{A}}}^{\mathrm{K}}(\boldsymbol{\xi}) \therefore \underset{\sim}{\underline{\mathbf{K}}}(\boldsymbol{x}) \right) \right. \\
&\qquad \left. : \left(\underset{\approx}{\mathbf{A}}^{\mathrm{E}}(\boldsymbol{\xi}) : \underset{\sim}{\mathbf{E}}(\boldsymbol{x}) + \underset{\approx}{\mathbf{A}}^{e}(\boldsymbol{\xi}) : \underset{\sim}{\mathbf{e}}(\boldsymbol{x}) + \underset{\approx}{\underline{\mathbf{A}}}^{\mathrm{K}}(\boldsymbol{\xi}) \therefore \underset{\sim}{\underline{\mathbf{K}}}(\boldsymbol{x}) \right) dV_y \right\} \\
\underset{\sim}{\underline{\boldsymbol{S}}} &:= \frac{\partial W_M(\underset{\sim}{\mathbf{E}},\, \underset{\sim}{\mathbf{e}},\, \underset{\sim}{\underline{\mathbf{K}}})}{\partial \underset{\sim}{\underline{\mathbf{K}}}} = \underset{\underset{\sim}{\boldsymbol{u}} \in H^1_{per}(Y)}{Min} \frac{\partial}{\partial \underset{\sim}{\underline{\mathbf{K}}}} \left\{ \int_Y \frac{1}{2} \underset{\approx}{\boldsymbol{C}}(\boldsymbol{\xi}) : \left(\underset{\approx}{\mathbf{A}}^{\mathrm{E}}(\boldsymbol{\xi}) : \underset{\sim}{\mathbf{E}}(\boldsymbol{x}) + \underset{\approx}{\mathbf{A}}^{e}(\boldsymbol{\xi}) : \underset{\sim}{\mathbf{e}}(\boldsymbol{x}) + \underset{\approx}{\underline{\mathbf{A}}}^{\mathrm{K}}(\boldsymbol{\xi}) \therefore \underset{\sim}{\underline{\mathbf{K}}}(\boldsymbol{x}) \right) \right. \\
&\qquad \left. : \left(\underset{\approx}{\mathbf{A}}^{\mathrm{E}}(\boldsymbol{\xi}) : \underset{\sim}{\mathbf{E}}(\boldsymbol{x}) + \underset{\approx}{\mathbf{A}}^{e}(\boldsymbol{\xi}) : \underset{\sim}{\mathbf{e}}(\boldsymbol{x}) + \underset{\approx}{\underline{\mathbf{A}}}^{\mathrm{K}}(\boldsymbol{\xi}) \therefore \underset{\sim}{\underline{\mathbf{K}}}(\boldsymbol{x}) \right) dV_y \right\}
\end{aligned}
\tag{3.90}
$$

Eq. 3.90 leads to the stress, relative stress, and hyperstress tensors, successively identified as:

$$
\begin{aligned}
\bar{\underset{\sim}{\boldsymbol{\sigma}}} &= \int_Y \underset{\approx}{\mathbf{C}}(\boldsymbol{\xi}) : \left(\underset{\approx}{\mathbf{A}}^{\mathrm{E}}(\boldsymbol{\xi}) : \underset{\sim}{\mathbf{E}}(\boldsymbol{x}) + \underset{\approx}{\mathbf{A}}^{e}(\boldsymbol{\xi}) : \underset{\sim}{\mathbf{e}}(\boldsymbol{x}) + \underset{\approx}{\underline{\mathbf{A}}}^{\mathrm{K}}(\boldsymbol{\xi}) \therefore \underset{\sim}{\underline{\mathbf{K}}}(\boldsymbol{x}) \right) : \underset{\approx}{\mathbf{A}}^{\mathrm{E}}(\boldsymbol{\xi})\, dV_y \\
&= \left\{ \int_Y \underset{\approx}{\mathbf{C}} : \underset{\approx}{\mathbf{A}}^{\mathrm{E}}(\boldsymbol{\xi}) : \underset{\approx}{\mathbf{A}}^{\mathrm{E}}(\boldsymbol{\xi}) dV_y \right\} : \underset{\sim}{\mathbf{E}}(\boldsymbol{x}) + \left\{ \int_Y \underset{\approx}{\mathbf{C}} : \underset{\approx}{\mathbf{A}}^{e}(\boldsymbol{\xi}) : \underset{\approx}{\mathbf{A}}^{\mathrm{E}}(\boldsymbol{\xi}) dV_y \right\} : \underset{\sim}{\mathbf{e}}(\boldsymbol{x}) + \left\{ \int_Y \underset{\approx}{\mathbf{C}} : \underset{\approx}{\underline{\mathbf{A}}}^{\mathrm{K}}(\boldsymbol{\xi}) : \underset{\approx}{\mathbf{A}}^{\mathrm{E}}(\boldsymbol{\xi}) dV_y \right\} \therefore \underset{\sim}{\underline{\mathbf{K}}}(\boldsymbol{x}) \\
\underset{\sim}{\boldsymbol{s}} &= \int_Y \underset{\approx}{\mathbf{C}}(\boldsymbol{\xi}) : \left(\underset{\approx}{\mathbf{A}}^{\mathrm{E}}(\boldsymbol{\xi}) : \underset{\sim}{\mathbf{E}}(\boldsymbol{x}) + \underset{\approx}{\mathbf{A}}^{e}(\boldsymbol{\xi}) : \underset{\sim}{\mathbf{e}}(\boldsymbol{x}) + \underset{\approx}{\underline{\mathbf{A}}}^{\mathrm{K}}(\boldsymbol{\xi}) \therefore \underset{\sim}{\underline{\mathbf{K}}}(\boldsymbol{x}) \right) : \underset{\approx}{\mathbf{A}}^{e}(\boldsymbol{\xi})\, dV_y \\
&= \left\{ \int_Y \underset{\approx}{\mathbf{C}} : \underset{\approx}{\mathbf{A}}^{\mathrm{E}}(\boldsymbol{\xi}) : \underset{\approx}{\mathbf{A}}^{e}(\boldsymbol{\xi}) dV_y \right\} : \underset{\sim}{\mathbf{E}}(\boldsymbol{x}) + \left\{ \int_Y \underset{\approx}{\mathbf{C}} : \underset{\approx}{\mathbf{A}}^{e}(\boldsymbol{\xi}) : \underset{\approx}{\mathbf{A}}^{e}(\boldsymbol{\xi}) dV_y \right\} : \underset{\sim}{\mathbf{e}}(\boldsymbol{x}) + \left\{ \int_Y \underset{\approx}{\mathbf{C}} : \underset{\approx}{\underline{\mathbf{A}}}^{\mathrm{K}}(\boldsymbol{\xi}) : \underset{\approx}{\mathbf{A}}^{e}(\boldsymbol{\xi}) dV_y \right\} \therefore \underset{\sim}{\underline{\mathbf{K}}}(\boldsymbol{x}) \\
\underset{\sim}{\underline{\mathbf{S}}} &= \int_Y \underset{\approx}{\mathbf{C}}(\boldsymbol{\xi}) : \left(\underset{\approx}{\mathbf{A}}^{\mathrm{E}}(\boldsymbol{\xi}) : \underset{\sim}{\mathbf{E}}(\boldsymbol{x}) + \underset{\approx}{\mathbf{A}}^{e}(\boldsymbol{\xi}) : \underset{\sim}{\mathbf{e}}(\boldsymbol{x}) + \underset{\approx}{\underline{\mathbf{A}}}^{\mathrm{K}}(\boldsymbol{\xi}) \therefore \underset{\sim}{\underline{\mathbf{K}}}(\boldsymbol{x}) \right) : \underset{\approx}{\underline{\mathbf{A}}}^{\mathrm{K}}(\boldsymbol{\xi})\, dV_y \\
&= \left\{ \int_Y \underset{\approx}{\mathbf{C}} : \underset{\approx}{\mathbf{A}}^{\mathrm{E}}(\boldsymbol{\xi}) : \underset{\approx}{\underline{\mathbf{A}}}^{\mathrm{K}}(\boldsymbol{\xi}) dV_y \right\} : \underset{\sim}{\mathbf{E}}(\boldsymbol{x}) + \left\{ \int_Y \underset{\approx}{\mathbf{C}} : \underset{\approx}{\mathbf{A}}^{e}(\boldsymbol{\xi}) : \underset{\approx}{\underline{\mathbf{A}}}^{\mathrm{K}}(\boldsymbol{\xi}) dV_y \right\} : \underset{\sim}{\mathbf{e}}(\boldsymbol{x}) + \left\{ \int_Y \underset{\approx}{\mathbf{C}} : \underset{\approx}{\underline{\mathbf{A}}}^{\mathrm{K}}(\boldsymbol{\xi}) : \underset{\approx}{\underline{\mathbf{A}}}^{\mathrm{K}}(\boldsymbol{\xi}) dV_y \right\} \therefore \underset{\sim}{\underline{\mathbf{K}}}(\boldsymbol{x})
\end{aligned}
\tag{3.91}
$$

These writings, together with the symmetry of the average quantities therein, lead to the following expression of the effective micromorphic moduli (their determination in index format is exposed in Appendix F):

$$
\begin{aligned}
&\underset{\approx}{\mathbf{C}}^{\mathrm{hom}} = \int_Y \underset{\approx}{\mathbf{A}}^{\mathrm{E}}(\boldsymbol{\xi}) : \underset{\approx}{\mathbf{C}} : \underset{\approx}{\mathbf{A}}^{\mathrm{E}}(\boldsymbol{\xi}) dV_y,\ \underset{\approx}{\mathbf{B}}^{\mathrm{hom}} = \int_Y \underset{\approx}{\mathbf{A}}^{e}(\boldsymbol{\xi}) : \underset{\approx}{\mathbf{C}} : \underset{\approx}{\mathbf{A}}^{\mathrm{E}}(\boldsymbol{\xi}) dV_y,\ \underset{\approx}{\underline{\mathbf{D}}}^{\mathrm{hom}} = \int_Y \underset{\approx}{\underline{\mathbf{A}}}^{\mathrm{K}}(\boldsymbol{\xi}) : \underset{\approx}{\mathbf{C}} : \underset{\approx}{\mathbf{A}}^{\mathrm{E}}(\boldsymbol{\xi}) dV_y, \\
&\underset{\approx}{\mathbf{H}}^{\mathrm{hom}} = \int_Y \underset{\approx}{\mathbf{A}}^{e}(\boldsymbol{\xi}) : \underset{\approx}{\mathbf{C}} : \underset{\approx}{\mathbf{A}}^{e}(\boldsymbol{\xi}) dV_y,\ \underset{\approx}{\underline{\mathbf{G}}}^{\mathrm{hom}} = \int_Y \underset{\approx}{\underline{\mathbf{A}}}^{\mathrm{K}}(\boldsymbol{\xi}) : \underset{\approx}{\mathbf{C}} : \underset{\approx}{\mathbf{A}}^{e}(\boldsymbol{\xi}) dV_y,\ \underset{\approx}{\mathbf{K}}^{\mathrm{hom}} = \int_Y \underset{\approx}{\underline{\mathbf{A}}}^{\mathrm{K}}(\boldsymbol{\xi}) : \underset{\approx}{\mathbf{C}} : \underset{\approx}{\underline{\mathbf{A}}}^{\mathrm{K}}(\boldsymbol{\xi}) dV_y
\end{aligned}
\tag{3.92}
$$

It can easily be checked from previous expression the transpose property of the coupling tensors leading to the overall symmetry of the effective stiffness rigidity tensor.

The strain energy of the effective micromorphic continuum writes as the following bilinear form of the kinematic measures, as the result of the obtained homogenized constitutive law Eq. 3.92 and Euler's theorem for quadratic functions of their tensor arguments:

$$\begin{aligned} W_M\left(\underset{\sim}{\mathbf{E}},\, \underset{\sim}{\mathbf{e}},\, \underset{\sim}{\mathbf{K}}\right) &= \frac{1}{2}\underset{\sim}{\mathbf{E}} : \underset{\approx}{\mathbf{C}}^{\text{hom}} : \underset{\sim}{\mathbf{E}} + \frac{1}{2}\underset{\sim}{\mathbf{e}} : \underset{\approx}{\mathbf{H}}^{\text{hom}} : \underset{\sim}{\mathbf{e}} + \frac{1}{2}\underset{\sim}{\mathbf{K}} \therefore \underset{\approx}{\mathbf{K}}^{\text{hom}} \therefore \underset{\sim}{\mathbf{K}} + \underset{\sim}{\mathbf{E}} : \left(\underset{\approx}{\mathbf{B}}^{\text{hom}} + \underset{\approx}{\mathbf{B}}^{\text{hom},T}\right) : \underset{\sim}{\mathbf{e}} \\ &+ \underset{\sim}{\mathbf{E}} : \left(\underset{\approx}{\underset{\sim}{\mathbf{D}}}^{\text{hom}} + \underset{\approx}{\underset{\sim}{\mathbf{D}}}^{\text{hom},T}\right) \therefore \underset{\sim}{\mathbf{K}} + \underset{\sim}{\mathbf{e}} : \left(\underset{\approx}{\underset{\sim}{\mathbf{G}}}^{\text{hom}} + \underset{\approx}{\underset{\sim}{\mathbf{G}}}^{\text{hom},T}\right) \therefore \underset{\sim}{\mathbf{K}} \\ &= \left\langle w_\mu\left(\underset{\sim}{\boldsymbol{\xi}}\right)\right\rangle_Y = \left\langle \frac{1}{2}\underset{\sim}{\boldsymbol{\xi}}(\boldsymbol{y}) : \underset{\approx}{\mathbf{C}}(\boldsymbol{y}) : \underset{\sim}{\boldsymbol{\xi}}(\boldsymbol{y})\right\rangle_Y \end{aligned} \tag{3.93}$$

with $\underset{\approx}{\mathbf{K}}^{\text{hom}}$, $\underset{\approx}{\mathbf{H}}^{\text{hom}}$, and $\underset{\approx}{\mathbf{C}}^{\text{hom}}$ therein the sixth order tensor of micromorphic moduli, fourth-order tensor of relative moduli, and fourth-order tensor of Cauchy moduli. $\underset{\approx}{\mathbf{B}}^{\text{hom}}$ is the fourth-order tensor of coupling moduli for the Cauchy strain and relative strain, $\underset{\approx}{\underset{\sim}{\mathbf{D}}}^{\text{hom}}$ and $\underset{\approx}{\underset{\sim}{\mathbf{G}}}^{\text{hom}}$ are fifth-order tensors of coupling moduli of Cauchy and relative strains with the microdeformation gradient. The presence of the sums $\left(\underset{\approx}{\mathbf{B}}^{\text{hom}} + \underset{\approx}{\mathbf{B}}^{\text{hom},T}\right)$, $\left(\underset{\approx}{\underset{\sim}{\mathbf{D}}}^{\text{hom}} + \underset{\approx}{\underset{\sim}{\mathbf{D}}}^{\text{hom},T}\right)$ and $\left(\underset{\approx}{\underset{\sim}{\mathbf{G}}}^{\text{hom}} + \underset{\approx}{\underset{\sim}{\mathbf{G}}}^{\text{hom},T}\right)$ is the consequence of the existence of a strain energy potential which guarantees the symmetry of the effective overall stiffness matrix, by Schwarz relation. The macroscopic micromorphic energy density entails the following micromorphic constitutive law at the macroscopic level, relating the average Cauchy type macroscopic stress $\bar{\underset{\sim}{\boldsymbol{\sigma}}}$, $\underset{\sim}{\mathbf{s}}$ and hyperstress $\underset{\sim}{\underset{\sim}{\mathbf{S}}}$ to the Cauchy strain, relative strain and micromorphic kinematic tensors, respectively:

$$\begin{aligned} \bar{\underset{\sim}{\boldsymbol{\sigma}}} &:= \frac{\partial W_M\left(\underset{\sim}{\mathbf{E}},\, \underset{\sim}{\mathbf{e}},\, \underset{\sim}{\mathbf{K}}\right)}{\partial \underset{\sim}{\mathbf{E}}} \equiv \underset{\approx}{\mathbf{C}}^{\text{hom}} : \underset{\sim}{\mathbf{E}} + \underset{\approx}{\mathbf{B}}^{\text{hom}} : \underset{\sim}{\mathbf{e}} + \underset{\approx}{\underset{\sim}{\mathbf{D}}}^{\text{hom}} \therefore \underset{\sim}{\mathbf{K}} \\ \underset{\sim}{\mathbf{s}} &= \frac{\partial W_M\left(\underset{\sim}{\mathbf{E}},\, \underset{\sim}{\mathbf{e}},\, \underset{\sim}{\mathbf{K}}\right)}{\partial \underset{\sim}{\mathbf{e}}} \equiv \underset{\approx}{\mathbf{B}}^{\text{hom},T} : \underset{\sim}{\mathbf{E}} + \underset{\approx}{\mathbf{H}}^{\text{hom}} : \underset{\sim}{\mathbf{e}} + \underset{\approx}{\underset{\sim}{\mathbf{G}}}^{\text{hom}} \therefore \underset{\sim}{\mathbf{K}} \\ \underset{\sim}{\underset{\sim}{\mathbf{S}}} &:= \frac{\partial W_M\left(\underset{\sim}{\mathbf{E}},\, \underset{\sim}{\mathbf{e}},\, \underset{\sim}{\mathbf{K}}\right)}{\partial \underset{\sim}{\mathbf{K}}} \equiv \underset{\approx}{\underset{\sim}{\mathbf{D}}}^{\text{hom},T} : \underset{\sim}{\mathbf{E}} + \underset{\approx}{\underset{\sim}{\mathbf{G}}}^{\text{hom},T} : \underset{\sim}{\mathbf{e}} + \underset{\approx}{\mathbf{K}}^{\text{hom}} \therefore \underset{\sim}{\mathbf{K}} \end{aligned} \tag{3.94}$$

3.6 Computation of the micromorphic properties of lattice structures and composite materials

The unit cell BVPs for determining the displacement localization functions are solved with the general open-source code Freefem++, as explained synthetically in Fig. 3.4.

3.6.1 Homogeneous micromorphic BVP

Considering $\underset{\sim}{\boldsymbol{\sigma}} = \underset{\sim}{\boldsymbol{\Sigma}} - \underset{\sim}{\boldsymbol{s}}$ and multiplying Eqs. 3.6 and 3.7 by virtual displacement and micromorphic deformation, variables $\underset{\sim}{\boldsymbol{v}}$ and $\underset{\sim}{\boldsymbol{\psi}}$, respectively and integrating over the macroscopic homogeneous volume

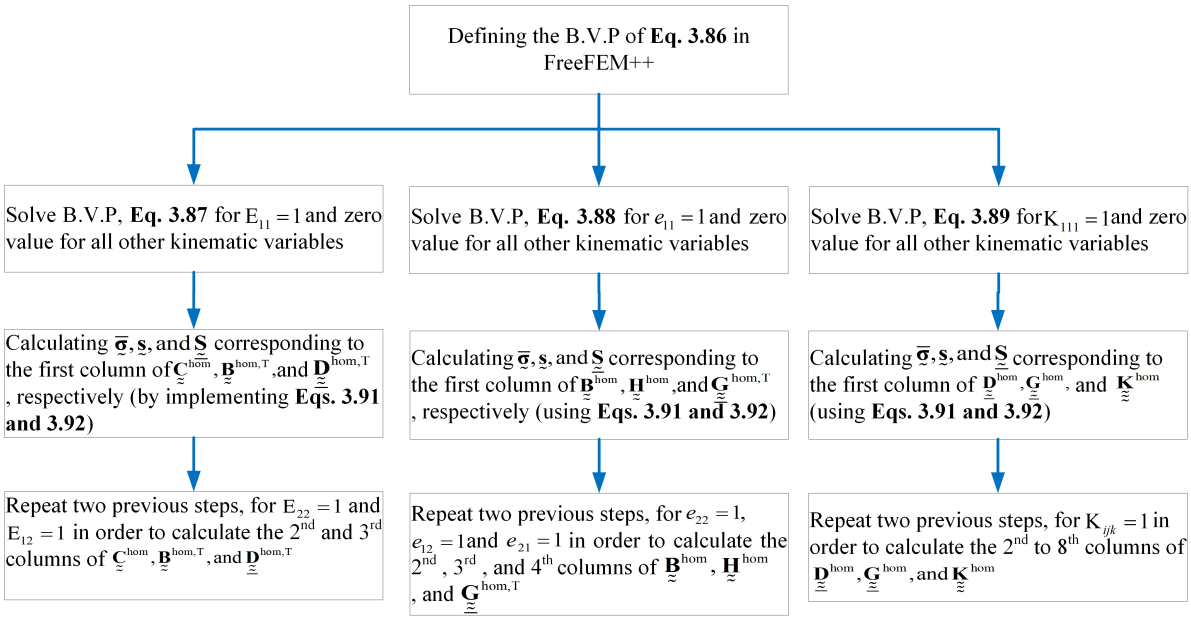

Figure 3.4 Schematic diagram for the computation of the effective micromorphic moduli.

V(x) depicted in Fig. 3.2, leads to the following relations.

$$-\int_{V(x)} \underset{\sim}{\sigma} : \nabla \underset{\sim}{\nu}\, dV(x) + \int_{\partial V(x)} \underset{\sim}{\sigma} \cdot \underset{\sim}{\nu}\, dS(x) = 0 \tag{3.95}$$

$$-\int_{V(x)} \underset{\sim}{\underset{\sim}{S}} \therefore \nabla \underset{\sim}{\psi}\, dV(x) - \int_{V(x)} \underset{\sim}{\sigma} : \underset{\sim}{\psi}\, dV(x) + \int_{\partial V(x)} \underset{\sim}{\underset{\sim}{S}} : \underset{\sim}{\psi}\, dS(x) = 0 \tag{3.96}$$

Substituting the micromorphic constitutive law, Eq. 3.94 into relations 3.95 and 3.96 and subtracting Eq. 3.95 from Eq. 3.96 leads to the following homogeneous micropolar BVP to be solved at the macroscale:

$$\int_{V(x)} \mathbf{E}(\nu) : \left(\underset{\approx}{\mathbf{C}}^{\text{hom}} : \underset{\sim}{\mathbf{E}}(u) + \underset{\approx}{\mathbf{B}}^{\text{hom}} : \underset{\sim}{\mathbf{e}}(u,\chi) + \underset{\approx}{\mathbf{D}}^{\text{hom}} \therefore \underset{\sim}{\mathbf{K}}(\chi) \right) dV(x) - \int_{V(x)} \underset{\sim}{\mathbf{K}}(\psi) \therefore \left(\underset{\approx}{\mathbf{D}}^{\text{hom},T} : \underset{\sim}{\mathbf{E}}(u) + \underset{\approx}{\mathbf{G}}^{\text{hom},T} : \underset{\sim}{\mathbf{e}}(u,\chi) + \underset{\approx}{\mathbf{K}}^{\text{hom}} \therefore \underset{\sim}{\mathbf{K}}(\chi) \right) dV(x)$$
$$- \int_{V(x)} \chi(\psi) : \left(\underset{\approx}{\mathbf{C}}^{\text{hom}} : \underset{\sim}{\mathbf{E}}(u) + \underset{\approx}{\mathbf{B}}^{\text{hom}} : \underset{\sim}{\mathbf{e}}(u,\chi) + \underset{\approx}{\mathbf{D}}^{\text{hom}} \therefore \underset{\sim}{\mathbf{K}}(\chi) \right) dV(x) - \int_{\partial V(x)} \underset{\sim}{\underset{\sim}{S}} : \underset{\sim}{\psi}\, dS(x) - \int_{\partial V(x)} \underset{\sim}{\sigma} \cdot \underset{\sim}{\nu}\, dS(x) = 0, \ \forall \left(\underset{\sim}{\nu}, \underset{\sim}{\psi} \right) \tag{3.97}$$

3.6.1.1 Axial loading of the plate lattice structure

In this section, the benchmark example of the tetrachiral lattices is considered in a plane strain condition in order to underline the correctness and accuracy of the proposed micromorphic model. We consider the lattice structure shown in Fig. 3.6, comprising a sufficient number of 12×15 tetrachiral unit cells (Fig. 3.5), such that edge effects can be minimized in the central part of the network. Roller boundary conditions are imposed at the left, bottom, and top surfaces, and a uniform displacement U is prescribed along the right surface. A simple uniaxial loading case is considered to illustrate the capability of the proposed homogenization approach in capturing the coupling effect between rotational and stretching mechanisms. The material and geometrical parameters of the isotropic base material are chosen as Table 3.2 in order to compare the model predictions with those of [111].

Table 3.1 Values of the geometrical and mechanical parameters of the tetrachiral lattice.

Elastic modulus (GPa)	Poisson's ratio	R (mm)	t (mm)	$L/2$ (mm)
200	0.3	0.15	0.052	0.48

The effective macroscopic tensors employed as the mechanical properties of the homogeneous micromorphic plate calculated by the proposed homogenization method are computed over the tetrachiral single unit cell with periodicity conditions:

$$\boldsymbol{C}^{\text{hom}} = \begin{bmatrix} 3496.65 & -2725.82 & -830.62 \\ -2721.77 & 3494.67 & 829.92 \\ -834.57 & 834.86 & 244.17 \end{bmatrix} \quad MPa$$

$$\mathbf{B}^{\text{hom}} = \begin{bmatrix} -7761.8 & 5993.44 & 1839.57 & 1839.57 \\ 6054.22 & -7743.52 & -1844.42 & -1844.43 \\ 1838.51 & -1838.1 & -540.54 & -540.55 \\ 1838.51 & -1838.1 & -540.54 & -540.55 \end{bmatrix} \quad MPa$$

$$\boldsymbol{H}^{\text{hom}} = \begin{bmatrix} 17249.52 & -13318.22 & -4087.86 & -4087.86 \\ -13318.22 & 17208.38 & 4098.84 & 4098.84 \\ -4085.44 & 4084.5 & 1201.15 & 1201.16 \\ -4085.49 & 4084.62 & 1201.17 & 1201.18 \end{bmatrix} \quad MPa$$

$$\mathbf{K}^{\text{hom}} = \begin{bmatrix} 1.427 & 1.425 & -1.721 & -1.721 & -3.564 & -3.564 & 0 & 0 \\ 2.481 & 2.479 & -2.05 & -2.05 & -2.981 & -2.981 & 0 & 0 \\ -0.5165 & -0.5165 & 7.813 & 7.813 & 0.302 & 0.302 & 0 & 0 \\ -0.5165 & -0.5165 & 7.813 & 7.813 & 0.302 & 0.302 & 0 & 0 \\ 0 & 0 & -0.301 & -0.301 & 7.818 & 7.818 & -0.519 & -0.520 \\ 0 & 0 & -0.301 & -0.301 & 7.818 & 7.818 & -0.519 & -0.520 \\ 0 & 0 & 3.05 & 3.05 & -2.022 & -2.022 & 2.497 & 2.497 \\ 0 & 0 & 3.646 & 3.646 & -1.694 & -1.694 & 1.45 & 1.45 \end{bmatrix} \quad MPa.mm$$

and the other homogeneous tensors take nil values.

These effective micromorphic moduli feed the macroscopic FE computations performed over the homogeneous (micromorphic) plate in Fig. 3.6(b), whereby the variational Eq. 3.97 is solved to find the spatial distribution of the effective micromorphic variables (u, χ) over the plate. The proposed homogenization method is validated by comparing the predictions of the fully resolved microstructure in Fig. 3.6(a) with those of the homogeneous micromorphic plate of Fig. 3.6(b) at both global and local levels.

The reaction forces along the x_1 direction is plotted in Fig. 3.7 for both the homogeneous micromorphic plate and the whole periodic lattice. The homogenized micromorphic model can predict the force-

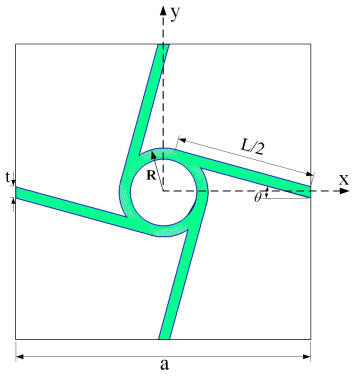

Figure 3.5 Centro-symmetric tetrachiral unit cell.

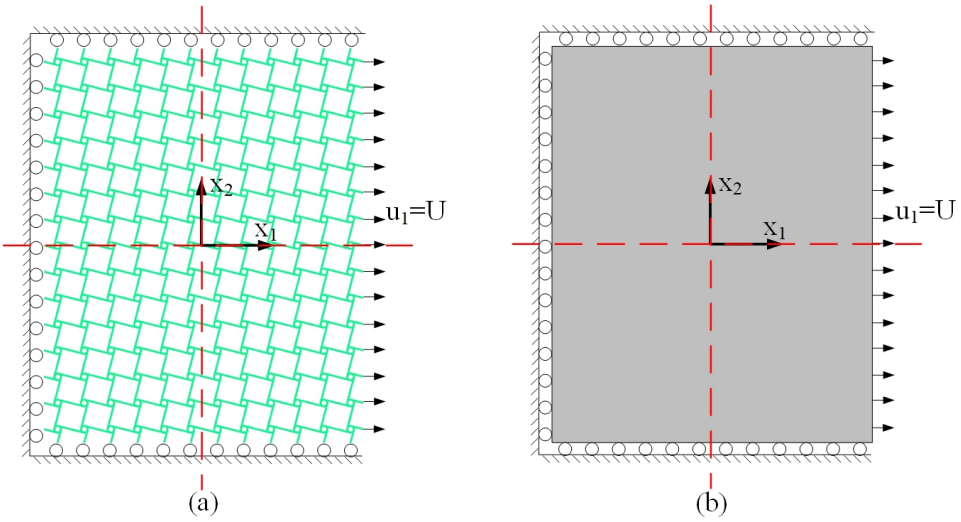

Figure 3.6 a) Full periodic network and b) homogenized representation of a tetra-chiral plate consisting of 12x15 unit cells.

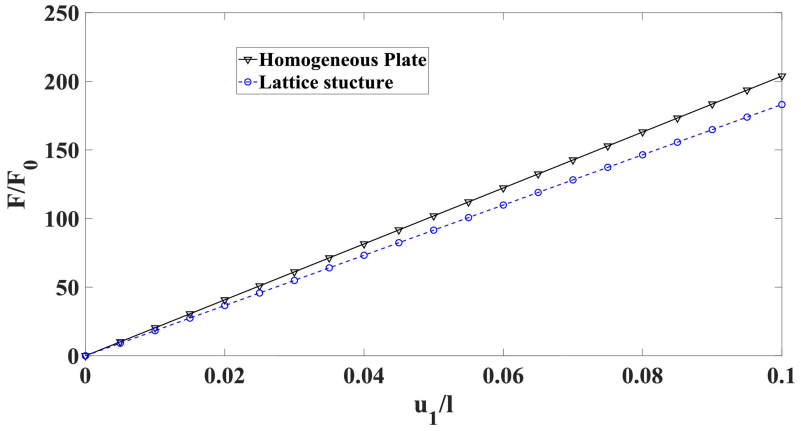

Figure 3.7 Load-displacement responses of the tetra-chiral plate, under axial loading normalized with respect to $F_0 = 1$.

displacement responses of the lattice structure with a maximum error of about 11%. To confirm the local predictive capability of the presented micromorphic model, vertical and horizontal displacements on the dashed red lines in Fig. 3.6 are compared with Biswas's results [111]. In this paper, the authors define the macro kinematic fields as the macro distortion tensor (for the standard Cauchy type homogenization), completed by the micromorphic variable, a second-order tensor specific to the considered tetra-chiral geometry. It does not include general definitions and elaborations of the effective micromorphic continuum's kinematics since the proposed work aims to elaborate a rather specific model applicable to the considered tetra-chiral unit cell. The effective stress measures dual to the two kinematic variables are obtained recoursing to the extended Hill-Mandel condition.

In comparison, we pursue a general modeling approach, proposing general definitions of the effective kinematic and static micromorphic tensors. We bring the proof of the extended Hill macrohomogeneity condition for the effective micromorphic continuum, which provides constructive proof of the introduced kinematic and static homogenized tensors. To summarize, we believe our homogenization method has great potential in future developments to construct homogenized enriched models of micromorphic or higher gradient types for composites and architectured media prone to such behaviors.

Fig. 3.8 shows that the proposed micromorphic model coincides with the results of the Biswas, and it can accurately predict the response of the plate for the regions that are far from the boundaries. The displacement contours u_1 and u_2 for the homogenized plate and tetrachiral lattice structure are shown in Fig. 3.9, illustrating that the homogenous micromorphic plate reproduces the local displacement pattern shown over the entire lattice.

3.6.2 Micromorphic deformation modes and energetic contribution of the displacement fluctuation

The $3D$ non-centrosymmetric composite unit cell depicted in Fig. 3.10 is considered; the unit cell is assumed to have a much larger thickness in the y_3 direction compared to its plane size so that a plane strain

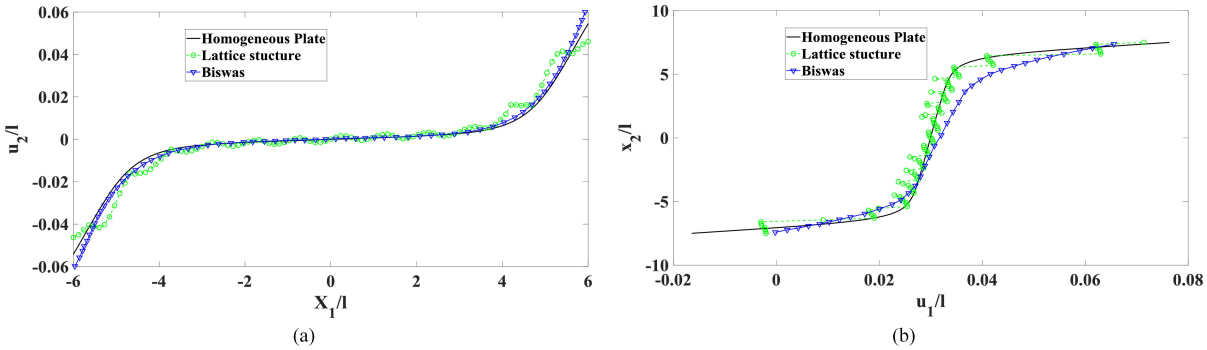

Figure 3.8 (a) Normalized displacement profiles u_2 along the horizontal center line of the plate, (b) Normalized displacement profiles u_1 along the vertical center line of the plate at prescribed displacement $U = 0.06l$.

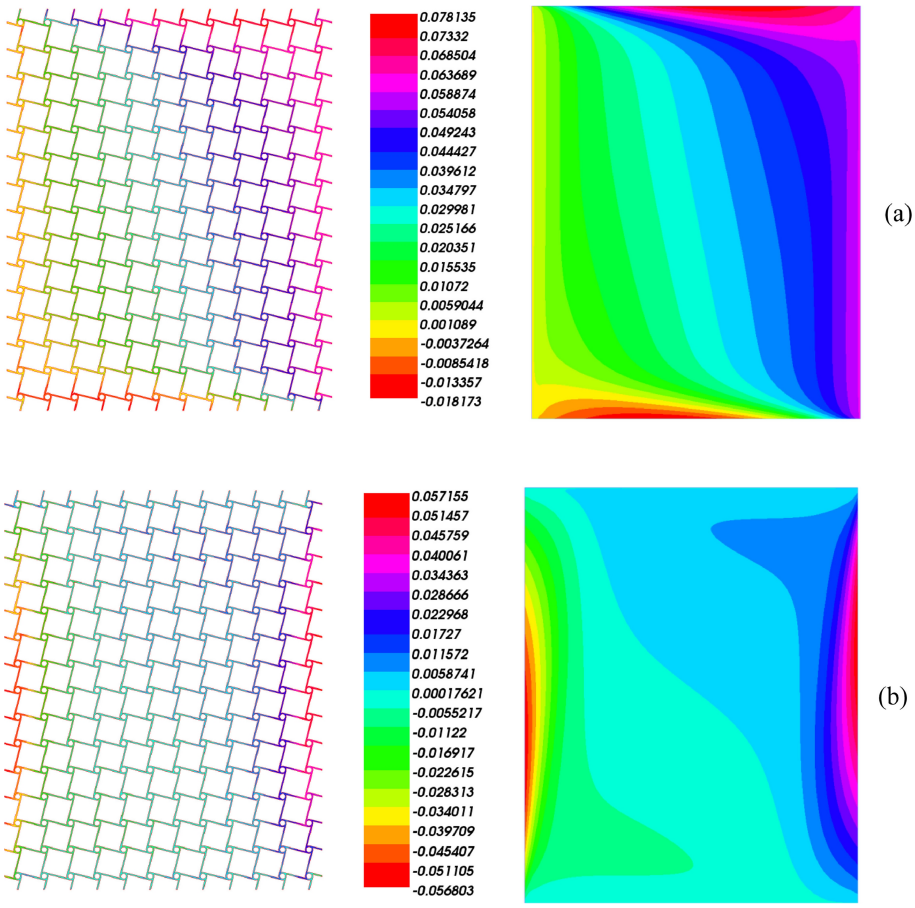

Figure 3.9 (a) Normalized horizontal displacement contour u_1, (b) Normalized vertical displacement contour u_2 of the tetrachiral lattice structure and homogenized plate at prescribed displacement $U = 0.06l$.

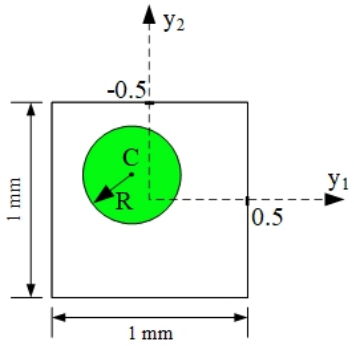

Figure 3.10 Non-centrosymmetric fibrous composite unit cell.

model is adopted. The center of the inclusion C with a circular shape is located at $(y_1, y_2) = (-0.1, 0.1)$, resulting in a non-centrosymmetric unit cell. The properties of the composite constituents, a carbon fiber within an epoxy matrix, are indicated in Table 3.2.

Table 3.2 Mechanical properties of Fiber and Matrix.

	Fiber (Carbon)	Matrix (Epoxy)
Elastic modulus (MPa)	228000	1400
Poisson's ratio	0.26	0.3

The total deformation modes of the unit cell induced by the successive independent components of the Cauchy strain, relative strain, and micromorphic kinematic tensors are depicted in Fig. 3.11.

Different kinematic loadings lead to the same deformed shape due to the existing index symmetries of the effective moduli. Fig. 3.11(f) shows that the eight total micromorphic deformation modes related to the components e_{11}, e_{22}, e_{12}, e_{21}, K_{111}, K_{122}, K_{211}, K_{222} are not activated in the present situation (since the macroscopic deformed shape is compensated by the fluctuation induced deformed shape), since the microscopic energy vanishes as shown in Table 3.3. However, as shown in Fig. 3.12, these macroscopic deformation modes cause microscopic deformation modes in the unit cell. The total deformation modes (especially the two in-plane bending modes in Fig. 3.6 are not periodic. The homogeneous part of the microscopic displacement imposed as a kinematic loading over the unit cell boundary is not compatible with periodicity.

The distribution of the fluctuating displacement component $\tilde{\mathrm{u}}_{y_2}$ in y_2 direction is evaluated, resulting from the components E_{11} and K_{112} of the macroscopic Cauchy strain and micromorphic deformation, respectively. To this end, the unit cell is subjected to successive applied kinematic loadings $\mathrm{E}_{11} = 1$ and $\mathrm{K}_{112} = 1$, and the variation of $\tilde{\mathrm{u}}_{y_2}$ is computed along the vertical line crossing the centers of the inclusion (the dashed line in Fig. 3.13); the results are shown in Fig. 3.14. The displacement is continuous across the fiber/matrix interface, where its derivative experiences a jump, while the displacement periodicity is apparent from Fig. 3.9.

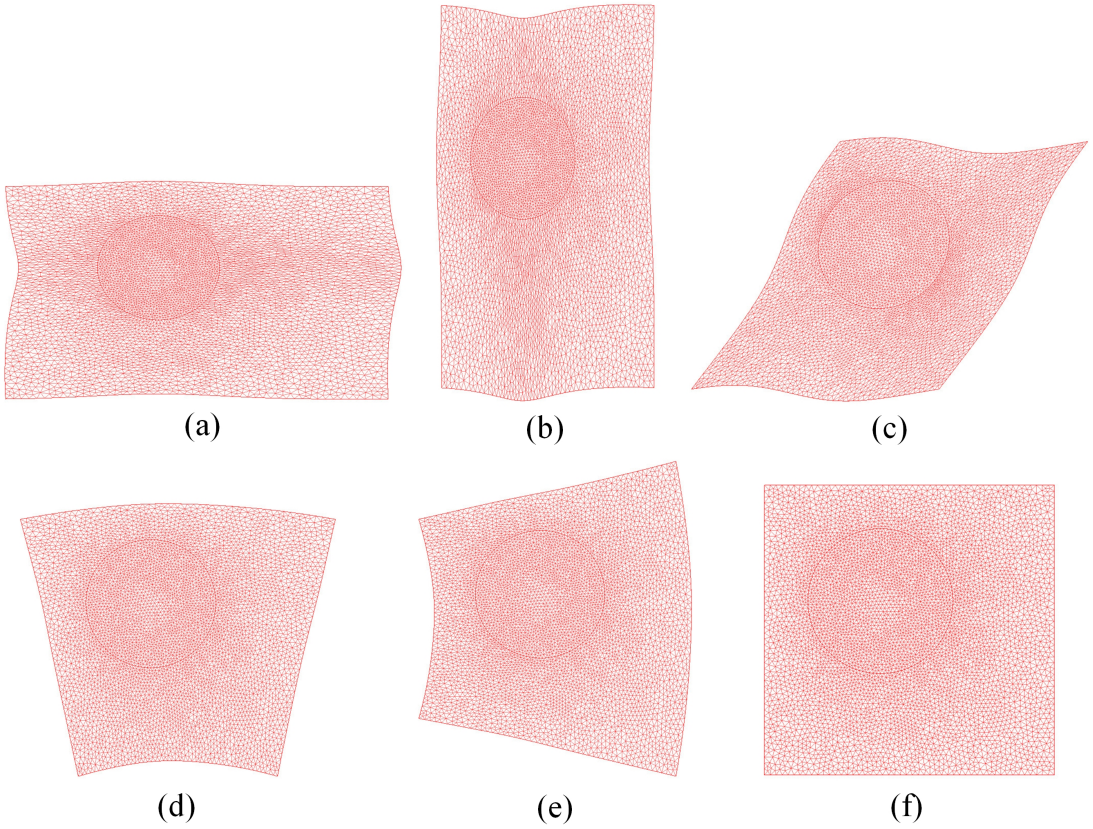

Figure 3.11 Microscopic total deformation modes induced by the imposed: (a)E_{11}, (b)E_{22}, (c)E_{12}, (d)K_{112}, K_{121}, (e)K_{221}, K_{212}, (f) e_{11}, e_{22}, e_{12}, e_{21}, K_{111}, K_{122}, K_{211}, K_{222}.

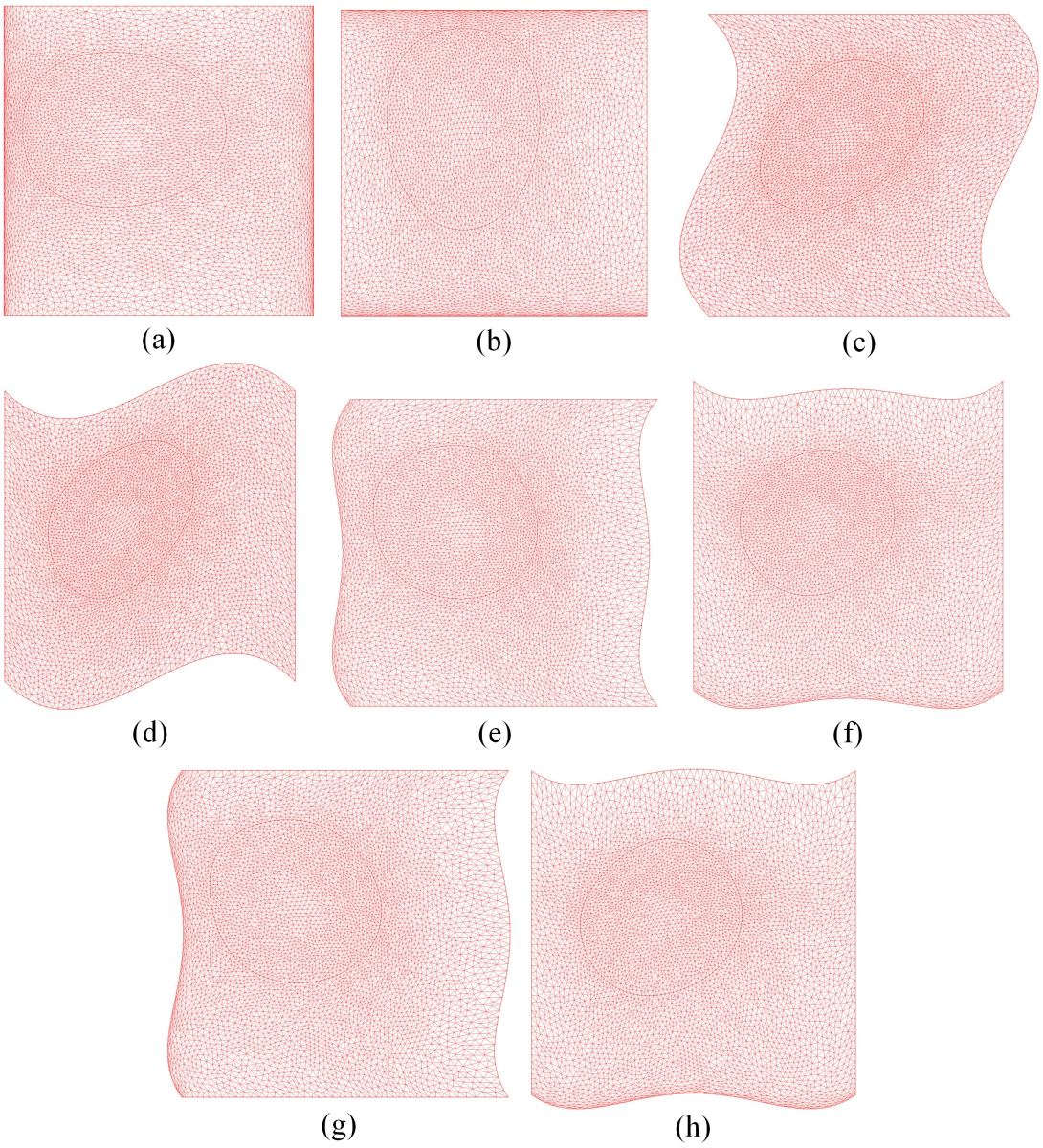

Figure 3.12 Microscopic fluctuation deformation modes induced by the imposed micromorphic components: (a) e_{11}, (b) e_{22}, (c) e_{12}, (d) e_{21}, (e) K_{111}, (f) K_{222}, (g) K_{122}, (h) K_{211}.

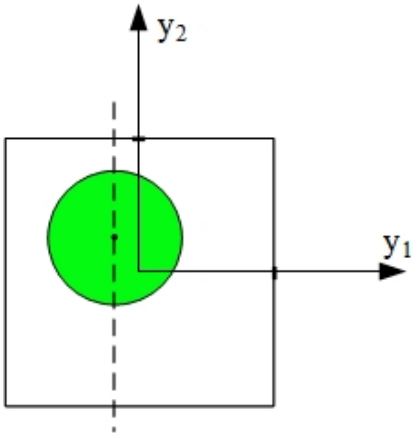

Figure 3.13 Non-centrosymmetric unit cell with indicated inclusion centerline.

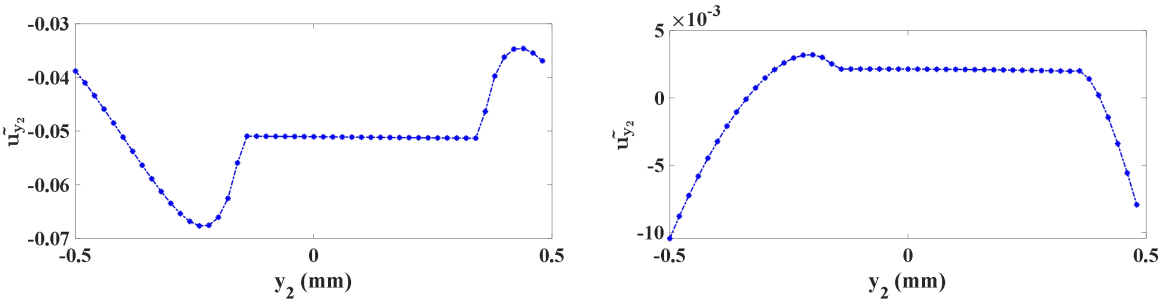

Figure 3.14 Distribution of the fluctuating displacement under the following kinematic loadings: $E_{11} = 1$, (b) $K_{112} = 1$.

To investigate the accuracy of modeling the composite by a micromorphic continuum, the relative contribution of the fluctuation energy to the total macroscopic energy for the successive components of the Cauchy strain, relative strain, and micromorphic kinematic measures are evaluated.

Table 3.3 shows the macroscopic, microscopic, and fluctuation energies for the unit cell of Fig. 3.10, for an inclusion with radius R = 0.25 mm; these energetic terms are successively defined as

$$W_{Macro} = \bar{\boldsymbol{\sigma}} : \underset{\sim}{\mathbf{E}} + \underset{\sim}{\mathbf{s}} : \underset{\sim}{\mathbf{e}} + \underset{\approx}{\mathbf{S}} : \underset{\approx}{\mathbf{K}}$$

$$W_{micro} = \left\langle \boldsymbol{\sigma} : \underset{\sim}{\boldsymbol{\varepsilon}}(\underset{\sim}{\mathbf{u}}^{\text{hom}} + \tilde{\underset{\sim}{\mathbf{u}}}) \right\rangle_Y$$

$$W_{fluctuation} = \left\langle \boldsymbol{\sigma} : \underset{\sim}{\boldsymbol{\varepsilon}}(\tilde{\underset{\sim}{\mathbf{u}}}) \right\rangle_Y$$

Overall, the energy of the fluctuation is about 0.5% for most of the deformation modes, except for those modes depicted in Fig. 3.12, a fact that will be discussed later on.

3.6.3 Effect of inclusion volume fraction and contrast of fiber and matrix Young's modulus

Consider the unit cell of Fig. 3.10 with properties given in Table 3.2. Fig. 3.15 shows the variation of the effective moduli components for one representative component of each effective moduli tensor versus inclusion volume fraction. Fig. 3.15(b) shows that by reducing the volume fraction of the inclusion, the coupling tensor $\underset{\approx}{\mathbf{D}}^{\text{hom}}$ tend to zero, since for a homogeneous material there is no coupling moduli. Analyzing the response of the unit cell for different inclusion volume fractions shows that the coupling tensors $\underset{\approx}{\mathbf{B}}^{\text{hom}}$, and $\underset{\approx}{\mathbf{H}}^{\text{hom}}$ tend to zero for all values of inclusion volume fraction; this follows from the vanishing of the relative stress in this case, expressed in Eq. 3.18. The explanation of this vanishing is due to the absence of body forces that have been discarded in the present simulations; although body forces do not explicitly appear in the expressions of the effective stress measures, Eq. 3.8, they indirectly contribute to all stress measures, classical and higher-order ones.

The effect of the contrast in Young's modulus of inclusion and matrix over the effective properties of the homogenous unit cell is next analyzed. To this end, the unit cell of Fig. 3.10 with an inclusion

Table 3.3 Elastic and Shear Moduli for various Materials [7].

Applied component	Macroscopic Energy	Total microscopic energy	Fluctuation Energy	Contribution of the fluctuation (%)
E_{11}	1291.962	1284.858	-7.104	0.553
E_{22}	1291.95	1284.831	-7.119	0.554
E_{12}	356.569	354.914	-1.655	0.466
e_{11}	0.08	0	-0.08	–
e_{22}	0.08	0	-0.08	–
e_{12}	0.002	0	-0.002	–
e_{21}	0.002	0	-0.002	–
K_{111}	0.017	0	-0.017	–
K_{122}	0.013	0	-0.013	–
K_{212}, K_{221}	18.261	18.19	-0.071	0.390
K_{112}, K_{121}	18.260	18.19	-0.07	0.385
K_{211}	0.013	0	-0.013	–
K_{222}	0.018	0	-0.018	–

radius R = 0.35 mm is considered. The mechanical properties of the epoxy matrix are chosen as $E_m = 1.4\,GPa$, $\nu_m = 0.3$, while those of the inclusion are being varied. Fig. 3.16(a) shows that for the homogenous unit cell ($E_f/E_m = 1$) the effective Cauchy tensor of moduli coincides with the mechanical properties of Epoxy, and it increases rapidly with the ratio of inclusion to matrix Young's modulus up to a plateau. It can be seen from Fig. 3.16(b) that some components of the effective micromorphic tensor $\underset{\approx}{\underset{\approx}{\mathbf{K}}}^{\text{hom}}$ start from the nil value for a homogeneous unit cell and asymptotically converge to a constant value with the ratio of tensile moduli. In contrast to this, some other components of $\underset{\approx}{\underset{\approx}{\mathbf{K}}}^{\text{hom}}$ start from a non-nil value even for a homogenous unit cell when $E_f/E_m = 1$ ($K_{112112} = 32$ MPa.mm in Fig. 3.16(b)).

3.6.4 Analysis of unit cell size effects

A centrosymmetric composite with a circular in-plane section of the inclusions is considered, as pictured in Fig. 3.17. The inclusions are aligned in the third out-of-plane direction and are periodically distributed in the (y_1, y_2) plane. The elastic coefficients of the fiber and matrix are given in Table 3.2, and the radius of the inclusion is selected as R = 0.25 mm in all unit cells. In Fig. 3.17, three unit cells containing N = 1, 4, 9 irreducible cells are shown to investigate the possible effects of unit cell size on the effective mechanical properties of the composite.

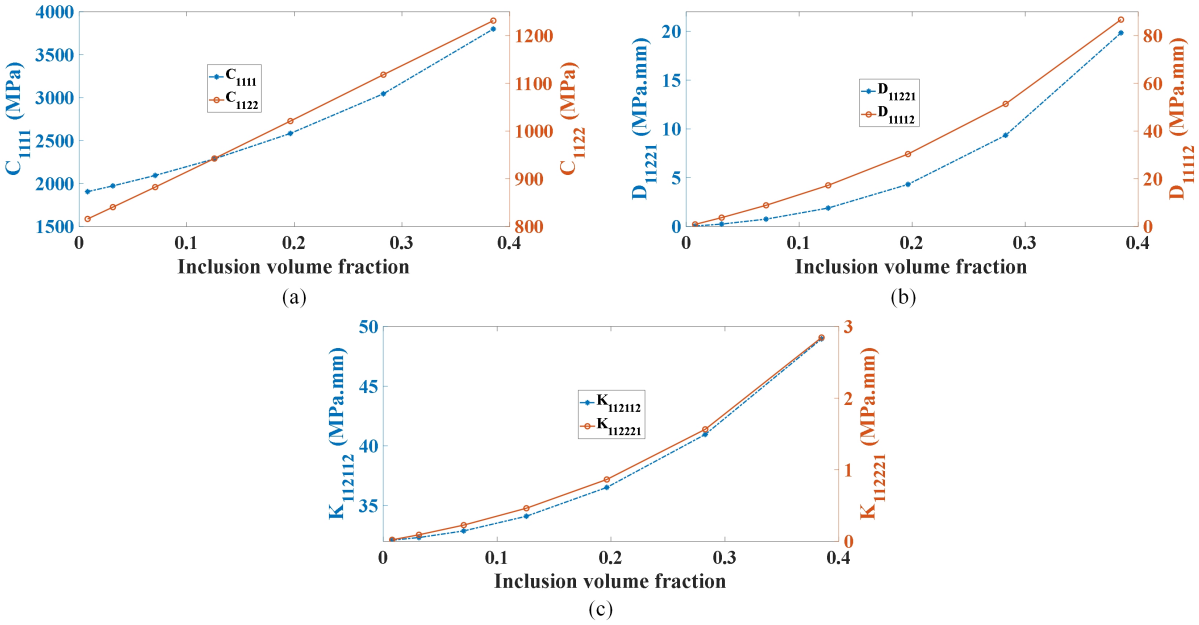

Figure 3.15 Variation of the effective moduli with the inclusion volume fraction.

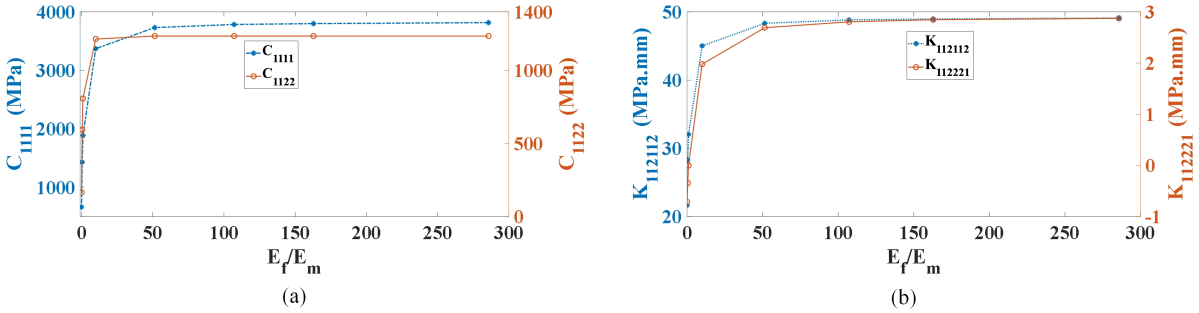

Figure 3.16 Variation of the effective moduli with the ratio of inclusion to matrix Young's modulus.

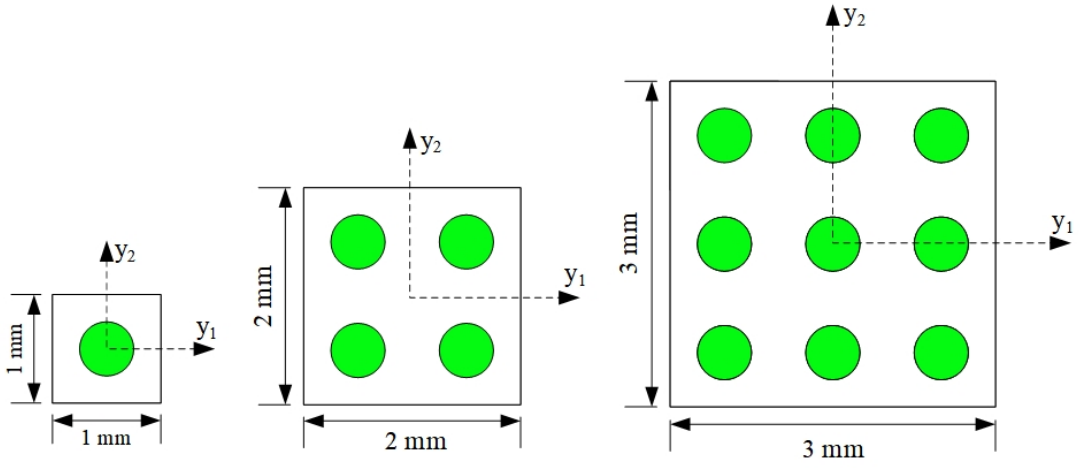

Figure 3.17 Unit cells including an increasing number of repetitions of the irreducible unit cell.

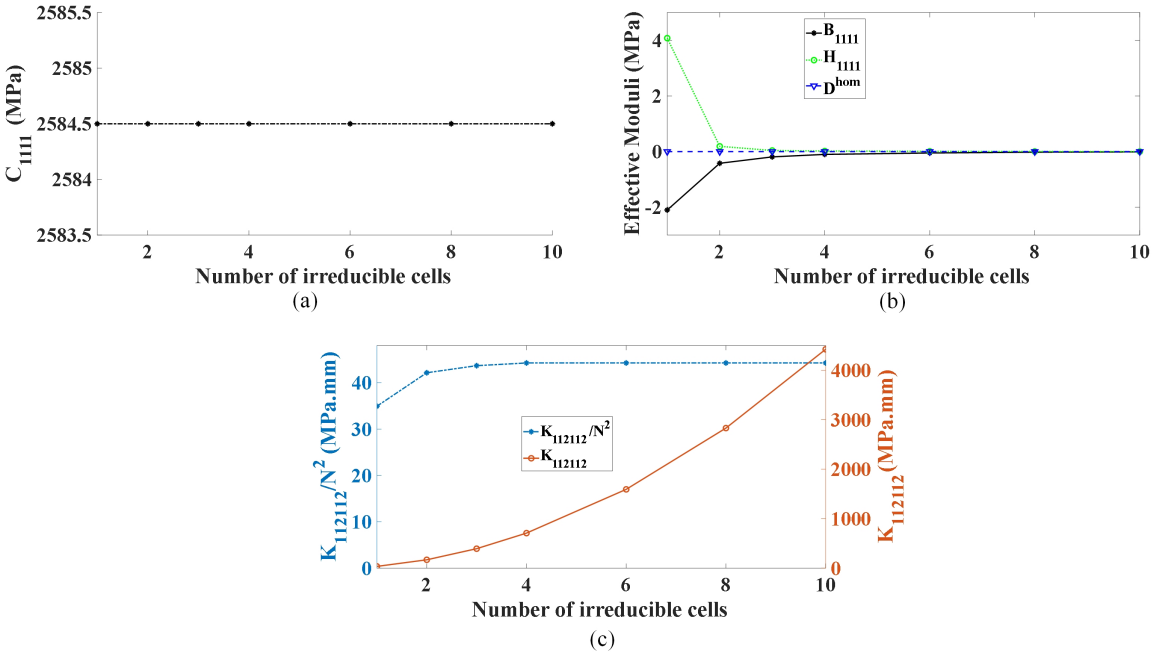

Figure 3.18 Variation of the effective moduli versus the number of irreducible unit cells, N.

For a centrosymmetric unit cell, the coupling tensor $\underset{\approx}{\mathbf{D}}^{\text{hom}}$ vanishes, as shown in Fig. 3.18(b). To investigate the behavior exhibited by other effective moduli, the variation of one representative component of each tensor versus the number of irreducible unit cells is depicted in Fig. 3.18.

As can be seen from Fig. 3.18(a), the effective Cauchy stress tensor $\underset{\approx}{\mathbf{C}}^{\text{hom}}$ is invariant with respect to the size of the unit cell, and the effective tensors $\underset{\approx}{\mathbf{B}}^{\text{hom}}$ and $\underset{\approx}{\mathbf{H}}^{\text{hom}}$ experience a slight change from N = 1 to N = 4 as shown in Fig. 3.18(b) while rapidly reaching the nil value for higher values of N, proving that these two tensors vanish. Fig. 3.18(b) shows the variation of the normalized micromorphic moduli normalized by the square of N ($\underset{\approx\approx}{\mathbf{K}}^{\text{hom}}/\text{N}^2$): the normalized values experience a rapid change from N = 1 to N = 2, but they quickly reach a plateau beyond this last value.

A few words about the assumption of a periodic displacement fluctuation are in order. The effective tensors $\underset{\approx}{\mathbf{B}}^{\text{hom}}$, $\underset{\approx}{\mathbf{H}}^{\text{hom}}$, and $\underset{\approx\approx}{\mathbf{K}}^{\text{hom}}/\text{N}^2$ (the last moduli being normalized by the square of the number of unit cells) experience a change from N = 1 to N = 4 as shown in Fig. 3.18. This variation is attributed to the fact that the fluctuation is expectedly not perfectly periodic, so a sufficiently large number of repetitions of the unit cell is needed to reach the stabilized value of the effective higher-order moduli.

The effective tensors $\underset{\approx}{\mathbf{B}}^{\text{hom}}$ and $\underset{\approx}{\mathbf{H}}^{\text{hom}}$ are related to the non-centrosymmetry of the unit cell; results of Fig. 3.17(b) shows that by increasing the number of the unit cell repetitions, these tensors tend to zero. This result confirms that for the entire structure, the fictitious non-centrosymmetric nature of the unit cell (it is due to the choice of the unit cell that can be arbitrarily translated, whereas the inclusion itself remains centrosymmetric) is meaningless since this effect becomes vanishingly small for a large number of unit cells repetitions. Moreover, the boundary of the unit cell can be translated concerning the microstructure in a way that the unit cell remains centrosymmetric.

The quadratic increase of the micromorphic moduli with the number of unit cells amount to decreasing the unit cell size, parameter 'a', considering that the homogenization of the initially heterogeneous periodic composite amounts to increasing the density of unit cells within a fixed macro domain tessellated with unit cells (thus the total area $\mathrm{N}^2 a$ remains constant). The performed normalization by factor N^2 is equivalent to homogenizing a fixed unit cell size so that the absolute size 'a' will be absorbed into the normalization process.

3.7 Discussion

The proposed homogenization method towards micromorphic substitution media relies on a variational formulation of equilibrium combined with a decomposition of the microscopic displacement into a homogeneous part and a fluctuation. At the microlevel, a linear elastic constitutive law without body forces is assumed. The homogeneous part of the microscopic displacement describes a heterogeneous medium that would exactly behave as the postulated micromorphic continuum. This homogenous displacement is corrected by an additional fluctuation at the microlevel, evaluated due to the linearity of the BVP using displacement localization operators, which are characterized by three-unit cell BVP.

After recoursing to the potential energy and complementary energy formulations, the proposed analysis provides a fourth-order polynomial homogeneous microscopic displacement field (this last formulation provides a third-order polynomial microscopic stress field). Moreover, it has been proved that this fourth-order displacement is complete because no more terms need to be added to capture the effective micromorphic continuum. The quadratic approximation of the homogeneous displacement is sufficient to capture the Cauchy stress and relative stress expressions of the micromorphic continuum. Thereby, a full displacement field at the microlevel in comparison to [187] has been provided. As proven in Appendix H, all kinematic and static macroscopic variables can be converted into surface integrals of the microscopic fields over the unit cell. This allows applying all kinematic measures fully over the unit cell boundary. The obtained expressions of the homogenized static variables are conveniently summarized as follows:

$$\bar{\underset{\sim}{\boldsymbol{\sigma}}} := \frac{1}{|Y|}\sum_{i=1,2}\left(\int_{\partial Y}\left(\underset{\sim}{\boldsymbol{\sigma}}\cdot\underline{\boldsymbol{n}}\right)ds\right)\otimes\underline{\boldsymbol{Y}}^{\delta}$$

$$\underset{\sim}{\mathbf{s}} := \frac{1}{|Y|}\sum_{i=1,2}\left(\left(\int_{\partial Y}\left(\underset{\sim}{\boldsymbol{\sigma}}\cdot\underline{\boldsymbol{n}}\right)ds_y\right)\otimes\left(\underline{\boldsymbol{Y}}^{\delta}\otimes\underline{\boldsymbol{Y}}^{\delta}\otimes\underline{\boldsymbol{Y}}^{\delta}\right)\right)\therefore\underset{\approx}{\Upsilon}-\frac{1}{|Y|}\sum_{i=1,2}\left(\int_{\partial Y}\left(\underset{\sim}{\boldsymbol{\sigma}}\cdot\underline{\boldsymbol{n}}\right)ds\right)\otimes\underline{\boldsymbol{Y}}^{\delta}\cdot\underset{\sim}{\boldsymbol{\Gamma}}$$

$$\begin{aligned}\underset{\approx}{\mathbf{S}} := &\frac{1}{|Y|}\sum_{i=1,2}\left(\left(\int_{\partial Y}\left(\underset{\sim}{\boldsymbol{\sigma}}\cdot\underline{\boldsymbol{n}}\right)ds_y\right)\otimes\left(\underline{\boldsymbol{Y}}^{\delta}\otimes\underline{\boldsymbol{Y}}^{\delta}\right)\right)\\&-\mathrm{P}^{-1}\underset{\sim}{\mathbf{G}}\otimes\underset{\approx}{\boldsymbol{\Lambda}}::\left(\underset{\approx}{\boldsymbol{\Omega}}:\frac{1}{|Y|}\sum_{i=1,2}\left(\left(\int_{\partial Y}\left(\underset{\sim}{\boldsymbol{\sigma}}\cdot\underline{\boldsymbol{n}}\right)ds_y\right)\otimes\left(\underline{\boldsymbol{Y}}^{\delta}\otimes\underline{\boldsymbol{Y}}^{\delta}\right)\right)+\frac{1}{|Y|}\sum_{i=1,2}\left(\left(\int_{\partial Y}\left(\underset{\sim}{\boldsymbol{\sigma}}\cdot\underline{\boldsymbol{n}}\right)ds_y\right)\otimes\left(\underline{\boldsymbol{Y}}^{\delta}\otimes\underline{\boldsymbol{Y}}^{\delta}\otimes\underline{\boldsymbol{Y}}^{\delta}\otimes\underline{\boldsymbol{Y}}^{\delta}\right)\right)\right)\end{aligned}$$

This contrasts with the recent approach [187], wherein the author cannot entirely convert all kinematic and static micro-macro relations into surface integrals, so they are instead expressed as integral constraints using Lagrange multipliers.

The presented method for determining the microscopic stress field relying upon the complementary energy leads to stress boundary conditions as an alternative to the employed kinematic boundary

conditions; the numerical efficiency of such stress-based boundary conditions will deserve further developments.

Moreover, the energy associated with the fluctuation shows a minimal relative contribution to the total average energy evaluated over the unit cell, less than 0.5%, as shown in Table 3.3.

A critical issue of the homogenization towards generalized continua raising controversies in the relevant literature is whether the higher-order moduli should identically vanish for a homogeneous composite; this fact has been acknowledged in the literature, see, e.g. [191]. Present numerical results for composites show that some higher-order moduli vanish for uniform unit cell domains, whereas some other higher moduli do not vanish. This behavior is attributed to the fact that the presence of neighboring unit cells (due to the periodicity assumption) constraints the deformed shape of the unit cell so that the Cauchy part of the response is also activated when imposing a given higher kinematic loading (even not including any Cauchy type kinematic measure). This amounts that the unit cell cannot deform as an infinite homogeneous domain would under the same kinematic loading, as recognized in [191].

The numerical results highlight that the effective higher-order moduli converge quickly with the unit cell size, so the proposed method does not exhibit a minimal size effect. Fig. 3.18(b)shows a rapid convergence towards a nil value of the pure relative stress to relative strain moduli and of that of the coupling moduli between relative stress and classical strains, tensors $\underset{\approx}{\mathbf{B}}^{\mathrm{hom}}, \underset{\approx}{\mathbf{H}}^{\mathrm{hom}}$, with unit cell size. On the other hand, the $\underset{\approx}{\mathbf{D}}^{\mathrm{hom}}$ moduli does not vanish for a non-centrosymmetric unit cell, as shown in Fig. 3.15(b). The closed-form expression of the microscopic displacement and stress shows that the absolute position of the inclusion within the unit cell matters (and thus not only the inclusion shape, centrosymmetric or not). Therefore, the integrated energy density of the unit cell is indeed dependent on the relative position of the origin of the local Cartesian basis attached to the unit cell so that a translation of it cannot be operated to cancel centrosymmetric effects).

In contrast, the pure micromorphic moduli show a convergence after proper normalization of the original homogenization problem by the unit cell size. This convergence is attributed to the incorporation of the displacement fluctuation into the variational-based homogenization method. Another explanation is the consideration of the higher moments of inertia Appendix G into the coefficients of macro kinematic measures that correct the potential unit cell size-dependency, which eliminates the need to define an artificial correction factor defined by the other authors, e.g. [192] for strain gradient homogenization. These corrections are captured into the expressions of the relative stress and hyperstress, here conveniently rewritten:

$$\underset{\sim}{\mathbf{s}} := 3\left\langle \underline{\boldsymbol{\xi}} \otimes \underline{\boldsymbol{\xi}} \otimes \underset{\sim}{\boldsymbol{\sigma}} \right\rangle_Y \therefore \underset{\approx}{\boldsymbol{\Upsilon}} - \langle \underset{\sim}{\boldsymbol{\sigma}} \rangle_Y \cdot \underset{\sim}{\boldsymbol{\Gamma}}$$

$$\underline{\mathbf{S}} := 2\left\langle \underline{\boldsymbol{\xi}} \otimes \underset{\sim}{\boldsymbol{\sigma}} \right\rangle_Y - 2\mathrm{P}^{-1}\underset{\sim}{\mathbf{G}} \otimes \underset{\approx}{\boldsymbol{\Lambda}} :: \left(\underset{\approx}{\boldsymbol{\Omega}} : \left\langle \underline{\boldsymbol{\xi}} \otimes \underset{\sim}{\boldsymbol{\sigma}} \right\rangle_Y + 2\left\langle \underline{\boldsymbol{\xi}} \otimes \underline{\boldsymbol{\xi}} \otimes \underline{\boldsymbol{\xi}} \otimes \underset{\sim}{\boldsymbol{\sigma}} \right\rangle_Y \right)$$

Previous expressions show that the relative stress and hyperstress tensors involve an additional quadratic and cubic terms in their expansion, respectively.

As an alternative to the proposed variational approach of micromorphic homogenization, some insights

into an asymptotic approach of micromorphic homogenization can be given see [193] for an overview of asymptotic homogenization. Cosserat models have been derived from an asymptotic homogenization of the microscopic BVP of Cosserat elasticity in [105]; [130]; [131] and micromorphic substitution models for a mixture of micromorphic continua established in [188]. The definition of a hierarchy of characteristic lengths allows classification and ranking of the derived effective medium, which can be Cauchy, micropolar, microstrain, or full micromorphic type according to the considered scheme of hypothesis. The difficulty of the emergence of a micromorphic effective continuum arises when the medium is of Cauchy type at the microscopic level of the individual constituents. At the macro level, the effective constitutive law shall involve new micromorphic degrees of freedom that are not present at the microscale. One, therefore, has to set a link between the microscopic displacement and the micromorphic DOFs. One possible strategy in line with the methodology adopted in the present work would be to embed the higher-order averaging of the microbalance laws, Eq. 3.6-3.8 into a family of balance laws index by the small scale parameter η, letting $\underline{\boldsymbol{\xi}} = \underline{\mathbf{x}}/\eta$. This entails from a kinematic viewpoint that the homogeneous part of the displacement will appear at leading orders of the scale parameter and its fluctuation at higher orders. A ranking of the different terms composing the homogeneous part of the micro displacement versus the small-scale parameter will appear, with Cauchy effective continuum to be recovered in the limit of a vanishing parameter; the fluctuating part of the displacement will appear at a higher order of the small-scale parameter. The so formulated asymptotic expansion of the displacement will lead to a corresponding asymptotic expansion of the effective macroscopic energy (using the extended Hill macrohomogeneity condition), highlighting the effective micromorphic constitutive tensors ranked at successive orders of the small-scale parameter.

Instead of a local (strong) form of the asymptotic homogenization scheme, one may resort to a variational-based asymptotic formulation, as done in [194]; for strain gradient homogenization. The benefit of the variational formulation compared to standard asymptotic models is to account for the finiteness of the scale parameter. Moreover, it can estimate the norm of the successive higher-order terms and the convergence of the solution obtained at the subsequent orders of the small scale parameter versus the actual solution.

3.7.1 Classification of generalized continua

Suitable degeneracy conditions of the introduced kinematic micromorphic variables lead to various subclasses of generalized continua issued from the micromorphic medium. For each generalized continuum, the balance equations and constitutive laws could be derived from applying the principle of virtual power. In order to set the stage for future developments, different generalized continua degenerated from the micromorphic continuum are introduced along with kinematic DOFs.

The micromorphic deformation $\underset{\sim}{\boldsymbol{\chi}}(\boldsymbol{x})$ is decomposed into symmetrical and skew-symmetrical

contributions:

$$\underset{\sim}{\underset{\sim}{\boldsymbol{\chi}}} = \underset{\sim}{\underset{\sim}{\boldsymbol{\chi}}}^{sym} + \underset{\sim}{\underset{\sim}{\boldsymbol{\chi}}}^{skew}$$

Another decomposition that will be helpful is in terms of the hydrostatic and deviatoric parts of the micro deformation, splitting into the hydrostatic, symmetrical deviatoric, and skew-symmetrical parts successively:

$$\underset{\sim}{\chi} = \underset{\sim}{\chi}^{H} + \underset{\sim}{\chi}^{D} \equiv \chi^{H}\underset{\sim}{\mathbf{I}} + \underset{\sim}{\chi}^{D} = \underbrace{\chi^{H}\underset{\sim}{\mathbf{I}} + \underset{\sim}{\chi}^{D,Sym}}_{\chi^{Sym}} + \underset{\sim}{\chi}^{skew}$$

The four introduced micromorphic tensors in the two previous relations can also be obtained from the full micromorphic kinematic variable $\underset{\sim}{\underset{\sim}{\boldsymbol{\chi}}}$ by the application of linear projection operators (fourth-order tensors) $\underset{\approx}{P}^{H}$, $\underset{\approx}{S}, \underset{\approx}{W}$, successively extracting the hydrostatic, symmetrical, and skew-symmetrical parts of any second-order tensor:

$$\begin{aligned}
P^{H}_{ijkl} &= \frac{1}{3}\delta_{ij}\delta_{kl} \Rightarrow \underset{\approx}{P}^{H} := \frac{1}{3}\underset{\sim}{\mathbf{I}} \otimes \underset{\sim}{\mathbf{I}} \\
S_{ijkl} &= \frac{1}{2}\left(\delta_{ik}\delta_{jl} + \delta_{il}\delta_{jk}\right) \Rightarrow \underset{\approx}{\underset{\approx}{P}}^{Sym} := \frac{1}{2}\left(\underset{\sim}{\mathbf{I}}\underline{\otimes}\underset{\sim}{\mathbf{I}} + \underset{\sim}{\mathbf{I}}\overline{\otimes}\underset{\sim}{\mathbf{I}}\right) \\
W_{ijkl} &= \frac{1}{2}\left(\delta_{ik}\delta_{jl} - \delta_{il}\delta_{jk}\right) \Rightarrow \underset{\approx}{\underset{\approx}{P}}^{Skew} := \frac{1}{2}\left(\underset{\sim}{\mathbf{I}}\underline{\otimes}\underset{\sim}{\mathbf{I}} - \underset{\sim}{\mathbf{I}}\overline{\otimes}\underset{\sim}{\mathbf{I}}\right)
\end{aligned}$$

The previous two decompositions entail the following classification of the considered generalized continua, whereby the respective practical macroscopic degrees of freedom are obtained as suitable projections of the full micromorphic kinematic DOFs.

Table 3.4 shows degenerated generalized continua resulting from the micromorphic continuum obtained by applying suitable constraint over kinematic degrees of freedom. The conjugated static variables of each media can be computed by implementing Hill macrohomogenity conditions.

Table 3.4 Micromorphic's degenerated generalized continua and their kinematic variables.

Type of generalized medium	**Kinematic degrees of freedom**
Micromorphic	$\{\mathbf{E}(\mathbf{x}), \boldsymbol{\chi}(\mathbf{x}), \mathbf{K}(\mathbf{x}) := \boldsymbol{\chi}(\mathbf{x}) \otimes \nabla_x\}$
Microstretch	$\left\{\begin{array}{l}\mathbf{E}(\mathbf{x}) := \mathbf{U} \otimes \nabla_x + \boldsymbol{\epsilon}.\boldsymbol{\chi}^{skew},\ \mathbf{K}(\mathbf{x}) := \chi^{skew} \otimes \nabla_x, \\ \mathbf{e}(\mathbf{x}) := Tr(\mathbf{E}(\mathbf{x})) - \chi^{H}(\mathbf{x}),\ \tau := \chi^{H}\nabla_x\end{array}\right\}$
Micropolar	$\left\{\mathbf{E}(\mathbf{x}), \boldsymbol{\chi}^{skew}(\mathbf{x}), \mathbf{K}(\mathbf{x})\right\}$
Microdilatation	$\left\{\mathbf{E}(\mathbf{x}), \chi^{H}(\mathbf{x}), \chi^{H}\nabla_x\right\}$
Microstrain	$\{\mathbf{E}(\mathbf{x}), \boldsymbol{\chi}^{sym}(\mathbf{x}), \boldsymbol{\chi}^{sym} \otimes \nabla_x\}$
Microshear	$\left\{\mathbf{E}(\mathbf{x}) := \mathbf{U} \otimes \nabla_x, \boldsymbol{\chi}^{D}, \mathbf{K}\right\}$
Strain gradient	$\{\mathbf{E}(\mathbf{x}) := \mathbf{U} \otimes \nabla_x, \mathbf{K} := \mathbf{E}(\mathbf{x}) \otimes \nabla_x\}$

The classification of the generalized continua arising from Table 3.4 is the picture in a synthetic format in Fig. 3.19, showing three hierarchical levels of degeneration of the micromorphic continuum.

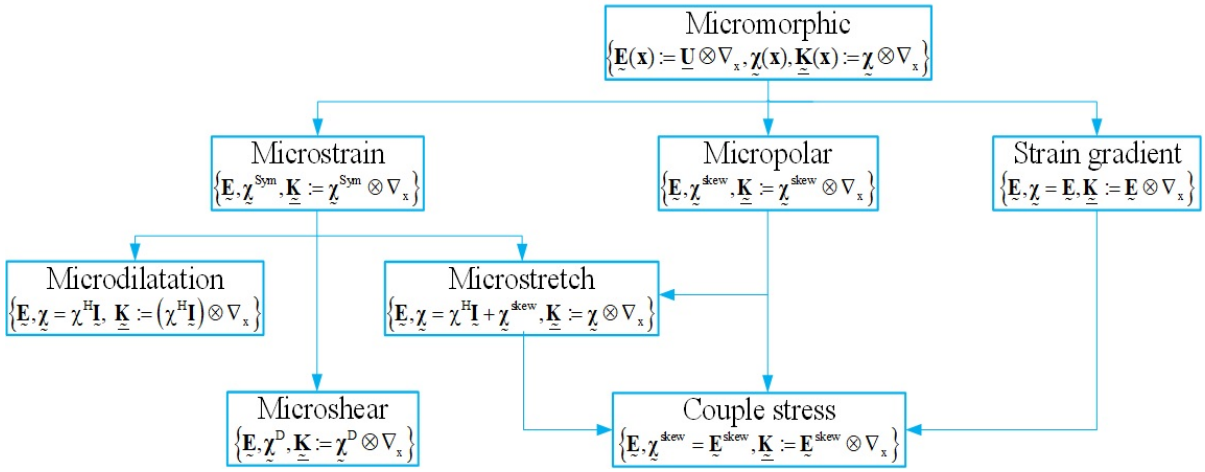

Figure 3.19 Classification of micromorphic effective medium and its degenerate media arising from Table 3.4.

3.8 Conclusion

The homogenization of heterogeneous media towards micromorphic substitution media is investigated in this chapter by revisiting the higher-order homogenization schemes. Starting from the microscopic balance equations, the local balance equations of the micromorphic continuum satisfied by the stress measures are formulated. The Hill macrohomogeneity condition is proven, highlighting the stress measures of the effective micromorphic medium as surface integrals over the representative unit cell. Relying on both the energy and complementary energy articulated with the extended Hill macrohomogeneity condition, the homogeneous displacement field representative of the micromorphic substitution medium is derived as a quartic polynomial in the microscopic relative position. This procedure leads to a higher-grade micromorphic theory, with the relative stress and hypertress tensors including respectively second-order and third-order polynomials in the relative position within the unit cell. A fluctuating part completes the displacement field evaluated from a variational principle and characterized by three unit cell BVPs. Numerical applications for inclusion-based composite materials highlighted that the higher-order moduli converge very quickly with unit cell size due to considering correction factors accounting for the higher-order moment of inertia. The obtained homogenized micromorphic model has been validated by comparing its predictions for a homogeneous plate architected with a tetrachiral lattice with the whole network model's.

In terms of perspectives, the proposed homogenization method has been implemented into a general-purpose FE code, so that it can potentially handle a wide diversity of regular heterogeneous materials, covering composites and architectured materials for which micromorphic models will be identified in future developments.

Part II

Beyond continuous homogenization: phenomenological beam models and discrete homogenization of architected materials towards Cosserat media

Chapter 4

Development of size-dependent consistent couple stress theory of Timoshenko beams

Summary

This chapter develops a nonlinear size-dependent Timoshenko beam model based on the consistent couple stress theory to capture the size effects. The extended Hamilton's principle is utilized to obtain the governing differential equations and boundary conditions. The general form of boundary conditions and the concentrated loading determines the beam's exact static/dynamic solution. Utilizing this solution for the beam's deformation and rotation, the exact shape functions of the consistent couple stress theory (C-CST in short) are extracted, leading to the stiffness and mass matrices of a two-node C-CST finite element beam. Due to the complexity and high computational cost of using the exact solution's shape functions, in addition to the Ritz approximate solution, a two primary variable finite element model of C-CST is proposed, and the corresponding general deformation and rotation fields, shape functions, mass and stiffness matrices are calculated. For the fully and partially clamped cantilever and free-free beams, the size dependency of the formulations is investigated. The static solutions of the classical and consistent couple stress Timoshenko beam models are compared, and a criterion for selecting the proper model is proposed. The relation between the beam length and length scale parameter is derived for a wide range of material properties. It is shown that the validity domain of the consistent couple stress Timoshenko model barely depends on the beam's constituent material.

4.1 Introduction

Beams as structural elements have found critical micro-scale applications such as biosensors [195], open foam cellular structures produced by additive manufacturing in bio-implants, and simulation of bone tissue internal remodeling. In these applications, the beam thickness is typical of the order of a micron, and the size effect is often observed [77, 78].

Due to the lack of an internal material length scale parameter in the classical beam models, extended continuum theories incorporating the material length scale parameters are needed. Several continuum-based theories have been proposed and, different parameters related to the material length scale are included to take into account the size effects. The most important theories are the couple stress theory (CST), micropolar elasticity, strain gradient theory, and the nonlocal elasticity theory [196]. In the 1960s, prominent researchers like Mindlin-Tiersten [197], Koiter [76], and Eringen [174] introduced the CST and micropolar theory. For linear isotropic elastic materials, constitutive equations of micropolar theory require four more constants and two Lame constants. The CST is the confined Cosserat model with restricted rotations, i.e., in which the Cosserat rotations coincide with the continuum macrorotations [198]. In the context of the linear isotropic elastic materials, two higher-order material length scale parameters appear in the constitutive equations of the CST in addition to the two Lame constants.

Furthermore, the CST can be considered a particular case of the micropolar theory due to the identity of the rotation vector of the microstructure with the macrorotation vector [199]. This assumption reduces the number of the higher-order material length scale parameters in constitutive equations for linear isotropic elastic materials from four in the micropolar theory to two parameters in the couple stress theory. Asghari et al. [200] investigated the size effects in Timoshenko beams based on the couple stress theory. In this work, the closed-form solutions for the axial deformation, bending deflection, and the rotation angle of cross-sections in the static cases, in the form of unknown coefficients, were presented, but the unknown constants were calculated only for a cantilever beam under a concentrated shear force at a free end. Alotta et al. [201] presented a finite element model for a nonlocal Timoshenko beam. The stiffness matrix was calculated for the axial deformation, bending deflection, and beam rotation. Dehrouyeh-Semnani and Bahrami [202] investigated size-dependent Timoshenko beam elements' accuracy, reliability, and stability properties based on the modified couple stress theory.

It should be mentioned that due to the difficulties associated with experimentally determining the higher-order material length scale parameters, applying a theory capable of a factor in the small-scale effects even with fewer of these parameters is preferred [203]. To this end, the modified couple stress theory (M-CST) was presented by Yang et al. [204], which included a single higher-order material length scale parameter in the constitutive equations. Ma et al. [205] developed or proposed a microstructure-dependent Timoshenko beam model based on the modified couple stress theory. Their work investigated the static bending and free vibrations of a simply-supported beam using the M-CST. Kahrobaiyan et al. [206] developed a Timoshenko beam model based on the M-CST. The DOF corresponding to the

slope of the beam was neglected, and the approximate mass and stiffness matrices of the two-node beam were calculated. based on the M-CST, Goncalves et al. [207] investigated the linear buckling and free vibrations of Timoshenko sandwich beams. The shape functions were calculated using the polynomial approximation. Karttunen et al. [208] studied the microstructure-dependent Timoshenko beam based on the M-CST and found the general close form solutions and the corresponding stiffness matrix. Yu et al. [196] analyzed the size-dependent mechanical behavior of functionally graded microbeams. In order to capture the size effects, they made an extension of a quasi-3D theory merged with M-CST. They have considered both normal and shear deformations, while no shear correction factor was needed. In another study [209], the authors developed a two-directional functionally graded microbeam model using the NURBS-based isogeometric analysis. The proposed model was used to investigate the natural frequency and mechanical bending of microbeams. Goncalves et al. [210] proposed a nonlinear model for periodic sandwich structures based on the modified couple stress Timoshenko beam theory. They show that their model is equivalent to the thick-face sandwich beam theory.

The M-CST restricts symmetric couple stress tensor to achieve a simple theory; the obtained equations are not consistent with proper boundary conditions and the virtual work principle energy conjugacy, which violates the fundamental rules of mechanics [211]. Recently, Hadjesfandiari and Dargush [211,212] developed the consistent couple stress theory (C-CST), which has no inconsistencies of the original couple stress or modified couple stress theories. Hadjesfandiari et al. [213] developed the C-CST for Timoshenko beams and obtained the exact solution for the deflection and rotation fields in some particular cases. Most previous studies have found the solution based on the other couple stress theories such as the modified couple stress theory, and indeterminate couple stress theory for some special cases of Timoshenko beam by using approximate shape functions. The constitutive equations of the abovementioned theories and their associated assumptions on the Timoshenko beam model are summarized in Table 1. It appears that C-CST and M-CST involve fewer material parameters compared to the other size-dependent beam theories. The validation of the C-CST model will be done later on.

The outline of the chapter is as follows. Section 4.2 is devoted to deriving the governing equilibrium equations and boundary conditions of the Timoshenko beam in the context of the C-CST. Various solution methodologies are exposed namely the exact solution, the two primary variables solution method, and the Ritz approximation method. In section 4.3, through some case studies, the effect of using various solution approaches on the beam response is investigated. Furthermore, the solutions of the C-CST and classical Timoshenko beam theory are compared. In the last part of section 4.3, for a broad range of material properties, based on the criterion of less than 1% discrepancy between the exact C-CST and classical Timoshenko solutions, the relation between the length and the length scale parameter of the beam is investigated. In section 4.4, for various material properties and boundary conditions, the range of values of dimensionless length for which the classical Timoshenko theory is not accurate enough and the C-CST solution should be used instead are determined. Section 4.5 concludes the chapter with a summary of the proposed model and a few perspectives of the development of the present contribution.

Table 4.1 Constitutive law and assumptions of classical and couple stress continuum theories.

Continuum theory	material constants (Linear isotropic elastic)	Constitutive equations	Timoshenko beam assumptions
Classical	2	$\sigma_{ji} = \lambda e_{kk}\delta_{ij} + 2\mu e_{ij}$	H1, H2, H8
		$\sigma_{ji} = \lambda\varepsilon_{kk}\delta_{ij} + \mu\varepsilon_{ij} + \mu'\varepsilon_{ji}$	
Micropolar	6	$\mu_{ji} = \alpha k_{kk}\delta_{ij} + \beta k_{ij} + \gamma k_{ji}$	H2, H3, H7
		$\varepsilon_{ij} = u_{i,j} - \epsilon_{ijk}\varphi_k$	
		$k_{ij} = \varphi_{i,j}$	
		$\sigma_{(ji)} = \lambda e_{kk}\delta_{ij} + 2\mu e_{ij}$	
CS	4	$\mu_{ij} = Q\delta_{ij} + 4\eta\omega_{j,i} + 4\mu'\omega_{i,j}$	H1, H3, H7
		$Q = \frac{1}{3}\mu_{kk}$	
		$\sigma_{(ji)} = \lambda e_{kk}\delta_{ij} + 2Ge_{ij}$	
MCS	3	$\mu_{ij} = 2Gl^2{\kappa'}_{ij}$	H1, H3, H7, H4
		${\kappa'}_{ij} = \frac{1}{2}(\omega_{i,j} + \omega_{j,i})$	
		$\sigma_{(ji)} = \lambda e_{kk}\delta_{ij} + 2Ge_{ij}$	
CCS	3	$\mu_{ij} = -8Gl^2\kappa_{ij}$	H1, H3, H7, H5
		$\kappa_{ij} = \frac{1}{2}(\omega_{i,j} - \omega_{j,i})$	
		$\sigma_{(ji)} = \lambda e_{kk}\delta_{ij} + 2Ge_{ij}$	
2PV	3	$\mu_{ij} = -8Gl^2\kappa_{ij}$	H1, H3, H8, H5,H6
		$\kappa_{ij} = \frac{1}{2}(\omega_{i,j} - \omega_{j,i})$	

H0: Deformation is only specified by the displacement field (u_i).

H1: Deformation is specified by displacement and micro rotation fields (u_i and φ_i).

H2: The rigid body motion of an infinitesimal element of matter at each point of the continuum is described by three translational degrees of freedom.

H3: The rigid body motion of an infinitesimal element of matter at each point of the continuum is described by six degrees of freedom (three translational and three rotational).

H4: The couple-stress tensor is assumed to be symmetric.

H5: The couple-stress tensor is assumed to be skew-symmetric.

H6: The contribution of the moment M_θ in the total moment M is disregarded, i.e. $M \approx M_\phi$ (see Eq.4.45).

H7: u_z, ϕ, and θ are primary variables in the transverse deflection (see Fig. 4.1).

H8: u_z and ϕ are primary variables in the transverse deflection (see Fig. 4.1).

4.2 Consistent Couple Stress Theory (C-CST)

In order to set the stage, we recall the main achievement of the consistent couple stress theory proposed by Hadjesfandiari et al. [211], which is the skew-symmetric character of the couple-stress tensor, viz

$$\mu_{ji} = -\mu_{ij} \tag{4.1}$$

Since the stress tensor σ_{ij} is in general a non-symmetric tensor, it can be decomposed into symmetric and antisymmetric parts denoted respectively with parentheses and brackets confined subscripts as

$$\sigma_{ij} = \sigma_{(ij)} + \sigma_{[ij]} \tag{4.2}$$

Surface forces and couples are represented by force-stress σ_{ij} and couple-stress μ_{ij} tensors

$$t_i^{(n)} = \sigma_{ji} n_j \tag{4.3}$$

$$m_i^{(n)} = \mu_{ji} n_j \tag{4.4}$$

where, $t_i^{(n)}$ and $m_i^{(n)}$ are force and moment traction vectors, respectively, and n_j is the normal unit vector on a surface element dS. The equilibrium equations can be written in the following tensor format

$$\sigma_{ji,j} + f_i = 0 \tag{4.5}$$

$$\mu_{ji,j} + \epsilon_{ijk}\sigma_{jk} = 0 \tag{4.6}$$

where f_i and ϵ_{ijk} are the body force and permutation symbol, respectively, and $(,)$ refers to the partial derivative. The antisymmetric part of Cauchy stress tensor is obtained as

$$\sigma_{[ij]} = \frac{1}{2}\epsilon_{ijk}\mu_{lk,l} = -\mu_{[i,j]} \tag{4.7}$$

By assuming infinitesimal deformations and adopting Cartesian coordinates, the displacement gradient tensor $u_{i,j}$ can be decomposed into a symmetric $(e_{i,j})$ and a skew-symmetric (ω_{ij}) part

$$\sigma_{[ij]} = \frac{1}{2}\epsilon_{ijk}\mu_{lk,l} = -\mu_{[i,j]} \tag{4.8}$$

$$\omega_{ij} = \frac{1}{2}\left(u_{i,j} - u_{j,i}\right) \tag{4.9}$$

where $e_{i,j}$ and ω_{ij} are the strain and rotation fields, respectively. The skew-symmetric part of the bend-twist tensor $(\kappa_{ij} = \omega_{i,j})$ is the curvature tensor, so that it holds

$$\kappa_{ij} = \omega_{[i,j]} = \frac{1}{2}\left(\omega_{i,j} - \omega_{j,i}\right) \tag{4.10}$$

The skew-symmetric tensors μ_{ij} and κ_{ij} can be represented by their dual true couple-stress vectors μ_i and the true mean curvature vector κ_i [213], successively, in the following form

$$\mu_i = \frac{1}{2}\epsilon_{ijk}\mu_{kj} \tag{4.11}$$

$$\kappa_i = \frac{1}{2}\epsilon_{ijk}\kappa_{kj} \tag{4.12}$$

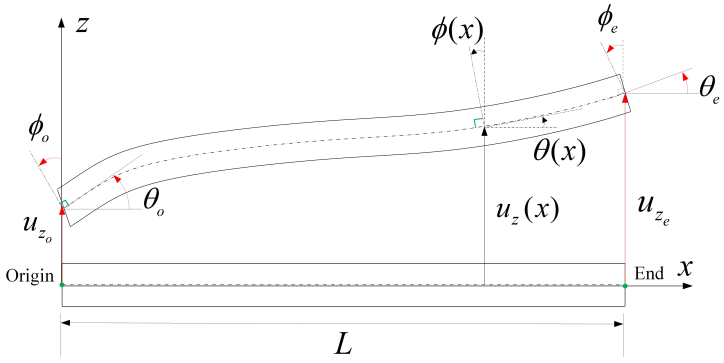

Figure 4.1 Timoshenko beam element coordinates and displacements

The constitutive relations of a linear isotropic elastic material writes as follows [211],

$$\sigma_{(ij)} = \lambda e_{kk}\delta_{ij} + 2Ge_{ij} \tag{4.13}$$

$$\mu_{ij} = -8\eta\kappa_{ij} = -4\eta\left(\omega_{i,j} - \omega_{j,i}\right) \tag{4.14}$$

where λ and G are the Lame constant and shear modulus, respectively, and η is the C-CST material constant for isotropic materials. λ and G are related to the Young's modulus, E, with the following relation

$$\lambda = \frac{G\left(E - 2G\right)}{3G - E}$$

The ratio η/G is related to the characteristic material length, l as follows

$$\frac{\eta}{G} = l^2 \tag{4.15}$$

so it appears that C-CST only requires a single couple-stress material parameter. The antisymmetric part of stress tensor becomes

$$\sigma_{[ji]} = 2Gl^2\nabla^2\omega_{ji} \tag{4.16}$$

As a result, the stress tensor, and the energy density function take the following form

$$\sigma_{ji} = \lambda e_{kk}\delta_{ij} + 2Ge_{ij} + 2Gl^2\nabla^2\omega_{ji} \tag{4.17}$$

$$W = \frac{1}{2}\lambda e_{jj}e_{kk} + Ge_{ij}e_{ij} + 4\eta\kappa_{ij}\kappa_{ij} \tag{4.18}$$

4.2.1 Timoshenko Beam with size-dependency effect

A prismatic homogeneous isotropic beam element, including shear deformation and rotary inertia, is considered. The displacement function $u_z\left(x\right)$ describe the translation of the beam's neutral axis, in the z direction, while function $\phi\left(x\right)$ denotes the rotation of the cross-section at the mid-plane, and $\theta\left(x\right)$ is the slope of the central axis of the beam. The beam element coordinates and displacements are shown in Fig. 4.1

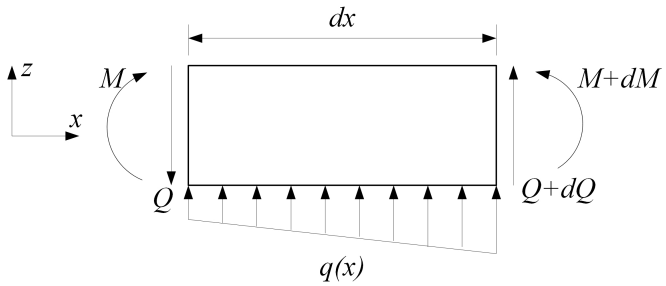

Figure 4.2 An infinitesimal element of the beam and applied forces and moments.

The governing equilibrium equations for an infinitesimal beam element shown in Fig. 4.2 are

$$\begin{cases} \dfrac{dQ}{dx} + q = 0 & (4.19) \\ \dfrac{dM}{dx} + Q = 0 & (4.20) \end{cases}$$

where Q, M, and q are the resultant shear force, the resultant bending moment, and the distributed shear load, respectively. The very definition of these quantities will be explicated in the sequel, based on the introduced couple stress continuum model that has been reduced to a beam model.

The displacement field in Timoshenko beam theory is assumed to take the form

$$\begin{aligned} u_x &= -z\phi\,(x,t) \\ u_y &= 0 \\ u_z &= u_z\,(x,t) \end{aligned} \tag{4.21}$$

in which the slope of the central axis of the beam is given by

$$\theta = \frac{du_z}{dx} \tag{4.22}$$

The non-zero strains, rotation, and curvature tensors, as well as the corresponding curvature vector component are respectively

$$e_{xx} = \frac{du_x}{dx} = -z\frac{d\phi}{dx} \tag{4.23}$$

$$e_{xz} = \frac{1}{2}\left(\frac{du_z}{dx} - \phi\right) \tag{4.24}$$

$$\omega_y = -\frac{1}{2}\left(\frac{du_z}{dx} + \phi\right) \tag{4.25}$$

$$\kappa_{xy} = -\kappa_z = -\frac{1}{2}\frac{\partial \omega_y}{\partial x} = \frac{1}{4}\left(\frac{d^2u_z}{dx^2} + \frac{d\phi}{dx}\right) \tag{4.26}$$

The engineering shear strain γ and the engineering curvature K are defined as

$$\gamma = 2e_{xz} = \frac{\partial u_z}{\partial x} - \phi \tag{4.27}$$

$$\mathrm{K} = -2\kappa_z = \frac{1}{2}\left(\frac{d^2u_z}{dx^2} + \frac{d\phi}{dx}\right) \tag{4.28}$$

The non-zero stress components follow from Eq. 4.13 and Eq. 4.14

$$\sigma_{xx} = Ee_{xx} = -Ez\frac{d\phi}{dx} \tag{4.29}$$

$$\sigma_{(xz)} = 2Ge_{xz} = G\gamma = G\left(\frac{du_z}{dx} - \phi\right) \tag{4.30}$$

$$\mu_z = -\mu_{xy} = 4Gl^2\mathrm{K} = 2Gl^2\left(\frac{d^2u_z}{dx^2} + \frac{d\phi}{dx}\right) \tag{4.31}$$

Therefore, it holds

$$\sigma_{[xz]} = -\frac{1}{2}\frac{d\mu_z}{dx} = -Gl^2\frac{d}{dx}\left(\frac{d^2u_z}{dx^2} + \frac{d\phi}{dx}\right) \tag{4.32}$$

According to Eq. 4.29 through Eq. 4.32, the resultant shear force and bending moment can be decomposed as [213]

$$\begin{aligned} M &= M_\sigma + M_\mu \\ Q &= Q_\sigma + Q_\mu \end{aligned} \tag{4.33}$$

with

$$\begin{aligned} M_\sigma &= -\int_A z\sigma_{xx}dA,\ M_\mu = -\int_A \mu_{xy}dA \\ Q_\sigma &= \int_A \sigma_{(xz)}dA,\ Q_\mu = \int_A \sigma_{[xz]}dA \end{aligned}$$

The equations of motion are next derived using the extended Hamilton's principle, viz

$$\begin{aligned} \delta\int_0^t \mathcal{L}\ dt &= 0 \\ \mathcal{L} &= T - U + W_e \end{aligned} \tag{4.34}$$

where $\mathcal{L}$, T, U and W_e are the Lagrangian, kinetic energy, strain energy, and work of the external loads, respectively. The strain energy is given by,

$$\begin{aligned} U = \frac{1}{2}\int_\Omega \left(\sigma_{(ij)}e_{ij} + \mu_{ij}\omega_{i,j}\right)d\Omega = \int_0^L \left[\frac{1}{2}EI\left(\frac{d\phi}{dx}\right)^2 + \frac{1}{2}k_sGA\left(\frac{du_z}{dx} - \phi\right)^2\right. \\ \left. + \frac{1}{2}k_\mu GAl^2\left(\frac{d^2u_z}{dx^2} + \frac{d\phi}{dx}\right)^2\right]dx \end{aligned} \tag{4.35}$$

or in matrix form

$$U = \frac{1}{2}\int_0^L \begin{Bmatrix} \frac{d\phi}{dx} \\ \frac{du_z}{dx} - \phi \\ \frac{d^2u_z}{dx^2} + \frac{d\phi}{dx} \end{Bmatrix}^{\mathrm{T}} \begin{bmatrix} EI & 0 & 0 \\ 0 & k_sGA & 0 \\ 0 & 0 & k_\mu GAl^2 \end{bmatrix} \begin{Bmatrix} \frac{d\phi}{dx} \\ \frac{du_z}{dx} - \phi \\ \frac{d^2u_z}{dx^2} + \frac{d\phi}{dx} \end{Bmatrix} dx \tag{4.36}$$

The kinetic energy of the beam is given by

$$T = \frac{1}{2}\int_\Omega \rho\left(\left(\frac{\partial u_x}{\partial t}\right)^2 + \left(\frac{\partial u_z}{\partial t}\right)^2\right)d\Omega \tag{4.37}$$

Integrating over the cross-section allows to rewrite this last quantity in matrix form as follows

$$T = \frac{1}{2}\int_0^L \begin{Bmatrix} \frac{\partial u_z}{\partial t} \\ \frac{\partial \phi}{\partial t} \end{Bmatrix}^{\mathrm{T}} \begin{bmatrix} \rho A & 0 \\ 0 & \rho I \end{bmatrix} \begin{Bmatrix} \frac{\partial u_z}{\partial t} \\ \frac{\partial \phi}{\partial t} \end{Bmatrix} dx \tag{4.38}$$

Finally, the work of the external distributed force 'q' and moment 'm' is given by the following line integral

$$W_e = \int_0^L \left\{ \begin{array}{c} u_z \\ \phi \end{array} \right\}^{\mathrm{T}} \left\{ \begin{array}{c} q \\ m \end{array} \right\} dx \tag{4.39}$$

Using Eq. 4.36, Eq. 4.38 and Eq. 4.39, the Lagrangian function of the beam is

$$\begin{aligned} \mathcal{L} &= \frac{1}{2}\int_0^L \rho\left(\left(\frac{\partial u_x}{\partial t}\right)^2 + \left(\frac{\partial u_z}{\partial t}\right)^2\right)dx - \frac{1}{2}\int_0^L \left(\sigma_{(ij)}e_{ij} + \mu_{ij}\omega_{i,j}\right)dx + \int_0^L (qu_z + m\phi)dx \\ &= \int_0^L \left[-\frac{1}{2}EI\left(\frac{d\phi}{dx}\right)^2 - \frac{1}{2}k_sGA\left(\frac{du_z}{dx} - \phi\right)^2 - \frac{1}{2}k_\mu GAl^2\left(\frac{d^2u_z}{dx^2} + \frac{d\phi}{dx}\right)^2 + \frac{1}{2}\rho A\left(\frac{\partial u_z}{\partial t}\right)^2 + \frac{1}{2}\rho I\left(\frac{\partial \phi}{\partial t}\right)^2 + qu_z + m\phi\right]dx \end{aligned} \tag{4.40}$$

Substituting the Lagrangian function in the extended Hamilton's principle, Eq. 4.34, and performing a few mathematical manipulations results in

$$\begin{aligned} \delta\int_0^t \mathcal{L}\,dt = \int_0^t \Bigg(& -EI\left(\frac{d\phi}{dx}\right)\delta\phi\Big|_0^L + \int_0^L EI\frac{d^2\phi}{dx^2}\delta\phi dx + \int_0^L k_sGA\left(\frac{du_z}{dx} - \phi\right)\delta\phi dx - k_sGA\left(\frac{du_z}{dx} - \phi\right)\delta u_z\Big|_0^L \\ & + \int_0^L k_sGA\left(\frac{d^2u_z}{dx^2} - \frac{d\phi}{dx}\right)\delta u_z dx - k_\mu GAl^2\left(\frac{d^2u_z}{dx^2} + \frac{d\phi}{dx}\right)\delta\phi\Big|_0^L + \int_0^L k_\mu GAl^2\left(\frac{d^3u_z}{dx^3} + \frac{d^2\phi}{dx^2}\right)\delta\phi dx \\ & - k_\mu GAl^2\left(\frac{d^2u_z}{dx^2} + \frac{d\phi}{dx}\right)\delta\frac{du_z}{dx}\Big|_0^L + k_\mu GA\,l^2\left(\frac{d^3u_z}{dx^3} + \frac{d^2\phi}{dx^2}\right)\delta u_z\Big|_0^L - \int_0^L k_\mu GAl^2\left(\frac{d^4u_z}{dx^4} + \frac{d^3\phi}{dx^3}\right)\delta u_z dx \\ & + \int_0^L q\delta u_z dx + \int_0^L m\delta\phi dx\Bigg)dt - \int_0^L\int_0^t \left(\rho A\frac{\partial^2 u_z}{\partial t^2}\delta u_z + \rho I\frac{\partial^2\phi}{\partial t^2}\delta\phi\right)dtdx + \int_0^L\left[\rho A\frac{\partial u_z}{\partial t}\delta u_z\Big|_0^t + \rho A\frac{\partial\phi}{\partial t}\delta\phi\Big|_0^t\right]dx = 0 \end{aligned} \tag{4.41}$$

where k_s and k_μ are the beam correction factors which takes into account the non-uniformity of the shear stress $\sigma_{(xz)}$ and couple stress μ_{xy}, respectively. Eq. 4.41 yields the dynamical equilibrium equations as follows

$$\begin{cases} EI\left(\frac{d^2\phi}{dx^2}\right) + k_sGA\left(\frac{du_z}{dx} - \phi\right) + k_\mu GAl^2\left(\frac{d^3u_z}{dx^3} + \frac{d^2\phi}{dx^2}\right) + m = \rho I\frac{\partial^2\phi}{\partial t^2} \\ k_sGA\left(\frac{d^2u_z}{dx^2} - \frac{d\phi}{dx}\right) - k_\mu GAl^2\left(\frac{d^4u_z}{dx^4} + \frac{d^3\phi}{dx^3}\right) + q = \rho A\frac{\partial^2 u_z}{\partial t^2} \end{cases} \tag{4.42}$$

with the following initial conditions

$$u_z(x,0) = u_i, \quad \frac{\partial u_z(x,0)}{\partial t} = \dot{u}_i, \quad \phi(x,0) = \phi_i, \quad \frac{\partial\phi(x,0)}{\partial t} = \dot{\phi}_i \tag{4.43}$$

The corresponding natural and essential boundary conditions are

$$\begin{aligned} M_\phi = 0 \;\; or \;\; \delta\phi = 0 \\ Q = 0 \;\; or \;\; \delta u_z = 0 \\ M_\theta = 0 \;\; or \;\; \delta\frac{du_z}{dx} = 0 \end{aligned} \tag{4.44}$$

where the moments and transverse force are elaborated as:

$$\begin{aligned} M_\phi &= EI\left(\frac{d\phi}{dx}\right) + k_\mu GAl^2\left(\frac{d^2u_z}{dx^2} + \frac{d\phi}{dx}\right) \\ Q &= k_sGA\left(\frac{du_z}{dx} - \phi\right) - k_\mu GAl^2\left(\frac{d^3u_z}{dx^3} + \frac{d^2\phi}{dx^2}\right) \\ M_\theta &= k_\mu GAl^2\left(\frac{d^2u_z}{dx^2} + \frac{d\phi}{dx}\right) \end{aligned} \tag{4.45}$$

In the classical Timoshenko beam theory $u_z(x)$ and $\phi(x)$ are the kinematic primary variables, but as one can observe in Eq. 4.44 in the size-dependent couple stress Timoshenko theory, $\theta = du_z(x)/dx$ becomes

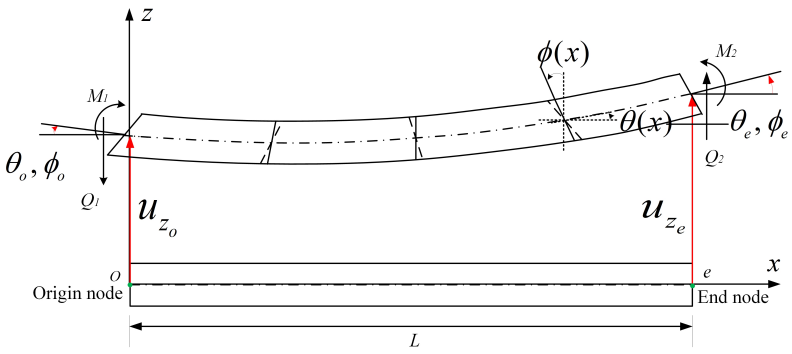

Figure 4.3 Beam element subjected to concentrated bending moments at the ends with general boundary conditions.

a primary variable, too. Besides, it can be concluded that the displacement DOF u_z is energetically conjugate to the transverse force Q, while the slopes θ and ϕ are primary variables with their conjugate bending moments M_θ and, M_ϕ, respectively. The total bending moment is the sum of moments M_θ and M_ϕ.

In what follows, three different solutions to the general form of the consistent couple stress Timoshenko beam under a concentrated load at nodal points are presented. These solutions are the exact solution, the two primary variables (2PV) approximation, and Ritz approximation; they are employed to find the solutions for the deflection and rotation vectors and the stiffness and mass matrices of the beam. It should be mentioned that while the aim of the present study is the static analysis, the general equilibrium equations, that is dynamic, are derived from being used in future studies.

4.2.2 Exact Solution

According to Eq.(45), the total bending moment M becomes,

$$M = M_\theta + M_\phi = \left(EI + 2k_\mu GAl^2\right)\frac{d\phi}{dx} + 2k_\mu GAl^2\frac{d^2u_z}{dx^2} \tag{4.46}$$

Consider next an element of the beam with length L, subjected to the concentrated bending moments M_1 and M_2 and concentrated shear forces Q_1 and Q_2 at node o (at $x = 0$) and node e (at $x = L$), as shown in Fig. 4.3. In the absence of the distributed load and considering the beam in a static condition, based on Eq. 4.19 and Eq. 4.20, it can be concluded that the shear force is constant and the bending moment varies linearly along the length of the beam as follows

$$M = \left(EI + 2k_\mu GAl^2\right)\frac{d\phi}{dx} + 2k_\mu GAl^2\frac{d^2u_z}{dx^2} = -M_1\left(1 - \frac{x}{L}\right) + M_2\left(\frac{x}{L}\right) \tag{4.47}$$

$$Q = GA\left(k_s\frac{du_z}{dx} - k_\mu l^2\frac{d^3u_z}{dx^3}\right) - GA\left(k_s\phi + k_\mu l^2\frac{d^2\phi}{dx^2}\right) = -\frac{M_1 + M_2}{L} \tag{4.48}$$

Using Eq. 4.44, the general form of the boundary conditions are

$$\begin{aligned} x=0: \quad & u_z = u_{zo}, \quad \phi = \phi_o, \quad \theta = \frac{du_z}{dx} = \theta_o \\ x=L: \quad & u_z = u_{ze}, \quad \phi = \phi_e, \quad \theta = \frac{du_z}{dx} = \theta_e \end{aligned} \tag{4.49}$$

Integrating Eq. 4.47 and applying the boundary conditions of $du_z(x)/dx = \theta_o$ and $\phi = \phi_o$ at $x = 0$, yields

$$\left(EI + 2k_\mu GAl^2\right)(\phi - \phi_o) + 2k_\mu GAl^2\left(\frac{du_z}{dx} - \theta_o\right) = -M_1\left(x - \frac{x^2}{2L}\right) + M_2\left(\frac{x^2}{2L}\right) \tag{4.50}$$

Eq. 4.50 can be rewritten as

$$\frac{du_z}{dx} = -\left(EI + 2k_\mu GAl^2\right)(\phi - \phi_o) + \theta_o - \frac{M_1\left(x - \frac{x^2}{2L}\right) - M_2\left(\frac{x^2}{2L}\right)}{2k_\mu GAl^2} \tag{4.51}$$

Substituting Eq. 4.47 and Eq. 4.48 in Eq. 4.20 results in

$$\left(EI + 2k_\mu GAl^2\right)\frac{d^2\phi}{dx^2} + 2k_\mu GAl^2\frac{d^3u_z}{dx^3} - \frac{M_1 + M_2}{L} = 0 \tag{4.52}$$

Inserting Eq. 4.50 in Eq. 4.51, the following second order linear differential equation for the rotation ϕ can be derived

$$\begin{aligned} \left(EI + 4k_\mu GAl^2\right)\phi - \frac{k_\mu l^2}{k_s}EI\frac{d^2\phi}{dx^2} = \left(EI + 2k_\mu GAl^2\right)\phi_o + \frac{k_\mu l^2}{k_s}\left(\frac{M_1 + M_2}{L}\right) \\ + 2k_\mu GAl^2\theta_o - M_1\left(x - \frac{x^2}{2L}\right) + M_2\left(\frac{x^2}{2L}\right) \end{aligned} \tag{4.53}$$

Using the boundary conditions $\phi = \phi_o$ and $\phi = \phi_e$ at $x = 0$ and $x = L$, respectively, the solution of BVP of Eq. 4.53 writes

$$\begin{aligned} \phi(x) = (\phi_o - C_0)\frac{sinh\lambda(L-x)}{sinh\lambda L} + \frac{1}{sinh\lambda L}\left(\phi_e - C_0 - \frac{a_4}{(a_1+2a_3)}L - \frac{a_5}{(a_1+2a_3)}\right)sinh\lambda x \\ + C_0 + \frac{a_4}{(a_1+2a_3)}x + \frac{a_5}{(a_1+2a_3)}x^2 \end{aligned} \tag{4.54}$$

with the following constants therein

$$a_1 = EI, \quad a_2 = -\frac{k_\mu}{k_s}l^2, \qquad a_3 = 2k_\mu GAl^2, \quad a_4 = -M_1, \qquad a_5 = \frac{M_1 + M_2}{2L}$$

$$b_0 = (a_1 + a_3)\phi_o - 2a_2a_5 + a_3\theta_o, \qquad C_0 = \frac{b_0}{a_1 + 2a_3} - \frac{2a_1a_2a_5}{(a_1+2a_3)^2}, \qquad \lambda = \sqrt{\frac{-(a_1+2a_3)}{a_1a_2}}$$

Substituting the rotation field $\phi(x)$ from Eq. 4.54 into Eq. 4.51 gives

$$\begin{aligned} \frac{du_z}{dx} = d_0\left[(\phi_o - C_0)\frac{sinh\lambda(L-x)}{sinh\lambda L} + \frac{1}{sinh\lambda L}\left(\phi_e - C_0 - \frac{a_4}{(a_1+2a_3)}L - \frac{a_5}{(a_1+2a_3)}\right)sinh\lambda x\right. \\ \left. + C_0 + \frac{a_4}{(a_1+2a_3)}x + \frac{a_5}{(a_1+2a_3)}x^2\right] - d_0\phi_o + \theta_o + \frac{a_4}{a_3}x + \frac{a_5}{a_3}x^2 \end{aligned} \tag{4.55}$$

where

$$d_0 = -\frac{(a_1 + a_3)}{a_3}$$

Integrating Eq. 4.55, and using the boundary condition $u_z = u_{z_o}$ at $x = 0$ results in

$$\begin{aligned} u_z(x) = d_0 \left[\frac{(\phi_o - C_0)}{-\lambda} \frac{cosh\lambda(L-x)}{sinh\lambda L} + \frac{1}{\lambda sinh\lambda L} \left(\phi_e - C_0 - \frac{a_4}{(a_1+2a_3)} L - \frac{a_5}{(a_1+2a_3)} L^2 \right) cosh\lambda x \right] \\ + \left(\frac{-4(a_1+a_3)a_2a_5}{(a_1+2a_3)^2} + \frac{(a_1+a_3)}{(a_1+2a_3)} \phi_o + \frac{a_3}{(a_1+2a_3)} \theta_o \right) x + \frac{a_4}{2(a_1+2a_3)} x^2 + \frac{a_5}{3(a_1+2a_3)} x^3 + A_1 \end{aligned} \tag{4.56}$$

where

$$A_1 = u_{z_o} - d_0 \left[-\frac{(\phi_o - C_0)}{\lambda} coth\lambda L + \frac{\phi_e - C_0 - \frac{a_4}{(a_1+2a_3)} L - \frac{a_5}{(a_1+2a_3)} L^2}{\lambda sinh\lambda L} \right]$$

Using the two remaining boundary conditions of $u_z = u_{z_e}$ and $\theta = \theta_e$ at $x = L$, the coefficients a_4 and a_5 which are related to the moments M_1 and M_2 are obtained as

$$\begin{aligned} a_4 = & \left(\begin{array}{l} \left(\frac{-1}{L^2} \left(a_3(\theta_e - \theta_o - d_0(\phi_e - \phi_o)) \left(-\frac{2d_0a_1a_2L}{(a_1+2a_3)^2} + \frac{L^3}{3(a_1+2a_3)} - \frac{2d_0a_2L}{(a_1+2a_3)} \right. \right. \right. \\ \left. \left. \left. + \frac{d_0(-1+\cosh(\lambda L)) \left(\frac{4a_2}{(a_1+2a_3)} + \frac{4a_1a_2}{(a_1+2a_3)^2} - \frac{L^2}{(a_1+2a_3)} \right)}{\lambda \sinh(\lambda L)} \right) \right) - \theta_o L - u_{z_o} \\ + u_{z_e} - \frac{d_0(-1+\cosh(\lambda L)) \left(\phi_e + \phi_o - \frac{2(a_1+a_3)\phi_o}{(a_1+2a_3)} - \frac{2a_3\theta_o}{(a_1+2a_3)} \right)}{\lambda \sinh(\lambda L)} \\ \left. + \frac{(a_1+a_3)L\phi_o}{(a_1+2a_3)} + \frac{a_3L\theta_o}{(a_1+2a_3)} - \phi_o L \right) \end{array} \right) \\ & \left(\frac{L^2}{6(a_1+2a_3)} + \left(1 - \frac{2(-1+\cosh(\lambda L))}{L\lambda \sinh(\lambda L)} \right) \left(\frac{2d_0a_2}{(a_1+2a_3)} + \frac{2d_0a_1a_2}{(a_1+2a_3)^2} \right) \right) \\ a_5 = & \frac{a_3(\theta_e - \theta_o - d_0(\phi_e - \phi_o))}{L^2} - \frac{a_4}{L} \end{aligned}$$

By substituting the coefficients a_4 and a_5 in Eq.(54) and Eq.(56), the shape functions that satisfy the dynamical equilibrium equations of Eq.(42) can be calculated. These shape functions lead to a two-node (3PV/node) Timoshenko beam bending element. The unknown primary variables can be expressed in terms of the shape functions $\boldsymbol{N}_i$ $(i = u_z,\ \phi)$ and the node variables $\boldsymbol{\Delta}(t)$ as

$$\left\{ \begin{array}{c} u_z \\ \phi \end{array} \right\} = \left[\begin{array}{c} \boldsymbol{N}_{u_z} \\ \boldsymbol{N}_{\phi} \end{array} \right] \boldsymbol{\Delta}(t) \tag{4.57}$$

where

$$\begin{aligned} \boldsymbol{\Delta}(t)^{\mathrm{T}} &= \{u_{z_o},\ \phi_o,\ \theta_o,\ u_{z_e},\ \phi_e,\ \theta_e\} \\ \boldsymbol{N}_{u_z} &= [U_1\ U_2\ U_3\ U_4\ U_5\ U_6] \\ \boldsymbol{N}_{\phi} &= [U_7\ U_8\ U_9\ U_{10}\ U_{11}\ U_{12}] \end{aligned}$$

The elements of matrices $\boldsymbol{N}_{u_z}$ and $\boldsymbol{N}_{\phi}$ are given in Appendix J. The finite element representation of the equations of motion are obtained by substituting the displacement distributions, Eq. 4.57, into the extended Hamilton's principle, Eq. 4.34, and integrating over the beam length; those equations write in matrix form

$$\boldsymbol{M}\ddot{\boldsymbol{\Delta}} + \boldsymbol{K}\boldsymbol{\Delta} = \boldsymbol{F} \tag{4.58}$$

where the stiffness and mass matrices are successively given by

$$\boldsymbol{K} = \int_0^L \begin{bmatrix} \frac{\partial \boldsymbol{N}_\phi}{\partial x} \\ \frac{\partial \boldsymbol{N}_{u_z}}{\partial x} - \boldsymbol{N}_\phi \\ \frac{\partial^2 \boldsymbol{N}_{u_z}}{\partial x^2} + \frac{\partial \boldsymbol{N}_\phi}{\partial x} \end{bmatrix}^{\mathrm{T}} \begin{bmatrix} EI & 0 & 0 \\ 0 & k_s GA & 0 \\ 0 & 0 & k_\mu GAl^2 \end{bmatrix} \begin{bmatrix} \frac{\partial \boldsymbol{N}_\phi}{\partial x} \\ \frac{\partial \boldsymbol{N}_{u_z}}{\partial x} - \boldsymbol{N}_\phi \\ \frac{\partial^2 \boldsymbol{N}_{u_z}}{\partial x^2} + \frac{\partial \boldsymbol{N}_\phi}{\partial x} \end{bmatrix} dx \tag{4.59}$$

$$\boldsymbol{M} = \int_0^L \begin{bmatrix} \boldsymbol{N}_{u_z} \\ \boldsymbol{N}_\phi \end{bmatrix}^{\mathrm{T}} \begin{bmatrix} \rho A & 0 \\ 0 & \rho I \end{bmatrix} \begin{bmatrix} \boldsymbol{N}_{u_z} \\ \boldsymbol{N}_\phi \end{bmatrix} dx \tag{4.60}$$

$$\boldsymbol{F} = \int_0^L \begin{bmatrix} \boldsymbol{N}_{u_z} \\ \boldsymbol{N}_\phi \end{bmatrix}^{\mathrm{T}} \begin{Bmatrix} q \\ m \end{Bmatrix} dx \tag{4.61}$$

As observed from the above expressions, the shape functions have polynomial and hyperbolic components in x. So, calculating the stiffness and mass matrices using the exact shape functions requires a substantial computational effort. For this reason, a simple and still accurate approximate solution for the consistent couple stress Timoshenko beam is sought. To this end, two approximations will be made: first, taking the beam as a (2PV/node) Timoshenko beam using the C-CST (section 4.2.3); secondly, finding the approximation of the shape functions using the Ritz method utilizing the C-CST (section 4.2.4).

4.2.3 Two Primary Variable consistent couple stress Timoshenko Beam

In section 4.2.1, it was observed that in the size-dependent couple stress Timoshenko theory, the rotation $\theta = du_z/dx$ was one of the primary variables. As the next step, in order to reduce the number of primary variables from three to two, namely $u_z(x)$ and $\phi(x)$, the contribution of the moment M_θ in the total moment M is disregarded, i.e. $M \approx M_\phi$.

It is known from the classical Timoshenko beam theory that the equilibrium equations are satisfied by taking functions $u_z(x)$ and $\phi(x)$ as cubic and quadratic polynomials, respectively [214]. Hence, accordingly, it is assumed that $u_z(x)$ and $\phi(x)$ have the following forms

$$u_z(x) = C_1 + C_2 x + C_3 x^2 + C_4 x^3 \tag{4.62}$$

$$\phi(x) = C_5 + C_6 x + C_7 x^2 \tag{4.63}$$

where C_i $(i = 1, ..., 7)$ are unknown constants that can be determined by using the following boundary conditions,

$$\begin{aligned} x = 0: &\quad u_z = u_{z_o}, \quad \phi = \phi_o \\ x = L: &\quad u_z = u_{z_e}, \quad \phi = \phi_e \end{aligned} \tag{4.64}$$

By substituting Eq. 4.62 and Eq. 4.63 in the first relation of Eq. 4.42, the unknown coefficients can be found:

$$EI(2C_7) + k_s GA\left[\left(C_2 + 2C_3 x + 3C_4 x^2\right) - \left(C_5 + C_6 x + C_7 x^2\right)\right] + k_\mu GAl^2(6C_4 + 2C_7) = 0$$

By setting coefficients of x^i $(i = 0,\ 1,\ 2)$ equal to zero we have

$$\begin{cases} x^0 : 2EIC_7 + k_sGA(C_2 - \phi_o) + k_\mu GAl^2(6C_4 + 2C_7) = 0 & (4.65) \\ x^1 : k_sGA(2C_3 - C_6) = 0 \ \rightarrow \ C_6 = 2C_3 & (4.66) \\ x^2 : k_sGA(3C_4 - C_7) = 0 \ \rightarrow \ C_7 = 3C_4 & (4.67) \end{cases}$$

and from the second relation of Eq. 4.42, we get:

$$k_sGA(2C_3 + 6C_4x) - (C_6 + 2C_7x) = 0$$

which leads to Eq. 4.66 and Eq. 4.67.

After some simple calculations, $u_{z_e}(x)$ and $\phi(x)$ take the following form

$$u_z(x) = u_{z_o} + C_2x + C_3x^2 + C_4x^3 \tag{4.68}$$

$$\phi(x) = \phi_o + 2C_3x + 3C_4x^2 \tag{4.69}$$

where

$$C_2 = \frac{k_sGAL^3\phi_o + \left(12k_\mu GAl^2L + 6EIL\right)(\phi_o - \phi_e) + \left(24k_\mu GAl^2 + 12EI\right)(u_{z_e} - u_{z_o})}{L\left(k_sGAL^2 + 24k_\mu GAl^2 + 12EI\right)}$$

$$C_3 = -\frac{\left(2k_sAGL^2 + 12k_\mu AGl^2 + 6EI\right)\phi_o + \left(k_sAGL^2 - 12k_\mu AGl^2 - 6EI\right)\phi_e + 3k_sAGL(u_{z_o} - u_{z_e})}{L\left(k_sGAL^2 + 24k_\mu GAl^2 + 12EI\right)}$$

$$C_4 = \frac{k_sGA(L\phi_o + L\phi_e + 2u_{z_o} - 2u_{z_e})}{L\left(k_sGAL^2 + 24k_\mu GAl^2 + 12EI\right)}$$

From Eq. 4.68 and Eq. 4.69, the shape functions can be calculated, which leads to a two-node (2PV/node) Timoshenko bending element. The unknown variables can be expressed in terms of the shape functions $\boldsymbol{N}_{i(2PV)}$ $(i = u_z,\ \phi)$ and the node variables $\boldsymbol{\Delta}_{(2PV)}(t)$

$$\begin{Bmatrix} u_z \\ \phi \end{Bmatrix} = \begin{bmatrix} \boldsymbol{N}^{\mathrm{T}}_{u_z(2PV)} \\ \boldsymbol{N}^{\mathrm{T}}_{\phi(2PV)} \end{bmatrix} \boldsymbol{\Delta}_{(2PV)}(t) \tag{4.70}$$

where

$$\boldsymbol{\Delta}^{\mathrm{T}}_{(2PV)} = \{u_{z_o},\ \phi_o,\ u_{z_e},\ \phi_e\}$$

and

$$\boldsymbol{N}^{\mathrm{T}}_{u_z(2PV)} = \begin{bmatrix} \frac{1}{(1+\alpha+\beta)}\left\{2\left(\frac{x}{L}\right)^3 - 3\left(\frac{x}{L}\right)^2 - (\alpha+\beta)\left(\frac{x}{L}\right) + (1+\alpha+\beta)\right\} \\ \frac{L}{(1+\alpha+\beta)}\left\{\left(\frac{x}{L}\right)^3 - \left(2+\frac{\alpha+\beta}{2}\right)\left(\frac{x}{L}\right)^2 + \left(1+\frac{\alpha+\beta}{2}\right)\left(\frac{x}{L}\right)\right\} \\ \frac{1}{(1+\alpha+\beta)}\left\{-2\left(\frac{x}{L}\right)^3 + 3\left(\frac{x}{L}\right)^2 + (\alpha+\beta)\left(\frac{x}{L}\right)\right\} \\ \frac{L}{(1+\alpha+\beta)}\left\{\left(\frac{x}{L}\right)^3 - \left(1-\frac{\alpha+\beta}{2}\right)\left(\frac{x}{L}\right)^2 - \frac{\alpha+\beta}{2}\left(\frac{x}{L}\right)\right\} \end{bmatrix} \tag{4.71}$$

$$\boldsymbol{N}^{\mathrm{T}}_{u_z(2PV)} = \begin{bmatrix} \frac{1}{(1+\alpha+\beta)}\left\{2\left(\frac{x}{L}\right)^3 - 3\left(\frac{x}{L}\right)^2 - (\alpha+\beta)\left(\frac{x}{L}\right) + (1+\alpha+\beta)\right\} \\ \frac{L}{(1+\alpha+\beta)}\left\{\left(\frac{x}{L}\right)^3 - \left(2+\frac{\alpha+\beta}{2}\right)\left(\frac{x}{L}\right)^2 + \left(1+\frac{\alpha+\beta}{2}\right)\left(\frac{x}{L}\right)\right\} \\ \frac{1}{(1+\alpha+\beta)}\left\{-2\left(\frac{x}{L}\right)^3 + 3\left(\frac{x}{L}\right)^2 + (\alpha+\beta)\left(\frac{x}{L}\right)\right\} \\ \frac{L}{(1+\alpha+\beta)}\left\{\left(\frac{x}{L}\right)^3 - \left(1-\frac{\alpha+\beta}{2}\right)\left(\frac{x}{L}\right)^2 - \frac{\alpha+\beta}{2}\left(\frac{x}{L}\right)\right\} \end{bmatrix} \tag{4.72}$$

where

$$\alpha = \frac{12EI}{k_s AGL^2}$$
$$\beta = \frac{24k_\mu l^2}{k_s L^2}$$

The stiffness matrix can be found by substituting the shape functions of Eq.(71) and Eq.(72) into Eq.(59) and integrating over the beam length

$$\boldsymbol{K}_{(2PV)} = \begin{bmatrix} K_{11} & K_{12} & K_{13} & K_{14} \\ & K_{22} & K_{23} & K_{24} \\ & & K_{33} & K_{34} \\ sym & & & K_{44} \end{bmatrix} \tag{4.73}$$

where

$$K_{11} = \frac{12\left[2k_\mu AGl^2(2+\beta) + EI(1+\alpha+2\beta)\right]}{L^3(1+\alpha+\beta)^2}$$
$$K_{12} = \frac{6\left[2k_\mu AGl^2(2+\beta) + EI(1+\alpha+2\beta)\right]}{L^2(1+\alpha+\beta)^2}$$
$$K_{22} = \frac{k_\mu AGl^2\left(16+14\beta+4\beta^2+8\alpha^2\right) + EI\left(4+12\beta+5\beta^2+5\alpha+\alpha^2\right)}{L(1+\alpha+\beta)^2}$$
$$K_{24} = -\frac{k_\mu AGl^2\left(-8+2\beta+4\beta^2+8\alpha^2\right) + EI\left(-2+5\beta^2-\alpha+\alpha^2\right)}{L(1+\alpha+\beta)^2}$$
$$K_{33} = K_{11} = -K_{13}, \quad K_{34} = K_{23} = -K_{12} = -K_{14}, \quad K_{44} = K_{22}$$

Substituting the shape functions of Eq. 4.71 and Eq. 4.72 into Eq. 4.60 and integrating over the beam length gives the mass matrix,

$$\boldsymbol{M}_{(2PV)} = \boldsymbol{M}_{\rho A(2PV)} + \boldsymbol{M}_{\rho I(2PV)} \tag{4.74}$$

where $\boldsymbol{M}_{\rho A(2PV)}$ and $\boldsymbol{M}_{\rho I(2PV)}$ are the mass matrices corresponding to the translational and rotary inertia, respectively,

$$\boldsymbol{M}_{\rho A(2PV)} = \gamma_1 \begin{bmatrix} 4\left(78+147(\alpha+\beta)+70(\alpha+\beta)^2\right) & L\left(44+77(\alpha+\beta)+35(\alpha+\beta)^2\right) & 4\left(27+63(\alpha+\beta)+35(\alpha+\beta)^2\right) & -L\left(26+63(\alpha+\beta)+35(\alpha+\beta)^2\right) \\ & L^2\left(8+14(\alpha+\beta)+7(\alpha+\beta)^2\right) & L\left(26+63(\alpha+\beta)+35(\alpha+\beta)^2\right) & -L^2\left(6+14(\alpha+\beta)+7(\alpha+\beta)^2\right) \\ & & 4\left(78+147(\alpha+\beta)+70(\alpha+\beta)^2\right) & -L\left(44+77(\alpha+\beta)+35(\alpha+\beta)^2\right) \\ sym & & & L^2\left(8+14(\alpha+\beta)+7(\alpha+\beta)^2\right) \end{bmatrix} \tag{4.75}$$

$$\boldsymbol{M}_{\rho I(2PV)} = \gamma_2 \begin{bmatrix} \frac{180}{L^2} & -\frac{3(5(\alpha+\beta)-1)}{L} & -\frac{180}{L^2} & -\frac{3(5(\alpha+\beta)-1)}{L} \\ & 10(\alpha+\beta)^2+5(\alpha+\beta)+4 & \frac{3(5(\alpha+\beta)-1)}{L} & 5(\alpha+\beta)^2-5(\alpha+\beta)-1 \\ & & \frac{180}{L^2} & \frac{3(5(\alpha+\beta)-1)}{L} \\ sym & & & 10(\alpha+\beta)^2+5(\alpha+\beta)+4 \end{bmatrix} \tag{4.76}$$

where

$$\gamma_1 = \frac{\rho AL}{840(1+\alpha+\beta)^2}, \quad \gamma_2 = \frac{\rho IL}{30(1+\alpha+\beta)^2}$$

4.2.4 Ritz approximation for the consistent couple stress Timoshenko beam

In Ritz method, one searches for an approximate solution $u_z(x)$, and $\phi(x)$, to the problem as a finite linear combination of admissible functions as [215]

$$u_z(x) \approx \sum_{s=1}^{N} b_{s_u} \psi_{s_u}(x) + \psi_{0_u}(x) \tag{4.77}$$

$$\phi(x) \approx \sum_{s=1}^{N} b_{s_\phi} \psi_{s_\phi}(x) + \psi_{0_\phi}(x) \tag{4.78}$$

in which $\psi_{0_u}(x)$ and $\psi_{0_\phi}(x)$ must satisfy the nonhomogeneous essential boundary conditions of Eq. 4.49.

Furthermore, $\psi_{s_u}(x)$ and $\psi_{s_\phi}(x)$ must satisfy the homogenous essential boundary conditions related to u_z and ϕ, respectively. To this end, $\psi_{0_u}(x)$ and $\psi_{0_\phi}(x)$ should have the following form

$$\psi_{0_u}(x) = \left(\frac{2u_{z_o} - 2u_{z_e}}{L^3} + \frac{\theta_o + \theta_e}{L^2}\right)x^3 + \left(-\frac{3}{2}\frac{\theta_o + \theta_e}{L} - \frac{3u_{z_o} - 3u_{z_e}}{L^2} - \frac{1}{2}\frac{\theta_o - \theta_e}{L}\right)x^2 + \theta_o x + u_{z_o} \tag{4.79}$$

$$\psi_{0_\phi}(x) = \phi_o - \frac{x(\phi_o - \phi_e)}{L} \tag{4.80}$$

As for $\psi_{s_u}(x)$ and $\psi_{s_\phi}(x)$, previous functions are approximated by polynomial series as

$$\psi_{s_u}(x) = x^{1+r}(x-L)^{1+q}, \qquad r, q = 1,\ 2,\ \ldots \tag{4.81}$$

$$\psi_{s_\phi}(x) = x^{r}(x-L)^{q}, \qquad r, q = 1,\ 2,\ \ldots \tag{4.82}$$

Taking only the first three terms of $\psi_{s_u}(x)$ and $\psi_{s_\phi}(x)$,, and substituting them along with Eq. 4.79 and Eq. 4.80 into Eq. 4.77 and Eq. 4.78 leads to

$$\begin{aligned} u_z(x) = {} & b_{1u}x^2(x-L)^2 + b_{2u}x^3(x-L)^2 + b_{3u}x^2(x-L)^3 + b_{4u}x^3(x-L)^3 \\ & + \left(\frac{2u_{z_o} - 2u_{z_e}}{L^3} + \frac{\theta_o + \theta_e}{L^2}\right)x^3 + \left(-\frac{3}{2}\frac{\theta_o + \theta_e}{L} - \frac{3u_{z_o} - 3u_{z_e}}{L^2} - \frac{1}{2}\frac{\theta_o - \theta_e}{L}\right)x^2 + \theta_o x + u_{z_o} \end{aligned} \tag{4.83}$$

$$\phi(x) = x^1(x-L)^1 b_{1\phi} + x^2(x-L)^1 b_{2\phi} + x^1(x-L)^2 b_{3\phi} + x^2(x-L)^2 b_{4\phi} + \phi_o - \frac{x(\phi_o - \phi_e)}{L} \tag{4.84}$$

Upon substitution of the approximate solutions of Eq. 4.83 and Eq. 4.84 in Eq. 4.41, it can be concluded that the variation of the Lagrangian function is a function of parameters b_{s_u} and b_{s_ϕ} $(s = 1,\ 2,\ 3,\ 4)$. After integrating over the beam length, the coefficients b_{s_u} and b_{s_ϕ} are determined such that the coefficients of the variations δb_{s_u} and δb_{s_ϕ} vanish; this leads to N linearly independent equations for the unknowns b_{s_u} and b_{s_ϕ}. Now taking the first three terms of each series, functions $u_z(x)$ and $\phi(x)$ become

$$\begin{aligned} u_z(x) = {} & u_{z_o} + x^3\left(\frac{2u_{z_o} - 2u_{z_e}}{L^3} + \frac{\theta_o + \theta_e}{L^2}\right) + \theta_o x - x^2\left(\frac{3\theta_o + 3\theta_e}{2L} + \frac{3w_o - 3w_e}{L^2} + \frac{\theta_o - \theta_e}{2L}\right) \\ & + \frac{x^3(L-x)^2\chi_1}{\xi_1} - \frac{x^2(L-x)^2\chi_2}{\xi_2} \end{aligned} \tag{4.85}$$

where

$$\xi_1 = L^5\left(60 + 280\beta + 56\alpha + 105\beta^2 + 210\alpha\beta\right)$$

$$\xi_2 = L^4\left(4\alpha + 8\beta + 7\alpha\beta\right)\left(60 + 280\beta + 56\alpha + 105\beta^2 + 210\alpha\beta\right)$$

$$\chi_1 = 252\left[2(\alpha+\beta)(u_{z_o} - u_{z_e}) + L(\alpha+\beta+1)(\theta_o + \theta_e) - L(\phi_o + \phi_e)\right]$$

$$\chi_2 = \begin{bmatrix} 36\left(28\alpha^2+49\alpha^2\beta+56\beta^2+50\alpha\beta^2+84\alpha\beta\right)\left(u_{z_o}-u_{z_e}\right)+L\left(\phi_e-\phi_o\right)\left(392\alpha^2+1960\beta^2+735\beta^3+1470\alpha^2\beta+2205\alpha\beta^2\right) \\ +L\theta_o\left(896\alpha^2+2352\alpha^2\beta+2968\beta^2+924\alpha+735\beta^3+1428\beta+3087\alpha\beta^2+4746\alpha\beta\right)-42L\phi_o\left(22\alpha+34\beta+77\alpha\beta\right) \\ +L\theta_e\left(112\alpha^2-588\alpha^2\beta-952\beta^2+84\alpha-735\beta^3+588\beta-1323\alpha\beta^2+42\alpha\beta\right)-42L\phi_o\left(2\alpha+14\beta-35\alpha\beta\right) \end{bmatrix}$$

and

$$\phi(x) = \phi_o - \frac{\left(\phi_o-\phi_e\right)x}{L} + \frac{(28\beta)\left(\phi_o-\phi_e-\theta_o+\theta_e\right)x^2\left(L-x\right)}{L^3\left(8\beta+4\alpha+7\alpha\beta\right)} - \frac{x\left(L-x\right)\chi_3}{\xi_3} \tag{4.86}$$

where

$$\xi_3 = L^3\left(4\alpha+8\beta+7\alpha\beta\right)\ \left(60+280\beta+56\alpha+105\beta^2+210\alpha\beta\right)$$

$$\chi_3 = \begin{bmatrix} 6\left(240\alpha-735\alpha\beta^3+1792\beta^2-840\beta^3+480\beta+1148\alpha\beta^2+1316\alpha\beta\right)\left(u_{z_o}-u_{z_e}\right)+3L\left(\theta_o+\theta_e\right)\left(16\alpha-735\alpha\beta^3\right) \\ +1470L\beta^3\left(\phi_o-\phi_e\right)+672L\alpha\left(\phi_o+\phi_e\right)-L\theta_o\left(3584\beta^2+3990\beta^3+744\beta+3906\alpha\beta^2+532\alpha\beta\right) \\ +L\phi_o\left(8960\beta^2+2184\beta+7350\alpha\beta^2+4480\alpha\beta\right)+L\phi_e\left(1120\beta^2+504\beta+1470\alpha\beta^2+2912\alpha\beta\right) \\ +L\theta_e\left(4256\beta^2-1050\beta^3+936\beta+1974\alpha\beta^2+1036\alpha\beta\right) \end{bmatrix}$$

The shape function coefficients can be calculated; they lead to a two-node (3PV/node) Timoshenko beam bending element. The unknown variables can be expressed in terms of the shape functions $\boldsymbol{N}_{i(Ritz)}\ \ (i=u_z,\ \phi)$ and the node variables $\boldsymbol{\Delta}_{(Ritz)}(t)$ as

$$\left\{ \begin{array}{c} u_z \\ \phi \end{array} \right\} = \left[\begin{array}{c} \boldsymbol{N}_{u_z(Ritz)} \\ \boldsymbol{N}_{\phi(Ritz)} \end{array} \right] \boldsymbol{\Delta}_{(Ritz)}(t) \tag{4.87}$$

where

$$\boldsymbol{\Delta}^{\mathrm{T}}_{(Ritz)} = \{u_{z_o},\ \phi_o,\ \theta_o, u_{z_e},\ \phi_e,\ \theta_e\}$$

Substituting the shape functions in Eq. 4.59 yields the stiffness matrix

$$\boldsymbol{K}_{(Ritz)} = \left[\begin{array}{cccccc} K'_{11} & K'_{12} & K'_{13} & K'_{14} & K'_{15} & K'_{16} \\ & K'_{22} & K'_{23} & K'_{24} & K'_{25} & K'_{26} \\ & & K'_{33} & K'_{34} & K'_{35} & K'_{36} \\ & & & K'_{44} & K'_{45} & K'_{46} \\ & sym & & & K'_{55} & K'_{56} \\ & & & & & K'_{66} \end{array} \right] \tag{4.88}$$

The elements of the stiffness matrix are given in the Appendix K. Inserting the shape functions in Eq. 4.60 results in the mass matrix, $\boldsymbol{M}_{(Ritz)}$ which includes two parts:

$$\boldsymbol{M}_{(Ritz)} = \boldsymbol{M}_{\rho A(Ritz)} + \boldsymbol{M}_{\rho I(Ritz)} \tag{4.89}$$

where $\boldsymbol{M}_{\rho A(Ritz)}$ and $\boldsymbol{M}_{\rho I(Ritz)}$ are the mass matrices corresponding to the translational and rotary inertia,

$$\boldsymbol{M}_{\rho A(Ritz)} = \left[\begin{array}{cccccc} M^{'\rho A}_{11} & M^{'\rho A}_{12} & M^{'\rho A}_{13} & M^{'\rho A}_{14} & M^{'\rho A}_{15} & M^{'\rho A}_{16} \\ & M^{'\rho A}_{22} & M^{'\rho A}_{23} & M^{'\rho A}_{24} & M^{'\rho A}_{25} & M^{'\rho A}_{26} \\ & & M^{'\rho A}_{33} & M^{'\rho A}_{34} & M^{'\rho A}_{35} & M^{'\rho A}_{36} \\ & & & M^{'\rho A}_{44} & M^{'\rho A}_{45} & M^{'\rho A}_{46} \\ & sym & & & M^{'\rho A}_{55} & M^{'\rho A}_{56} \\ & & & & & M^{'\rho A}_{66} \end{array} \right] \tag{4.90}$$

$$\boldsymbol{M}_{\rho I(Ritz)} = \begin{bmatrix} M_{11}^{'\rho I} & M_{12}^{'\rho I} & M_{13}^{'\rho I} & M_{14}^{'\rho I} & M_{15}^{'\rho I} & M_{16}^{'\rho I} \\ & M_{22}^{'\rho I} & M_{23}^{'\rho I} & M_{24}^{'\rho I} & M_{25}^{'\rho I} & M_{26}^{'\rho I} \\ & & M_{33}^{'\rho I} & M_{34}^{'\rho I} & M_{35}^{'\rho I} & M_{36}^{'\rho I} \\ & & & M_{44}^{'\rho I} & M_{45}^{'\rho I} & M_{46}^{'\rho I} \\ & sym & & & M_{55}^{'\rho I} & M_{56}^{'\rho I} \\ & & & & & M_{66}^{'\rho I} \end{bmatrix} \tag{4.91}$$

4.3 Case studies

A beam of length L, and a circular cross-section of diameter 'd' is shown in Fig. 4.1. Since the present study will be served as a benchmark for a future research and will be compared with the result of the experimental study and simulation data for bone structure provided in [216], the length to diameter ratio of $L/d = 5$ is adopted. It is also assumed that the beam is made of Epoxy with the following material properties [217]:

$$E = 1.44\ GPa, \qquad G = 521.7\ MPa, \qquad l = 17.6\ \mu m$$

The beam correction factors are taken unity as a matter of simplicity $k_s = k_\mu = 1$ (these factors will take values close to unity depending on the specific shape of the beam cross-section).

4.3.1 Verification of C-CST and comparison with other size-dependent beam theories

In order to compare and validate the result of C-CST, the size-dependent static behavior of cantilever Timoshenko beam under a concentrated force p at its extremity using C-CST is investigated and compared with the predictions of CST [200], MCST [210], classical Timoshenko, and a homogenized micropolar continuum [57]. It was mentioned that the micropolar theory includes less restrictive assumptions in comparison to the couple stress theory, so its results can be used as a benchmark for comparing predictions of different couple stress theories. We consider a beam including repetitive periodic microstructure of a square lattice, with geometric and base modulus chosen to comply with previous values of the homogenized unit cell properties given in the introduction of this section. Relying on the results obtained in Table 1 in reference [57], and considering the above-mentioned homogenous properties for the beam, we derive by solving the inverse homogenization problem the values of modulus $E_s = 1.6916\ GPa$, and aspect ratio $\eta_b = 0.08512$, for the base material of the square lattice. Utilizing Eq. 4.14 and Eq. 4.15, results from Table 4.1 in [57], and noticing that γ is micropolar modulus, the length scale parameter of the micropolar theory l_c, for the above-mentioned beam will be evaluated as follows

$$\gamma = 8\eta = 8G_h l^2 = 8 \times 521.7 \times (17.6)^2 \times 10^{-6} = 1.2928\ N$$
$$l_c = \frac{1}{2}\sqrt{\frac{\gamma}{G_h}} = 24.89\ \mu m$$

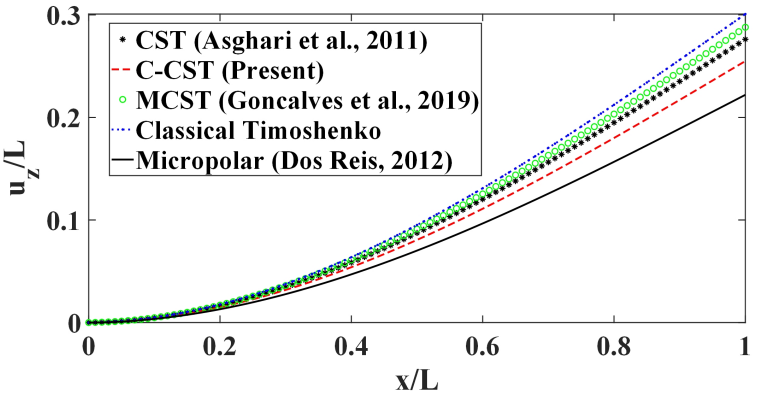

Figure 4.4 Comparison of dimensionless deflection of a fully clamped cantilever beam under a concentrated shear force.

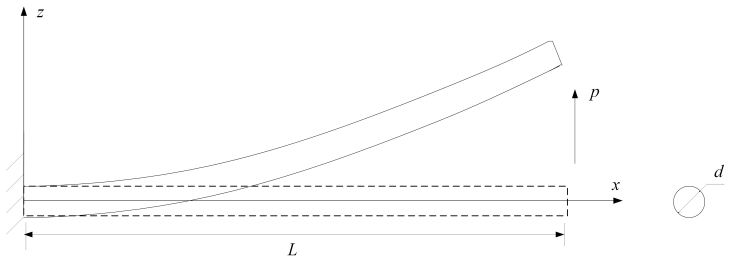

Figure 4.5 Cantilever beam under a shear force at the tip

The comparison of the beam deflection based on micropolar theory and the classical Timoshenko beam model shows a stiffer behavior (higher bending rigidity) for micropolar theory, reducing tip deformation by 36.11% compared to the classical beam theory. An increase in tip vertical displacement of the beam in the MCST, CST, and C-CST compared to the micropolar theory by 30.32%, 24.98%, and 15.38%, is obtained respectively; this entails that C-CST provides a better description of the beam response compared to the other couple stress theories. In comparison to CST and MCST, C-CST yields deflection closer to that obtained from the micropolar theory. The only advantage of MCST over CST is the reduction in the required number of independent material constants for linear isotropic elastic materials from 4 to 3. These results further show that the assumption underlying the C-CST (skew-symmetricity of the couple-stress tensor) is correct.

4.3.2 Fully clamped cantilever beam

A cantilever beam subjected to a concentrated transverse force p on its free end is depicted in Fig. 4.5. The force is assumed to be proportional to the beam length ($p = aL$), where 'a' is a constant. This assumption leads to a constant deflection of the beam in classical Timoshenko theory.

The boundary conditions at the clamped and free ends are as follows

$$\begin{aligned} x = 0: \quad & u_z(x) = 0, \quad \phi(x) = 0, \quad \theta(x) = 0 \\ x = L: \quad & Q(x) = p, \quad M_\theta(x) = 0, \quad M_\phi(x) = 0 \end{aligned} \tag{4.92}$$

The exact solution of this case study follows from the general solutions, Eq. 4.54 and Eq. 4.56,

$$\phi(x) = \frac{p}{(a_1 + 2a_3)}\left(Lx - \frac{x^2}{2}\right) + 2a_2 p \frac{a_1 + a_3}{(a_1 + 2a_3)^2}\left(1 - \frac{\cosh(\lambda(L-x))}{cosh(\lambda L)}\right) \tag{4.93}$$

$$u_z(x) = \frac{p}{a_1 + 2a_3}\left(\frac{Lx^2}{2} - \frac{x^3}{6}\right) - \frac{2a_2 p}{a_3}\frac{(a_1 + a_3)^2}{(a_1 + 2a_3)^2}\left(x - \frac{\tanh(\lambda L)}{\lambda} + \frac{\sinh(\lambda(L-x))}{\lambda cosh(\lambda L)}\right) \tag{4.94}$$

Note that Eq. 4.93 and Eq. 4.94 are identical with those calculated in [213].

The approximate solution with the 2PV method can be obtained from the stiffness matrix of Eq. 4.73 and the boundary conditions of Eq. 4.92. Consequently, the master stiffness equations for this case study are

$$\begin{bmatrix} K_{11} & K_{12} & K_{13} & K_{14} \\ & K_{22} & K_{23} & K_{24} \\ & & K_{33} & K_{34} \\ sym & & & K_{44} \end{bmatrix} \begin{Bmatrix} u_{z_o} = 0 \\ \phi_o = 0 \\ u_{z_e} \\ \phi_e \end{Bmatrix} = \begin{Bmatrix} f_1 \\ f_2 \\ p \\ 0 \end{Bmatrix} \tag{4.95}$$

in which f_1 and f_2 are the unknown mechanical reactions, and the known force and displacements have been marked. Because the prescribed displacements are zero, the reduced system is simply

$$\begin{Bmatrix} u_{z_e} \\ \phi_e \end{Bmatrix} = \begin{bmatrix} K_{33} & K_{34} \\ K_{34} & K_{44} \end{bmatrix}^{-1} \begin{Bmatrix} p \\ 0 \end{Bmatrix} \tag{4.96}$$

which can be solved using MATLAB. By substituting u_{z_e} and ϕ_e from Eq. 4.96 into Eq. 4.68 and Eq. 4.69, the 2PV approximate solution for the kinematic variables $u_z(x)$ and $\phi(x)$ of the cantilever beam under a concentrated shear force at its tip can be determined.

Using the same procedure and utilizing the stiffness matrix of Eq. 4.88 and boundary conditions in Eq. 4.91, the Ritz approximate solution of $u_z(x)$ and $\phi(x)$ for the cantilever beam is calculated. Fig. 4.6(a) provides a comparison of the deflections of the cantilever beam under a concentrated shear force at the free end based on the exact solution for C-CST, Ritz approximate solution, 2PV approximation, and classical Timoshenko beams. In Table 4.2, for the sake of comparison, the error of the tip deflection for the approximate and classical solutions are compared with the exact one. Setting the criterion of acceptable discrepancy at 1%, it can be concluded that the consistent couple stress Timoshenko model, which is stiffer than the classical one, for beams with a dimensionless length of less than $L/l = 240$, is unable to predict the beam's response accurately when L/l lies in this range. Also, the obtained results show that the Ritz approximation and the 2PV approximation solutions lead to relatively more minor discrepancies in comparison with the exact solution.

Fig. 4.6(b) shows the rotation of the free end for this beam based on the C-CST solutions and Classical Timoshenko solution. Similar to the deflection diagram, the classical Timoshenko predictions are not

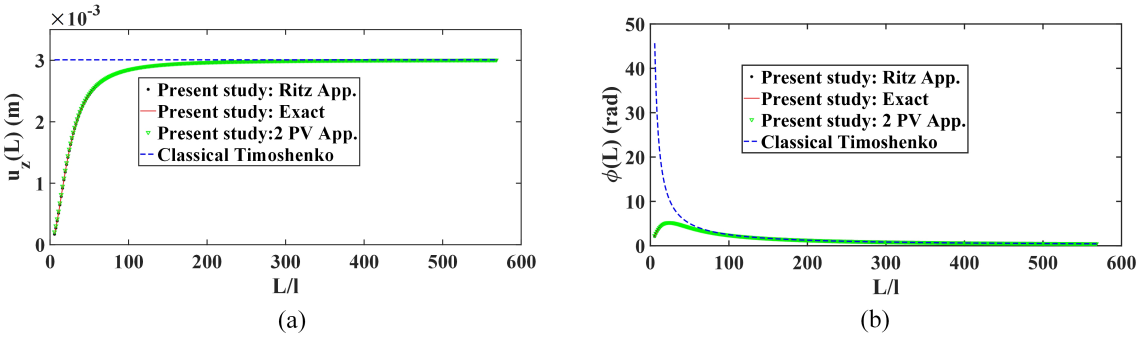

Figure 4.6 Tip deflection of a Fully clamped cantilever beam under a concentrated shear force: (a) tip deflection, (b) tip rotation.

accurate for beams with a dimensionless length of less than about $L/l = 240$. The amount of rotation predicted by this theory is much more significant than the exact solution calculated using the C-CST in this range.

Table 4.2 Error of the tip deflection: fully clamped cantilever beam under a concentrated shear force at free end.

$\frac{L}{l}$	Percentage Error (%)		
	Ritz	2PV	Classical Timoshenko
10	0.1063	7.1421	564.17
100	0.063335	0.13423	5.8158
241	0.073093	0.028522	1.0064
400	0.076191	0.012397	0.36736
500	0.07716	0.008736	0.23546

For a cantilever beam with a length of $L = 0.001$ m (which is equivalent to the dimensionless length of $L/l = 56.8$) there is about 18% relative difference between the tip deflection and rotation in C-CST and classical models, deciphered from Fig. 4.7(a) and Fig. 4.7(b).

4.3.3 Inflexurable couple stress theory $l \to \infty$

From Eq. 4.15, when the internal length becomes very large, so when $l \to \infty$, this entails that $\eta \to \infty$. According to the last term of Eq. 4.18 and the fact that the energy density is finite, it can be concluded that when $l \to \infty$, the curvature of the beam should vanish, $\kappa \to \infty$. This means that under these circumstances, the beam is rigid concerning curvature deformations.

For the cantilever beam studied in section 4.3.2, a sensitivity analysis of the deflection and engineering curvature versus the length scale parameter has been performed and shown in Fig. 4.8(a) and Fig. 4.8(b).

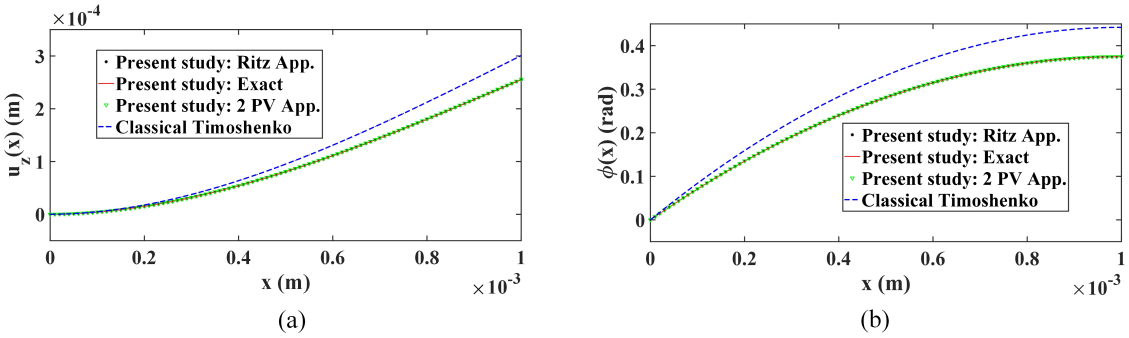

Figure 4.7 Fully clamped cantilever beam under a concentrated shear force: (a) deflection at $L = 0.001$ m, (b) rotation at $L = 0.001$ m.

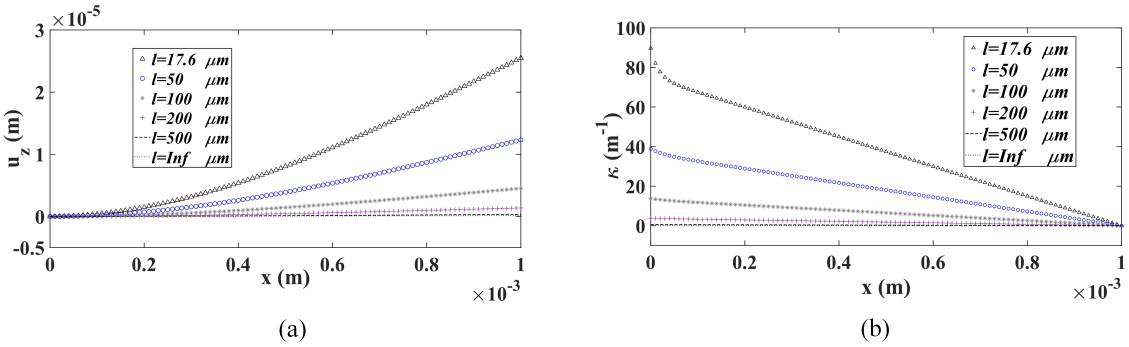

Figure 4.8 Effect of the length scale parameter of a fully clamped cantilever beam under a concentrated shear force: (a) on the deflection, (b) on the microcurvature. $L = 0.001$ m

In the case $l \to \infty$ the exact solution of the C-CST is,

$$\lim_{l\to\infty} u_z(x) = \frac{p}{4k_sGA}\left(x - \frac{\tanh(\lambda_\infty L)}{\lambda_\infty} + \frac{\sinh(\lambda_\infty(L-x))}{\lambda_\infty cosh(\lambda_\infty L)}\right)$$
$$\lim_{l\to\infty} \phi(x) = \frac{-p}{4k_sGA}\left(1 - + \frac{\cosh(\lambda_\infty(L-x))}{cosh(\lambda_\infty L)}\right)$$
$$\kappa_{xy} = -\kappa_z = \frac{1}{4}\left(\frac{d^2u_z}{dx^2} + \frac{d\phi}{dx}\right) = 0$$

where

$$\lambda_\infty = 2\sqrt{\frac{GAk_s}{EI}}$$

Fig. 4.8(a) shows a reduced deflection as the internal length parameter increases, while the microcurvature becomes negligible for high enough values of l (Fig. 4.8(b)).

4.3.4 Free-free beam

In the next example, a free-free beam subjected to concentrated bending moments M_0 at the free ends, Fig. 4.9(a), is considered. This case is equivalent to a fully clamped beam with a length of $L/2$ subjected to a bending moment M_0 at its free end, Fig. 4.9(b).

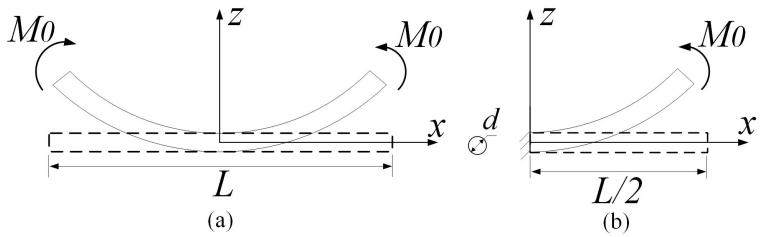

Figure 4.9 (a) Pure bending of a free-free beam with length L, (b) Pure bending of a fully clamped cantilever beam with length $L/2$.

It is assumed that M_0 is proportional to the squared length ($M_0 = bL^2$), where 'b' is a constant; this assumption leads to a constant deflection of the beam in the classical Timoshenko theory. The boundary conditions at the clamped and free ends are as follows:

$$\begin{aligned} x = 0: &\quad u_z(x) = 0, \quad \phi(x) = 0, \quad \theta(x) = 0 \\ x = L: &\quad Q(x) = 0, \quad M_\theta(x) + M_\phi(x) = \mathrm{M}_0 \end{aligned} \tag{4.97}$$

The exact solution to this case study thus follows from the general solutions of Eq. 4.54 and Eq. 4.56, as

$$\phi(x) = \frac{-M_0 sinh(\lambda x)}{\lambda cosh(\lambda L/2)(a_1 + 2a_3)} + \frac{M_0 x}{(a_1 + 2a_3)} \tag{4.98}$$

$$u_z(x) = -\frac{(a_1 + a_3)}{a_3}\left(\frac{-M_0 \cosh(\lambda x)}{\lambda^2 \cosh\left(\frac{\lambda L}{2}\right)(a_1 + 2a_3)} + \frac{M_0 x^2}{2(a_1 + 2a_3)}\right) + \frac{M_0 x^2}{2a_3} - \frac{M_0(a_1 + a_3)}{a_3 \lambda^2 \cosh\left(\frac{\lambda L}{2}\right)(a_1 + 2a_3)} \tag{4.99}$$

Note that the rotation $\phi(x)$ for this case study is different from $\phi(x)$ which is calculated in [213]. It seems that in the mentioned study only the particular part of the solution is taken into the account. Substituting Eq. 4.98 and Eq. 4.99 into the natural boundary conditions of Eq. 4.44, gives the contribution of the external bending moment in the moments of M_θ and M_ϕ

$$\begin{aligned} M_\theta|_{x=L/2} &= \frac{a_3}{2}\left(\frac{d^2 u_z}{dx^2} + \frac{d\phi}{dx}\right) = \frac{M_0}{2} \\ M_\phi|_{x=L/2} &= a_1\left(\frac{d\phi}{dx}\right) + \frac{a_3}{2}\left(\frac{d^2 u_z}{dx^2} + \frac{d\phi}{dx}\right) = \frac{M_0}{2} \end{aligned} \tag{4.100}$$

Using the same method as in section 4.3.2, the Ritz and 2PV approximation solutions can be obtained from their stiffness matrices.

Fig. 4.10(a) and Fig. 4.10(b), respectively, represent the deflection and rotation of the free end calculated by the classical Timoshenko beam theory, the C-CST exact solution, the 2PV approximation, and Ritz approximation. From these figures and the accompanying data provided in Table 4.3, it is apparent that the classical Timoshenko beam theory loses its accuracy for beams having a dimensionless length $L/2l > 180$. Recall that the internal length is defined in expression 4.23. Within the range $L/2l > 284$, the maximum discrepancy between the approximate solutions of Ritz and the 2PV and the exact solution

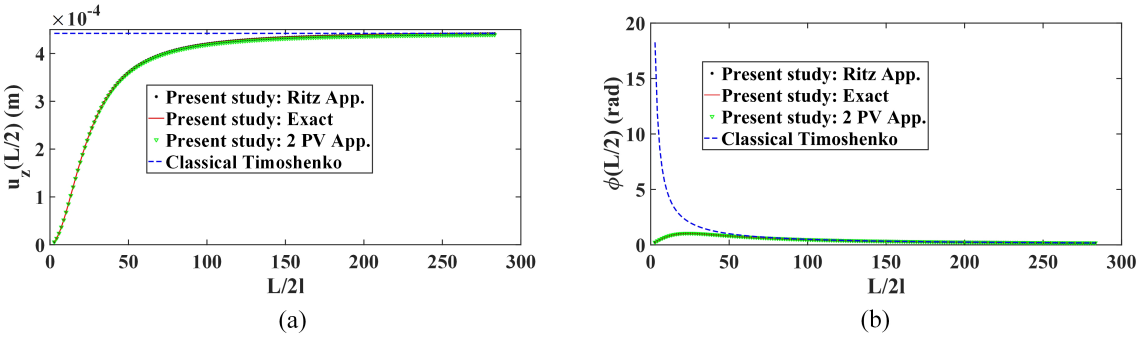

Figure 4.10 Free-free beam under pure bending: (a) tip deflection, (b) rotation.

take low values, respectively 0.136% and 0.68%. For the studied cantilever beam under a pure bending moment and concentrated shear force, based on the 1% discrepancy criterion, the acceptable dimensionless length is 360 and 240, respectively. It can be concluded that when the beam is subjected to a pure bending moment, the classical Timoshenko theory is still accurate for a large range of dimensionless lengths.

Table 4.3 Error of the tip deflection: fully clamped cantilever beam under pure bending at free end.

$\frac{L}{2l}$	Percentage Error (%)		
	Ritz	2PV	Classical Timoshenko
9	0.0240	0.3858	712.49
51	0.0.10736	0.62326	21.524
102	0.12841	0.66736	4.867
180	0.1342	0.6793	1.0976
280	0.13585	0.68281	0.051789

4.3.5 Partially clamped cantilever beam

In this example, a cantilever beam that is not fully clamped is considered (Fig. 4.4). The boundary conditions of this so-called partially clamped cantilever beam are as follows:

$$\begin{aligned} x=0: &\quad u_z=0, \quad \phi(x)=0, \quad M_\theta(x)=0 \\ x=L: &\quad Q(x)=p, \quad M_\theta(x)=0 \quad M_\phi(x)=0 \end{aligned} \tag{4.101}$$

The loading conditions are similar to the fully clamped ones. The exact solution can be calculated from Eq. 4.54 and Eq. 4.56 as,

$$\phi(x)=\frac{p}{(a_1+2a_3)}\left(Lx-\frac{x^2}{2}\right)-2a_3pL\frac{(\cosh(\lambda(L-x))-cosh(\lambda L))}{\lambda a_1(a_1+2a_3)sinh(\lambda L)} \tag{4.102}$$

$$\begin{aligned} u_z(x)=&\frac{p}{(a_1+2a_3)}\left(\frac{Lx^2}{2}-\frac{x^3}{6}\right)+\frac{2a_3pLx}{\lambda a_1(a_1+2a_3)tanh(\lambda L)} \\ &-\frac{2a_2(a_1+a_3)pL}{(a_1+2a_3)^2}\left(1-\frac{\sinh(\lambda(L-x))}{\sinh(\lambda L)}\right)-\frac{2a_2\left(3a_1a_3+2a_3^2+a_1^2\right)xp}{a_3(a_1+2a_3)^2} \end{aligned} \tag{4.103}$$

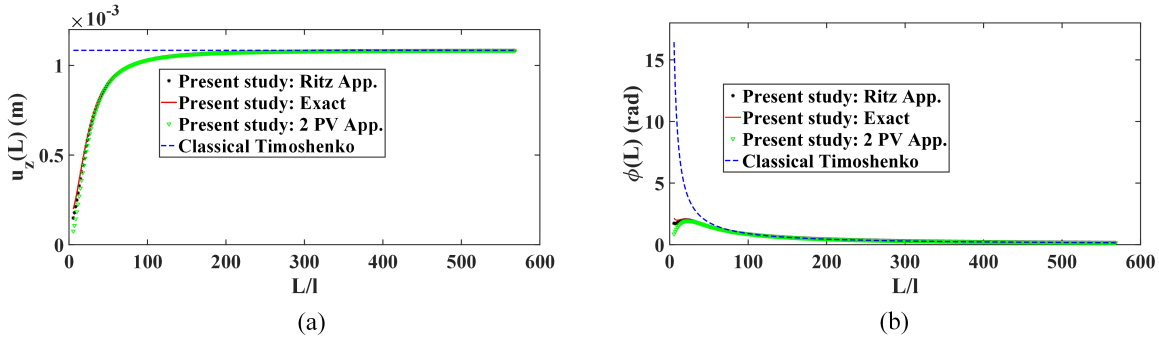

Figure 4.11 Partially clamped cantilever beam under a concentrated shear force: (a) tip deflection, (b) rotation.

It should be mentioned that Eq. 4.102 and Eq. 4.103 are the same as $\phi(x)$ and $u_z(x)$ in [213].

The 2PV approximate solution is analogous to the solution of the first case study. As for the Ritz approximate solution, the unknown nodal variables can be obtained from the stiffness matrix of Eq. 4.88 as

$$\begin{Bmatrix} \theta_o \\ u_{z_e} \\ \phi_e \\ \theta_e \end{Bmatrix} = \begin{bmatrix} K'_{33} & K'_{34} & K'_{35} & K'_{36} \\ & K'_{44} & K'_{45} & K'_{46} \\ & & K'_{55} & K'_{56} \\ Sym & & & K'_{66} \end{bmatrix}^{-1} \begin{Bmatrix} 0 \\ p \\ 0 \\ 0 \end{Bmatrix} \tag{4.104}$$

By substituting the amount of non-zero nodal variables in Eq. 4.85 and Eq. 4.86, an approximate solution of $u_z(x)$ and $\phi(x)$ can be calculated.

Table 4.4 Error of the tip deflection: partially clamped cantilever beam under a concentrated shear force at free end.

$\frac{L}{l}$	Percentage Error (%)		
	Ritz	2PV	Classical Timoshenko
10	13.704	36.417	275.74
100	0.15269	0.20586	6.2496
230	0.011882	0.013318	1.00
400	0.002353	0.002509	0.33262
500	0.001218	0.001282	0.21278

Fig. 4.11(a) and Fig. 4.11(b), respectively, illustrate the deflections and rotations of the partially clamped cantilever beam under a concentrated shear force at its free end calculated based on the exact solution of the C-CST, Ritz approximate solution, the 2PV approximation, and the classical Timoshenko beam model. From these figures and Table 4.4, it can be observed that the consistent couple stress Timoshenko beam model is stiffer than the classical one for beams with a dimensionless length less than 230; the classical model is unable to accurately predict the beam's response when the dimensionless beam length is in this range. Furthermore, the results show that the deviation of the 2PV and Ritz

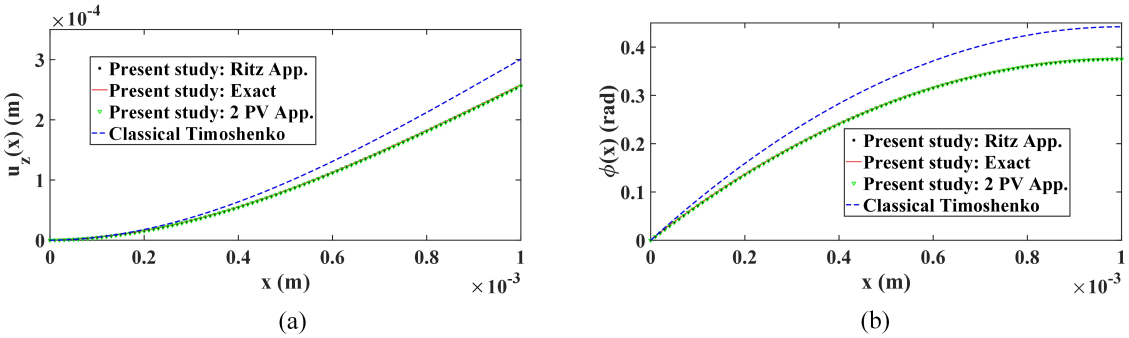

Figure 4.12 Partially clamped cantilever beam with $L = 0.001$ m under a concentrated shear force: (a) deflection, (b) rotation.

approximations from the exact solution is very small, and errors are close for beams with dimensionless length $L/l > 230$. For beams with dimensionless length $L/l > 230$, the error of the classical Timoshenko is less than one percent; hence, it can be concluded that when the dimensionless length is greater than 230, the classical Timoshenko beam theory can be used with acceptable accuracy.

As an example, for a cantilever beam with a length of $L = 0.001$ m (which is equivalent to the dimensionless length of $L/l = 56.8$) there is about 16.55% and 17.27% relative difference between the tip deflection and rotation in C-CST and classical models, respectively, as depicted in Fig. 4.12(a) and Fig. 4.12(b). Comparing Fig. 4.12 with Fig. 4.7 reveals that the classical Timoshenko theory produces the same result for fully and partially clamped beams. This is not surprising, in the classical Timoshenko beam model, the angular variable θ is not a primary variable; hence there is no control on it for either partially or fully clamped beams. Comparing the data from Table 4.2 and Table 4.4 reveals that the error of C-CST and classical Timoshenko models for the partially clamped beam is less than for the fully clamped beam. The results of Table 4.2 and Table 4.4 show that the approximate and exact solutions are in good agreement.

4.3.6 Material dependency of the domain of validity of C-CST

In the remainder of this section, the range of the ratio of beam length to the length scale for which the difference between the exact C-CST and classical Timoshenko deflections is about 1% is determined. For a broad range of mechanical properties (corresponding to different materials) listed in Table 4.5, covering more than four orders of magnitude, the effect of the beam properties on the outcome of the study is investigated. Cantilever beams subjected to either a concentrated shear force or a pure bending moment with the length scale parameter l varying in the range $0 \leq l \leq 400$ μm are assessed.

Fig. 4.13(a) and Fig. 4.13(b) show the variation of beam length versus the length scale for fully/partially clamped cantilever beams under a concentrated shear force and pure bending moment, respectively. These graphs are obtained for the range of beam lengths where classical Timoshenko theory and C-CST show less than 1% difference in deflection; this small percentage is selected as the limit of the domain of validity

Table 4.5 Elastic and Shear Moduli for various Materials [7].

Property \ Material	Aluminum Oxide (Al_2O_3)	Steel	Aluminum	Polystyrene (PS)	Epoxy	PTFE
Young's Modulus (GPa)	393	207	69	2.28	1.44	0.4
Shear Modulus (GPa)	161.1	83	25	0.8571	0.5217	0.137

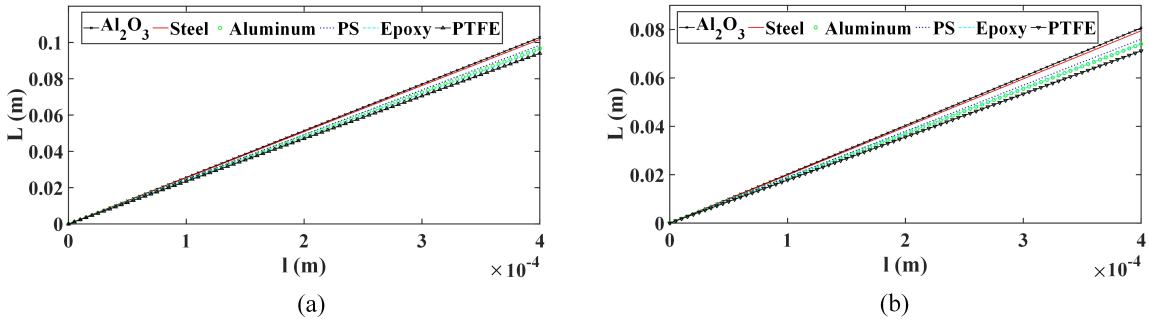

Figure 4.13 Concentrated shear force at the free end of: (a) a fully/partially clamped cantilever beam, (b) a free-free beam.

of classical Timoshenko beam theory. Fig. 4.13(a) and Fig. 4.13(b) show a linear relationship with slight changes in the slope, which is due to the variation of mechanical properties. It can be observed that at a constant length scale, as the material gets stiffer, namely moving from PTFE to Al_2O_3, the minimum length to achieve accurate results by classical Timoshenko beam increases.

4.4 Relevance of the C-CST based on a dimensionless length

In this section, the range of beam length to internal length ratio, L/l, for which the predictions of the classical Timoshenko model are not accurate enough and thus the consistent couple stress Timoshenko model should be used instead is assessed. For this purpose, the curves of deflection percentage error versus L/l for the case studies of section 4.3 are plotted in Fig. 4.14(a). For small enough values of the dimensionless length, here $L/l < 40$, as this ratio decreases the error increases exponentially. This entails that, for the epoxy beam under study, when the length is less than 40 times the internal length the C-CST should be employed instead of Timoshenko beam theory.

For a partially clamped cantilever beam, the variations of the deflection errors versus the dimensionless length for the materials of Table 4.5 are depicted in Fig. 4.14(b). It can be concluded that the application range of the consistent couple stress Timoshenko model hardly depends on the constituent material since all plots condense to a single master response. From Fig. 4.14(b), the range of L/l for which the classical Timoshenko theory is accurate enough can accordingly be extracted.

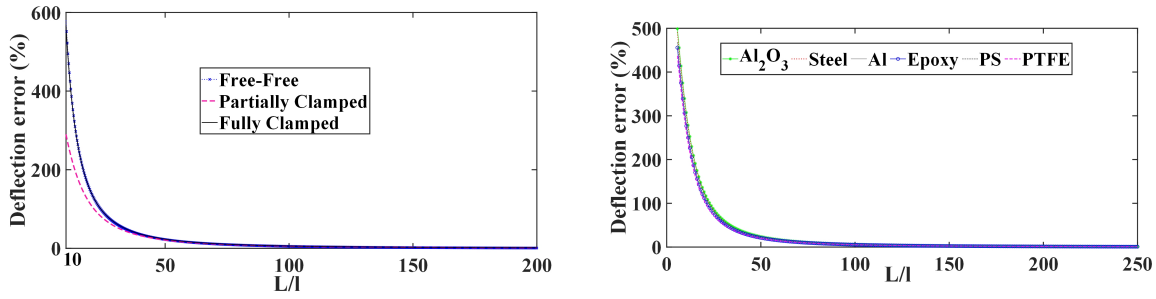

Figure 4.14 Variations of the deflection percentage error versus the dimensionless length for: (a) an Epoxy beam with different boundary conditions, (b) a partially clamped cantilever beam made of different materials.

4.5 Conclusion

For the first time, based on the consistent couple stress theory (C-CST), a general solution of a Timoshenko beam has been developed herewith. Using Hamilton's extended principle, the governing equations and the general form of the boundary conditions have been derived. The exact solution of the beam with general boundary conditions was then obtained. The deformation and rotation fields derived the exact shape functions, stiffness, and mass matrices of the two-node consistent couple stress Timoshenko beam. Due to these derivations' complexity and computational cost, Ritz's approximate solution and two primary variable (2PV) solutions were proposed. The following novel aspects have been proposed in this chapter.

- The 2PV approximation using only u_z and ϕ as the primary variables retained from the consistent couple stress Timoshenko beam theory leads to a significant decrease in the computational effort and a more simple formulation; in addition, it can incorporate the size effect properly into the formulation.
- In order to verify and assess the derived formulations, the deflection predicted by the different size-dependent beam models was compared to that computed by the complete micropolar theory, showing that C-CST provides the best approximation amongst all theories. Moreover, fully/partially clamped cantilever and free-free beams were studied to apply the proposed C-CST theory.
- While comparing the static solutions of the classical and consistent couple stress Timoshenko models, specific values of the dimensionless length were calculated as a criterion of validity of the classical method. The numerical results obtained from the 2PV method show relatively low error compared to the exact solutions over the entire beam length range.
- A criterion for deciding when the consistent couple stress Timoshenko beam model needs to be employed rather than its classical version has been proposed, involving a relation between beam length and internal length.

- The validity domain of the C-CST hardly depends on the beam's constituent material.

We have presented a phenomenological approach of couple stress media, starting from a reduced beam description. This approach implicitly assumes that the base material is endowed with some internal length scale intrinsic to the base material properties. However, this is a kind of 'black box approach' in the sense that no underlying microstructure responsible for such an additional internal parameter is introduced to support its existence. The developed consistent couple stress beam model could be applied in future works to the biomechanics of bone. Such a beam may represent either a single trabecula or a network of trabeculae within a (trabecular) bone. The following developments' objective is to recover additional such parameters from considering a periodic microstructure within the body, giving rise to an enhanced behavior when upscaling methods are employed. These enriched beam models could be used in future works to describe the size effects encountered in network materials.

Chapter 5

Continualization method towards homogenized Cosserat media and size effects in architected macro-beams under bending

Summary

The effective classical and higher-order mechanical properties of repetitive lattice materials are evaluated using Timoshenko beam models at a microlevel, and a continualization method towards a Cosserat effective substitution medium is applied. The proposed method combines a reduced number of degrees of freedom at a unit cell level with the continuous set of kinematic variables, representative of a Cosserat continuum at the macroscale. The effective classical and Cosserat moduli are obtained as closed-form expressions of the lattice microstructural and mechanical parameters for the specific case of honeycomb lattices. The proposed continualization method proves to be accurate and computationally efficient compared to fully resolved finite element simulations. One main hallmark of this chapter is the quantification of edge effects in the response of lattice structures, which are accounted for here by exploiting an effective macroscopic height and considering the micropolar contribution to the total bending moment. When the number of unit cells is high enough across the macrostructure height, the micropolar contribution to the total bending moment becomes negligible so that the classical Timoshenko macro beam model suffices to capture the bending behavior.

5.1 Introduction

Additively manufactured (AM in short) cellular materials gradually become an inseparable class of advanced materials. Cellular solids are widely used in various applications, from cores of sandwich panels in the aerospace, automotive, marine, and infrastructures, to medical devices and bio-implants. In sandwich panels, the separation of stiff and strong faces (for instance, fiber-reinforced composite laminates) by a lightweight and typically cellular core increases the moment of inertia of the panels with a slight increase in weight, making them efficient to resist against bending and buckling loads [218–220]. Lattice materials define a specific class of functional and structural materials with tunable mechanical and multiphysical properties that find increasing usage in engineering applications due to their wide span of properties that conventional materials cannot attain. A new paradigm entered the field of material science, bearing the name material design, sustained by the idea that the engineering properties of such lattice materials can be tuned by the sole modification of their inner topology and structure, independent of the choice of their base material [154]. This concept has led to a new class of artificial materials, named metamaterials [153] due to their distinctive properties far exceeding the range of properties that conventional and bulky materials can reach are devoid of such an engineered inner microstructure. Metamaterials with architected micro/meso structures usually rely on the periodic repetition of a unit cell , which is conceived to reach targeted static or dynamic properties. The notion of basic unit cell of the lattice here substitutes the atoms in conventional materials [159]. Lattice materials, as a category of cellular solids or porous materials with reticulated structures, often have a regular or quasi-periodic microstructure. This feature allows for the efficient design of structures with exceptional mechanical properties that modern additive manufacturing technologies can realize them from an excellent scale of a few nanometers [221].

The prediction of the effective properties of architected materials is an active field of research. Many theoretical models have been proposed to predict the effective properties of the unit cell with arbitrary topologies. When performing such analyses, two critical issues should be considered: Firstly, the appropriate choice of the continuum theory chosen for the substituted homogeneous medium depending on the inner lattice architecture and deformation mechanisms; secondly, the ability to evaluate the proper scaling of higher-order mechanical properties concerning suitable to microstructural parameters.

A distinction can be made between the continuous type homogenization methods traditionally employed for composite materials and the so-called discrete homogenization that employs reduced, discrete type models for the structural elements defining the unit cell as either a collection of bars or beams. Discrete homogenization is adequate for low-density lattice and architected materials since their inner structural elements can be naturally modeled as beams or rods at an affordable computational cost compared to continuous homogenization schemes.

These discrete modeling approaches have the advantage of considering a finite number of DOFs at the microscale and can sometimes provide closed-form expressions for the effective moduli [3, 58]. Amongst

the class of discrete homogenization methods, the so-called continualization methods introduced in [61] have deserved some particular interest in the literature since then.

On the side of continuous homogenization, a common strategy to compute higher-order moduli is to adopt suitable polynomial boundary conditions over the RVE as the minimum kinematic loading to capture conjugated higher-order macroscopic static variables; as followed in chapters 2 and 3.

Derivation of Cosserat effective moduli that are intrinsic to the microstructure and not depending on the size of the RVE remains a significant issue in the field of discrete or continuous homogenization. We propose a methodology to address this issue in the present chapter, recoursing to discrete homogenization of the lattice materials using the Timoshenko beam elements to describe their effective mechanical behavior as an effective micropolar continuum at the macro scale level. The articulation between the discrete formulation and the postulated effective Cosserat continuum is provided by the extended Hill macrohomogeneity condition, requiring a proper elaboration of the macroscopic (continuous) kinematic and static variables their discrete counterparts. The second novel aspect investigated in the present contribution is the analysis of edge effects, which play an essential role in the mechanical response of a macrodomain tessellated with a finite number of unit cells.

The outline of this chapter is as follows: a few general definitions related to the lattice description in terms of an irreducible unit cell and preliminary steps for the subsequent continualization towards an effective Cosserat continuum are introduced in section 5.2. The material description at both discrete and effective continuum levels is exposed in section 5.3, including the two nodes Timoshenko beam element model employed at the micro-level and the postulated Cosserat continuum at the macro-level. The general methodology underlying the proposed lattice continualization method deserves the developments of section 5.4, ending with the closed-form expression of the effective micropolar honeycomb properties. The validation of the computed homogenized properties from FE unit cell-based continuous simulation is conducted in section 5.5. Sensitivity analyses, size effects, and implementation of the Cosserat model into a macro beam bending problem are the subjects of section 5.7. We conclude in section 5.8 with a summary of the work and a few perspectives.

A few words regarding the employed notations are in order. The physical space is embedded with the Euclidean space and vectors and higher-order tensors are implicitly decomposed into an orthonormal basis of the underlying vector space. Vectors and higher-order tensors are denoted by boldface symbols. The gradient of a scalar or tensor field with respect to the position is denoted with the nabla operator and the position as a subscript, viz $\nabla_x \mathbf{E}(\mathbf{x})$, represents the gradient of the tensor field $\mathbf{E}(\mathbf{x})$ with respect to $\mathbf{x}$. The transpose of a tensor is written with a superscript notation, for instance $\mathbf{B}^T$. The gradient of a tensor field $\mathbf{A}(\mathbf{y})$ is denoted $\mathbf{A}(\mathbf{y}) \otimes \nabla_y$ ($\otimes$ represents the tensor product), and its divergence is obtained as the trace of the gradient, denoted $\mathbf{A}(\mathbf{y}).\nabla_y$. The dot product therein represents the internal product in the space of Cartesian tensors. The vector product of two arbitrary vectors $\mathbf{U}, \mathbf{V}$ is denoted as $(\mathbf{U} \times \mathbf{V})$, with components $(\mathbf{U} \times \mathbf{V})_i = \epsilon_{ijk} U_j V_k$. The vector product of a second-order tensor and a vector is the second-order tensor defined as $(A \times v)_{ij} = \epsilon_{jmk} A_{im} v_k$.

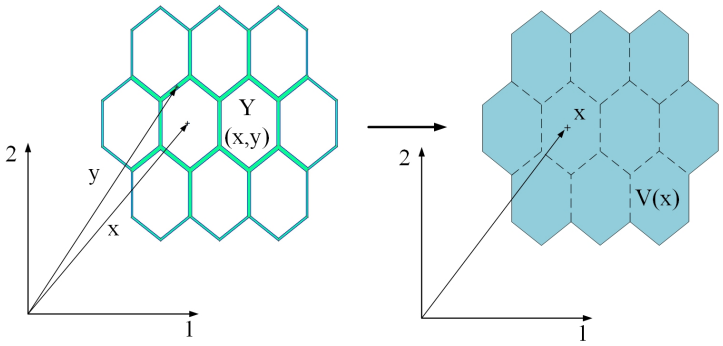

Figure 5.1 (left)Lattice material domain made of hexagon unit cell, (right) The homogeneous substitution medium (right) with domain $V(\boldsymbol{x})$ centered around point $\boldsymbol{x}$.

5.2 Homogenization of lattice materials towards generalized continua

Fig. 5.1 shows repetitive cellular material's heterogeneous periodic domain Y (x, y) of and its homogenized domain $V(x)$. In the homogenization theory, the period length is assumed to be very small compared to the dimensions of the overall domain. Hence the characteristic functions of these highly heterogeneous media will rapidly vary within a very small neighborhood of a point x. This fact inspires the consideration of two different scales of dependencies for all quantities: one on the macroscopic or global level x, which indicates slow variations, and the other on the microscopic or local level y, which describes rapid oscillations [4]. In the present context of periodic homogenization, the microstructure is identified within a representative unit cell, which generates the entire cellular composite domain by periodic translation. The unit cell domain consists of at least two phases or constituents with specific mechanical properties; in the context of lattice materials (Fig. 5.1), the second phase consists of air, for which the contrast of properties is infinite.

Point $\boldsymbol{x}$ on Fig. 5.1(left) represents the unit cells center of area in the cellular macrodomain; it is defined implicitly by following integral relation adopting a fixed Cartesian basis

$$\frac{1}{|Y|}\int_{Y}(\boldsymbol{y}-\boldsymbol{x})dV_y=\boldsymbol{0} \tag{5.1}$$

In Eq. 5.1, integration is performed over all micropoints labeled with the position vector $\boldsymbol{y}$ within the RVE. The relative position $(\boldsymbol{y}-\boldsymbol{x})$ of the micropoints has zero average over the volume Y. It should be noted that the definition presented in Eq. 5.1 could be simplified when the origin of coordinates is selected at the center of the area of the RVE, which further guarantees the objectivity of the virtual power of internal forces [126]. That will be our choice here and, in the sequel, the relative position vector coincides with the microscopic position.

RVEs and unit cells have become a popular means of multiscale modeling as modern physical science and engineering methodology. So, in the following brief, related definitions tied to unit cell description

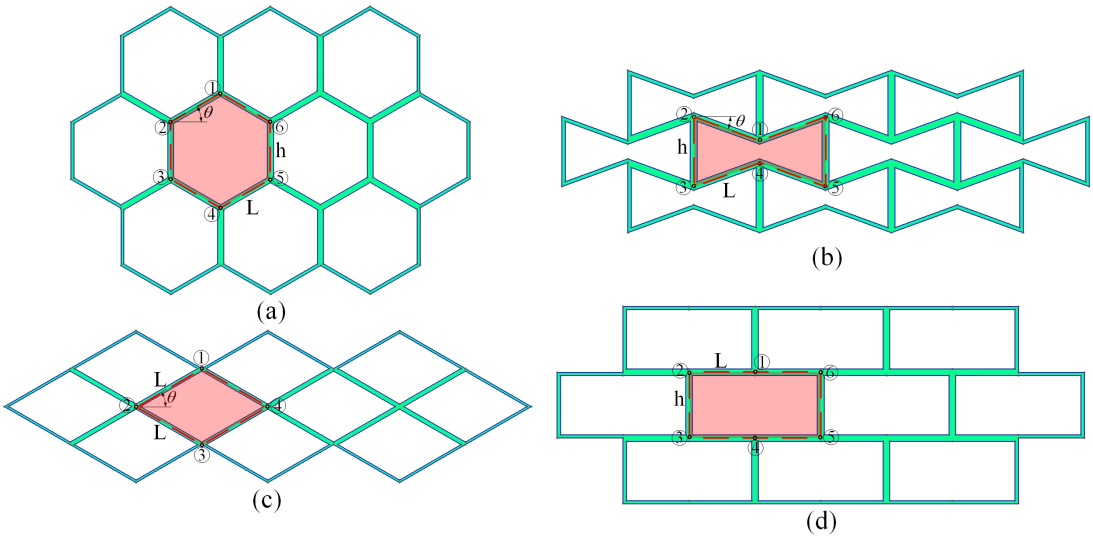

Figure 5.2 Schematic representation of periodic (a) Hexagonal ($\theta > 0$), (b) Re-entrant ($\theta < 0$), (c) Pantograph ($h = 0$), and (d) Rectangular $\theta = 0$ honeycombs; unit cell boundaries are indicated with dashed lines for each microarchitecture.

and modeling are presented. For the first time, Hill [180], has used the RVE term, defined as the smallest material volume element which its behavior in an average sense is the truthful behavior of the whole material. In the context of periodic cellular solids, the unit cell can easily be selected as an RVE, the duplication of which provides the material distribution over large scales (Fig. 5.2). Accordingly, in the present chapter, the unit cell is employed for the periodic structures under consideration.

In modeling the cellular materials using a periodic unit cell, the deformation of the unit cell under different types of loading at the boundary of the unit cell should be investigated. In homogenous material, constant stress and strain states stand under uniform loading, but this is not the case in cellular materials where a large percentage of its volume is filled with air. However, since the unit cell behavior is identical within the macrostructure, it should provide the same stress and strain fields. Thus, generally, the stress and strain fields are periodic, except in a narrow boundary layer close to the external boundary of a cellular domain where the (external) load is applied. These periodicity constraints are implemented into numerical schemes to determine the proper displacement constraint at the boundary of the unit cell.

In the context of the generalized continuum theory, the cellular materials can be modeled as a higher-order homogenous anisotropic medium with specified effective moduli, which characterize the homogenized lattice material response. Averaging the classical and higher-order stress and strain tensors over the volume of the unit cell leads to the definition of a macroscopically homogeneous medium containing the macro-stress and macro-strain fields. Using the Hill-Mandel macrohomogeneity condition, the equivalence between the initially heterogeneous and effective homogeneous medium is guaranteed, and the effective elastic properties are calculated.

In the next section, the unit cell struts of the lattice materials, Fig. 5.2, are discretized as Timoshenko beam elements with two nodes, and their mechanical properties are calculated [222]. These properties

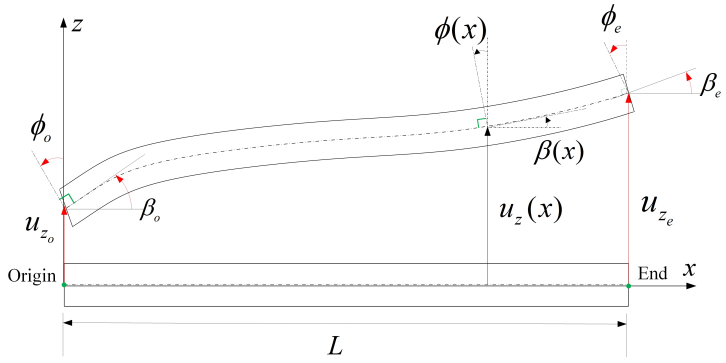

Figure 5.3 Beam element coordinates and displacements.

are subsequently used for the discrete homogenization approach introduced in the following sections.

5.3 Two-node Timoshenko beam element

As indicated in Fig. 5.2, each strut of the cellular material can be modeled as a beam element. Hence, a prismatic homogeneous isotropic beam element, including shear deformation and rotary inertia, is considered, as depicted in Fig. 5.3. The displacement functions $u_{y_1}(y_1)$ and $u_{y_2}(y_1)$ present the translation of the beam's neutral axis in the y_1 and y_2 direction, respectively; function $\phi(y_1)$ denotes the rotation of the cross-section at the mid-plane, and $\beta(y_1)$ is the slope of the central axis of the beam. The coordinates of the beam element along with displacements are shown in Fig. 5.3.

Next, considering the beam presented in Fig. 5.3 as a single element beam of length L with two nodes named 'o' (at $y_1 = 0$) and 'e' (at $y_1 = L$), the stiffness matrix of the Timoshenko beam is obtained as Eq. 5.2; wherein $\alpha = \frac{12E_sI}{k_sAG_sL^2}$is a dimensionless coefficient (chapter 4). E_s and G_s are the Young's and shear modulus of the beam. Also, k_s, I, and A are the beam shear correction factor, second moment of area, and area of the beam's cross-section, respectively. These expressions for the beam with rectangular cross-section are defined as follows:

$k_s = \frac{10(1+\nu_s)}{(12+11\nu_s)}, \quad I = \frac{1}{12}bt^3, \quad A = bt$

with t and b the thickness of the beam in y_2 and out-of-plane directions, respectively.

$$\boldsymbol{K} = \begin{bmatrix} \frac{E_sA}{L} & 0 & 0 & -\frac{E_sA}{L} & 0 & 0 \\ & \frac{12E_sI}{L^3(1+\alpha)} & \frac{6E_sI}{L^2(1+\alpha)} & 0 & -\frac{12E_sI}{L^3(1+\alpha)} & \frac{6E_sI}{L^2(1+\alpha)} \\ & & \frac{E_sI(4+\alpha)}{L(1+\alpha)} & 0 & -\frac{6E_sI}{L^2(1+\alpha)} & -\frac{E_sI(\alpha-2)}{L(1+\alpha)} \\ & & & \frac{E_sA}{L} & 0 & 0 \\ & sym & & & \frac{12E_sI}{L^3(1+\alpha)} & -\frac{6E_sI}{L^2(1+\alpha)} \\ & & & & & \frac{E_sI(4+\alpha)}{L(1+\alpha)} \end{bmatrix} \tag{5.2}$$

Discretizing the beam representing a strut that constitutes cellular materials, as a single two-node element leads to the deformation and rotation fields at nodes that coincide with the beam's analytical solution [223]. Moreover, it is well-known from FE methods that any loading can be replaced with equivalent loads

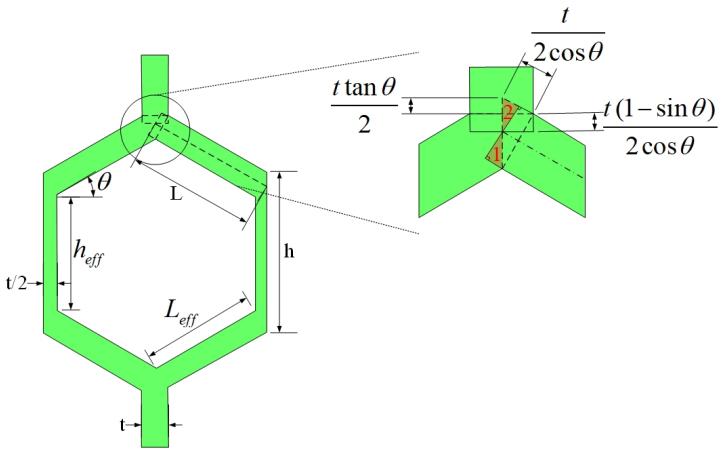

Figure 5.4 Effective lengths for the general periodic unit cell.

at nodes (chapter 4). Accordingly, discretizing struts of the unit cells in Fig. 5.2 as a single beam element produces the exact classical solution of the nodal deformation field that results in the effective in-plane properties of the unit cell. Before describing the homogenization method, some definitions related to unit cell effective lengths, discrete strain energy of the beam, and a summary of the Cosserat continuum theory (chapter 2) should be introduced.

5.3.1 The effective length of the beam

Discretizing the unit cell leads to an assembly of the beam elements described by their neutral axis. However, in the actual case of the lattice materials, struts have overlapped at the intersection points, implying the necessity of defining the effective length of the beam for calculations. Fig. 5.4 depicts the intersection of the beams in the honeycomb unit cell. Utilizing the similarity of triangles 1 and 2 and the geometrical relations shown in the magnified subset of Fig. 5.4, the effective lengths of struts are evaluated as:

$$h_{eff} = h - \frac{t(1-\sin\theta)}{\cos\theta} L_{eff} = L - \frac{t}{2\cos\theta} \tag{5.3}$$

herein, the angular parameter θ can take negative, zero, or positive values to build all the unit cells mentioned in Fig. 5.2. Here and in the sequel, the dimensionless variables are denoted with the '*' superscript symbol. The effective relative density for a honeycomb unit cell can be determined by subtracting the void area in 2D (volume in 3D) within the cell, evaluated in closed form as [224]:

$$\rho_f^* = \left(1 - \frac{V^{void}}{V^{cell}}\right) = \left(1 - \frac{L_{eff}\,(h_{eff} + L_{eff}\sin\theta)}{L\,(h + L\sin\theta)}\right) \tag{5.4}$$

Contour plots of the effective dimensionless tensile modulus modulus $\mathrm{E}_{x_1}^* = \mathrm{E}_{x_1}^{\mathrm{hom}}/\mathrm{E}_s$ and relative density using either the initial length parameters L and h or the effective lengths L_{eff} and h_{eff} shown in Fig. 5.5 reflect differences that become more significant as the relative density increases beyond 0.2. The importance of using these effective length parameters will be more apparent in subsequent developments of section 5.7.

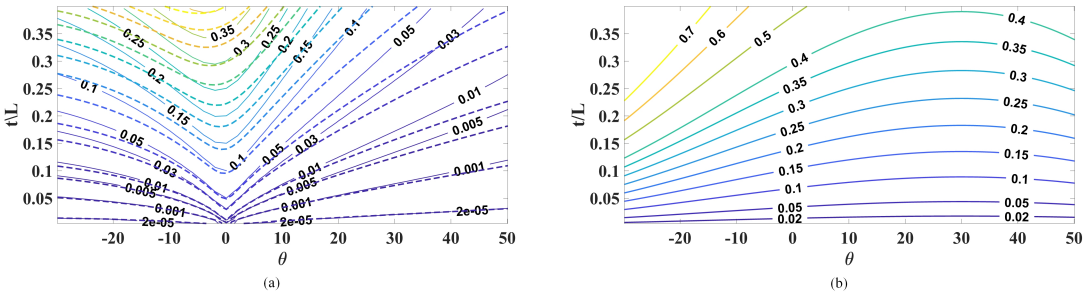

Figure 5.5 Contours of (a)$\mathrm{E}^*_{x_1}$, (b)ρ^*_f, versus θ and t/L; solid lines use L and h, and dotted lines use L_{eff} and h_{eff}.

5.3.2 Discrete expression of the beam energy

Following the general approach described in section 5.3, each strut of the unit cell is discretized as a two-node Timoshenko beam. The discrete energy expression of the unit cell will be computed using the summation of the beam's energy within the unit cell. The general expression of the internal deformation energy associated with the beam element under normal and shearing forces, and the bending moment, is obtained straightforwardly as (the reader can refer to [225] for a more detailed expression)

$$\begin{aligned} W = \tfrac{1}{2(1+\alpha)} \Big[\tfrac{E_s A}{L} (1+\alpha) \left(u_{y_{1_e}} - u_{y_{1_o}}\right)^2 + \tfrac{12 E_s I}{L^3} \left(u_{y_{2_e}} - u_{y_{2_o}}\right)^2 + \tfrac{12 E_s I \alpha}{L} (\phi_e - \phi_o)^2 \\ + \tfrac{4 E_s I}{L^2} \left(L(\phi_e + \phi_o)^2 - L\phi_e\phi_o - 3\left(\phi_e + \phi_o\right)\left(u_{y_{2_e}} - u_{y_{2_o}}\right) \right) \Big] \end{aligned} \tag{5.5}$$

The first term in Eq. 5.5 corresponds to the axial deformation due to the normal force, followed by two terms related to the vertical deformation and rotation of the beam element due to the shearing force and bending moment. The last term in Eq. 5.5 is the coupling of the bending and rotation terms. We next expose the Cosserat continuum formulation of the posited effective medium, the objective being to express the macroscopic displacement and rotation field versus the Cosserat continuous kinematic variables.

5.3.3 Summary of Cosserat continuum formulation

In Cosserat mechanics, the strain tensor e_{ij} is elaborated as the difference of the microscopic displacement gradient to the local microrotation at a given material point (chapter 2), viz

$$e_{ij} = \frac{\partial u_i}{\partial x_j} - \epsilon_{ijk}\phi_k, i = 1, 2, 3 \tag{5.6}$$

where the $\epsilon_{ijk}$is the Levi-Civita symbol, the total strain is not a symmetrical tensor. Its symmetrical part coincides with the linearized strain of Cauchy elasticity, whereas its skew-symmetric part includes a contribution from the microrotation. Cosserat theory also introduces micro curvature measures, elaborated as the spatial gradients of the micro-rotation vector $\boldsymbol{\phi}(\boldsymbol{y})$, which is defined in the index and tensor notation as:

$$\begin{aligned} \kappa_{ij} &= \frac{\partial \phi_i}{\partial y_j} \\ \boldsymbol{\kappa}(\boldsymbol{y}) &= \boldsymbol{\phi} \otimes \nabla_y \end{aligned} \tag{5.7}$$

Using Eq. 5.6 and Eq. 5.7, the second-order micropolar strain and the macro curvature tensors $\boldsymbol{E}(\boldsymbol{x})$ and $\mathbf{K}(\boldsymbol{x})$ can be defined, respectively:

$$\boldsymbol{E}(\boldsymbol{x}) : = \nabla_x \boldsymbol{U} - \epsilon \cdot \boldsymbol{\Phi}(\boldsymbol{x}) \tag{5.8}$$

$$\mathbf{K}\left(\boldsymbol{x}\right) : = \nabla_x \boldsymbol{\Phi}(\boldsymbol{x}) \tag{5.9}$$

wherein the following set of relations defines the averaged kinematic tensors:

$$\begin{aligned} &\boldsymbol{E}^{sym}(\boldsymbol{x}) := \tfrac{1}{2}\left(\boldsymbol{E}(\boldsymbol{x}) + \boldsymbol{E}^{T}(\boldsymbol{x})\right) \\ &\boldsymbol{E}^{Tskew}(\boldsymbol{x}) = skew(\boldsymbol{U} \otimes \nabla_x)^{skew} - \boldsymbol{\epsilon} \cdot \boldsymbol{\Phi}(\boldsymbol{x}) \\ &\boldsymbol{E} = \boldsymbol{E}^{sym} + \boldsymbol{E}^{Tskew} \\ &\mathbf{K}(\boldsymbol{x}) := \boldsymbol{\Phi}(\boldsymbol{x}) \otimes \nabla_x \end{aligned} \tag{5.10}$$

where $\boldsymbol{E}^{skew,T}$ is the second-order skew-symmetric macro strain tensor. The tensor $\mathbf{K}(\boldsymbol{x})$ in the last relation designates the macro curvature, defined as the macroscopic gradient of the macro-rotation vector $\boldsymbol{\Phi}(\boldsymbol{x})$. The skew-symmetric part of the macro-strain can be expressed by the follow infinitesimal rotation tensor as:

$$\begin{aligned} &\boldsymbol{\omega} = \tfrac{1}{2}\left((\boldsymbol{U} \otimes \nabla_x) - (\boldsymbol{U} \otimes \nabla_x)^{T}\right) \\ &\boldsymbol{\varpi} = \boldsymbol{\epsilon} : \boldsymbol{\omega} \\ &\mathbf{E}^{skew} = \boldsymbol{\varpi} - 2\boldsymbol{\Phi} \end{aligned} \tag{5.11}$$

where $\mathbf{E}^{skew}$ is the pseudo-vector dual to the antisymmetric tensor $\mathbf{E}^{skew,T}$(similarly, the vector $\boldsymbol{\varpi}$ is dual to the skew-symmetric tensor $\boldsymbol{\omega}$). The readers are referred to (chapter 2) for more details on the Cosserat continuum formulation. The variation of the macroscopic energy density of the effective micropolar continuum function is expressed as:

$$\delta \mathbf{W}_{\mathrm{M}} = \boldsymbol{\Sigma} : (\delta \boldsymbol{E} + \boldsymbol{\epsilon} \cdot \delta \boldsymbol{\Phi}) + \boldsymbol{M} : \delta \mathbf{K} \rightarrow \delta \mathbf{W}_{\mathrm{M}} = \boldsymbol{\Sigma}^{\mathrm{sym}} : \delta \boldsymbol{E}^{\mathrm{sym}} + \boldsymbol{\Sigma}^{\mathrm{skew}} \cdot \delta \boldsymbol{E}^{\mathrm{skew}} + \boldsymbol{M} : \delta \mathbf{K} \tag{5.12}$$

wherein $\mathbf{M}$ is the couple stress tensor, and $\boldsymbol{\Sigma}^{\mathrm{skew}}$and $\boldsymbol{\Sigma}^{\mathrm{Tskew}}$ are the macroscopic stresses, elaborated by:

$$\begin{aligned} &\boldsymbol{\Sigma}^{\mathrm{sym}}(\boldsymbol{x}) := \tfrac{1}{2}\left(\boldsymbol{\Sigma}(\boldsymbol{x}) + \boldsymbol{\Sigma}^{\mathrm{T}}(\boldsymbol{x})\right) \\ &\boldsymbol{\Sigma}^{\mathrm{Tskew}} = -\boldsymbol{\epsilon} \cdot \boldsymbol{\Sigma}^{\mathrm{skew}} \\ &\boldsymbol{\Sigma} = \boldsymbol{\Sigma}^{\mathrm{sym}} + \boldsymbol{\Sigma}^{\mathrm{Tskew}} \end{aligned} \tag{5.13}$$

Here, $\boldsymbol{\Sigma}^{\mathrm{skew}}$ is the pseudo-vector dual to the second-order skew-symmetric tensor $\boldsymbol{\Sigma}^{\mathrm{Tskew}}$. The general constitutive law for the proposed Cosserat model writes as (chapter 2):

$$\begin{aligned} &\Sigma_{ij}^{sym} = C_{ijkl}\mathrm{E}_{kl}^{\mathrm{sym}} + B_{ijk}\mathrm{E}_{k}^{\mathrm{skew}} + D_{ijkl}\mathrm{K}_{kl} \\ &\Sigma_{i}^{skew} = B_{ijk}\mathrm{E}_{jk}^{\mathrm{sym}} + R_{ij}\mathrm{E}_{j}^{\mathrm{skew}} + G_{ijk}\mathrm{K}_{jk} \\ &\mathrm{M}_{ij} = D_{ijkl}\mathrm{E}_{kl}^{\mathrm{sym}} + G_{ijk}\mathrm{E}_{k}^{\mathrm{skew}} + S_{ijkl}\mathrm{K}_{kl} \end{aligned} \tag{5.14}$$

wherein the macroscopic kinematic variables are related to the macro displacement field as (chapter 2):

$$\boldsymbol{U}\left(\boldsymbol{y}, \boldsymbol{x}\right) = \boldsymbol{U}^{0} + \boldsymbol{E}^{\mathrm{sym}}\left(\boldsymbol{x}\right) \cdot \boldsymbol{y} - \boldsymbol{\epsilon} \cdot \boldsymbol{E}^{\mathrm{skew}}\left(\boldsymbol{x}\right) \cdot \boldsymbol{y} + \boldsymbol{\epsilon} \cdot \mathbf{K} : (\boldsymbol{y} \otimes \boldsymbol{y}) \tag{5.15}$$

in which $\boldsymbol{U}^0(\boldsymbol{x})$ is a rigid body motion. Instead of the classical Taylor series expansion, we will use the discrete form of the Eq. 5.15 of the macroscopic continuous displacement field at the lattice level, using the index 'i' for the node number within the unit cell, and variable $\boldsymbol{y}_i$ as the lattice nodal position:

$$\boldsymbol{U}_i(\boldsymbol{y},\boldsymbol{x}) = \boldsymbol{U}^0 + \boldsymbol{E}^{\text{sym}}(\boldsymbol{x})\cdot\boldsymbol{y}_i - \boldsymbol{\epsilon}\cdot\boldsymbol{E}^{\text{skew}}(\boldsymbol{x})\cdot\boldsymbol{y}_i + \boldsymbol{\epsilon}\cdot\mathbf{K}:(\boldsymbol{y}_i\otimes\boldsymbol{y}_i) \tag{5.16}$$

In the next section, the continualization method for discretized lattices is first explained and then is employed to find the Cosserat formulation for the effective medium.

5.4 Continualization towards generalized continua

In this section, an equivalent continuum model based on the FE discretization method in conjunction with the continualization technique derived from the Taylor series expansion of the kinematics is employed. The honeycomb lattices are considered in this contribution to illustrate the homogenization method, which is quite general in scope and can be potentially applied to all repetitive lattices prone to Cosserat effects.

The general idea of the continualization method may be summarized as follows:

- The unit cell is chosen from the material with a periodic microstructure that reflects all the microstructure properties, e.g., the unit cell here is represented as a red-colored part of the micro-lattice surrounded by the dotted lines in Fig. 5.6(a).
- Each strut of the unit cell is discretized as two-node beam elements depicted in Fig. 5.3 (one can implement different beam theories such as Euler-Bernoulli, Timoshenko beam model, or enriched beam models with more number of nodes per element).
- The discrete strain energy of the unit cell is evaluated in terms of the nodal degrees of freedom.
- Dependent and independent nodes (Fig. 5.6 (c) and Table 5.1) in the unit cell are determined, and the periodicity over the unit cell is applied to them.
- The dependent nodal displacements and rotations are formulated as a continuous field in the lattice material by implementing the macroscopic Cosserat displacement expansion of Eq. 5.16.
- The balance of linear and angular momentum is solved to express the independent nodal degrees of freedom regarding the meso kinematic variables, Eq. 5.21.
- The continuum strain energy density is obtained by introducing the continuous displacement field into the discrete strain energy (L.19) and normalizing it by the unit cell area in 2D (volume in 3D).
- The homogenized media's effective moduli are obtained by equating the micro and macro strain energy densities, relying on Hill's macrohomogeneity condition proven in Appendix M.

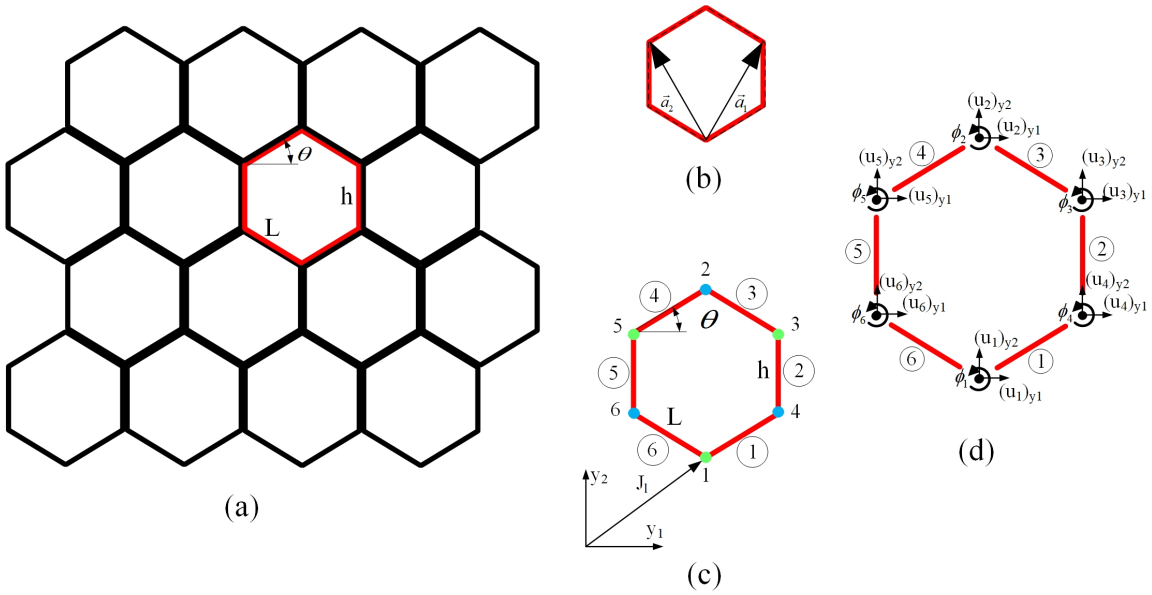

Figure 5.6 (a) Generic Honeycomb lattice material, (b) periodicity vectors of unit cell, (c) unit cell with dependency groups of nodes, and (d) unit cell nodal DOFs.

5.4.1 Homogenization of generic hexagonal honeycomb to a Cosserat effective medium

The topology of the unit cell is parameterized by the two lengths L, h, the beam thickness t, and the angular variable θ , all shown in Fig. 5.6, which generates the effective continuum model of a generic honeycomb lattice. The procedure leading to the effective continuum and the continualization technique based on the Taylor series expansion is explained [226]; [227]; [228]. In this section, the continualization process expanded in Appendix L is implemented to determine the classical and Cosserat effective mechanical properties of the 2D hexagonal honeycombs.

5.4.1.1 Continualization method for generalized hexagon lattices towards Cosserat media

Fig. 5.6 shows the lattice topology, the periodicity vectors, and the unit cell nodal DOFs; the unit cell of the honeycomb lattice contains six nodes and six-bar elements, as shown in Fig. 5.6(c). The node base group (Fig. 5.6(c) (see Appendix L for the employed terminology) are:

$$G_N = \left\{ \begin{array}{l} (0, h/2 + L\sin(\theta)),\ (-L\cos(\theta), h/2),\ (-L\cos(\theta), -h/2),\\ (0, -h/2 - L\sin(\theta)),\ (L\cos(\theta), -h/2),\ (L\cos(\theta), h/2) \end{array} \right\} \tag{5.17}$$

From the geometry of the unit cell, the direct translational bases are (Fig. 5.6(b)):

$$\vec{a}_1 = (L\cos(\theta), h + L\sin(\theta)), \quad \vec{a}_2 = (-L\cos(\theta), h + L\sin(\theta)) \tag{5.18}$$

The dependency between the unit cell node position vectors is computed on a unit cell basis using Eq. L.7; this test reveals the exhibit dependencies of the nodes, as shown in Table 5.1.

Table 5.1 Dependency relations of the unit cell nodes.

Independent node	Dependent node	$\hat{x}_1$	$\hat{x}_2$
1	3	1	0
1	5	0	1
2	4	0	-1
2	6	-1	0

The dependency relations are used to generate the transformation matrix essential for reducing the kinematics and the equilibrium systems to their periodic forms. For the hexagonal honeycomb lattice shown in Fig. 5.6, the nodal displacements and the nodal forces transformation matrix systems are formulated respectively in Eqs. 5.19 and 5.20 as:

$$\boldsymbol{u}^d = \boldsymbol{T} u^i \tag{5.19}$$

$$\boldsymbol{f}^i = \boldsymbol{T}^{Transpose} \boldsymbol{f}^d = 0 \tag{5.20}$$

where $\boldsymbol{u}^d$, $\boldsymbol{u}^i$, $\boldsymbol{f}^d$, $\boldsymbol{f}^i$, and $\boldsymbol{T}$ are vectors of the nodal degrees of freedom for dependent and independent nodes, vectors of the nodal forces for dependent and independent nodes, and transformation matrix which are defined as:

$$\boldsymbol{u}^{d,Transpose} = \begin{bmatrix} (u_1)_{y_1} & (u_1)_{y_2} & \phi_1 & (u_2)_{y_1} & (u_2)_{y_2} & \phi_2 & (u_3)_{y_1} & (u_3)_{y_2} & \phi_3 & (u_4)_{y_1} & (u_4)_{y_2} & \phi_4 & (u_5)_{y_1} & (u_5)_{y_2} & \phi_5 & (u_6)_{y_1} & (u_6)_{y_2} & \phi_6 \end{bmatrix}$$
$$\boldsymbol{u}^{i,Transpose} = \begin{bmatrix} (u_1)_{y_1} & (u_1)_{y_2} & \phi_1 & (u_2)_{y_1} & (u_2)_{y_2} & \phi_2 \end{bmatrix}$$
$$\boldsymbol{f}^{d,Transpose} = \begin{bmatrix} (f_1)_{y_1} & (f_1)_{y_2} & m_1 & (f_2)_{y_1} & (f_2)_{y_2} & m_2 & (f_3)_{y_1} & (f_3)_{y_2} & m_3 & (f_4)_{y_1} & (f_4)_{y_2} & m_4 & (f_5)_{y_1} & (f_5)_{y_2} & m_5 & (f_6)_{y_1} & (f_6)_{y_2} & m_6 \end{bmatrix}$$
$$\boldsymbol{f}^{i,Transpose} = \begin{bmatrix} (f_1)_{y_1} & (f_1)_{y_2} & m_1 & (f_2)_{y_1} & (f_2)_{y_2} & m_2 \end{bmatrix}$$

$$\boldsymbol{T}^{Transpose} = \begin{bmatrix} 1 & 0 & 0 & 0 & 0 & 0 & 1 & 0 & 0 & 0 & 0 & 0 & 1 & 0 & 0 & 0 & 0 & 0 \\ 0 & 1 & 0 & 0 & 0 & 0 & 0 & 1 & 0 & 0 & 0 & 0 & 0 & 1 & 0 & 0 & 0 & 0 \\ 0 & 0 & 1 & 0 & 0 & 0 & 0 & 0 & 1 & 0 & 0 & 0 & 0 & 0 & 1 & 0 & 0 & 0 \\ 0 & 0 & 0 & 1 & 0 & 0 & 0 & 0 & 0 & 1 & 0 & 0 & 0 & 0 & 0 & 1 & 0 & 0 \\ 0 & 0 & 0 & 0 & 1 & 0 & 0 & 0 & 0 & 0 & 1 & 0 & 0 & 0 & 0 & 0 & 1 & 0 \\ 0 & 0 & 0 & 0 & 0 & 1 & 0 & 0 & 0 & 0 & 0 & 1 & 0 & 0 & 0 & 0 & 0 & 1 \end{bmatrix}$$

The Cosserat macro displacement field 5.16, along with the macro kinematic variables 5.10, results in the following polynomial expression of the displacement and rotation fields of the 2D Cosserat media:

$$\begin{aligned} (U_i)_{x_1} &= \left(U_i^0\right)_{x_1} + (y_1)_i \mathrm{E}^{sym}_{x_1x_1} + 0.5(y_2)_i \mathrm{E}^{sym}_{x_1x_2} + (y_2)_i \mathrm{E}^{skew}_{x_3} - (y_1)_i (y_2)_i \mathrm{K}_{x_3x_1} - (y_2)_i{}^2 \mathrm{K}_{x_3x_2} \\ (U_i)_{x_2} &= \left(U_i^0\right)_{x_2} + (y_2)_i \mathrm{E}^{sym}_{x_2x_2} + 0.5(y_1)_i \mathrm{E}^{sym}_{x_1x_2} - (y_1)_i \mathrm{E}^{skew}_{x_3} + (y_1)_i (y_2)_i \mathrm{K}_{x_3x_2} + (y_1)_i{}^2 \mathrm{K}_{x_3x_1} \\ \phi_i &= (y_1)_i \mathrm{K}_{x_3x_1} + (y_2)_i \mathrm{K}_{x_3x_2} \end{aligned} \tag{5.21}$$

The relation between the dependent and independent nodal microscopic DOFs and the averaged kinematic variables is derived using Eq. 5.21 along with Eq. L.16 in Appendix L as:

$$
\begin{bmatrix}
(u_1)_{y_1}\\ (u_1)_{y_2}\\ \phi_1\\ (u_2)_{y_1}\\ (u_2)_{y_2}\\ \phi_2\\ (u_3)_{y_1}\\ (u_3)_{y_2}\\ \phi_3\\ (u_4)_{y_1}\\ (u_4)_{y_2}\\ \phi_4\\ (u_5)_{y_1}\\ (u_5)_{y_2}\\ \phi_5\\ (u_6)_{y_1}\\ (u_6)_{y_2}\\ \phi_6
\end{bmatrix}
=
\begin{bmatrix}
1&0&0&0&0&0\\ 0&1&0&0&0&0\\ 0&0&1&0&0&0\\ 0&0&0&1&0&0\\ 0&0&0&0&1&0\\ 0&0&0&0&0&1\\
1&0&0&0&0&0\\ 0&1&0&0&0&0\\ 0&0&1&0&0&0\\ 0&0&0&1&0&0\\ 0&0&0&0&1&0\\ 0&0&0&0&0&1\\
1&0&0&0&0&0\\ 0&1&0&0&0&0\\ 0&0&1&0&0&0\\ 0&0&0&1&0&0\\ 0&0&0&0&1&0\\ 0&0&0&0&0&1
\end{bmatrix}
\begin{bmatrix}
(u_1)_{y_1}\\ (u_1)_{y_2}\\ \phi_1\\ (u_2)_{y_1}\\ (u_2)_{y_2}\\ \phi_2
\end{bmatrix}
+
\begin{bmatrix}
0&0&0&0&0&0\\ 0&0&0&0&0&0\\ 0&0&0&0&0&0\\ 0&0&0&0&0&0\\ 0&0&0&0&0&0\\ 0&0&0&0&0&0\\
((y_1)_3-(y_1)_1)&0&0.5((y_2)_3-(y_2)_1)&((y_2)_3-(y_2)_1)&-((y_1)_3(y_2)_3-(y_1)_1(y_2)_1)&-\left((y_2)_3{}^2-(y_2)_1{}^2\right)\\
0&((y_2)_3-(y_2)_1)&0.5((y_1)_3-(y_1)_1)&-((y_1)_3-(y_1)_1)&\left((y_1)_3{}^2-(y_1)_1{}^2\right)&((y_1)_3(y_2)_3-(y_1)_1(y_2)_1)\\
0&0&0&0&((y_1)_3-(y_1)_1)&((y_2)_3-(y_2)_1)\\
((y_1)_4-(y_1)_2)&0&0.5((y_2)_4-(y_2)_2)&((y_2)_4-(y_2)_2)&-((y_1)_4(y_2)_4-(y_1)_2(y_2)_2)&-\left((y_2)_4{}^2-(y_2)_2{}^2\right)\\
0&((y_2)_4-(y_2)_2)&0.5((y_1)_4-(y_1)_2)&-((y_1)_4-(y_1)_2)&\left((y_1)_4{}^2-(y_1)_2{}^2\right)&((y_1)_4(y_2)_4-(y_1)_2(y_2)_2)\\
0&0&0&0&((y_1)_4-(y_1)_2)&((y_2)_4-(y_2)_2)\\
((y_1)_5-(y_1)_1)&0&0.5((y_2)_5-(y_2)_1)&((y_2)_5-(y_2)_1)&-((y_1)_5(y_2)_5-(y_1)_1(y_2)_1)&-\left((y_2)_5{}^2-(y_2)_1{}^2\right)\\
0&((y_2)_5-(y_2)_1)&0.5((y_1)_5-(y_1)_1)&-((y_1)_5-(y_1)_1)&\left((y_1)_5{}^2-(y_1)_1{}^2\right)&((y_1)_5(y_2)_5-(y_1)_1(y_2)_1)\\
0&0&0&0&((y_1)_5-(y_1)_1)&((y_2)_5-(y_2)_1)\\
((y_1)_6-(y_1)_2)&0&0.5((y_2)_6-(y_2)_2)&((y_2)_6-(y_2)_2)&-((y_1)_6(y_2)_6-(y_1)_2(y_2)_2)&-\left((y_2)_6{}^2-(y_2)_2{}^2\right)\\
0&((y_2)_6-(y_2)_2)&0.5((y_1)_6-(y_1)_2)&-((y_1)_6-(y_1)_2)&\left((y_1)_6{}^2-(y_1)_2{}^2\right)&((y_1)_6(y_2)_6-(y_1)_2(y_2)_2)\\
0&0&0&0&((y_1)_6-(y_1)_2)&((y_2)_6-(y_2)_2)
\end{bmatrix}
\begin{bmatrix}
\mathrm{E}^{sym}_{x_1x_1}\\ \mathrm{E}^{sym}_{x_2x_2}\\ \mathrm{E}^{sym}_{x_1x_2}\\ \mathrm{E}^{skew}_{x_3}\\ \mathrm{K}_{x_3x_1}\\ \mathrm{K}_{x_3x_2}
\end{bmatrix}
\tag{5.22}
$$

Considering the honeycomb unit cell of Fig. 5.6, the independent nodal displacement fields in Eq. 5.22 should be evaluated versus the introduced Cosserat macro kinematic variables. This step completes the localization process from the lattice material to the Cosserat homogenized continuum. To this end, the linear and angular momentum balance equations, Eq. L.13, are solved for a self-equilibrated unit cell (the applied forces result from the applied kinematic control over the unit cell boundary) for the independent DOFs at nodes 1 and 2 for the set of independent microscopic nodal deformations $\Big((u_1)_{y_1},\ (u_1)_{y_2},\ \phi_1,\ (u_2)_{y_1},\ (u_2)_{y_2},\ \phi_2\Big)$. To eliminate the rigid body motion, one of these nodes is selected as a reference node with nil displacement (e.g. $(u_1)_{y_1} = (u_1)_{y_2} = 0$), while periodicity prohibits the unit cell rigid body rotation. Then the set of algebraic balance equations is solved for the set of independent microscopic nodal deformations $\Big(\phi_1,\ (u_2)_{y_1},\ (u_2)_{y_2}, \phi_2\Big)$ versus the macro kinematic variables. This step leads to the full expression of the displacement field and consequently of the strain energy expressed in terms of the sole continuous macro Cosserat kinematic variables. Substituting these expressions along with Eqs. 5.19, 5.20, and 5.22 into the expression of the strain energy density Eq. L.19

gives the continuous Cosserat strain energy density expression of the honeycomb unit cell.

5.4.1.2 Evaluation of the Classical and Cosserat effective moduli

The constitutive law of the Cosserat equivalent medium can be written using Hill lemma as (section 2.3):

$$W_M = W_M\left(\mathrm{E}_{ij}^{sym}, \mathrm{E}_i^{skew}, \mathrm{K}_{ij}\right) = \frac{1}{2}\left(\Sigma_{ij}^{sym}\mathrm{E}_{ij}^{sym} + \Sigma_i^{skew}\mathrm{E}_i^{skew} + \mathrm{M}_{ij}\mathrm{K}_{ij}\right) \tag{5.23}$$

The stress measures are defined as a partial derivative of the strain energy density versus macro kinematic variables:

$$\Sigma_{ij}^{sym} = \frac{\partial W_M}{\partial \mathrm{E}_{ij}^{sym}}, \quad \Sigma_i^{skew} = \frac{\partial W_M}{\partial \mathrm{E}_i^{skew}}, \quad \mathrm{M}_{ij} = \frac{\partial W_M}{\partial \mathrm{K}_{ij}} \tag{5.24}$$

Inserting the continuous Cosserat strain energy density expression calculated in section 2.3 into Eq. 5.24 delivers the definition of the macro static variables versus the macro kinematic variables. Finally, in the present 2D context, the previous general constitutive law specializes in the 2D formulation of Eq. 5.14, considering i, j, k, $l = x_1, x_2$:

$$\begin{aligned}
&\begin{Bmatrix} \Sigma_{x_1x_1}^{sym} \\ \Sigma_{x_2x_2}^{sym} \\ \Sigma_{x_1x_2}^{sym} \end{Bmatrix} = \begin{bmatrix} C_{11} & C_{12} & 0 \\ C_{12} & C_{22} & 0 \\ 0 & 0 & C_{33} \end{bmatrix} \begin{Bmatrix} \mathrm{E}_{x_1x_1}^{sym} \\ \mathrm{E}_{x_2x_2}^{sym} \\ \mathrm{E}_{x_1x_2}^{sym} \end{Bmatrix} + \begin{bmatrix} B_{113} \\ B_{223} \\ B_{123} \end{bmatrix} \left\{\mathrm{E}_{x_3}^{skew}\right\} + \begin{bmatrix} D_{11} & D_{12} \\ D_{21} & D_{22} \\ D_{31} & D_{32} \end{bmatrix} \begin{Bmatrix} \mathrm{K}_{x_3x_1} \\ \mathrm{K}_{x_3x_2} \end{Bmatrix} \\
&\left\{\Sigma_{x_3}^{skew}\right\} = \begin{bmatrix} B_{113} & B_{223} & B_{123} \end{bmatrix} \begin{Bmatrix} \mathrm{E}_{x_1x_1}^{sym} \\ \mathrm{E}_{x_2x_2}^{sym} \\ \mathrm{E}_{x_1x_2}^{sym} \end{Bmatrix} + [R_{13}]\left\{\mathrm{E}_{x_3}^{skew}\right\} + \begin{bmatrix} G_{331} & G_{332} \end{bmatrix} \begin{Bmatrix} \mathrm{K}_{x_3x_1} \\ \mathrm{K}_{x_3x_2} \end{Bmatrix} \\
&\begin{Bmatrix} \mathrm{M}_{x_3x_1} \\ \mathrm{M}_{x_3x_2} \end{Bmatrix} = \begin{bmatrix} D_{11} & D_{21} & D_{31} \\ D_{12} & D_{22} & D_{32} \end{bmatrix} \begin{Bmatrix} \mathrm{E}_{x_1x_1}^{sym} \\ \mathrm{E}_{x_2x_2}^{sym} \\ \mathrm{E}_{x_1x_2}^{sym} \end{Bmatrix} + \begin{bmatrix} G_{331} \\ G_{332} \end{bmatrix} \left\{\mathrm{E}_{x_3}^{skew}\right\} + \begin{bmatrix} S_{11} & S_{12} \\ S_{21} & S_{22} \end{bmatrix} \begin{Bmatrix} \mathrm{K}_{x_3x_1} \\ \mathrm{K}_{x_3x_2} \end{Bmatrix}
\end{aligned} \tag{5.25}$$

In Eq. 5.25, the following constitutive tensors have been introduced:

$$\begin{aligned}
&\boldsymbol{C} = \begin{bmatrix} C_{11} & C_{12} & 0 \\ C_{12} & C_{22} & 0 \\ 0 & 0 & C_{33} \end{bmatrix}, \boldsymbol{S} = \begin{bmatrix} S_{11} & S_{12} \\ S_{21} & S_{22} \end{bmatrix}, \boldsymbol{R} = [R_{13}], \\
&\boldsymbol{B} = \begin{bmatrix} B_{113} \\ B_{223} \\ B_{123} \end{bmatrix}, \boldsymbol{D} = \begin{bmatrix} D_{11} & D_{12} \\ D_{21} & D_{22} \\ D_{31} & D_{32} \end{bmatrix}, \boldsymbol{G} = \begin{bmatrix} G_{331} & G_{332} \end{bmatrix}
\end{aligned} \tag{5.26}$$

Successively in the first line of Eq. 5.26, the Cauchy, Cosserat, skew-symmetric homogenized tensors are presented, while the second line in Eq. 5.26 defines the coupling tensors. In previous constitutive tensors of Eq. 5.25, the non-nil Cauchy, coupling, and Cosserat effective moduli components have been evaluated by taking the partial differential of the static measures in Eq. 5.25 versus the related Cosserat macro kinematic variables, which receive the following closed-form expressions in terms of the microscopic parameters of the honeycomb unit cell as shown in Fig. 5.2.

Table 5.2 Closed-from expressions for effective properties of general hexagonal lattices.

Effective Moduli	Closed-form expression
C_{11}	$\frac{AE_s\cos(\theta)\left[(1+\alpha_1)\cos^2(\theta)+\beta_1\left(\sin^2(\theta)+2\eta_{eff}\right)\right]}{bL_{eff}\gamma_1(\eta+\sin(\theta))}$
C_{22}	$\frac{AE_s(\eta+\sin(\theta))\left[(1+\alpha_1)\sin^2(\theta)+\beta_1\cos^2(\theta)\right]}{bL_{eff}\gamma_1\cos(\theta)}$
C_{12}	$\frac{AE_s\sin(2\theta)(1+\alpha_1-\beta_1)}{2bL_{eff}\gamma_1}$
C_{33}	$\frac{3E_sI\left[\cos(\theta)(\eta+\eta_{eff})^2+4\sin(\theta)\cos(\theta)(\eta+\eta_{eff}+\sin(\theta))\right]}{bL_{eff}^3(\eta+\sin(\theta))\gamma_2}$
B_{123}	$\frac{6E_sI\cos(\theta)(\eta_{eff}-\eta)(\eta_{eff}+\eta+2\sin(\theta))}{bL_{eff}^3(\eta+\sin(\theta))\gamma_2}$
R_{13}	$\frac{12E_sI\cos(\theta)(\eta_{eff}-\eta)^2}{bL_{eff}^3(\eta+\sin(\theta))\gamma_2}$
S_{11}	$\frac{E_sIL^2\cos(\theta)\left[12\eta_{eff}\left(\alpha_1+\eta_{eff}^2\right)\gamma_3+24(1+\alpha_1)\gamma_4+\eta_{eff}(1+\alpha_1)\left(\alpha_1+\eta_{eff}^2\right)\gamma_5\right]}{4bh_{eff}L_{eff}^2(\eta+\sin(\theta))(1+\alpha_1)\left(\alpha_1+\eta_{eff}^2\right)}$
S_{22}	$\frac{2E_s\left[2\eta_{eff}I(\eta+\sin(\theta))^2\gamma_6+6I\eta_{eff}(1+2\eta_{eff})\left(\frac{L}{L_{eff}}\right)^2\gamma_7+AL^2\cos^2(\theta)(1+\alpha_1)\gamma_8\right]}{bh_{eff}}$

wherein b, $A=bt$, $I=\frac{1}{12}bt^3$ are the out-of-plane thickness of the unit cell, cross-sectional area of the elements, and second moment of area of the elements, respectively. The following non-dimensional parameters in Table 5.2 are introduced:

$$\alpha_1=\frac{12E_sI}{k_sAG_sL_{eff}^2};\quad \beta_1=\frac{12I}{AL_{eff}^2};\quad \eta_{eff}=\frac{h_{eff}}{L_{eff}};\quad \eta=\frac{h}{L}$$

$$\gamma_1=(1+\alpha_1)\left(1+2\eta_{eff}\sin^2(\theta)\right)+2\beta_1\eta_{eff}\cos^2(\theta)$$

$$\gamma_2=\beta_1(1+\eta_{eff}\sin(\theta))(2+\eta_{eff}\sin(\theta))+\eta_{eff}\cos^2(\theta)\left[\alpha_1(2+\eta_{eff})+\eta_{eff}(1+2\eta_{eff})\right]$$

$$\gamma_3=\left(\frac{L_{eff}}{L}+\eta\sin(\theta)-2\cos^2(\theta)\right)^2$$

$$\gamma_4=\left(\eta-\frac{h_{eff}}{L}\right)^2$$

$$\gamma_5=\left(\frac{L_{eff}}{L}\right)^2+\frac{AL_{eff}^2}{I}\cos(\theta)\left(\eta^2\cos(\theta)+4\sin(\theta)(\eta+\sin(\theta))\right)$$

$$\gamma_6=3(1+2\eta_{eff})+1+\alpha_1$$

$$\gamma_7=\left[2\sin^3(\theta)+\eta\left(1+\sin^2(\theta)\right)\right]^2-2\left(\frac{L_{eff}}{L}\right)(\eta+\sin(\theta))\left[2\sin^3(\theta)+\eta\left(1+\sin^2(\theta)\right)\right]$$

$$\gamma_8=2\eta_{eff}\sin^3(\theta)\left[\sin(\theta)(1+2\eta_{eff})+\eta+2\eta_{eff}\right]+\eta^2\left[\cos^2(\theta)+\sin^2(\theta)(1+\eta_{eff})^2+3.5\eta_{eff}\right]$$

The expressions of the effective Cauchy and coupling moduli reveal that these properties do not depend on the unit cell absolute dimension; on the other hand, the Cosserat effective properties have a quadratic dependency upon the absolute size of the unit cell.

The representation of the effective Cauchy properties in the form of engineering effective properties is more practical. Hence, the following subsection is devoted to the calculation of these parameters for the proposed honeycomb materials.

5.4.1.3 Effective engineering material properties of the honeycomb unit cell

Considering the plane strain condition, and according to the 2D Cauchy stiffness matrix $\boldsymbol{C}^{\text{hom}}$in Eq. 5.25, the general honeycomb's effective behavior can be regarded as an orthotropic elastic solid with four independent coefficients in 2D. The compliance matrix for the purely 2D geometry pictured in Fig. 5.6 with vector e_3 orthogonal to the symmetry plane receives the expression of an orthotropic body:

$$\begin{pmatrix} E^{sym}_{x_1x_1} \\ E^{sym}_{x_2x_2} \\ E^{sym}_{x_1x_2} \end{pmatrix} = \begin{bmatrix} \frac{1}{\mathrm{E}^{\text{hom}}_{x_1}} & -\frac{\nu^{\text{hom}}_{x_2x_1}}{\mathrm{E}^{\text{hom}}_{x_2}} & 0 \\ -\frac{\nu^{\text{hom}}_{x_1x_2}}{\mathrm{E}^{\text{hom}}_{x_1}} & \frac{1}{\mathrm{E}^{\text{hom}}_{x_2}} & 0 \\ 0 & 0 & \frac{1}{\mathrm{G}^{\text{hom}}_{x_1x_2}} \end{bmatrix} \begin{pmatrix} \Sigma^{sym}_{x_1x_1} \\ \Sigma^{sym}_{x_2x_2} \\ \Sigma^{sym}_{x_1x_2} \end{pmatrix} \tag{5.27}$$

The symmetry of the compliance matrix entails the following relation:

$$\frac{\nu^{\text{hom}}_{x_2x_1}}{\mathrm{E}^{\text{hom}}_{x_2}} = \frac{\nu^{\text{hom}}_{x_1x_2}}{\mathrm{E}^{\text{hom}}_{x_1}};$$

The effective Cauchy properties are then easily extracted to be:

$$\mathrm{E}^{\text{hom}}_{x_1} = \frac{\mathrm{C}_{11}\mathrm{C}_{22} - \mathrm{C}^2_{12}}{\mathrm{C}_{22}}; \quad \mathrm{E}^{\text{hom}}_{x_2} = \frac{\mathrm{C}_{11}\mathrm{C}_{22} - \mathrm{C}^2_{12}}{\mathrm{C}_{11}}; \quad \nu^{\text{hom}}_{x_1x_2} = \frac{\mathrm{C}_{12}}{\mathrm{C}_{22}}; \quad \nu^{\text{hom}}_{x_2x_1} = \frac{\mathrm{C}_{12}}{\mathrm{C}_{11}} \tag{5.28}$$

In the following section, the effective classical and micropolar properties evaluated using the continualization method are validated based on the unit cell FE periodic homogenization.

5.5 Homogenization of lattice materials towards generalized continua

The FE validation of the homogenized Cosserat moduli derived in the previous section is based on sequential kinematic loadings, with polynomial type displacements (see Eq. 5.21) applied over the unit cell boundary to reproduce the effective unit cell kinematics. The effective moduli are obtained relying on the equivalence of the macroscopic energy and the average of the microscopic energy, traducing Hill macrohomogeneity condition. Many authors in the literature have addressed the proper way of formulating kinematic boundary conditions over the unit cell, and we only mention a few of them. They maintain unit cells planar boundary surfaces after deformation [229] or apply homogeneous displacement boundary conditions [230], which only hold for a transversely isotropic unit cell under longitudinal and transverse strains, over constraints the unit cell for general anisotropic materials. This overestimation happens especially under shear loading conditions - since straight lines remain straight after deformation - leading to overestimated properties [181]. The implementation into ABAQUS of periodic homogenization conditions over the unit cell in an automated way has been done [231], relying on [232]; [233] for calculating Cauchy effective properties. This method has been extended in chapter 2 towards computing Cosserat effective properties. The novelty of the present work lies in applying such PBCs for the hexagon without introducing over-constraints to evaluate the Cauchy and Cosserat effective moduli.

In the following section, PBCs are described that characterize the Cauchy and Cosserat effective properties of lattice materials via unit cell.

5.5.1 Periodic boundary conditions

PBCs are applied to the unit cell to establish the bulk response of the material without any edge effect. These boundary conditions will ensure that the deformed shape of the unit cell on external surfaces remains periodic. The periodicity conditions on the boundary are [181]:

$$u_i = \bar{\varepsilon}_{ik} y_k + \hat{u}_i \tag{5.29}$$

where $\hat{u}_i$, and $\bar{\varepsilon}_{ik}$ are the periodic fluctuating part of the displacement, and the average strain fields, respectively. Eq. 5.29 includes the unknown fluctuating part of the displacement (the method applies for both periodic and non-periodic microstructures). Thus, it would be easier to impose the following relative boundary conditions on the opposite boundary surfaces of unit cell,

$$u_i^{j+} - u_i^{j-} = \bar{\varepsilon}_{ik} \left(y_k^{j+} - y_k^{j-} \right) = \bar{\varepsilon}_{ik} \Delta \mathrm{y}_k^j \tag{5.30}$$

where indices $j+$ and $j-$ denote the positive and negative y_j directions, respectively. One can see from Eq. 5.30 that although the difference of the displacements on the two opposite boundary surfaces is determined, the individual displacement component is a function of the coordinates, and a plane does not necessarily remain planar after deformation.

5.5.2 Applying PBCs in the FE method

Application of PBCs on the non-cubic unit cells is not reported in the literature to the authors' knowledge. Accordingly, this chapter presents, the detailed expression of the PBCs over the general hexagonal unit cells with three periodicity vector for calculating the Cosserat effective properties. These results are used as a reference solution for the effective properties.

PBCs of Eq. 5.30 have to be applied node-by-node over the boundaries of the unit cell depicted in Fig. 5.7. To this end, the opposite faces should have the same type of mesh with an equal number of elements. The nodal degrees of freedom in FE method are linked together, based on the kinematic constraints in Eq. 5.30, as illustrated in Table 5.3. u_i $(i = y_1,\ y_2,\ y_3)$ is the displacement component, and $u_i^{F_j^2}$ is the displacement of the node 'j' of face 'F^2' in y_i direction. The PBCs are applied over the unit cell using the reference point $RP_i (i = y_1,\ y_2,\ y_3)$, and $RP_i^{F_j^2, F_j^1}$ is considered for applying the PBCs over node 'j' of face 'F^2' and 'F^1'.

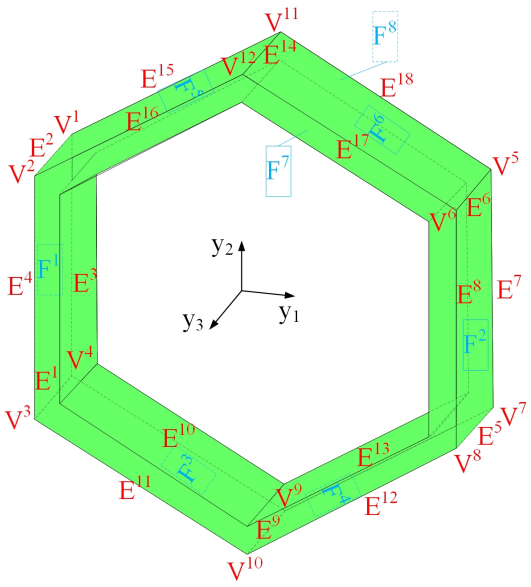

Figure 5.7 Hexagon unit cell with faces (F^i), edges (E^i) and vertices (V^i) and their numbering.

Table 5.3 Boundary constraint equations for faces, edges, and vertices.

$u_i^{F_j^2} - u_i^{F_j^1} - RP_i^{F_j^2,F_j^1} = 0$	$u_i^{E_j^4} - u_i^{E_j^3} - RP_i^{E_j^4,E_j^3} = 0$	$u_i^{V_{12}} - u_i^{V_{11}} - RP_i^{V_{12},V_{11}} = 0$
$u_i^{F_j^4} - u_i^{F_j^5} - RP_i^{F_j^4,F_j^5} = 0$	$u_i^{E_j^3} - u_i^{E_j^7} - RP_i^{E_j^3,E_j^7} = 0$	$u_i^{V_{11}} - u_i^{V_8} - RP_i^{V_{11},V_8} = 0$
$u_i^{F_j^6} - u_i^{F_j^3} - RP_i^{F_j^6,F_j^3} = 0$	$u_i^{E_j^{16}} - u_i^{E_j^{12}} - RP_i^{E_j^{16},E_j^{12}} = 0$	$u_i^{V_8} - u_i^{V_7} - RP_i^{V_8,V_7} = 0$
$u_i^{F_j^8} - u_i^{F_j^7} - RP_i^{F_j^8,F_j^7} = 0$	$u_i^{E_j^{12}} - u_i^{E_j^{13}} - RP_i^{E_j^{12},E_j^{13}} = 0$	$u_i^{V_7} - u_i^{V_4} - RP_i^{V_7,V_4} = 0$
$u_i^{E_j^6} - u_i^{E_j^2} - RP_i^{E_j^6,E_j^2} = 0$	$u_i^{E_j^{13}} - u_i^{E_j^{15}} - RP_i^{E_j^{13},E_j^{15}} = 0$	$u_i^{V_2} - u_i^{V_{10}} - RP_i^{V_2,V_{10}} = 0$
$u_i^{E_j^2} - u_i^{E_j^9} - RP_i^{E_j^2,E_j^9} = 0$	$u_i^{E_j^{17}} - u_i^{E_j^{11}} - RP_i^{E_j^{17},E_j^{11}} = 0$	$u_i^{V_{10}} - u_i^{V_9} - RP_i^{V_{10},V_9} = 0$
$u_i^{E_j^5} - u_i^{E_j^1} - RP_i^{E_j^5,E_j^1} = 0$	$u_i^{E_j^{11}} - u_i^{E_j^{10}} - RP_i^{E_j^{11},E_j^{10}} = 0$	$u_i^{V_9} - u_i^{V_5} - RP_i^{V_9,V_5} = 0$
$u_i^{E_j^1} - u_i^{E_j^{14}} - RP_i^{E_j^1,E_j^{14}} = 0$	$u_i^{E_j^{10}} - u_i^{E_j^{18}} - RP_i^{E_j^{10},E_j^{18}} = 0$	$u_i^{V_5} - u_i^{V_6} - RP_i^{V_5,V_6} = 0$
$u_i^{E_j^8} - u_i^{E_j^4} - RP_i^{E_j^8,E_j^4} = 0$	$u_i^{V_3} - u_i^{V_{12}} - RP_i^{V_3,V_{12}} = 0$	$u_i^{V_6} - u_i^{V_1} - RP_i^{V_6,V_1} = 0$

Table 5.4 . Kinematic loadings corresponding to the Cauchy and Cosserat rigidity components.

Effective component	$RP_{y_1}^{\psi_1,\psi_2}$	$RP_{y_2}^{\psi_1,\psi_2}$
$C_{11} = \frac{2U^{cell}}{V^{cell}}$	$\left({y_1}^{\psi_2} - {y_1}^{\psi_1}\right) \mathrm{E}_{x_1x_1}$	0
$C_{22} = \frac{2U^{cell}}{V^{cell}}$	0	$\left({y_2}^{\psi_1} - {y_2}^{\psi_2}\right) \mathrm{E}_{x_2x_2}$
$C_{12} = \frac{U^{cell}}{V^{cell}} - \frac{C_{11}+C_{22}}{2}$	$\left({y_1}^{\psi_2} - {y_1}^{\psi_1}\right) \mathrm{E}_{x_1x_1}$	$\left({y_2}^{\psi_1} - {y_2}^{\psi_2}\right) \mathrm{E}_{x_2x_2}$
$C_{33} = \frac{U^{cell}}{2V^{cell}}$	$\left({y_2}^{\psi_1} - {y_2}^{\psi_2}\right) \mathrm{E}_{x_1x_2}$	$\left({y_1}^{\psi_1} - {y_1}^{\psi_2}\right) \mathrm{E}_{x_1x_2}$
$S_{11} = \frac{2U^{cell}}{V^{cell}}$	$-\left({y_1}^{\psi_1}{y_2}^{\psi_1} - {y_1}^{\psi_2}{y_2}^{\psi_2}\right) \mathrm{K}_{x_3x_1}$	$\left(\left({y_1}^{\psi_1}\right)^2 - \left({y_1}^{\psi_2}\right)^2\right) \mathrm{K}_{x_3x_1}$
$S_{22} = \frac{2U^{cell}}{V^{cell}}$	$-\left(\left({y_2}^{\psi_1}\right)^2 - \left({y_2}^{\psi_2}\right)^2\right) \mathrm{K}_{x_3x_2}$	$\left({y_1}^{\psi_1}{y_2}^{\psi_1} - {y_1}^{\psi_2}{y_2}^{\psi_2}\right) \mathrm{K}_{x_3x_2}$

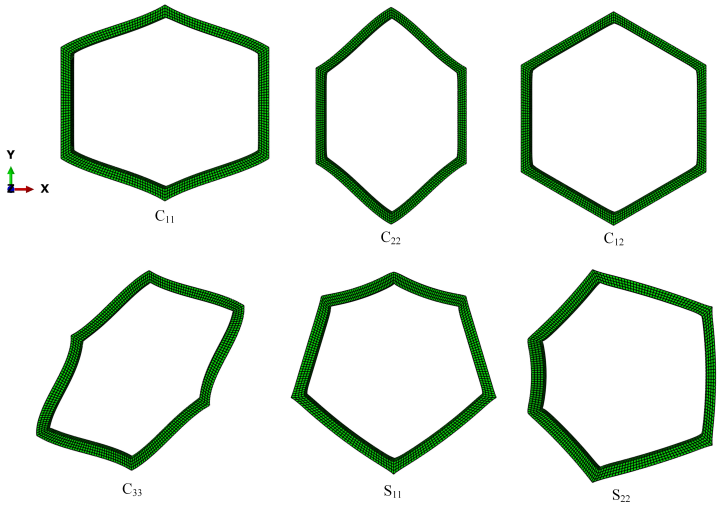

Figure 5.8 Schematic representation of different modes related to the effective Cauchy and Cosserat moduli for a hexagonal honeycomb $\theta = 30$.

In Table 5.4, the quantities U^{cell} and V^{cell} are the strain energy and volume of the unit cell occupied by the outer faces, respectively. Also ψ_1, ψ_2 are the notations that represent nodal points over the opposite faces, edges, and vertices. For each FE test, the total strain energy of the unit cell corresponding to the known applied strain on the unit cell boundary is used to evaluate the corresponding homogenized modulus. Considering only nonzero strain terms gives the relation between each effective modulus and the total strain energy of the unit cell as written in Table 5.4.

5.5.3 Micropolar deformation modes

Unit cell homogenization requires imposing strains on the boundaries of the unit cell to calculate the effective properties. Fig. 5.8 shows the schematic of deformed modes of the unit cell in the computation of rigidity coefficients C_{11}, C_{22}, C_{12}, C_{33}, S_{11}, and S_{22}.

5.6 Numerical results

The effective moduli expressed in section 5.4 will be compared with numerical predictions based on unit cell FE computations of section 5 using the FE software ABAQUS to validate them and study their sensitivity to the geometrical unit cell design parameters. For the unit cell computations in ABAQUS, we have considered the PBC in the out-of-plane direction (an infinite length is considered in the third direction), which is the needed condition for a 2D plane strain analysis implemented in the continualization method.

5.6.1 Validation and sensitivity analysis of the effective moduli

The design variables are the dimensionless ratio $t/L \in [0.004, 0.4]$ and the angular variable, adopted to validate the homogenized moduli evaluated in section 5.4 (Table 5.2), as a discrete homogenization method. The variation of these parameters is adapted to be $t/L \in [0.04, 0.36], \theta \in [-15, 45]$ in FE simulations of section 5.5, employing the C3D20 element in the ABAQUS software. The ratio h/L is kept to a constant unity value in all subsequent analyses. In all coming plots, the dotted lines represent FE predictions of moduli using 3D solid elements using the Abaqus software, considering a linear isotropic constitutive law at the microscopic level, with parameters given in Table 5.5. The FE simulation results are then compared with the corresponding values of the moduli computed with the previous discrete (beam) homogenization method (section 5.4), with the last predictions pictured using solid lines. The dimensionless density defined in Eq. 5.4 varies according to the range of design parameters ${\rho_f}^* \in [0.02, 0.7]$; ratios above 0.5 (see Fig. 5.9(j)) are not accepted due to the existing geometrical constraints that pertain to the considered unit cell (overlap of struts have to be prevented). where $\mathrm{E}^*_{x_1} = \mathrm{E}^{\mathrm{hom}}_{x_1}/\mathrm{E}_s$, $\mathrm{E}^*_{x_2} = \mathrm{E}^{\mathrm{hom}}_{x_2}/\mathrm{E}_s$, and $\mathrm{G}^*_{x_1x_2} = \mathrm{G}^{\mathrm{hom}}_{x_1x_2}/\mathrm{E}_s$ are dimensionless Young's moduli along x1 and x2 directions, and in-plane shear modulus, respectively.

Fig. 5.9(a),(b),(c),(d),(e) show a perfect agreement of the effective mechanical Cauchy properties predicted by discrete homogenization with those provided by FE simulations over the entire range of considered design parameters and over the believed range of variation of the tolerable relative density. Discrepancies appear at higher values of relative density due to the overlap of structural members within the unit cell for continuous FE homogenization. In contrast, discrete homogenization does not face this issue since only the mainline of the beams is considered. The contour plots of the dimensionless coupling moduli $B^*_{123} = B_{123}/\mathrm{E}_s$ and $R^*_{13} = R_{13}/\mathrm{E}_s$ of the skew-symmetric response are shown in Fig. 5.9(f) and Fig. 5.9(g), respectively, relying on discrete homogenization. The internal bending length $l^*_{x_1} = \sqrt{S_{11}/\left(\mathrm{E}^{\mathrm{hom}}_{x_1}\mathrm{L}^2\right)}$ and $l^*_{x_2} = \sqrt{S_{22}/\left(\mathrm{E}^{\mathrm{hom}}_{x_2}\mathrm{L}^2\right)}$ contour lines plotted in Fig. 5.9(h) and Fig. 5.9(i) highlight that the validity range of Cosserat moduli predicted by the beam continualization method is lower than Cauchy moduli, with a good agreement versus FE predictions holding for relative densities less than 0.25. Two main reasons can cause this behavior; Firstly, the finite sampling of variables in discrete homogenization (the kinematic variables are interpolated at a finite number of points within the microstructure) may not be sufficient. Secondly, the adopted Cosserat continuum model may not adequately describe the effective behavior at higher relative density, so more enriched generalized continuum descriptions may be needed. Plots of internal bending lengths reveal that auxetic configurations (Negative Poisson's ratio) have smaller $l^*_{x_1}$ values than classical hexagon geometries with positive Poisson's ratio. We notice the significant Cosserat effects due to the value of the normalized bending length $l^*_{x_2}$ well above unity. For a constant relative density, the internal bending length $l^*_{x_1}$ varies by a factor of 8 over the range of explored parameters, which remains almost constant by the way more than the other length $l^*_{x_2}$.

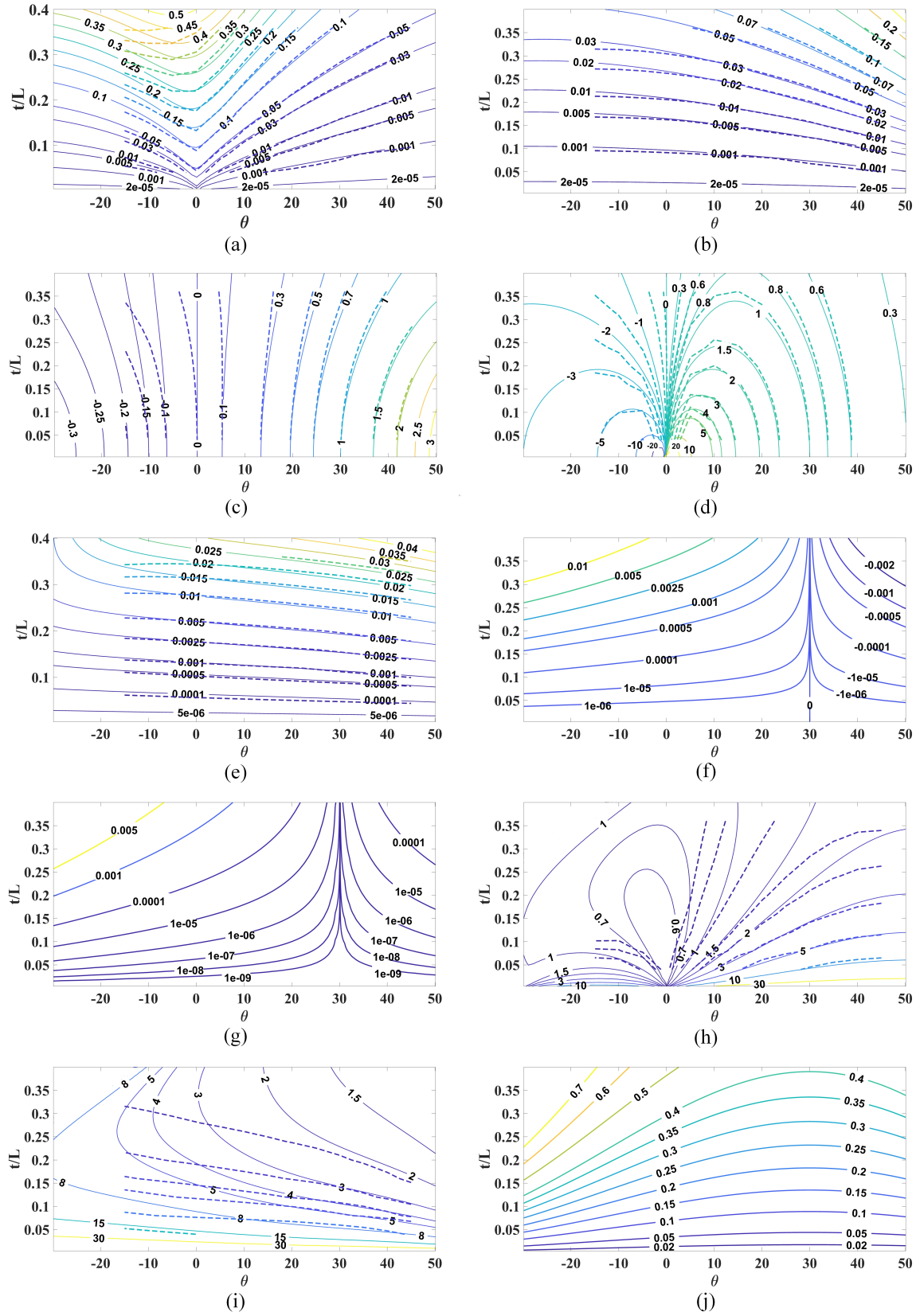

Figure 5.9 Contours of the (a) $\mathrm{E}^*_{x_1}$, (b) $\mathrm{E}^*_{x_2}$, (c) $\nu^*_{x_2x_1}$, (d) $\nu^*_{x_1x_2}$, (e) $\mathrm{G}^*_{x_1x_2}$, (f) B^*_{123}, (g) R^*_{13}, (h) $l^*_{x_1}$, (i) $l^*_{x_2}$, (j) ρ^*_f versus θ and t/L; solid lines are results from continualization and dotted lines FE results.

5.6.2 Window analysis size effect

In order to show that the computed Cosserat moduli are intrinsic to the microstructure and do not depend on the size of the window of analysis, 2D hexagonal windows, including an increasing number of repeated unit cells, are considered, pictured in Fig. 5.10. The lattices are aligned in the third out-of-plane direction and are periodically distributed in the (y_1, y_2) plane. The mechanical and geometrical parameters of the honeycomb unit cell of Fig. 5.10 are given in Table 5.5. shown in Table 5.1.

Table 5.5 Values of the geometrical and mechanical parameters of the hexagonal lattice.

E_s (MPa)	ν_s	L (mm)	h (mm)	θ (deg)	t (mm)	b (mm)
69000	0.33	5	5	30	0.2	1

Here, the effective Cosserat kinematic and static variables entering the Hill macrohomogeneity condition are fully expressible as surface integrals over the considered macrodomain of analysis, here coined the window of analysis. The proof of the derived extended macrohomogeneity lemma for the Cosserat media is given in Appendix M; the expressions reached in Eqs. M.11-M.13 define the surface integral of the macro static variables of the effective Cosserat medium. According to this, the total cumulated length of the external edges of unit cells crossing the window of analysis boundaries (the variable L^{be} is defined as a total length of the struts over the boundary of the windows of analysis normalized by the perimeter of the single unit cell window of analysis in Fig. 5.10(a)) is the essential variable for measuring the macro kinematic and static variables. Consequently, the effective properties relating to them mutually also depend on this parameter.

As indicated in Fig. 5.11(a), the effective Cauchy coefficients are invariant versus the window size shown in Fig. 5.10. Moreover, Fig. 5.11(b) illustrates the fast convergence of the normalized micropolar moduli (by the total length L^{be}), a fact that highlights the size-independency of the represented homogenization method. Note that enough large window (about eight repetitions of the single unit cell) is needed to reach the converged intrinsic higher-order moduli.

The relevance of using a Cosserat effective model at the unit cell level for describing the macroscale response at the structural level is next investigated. The mechanical response of a macro beam made of the honeycomb unit cells is analyzed in detail in the next section; for this purpose, we develop an extended Timoshenko beam theory and investigate the relative importance of Cauchy versus micropolar effects in the beam response under extension and pure bending loadings.

5.6.3 Extended Timoshenko beam theory

A prismatic homogeneous isotropic beam element of Fig. 5.3, including shear deformation, is considered at the macro level. The displacement function $u_{y_2}(x_1)$ describes the translation of the beam's neutral axis in the $x2_2$-direction, while function $\phi(x_1)$ denotes the rotation of the cross-section at the mid-plane,

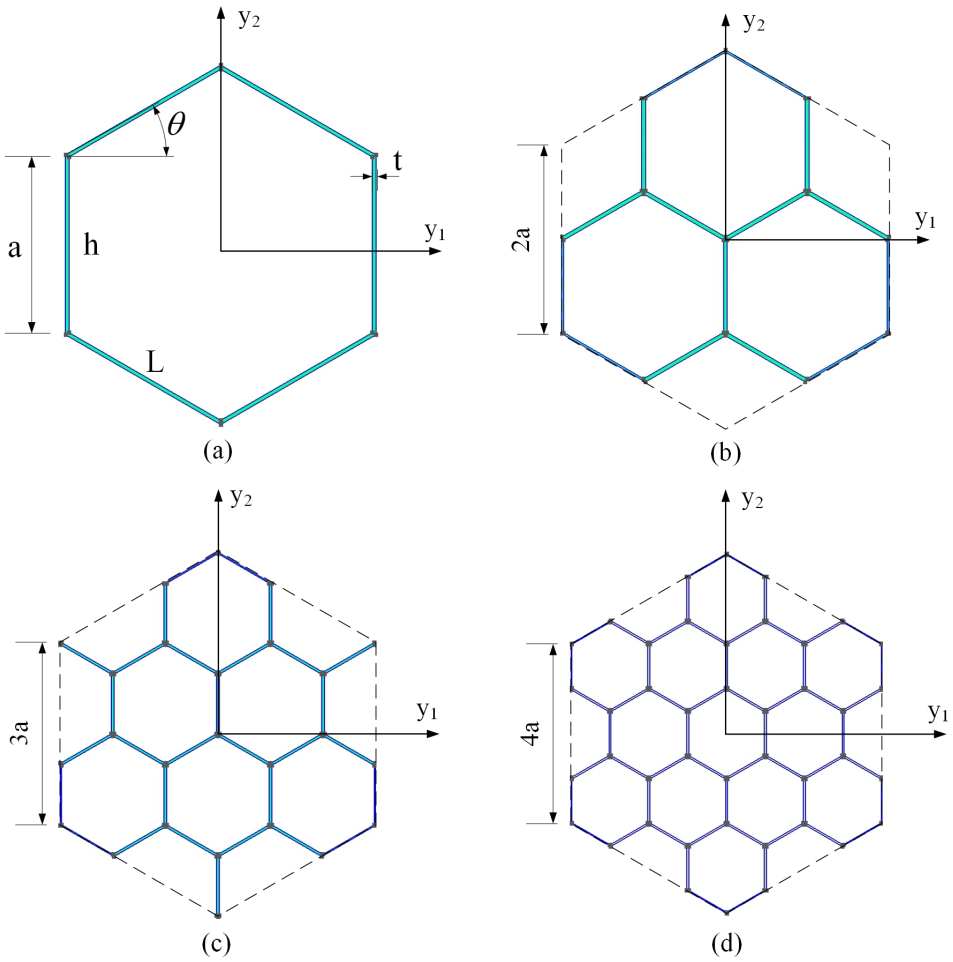

Figure 5.10 Window of analysis comprising a unit cell with the side length: (a) 'a', (b) '2a', (c) '3a', (d) '4a'.

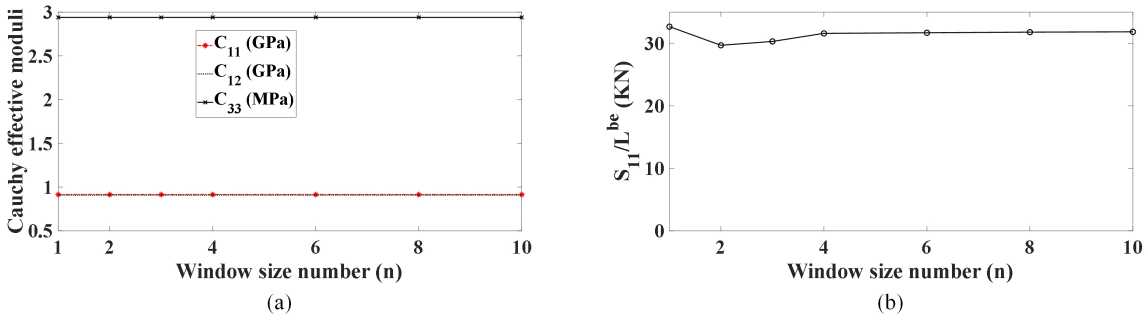

Figure 5.11 Variation of the effective moduli versus the window size number 'n':(a) Cauchy effective moduli (b) Micropolar effective modulus.

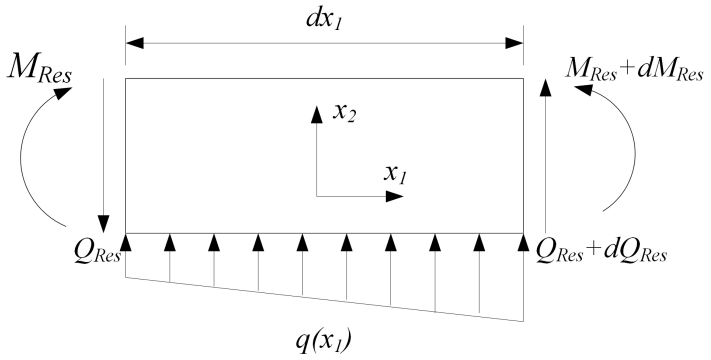

Figure 5.12 An infinitesimal element of the beam and applied forces and moments.

and $\theta(x_1)$ is the slope of the beam's central axis. The governing equilibrium equations for an infinitesimal beam element shown in Fig. 5.12 are

$$\frac{dQ}{dx_1} + q = 0 \tag{5.31}$$

$$\frac{dM}{dx_1} + Q = 0 \tag{5.32}$$

Q_{Res} , M_{Res} , and q are the resultant shear force, the resultant bending moment and the distributed shear load, respectively. The very definition of these quantities will be explicated in the sequel, based on the micropolar continuum model that has been reduced to a beam model.

The displacement field in Timoshenko beam theory is assumed to take the following form:

$$\begin{aligned} u_{x_1} &= -x_2\phi(x_1) \\ u_{x_2} &= u_{x_2}(x_1) \\ u_{x_3} &= 0 \end{aligned} \tag{5.33}$$

in which the slope of the central axis of the beam is given by

$$\theta = \frac{du_{x_2}}{dx_1} \tag{5.34}$$

The non-zero strains, rotation, and curvature tensors, as well as the corresponding curvature vector component, are given respectively as:

$$\mathrm{E}^{sym}_{x_1x_1} = \frac{du_{x_1}}{dx_1} = -x_2\frac{d\phi}{dx_1} \tag{5.35}$$

$$\mathrm{E}^{sym}_{x_1x_2} = \frac{1}{2}\left(\frac{du_{x_2}}{dx_1} - \phi\right) \tag{5.36}$$

$$\mathrm{E}^{skew}_{x_3} = -\frac{1}{2}\left(\frac{du_{x_2}}{dx_1} + \phi\right) \tag{5.37}$$

$$\mathrm{K}_{x_3x_1} = \frac{d\phi}{dx_1} \tag{5.38}$$

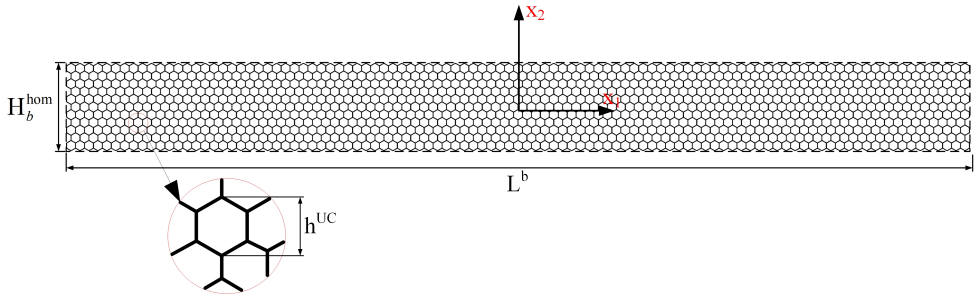

Figure 5.13 Architected Macro beam made of honeycomb unit cells with its geometrical descriptors. h^{UC} is the total height of the unit cell shown in the magnified part.

The stress components and Cosserat bending moment follow from Eq. 5.25(25) and Eq. 5.27

$$\Sigma^{sym}_{x_1x_1} = -\mathrm{E}^{\mathrm{hom}}_{x_1} x_2 \frac{d\phi}{dx_1} \tag{5.39}$$

$$\Sigma^{sym}_{x_1x_2} = 2G^{\mathrm{hom}}_{x_1x_2}\mathrm{E}^{sym}_{x_1x_2} = G^{\mathrm{hom}}_{x_1x_2}\left(\frac{du_{x_2}}{dx_1} - \phi\right) \tag{5.40}$$

$$\Sigma^{skew}_{x_3} = B_{123}\mathrm{E}^{sym}_{x_1x_2} + R_{13}\mathrm{E}^{skew}_{x_3} \tag{5.41}$$

$$M_{x_3x_1} = S_{11}(x_2)\mathrm{K}_{x_3x_1} = S_{11}(x_2)\frac{d\phi}{dx_1} \tag{5.42}$$

According to Eqs. 5.39 and 5.42, the bending moment can be additively decomposed into a classical and higher order micropolar contribution, successively:

$$M_{Res} = M^{\Sigma}_{\mathrm{Res}} + M^{M}_{\mathrm{Res}} \tag{5.43}$$

with

$$\begin{aligned} M^{\Sigma}_{\mathrm{Res}} &= -\int_A x_2 \Sigma^{sym}_{x_1x_1} dA \\ M^{M}_{\mathrm{Res}} &= \int_A M_{x_3x_1} dA \end{aligned} \tag{5.44}$$

wherein $M^{\Sigma}_{\mathrm{Res}}$, M^{M}_{Res}, and A are the Cauchy part of resultant bending moment, the Cosserat part of resultant bending moment , and the cross-sectional area of the beam, respectively. The first integral in Eq. 5.44 leads to the Cauchy contribution of the bending moment expressing as:

$$M^{\Sigma}_{\mathrm{Res}} = -\int_A x_2 \Sigma^{sym}_{x_1x_1} dA = \int_A \mathrm{E}^{\mathrm{hom}}_{x_1} {x_2}^2 \frac{d\phi}{dx_1} dA = \mathrm{E}^{\mathrm{hom}}_{x_1}\mathrm{I}_{x_1x_1}\frac{d\phi}{dx_1} \tag{5.45}$$

where $\mathrm{I}_{x_1x_1}$ is the second momentum of the area of the beam cross section.

The macroscopic bending relation can be obtained by upscaling the internal virtual work of bending moments over the entire set of lattice unit cells filling the macro beam domain, with the first relation Eq. M.19 in Appendix M:

$$\sum_{k=1}^{N^{be}_L \times N^{be}_H} \frac{1}{|Y|} \sum_{i=1,2,3} \left(\left((\mathbf{K}) \cdot \boldsymbol{Y}^i \right) \otimes \boldsymbol{N}^i \right) : \sum_{j=1,2,3} \left(\int_{\partial Y} (epsilon \cdot \boldsymbol{\sigma} \cdot \boldsymbol{n})\, ds_y \cdot \boldsymbol{Y}^j \otimes \boldsymbol{Y}^j \right) \equiv \sum_{k=1}^{N^{be}_L + N^{be}_H} \mathbf{K} : \boldsymbol{M}_k \equiv \mathbf{K} : \left(\sum_{k=1}^{N^{be}_H} \boldsymbol{M}_k \right) \tag{5.46}$$

In Eq. 5.46, the first equality results from the fact that the unit cells within the macrodomain can be paired so that the external unit normal vectors are opposite. Moreover, the normal to the upper and

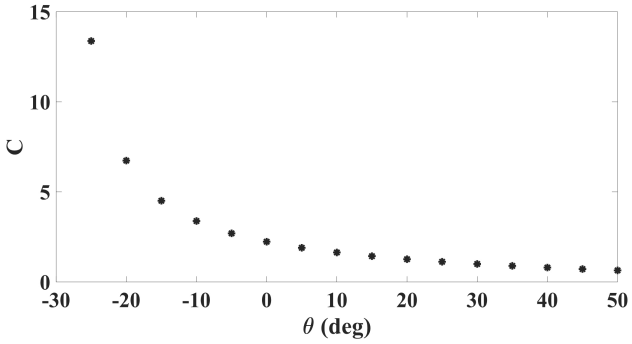

Figure 5.14 Variation of the Constant 'C' with the unit cell angular variable θ.

lower macrodomain edges are also opposite. Only the edge integral over the vertical boundaries remains, a result traduced by the last equality.

Considering the macro beam of Fig. 5.13, and as a result of the extended Hill macro homogeneity condition proven in Appendix M, S_{11} is a function of the struts crossing the boundaries. The number of boundary elements in the vertical direction along the macrodomain edges is crucial for determining the resultant bending moment from the previous analysis, quantity $M^M_{\text{Res}} := \sum_{k=1}^{N_H^{be}} M_k.e_3$ in Eq. 5.46. Utilizing Eq. 5.42 leads to the following double edge integral over the vertical boundary of the macro beam:

$$\begin{aligned} &M^M_{\text{Res}} = \int_A S_{11}(x_2)\frac{d\phi}{dx_1}dA = \int_{H^b} dx_2 \left\{ B\left(\int_{h^{UC}} \left(\frac{S_{11}}{h^{UC}}\right)\frac{d\phi}{dx_1}dx_2 \right) \right\}(X_2) \\ &dX_2/dx_2 = dH_b^{\text{hom}}/dh^{UC} \equiv Cf\left(l^*_{x_1}\right) \end{aligned} \tag{5.47}$$

wherein C is a constant, 'B' is the out-of-plane width of the macro beam and $f\left(l^*_{x_1}\right)$ is a function of the internal length $l^*_{x_1}$ defined in section 5.6.1. The height parameter H_b^{hom} is the effective height of the macro beam.

The constant 'C' involved in Eq. 5.47 is evaluated from fully resolved lattice bending FE simulations in ABAQUS software. 'C' is shown to decrease versus the angular variable θ, and it reaches the unity value for a regular hexagon. Considering the function $f\left(l^*_{x_1}\right) = \left(l^*_{x_1}\right)^2$, the last integral of Eq. 5.47 leads to the following scaling law of the resultant Cosserat bending moment:

$$M^M_{\text{Res}} \propto \frac{1}{2C}\left(\frac{S_{11}}{h^{UC}}\right)\left(\frac{H_b^{\text{hom}}}{l^*_{x_1}}\right)^2 B\frac{d\phi}{dx_1} \tag{5.48}$$

Substituting Eqs. 5.45 and 5.48 into relation 5.43 leads to the following relation for the bending moment of the extended macro Timoshenko beam as:

$$M_{\text{Res}} = \left(\mathrm{E}^{\text{hom}}_{x_1}\mathrm{I}_{x_1x_1} + \frac{1}{2}\left(\frac{S_{11}}{h^{UC}}\right)\left(\frac{H_b^{\text{hom}}}{l^*_{x_1}}\right)^2 B \right)\frac{d\phi}{dx_1} \tag{5.49}$$

The effect of the absolute lengths, angular variable θ and h/L ratio on the architected macro beam bending behavior will be investigated. In Eq. 5.49, the ratio $\left(H_b^{\text{hom}}/l^*_{x_1}\right)$ implicitly represents the number of unit cells on the vertical edge. The first term on the right-hand side of Eq. 5.49 is descriptive of Cauchy effects, while the second term describes Cosserat effects.

Computations of the macroscopic bending response of the macro beam with two configurations of the horizontal edges, one with full unit cell intersecting the macrodomain boundary and the other one

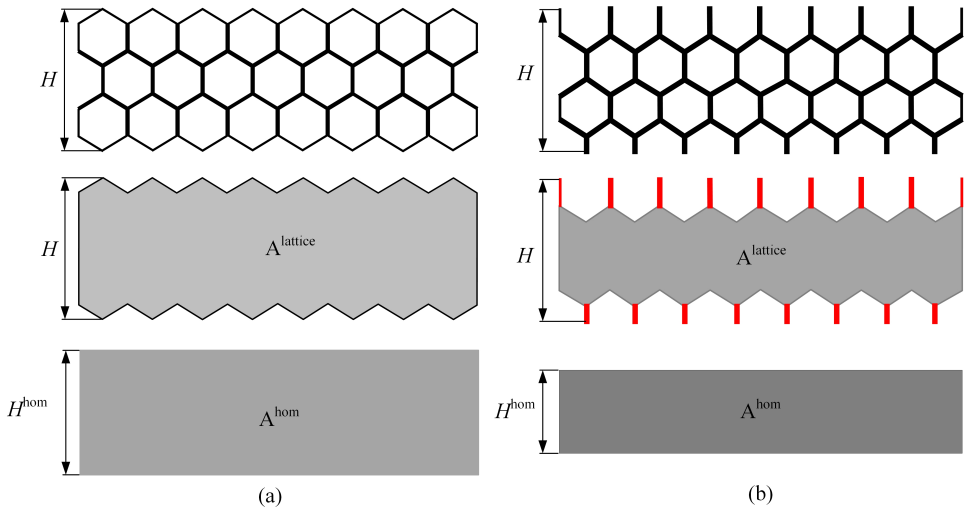

Figure 5.15 Representation of the homogenized area and height for (a) complete lattice, (b) cut edge lattice.

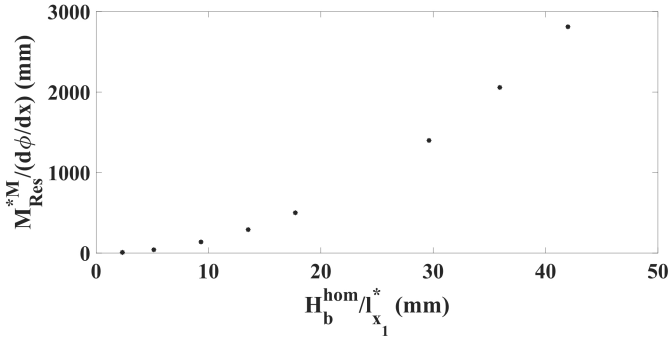

Figure 5.16 Variation of the normalized Cosserat bending moduli versus normalized height of the macro beam for a hexagonal unit cell of Table 5.5, based on fully resolved FE computations.

with cut edges, are next performed to assess edge effects (Fig. 5.15). A new homogenized lattice height denoted H^{hom} is introduced such that the effective domain with a zigzag horizontal edge (middle shape in Fig. 5.15(a)) is replaced by a rectangular domain of the same area $A^{\text{hom}} = A^{lattice}$. The truncated domain on Fig. 5.15(b) has floppy filaments on the horizontal edge, which do not contribute to the bending response and axial deformation (in red color in Fig. 5.15(b)); their contribution is accordingly removed on building the rectangular domain in Fig. 5.15(b). The Cosserat contribution to the overall bending moment in Eq. 5.49 is evaluated from lattice-based (fully resolved) FE bending computations (Fig. 5.16); it shows the quadratic increase predicted by the scaling law in Eq. 5.48 versus the number of unit cells within the ratio $\left(\frac{H_b^{\text{hom}}}{l^*_{x_1}}\right)$.

5.6.3.1 Effect of the unit cell geometrical parameters on the macro beam bending response

The benchmark examples of the honeycomb lattices are considered in a plane strain condition in order to underline the effect of the geometrical parameters of the unit cell, θ, h/L, and the absolute length L

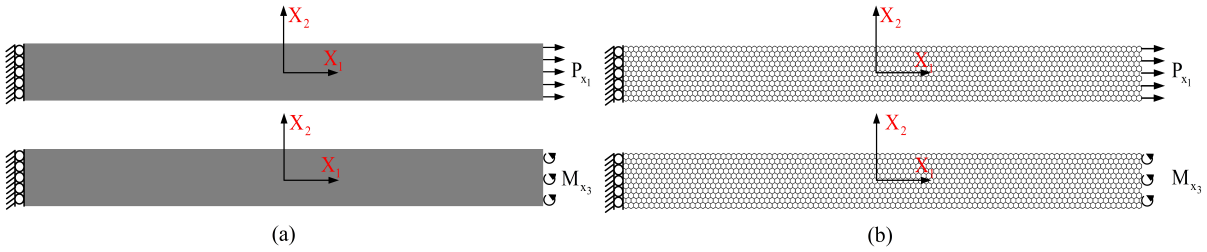

Figure 5.17 Architected macro beam comprising: (a) honeycomb unit cells and (b) the equivalent homogenized macro beam, under uniaxial (top view) and pure bending loads (bottom view).

on the macroscopic bending response of the macro beam. The lattice beam structure shown in Fig. 5.17 is considered, comprising $N_L^{be} \times N_H^{be}$ honeycomb unie cells. The left bottom corner is completely fixed to eliminate the effect of boundary conditions over the beam, but the other points on the left boundary are free to move vertically. Free boundary conditions are imposed at the bottom and top surfaces, and two different types of loading, a uniform axial load P_{x_1}, and a pure bending moment M_{x_3} are prescribed along the right surface to compute the effective Young's and Cosserat moduli, respectively. Two different loading conditions have been applied in Fig. 5.17(a), uniaxial loading, and pure bending.

The first load allows calculating the effective Young's modulus of the beam lattice by considering it as an effective homogenized beam (Fig. 5.17(b)). We compare the effective Young's modulus with that calculated at the unit cell level from the continualization method. The pure bending aims to compare the curvature of the macro-architected beam with that of the effective homogenized macro Timoshenko beam (Fig. 5.17(b)).

In the following examples, the varying parameters are indicated precisely in Table 5.6-5.9. The mechanical properties of the base material and other fixed geometrical parameters of the honeycomb unit cell are listed in Table 5.5, and the uniform axial load $P_{x_1} = 100$ N, and a pure bending moment $M_{x_3} = 100$ N.mm are prescribed over the beam's right boundary

Table 5.6 Effect of the absolute unit cell size in a macro beams comprising 440×13 unit cells, with a ratio $L^b/H^b = 20$. Error is the difference between the macro beam measured values of $\mathrm{E}^*_{x_1}$ and $l^*_{x_1}$, and those calculated by unit cell homogenization approach.

h = L	t (mm)	b (mm)	$l^*_{x_1}$	$\mathrm{E}^*_{x_1}$ $(\times 10^{-6})$	Error of $l^*_{x_1}$(%)	Error of $\mathrm{E}^*_{x_1}$ (%)	Cauchy contribution (%)	Cosserat contribution (%)
1	0.04	0.2	10.662	158.2	0.512	3	92.48	7.52
3	0.12	0.6	10.627	158.3	0.837	3.05	92.53	7.47
5	0.2	1	10.627	158.3	0.838	3.05	92.53	7.47
7	0.28	1.4	10.627	158.3	0.838	3.05	92.53	7.47
10	0.4	2	10.627	158.3	0.837	3.05	92.53	7.47

We have considered different macro beams with the same number of unit cells and the same aspect ratio. The absolute lengths of the comprising unit cell are changed to check the effect of the unit cell absolute size in the macro beam result. The dimensionless Young's modulus of the macro beam is shown as $\mathrm{E}^*_{x_1}$, and the error is computed by comparing this value to the one calculated by the continualization

method at the unit cell level. The internal bending length, variable $l^*_{x_1}$, is calculated using Eq. 5.49 (in which all values are known for the macro beam except $l^*_{x_1}$) and then the error is computed by comparing this value by the one calculated by the continualization method at the unit cell level. Table 5.6 highlights that the absolute size of the unit cell does not impact the macro beam properties identified from Eq. 5.49. Table 5.7 shows that the varying parameters θ and h/L do not affect the macro beam response when the number of unit cells at the vertical direction is constant and the macro beam aspect ratio is $L^b/H^b = 20$. Moreover, rotation of the unit cells within the macro beam by 90 degrees does not influence on the macroscopic Cauchy and Cosserat behavior of the beam (the modulus $E^*_{x_1}$ is replaced by $E^*_{x_2}$ and $l^*_{x_1}$ is replaced with $l^*_{x_2}$). Note that the situation of vanishing height 'h' describes the pantograph pictured in Fig. 5.2.

Table 5.7 Effect of the uit cell geometrical parameters in the response of the macro beam; Cauchy and Cosserat represent their percentage contributions, respectively.

$N_L^{be} \times N_H^{be}$	θ (deg)	Cauchy	Cosserat	$N_L^{be} \times N_H^{be}$	h/L	Cauchy	Cosserat
161×10	-10	91	9	555×10	2	90.5	9.5
190×10	0	90.7	9.3	445×10	1.5	90.5	9.5
228×10	10	90.5	9.5	335×10	1	90.5	9.5
275×10	20	90.5	9.5	225×10	0.5	90.6	9.4
335×10	30	90.5	9.5	115×10	0	90.5	9.5
416×10	40	90.5	9.5				
565×10	50	91	9				

5.6.3.2 Effect of the number of unit cells along vertical edge N_H^{be} on the macro beam response

In this section, we investigate the effect of the number of vertical unit cells in the macro beam bending response, namely parameter N_H^{be} and the aspect ratio of the macro beam L^b/H^b, using Eq. 5.49. The internal bending length identified from Eq. 5.49 shows a difference with the one obtained from the beam continualization, decreasing with the increasing number of unit cells in the vertical direction. The macro beam aspect ratio, L^b/H^b, does not impact the relative contribution of the micropolar bending moment. Results in Table 5.8 show that the accuracy of unit cell-based homogenized moduli for predicting the effective beam properties increases with the number of unit cells in height up to a stage where edge effects become negligible.

It should be noted that there are enough unit cell in the axial direction; this entails that the beam macroscopic behavior can be considered to be invariant in the axial direction. The sole Cauchy bending prediction is not sufficient to capture the bending response of the macro beam when the number of unit cells in the vertical direction is not high enough (here below 26) since the Cosserat bending modulus

Table 5.8 Effective Cauchy compliance components and Cosserat effective moduli. Error is the difference between the macro beam measured values of $\mathrm{E}^*_{x_1}$ and $l^*_{x_1}$, and those calculated by unit cell homogenization approach; Cauchy and Cosserat represent their percentage contributions, respectively.

$N_L^{be} \times N_H^{be}$	L^b/H^b	$l^*_{x_1}$	$\mathrm{E}^*_{x_1}$ $(\times 10^{-6})$	Error of $l^*_{x_1}$ (%)	Error of $\mathrm{E}^*_{x_1}$ (%)	Cauchy	Cosserat
30×2	10	9.74	202.8	11.41	32.01	59.55	40.45
60×2	20	9.74	202.95	11.41	32.1	59.55	40.45
125×4	20	10.28	173.96	6.45	13.24	77.61	22.39
230×7	20	10.49	163.92	4.52	6.7	86.57	13.43
335×10	20	10.58	160.23	3.74	4.3	90.4	9.6
445×13	20	10.63	158.3	3.29	3.05	92.53	7.47
360×22	10	11.19	155.72	1.82	1.37	94.99	5.01
445×26	10	10.94	155.6	0.43	1.29	96.02	3.98
520×30	10	11.01	153.47	0.19	0.1	98.4	1.6

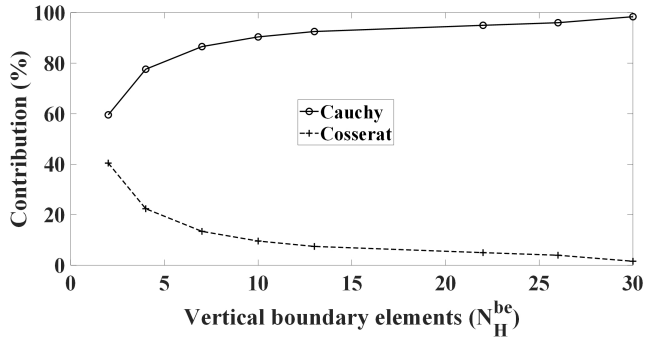

Figure 5.18 Contribution of the Cauchy and Cosserat bending moments in the pure bending response of the macro beam.

contribution to the total bending modulus of the macro beam still represents a non-negligible part of it. The plot of the relative contribution of the Cauchy and Cosserat bending moments in the pure bending of the macro beam, shown in Fig. 5.18, highlights that the Cosserat effect becomes vanishing importance for a high enough number of unit cells in the vertical direction. In this case, the pure classical, Cauchy-induced bending response in Eq. 5.45 becomes sufficient for capturing the macro beam response.

The following example investigates the effect of the number of vertical unit cells in the bending response of a macro beam with cut edges unit cells. The importance of edge effects is decisive for a low number of unit cells. It decreases to a negligible amount for the number of uit cells in a vertical direction higher than 30, as shown in Table 5.9.

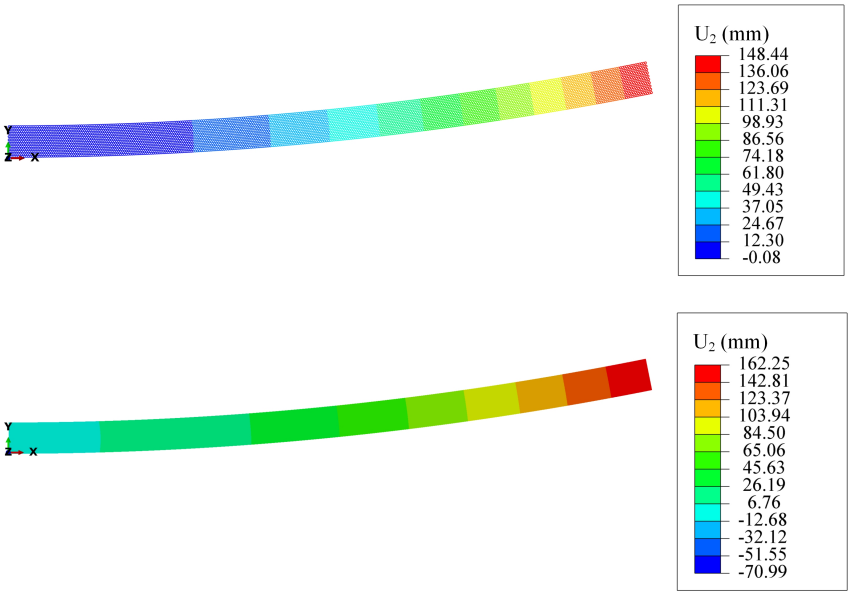

Figure 5.19 Vertical displacement contour of a cantilever (top) Hexagon lattice beam with 335×10 unit cells, (bottom) Homogeneous beam, under pure bending moment $M_{x_3} = 100$ N.mm.

Table 5.9 Effective Cauchy compliance components and Cosserat effective moduli for a macro beam with cut edges unit cells. Error is the difference between the macro beam measured values of $\mathrm{E}^*_{x_1}$ and $l^*_{x_1}$, and those calculated by unit cell homogenization approach; Cauchy and Cosserat represent their percentage contributions, respectively.

$N_L^{be} \times N_H^{be}$	L^b/H^b	$l^*_{x_1}$	$\mathrm{E}^*_{x_1}$ $(\times 10^{-6})$	Error of $l^*_{x_1}$(%)	Error of $\mathrm{E}^*_{x_1}$ (%)	Cauchy	Cosserat
30×2	10	9.275	215.909	15.58	43.61	50.06	49.94
60×4	10	10.534	169.352	4.123	12.64	75.27	24.73
115×7	10	10.88	157.887	0.97	5.01	85.82	14.18
168×10	10	10.983	154.052	0.037	2.46	90.03	9.97
223×13	10	11.001	152.175	0.127	1.22	92.27	7.73
360×22	10	10.956	149.966	0.283	0.26	95.33	4.67
445×26	10	10.969	149.785	0.164	0.38	96.02	3.98
520×30	10	10.98	150.04	0.064	0.21	98.4	1.6

The bending response of the homogeneous beam is compared to that of the architected beam comprising 335×10 unit cells with the geometrical and mechanical parameters indicated in Table 5.5. Fig. 5.19 shows a relative difference of maximum displacement (at the beam right end) of about 9%, corresponding to the Cosserat contribution to the bending moment, referring to Table 5.8.

5.7 Discussion

In summary, the main thrust of the chapter and the principal results are the following ones:

- The developed beam mechanics based on the continualization method towards Cosserat media proves to be much more efficient than continuous homogenization schemes due to the finite number of degrees of freedom of the inherent formulation. The proposed method combines the continualization of the discrete lattice modeling with the continuous kinematic and static description of the effective posited Cosserat medium, relying on the extended Hill energy equivalence between the micro and macro scales (Appendix L). Discrete homogenization leads as a chief advantage over continuous homogenization schemes to a closed-form expression of classical and Cosserat moduli versus the unit cell geometrical and mechanical parameters. The closed-form expression of the Cosserat moduli has been exploited to provide a sensitivity analysis of the micro geometrical parameters on these moduli and internal bending lengths.
- We provide constructive proof of Hill's macrohomogeneity condition for the effective Cosserat continuum, underlining the continuous static variables conjugated to the introduced kinematic variables. Moreover, the macroscopic stress tensors have been formulated as surface integrals over the unit cell boundary.
- The effective moduli obtained by the continualization method have been predicted with reasonable accuracy, as revealed by comparison with fully resolved FE computations implementing PBCs over the honeycomb unit cell for calculating both classical and Cosserat properties. Polynomial higher-order kinematic loadings are applied over the unit cell boundaries to capture the Cosserat properties.
- The provided sensitivity analyses show that Cosserat effects proved to be significant at the unit cell level over the entire range of considered parameters, following the fact that the hexagon lattice is bending-dominated. The computed internal bending length may rise to 8 times the unit cell size. These Cosserat effects account for the pronounced bending response of the hexagonal unit cell, reflecting in the enhanced kinematics of the effective continuum (the microrotation emerges as an additional DOF) and the existence of a bending rigidity controlled by the (bending) internal length.
- The importance of micropolar effects has been analyzed at the upper scale of a macro beam under pure bending, revealing the importance of micropolar edge effects, relying on the surface formulation of the extended Hill macrohomogeneity condition proven in Appendix M. The bending moment to curvature relation involves a classical term and a micropolar bending moment (controlled by a micropolar modulus and some geometrical parameters). The importance of this last one is decreasing asymptotically up to a nil value by increasing the number of unit cells within the macrodomain. The essential geometrical determining parameter quantifying the Cosserat effects at the macroscale is the number of unit cells in the height of the macro beam.

- Edge effects arise from truncation of the unit cell edges (these stress-free cut edges do not contribute to the overall mechanical response) crossing the external domain boundary. Edge effects are incorporated into our formulation by introducing an effective height accounting for the actual amount of lattice material within the macro domain, such that the macro bending modulus will be reduced. The additional higher-order stiffness is needed to adequately capture the macro beam bending response, which is always positive. In contrast, some authors [136,139] introduce softening effects associated with a negative higher-order rigidity to account for edge effects (a negative higher-order stiffness corrects Cauchy contribution to the overall beam response). Our analysis shows that this is incorrect due to the lack of consideration of the appropriate, effective height of the considered architected macrostructure.
- Experimental results with bending tests [133] show a significant increase of the bending rigidity when the beam thickness is reduced, the departure from the conventional bending solution arising below a thickness of 80 μm. This effect is attributed in the opinion of [133] to the decisive importance of strain gradient effects for the selected beam dimensions. These last authors invoke a microscopic internal length, but they do not consider the impact of lattice topology and the number of unit cells within the macro beam domain. Our analysis shows that such arising size effects are partly due to the material higher-order effects triggered by the Cosserat moduli, but most importantly, the number of unit cells within the macro beam height.
- The proposed analysis of size effects provides a sound and rationale methodology to design experimental protocols for testing and measuring Cosserat and size effects in lattice materials in future developments.

5.8 Conclusion

This chapter addresses the efficient and accurate computation of repetitive lattice materials' effective classical and high order moduli. The continualization method has been employed on the adopted beam mechanics description at the unit cell level to obtain the effective Cosserat continuum model considered at the macroscale. Closed-form expressions of the effective moduli versus the microstructural geometrical and mechanical lattice parameters have been obtained for the honeycomb lattices. Comparing these discrete homogenization predictions of the moduli with fully resolved unit cell-based FE computations has revealed an excellent accuracy of the proposed continualization scheme. The existing differences are due to the mesh's fineness and can be reduced by increasing the number of nodes along the lattice struts.

Beyond achieving a closed-form expression of the effective properties, the chief advantage of beam mechanics at the micro level over continuous homogenization schemes (chapters 2 and 4) lies in its much lower numerical cost due to the finite number of DOFs (whereas FE based method involve an infinite number of DOFs). We have performed sensitivity analyses of the effective computed moduli, internal bending lengths, and relative density to plot their contours in a plane sustained by two configuration

variables of the lattice. These contour plots will prove helpful as design guides to tune the lattice geometry to reach targeted properties. The Cosserat effects prove significant over the entire range of considered parameters; this reflects that the hexagon is bending-dominated so that nodal rotations are translated into a field of microrotation at the macroscale.

As the main conclusion of this chapter, edge effects play an essential role in the macro beam response. A classical Timoshenko beam can model the homogenized macro beam for a high enough number of unit cells in the vertical direction. In contrast, Cosserat effects have to be considered when the number of unit cell in the same vertical directions is not high enough.

We have restricted this chapter to considering an effective micropolar continuum to reflect the bending-dominated response of the selected honeycomb. However, standard micropolar models may be inadequate for lattices witnessing complex couplings between deformation modes, especially to capture the rotational-stretching coupling mechanisms arising in chiral microstructures, as underlined in [111] and references therein. The micromorphic continuum offers a more general framework to efficiently capture both rotation and distorsion effects [111] and chapter 3. These considerations will deserve future developments.

Part III

Continuous homogenization methods for quasi-periodic media and case of conformal transformations of the geometry

Chapter 6

Homogenization of quasi-periodic heterogeneous materials and applications to functionally graded materials

Summary

We extend the asymptotic homogenization method for quasi-periodic continuous media, assuming that the initial non-periodic geometry can be mapped to a periodic parent domain in which a periodic unit cell can be identified. The theoretical background underlying quasi-periodic asymptotic homogenization in the framework of linearized anisotropic elasticity is exposed in the first part of the chapter. Different methodologies for evaluating the effective quasi-periodic properties are developed; when assimilating the heterogeneous unit cells to their effective homogeneous media, the tensors of effective periodic and quasi-periodic moduli can be directly related, bypassing the need to solve the unit cell BVP in either periodic or quasi-periodic domains. The second class of more advanced strategies relies on a mapping of the periodic unit cell problem onto the quasi-periodic unit cell problem, whereby the microstructural strain fluctuation within the unit cell is taken into account by solving a localization problem at the unit cell level before evaluating the tensor of quasi-periodic effective moduli. In both strategies, the extended quasi-periodic Hill macrohomogeneity condition plays a prominent role.

6.1 Introduction

Two methods can be followed for the derivation of the quasi-periodic properties: in the first class of methods, the unit cell $\mathrm{Y} = \mathrm{Y}(\mathrm{x})$ depends on the macroscale position, thus one may write the dependency of the tensor of microscopic moduli into the form $\boldsymbol{C}^{\varepsilon}(\boldsymbol{x}) = \boldsymbol{C}\left(\boldsymbol{x}, \frac{\eta(\boldsymbol{x})}{\eta}\right)$, with $\varphi(\boldsymbol{x})$ a smooth diffeomorphism, with the meaning that $\boldsymbol{C}$ is still periodic in the second variable, provided the quasi-periodic variable is mapped by $\varphi(\boldsymbol{x})$ to a periodic one. In this case, the image of the periodic unit cell by function φ^{-1} will depend on the macroposition $\boldsymbol{x}$. The second class of methods transforms the BVP posed over the quasi-periodic domain over a periodic parent domain, e.g., using a parameterization change like in [234]. This way, a periodic BVP is still formulated with an apparently modified tensor of microscopic moduli, which can further be expanded versus the small-scale parameter. The assumption of a quasi-affine geometrical transformation done in [234] allows to formulate the unit cell BVP as the periodic one, by extracting a term function of the sole macroscopic variable. Doing so amounts neglecting the grading within neighbouring unit cells and considering a variation of the effective properties due to the sole macroscale variation of the unit cell geometry.

The present chapter aims to develop a theory of quasi-periodic homogenization accounting for macroscopic and microscopic geometry variations. The elaboration of a second gradient effective model is a way to account for the variation of microgeometry within the unit cell when elaborating models to be incorporated at the macroscale of the composite. This work's main objective is to develop a suitable higher-order homogenization framework for quasi-periodic microstructures so that the tensor of effective moduli of the quasi-periodic design can, in turn, be evaluated from that of a parent design of a macrostructure tessellated with periodic unit cells.

More precisely, the following scientific questions are addressed:

(i) Can one extend the classical framework of periodic asymptotic homogenization to quasi-periodic microstructures, based on some assumptions on the smoothness of a mapping of the quasi-periodic microstructure onto a periodic parent domain?

(ii) In the context of such an extension, can one formally and numerically relate the tensor of effective quasi-periodic moduli to those of the parent periodic microstructure and under what conditions?

(iii) What are the possible mappings satisfying the kinematic compatibility conditions needed to generate a locally and globally compatible design from an initially periodic domain?

(iv) Can one establish a classification of arising subcases of quasi-periodic homogenization, including conformal transformations and quasi-affine mappings?

The main thrust of the chapter is to elaborate on a general theory of quasi-periodic homogenization based on double-scale asymptotic expansion. It extends the well-established theory of asymptotic homogenization for periodic media to heterogeneous media having a non-periodic although regular microstructure, for which the notion of effective mechanical properties still makes sense. As an outcome of the developed theory, several schemes for the computation of the effective properties based on periodic

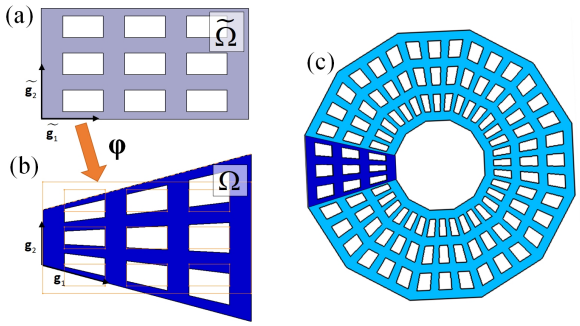

Figure 6.1 (a) Illustration of the transformation introduced in the present approach, defined by a mapping $\boldsymbol{\varphi}$ between the perfectly periodic domain $\tilde{\omega}$ (b) A quasi-periodic domain, (c) aiming at studying more complex special domains.

parent material are developed, considering the class of functionally graded materials.

The chapter is organized as follows: the classical theory of periodic homogenization of heterogeneous materials is shortly exposed in section 6.2, relying on the double scale asymptotic homogenization method. It will be the basis for its extension towards structures exhibiting a regular in space but non-strictly periodic microstructure that can be mapped to a periodically organized microstructure using a geometrical transformation. A general double scale asymptotic theory of quasi-periodic homogenization is expanded in section 6.3, whereby different formulations are proposed and specific situations are analyzed. The smoothness condition of quasi-periodic mapping is considered in section 6.4 wherein criteria for the adopted geometrical design mappings are set.

6.2 General properties of quasi-periodic homogenization

A quasi-periodic structure is defined as a structure with a well-identified unit cell (the basic pattern), which is repeated in space but with varying geometry. The macrostructure is thus no longer macroscopically homogeneous: since the macroscopic heterogeneity also impacts the microstructure, the effective mechanical properties of the unit cell depend on its varying dimensions at the macroscale.

6.2.1 Preliminary steps

The main idea of the proposed homogenization method is to map the non-periodic domain into an exactly periodic one as illustrated in Fig. 6.1, onto which homogenization can be performed as reminded in previous section. We assume that the parent unit cell and its periodic transform are related by a mapping $Y = \varphi\left(\tilde{Y}\right) \Leftrightarrow \tilde{Y} = \varphi^{-1}\left(Y\right)$.

It is convenient to introduce the transition mapping between two systems of coordinates as the one-to-one point mapping $\tilde{\boldsymbol{x}} \mapsto \boldsymbol{x} = \boldsymbol{\varphi}(\tilde{\boldsymbol{x}})$ from the periodic parent domain to the quasi-periodic domain. This entails the existence of a system of coordinates $\tilde{\boldsymbol{x}} = \varphi^{-1}\left(\boldsymbol{x}\right)$ on the parent periodic domain. Note that both microscopic and macroscopic scales will be affected by this geometrical transformation of coordinates.

The point mapping is simplified to its tangent $\boldsymbol{A}(\tilde{\boldsymbol{x}}) := \nabla_{\tilde{\boldsymbol{x}}}\boldsymbol{\varphi}(\tilde{\boldsymbol{x}})$, which maps 'small' vectors from the periodic domain $\tilde{\Omega}$ to 'small' vectors in the quasi-periodic domain Ω. Let call

$$\boldsymbol{A} := \nabla_{\tilde{x}}\boldsymbol{\varphi} = \nabla_{\tilde{x}}\boldsymbol{x} \Leftrightarrow A^i_{.j} = \frac{\partial x^i}{\partial \tilde{x}^j} = A^i_{.j}(\tilde{\boldsymbol{x}}) \tag{6.1}$$

the tangent mapping of (tangent) vectors in the quasi-periodic domain to (tangent) vectors in the periodic parent domain; it is supposed to admit an inverse mapping with components

$$\frac{\partial \tilde{x}^p}{\partial x^q} = \tilde{x}^p_{.,q} \equiv \left(A^{-1}\right)^p_{.q}(\boldsymbol{x}) \tag{6.2}$$

In the present context of periodic homogenization, the microstructure is defined within a RVE, which generates the entire macrodomain by periodic translation (section 3.2).

We will use in the sequel the transformation of the coordinates under the effect of the mapping between the quasi-periodic and periodic configurations (Fig. 6.1). In order to set the stage, we recall the transformation rules for vectors and tensors. The volume element transforms as

$$\begin{aligned} &d\boldsymbol{x} = \nabla_{\tilde{x}}\boldsymbol{\varphi}.d\tilde{\boldsymbol{x}} \rightarrow dV_x = \det\left(\nabla_{\tilde{x}}\boldsymbol{\varphi}\right) dV_{\tilde{x}} = JdV_{\tilde{x}} \\ &J := \det\left(\nabla_{\tilde{x}}\boldsymbol{\varphi}\right) \end{aligned} \tag{6.3}$$

In the subsequent weak form of the BVP, depending on the utilized quasi-periodic homogenization matter, the integrals are expressed in the periodic parent domain or in the transformed quasi-periodic domain, over which homogenization can be performed. As a prerequisite for the elaboration of a quasi-periodic homogenization theory to follow, the classical asymptotic homogenization theory of periodic media is exposed synthetically in the following subsection.

6.2.2 A reminder of asymptotic homogenization of periodic media

The BVP to be solved writes over the periodic unit cell as follows:

$$\left|\begin{aligned} &\tilde{C}_{rpqs}\tilde{u}_{s,pq} + \tilde{b}_r = 0 \Leftrightarrow div_{\tilde{x}}\left(\tilde{\boldsymbol{C}} : \tilde{\nabla}\tilde{\boldsymbol{u}}\right) + \tilde{\boldsymbol{b}}_r = \boldsymbol{0} \\ &\tilde{\boldsymbol{u}} = \boldsymbol{A}^T.\boldsymbol{u} \\ &\tilde{\sigma}_{ij} = \tilde{C}_{ijkl}(\nabla d_{\tilde{x}}\tilde{\boldsymbol{u}})_{kl} = \tilde{C}_{ijkl}\tilde{\eta}_{kl} \Leftrightarrow \tilde{\boldsymbol{\sigma}} = \tilde{\boldsymbol{C}} : \tilde{\boldsymbol{\varepsilon}} \end{aligned}\right. \tag{6.4}$$

Note that the mapping of the displacement, relation $\tilde{\boldsymbol{u}} = \boldsymbol{A}^T.\boldsymbol{u}$, needed to reach a consistent formulation, corresponds to an active transformation. It represents the freedom of mapping the displacement between both domains, otherwise called gauge freedom in the literature on the topic [235]; [236]. The gauge is here fixed by selecting the mapping such that the BVP of linear anisotropic elasticity remains invariant and with the same stiffness coefficients. A double scale asymptotic homogenization is next performed over the periodic domain (in which homogenization can be done), considering the macroscale and microscale variables so that all fields depend now on the two-scale variables. The classical multiscale derivative rule is used for a function f^η depending on the small-scale parameter η (ratio of the unit cell size to a characteristic macroscopic dimension); it allows for any field expressing the derivative of any function in

the periodic domain when considered as a function of both scale variables:

$$f^{\eta}\left(\tilde{\boldsymbol{x}}\right)=f^{\eta}\left(\tilde{\boldsymbol{x}},\tilde{\boldsymbol{y}}=\frac{\tilde{\boldsymbol{x}}}{\eta}\right)\Rightarrow\frac{df^{\eta}\left(\tilde{\boldsymbol{x}}\right)}{d\tilde{\boldsymbol{x}}}=\frac{\partial f^{\eta}}{\partial\tilde{\boldsymbol{x}}}+\frac{1}{\eta}\frac{\partial f^{\eta}}{\partial\tilde{\boldsymbol{y}}} \tag{6.5}$$

One looks for a periodic displacement and stress tensor written in asymptotic expansion form as

$$\begin{aligned}\tilde{\boldsymbol{u}}^{\eta}(\tilde{\boldsymbol{x}})&=\tilde{\boldsymbol{u}}^{0}(\tilde{\boldsymbol{x}})+\eta\tilde{\boldsymbol{u}}^{1}(\tilde{\boldsymbol{x}},\frac{\tilde{\boldsymbol{x}}}{\eta})+\eta^{2}\tilde{\boldsymbol{u}}^{2}(\tilde{\boldsymbol{x}},\frac{\tilde{\boldsymbol{x}}}{\eta})+...\\\tilde{\boldsymbol{\sigma}}^{\eta}(\tilde{\boldsymbol{x}})&=\tilde{\boldsymbol{\sigma}}^{0}(\tilde{\boldsymbol{x}})+\eta\tilde{\boldsymbol{\sigma}}^{1}(\tilde{\boldsymbol{x}},\frac{\tilde{\boldsymbol{x}}}{\eta})+\eta^{2}\tilde{\boldsymbol{\sigma}}^{2}(\tilde{\boldsymbol{x}},\frac{\tilde{\boldsymbol{x}}}{\eta})+...\end{aligned} \tag{6.6}$$

Classical developments deliver the following unit cell BVP at the successive orders η^{-1},η^{0} for the searched solutions $\tilde{\boldsymbol{u}}^{0},\tilde{\boldsymbol{u}}^{1}$:

$$\left|\begin{array}{l}\nabla^{S}{}_{\tilde{y}}\tilde{\boldsymbol{u}}^{0}\left(\tilde{\boldsymbol{x}},\tilde{\boldsymbol{y}}\right)=\boldsymbol{0}\Rightarrow\tilde{\boldsymbol{u}}^{0}\left(\tilde{\boldsymbol{x}},\tilde{\boldsymbol{y}}\right)=\tilde{\boldsymbol{u}}^{0}\left(\tilde{\boldsymbol{x}}\right)\\div_{\tilde{y}}\tilde{\boldsymbol{\sigma}}^{0}\left(\tilde{\boldsymbol{x}},\tilde{\boldsymbol{y}}\right)=\boldsymbol{0}\\\tilde{\boldsymbol{\sigma}}^{0}\left(\tilde{\boldsymbol{x}},\tilde{\boldsymbol{y}}\right)=\tilde{\boldsymbol{C}}\left(\tilde{\boldsymbol{y}}\right):\tilde{\boldsymbol{\varepsilon}}^{0}\left(\tilde{\boldsymbol{x}},\tilde{\boldsymbol{y}}\right)\\\tilde{\boldsymbol{\varepsilon}}^{0}\left(\tilde{\boldsymbol{x}},\tilde{\boldsymbol{y}}\right):=\nabla_{\tilde{x}}\tilde{\boldsymbol{u}}^{0}\left(\tilde{\boldsymbol{x}}\right)+\nabla_{\tilde{y}}\tilde{\boldsymbol{u}}^{1}\left(\tilde{\boldsymbol{x}},\tilde{\boldsymbol{y}}\right)\\\tilde{\boldsymbol{u}}^{1}\tilde{Y}-periodic,\,\tilde{\boldsymbol{\sigma}}^{0}.\boldsymbol{n}\text{ antiperiodic}\end{array}\right. \tag{6.7}$$

Using the anti-periodicity condition of the traction vector $\tilde{\boldsymbol{\sigma}}^{1}.\boldsymbol{n}$, the weak form of the balance of linear momentum at first order of the small scale parameter over the unit cell delivers:

$$\int_{\tilde{Y}}div_{\tilde{y}}\tilde{\boldsymbol{\sigma}}^{0}d\tilde{V}_{y}=\boldsymbol{0} \tag{6.8}$$

By linearity of the previous BVP, one can express the solution $\tilde{\boldsymbol{u}}^{1}$ using the third-order tensor $\boldsymbol{H}^{E}\left(\tilde{\boldsymbol{y}}\right)$ of displacement localization (up to a macroscopic displacement that will be discarded here):

$$\begin{aligned}&\tilde{\boldsymbol{u}}^{1}\left(\tilde{\boldsymbol{y}}\right)=\boldsymbol{H}^{E}\left(\tilde{\boldsymbol{y}}\right):\tilde{\boldsymbol{E}}^{0}\left(\tilde{\boldsymbol{x}}\right)+\tilde{\boldsymbol{U}}^{1}\left(\tilde{\boldsymbol{x}}\right),\\&\tilde{\boldsymbol{E}}^{0}\left(\tilde{\boldsymbol{x}}\right):=\nabla^{S}{}_{\tilde{x}}\tilde{\boldsymbol{u}}^{0}\left(\tilde{\boldsymbol{x}}\right)\end{aligned} \tag{6.9}$$

with $\tilde{\boldsymbol{U}}^{1}\left(\tilde{\boldsymbol{x}}\right)$ a macroscopic displacement resulting from the integration of the set of Eq. 6.9. The unit cell BVP writes by linearity versus the kinematic loading $\tilde{\boldsymbol{E}}^{0}\left(\tilde{\boldsymbol{x}}\right)$:

$$\left|\begin{array}{l}div_{\tilde{y}}\left(\tilde{\boldsymbol{C}}:\left(\boldsymbol{I}_{4}+\nabla_{\tilde{y}}\boldsymbol{H}^{E}\left(\tilde{\boldsymbol{y}}\right)\right)\right):\tilde{\boldsymbol{E}}^{0}\left(\tilde{\boldsymbol{x}}\right)+\tilde{\boldsymbol{b}}=\boldsymbol{0}\\\boldsymbol{H}^{E}\left(\tilde{\boldsymbol{y}}\right)\text{ periodic}\end{array}\right. \tag{6.10}$$

with $\boldsymbol{I}_{4}$ the fourth-order identity tensor. Previous BVP leads to the tensor of homogenized moduli given by

$$\tilde{\boldsymbol{C}}^{hom}=\left\langle\tilde{\boldsymbol{C}}:\left(\boldsymbol{I}_{4}+\nabla_{\tilde{y}}\boldsymbol{H}^{E}\left(\tilde{\boldsymbol{y}}\right)\right)\right\rangle_{\tilde{Y}} \tag{6.11}$$

Defining the strain localization function $\tilde{\boldsymbol{A}}^{E}$ as

$$\tilde{\boldsymbol{A}}^{E}:=\boldsymbol{I}_{4}+\nabla_{\tilde{y}}\boldsymbol{H}^{E}\left(\tilde{\boldsymbol{y}}\right) \tag{6.12}$$

Moreover, considering the Eqs. 6.9 - 6.12, the homogenized tensor $\tilde{\boldsymbol{C}}^{hom}$ of the periodic parent domain therein relates the average stress to the average strain $\tilde{\boldsymbol{E}}^{0}\left(\tilde{\boldsymbol{x}}\right)$ in the form (dependency of the fields on

their arguments is dropped here):

$$\tilde{\boldsymbol{\Sigma}}^0 := \left\langle \tilde{\boldsymbol{\sigma}}^0 \right\rangle_{\tilde{Y}} := \frac{1}{|\tilde{Y}|} \int_{\tilde{Y}} \tilde{\boldsymbol{\sigma}}^0 d\tilde{V}_y = \left\langle \tilde{\boldsymbol{C}} : \left(\boldsymbol{I}_4 + \nabla_{\tilde{y}} \boldsymbol{H}^E \left(\tilde{\boldsymbol{y}} \right) \right) \right\rangle_{\tilde{Y}} : \tilde{\boldsymbol{E}}^0 \equiv \left\langle \tilde{\boldsymbol{C}} : \tilde{\boldsymbol{A}}^E \right\rangle_{\tilde{Y}} : \tilde{\boldsymbol{E}}^0 = \tilde{\boldsymbol{C}}^{hom} : \tilde{\boldsymbol{E}}^0 \quad (6.13)$$

The tensor of effective moduli introduced in Eq. 6.13 is classically given by the average product of the microscopic rigidity tensor with the fourth-order strain localization operator $\boldsymbol{A}^E \left(\tilde{\boldsymbol{y}} \right)$. A more symmetrical form of the tensor of effective Cauchy moduli can easily be obtained, reflecting the inherent major and minor symmetries of $\tilde{\boldsymbol{C}}^{hom}$:

$$\tilde{\boldsymbol{C}}^{hom} = \left\langle \left(\tilde{\boldsymbol{A}}^E \right)^T : \tilde{\boldsymbol{C}} : \tilde{\boldsymbol{A}}^E \right\rangle_{\tilde{Y}} \quad (6.14)$$

The period is assumed to vary in its geometry slowly at the macroscale, a condition to be set in the sequel by an asymptotic expansion of the quasi-periodic domain versus the parent (periodic) domain. Note that the quasi-periodicity of the geometry shall be distinguished from the quasi-periodicity of the constitutive law, which would imply that the microscopic properties experience a macroscopic spatial variation in addition to microscopic dependency thus $\boldsymbol{C} = \boldsymbol{C}^\eta \left(\boldsymbol{x}, \frac{\boldsymbol{x}}{\eta} \right) = \boldsymbol{C}^0 \left(\boldsymbol{x}, \frac{\boldsymbol{x}}{\eta} \right) + \eta \boldsymbol{C}^1 \left(\boldsymbol{x}, \frac{\boldsymbol{x}}{\eta} \right) + ...$ We will not consider such variation of microscopic properties in this contribution but focus on the sole effect of a variation of the unit cell geometry.

6.3 Quasi-periodic homogenization

In this section, two main alternative methods for the derivation of the tensor of effective quasi-periodic moduli versus those of the periodic parent domain will be exposed. The first method relies on the relation between the average unit cell energies in periodic and quasi-periodic domains; the second method relies on relating the BVP within the quasi-periodic unit cell to the periodic BVP written in the parent (periodic) unit cell. In order to set the stage, we elaborate the mappings of the microscopic displacement gradient and stress tensors from the periodic domain to its quasi-periodic counterpart.

6.3.1 Preliminary steps

The microscopic periodic position in the physical domain is split in vector format into a macroscopic position of the center of the area $\tilde{\boldsymbol{x}}$ and a microscopic position $\tilde{\boldsymbol{y}}$ representing the relative position around the center of the area, pictured in Fig. 6.2:

$$\begin{aligned} &\tilde{\boldsymbol{y}} = \tilde{\boldsymbol{x}}/\eta \Rightarrow d\tilde{\boldsymbol{y}} = d\tilde{\boldsymbol{x}}/\eta \Rightarrow \\ &\left| \begin{aligned} &d\boldsymbol{x} \left(\tilde{\boldsymbol{x}} \right) = \nabla_{\tilde{\boldsymbol{x}}} \left(\boldsymbol{x} = \boldsymbol{\varphi}_{\tilde{x}} \left(\tilde{\boldsymbol{x}} \right) \right) . d\tilde{\boldsymbol{x}} \\ &\frac{d\boldsymbol{y}}{d\tilde{\boldsymbol{x}}} \left(\tilde{\boldsymbol{x}}, \tilde{\boldsymbol{y}} = \tilde{\boldsymbol{x}}/\eta \right) = \nabla_{\tilde{\boldsymbol{x}}} \boldsymbol{y} + \eta^{-1} \nabla_{\tilde{y}} \boldsymbol{y} \end{aligned} \right. \end{aligned} \quad (6.15)$$

One then identifies from Eq. 6.15 the following differential relations of the order η^0 of position vectors in periodic and quasi-periodic domains

$$\left| \begin{aligned} &d\boldsymbol{x} = \nabla_{\tilde{\boldsymbol{x}}} \boldsymbol{\varphi}_{\tilde{x}} \left(\tilde{\boldsymbol{x}} \right) . d\tilde{\boldsymbol{x}} \\ &d\boldsymbol{y} = \nabla_{\tilde{\boldsymbol{x}}} \boldsymbol{y} . d\tilde{\boldsymbol{x}} + \nabla_{\tilde{y}} \boldsymbol{y} . d\tilde{\boldsymbol{y}} \end{aligned} \right. \quad (6.16)$$

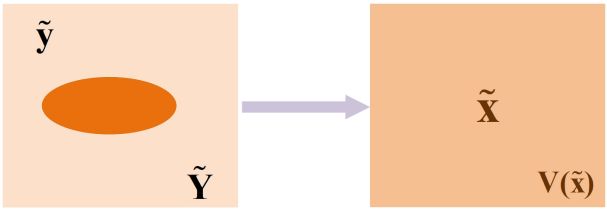

Figure 6.2 (left) Composite periodic unit cell of made of two elastic materials, (right)The homogeneous substitution medium. The inner material could be an inclusion or void in case of an architected material. Non-connected constituents can be envisaged.

relations 6.15 and 6.16 lead to the following global tangent map:

$$\begin{aligned}
&\left|\frac{d\boldsymbol{y}^{\eta}\left(\tilde{\boldsymbol{x}}\right)}{d\tilde{\boldsymbol{x}}}=\frac{\partial \boldsymbol{y}^{\eta}}{\partial \tilde{\boldsymbol{x}}}+\frac{1}{\eta}\frac{\partial \boldsymbol{y}^{\eta}}{\partial \tilde{\boldsymbol{y}}}\right. \Rightarrow \eta d\boldsymbol{y}\left(\tilde{\boldsymbol{x}},\tilde{\boldsymbol{y}}=\tilde{\boldsymbol{x}}/\eta\right)=\left(\eta\nabla_{\tilde{\boldsymbol{x}}}\boldsymbol{y}.d\tilde{\boldsymbol{x}}+\nabla_{\tilde{\boldsymbol{y}}}\boldsymbol{y}.d\eta\tilde{\boldsymbol{y}}\right)\\
&\Rightarrow\begin{pmatrix} d\boldsymbol{x} \\ \eta d\boldsymbol{y}\end{pmatrix}=\begin{pmatrix}\nabla_{\tilde{\boldsymbol{x}}}\varphi_{\tilde{x}}\left(\tilde{\boldsymbol{x}}\right) & \boldsymbol{0}\\ \eta\nabla_{\tilde{\boldsymbol{x}}}\boldsymbol{y} & \nabla_{\tilde{y}}\boldsymbol{y}\end{pmatrix}.\begin{pmatrix} d\tilde{\boldsymbol{x}} \\ \eta d\tilde{\boldsymbol{y}}\end{pmatrix}=\boldsymbol{A}\left(\tilde{\boldsymbol{x}},\tilde{\boldsymbol{y}}\right).\begin{pmatrix} d\tilde{\boldsymbol{x}} \\ \eta d\tilde{\boldsymbol{y}}\end{pmatrix}
\end{aligned} \tag{6.17}$$

The microscopic spatial position in the periodic unit cell $\tilde{\boldsymbol{y}}$ has been de-zoomed so that it can be defined in the same unit cell of the center of gravity $\tilde{\boldsymbol{x}}$ as a microscopic position vector with respect to the center of the area of the unit cell. The geometrical point mapping between macroscopic and microscopic variables in both periodic and quasi-periodic unit cells is a matter of choice of the designer.

A vector including macroscopic and microscopic spatial positions $\begin{pmatrix} d\tilde{\boldsymbol{x}} & \eta d\tilde{\boldsymbol{y}}\end{pmatrix}$ is then elaborated in the periodic unit cell, which is mapped to a corresponding vector $\begin{pmatrix} d\boldsymbol{x} & \eta d\boldsymbol{y}\end{pmatrix}$ in the quasi-periodic domain. Eq. 6.16 leads to a decomposition of the tangent into the sum of macroscopic and microscopic tangents, respectively $\boldsymbol{A}_M\left(\tilde{\boldsymbol{x}}\right)$ and $\boldsymbol{A}_m\left(\tilde{\boldsymbol{x}},\tilde{\boldsymbol{y}}\right)$. With $\boldsymbol{A}_M\left(\tilde{\boldsymbol{x}}\right)$ acting only at the macroscale and mapping tangent vectors attached to the center of the area from periodic to the quasi-periodic unit cell. In contrast, the microscopic tangent $\boldsymbol{A}_m\left(\tilde{\boldsymbol{x}},\tilde{\boldsymbol{y}}\right)$ maps microscopic tangent vectors attached to any micropoint within the periodic unit cell to corresponding tangent vectors attached to the image of the micropoint in the quasi-periodic unit cell. $\boldsymbol{A}_m\left(\tilde{\boldsymbol{x}},\tilde{\boldsymbol{y}}\right)$ is a priori depending on both macro and microscale positions in the periodic parent domain. Considering Eq. 6.17 in combination with the decomposition of the tangent, get

$$\begin{aligned}
&\boldsymbol{A}\left(\tilde{\boldsymbol{x}},\tilde{\boldsymbol{y}}\right):=\boldsymbol{A}_M\left(\tilde{\boldsymbol{x}}\right)+\eta\boldsymbol{A}_m\left(\tilde{\boldsymbol{x}},\tilde{\boldsymbol{y}}\right)\\
&\boldsymbol{A}_M\left(\tilde{\boldsymbol{x}}\right):=\begin{pmatrix}\nabla_{\tilde{\boldsymbol{x}}}\boldsymbol{\varphi}_{\tilde{x}}\left(\tilde{\boldsymbol{x}}\right) & \boldsymbol{0}\\ \boldsymbol{0} & \nabla_{\tilde{y}}\boldsymbol{y}\left(\tilde{\boldsymbol{x}},\tilde{\boldsymbol{y}}\right)\end{pmatrix},\ \boldsymbol{A}_m\left(\tilde{\boldsymbol{x}},\tilde{\boldsymbol{y}}\right):=\begin{pmatrix}\boldsymbol{0} & \boldsymbol{0}\\ \nabla_{\tilde{\boldsymbol{x}}}\boldsymbol{y}\left(\tilde{\boldsymbol{x}},\tilde{\boldsymbol{y}}\right) & \boldsymbol{0}\end{pmatrix}\\
&\begin{pmatrix} d\boldsymbol{x} \\ \eta d\boldsymbol{y}\end{pmatrix}=\boldsymbol{A}\left(\tilde{\boldsymbol{x}},\tilde{\boldsymbol{y}}\right).\begin{pmatrix} d\tilde{\boldsymbol{x}} \\ \eta d\tilde{\boldsymbol{y}}\end{pmatrix}
\end{aligned} \tag{6.18}$$

The macroscale tangent $\nabla_{\tilde{\boldsymbol{x}}}\boldsymbol{\varphi}_{\tilde{x}}\left(\tilde{\boldsymbol{x}}\right)$ describes the grading of geometry at the macroscale (thus ignoring the grading within unit cells). The micro gradient $\nabla_{\tilde{y}}\boldsymbol{y}\left(\tilde{\boldsymbol{x}},\tilde{\boldsymbol{y}}\right)$ shows the grading of the geometry within a single unit cell without considering the macro scale variations, whereas the microscale tangent $\nabla_{\tilde{\boldsymbol{x}}}\boldsymbol{y}\left(\tilde{\boldsymbol{x}},\tilde{\boldsymbol{y}}\right)$ describes the grading of geometry within unit cells, quantifies the varying of this micro-grading at the macroscale as well.

The macroscale quasi-periodic variable is thus only dependent on the macroscale periodic variable, as reflected by the fact that the macroscale tangent map $\boldsymbol{A}_M(\tilde{\boldsymbol{x}})$ in Eq. 6.18 only depends on the macroscale position. In contrast, the microscale position depends on both the macroscale and microscale periodic positions, thereby accounting for the grading of geometry within the unit cell. Thereby, the gradient of the microscopic position concerning the periodic macroscopic coordinate defines the higher-order tangent $\boldsymbol{A}_m(\tilde{\boldsymbol{x}},\tilde{\boldsymbol{y}})$. Note that higher-order terms η^2 will appear if previous expansion in Eqs. 6.16 - 6.18 is continued.

Based on the previous decomposition of Eq. 6.17, we elaborate on the transformation laws of the microscopic strain tensor concerning the micro and macro scale variables, considering their covariant and contravariant nature, respectively. When considered as a single scale function, the displacement and its spatial gradient can be decomposed into the local tangent basis in terms of its mixed components (in both the periodic and quasi-periodic domains),

$$\nabla_y \boldsymbol{u}(\boldsymbol{y}) = u^i{}_{,j}\boldsymbol{g}_i \otimes \boldsymbol{g}^j \tag{6.19}$$

The natural basis is denoted $\boldsymbol{g}_k$, $\tilde{\boldsymbol{g}}_k$ on the untransformed and transformed domains, respectively; each basis vector is defined as the tangent at each point to coordinate lines acting as curvilinear coordinates in both periodic and quasi-periodic domains. The transformation laws of vectors and tensors under a general non-affine change of coordinate are first written as a prerequisite for the homogenization of quasi-periodic structures. It is crucial to identify the variance of tensors since contravariant and covariant tensors transform differently [237]. Covariant tensors transform like the basis vectors using the transition matrix, whereas contravariant tensors (contra means 'opposite to') transform in a way opposite to the basis vectors, using the inverse of the transition matrix. Covariant tensors (resp. contravariant) are denoted with lower components (resp. upper indices). The tangent vectors building the natural basis transform between both configurations as follows:

$$\begin{aligned}
\tilde{\boldsymbol{g}}_h &:= \frac{\partial \boldsymbol{y}}{\partial \tilde{y}^h} = \frac{\partial \boldsymbol{y}}{\partial y^j}.\frac{\partial x^j}{\partial \tilde{y}^h} = \frac{\partial y^j}{\partial \tilde{y}^h}\boldsymbol{g}_j \Leftrightarrow \boldsymbol{g}_j = \tilde{\boldsymbol{g}}_k \frac{\partial \tilde{y}^k}{\partial y^j} \equiv \tilde{\boldsymbol{g}}_k \left(A^{-1}\right)^k_{.j} \\
d\boldsymbol{v}_i &= \frac{dv^i}{dy^l} dy^l \boldsymbol{g}_i \Rightarrow \tilde{\boldsymbol{g}}_k d\tilde{y}^k = \frac{\partial y^j}{\partial \tilde{y}^k}\boldsymbol{g}_j \frac{\partial \tilde{y}^k}{\partial y^p} dy^p \equiv \delta_{jp}\boldsymbol{g}_j dy^p = \boldsymbol{g}_q dy^q
\end{aligned} \tag{6.20}$$

Remark: the change of components of a vector or tensor from the quasi-periodic to the periodic domain can be expressed equivalently as a passive or an active transformation. In the passive viewpoint, a vector field holds the invariance of vectors $\tilde{\boldsymbol{v}} = \boldsymbol{v} = v^j \boldsymbol{g}_j$, $v^h(y^q) = A^h_{.k}\tilde{v}^k(\tilde{y}^p)$; in the active viewpoint, the vector is represented as a covariant vector. It transforms (its components) like the covariant base vectors; thus, the components of the same vector in both domains are the same:

$$\begin{aligned}
&\boldsymbol{g}^i = \boldsymbol{A}^{-T}.\tilde{\boldsymbol{g}}^i \\
&\boldsymbol{v} = v_i \boldsymbol{g}^i = \boldsymbol{A}^{-T}.\tilde{\boldsymbol{v}} = \tilde{v}_j \boldsymbol{A}^{-T}.\tilde{\boldsymbol{g}}^j = \tilde{v}_j \boldsymbol{g}^i \Rightarrow v_i = \tilde{v}_j
\end{aligned} \tag{6.21}$$

The single scale-dependent displacement field is expressed in terms of its covariant representation,

leading to the elaboration of the strain as a mixed tensor

$$\begin{aligned}&\nabla_{\tilde{\boldsymbol{y}}}\tilde{\boldsymbol{u}}\left(\tilde{\boldsymbol{y}}\right)=\tilde{u}^{i}_{,j}\tilde{\boldsymbol{g}}_{i}\otimes\tilde{\boldsymbol{g}}^{j},\ \nabla_{\boldsymbol{y}}\boldsymbol{u}\left(\boldsymbol{y}\right)=u^{i}{}_{,j}\boldsymbol{g}_{i}\otimes\boldsymbol{g}^{j}\\&\boldsymbol{g}^{i}.\boldsymbol{g}_{j}=\delta^{i}_{.j}=\tilde{\boldsymbol{g}}^{i}.\tilde{\boldsymbol{g}}_{j}\end{aligned}\tag{6.22}$$

We have introduced in previous relations the primal bases in periodic and quasi-periodic domains, the set of tangent vectors $\tilde{\boldsymbol{g}}_i, \boldsymbol{g}_i$, with dual (reciprocal) bases satisfying the product relations with the set of primal basis vectors in the last identity of Eq. 6.22. The strain and stress tensors are represented as mixed variant second-order tensors, with the following transformation rules:

$$\begin{aligned}&\tilde{\boldsymbol{\sigma}}=\tilde{\sigma}^{.q}_{p}\tilde{\boldsymbol{g}}^{p}\otimes\tilde{\boldsymbol{g}}_{q},\ \boldsymbol{\sigma}=\sigma^{.q}_{p}\boldsymbol{g}^{p}\otimes\boldsymbol{g}_{q}\\&\left|\begin{array}{l}\nabla_{\boldsymbol{y}}\boldsymbol{u}\left(\boldsymbol{y}\right)=\boldsymbol{A}.\nabla_{\tilde{\boldsymbol{y}}}\tilde{\boldsymbol{u}}\left(\tilde{\boldsymbol{y}}\right).\boldsymbol{A}^{-1},\\\boldsymbol{\sigma}\left(\boldsymbol{y}\right)=\boldsymbol{A}^{-T}.\tilde{\boldsymbol{\sigma}}.\boldsymbol{A}^{T}\Leftrightarrow\sigma^{.j}_{i}=\left(A^{-T}\right)^{.p}_{i}\tilde{\sigma}^{.q}_{p}\left(A^{T}\right)^{.j}_{q}\end{array}\right.\\&\Rightarrow\boldsymbol{\sigma}\left(\boldsymbol{y}\right):\nabla_{\boldsymbol{y}}\boldsymbol{u}\left(\boldsymbol{y}\right)=\tilde{\boldsymbol{\sigma}}:\nabla_{\tilde{\boldsymbol{y}}}\tilde{\boldsymbol{u}}\left(\tilde{\boldsymbol{y}}\right)\end{aligned}\tag{6.23}$$

In periodic homogenization theory, the period $\tilde{Y}$ is assumed to be very small compared to the dimensions of the overall domain; thus, the characteristic functions of such heterogeneous media will experience rapid variations within any small neighborhood of a macropoint $\tilde{\boldsymbol{x}}$. On the other hand, mechanical fields at the macroscale can be considered to experience slower variations. These considerations lead to considering all fields in both periodic and quasi-periodic domains as dependent on both the macroscopic and microscopic positions, experiencing respectively slow and fast variations concerning the first and second ones. The existing mapping between the periodic and quasi-periodic domain is assumed to be regular enough that the periodicity conditions that prevail in the periodic domain can be transferred in some sense to the quasi-periodic domain.

A similar double scale derivative as the one defined in the periodic domain in Eq. 6.5 will also hold in the quasi-periodic domain, in a form subsequent developments will show. Following the double scale dependency of the mechanical fields, the tangent map and its inverse are decomposed additively and in an asymptotic manner versus the small-scale parameter into macro and micro contributions, as follows:

$$\begin{aligned}&\boldsymbol{A}\left(\tilde{\boldsymbol{x}},\tilde{\boldsymbol{y}}\right)=\boldsymbol{A}_{M}\left(\tilde{\boldsymbol{x}}\right)+\eta\boldsymbol{A}_{m}\left(\tilde{\boldsymbol{x}},\tilde{\boldsymbol{y}}\right)=\boldsymbol{A}_{M}\left(\tilde{\boldsymbol{x}}\right).\left(\boldsymbol{I}+\eta\boldsymbol{A}_{M}\left(\tilde{\boldsymbol{x}}\right)^{-1}.\boldsymbol{A}_{m}\left(\tilde{\boldsymbol{x}},\tilde{\boldsymbol{y}}\right)\right),\\&\Rightarrow\det\boldsymbol{A}=\det\left(\boldsymbol{A}_{M}\right)\left(1+\eta Tr\left({\boldsymbol{A}_{M}}^{-1}.\boldsymbol{A}_{m}\right)\right)+o\left(\eta\right)\\&\Rightarrow\boldsymbol{A}(\tilde{\boldsymbol{x}},\tilde{\boldsymbol{y}})^{-1}=\left(\boldsymbol{I}+\eta\boldsymbol{A}_{M}^{-1}\left(\tilde{\boldsymbol{x}}\right).\boldsymbol{A}_{m}\left(\tilde{\boldsymbol{x}},\tilde{\boldsymbol{y}}\right)\right)^{-1}.\boldsymbol{A}_{M}^{-1}\left(\tilde{\boldsymbol{x}}\right)\\&\qquad\cong\left(\boldsymbol{I}-\eta\boldsymbol{A}_{M}^{-1}\left(\tilde{\boldsymbol{x}}\right).\boldsymbol{A}_{m}\left(\tilde{\boldsymbol{x}},\tilde{\boldsymbol{y}}\right)\right).\boldsymbol{A}_{M}^{-1}\left(\tilde{\boldsymbol{x}}\right)=\boldsymbol{A}_{M}^{-1}\left(\tilde{\boldsymbol{x}}\right)-\eta\boldsymbol{A}_{M}^{-1}\left(\tilde{\boldsymbol{x}}\right).\boldsymbol{A}_{m}\left(\tilde{\boldsymbol{x}},\tilde{\boldsymbol{y}}\right).\boldsymbol{A}_{M}^{-1}\left(\tilde{\boldsymbol{x}}\right)+o\left(\eta\right)\\&\det\left(\boldsymbol{A}^{-1}\right)=\det\left(\boldsymbol{A}_{M}^{-1}-\eta\boldsymbol{A}_{M}^{-1}.\boldsymbol{A}_{m}.\boldsymbol{A}_{M}^{-1}\right)\cong\det\left(\boldsymbol{A}_{M}^{-1}\right)\left(1-\eta Tr\left(\boldsymbol{A}_{M}^{-1}.\boldsymbol{A}_{m}\right)\right)+o\left(\eta\right)\end{aligned}\tag{6.24}$$

We write the asymptotic expansion of the strain in the periodic domain with the definition of the

successive terms:

$$\tilde{\boldsymbol{\varepsilon}}^{\eta}(\boldsymbol{y}) = \tilde{\boldsymbol{\varepsilon}}^{\eta}(\boldsymbol{x},\boldsymbol{y}) = \tilde{\boldsymbol{\varepsilon}}^{0}(\boldsymbol{x}) + \eta\tilde{\boldsymbol{\varepsilon}}^{1}(\boldsymbol{x},\boldsymbol{y}) + \eta^{2}\tilde{\boldsymbol{\varepsilon}}^{2}(\boldsymbol{x},\boldsymbol{y})$$
$$\begin{cases} \tilde{\boldsymbol{\varepsilon}}^{0} = \nabla^{S}{}_{\tilde{x}}\tilde{\boldsymbol{u}}^{0}(\tilde{\boldsymbol{x}}) + \nabla^{S}{}_{\tilde{y}}\tilde{\boldsymbol{u}}^{1} = \tilde{\boldsymbol{E}}_{0}(\tilde{\boldsymbol{x}}) + \nabla^{S}{}_{\tilde{y}}\tilde{\boldsymbol{u}}^{1} \\ \left\langle \nabla^{S}{}_{\tilde{y}}\tilde{\boldsymbol{u}}^{1} \right\rangle_{\tilde{Y}} = \boldsymbol{0} \Rightarrow \tilde{\boldsymbol{E}}_{0}(\tilde{\boldsymbol{x}}) = \left\langle \tilde{\boldsymbol{\varepsilon}}^{0} \right\rangle_{\tilde{Y}} \\ \tilde{\boldsymbol{\varepsilon}}^{k} = \nabla^{S}{}_{\tilde{x}}\tilde{\boldsymbol{u}}^{k}(\tilde{\boldsymbol{x}}) + \nabla^{S}{}_{\tilde{y}}\tilde{\boldsymbol{u}}^{k+1},\ \mathrm{k} \geqslant 1 \end{cases} \tag{6.25}$$

The transformation of the strain tensor at the subsequent orders of the small-scale parameter accordingly writes:

$$\boldsymbol{\varepsilon}^{\eta}(\boldsymbol{y}) = \boldsymbol{A}.\tilde{\boldsymbol{\varepsilon}}^{\eta}(\tilde{\boldsymbol{y}}).\boldsymbol{A}^{-1} = \left(\boldsymbol{A}_{M}(\tilde{\boldsymbol{x}}) + \eta\boldsymbol{A}_{m}(\tilde{\boldsymbol{x}},\tilde{\boldsymbol{y}})\right).\tilde{\boldsymbol{\varepsilon}}^{\eta}(\tilde{\boldsymbol{y}}).\left\{\boldsymbol{A}_{M}^{-1}(\tilde{\boldsymbol{x}}) - \eta\boldsymbol{A}_{M}^{-1}(\tilde{\boldsymbol{x}}).\boldsymbol{A}_{m}(\tilde{\boldsymbol{x}},\tilde{\boldsymbol{y}}).\boldsymbol{A}_{M}^{-1}(\tilde{\boldsymbol{x}})\right\} \tag{6.26}$$

Which gives the quasi-periodic strain components as

$$\begin{aligned} \boldsymbol{\varepsilon}^{0}(\boldsymbol{x},\boldsymbol{y}) &= \boldsymbol{A}_{M}(\tilde{\boldsymbol{x}}).\tilde{\boldsymbol{\varepsilon}}^{0}(\tilde{\boldsymbol{x}},\tilde{\boldsymbol{y}}).\boldsymbol{A}_{M}^{-1}(\tilde{\boldsymbol{x}}) = \boldsymbol{A}_{M}(\tilde{\boldsymbol{x}}).\left(\nabla^{S}{}_{\tilde{x}}\tilde{\boldsymbol{u}}^{0}(\tilde{\boldsymbol{x}}) + \nabla^{S}{}_{\tilde{y}}\tilde{\boldsymbol{u}}^{1}\right).\boldsymbol{A}_{M}^{-1}(\tilde{\boldsymbol{x}}) \\ \boldsymbol{\varepsilon}^{1}(\boldsymbol{x},\boldsymbol{y}) &= \boldsymbol{A}_{M}(\tilde{\boldsymbol{x}}).\tilde{\boldsymbol{\varepsilon}}^{1}(\tilde{\boldsymbol{y}}).\boldsymbol{A}_{M}^{-1}(\tilde{\boldsymbol{x}}) + \boldsymbol{A}_{m}(\tilde{\boldsymbol{y}}).\tilde{\boldsymbol{\varepsilon}}^{0}(\tilde{\boldsymbol{y}}).\boldsymbol{A}_{M}^{-1}(\tilde{\boldsymbol{x}}) - \boldsymbol{A}_{M}(\tilde{\boldsymbol{x}}).\tilde{\boldsymbol{\varepsilon}}^{0}(\tilde{\boldsymbol{y}}).\boldsymbol{A}_{M}^{-1}(\tilde{\boldsymbol{x}}).\boldsymbol{A}_{m}(\tilde{\boldsymbol{x}},\tilde{\boldsymbol{y}}).\boldsymbol{A}_{M}^{-1}(\tilde{\boldsymbol{x}}) \\ \boldsymbol{\varepsilon}^{2}(\boldsymbol{x},\boldsymbol{y}) &= \boldsymbol{A}_{M}^{-1}(\tilde{\boldsymbol{x}}).\tilde{\boldsymbol{\varepsilon}}^{2}\boldsymbol{A}_{M}(\tilde{\boldsymbol{x}}) + \boldsymbol{A}_{m}(\tilde{\boldsymbol{y}}).\tilde{\boldsymbol{\varepsilon}}^{1}(\tilde{\boldsymbol{y}}).\boldsymbol{A}_{M}^{-1}(\tilde{\boldsymbol{x}}) - \boldsymbol{A}_{M}(\tilde{\boldsymbol{x}}).\tilde{\boldsymbol{\varepsilon}}^{1}(\tilde{\boldsymbol{y}}).\boldsymbol{A}_{M}^{-1}(\tilde{\boldsymbol{x}}).\boldsymbol{A}_{m}(\tilde{\boldsymbol{x}},\tilde{\boldsymbol{y}}).\boldsymbol{A}_{M}^{-1}(\tilde{\boldsymbol{x}}) \\ &\quad - \eta^{2}\boldsymbol{A}_{M}^{-1}(\tilde{\boldsymbol{x}}).\boldsymbol{A}_{m}(\tilde{\boldsymbol{x}},\tilde{\boldsymbol{y}}).\boldsymbol{A}_{M}^{-1}(\tilde{\boldsymbol{x}}).\tilde{\boldsymbol{\varepsilon}}^{0}(\tilde{\boldsymbol{x}}).\boldsymbol{A}_{m}(\tilde{\boldsymbol{x}},\tilde{\boldsymbol{y}}) \end{aligned} \tag{6.27}$$

Eqs. 6.23- 6.25, and considering the leading order asymptotic expansion of $det(\boldsymbol{A}^{\eta})$ leads to the following asymptotic expansion of periodic displacement :

$$\begin{aligned} &\nabla^{S}{}_{\tilde{y}}\tilde{\boldsymbol{u}}^{\eta} = \left(\boldsymbol{A}_{M}^{-1}(\tilde{\boldsymbol{x}}) - \eta\boldsymbol{A}_{M}^{-1}(\tilde{\boldsymbol{x}}).\boldsymbol{A}_{m}(\tilde{\boldsymbol{x}},\tilde{\boldsymbol{y}}).\boldsymbol{A}_{M}^{-1}(\tilde{\boldsymbol{x}})\right).\nabla^{S}{}_{y}\boldsymbol{u}^{\eta}.\left(\boldsymbol{A}_{M}(\tilde{\boldsymbol{x}}) + \eta\boldsymbol{A}_{m}(\tilde{\boldsymbol{y}})\right) \\ &\Rightarrow \begin{cases} \nabla^{S}{}_{\tilde{x}}\tilde{\boldsymbol{u}}^{0} = \boldsymbol{A}_{M}^{-1}.\nabla^{S}{}_{x}\boldsymbol{u}^{0}.\boldsymbol{A}_{M} \\ \nabla^{S}{}_{\tilde{y}}\tilde{\boldsymbol{u}}^{1} = \boldsymbol{A}_{M}^{-1}.\left(\boldsymbol{I} - \boldsymbol{A}_{m}.\boldsymbol{A}_{M}^{-1}\right).\nabla^{S}{}_{y}\boldsymbol{u}^{1}.\boldsymbol{A}_{M} \end{cases} \end{aligned} \tag{6.28}$$

The leading order quasi-periodic microstrain tensor follows from Eqs. 6.27 and 6.28, using the leading order asymptotic expansion of $det(\boldsymbol{A}^{\eta})$:

$$\begin{aligned} \boldsymbol{\varepsilon}^{0}(\boldsymbol{x},\boldsymbol{y}) &= \nabla^{S}{}_{x}\boldsymbol{u}^{0}(\boldsymbol{x}) + \boldsymbol{A}_{M}.\left(\boldsymbol{A}_{M}^{-1}.\left(\boldsymbol{I} - \boldsymbol{A}_{m}.\boldsymbol{A}_{M}^{-1}\right).\nabla^{S}{}_{y}\boldsymbol{u}^{1}.\boldsymbol{A}_{M}\right).\boldsymbol{A}_{M}^{-1} \\ &= \nabla^{S}{}_{x}\boldsymbol{u}^{0}(\boldsymbol{x}) + \left(\boldsymbol{I} - \boldsymbol{A}_{m}.\boldsymbol{A}_{M}^{-1}\right).\nabla^{S}{}_{y}\boldsymbol{u}^{1}(\boldsymbol{x},\boldsymbol{y}) \end{aligned} \tag{6.29}$$

Eq. 6.27 in combination with Eq.6.25 leads to the macrostrain relation in the quasi-periodic domain $\boldsymbol{E}^{0}(\boldsymbol{x})$ to its counterpart $\tilde{\boldsymbol{E}}_{0}(\tilde{\boldsymbol{x}})$ in the periodic domain:

$$\begin{aligned} &\boldsymbol{E}^{0}(\boldsymbol{x}) := \left\langle \varepsilon^{0}(\boldsymbol{x},\boldsymbol{y}) \right\rangle_{Y} = \boldsymbol{A}_{M}(\tilde{\boldsymbol{x}}).\left\langle \left(\nabla^{S}{}_{\tilde{x}}\tilde{\boldsymbol{u}}^{0}(\tilde{\boldsymbol{x}}) + \nabla^{S}{}_{\tilde{y}}\tilde{\boldsymbol{u}}^{1}\right) det\left(\boldsymbol{A}_{M}(\tilde{\boldsymbol{x}})\right) \right\rangle_{\tilde{Y}}.\boldsymbol{A}_{M}^{-1}(\tilde{\boldsymbol{x}}) \\ &\Rightarrow \boldsymbol{E}^{0}(\boldsymbol{x}) : = \left\langle \boldsymbol{\varepsilon}^{0}(\boldsymbol{x},\boldsymbol{y}) \right\rangle_{Y} = det\left(\boldsymbol{A}_{M}(\tilde{\boldsymbol{x}})\right)\boldsymbol{A}_{M}(\tilde{\boldsymbol{x}}).\left\langle \nabla^{S}{}_{\tilde{x}}\tilde{\boldsymbol{u}}^{0}(\tilde{\boldsymbol{x}}) \right\rangle_{\tilde{Y}}.\boldsymbol{A}_{M}^{-1}(\tilde{\boldsymbol{x}}) \\ &\qquad = det\left(\boldsymbol{A}_{M}(\tilde{\boldsymbol{x}})\right)\boldsymbol{A}_{M}(\tilde{\boldsymbol{x}}).\tilde{\boldsymbol{E}}_{0}(\tilde{\boldsymbol{x}}).\boldsymbol{A}_{M}^{-1}(\tilde{\boldsymbol{x}}) \end{aligned} \tag{6.30}$$

The stress tensor conjugated to the strain tensor is also represented as a mixed tensor (Eq. 6.23), and it follows similar transformation rules (Eq. 6.24) when mapped from the periodic to quasi-periodic domains:

$$\begin{aligned} &\boldsymbol{A}(\tilde{\boldsymbol{x}},\tilde{\boldsymbol{y}})^{-1} = \boldsymbol{A}_{M}^{-1}(\tilde{\boldsymbol{x}}) - \eta\boldsymbol{A}_{M}^{-1}(\tilde{\boldsymbol{x}}).\boldsymbol{A}_{m}(\tilde{\boldsymbol{x}},\tilde{\boldsymbol{y}}).\boldsymbol{A}_{M}^{-1}(\tilde{\boldsymbol{x}}) + o(\eta) \\ &\boldsymbol{A}(\tilde{\boldsymbol{x}},\tilde{\boldsymbol{y}})^{-T} = \boldsymbol{A}_{M}^{-T}(\tilde{\boldsymbol{x}}) - \eta\boldsymbol{A}_{M}^{-T}(\tilde{\boldsymbol{x}}).\boldsymbol{A}_{m}^{T}(\tilde{\boldsymbol{x}},\tilde{\boldsymbol{y}}).\boldsymbol{A}_{M}^{-T}(\tilde{\boldsymbol{x}}) + o(\eta) \\ &\Rightarrow \boldsymbol{\sigma}^{\eta} = \left(\boldsymbol{A}_{M}^{-T}(\tilde{\boldsymbol{x}}) - \eta\boldsymbol{A}_{M}^{-T}(\tilde{\boldsymbol{x}}).\boldsymbol{A}_{m}^{T}(\tilde{\boldsymbol{x}},\tilde{\boldsymbol{y}}).\boldsymbol{A}_{M}^{-T}(\tilde{\boldsymbol{x}})\right).\tilde{\boldsymbol{\sigma}}^{\eta}.\left(\boldsymbol{A}_{M}^{T}(\tilde{\boldsymbol{x}}) + \eta\boldsymbol{A}_{m}^{T}(\tilde{\boldsymbol{x}},\tilde{\boldsymbol{y}})\right) \\ &\boldsymbol{\sigma}^{\eta}(\boldsymbol{x},\boldsymbol{y}) = \boldsymbol{\sigma}^{0}(\boldsymbol{x}) + \eta\boldsymbol{\sigma}^{1}(\boldsymbol{x},\boldsymbol{y}) + \eta^{2}\boldsymbol{\sigma}^{2}(\boldsymbol{x},\boldsymbol{y}) \end{aligned} \tag{6.31}$$

with the following quasi-periodic stress components

$$\left|\begin{array}{l}\boldsymbol{\sigma}^0(\boldsymbol{x}) = \boldsymbol{A}_M^{-T}(\boldsymbol{x}).\tilde{\boldsymbol{\sigma}}^0(\tilde{\boldsymbol{x}}).\boldsymbol{A}_M^T(\tilde{\boldsymbol{x}}),\\ \boldsymbol{\sigma}^1(\boldsymbol{x},\boldsymbol{y}) = \boldsymbol{A}_M^{-T}.\tilde{\boldsymbol{\sigma}}^1.\boldsymbol{A}_M^T + \boldsymbol{A}_M^{-T}.\tilde{\boldsymbol{\sigma}}^0.\boldsymbol{A}_m^T - \boldsymbol{A}_M^{-T}.\boldsymbol{A}_m^T.\boldsymbol{A}_M^{-T}.\tilde{\boldsymbol{\sigma}}^0.\boldsymbol{A}_M^T\\ \boldsymbol{\sigma}^2(\boldsymbol{x},\boldsymbol{y}) = \boldsymbol{A}_M^{-T}.\tilde{\boldsymbol{\sigma}}^2.\boldsymbol{A}_M^T + \boldsymbol{A}_M^{-T}.\tilde{\boldsymbol{\sigma}}^1.\boldsymbol{A}_m^T - \boldsymbol{A}_M^{-T}.\boldsymbol{A}_m^T.\boldsymbol{A}_M^{-T}.\tilde{\boldsymbol{\sigma}}^1.\boldsymbol{A}_M^T - \boldsymbol{A}_M^{-T}.\boldsymbol{A}_m^T.\boldsymbol{A}_M^{-T}.\tilde{\boldsymbol{\sigma}}^0.\boldsymbol{A}_m^T\end{array}\right. \tag{6.32}$$

As a consequence of the previous transformation relations 6.27 and 6.32 for the microstrain and stress tensor fields, it is straightforward to derive the invariance of the microscopic energy density:

$$w_\mu(\boldsymbol{y}) := \frac{1}{2}\boldsymbol{\sigma} : \boldsymbol{\varepsilon} = \frac{1}{2}Tr(\boldsymbol{\sigma}^T.\boldsymbol{\varepsilon}) = \frac{1}{2}\sigma_i^{\cdot j}\varepsilon^{\cdot i} = \frac{1}{2}\tilde{\sigma}_i^{\cdot j}\tilde{\varepsilon}^{\cdot i} = \frac{1}{2}\tilde{\boldsymbol{\sigma}} : \tilde{\boldsymbol{\varepsilon}} = \tilde{w}_\mu(\tilde{\boldsymbol{y}}) \tag{6.33}$$

6.3.2 Evaluation of the tensor of quasi-periodic effective moduli based on the unit cell BVP

As a starting point of the proposed method, the periodic unit cell BVP is mapped onto the quasi-periodic unit cell. Recall that the first-order constitutive relation in the periodic macrodomain $\tilde{\Omega}$ is written in the form Eq. 6.7. Both macroscopic and microscopic spatial gradients involved in Eq. 6.7 are push-forwarded into the quasi-periodic domain using Eqs. 6.24, 6.26 for the first order microstrain tensor and Eq. 6.31 for the microstress tensor:

$$\begin{array}{l}\left|\boldsymbol{\sigma}^0(\boldsymbol{x}) = \boldsymbol{A}_M^{-T}.\tilde{\boldsymbol{\sigma}}^0(\tilde{\boldsymbol{x}}).\boldsymbol{A}_M^T\right.\\ \left|\begin{array}{l}\nabla^S{}_{\tilde{x}}\tilde{\boldsymbol{u}}^0 = \boldsymbol{A}_M^{-1}.\nabla^S{}_x\boldsymbol{u}^0.\boldsymbol{A}_M\\ \nabla^S{}_{\tilde{y}}\tilde{\boldsymbol{u}}^1 = \boldsymbol{A}_M^{-1}.\left(\nabla^S{}_y\boldsymbol{u}^1 - \boldsymbol{A}_m.\boldsymbol{A}_M^{-1}.\nabla^S{}_y\boldsymbol{u}^1\right).\boldsymbol{A}_M\end{array}\right.\\ \Rightarrow \tilde{\boldsymbol{\sigma}}^0 = \tilde{\boldsymbol{C}} : \left(\nabla^S{}_{\tilde{x}}\tilde{\boldsymbol{u}}^0(\tilde{\boldsymbol{x}}) + \boldsymbol{A}_M^{-1}.\left(\boldsymbol{I} - \boldsymbol{A}_m.\boldsymbol{A}_M^{-1}\right).\nabla^S{}_y\boldsymbol{u}^1.\boldsymbol{A}_M\right)\end{array} \tag{6.34}$$

Recalling Eq. 6.30, mapping of the leading order microstress written in the periodic domain from the last relation in Eq. 6.35 onto the quasi-periodic domain leads to the following relation

$$\begin{aligned}\boldsymbol{\sigma}^0(\boldsymbol{x}) &= det(\boldsymbol{A}_M(\tilde{\boldsymbol{x}}))^{-1}\boldsymbol{A}_M^{-T}.\left\{\tilde{\boldsymbol{C}} : \boldsymbol{A}_M^{-1}.\left(\boldsymbol{E}_0(\boldsymbol{x}) + \boldsymbol{A}_M^{-1}.\left(\boldsymbol{I} - \boldsymbol{A}_m.\boldsymbol{A}_M^{-1}\right).\nabla^S{}_y\boldsymbol{u}^1\right).\boldsymbol{A}_M\right\}.\boldsymbol{A}_M^T\\ &= det(\boldsymbol{A}_M(\tilde{\boldsymbol{x}}))^{-1}\left(\boldsymbol{A}_M^{-T}\underline{\otimes}\boldsymbol{A}_M\right) : \tilde{\boldsymbol{C}} : \left(\boldsymbol{A}_M^{-1}\underline{\otimes}\boldsymbol{A}_M^T\right) : \left(\boldsymbol{E}_0(\boldsymbol{x}) + \boldsymbol{A}_M^{-1}.\left(\boldsymbol{I} - \boldsymbol{A}_m.\boldsymbol{A}_M^{-1}\right).\nabla^S{}_y\boldsymbol{u}^1\right)\end{aligned} \tag{6.35}$$

The leading order quasi-periodic stress tensor in Eq. 6.36 is of the form

$$\boldsymbol{\sigma}^0(\boldsymbol{x},\boldsymbol{y}) = L\left(\nabla^S{}_y\boldsymbol{u}^1(\boldsymbol{x},\boldsymbol{y}); \boldsymbol{E}_0(\boldsymbol{x})\right) \tag{6.36}$$

with $L\left(\nabla^S{}_y\boldsymbol{u}^1(\boldsymbol{x},\boldsymbol{y}); \boldsymbol{E}_0(\boldsymbol{x})\right)$ a linear operator acting on the second-order term $\nabla^S{}_{\tilde{y}}\tilde{\boldsymbol{u}}^1(\boldsymbol{x},\boldsymbol{y})$ and $\boldsymbol{E}_0(\boldsymbol{x})$ the macroscopic kinematic loading over the quasi-periodic unit cell, acting as a source term in the unit cell BVP.

Using the equality of microscopic energy densities in periodic and quasi-periodic domains and introducing the strain localization operator $\boldsymbol{A}^E(\boldsymbol{y})$ under the linearity of the quasi-periodic unit cell BVP versus the macrostrain $\boldsymbol{E}^0(\boldsymbol{x})$ leads to the following relations for isotropic microstructures, considering the leading order term in the microstrain:

$$\left(\tilde{C}\right)_{ijkl} = \lambda\delta_{ij}\delta_{kl} + \mu\left(\delta_{ik}\delta_{jl} + \delta_{il}\delta_{jk}\right) \Rightarrow \boldsymbol{\varepsilon C \varepsilon} = \tilde{\boldsymbol{\varepsilon}} \,\tilde{:}\tilde{\boldsymbol{C}}\tilde{:}\, \tilde{\boldsymbol{\varepsilon}} \tag{6.37}$$

On due account of Eq. 6.36, the BVP of Eq. 6.7 becomes in the quasi-periodic domain by consideration of the mapping of the leading order stress tensor considering the invariance of strain energy densities written for virtual velocity fields:

$$\begin{vmatrix} div_y\left(\det(\boldsymbol{A}^{-1})\boldsymbol{\sigma}^0\right) = \boldsymbol{0} \text{ order } \eta^{-1} \\ \boldsymbol{\sigma}^0(\boldsymbol{x},\boldsymbol{y}) = L\left(\nabla^S{}_y\boldsymbol{u}^1(\boldsymbol{x},\boldsymbol{y});\boldsymbol{E}_0(\boldsymbol{x})\right) \text{ order } \eta^0 \\ \boldsymbol{u}^0,\boldsymbol{u}^1 \text{ quasi - periodic, } \boldsymbol{\sigma}^0.\boldsymbol{n} \text{ antiperiodic} \end{vmatrix} \tag{6.38}$$

The first and second-order displacements satisfy quasi-periodicity conditions, and the first-order traction is anti-periodic; these notions of quasi-periodicity will be defined more accurately later in this contribution. The last expression of the quasi-periodic leading order stress tensor $\boldsymbol{\sigma}^0$ in Eq. 6.38 shows a linear dependency upon the second-order term $\nabla^S{}_y\boldsymbol{u}^1(\boldsymbol{x},\boldsymbol{y})$, with the macrostrain $\boldsymbol{E}_0(\boldsymbol{x})$ therein acting as a source term. Since the unit cell BVP in the quasi-periodic domain is linear in the kinematic loading $\boldsymbol{E}_0(\boldsymbol{x})$, one can introduce a fourth-order strain localization tensor such that it holds

$$\boldsymbol{u}^1(\tilde{\boldsymbol{y}}) = \boldsymbol{H}^E(\boldsymbol{y}) : \boldsymbol{E}^0(\boldsymbol{x}) \Rightarrow \nabla^S{}_y\boldsymbol{u}^1(\boldsymbol{x},\boldsymbol{y}) = \nabla_y\boldsymbol{H}^E(\boldsymbol{y}) : \boldsymbol{E}_0(\boldsymbol{x}) \tag{6.39}$$

thus, the leading-order stress tensor writes

$$\begin{aligned} &\boldsymbol{\varepsilon}^0(\boldsymbol{x}) = \left(\boldsymbol{I}_4 + \nabla_y\boldsymbol{H}^E(\boldsymbol{y})\right) : \boldsymbol{E}_0(\boldsymbol{x}) \ \equiv \boldsymbol{A}^E(\boldsymbol{x},\boldsymbol{y}) : \boldsymbol{E}_0(\boldsymbol{x}) \\ &\Rightarrow \boldsymbol{\sigma}^0(\boldsymbol{x}) = \boldsymbol{C}(\boldsymbol{x},\boldsymbol{y}) : \left(\boldsymbol{I}_4 + \nabla_y\boldsymbol{H}^E(\boldsymbol{y})\right) : \boldsymbol{E}_0(\boldsymbol{x}) \ \equiv \boldsymbol{C}(\boldsymbol{x},\boldsymbol{y}) : \boldsymbol{A}^E(\boldsymbol{x},\boldsymbol{y}) : \boldsymbol{E}_0(\boldsymbol{x}) \end{aligned} \tag{6.40}$$

with similar writing on the periodic domain.

By analogy with the elaboration of the periodic strain localization operator Eq. 6.12, the following expressions define

$$\begin{aligned} \nabla^S{}_y\boldsymbol{u}^1(\boldsymbol{x},\boldsymbol{y}) &= \nabla_y\boldsymbol{H}^E(\boldsymbol{y}) : \boldsymbol{E}_0(\boldsymbol{x}) \\ \boldsymbol{\varepsilon}_0(\boldsymbol{x},\boldsymbol{y}) &= \boldsymbol{A}^E(\boldsymbol{x},\boldsymbol{y}) : \boldsymbol{E}_0(\boldsymbol{x}) \end{aligned} \tag{6.41}$$

Starting from Eq. 6.29, the fourth-order tensor of quasi-periodic strain localization operator denoted $\boldsymbol{A}^E(\boldsymbol{x},\boldsymbol{y})$ is obtained from the following relation :

$$\begin{aligned} &\varepsilon^0(\boldsymbol{x}) = \boldsymbol{A}_M^{-1}.\left(\boldsymbol{E}_0(\boldsymbol{x}) + \left(\boldsymbol{I} - \boldsymbol{A}_m.\boldsymbol{A}_M^{-1}\right).\nabla^S{}_y\boldsymbol{u}^1\right).\boldsymbol{A}_M \\ &\Rightarrow \boldsymbol{A}^E(\boldsymbol{x},\boldsymbol{y}) : \boldsymbol{E}_0(\boldsymbol{x}) = \boldsymbol{A}_M^{-1}.\left(\boldsymbol{I}_4 + \boldsymbol{A}_M^{-1}.\left(\boldsymbol{I} - \boldsymbol{A}_m.\boldsymbol{A}_M^{-1}\right).\nabla_y\boldsymbol{H}^E(\boldsymbol{y})\right).\boldsymbol{A}_M.\boldsymbol{E}_0(\boldsymbol{x}) \\ &\Rightarrow \ \boldsymbol{A}^E(\boldsymbol{x},\boldsymbol{y}) = \boldsymbol{A}_M^{-1}(\boldsymbol{x}).\left(\boldsymbol{I}_4 + \boldsymbol{A}_M^{-1}(\boldsymbol{x}).\left(\boldsymbol{I} - \boldsymbol{A}_m(\boldsymbol{x},\boldsymbol{y}).\boldsymbol{A}_M^{-1}(\boldsymbol{x})\right).\nabla_y\boldsymbol{H}^E(\boldsymbol{y})\right).\boldsymbol{A}_M(\tilde{\boldsymbol{x}}) \end{aligned} \tag{6.42}$$

One may accordingly rewrite previous unit cell BVP in Eq. 6.38:

$$\begin{vmatrix} div_y\left(\det(\boldsymbol{A}^{-1})\ \boldsymbol{\sigma}^0\right) = \boldsymbol{0} \\ \boldsymbol{\varepsilon}^0(\boldsymbol{x}) = \left(\boldsymbol{I}_4 + \nabla_y\boldsymbol{H}^E(\boldsymbol{y})\right) : \boldsymbol{E}_0(\boldsymbol{x}) \ \equiv \boldsymbol{A}^E(\boldsymbol{x},\boldsymbol{y}) : \boldsymbol{E}_0(\boldsymbol{x}) \\ \Rightarrow \boldsymbol{\sigma}^0(\boldsymbol{x}) = \boldsymbol{C}(\boldsymbol{x},\boldsymbol{y}) : \boldsymbol{\varepsilon}^0(\boldsymbol{x}) \\ \boldsymbol{u}^0,\boldsymbol{u}^1 \text{ quasi - periodic, } \boldsymbol{\sigma}^0.\boldsymbol{n} \text{ antiperiodic} \end{vmatrix} \tag{6.43}$$

The strain localization operator $\boldsymbol{A}^E(\boldsymbol{x},\boldsymbol{y})$ further enables to express of the tensor of effective moduli $\boldsymbol{C}^{hom}(\boldsymbol{x})$ by taking the volume average of the leading order microscopic stress from Eq. 6.35:

$$\begin{aligned}
&\left|\begin{array}{l}\boldsymbol{\sigma}^0(\boldsymbol{x}) = Det(\boldsymbol{A}_M(\tilde{\boldsymbol{x}}))^{-1}\left(\boldsymbol{A}_M^{-T}\underline{\otimes}\boldsymbol{A}_M\right):\tilde{\boldsymbol{C}}:\left(\boldsymbol{A}_M^{-1}\underline{\otimes}\boldsymbol{A}_M^{T}\right):\left(\boldsymbol{E}_0(\boldsymbol{x})+\boldsymbol{A}_M^{-1}.\left(\boldsymbol{I}-\boldsymbol{A}_m.\boldsymbol{A}_M^{-1}\right).\nabla^S{}_y\boldsymbol{u}^1\right)\\ \nabla^S{}_y\boldsymbol{u}^1(\boldsymbol{x},\boldsymbol{y}) = \nabla_y\boldsymbol{H}^E(\boldsymbol{y}):\boldsymbol{E}_0(\boldsymbol{x})\end{array}\right.\\
&\Rightarrow \boldsymbol{\Sigma}^0(\boldsymbol{x}) := \left\langle\boldsymbol{\sigma}^0(\boldsymbol{x})\right\rangle_Y = \left\langle Det(\boldsymbol{A}_M(\tilde{\boldsymbol{x}}))^{-1}\left(\boldsymbol{A}_M^{-T}\underline{\otimes}\boldsymbol{A}_M\right):\tilde{\boldsymbol{C}}:\left(\boldsymbol{A}_M^{-1}\underline{\otimes}\boldsymbol{A}_M^{T}\right):\left(\boldsymbol{E}_0(\boldsymbol{x})+\boldsymbol{A}_M^{-1}.\left(\boldsymbol{I}-\boldsymbol{A}_m.\boldsymbol{A}_M^{-1}\right).\nabla^S{}_y\boldsymbol{u}^1\right)\right\rangle_Y \quad (6.44)\\
&\qquad = \boldsymbol{C}^{hom}(\boldsymbol{x}):\boldsymbol{E}_0(\boldsymbol{x})\\
&\Rightarrow\ \boldsymbol{C}^{hom}(\boldsymbol{x}) = \left(\boldsymbol{A}_M^{-T}\boldsymbol{A}_M\right):\left\langle\boldsymbol{C}:\left(\boldsymbol{I}_4+\boldsymbol{A}_M^{-1}.\left(\boldsymbol{I}-\boldsymbol{A}_m.\boldsymbol{A}_M^{-1}\right).\nabla_y\boldsymbol{H}^E(\boldsymbol{y})\right)\right\rangle_Y:\left(\boldsymbol{A}_M^{-1}\boldsymbol{A}_M^{T}\right)
\end{aligned}$$

Note that the body in a transformed domain is macroscopically non-homogeneous due to the position dependency (within the center of gravity of the mapped unit cells) of the effective moduli $\boldsymbol{C}^{hom}(\boldsymbol{x})$.

Taking the average of the balance of linear momentum of Eq. 6.38, using the strain localization introduced in Eq. 6.43 and Whitaker averaging theorem (the unit cell average of the microscopic gradient of a field is equal to the macroscopic gradient of its average) delivers the quasi-periodic unit cell BVP for the strain localization operator $\boldsymbol{A}^E(\boldsymbol{x},\boldsymbol{y})$ needed for the evaluation of the tensor of quasi-periodic moduli in the last relation of Eq. 6.44:

$$\left|\begin{array}{l} div_x\left(\left\langle\det(\boldsymbol{A}^{-1})\boldsymbol{\sigma}^0\right\rangle_Y\right)+\langle\boldsymbol{b}\rangle_Y=\boldsymbol{0}\\ \boldsymbol{\sigma}^0(\boldsymbol{x},\boldsymbol{y})=\boldsymbol{C}(\boldsymbol{x},\boldsymbol{y}):\boldsymbol{A}^E(\boldsymbol{x},\boldsymbol{y}):\boldsymbol{E}_0(\boldsymbol{x})\\ \boldsymbol{u}^0,\boldsymbol{u}^1\ \text{quasi - periodic},\ \boldsymbol{\sigma}^0.\boldsymbol{n}\ \text{antiperiodic}\end{array}\right. \quad (6.45)$$

Averaging the leading order microstress from the last relation over the microscopic relative position leads to the effective constitutive law in the quasi-periodic domain of the form:

$$\begin{aligned}
&\boldsymbol{\Sigma}^0(\boldsymbol{x}) := \left\langle\boldsymbol{\sigma}^0(\boldsymbol{x},\boldsymbol{y})\right\rangle_Y \equiv \boldsymbol{C}^{\hom}(\boldsymbol{x}):\boldsymbol{E}_0(\boldsymbol{x})\\
&\boldsymbol{C}^{\hom}(\boldsymbol{x}) = \left\langle\boldsymbol{C}(\boldsymbol{x},\boldsymbol{y}):\boldsymbol{A}^E(\boldsymbol{x},\boldsymbol{y})\right\rangle_Y
\end{aligned} \quad (6.46)$$

with the tensor of quasi-periodic effective moduli obtained from the unit cell averaging of the tensor of microscopic moduli with strain localization operator.

From the numerical point of view, it proves more convenient to have all quantities computed into the periodic unit cell and then mapped by push-forward operations onto the quasi-periodic unit cell. Having computed the strain localization $\tilde{\boldsymbol{A}}^E(\tilde{\boldsymbol{x}},\tilde{\boldsymbol{y}})^T$ in the periodic domain, one maps it to the quasi-periodic domain to get its quasi-periodic counterpart using the relation

$$\text{Recall}: \left|\begin{array}{l}\tilde{\varepsilon}^0(\tilde{\boldsymbol{x}},\tilde{\boldsymbol{y}})=\tilde{\boldsymbol{A}}^E:\tilde{\boldsymbol{E}}_0(\tilde{\boldsymbol{x}}),\ \varepsilon^0(\boldsymbol{x},\boldsymbol{y})=\boldsymbol{A}^E(\boldsymbol{x},\boldsymbol{y}):\boldsymbol{E}_0(\boldsymbol{x}),\\ \boldsymbol{E}^0(\boldsymbol{x})=det(\boldsymbol{A}_M(\tilde{\boldsymbol{x}}))\boldsymbol{A}_M(\tilde{\boldsymbol{x}}).\tilde{\boldsymbol{E}}_0(\tilde{\boldsymbol{x}}).\boldsymbol{A}_M^{-1}(\tilde{\boldsymbol{x}})\end{array}\right.$$

$$\begin{aligned}
&\varepsilon^0(\boldsymbol{x},\boldsymbol{y}) = \boldsymbol{A}_M(\tilde{\boldsymbol{x}}).\tilde{\varepsilon}^0(\tilde{\boldsymbol{x}},\tilde{\boldsymbol{y}}).\boldsymbol{A}_M^{-1}(\tilde{\boldsymbol{x}}) = \boldsymbol{A}_M(\tilde{\boldsymbol{x}}).\tilde{\boldsymbol{A}}^E:\tilde{\boldsymbol{E}}_0(\tilde{\boldsymbol{x}}).\boldsymbol{A}_M^{-1}(\tilde{\boldsymbol{x}}) = \boldsymbol{A}_M(\tilde{\boldsymbol{x}}).\tilde{\boldsymbol{A}}^E.\boldsymbol{A}_M^{-T}(\tilde{\boldsymbol{x}}):\tilde{\boldsymbol{E}}_0(\tilde{\boldsymbol{x}}) \quad (6.47)\\
&det\left(\boldsymbol{A}_M(\tilde{\boldsymbol{x}})^{-1}\right)\left(\boldsymbol{A}_M(\tilde{\boldsymbol{x}}).\tilde{\boldsymbol{A}}^E.\boldsymbol{A}_M^{-T}(\tilde{\boldsymbol{x}})\right):\left(\boldsymbol{A}_M^{-1}(\boldsymbol{x}).\boldsymbol{E}^0(\boldsymbol{x}).\boldsymbol{A}_M(\tilde{\boldsymbol{x}})\right) = det\left(\boldsymbol{A}_M(\tilde{\boldsymbol{x}})^{-1}\right)\tilde{\boldsymbol{A}}^E:\boldsymbol{E}^0(\boldsymbol{x})\\
&\Rightarrow \boldsymbol{A}^E(\boldsymbol{x},\boldsymbol{y}) = det\left(\boldsymbol{A}_M(\tilde{\boldsymbol{x}})^{-1}\right)\boldsymbol{A}_M(\tilde{\boldsymbol{x}}).\tilde{\boldsymbol{A}}^E(\tilde{\boldsymbol{x}},\tilde{\boldsymbol{y}}).\boldsymbol{A}_M^{-T}(\tilde{\boldsymbol{x}})
\end{aligned}$$

6.3.3 Evaluation of the effective quasi-periodic moduli based on energy and Hill lemma

Eq. 6.37, in conjunction with Hill macrohomogeneity condition in the periodic domain, leads to the following set of relations, when inserting into the microscopic energy the asymptotic expansion of stress and strain tensors a referring to Eq. 6.24 for the expansion of the determinant of the tangent map truncated to the leading order term, delivers the expression and asymptotic expansion of the quasi-periodic macroscopic energy density:

$$
\begin{aligned}
2w_{\mu}^{\eta}\left(\boldsymbol{y}\right) &= \boldsymbol{A}_M^T.\boldsymbol{\sigma}^0(\boldsymbol{x}).\boldsymbol{A}_M^{-T} : \begin{pmatrix} \boldsymbol{A}_M^{-1}.\boldsymbol{\varepsilon}^0(\boldsymbol{x},\boldsymbol{y}).\boldsymbol{A}_M + \boldsymbol{A}_M^{-1}.\boldsymbol{\varepsilon}^1(\boldsymbol{x},\boldsymbol{y}).\boldsymbol{A}_M - \\ \boldsymbol{A}_M^{-1}.\left\{\boldsymbol{A}_m.\tilde{\boldsymbol{\varepsilon}}^0(\tilde{\boldsymbol{x}},\tilde{\boldsymbol{y}}).\boldsymbol{A}_M^{-1} - \boldsymbol{A}_m.\tilde{\boldsymbol{\varepsilon}}^0(\tilde{\boldsymbol{x}}).\boldsymbol{A}_M^{-1}.\boldsymbol{A}_m.\boldsymbol{A}_M^{-1}\right\}.\boldsymbol{A}_M \end{pmatrix} + o\left(\eta\right) \\
&= \boldsymbol{\sigma}^0(\boldsymbol{x}) : \left(\boldsymbol{\varepsilon}^0(\boldsymbol{x},\boldsymbol{y}) + \boldsymbol{\varepsilon}^1(\boldsymbol{x},\boldsymbol{y})\right) + \boldsymbol{A}_M^T.\boldsymbol{\sigma}^0(\boldsymbol{x}) : \left\{\tilde{\boldsymbol{\varepsilon}}^0(\tilde{\boldsymbol{x}}).\left(\boldsymbol{A}_M^{-1} - \boldsymbol{A}_M^{-1}.\boldsymbol{A}_m.\boldsymbol{A}_M^{-1}\right)\right\} + o\left(\eta\right) \equiv 2w_{\mu}^{0}\left(\boldsymbol{y}\right) + o\left(\eta\right) \\
\det\left(\boldsymbol{A}^{-1}\right) &= \det\left(\boldsymbol{A}_M^{-1} - \eta\boldsymbol{A}_M^{-1}.\boldsymbol{A}_m.\boldsymbol{A}_M^{-1}\right) \cong \det\left(\boldsymbol{A}_M^{-1}\right) - \eta Tr\left(\boldsymbol{A}_M^{-1}.\boldsymbol{A}_m.\boldsymbol{A}_M^{-1}\right) + o\left(\eta\right) \\
\Rightarrow \tilde{W}_M &\cong \left(\frac{|Y|}{|\tilde{Y}|}\right)\det\left(\boldsymbol{A}_M^{-1}\right)\frac{1}{|Y|}\int\limits_Y w_{\mu}^{0}\left(\boldsymbol{y}\right)dV_y + o\left(\eta\right) = W_M + o\left(\eta\right)
\end{aligned}
\tag{6.48}
$$

with

$$
\begin{aligned}
&2w_{\mu}^{\eta}\left(\tilde{\boldsymbol{y}}\right) = \boldsymbol{\sigma}^{\eta} : \boldsymbol{\varepsilon}^{\eta} = \tilde{\boldsymbol{\sigma}}^{\eta} : \tilde{\boldsymbol{\varepsilon}}^{\eta} = \tilde{\underset{\sim}{\boldsymbol{Q}}}^0 : \tilde{\boldsymbol{\varepsilon}}^0 + o\left(\eta\right) = \tilde{\boldsymbol{\sigma}}^0\left(\tilde{\boldsymbol{x}}\right) : \left(\nabla_{\tilde{x}}\tilde{\boldsymbol{u}}^0\left(\tilde{\boldsymbol{x}}\right) + \nabla_{\tilde{y}}\tilde{\boldsymbol{u}}^1\left(\tilde{\boldsymbol{x}},\tilde{\boldsymbol{y}}\right)\right) + o\left(\eta\right) \equiv 2\tilde{w}_{\mu}^{0}\left(\tilde{\boldsymbol{y}}\right) + o\left(\eta\right) \\
&\begin{vmatrix}
\tilde{\boldsymbol{\sigma}}^0\left(\tilde{\boldsymbol{x}}\right) = \boldsymbol{A}_M^T.\boldsymbol{\sigma}^0(\boldsymbol{x}).\boldsymbol{A}_M^{-T}, \\
\tilde{\boldsymbol{\varepsilon}}^0\left(\tilde{\boldsymbol{x}},\tilde{\boldsymbol{y}}\right) := \left(\nabla_{\tilde{x}}\tilde{\boldsymbol{u}}^0\left(\tilde{\boldsymbol{x}}\right) + \nabla_{\tilde{y}}\tilde{\boldsymbol{u}}^1\left(\tilde{\boldsymbol{x}},\tilde{\boldsymbol{y}}\right)\right) \\
\nabla_{\tilde{x}}\tilde{\boldsymbol{u}}^0\left(\tilde{\boldsymbol{x}}\right) = \boldsymbol{A}_M^{-1}.\nabla_x\boldsymbol{u}^0\left(\boldsymbol{x}\right).\boldsymbol{A}_M \equiv \tilde{\boldsymbol{E}}_0(\tilde{\boldsymbol{x}}), \\
\nabla^S{}_{\tilde{y}}\tilde{\boldsymbol{u}}^1 = \boldsymbol{A}_M^{-1}.\left(\nabla^S{}_y\boldsymbol{u}^1 - \boldsymbol{A}_m.\boldsymbol{A}_M^{-1}.\nabla^S{}_y\boldsymbol{u}^1\right).\boldsymbol{A}_M
\end{vmatrix}
\end{aligned}
$$

We have used the following identity for arbitrary second-order tensors $\boldsymbol{R} : (\boldsymbol{S}.\boldsymbol{T}) = \boldsymbol{S}^T.\boldsymbol{R} : \boldsymbol{T}$ and the macroscopic change of area formula $\det\left(\boldsymbol{A}_M\right) = \left(\frac{|Y|}{|\tilde{Y}|}\right)$ in the previous derivation of the leading order term of the microscopic energy density $w_{\mu}^{\eta}\left(\boldsymbol{y}\right)$. The strain fluctuation $\boldsymbol{\varepsilon}^1(\boldsymbol{x},\boldsymbol{y})$ in Eq. 6.48 (it is the second-order strain in the asymptotic expansion) has to be evaluated numerically by solving the quasi-periodic unit cell BVP in Eq. 6.45 (with quasi-periodicity conditions) and inserted back into the microscopic energy density to evaluate the macroscopic strain energy density, $W_M = \frac{1}{|Y|}\int\limits_Y w_{\mu}^{0}\left(\boldsymbol{y}\right)dV_y$. This last quantity is related to the effective quasi-periodic moduli based on Hill macrohomogeneity condition, viz.

$$
\frac{1}{|Y|}\int\limits_Y w_{\mu}^{0}\left(\boldsymbol{y}\right)dV_y = W_M = \frac{1}{2}\boldsymbol{E}^0(\boldsymbol{x}) : \boldsymbol{C}^{\mathrm{hom}}(\boldsymbol{x}) : \boldsymbol{E}^0(\boldsymbol{x}) \tag{6.49}
$$

As explained in the sequel, the microscopic energy density is evaluated numerically by computing the higher-order strain tensor $\boldsymbol{\varepsilon}^1(\boldsymbol{x},\boldsymbol{y})$ by solving the quasi-periodic unit cell BVP. Taking the average energy density for a specific strain $\boldsymbol{E}^0(\boldsymbol{x})$ imposed over the quasi-periodic unit cell leads to the sequential identification of the effective quasi-periodic moduli as the components $\boldsymbol{C}^{\mathrm{hom}}(\boldsymbol{x})$. Instead of computing the higher-order strain $\boldsymbol{\varepsilon}^1(\boldsymbol{x},\boldsymbol{y})$ in the quasi-periodic domain, one may evaluate it more efficiently in the periodic domain and map it into the quasi-periodic domain.

6.3.4 Evaluation of the tensor of quasi-periodic moduli based on the effective homogeneous medium

Instead of solving the unit cell BVP in the quasi-periodic domain, we may follow a more straightforward approach, bypassing the need to account for the strain fluctuation (in quasi-periodic or periodic domains). Thereby, we replace from the onset the heterogeneous unit cell in both domains with the homogeneous domain and map their effective properties without considering the effect of the underlying microstructure. Using the last relation of Eq. 6.48 involving the sole macroscopic mapping at the leading-order of the small-scale parameter along with Eq. 6.49 leads to the expression of the tensor of effective quasi-periodic moduli versus the tensor of periodic homogenized moduli

$$\begin{aligned}
&\tilde{W}_M = \frac{1}{2}\tilde{\boldsymbol{E}}^0 : \tilde{\boldsymbol{C}}^{\hom} : \tilde{\boldsymbol{E}}^0 = \frac{1}{2}\boldsymbol{E}^0(\boldsymbol{x}) : \boldsymbol{C}^{\hom}(\boldsymbol{x}) : \boldsymbol{E}^0(\boldsymbol{x}) + o(\eta) \\
&\Rightarrow \frac{1}{2}\boldsymbol{A}_M^{-1}(\tilde{\boldsymbol{x}}).\boldsymbol{E}^0(\boldsymbol{x}).\boldsymbol{A}_M(\tilde{\boldsymbol{x}}) : \tilde{\boldsymbol{C}}^{\hom} : \boldsymbol{A}_M^{-1}(\tilde{\boldsymbol{x}}).\boldsymbol{E}^0(\boldsymbol{x}).\boldsymbol{A}_M(\tilde{\boldsymbol{x}}) = \frac{1}{2}\boldsymbol{E}^0(\boldsymbol{x}) : \boldsymbol{C}^{\hom}(\boldsymbol{x}) : \boldsymbol{E}^0(\boldsymbol{x}) \\
&\Rightarrow \boldsymbol{C}^{\hom}(\boldsymbol{x}) = \left(\boldsymbol{A}_M^{-1} \underline{\otimes} \boldsymbol{A}_M^T\right)(\boldsymbol{x}) : \tilde{\boldsymbol{C}}^{\hom} : \left(\boldsymbol{A}_M^{-1} \underline{\otimes} \boldsymbol{A}_M^T\right)(\boldsymbol{x}) + o(\eta)
\end{aligned} \tag{6.50}$$

Note that the previous relation Eq. 6.50 reflects the response of the homogenous unit cells, although the formal evaluation $\tilde{\boldsymbol{C}}^{\hom}$ accounts for the strain fluctuation.

General relation 6.37 in conjunction with Eq. 6.48 then leads to the following expression starting from mirco strain energy densities:

$$\boldsymbol{\varepsilon} : \boldsymbol{C} : \boldsymbol{\varepsilon} = \tilde{\boldsymbol{\varepsilon}} : \tilde{\boldsymbol{C}} : \tilde{\boldsymbol{\varepsilon}} \Rightarrow \langle \boldsymbol{\varepsilon} : \boldsymbol{C} : \boldsymbol{\varepsilon} \rangle_Y = \left\langle \tilde{\boldsymbol{\varepsilon}} : \tilde{\boldsymbol{C}} : \tilde{\boldsymbol{\varepsilon}} \right\rangle_Y = \left\langle \det(\boldsymbol{A}) \left(\tilde{\boldsymbol{\varepsilon}} : \tilde{\boldsymbol{C}} : \tilde{\boldsymbol{\varepsilon}}\right) \right\rangle_{\tilde{Y}} \tag{6.51}$$

For any order, it thus holds

$$W_M \equiv \frac{1}{2}\boldsymbol{E}(\boldsymbol{x}) : \boldsymbol{C}^{\hom}(\boldsymbol{x}) : \boldsymbol{E}(\boldsymbol{x}) = \left\langle \det(\boldsymbol{A}) \left(\tilde{\boldsymbol{\varepsilon}} : \tilde{\boldsymbol{C}} : \tilde{\boldsymbol{\varepsilon}}\right) \right\rangle_{\tilde{Y}} \tag{6.52}$$

As a consequence of previous relations, it holds at the leading order of the asymptotic expansion:

$$\begin{aligned}
\frac{1}{|Y|}\int_Y w_\mu^0(\boldsymbol{y})\, dV_y = \frac{1}{2}\langle \boldsymbol{\varepsilon} : \boldsymbol{c_\mu} : \boldsymbol{\varepsilon} \rangle_Y^0 = W_M^0 \equiv \frac{1}{2}\boldsymbol{E}^0(\boldsymbol{x}) : \boldsymbol{C}^{\hom}(\boldsymbol{x}) : \boldsymbol{E}^0(\boldsymbol{x}) = \left\langle \left(\tilde{\boldsymbol{\varepsilon}} : \tilde{\boldsymbol{C}} : \tilde{\boldsymbol{\varepsilon}}\right) \right\rangle_{\tilde{Y}}^0 \\
= \frac{1}{2}\tilde{\boldsymbol{E}}^0(\tilde{\boldsymbol{x}}) : \tilde{\boldsymbol{C}}^{\hom}(\boldsymbol{x}) : \boldsymbol{E}^0(\tilde{\boldsymbol{x}})
\end{aligned} \tag{6.53}$$

We thus obtain the same expression of the tensor of effective quasi-periodic moduli

$$\boldsymbol{C}^{\hom}(\boldsymbol{x}) = \left(\boldsymbol{A}_M^{-1} \underline{\otimes} \boldsymbol{A}_M^T\right)(\boldsymbol{x}) : \tilde{\boldsymbol{C}}^{\hom} : \left(\boldsymbol{A}_M^{-1} \underline{\otimes} \boldsymbol{A}_M^T\right)(\boldsymbol{x}) \tag{6.54}$$

As a summary of the developments done in this section, the main features of the proposed quasi-periodic homogenization theories are synthesized in Table 6.1. Specific cases of mappings are next considered, leading to some simplifications in deriving the expressions of the quasi-periodic effective moduli.

6.3.5 Specific case: mapping with homogeneous microscale volumetric part

We here rely on the following general transformation rule of the integral of a scalar-valued density (to be identified later on with the microscopic energy density) from the periodic parent domain to the quasi-

Table 6.1 Summary of the formulated quasi-periodic homogenization theories.

Nature of assumptions in the theory (with corresponding equation number)	**Advantages and drawbacks**
Direct mapping of the tensors of effective moduli in Eq. 6.54 at leading order of the small-scale parameter. The unit cell is considered as an equivalent homogeneous material, the effective properties of which being mapped to the quasi-periodic domain.	The relation between the effective quasi-periodic and periodic moduli is directly obtained at the macroscale using the macroscopic map $\boldsymbol{A}_M$. The formulation is simple to implement numerically since the unit cell BVP is solved in the periodic domain.
Solve the unit cell BVP in periodic domain to derive the strain localization operator which is mapped to the strain localization operator in quasi-periodic domain using Eq. 6.13 and BVP in Eq. 6.44.	The periodic strain fluctuation $\tilde{\boldsymbol{\varepsilon}}^1(\tilde{\boldsymbol{x}}, \tilde{\boldsymbol{y}})$ is computed from the strain localization operator as the solution of the periodic unit cell BVP, and then mapped to the quasi-periodic unit cell.
Solve the unit cell BVP directly in quasi-periodic domain via the quasi-periodic strain localization operator in Eq. 6.42.	The unit cell BVP is solved directly in the quasi-periodic domain, without recoursing to the periodic one. Quasi-PBCs may be complicated to implement.

periodic domain:

$$\left\langle \tilde{h}(\tilde{\boldsymbol{y}}) \right\rangle_{\tilde{Y}} := \frac{1}{|\tilde{Y}|} \int_{\tilde{Y}} \tilde{h}(\tilde{\boldsymbol{y}}) \, d\tilde{V}_y = \frac{1}{|\tilde{Y}|} \int_{Y} h(\boldsymbol{y}) \det\left(\boldsymbol{A}^{-1}\right)(\boldsymbol{y}) \, dV_y = \frac{|Y|}{|\tilde{Y}|} \frac{1}{|Y|} \int_{Y} h(\boldsymbol{y}) \det\left(\boldsymbol{A}^{-1}\right)(\boldsymbol{y}) \, dV_y \quad (6.55)$$

The previous identity holds especially at the leading order versus the small-scale parameter, at which the homogenized properties are evaluated. Suppose that the local change of area factor $\det(A)(\tilde{\boldsymbol{y}})$ is independent of the microscopic variable within the quasi-periodic unit cell as a specific situation. In that case, it becomes a function of the sole macroscale variable $\tilde{\boldsymbol{x}}$, evaluated at the center of the area of the unit cell, representing their area change under the coordinate transformation, viz.:

$$\det(A_M)(\tilde{\boldsymbol{x}}) = \frac{|Y|}{|\tilde{Y}|} \quad (6.56)$$

This last specific situation holds mainly when the mapping consists of a pure orthogonal transformation. Note that the deviatoric part associated with shape changes does not intervene in the previous assumption; thus, it may still depend on the microscopic position.

Considering Eq. 6.56 and relying on Eq. 6.48 by considering the leading term of $\det(A)(\tilde{\boldsymbol{x}})$ the equality of the normalized integrals of densities delivers as

$$\left\langle \tilde{h}(\tilde{\boldsymbol{y}}) \right\rangle_{\tilde{Y}} := \frac{1}{|\tilde{Y}|} \int_{\tilde{Y}} \tilde{h}(\tilde{\boldsymbol{y}}) \, d\tilde{V}_y = \frac{1}{|Y|} \int_{Y} h(\boldsymbol{y}) \, dV_y \equiv \left\langle h(\boldsymbol{y}) \right\rangle_{Y} \quad (6.57)$$

Using Eq. 6.57 for the identity of energy densities in articulation with Hill macrohomogeneity condition then directly leads to

$$\begin{aligned}
&\tilde{W}_M = \frac{1}{\left|\tilde{Y}\right|}\int\limits_{\tilde{Y}} \tilde{w}_\mu^\eta\left(\tilde{\boldsymbol{y}}\right) d\tilde{V}_y := \left\langle \frac{1}{2}\tilde{\boldsymbol{\sigma}}^\eta : \tilde{\boldsymbol{\varepsilon}}^\eta \right\rangle_{\tilde{Y}} = \frac{1}{|Y|}\int\limits_{Y} w_\mu^\eta\left(\boldsymbol{y}\right) dV_y = W_M \\
&\Rightarrow \tilde{W}_M = \frac{1}{2}\tilde{\boldsymbol{E}}^\eta : \tilde{\boldsymbol{C}}^{\mathrm{hom}} : \tilde{\boldsymbol{E}}^\eta = \frac{1}{2}\boldsymbol{E}^\eta(\boldsymbol{x}) : \boldsymbol{C}^{\mathrm{hom}}(\boldsymbol{x}) : \boldsymbol{E}^\eta(\boldsymbol{x}),
\end{aligned} \tag{6.58}$$

Note that the macrohomogeneity assumption within the periodic domain implies that the macrostrain $\tilde{\boldsymbol{E}}^\eta(\tilde{\boldsymbol{x}})$ does not depend on the macro-position (contrary to the quasi-periodic domain).

The previous identity then leads to the identification of the tensor of quasi-periodic moduli versus those of the periodic microstructure:

$$\boldsymbol{C}^{\mathrm{hom}}(\boldsymbol{x}) = \left(\boldsymbol{A}_M^{-1} \underline{\otimes} \boldsymbol{A}_M^T\right)(\boldsymbol{x}) : \tilde{\boldsymbol{C}}^{\mathrm{hom}} : \left(\boldsymbol{A}_M^{-1} \underline{\otimes} \boldsymbol{A}_M^T\right)(\boldsymbol{x}) \tag{6.59}$$

This last relation is valid at any order of the small scale parameter, whereas the corresponding relation Eq. 6.50 is only an approximation valid at the leading order.

6.3.6 More specific case of a microscopically homogeneous design transformation

When the entire mapping is not dependent on the microscale, we get the following macro strain relation dictated by the sole macro part of the mapping since it holds

$$\boldsymbol{A}_m\left(\tilde{\boldsymbol{x}}, \tilde{\boldsymbol{y}}\right) = \boldsymbol{0} \Rightarrow \boldsymbol{A} = \boldsymbol{A}_M\left(\tilde{\boldsymbol{x}}\right) \tag{6.60}$$

In this situation, the strain and stress fields transformation rules at the different asymptotic orders become using the general relations Eqs. 6.27 and 6.32, become:

$$\begin{aligned}
&\boldsymbol{\varepsilon}^\eta\left(\boldsymbol{y}\right) = \boldsymbol{\varepsilon}^0(\boldsymbol{x}) + \eta\boldsymbol{\varepsilon}^1(\boldsymbol{x},\boldsymbol{y}) + \eta^2\boldsymbol{\varepsilon}^2(\boldsymbol{x},\boldsymbol{y}), \\
&\boldsymbol{\varepsilon}^0(\boldsymbol{x},\boldsymbol{y}) = \boldsymbol{A}_M\left(\tilde{\boldsymbol{x}}\right).\tilde{\boldsymbol{\varepsilon}}^0\left(\tilde{\boldsymbol{x}},\tilde{\boldsymbol{y}}\right).\boldsymbol{A}_M^{-1}\left(\tilde{\boldsymbol{x}}\right) = \boldsymbol{A}_M\left(\tilde{\boldsymbol{x}}\right).\left(\nabla^S{}_{\tilde{x}}\tilde{\boldsymbol{u}}^0\left(\tilde{\boldsymbol{x}}\right) + \nabla^S{}_{\tilde{y}}\tilde{\boldsymbol{u}}^1\right).\boldsymbol{A}_M^{-1}\left(\tilde{\boldsymbol{x}}\right) \\
&\boldsymbol{\varepsilon}^1(\boldsymbol{x},\boldsymbol{y}) = \boldsymbol{A}_M\left(\tilde{\boldsymbol{x}}\right).\tilde{\boldsymbol{\varepsilon}}^1\left(\tilde{\boldsymbol{y}}\right).\boldsymbol{A}_M^{-1}\left(\tilde{\boldsymbol{x}}\right) \\
&\boldsymbol{\varepsilon}^2(\boldsymbol{x},\boldsymbol{y}) = \boldsymbol{A}_M^{-1}\left(\tilde{\boldsymbol{x}}\right).\tilde{\boldsymbol{\varepsilon}}^0\boldsymbol{A}_M\left(\tilde{\boldsymbol{x}}\right)
\end{aligned} \tag{6.61}$$

$$\begin{aligned}
&\boldsymbol{\sigma}^\eta(\boldsymbol{y}) = \boldsymbol{\sigma}^0(\boldsymbol{x}) + \eta\boldsymbol{\sigma}^1(\boldsymbol{x},\boldsymbol{y}) + \eta^2\boldsymbol{\sigma}^2(\boldsymbol{x},\boldsymbol{y}) \\
&\boldsymbol{\sigma}^0(\boldsymbol{x}) = \boldsymbol{A}_M^{-T}\left(\boldsymbol{x}\right).\tilde{\boldsymbol{\sigma}}^0.\boldsymbol{A}_M^T\left(\tilde{\boldsymbol{x}}\right) \\
&\boldsymbol{\sigma}^1(\boldsymbol{x},\boldsymbol{y}) = \boldsymbol{A}_M^{-T}.\tilde{\boldsymbol{\sigma}}^1.\boldsymbol{A}_M^T \\
&\boldsymbol{\sigma}^2(\boldsymbol{x},\boldsymbol{y}) = \boldsymbol{A}_M^{-T}.\tilde{\boldsymbol{\sigma}}^2.\boldsymbol{A}_M^T
\end{aligned} \tag{6.62}$$

The macrostrain tensors map according to the following relation:

$$\boldsymbol{E}^0\left(\boldsymbol{x}\right) := \boldsymbol{A}_M\left(\tilde{\boldsymbol{x}}\right).\left\langle\tilde{\boldsymbol{\varepsilon}}^0\right\rangle_{\tilde{Y}}.\boldsymbol{A}_M^{-1}\left(\tilde{\boldsymbol{x}}\right) = \boldsymbol{A}_M\left(\tilde{\boldsymbol{x}}\right).\tilde{\boldsymbol{E}}^0\left(\tilde{\boldsymbol{x}}\right).\boldsymbol{A}_M^{-1}\left(\tilde{\boldsymbol{x}}\right) \tag{6.63}$$

Use of Hill macrohomogeneity condition then leads to the following expression of the tensor of effective quasi-periodic moduli:

$$\boldsymbol{C}^{\text{hom}}(\boldsymbol{x}) = \left(\boldsymbol{A}_M^{-1} \underline{\otimes} \boldsymbol{A}_M^T\right)(\boldsymbol{x}) : \tilde{\boldsymbol{C}}^{\text{hom}} : \left(\boldsymbol{A}_M^{-1} \underline{\otimes} \boldsymbol{A}_M^T\right)(\boldsymbol{x}) \tag{6.64}$$

Here, the last relation is also valid at any order of the small scale parameter, whereas the corresponding relation Eq. 6.50 is an approximation only valid at the leading order.

6.3.6.1 Quasi-affine mapping

As a subcase of the previous situation, quasi-affine mappings are next considered, making here an important assumption regarding the way the microstructure transforms concerning the mapping of the macrostructure: a natural assumption is to assume an affine point transformation, obtained by truncating the resulting transformation of the microstructure position to a first gradient model in Eq. 6.18:

$$\tilde{\boldsymbol{y}} \mapsto \boldsymbol{y} = \boldsymbol{\varphi}_{\tilde{y}}(\tilde{\boldsymbol{y}}) = \nabla_{\tilde{\boldsymbol{x}}} \boldsymbol{\varphi}_{\tilde{x}}(\tilde{\boldsymbol{x}}) . \tilde{\boldsymbol{y}} = \boldsymbol{A}_M(\tilde{\boldsymbol{x}}) . \tilde{\boldsymbol{y}} \tag{6.65}$$

Eq. 6.65 means that the microstructure follows exactly the mapping of the macrostructure, which entails that the microscopic gradient of the point mapping is equal to the macroscopic tangent mapping, viz.

$$\nabla_{\tilde{y}} \boldsymbol{\varphi}_{\tilde{y}}(\tilde{\boldsymbol{y}}) = \nabla_{\tilde{x}} \boldsymbol{\varphi}_{\tilde{x}}(\tilde{\boldsymbol{x}}) \tag{6.66}$$

Such an assumption of the geometrical variation of the microstructure has been adopted in [234], who developed a quasi-periodic asymptotic homogenization theory for both elastic and thermal conduction problems in the linear context. In that situation, the unit cell BVP depends on the macroscale in a parametric way, and the tensor of effective properties incorporates the macroscale variation of the design, but it does not account for the variation of unit cell internal design. The identity of Eq. 6.66 has the far-reaching consequence that the transformation law of the microscopic tensor fields will depend not only on the microscale but also on the macroscale and that macroscopic and microscopic gradients transform in precisely the same way when performing asymptotic homogenization. The effective constitutive law can be determined on the quasi-periodic domain from the homogenized tensor computed in the periodic domain, using relation 6.65. The issue of smoothness conditions of the design mapping is next considered to delineate what types of mappings can be used to generate quasi-periodic domains from parent periodic architectured domains.

6.4 Smoothness conditions of quasi-periodic mappings

We define a mapping from the quasi-periodic domain to a parent periodic one by a point mapping inducing a tangent map as Eqs. 6.16- 6.18. In qualitative terms, the smoothness condition states that the point mapping has a slow variation of the design at the macroscale. Both macroscale and microscale mappings $\boldsymbol{A}_M(\tilde{\boldsymbol{x}}), \boldsymbol{A}_m(\tilde{\boldsymbol{x}}, \tilde{\boldsymbol{y}})$ - thus also the full tangent map $\boldsymbol{A}(\tilde{\boldsymbol{x}}, \tilde{\boldsymbol{y}})$ should satisfy the following requirements:

- Macroscopic fluctuations of the effective moduli should occur with a wavelength much larger than the unit cell size so that the assumption of effective behavior of Cauchy type still holds (otherwise, enriched effective continuum descriptions may be needed). This condition has to be verified a posteriori from computational results; this has motivated to limit the transformation mapping to its linearized version, meaning that the variation of the unit cell dimensions has to be 'slow enough' to the unit cell size, such that each unit cell witnesses a homogeneous tensor of effective elastic moduli.
- Due to the unit cell varying dimension(s) in the quasi-periodic domain, the deformation mechanisms should not change drastically from those observed in the periodic reference domain. This criterion could also limit the magnitude of the transformation mapping and has to be verified a posteriori from computational results. In case the geometry varies too fast in the quasi-periodic domain, interactions between neighboring unit cells may be generated, triggering higher-gradients in the macroscopic response of the quasi-periodic composite.

In mathematical terms, we require the following conditions to be satisfied by the conformal point mapping and its tangent:

(i) Boundedness of point mapping: $\lim_{\|\tilde{\boldsymbol{x}}\|\to\infty} \|\boldsymbol{\varphi}(\tilde{\boldsymbol{y}})\| \leqslant K$

(ii) Distributing an initially periodic microstructure within a periodic domain (of possibly infinite size) into a quasi-periodic domain having a finite size requires the condition $\lim_{\|\tilde{\boldsymbol{x}}\|\to\infty} \|A(\tilde{\boldsymbol{y}})\| = 0$ that the quasi-periodic position remains bounded.

(iii) The point mapping $\boldsymbol{\varphi}(\tilde{\boldsymbol{y}})$ should be a monotone growing function of the periodic spatial position variable.

A possible function satisfying these three requirements is the following two parameters exponential function (considered here as a function of a single scalar coordinate $\tilde{\boldsymbol{x}}$:

$$\boldsymbol{\varphi}_{\tilde{y}}(\tilde{\boldsymbol{y}}) = K\left(1 - \exp\left(-\tilde{\boldsymbol{y}}/c\right)\right) \tag{6.67}$$

with K the asymptotic limit, and c a parameter controlling the rate at which the function reaches its horizontal asymptote at infinity. Note that only its dilatational part intervenes in the conditions mentioned above for the considered conformal transformations since its rotation part is bounded. Note that many other choices of smooth mappings are possible, although it is not the aim of this chapter to find them all. Once the designer has selected a mapping, its smoothness can be checked by defining the following geometrical length in tensor format (it is as defined a third-order tensor) as the ratio

$$\underset{\sim}{\boldsymbol{l}} := \nabla_{\tilde{\boldsymbol{x}}}(\nabla_{\tilde{\mathbf{x}}}\varphi_{\tilde{\mathbf{x}}}(\tilde{\mathbf{x}}))(\nabla_{\tilde{\mathbf{x}}}\varphi_{\tilde{\mathbf{x}}}(\tilde{\mathbf{x}}))^{-1} \tag{6.68}$$

quantifying the importance of strain gradient effects in the design variation in different directions of space. This geometrical length may then be compared to the unit cell size, such that a criterion for smooth mappings can be set in the form:

$$l_{ijk} \ll l_{UC} \Rightarrow \nabla_{\tilde{\boldsymbol{x}}}(\nabla_{\tilde{\mathbf{x}}}\varphi_{\tilde{\mathbf{x}}}(\tilde{\mathbf{x}}))(\nabla_{\tilde{\mathbf{x}}}\varphi_{\tilde{\mathbf{x}}}(\tilde{\mathbf{x}}))^{-1}\frac{1}{l_{UC}} \ll 1 \Rightarrow l_{ijk} \ll l_{UC} = \eta L \Rightarrow l_{ijk} \propto \eta^{\theta},\ \theta > 1 \tag{6.69}$$

Thereby, a smooth geometrical transformation is one for which the associated characteristic length of variation is asymptotically more diminutive than the unit cell size.

6.5 Strain gradient models of quasi-periodic microstructures

In order to derive higher-order constitutive models, we perform an asymptotic expansion of the energy in the quasi-periodic domain up to second-order, relying on the identity of the microstrain energy density in both domains and inserting therein the previous expansions of the stress and strain fields of Eqs. 6.25 and 6.31:

$$
\begin{aligned}
&W_M^\eta := \frac{1}{|Y|}\int_Y w_\mu^\eta(\boldsymbol{y})\,dV_y := \left\langle \frac{1}{2}\boldsymbol{\sigma}^\eta : \boldsymbol{\varepsilon}^\eta \right\rangle_Y = \left(\frac{|\tilde{Y}|}{|Y|}\right)\frac{1}{|\tilde{Y}|}\int_{\tilde{Y}} w_\mu^\eta(\tilde{\boldsymbol{y}})\det(\boldsymbol{A})d\tilde{V}_y \\
&\det\boldsymbol{A} = \det(\boldsymbol{A}_M)\left(1+\eta Tr\left({\boldsymbol{A}_M}^{-1}.\boldsymbol{A}_m\right)\right)+o(\eta) \\
&\Rightarrow W_M^\eta = \det(\boldsymbol{A}_M)\left(\frac{|\tilde{Y}|}{|Y|}\right)\frac{1}{|\tilde{Y}|}\int_{\tilde{Y}} w_\mu^\eta(\tilde{\boldsymbol{y}})\,d\tilde{V}_y + \eta\det(\boldsymbol{A}_M)\left(\frac{|\tilde{Y}|}{|Y|}\right)\frac{1}{|\tilde{Y}|}\int_{\tilde{Y}} w_\mu^\eta(\tilde{\boldsymbol{y}})\,Tr\left({\boldsymbol{A}_M}^{-1}.\boldsymbol{A}_m\right)d\tilde{V}_y \\
&\qquad = \frac{1}{|\tilde{Y}|}\int_{\tilde{Y}} w_\mu^\eta(\tilde{\boldsymbol{y}})\,d\tilde{V}_y + \eta\frac{1}{|\tilde{Y}|}\int_{\tilde{Y}} w_\mu^\eta(\boldsymbol{y})\,Tr\left(\boldsymbol{A}_M^{-1}.\boldsymbol{A}_m\right)d\tilde{V}_y \\
&\qquad \equiv \left\langle w_\mu^\eta(\tilde{\boldsymbol{y}})\right\rangle_{\tilde{Y}} + \eta\left\langle w_\mu^\eta(\tilde{\boldsymbol{y}})\,Tr\left(\boldsymbol{A}_M^{-1}.\boldsymbol{A}_m\right)\right\rangle_{\tilde{Y}} + o(\eta)
\end{aligned}
\tag{6.70}
$$

Note that the expansion has been truncated to the second-order of the small-scale parameter in Eq. 6.70. We thereby assume that area variation is of higher-order compared to the variation of the mechanical fields within the unit cell (especially when there is a strong contrast of properties of constituents within the unit cell or/and in the non-diluted regime, for instance, for a high volume fraction of rigid inclusions within a softer matrix phase).

The microscopic strain energy density $w_\mu^\eta(\tilde{\boldsymbol{y}})$ in the periodic domain therein is next expanded up to the third-order of the small-scale parameter:

$$
\begin{aligned}
w_\mu^\eta(\boldsymbol{y}) &= \frac{1}{2}\boldsymbol{\sigma}^\eta : \boldsymbol{\varepsilon}^\eta = \frac{1}{2}\tilde{\boldsymbol{\sigma}}^\eta : \tilde{\boldsymbol{\varepsilon}}^\eta = \frac{1}{2}\tilde{\boldsymbol{\sigma}}^0 : \tilde{\boldsymbol{\varepsilon}}^0 + \eta\frac{1}{2}\left(\tilde{\boldsymbol{\sigma}}^0 : \tilde{\boldsymbol{\varepsilon}}^1 + \tilde{\boldsymbol{\sigma}}^1 : \tilde{\boldsymbol{\varepsilon}}^0\right) + \eta^2\frac{1}{2}\left(\tilde{\boldsymbol{\sigma}}^0 : \tilde{\boldsymbol{\varepsilon}}^2 + \tilde{\boldsymbol{\sigma}}^2 : \tilde{\boldsymbol{\varepsilon}}^0 + \tilde{\boldsymbol{\sigma}}^1 : \tilde{\boldsymbol{\varepsilon}}^1\right) \\
&\equiv \tilde{w}_\mu^0\left(\tilde{\boldsymbol{\varepsilon}}^0\right) + \eta\tilde{w}_\mu^1\left(\tilde{\boldsymbol{\varepsilon}}^0, \tilde{\boldsymbol{\varepsilon}}^1\right) + \eta^2\tilde{w}_\mu^2\left(\tilde{\boldsymbol{\varepsilon}}^1, \tilde{\boldsymbol{\varepsilon}}^2\right) + o\left(\eta^2\right) := \tilde{w}_\mu^\eta(\tilde{\boldsymbol{y}})
\end{aligned}
\tag{6.71}
$$

Inserting the previous expressions of the microscopic energy densities leads to the following expansion of

macroscopic energy in the quasi-periodic domain:

$$
\begin{aligned}
&W_M^\eta = \langle w_\mu^0\left(\tilde{\boldsymbol{\varepsilon}}^0\right)\rangle_{\tilde{Y}} + \eta\left(\langle w_\mu^0\left(\tilde{\boldsymbol{\varepsilon}}^0\right) Tr\left(\boldsymbol{A}_M{}^{-1}.\boldsymbol{A}_m\right)\rangle_{\tilde{Y}} + \langle w_\mu^1\left(\tilde{\boldsymbol{\varepsilon}}^0,\tilde{\boldsymbol{\varepsilon}}^1\right)\rangle_{\tilde{Y}}\right) + \eta^2\langle w_\mu^1\left(\tilde{\boldsymbol{\varepsilon}}^0,\tilde{\boldsymbol{\varepsilon}}^1\right) Tr\left(\boldsymbol{A}_m.\boldsymbol{A}_M^{-1}\right) + w_\mu^2\left(\tilde{\boldsymbol{\varepsilon}}^0,\tilde{\boldsymbol{\varepsilon}}^1,\tilde{\boldsymbol{\varepsilon}}^2\right)\rangle_{\tilde{Y}} + o\left(\eta^2\right)\\
&w_\mu^0\left(\tilde{\boldsymbol{\varepsilon}}^0\right) := \frac{1}{2}\tilde{\boldsymbol{\sigma}}^0 : \tilde{\boldsymbol{\varepsilon}}^0,\ w_\mu^1\left(\tilde{\boldsymbol{\varepsilon}}^0,\tilde{\boldsymbol{\varepsilon}}^1\right) := \frac{1}{2}\left(\tilde{\boldsymbol{\sigma}}^0 : \tilde{\boldsymbol{\varepsilon}}^1 + \tilde{\boldsymbol{\sigma}}^1 : \tilde{\boldsymbol{\varepsilon}}^0\right) \Rightarrow \langle w_\mu^1\left(\tilde{\boldsymbol{\varepsilon}}^0,\tilde{\boldsymbol{\varepsilon}}^1\right)\rangle_{\tilde{Y}} = \frac{1}{2}\left(\tilde{\boldsymbol{\sigma}}^0 : \langle\tilde{\boldsymbol{\varepsilon}}^1\rangle_{\tilde{Y}} + \langle\tilde{\boldsymbol{\sigma}}^1 : \tilde{\boldsymbol{\varepsilon}}^0\rangle_{\tilde{Y}}\right),\\
&w_\mu^2\left(\tilde{\boldsymbol{\varepsilon}}^0,\tilde{\boldsymbol{\varepsilon}}^1,\tilde{\boldsymbol{\varepsilon}}^2\right) := \frac{1}{2}\left(\tilde{\boldsymbol{\sigma}}^0 : \tilde{\boldsymbol{\varepsilon}}^2 + \tilde{\boldsymbol{\sigma}}^2 : \tilde{\boldsymbol{\varepsilon}}^0 + \tilde{\boldsymbol{\sigma}}^1 : \tilde{\boldsymbol{\varepsilon}}^1\right) \Rightarrow \langle w_\mu^2\left(\tilde{\boldsymbol{\varepsilon}}^0,\tilde{\boldsymbol{\varepsilon}}^1,\tilde{\boldsymbol{\varepsilon}}^2\right)\rangle_{\tilde{Y}} = \left\langle\frac{1}{2}\left(\tilde{\boldsymbol{\sigma}}^0\left(\tilde{\boldsymbol{x}}\right) : \tilde{\boldsymbol{\varepsilon}}^2 + \tilde{\boldsymbol{\sigma}}^2 : \tilde{\boldsymbol{\varepsilon}}^0 + \tilde{\boldsymbol{\sigma}}^1 : \tilde{\boldsymbol{\varepsilon}}^1\right)\right\rangle_{\tilde{Y}}\\
&\tilde{\boldsymbol{\varepsilon}}^0(\tilde{\boldsymbol{x}}) = \boldsymbol{A}_M^{-1}\left(\boldsymbol{x}\right).\tilde{\boldsymbol{\varepsilon}}^0(\boldsymbol{x},\boldsymbol{y}).\boldsymbol{A}_M\left(\tilde{\boldsymbol{x}}\right)\\
&\tilde{\boldsymbol{\varepsilon}}^1 = \nabla^S{}_{\tilde{x}}\tilde{\boldsymbol{u}}^1 + \nabla^S{}_{\tilde{y}}\tilde{\boldsymbol{u}}^2 \Rightarrow \langle\tilde{\boldsymbol{\varepsilon}}^1\rangle_{\tilde{Y}} = \langle\nabla^S{}_{\tilde{x}}\tilde{\boldsymbol{u}}^1\rangle_{\tilde{Y}} = \left\langle\boldsymbol{H}^E\left(\tilde{\boldsymbol{y}}\right)\right\rangle_{\tilde{Y}} : \nabla^S{}_{\tilde{x}}\tilde{\boldsymbol{E}}^0\\
&\Rightarrow W_M^\eta = \frac{1}{2}\boldsymbol{E}^\eta : \boldsymbol{C}^{\mathrm{hom},\eta} : \boldsymbol{E}^\eta =\\
&\qquad = \frac{1}{2}\tilde{\boldsymbol{E}}^0 : \tilde{\boldsymbol{C}}^{\mathrm{hom},0} : \tilde{\boldsymbol{E}}^0 + \eta\left(\langle w_\mu^0\left(\tilde{\boldsymbol{\varepsilon}}^0\right)\boldsymbol{A}_m\rangle_{\tilde{Y}} : \boldsymbol{A}_M^{-T} + \langle w_\mu^1\left(\tilde{\boldsymbol{\varepsilon}}^0,\tilde{\boldsymbol{\varepsilon}}^1\right)\rangle_{\tilde{Y}}\right) + \eta^2\langle w_\mu^1\left(\tilde{\boldsymbol{\varepsilon}}^0,\tilde{\boldsymbol{\varepsilon}}^1\right) Tr\left(\boldsymbol{A}_m.\boldsymbol{A}_M^{-1}\right) + w_\mu^2\left(\tilde{\boldsymbol{\varepsilon}}^0,\tilde{\boldsymbol{\varepsilon}}^1,\tilde{\boldsymbol{\varepsilon}}^2\right)\rangle_{\tilde{Y}} + o\left(\eta^2\right)\\
&\qquad = \frac{1}{2}\tilde{\boldsymbol{E}}^0 : \tilde{\boldsymbol{C}}^{\mathrm{hom},0} : \tilde{\boldsymbol{E}}^0 + \eta\left(\left\langle\frac{1}{2}\left(\tilde{\boldsymbol{\sigma}}^0 : \tilde{\boldsymbol{\varepsilon}}^0\right)\boldsymbol{A}_m\right\rangle_{\tilde{Y}} : \boldsymbol{A}_M^{-T} + \frac{1}{2}\left(\tilde{\boldsymbol{\sigma}}^0\left(\tilde{\boldsymbol{x}}\right) : \langle\nabla^S{}_{\tilde{x}}\tilde{\boldsymbol{u}}^1\rangle_{\tilde{Y}} + \langle\tilde{\boldsymbol{\sigma}}^1 : \tilde{\boldsymbol{\varepsilon}}^0\rangle_{\tilde{Y}}\right)\right)\\
&\qquad +\eta^2\left\langle\frac{1}{2}\left(\tilde{\boldsymbol{\sigma}}^0 : \langle\tilde{\boldsymbol{\varepsilon}}^1\rangle_{\tilde{Y}} + \langle\tilde{\boldsymbol{\sigma}}^1 : \tilde{\boldsymbol{\varepsilon}}^0\rangle_{\tilde{Y}}\right) Tr\left(\boldsymbol{A}_m.\boldsymbol{A}_M^{-T}\right) + \frac{1}{2}\left(\tilde{\boldsymbol{\sigma}}^0\left(\tilde{\boldsymbol{x}}\right) : \tilde{\boldsymbol{\varepsilon}}^2 + \tilde{\boldsymbol{\sigma}}^2 : \tilde{\boldsymbol{\varepsilon}}^0 + \tilde{\boldsymbol{\sigma}}^1 : \tilde{\boldsymbol{\varepsilon}}^1\right)\right\rangle_{\tilde{Y}} + o\left(\eta^2\right)
\end{aligned}
\tag{6.72}
$$

Note that all integrals building the asymptotic expansion of the macroscopic energy density W_M^η are performed over the periodic unit cell (by variable change).

The terms $\left\langle\nabla^S{}_{\tilde{x}}\tilde{\boldsymbol{u}}^1\right\rangle_{\tilde{Y}}, \left\langle\tilde{\boldsymbol{\varrho}}^1 : \tilde{\boldsymbol{\varepsilon}}^0\right\rangle_{\tilde{Y}}$ therein can only be evaluated numerically by solving the unit cell BVP in Eq. 6.10 for the displacement localization operator $\boldsymbol{H}^E\left(\tilde{\boldsymbol{y}}\right)$ in the periodic unit cell. Use of Maxwell-Betti reciprocity theorem for the two mechanical states $\left(\tilde{\boldsymbol{\varepsilon}}^0,\tilde{\boldsymbol{\sigma}}^0\right),\ \left(\tilde{\boldsymbol{\varepsilon}}^1,\tilde{\boldsymbol{\sigma}}^1\right)$ entails the equality of energy densities, viz. $\tilde{\boldsymbol{\sigma}}^0 : \tilde{\boldsymbol{\varepsilon}}^1 = \tilde{\boldsymbol{\sigma}}^1 : \tilde{\boldsymbol{\varepsilon}}^0$, thus resulting in

$$
\begin{aligned}
W_M^\eta = &\frac{1}{2}\tilde{\boldsymbol{E}}^0 : \tilde{\boldsymbol{C}}^{\mathrm{hom},0} : \tilde{\boldsymbol{E}}^0 + \eta\left(\left\langle\frac{1}{2}\left(\tilde{\boldsymbol{\sigma}}^0 : \tilde{\boldsymbol{\varepsilon}}^0\right)\boldsymbol{A}_m\right\rangle_{\tilde{Y}} : \boldsymbol{A}_M^{-T} + \tilde{\boldsymbol{\Sigma}}^0 : \left\langle\boldsymbol{H}^E\left(\tilde{\boldsymbol{y}}\right)\right\rangle_{\tilde{Y}} : \nabla^S{}_{\tilde{x}}\tilde{\boldsymbol{E}}^0\right)\\
&+\eta^2\left\langle\left(\tilde{\boldsymbol{\sigma}}^0 : \left\langle\tilde{\boldsymbol{\varepsilon}}^1\right\rangle_{\tilde{Y}}\right) Tr\left(\boldsymbol{A}_m.\boldsymbol{A}_M^{-T}\right) + \frac{1}{2}\left(\tilde{\boldsymbol{\sigma}}^0\left(\tilde{\boldsymbol{x}}\right) : \tilde{\boldsymbol{\varepsilon}}^2 + \tilde{\boldsymbol{\sigma}}^2 : \tilde{\boldsymbol{\varepsilon}}^0 + \tilde{\boldsymbol{\sigma}}^1 : \tilde{\boldsymbol{\varepsilon}}^1\right)\right\rangle_{\tilde{Y}} + o\left(\eta^2\right)
\end{aligned}
\tag{6.73}
$$

with $\tilde{\boldsymbol{\Sigma}}^0\left(\tilde{\boldsymbol{x}}\right) := \tilde{\boldsymbol{\sigma}}^0\left(\tilde{\boldsymbol{x}}\right)$ the macrostress tensor. Note, however, that the displacement localization operator can be selected to be of nil average so that one needs in full generality to expand the macroscopic energy in Eq. 6.73 to a higher-order. Thereby, a strain gradient model emerges at the second-order in the small-scale parameter.

Moreover, according to Eq. 6.18, it holds the following relation for any tangent $\boldsymbol{A}_M$ and $\boldsymbol{A}_m$.

$$
\boldsymbol{A}_m : \boldsymbol{A}_M^{-T} = Tr\left(\boldsymbol{A}_m.\boldsymbol{A}_M^{-1}\right) = Tr\left\{\begin{pmatrix}\boldsymbol{0} & \boldsymbol{0}\\ \nabla_{\tilde{\boldsymbol{x}}}\boldsymbol{y}\left(\tilde{\boldsymbol{x}},\tilde{\boldsymbol{y}}\right) & \boldsymbol{0}\end{pmatrix}.\begin{pmatrix}\nabla_{\tilde{\boldsymbol{x}}}\boldsymbol{\varphi}_{\tilde{x}}\left(\tilde{\boldsymbol{x}}\right) & \boldsymbol{0}\\ \boldsymbol{0} & \nabla_{\tilde{y}}\boldsymbol{y}\left(\tilde{\boldsymbol{x}},\tilde{\boldsymbol{y}}\right)\end{pmatrix}\right\} = 0 \tag{6.74}
$$

Insertion of Eq. 6.74 into Eq. 6.73 delivers recalling Eq. 6.17 the following expansion of the macroscopic energy density:

$$
\begin{aligned}
W_M^\eta = &\frac{1}{2}\tilde{\boldsymbol{E}}^0 : \tilde{\boldsymbol{C}}^{\mathrm{hom},0} : \tilde{\boldsymbol{E}}^0 + \eta\left(\boldsymbol{\Sigma}^0 : \left\langle\boldsymbol{H}^E\right\rangle_{\tilde{Y}} : \nabla^S{}_{\tilde{x}}\tilde{\boldsymbol{E}}^0\right)\\
&+\eta^2\frac{1}{2}\left(\tilde{\boldsymbol{\sigma}}^0\left(\tilde{\boldsymbol{x}}\right) : \langle\tilde{\boldsymbol{\eta}}^2\rangle_{\tilde{Y}} + \langle\tilde{\boldsymbol{\sigma}}^2 : \tilde{\boldsymbol{\eta}}^0\rangle_{\tilde{Y}} + \left\langle\left(\tilde{\boldsymbol{\sigma}}^1 : \boldsymbol{H}^E\right)\right\rangle_{\tilde{Y}} : \nabla^S{}_{\tilde{x}}\tilde{\boldsymbol{E}}^0\right) + o\left(\eta^2\right)
\end{aligned}
\tag{6.75}
$$

Thereby, the macroscopic energy in the quasi-periodic domain is expanded in terms of the Cauchy contribution at leading order, the second term at the next order traduces a coupling between Cauchy stress and strain gradient kinematics, which is only present for non-centrosymmetric media, and the last term represents the strain-gradient energy.

The higher-order stress tensor $\tilde{\boldsymbol{\sigma}}^1$ verifies the following balance of linear momentum, extending Eq. 6.7:

$$\left|\begin{array}{l} div_{\tilde{y}}\tilde{\boldsymbol{\sigma}}^1 + div_{\tilde{x}}\tilde{\boldsymbol{\sigma}}^0 + \tilde{\boldsymbol{f}} = \boldsymbol{0} \Rightarrow \left\langle div_{\tilde{x}}\tilde{\boldsymbol{\sigma}}^0 \right\rangle_{\tilde{Y}} + \left\langle \tilde{\boldsymbol{f}} \right\rangle_{\tilde{Y}} = \boldsymbol{0} \\ \tilde{\boldsymbol{\sigma}}^0 = \tilde{\boldsymbol{C}} : \tilde{\boldsymbol{\varepsilon}}^0 = \tilde{\boldsymbol{C}} : \left(\nabla_{\tilde{x}}\tilde{\boldsymbol{u}}^0\left(\tilde{\boldsymbol{x}}\right) + \nabla_{\tilde{y}}\tilde{\boldsymbol{u}}^1\right) : \tilde{\boldsymbol{E}}^0\left(\tilde{\boldsymbol{x}}\right) \\ \tilde{\boldsymbol{u}}^1 = \tilde{\boldsymbol{H}}^E : \tilde{\boldsymbol{E}}^0\left(\tilde{\boldsymbol{x}}\right) \Rightarrow \tilde{\boldsymbol{\varepsilon}}^1 = \nabla_{\tilde{x}}\tilde{\boldsymbol{u}}^1 + \nabla_{\tilde{y}}\tilde{\boldsymbol{u}}^2 = \tilde{\boldsymbol{H}}^E : \nabla_{\tilde{x}}\tilde{\boldsymbol{E}}^0\left(\tilde{\boldsymbol{x}}\right) + \nabla_{\tilde{y}}\tilde{\boldsymbol{u}}^2 \\ \tilde{\boldsymbol{\sigma}}^1 = \tilde{\boldsymbol{C}} : \tilde{\boldsymbol{\varepsilon}}^1 = \tilde{\boldsymbol{C}} : \left(\tilde{\boldsymbol{H}}^E : \nabla_{\tilde{x}}\tilde{\boldsymbol{E}}^0\left(\tilde{\boldsymbol{x}}\right) + \nabla_{\tilde{y}}\tilde{\boldsymbol{u}}^2\right) \end{array}\right. \tag{6.76}$$

$$\Rightarrow \left|\begin{array}{l} div_{\tilde{y}}\left(\tilde{\boldsymbol{C}} : \left(\tilde{\boldsymbol{H}}^E : \nabla_{\tilde{x}}\tilde{\boldsymbol{E}}^0\left(\tilde{\boldsymbol{x}}\right) + \nabla_{\tilde{y}}\tilde{\boldsymbol{u}}^2\right)\right) + \tilde{\boldsymbol{C}} : \tilde{\boldsymbol{A}}^E : \nabla_{\tilde{x}}\tilde{\boldsymbol{E}}^0 + \tilde{\boldsymbol{f}} = \boldsymbol{0} \\ \tilde{\boldsymbol{u}}^2 \text{periodic, } \tilde{\boldsymbol{\sigma}}^1.\boldsymbol{n} \text{ antiperiodic} \end{array}\right.$$

The consequence of the second-order equilibrium equation is defining a global compatibility condition stating that the stress $\tilde{\boldsymbol{\sigma}}^0$ has to be compatible with the average body force $\left\langle \tilde{\boldsymbol{f}} \right\rangle_{\tilde{Y}}$. The previous BVP for the displacement $\tilde{\boldsymbol{u}}^2$ is linear in the following kinematic loading tensors

$$\tilde{\boldsymbol{E}}^0\left(\tilde{\boldsymbol{x}}\right), \ \tilde{\boldsymbol{K}}^0\left(\tilde{\boldsymbol{x}}\right) := \nabla_{\tilde{x}}\tilde{\boldsymbol{E}}^0\left(\tilde{\boldsymbol{x}}\right) \tag{6.77}$$

Thus, a strain gradient localization operator $\tilde{\boldsymbol{H}}^K\left(\tilde{\boldsymbol{y}}\right)$ exists such that it holds (the macroscopic displacement appearing as an 'integration constant' is discarded):

$$\tilde{\boldsymbol{u}}^2\left(\tilde{\boldsymbol{x}}, \tilde{\boldsymbol{y}}\right) = \tilde{\boldsymbol{H}}^K\left(\tilde{\boldsymbol{y}}\right) \therefore \tilde{\boldsymbol{K}}^0\left(\tilde{\boldsymbol{x}}\right) + \tilde{\boldsymbol{U}}^2\left(\tilde{\boldsymbol{x}}\right) \tag{6.78}$$

in which $\tilde{\boldsymbol{U}}^2\left(\tilde{\boldsymbol{x}}\right)$ is a macroscopic displacement resulting from the integration of the higher-order unit cell BVP of Eq. 6.76.

Inserting the previous expression of the microscopic third-order displacement field into Eq. 6.75 delivers the asymptotic expansion of the macroscopic energy density within the quasi-periodic domain:

$$\begin{aligned} W_M^\eta = & \frac{1}{2}\tilde{\boldsymbol{E}}^0 : \tilde{\boldsymbol{C}}^{\hom,0} : \tilde{\boldsymbol{E}}^0 + \eta\left(\boldsymbol{\Sigma}^0 : \left\langle \boldsymbol{H}^E \right\rangle_{\tilde{Y}} : \tilde{\boldsymbol{K}}^0\right) \\ & + \eta^2 \frac{1}{2}\left(\tilde{\boldsymbol{\sigma}}^0\left(\tilde{\boldsymbol{x}}\right) : \left\langle \nabla_{\tilde{x}}\tilde{\boldsymbol{u}}^2 \right\rangle_{\tilde{Y}} + \left\langle \tilde{\boldsymbol{\sigma}}^2 : \tilde{\boldsymbol{\varepsilon}}^0 \right\rangle_{\tilde{Y}} + \left\langle \left(\tilde{\boldsymbol{C}} : \left(\tilde{\boldsymbol{H}}^E : \tilde{\boldsymbol{K}}^0 + \nabla_{\tilde{y}}\tilde{\boldsymbol{u}}^2\right) : \boldsymbol{H}^E\right) \right\rangle_{\tilde{Y}} : \tilde{\boldsymbol{K}}^0\right) + o\left(\eta^2\right) \end{aligned} \tag{6.79}$$

Since the term $\nabla_{\tilde{x}}\tilde{\boldsymbol{u}}^2$ involves the macro gradient tensor $\tilde{\boldsymbol{K}}^0\left(\tilde{\boldsymbol{x}}\right)$, it can be neglected in the present framework of strain gradient mechanics; the following transformation rules of the macroscopic gradient and strain gradient tensors will prove helpful:

$$\begin{aligned} & \tilde{\boldsymbol{E}}^0\left(\tilde{\boldsymbol{x}}\right) = \boldsymbol{A}_M^{-1}\left(\tilde{\boldsymbol{x}}\right).\boldsymbol{E}^0\left(\boldsymbol{x}\right).\boldsymbol{A}_M\left(\tilde{\boldsymbol{x}}\right), \\ & \left(\nabla_x \boldsymbol{A}_M\right)_{ijk} = \frac{\partial^2 x^i}{\partial\tilde{x}^k \partial\tilde{x}^j} \equiv x^i{}_{,jk} \Rightarrow \left(\nabla^T{}_x \boldsymbol{A}_M\right)_{ijk} = x^j{}_{,ik} = x^j{}_{,ki} \\ & \boldsymbol{K}^0 := \nabla_x \boldsymbol{E}^0 \Rightarrow \tilde{\boldsymbol{K}}^0\left(\tilde{\boldsymbol{x}}\right) := \nabla_{\tilde{x}}\tilde{\boldsymbol{E}}^0\left(\tilde{\boldsymbol{x}}\right) = \boldsymbol{A}_M^T.\nabla_x\left(\boldsymbol{A}_M^{-1}.\boldsymbol{E}^0.\boldsymbol{A}_M\right) \\ & \quad = -\boldsymbol{A}_M^T.\boldsymbol{A}_M^{-1}.\nabla_x\boldsymbol{A}_M.\boldsymbol{A}_M^{-1}.\boldsymbol{E}^0.\boldsymbol{A}_M + \boldsymbol{A}_M^T.\boldsymbol{A}_M^{-1}.\boldsymbol{E}^0.\nabla_x\boldsymbol{A}_M + \boldsymbol{A}_M^T.\boldsymbol{K}^0.\boldsymbol{A}_M \\ & \quad = -\boldsymbol{A}_M^T.\boldsymbol{A}_M^{-1}.\nabla_x\boldsymbol{A}_M.\left(\boldsymbol{A}_M^{-1}\underline{\otimes}\boldsymbol{A}_M^T\right) : \boldsymbol{E}^0 + \boldsymbol{A}_M^T.\boldsymbol{A}_M^{-1}.\nabla^T{}_x\boldsymbol{A}_M.\boldsymbol{E}^0 + \left(\boldsymbol{A}_M^T\underline{\otimes}\boldsymbol{A}_M^T\right) : \boldsymbol{K}^0 \end{aligned} \tag{6.80}$$

Previous expression Eq. 6.79 together with the set of relations Eq. 6.80 then delivers the following asymptotic expansion of the macroscopic energy density versus the quasi-periodic macroscopic kinematic

variables:

$$
\begin{aligned}
W_M^{\eta} &= \frac{1}{2}\tilde{\boldsymbol{E}}^0 : \tilde{\boldsymbol{C}}^{\hom,0} : \tilde{\boldsymbol{E}}^0 + \eta\left(\tilde{\boldsymbol{E}}^0 : \tilde{\boldsymbol{C}}^{\hom,0} : \left\langle \boldsymbol{H}^E \right\rangle_{\tilde{Y}} : \tilde{\boldsymbol{K}}^0\right) \\
&\quad + \eta^2 \frac{1}{2}\left(\left\langle\left(\left(\tilde{\boldsymbol{C}} : \left(\tilde{\boldsymbol{H}}^E : \tilde{\boldsymbol{K}}^0 + \nabla_{\tilde{y}}\tilde{\boldsymbol{H}}^K\left(\tilde{\boldsymbol{y}}\right) \therefore \tilde{\boldsymbol{K}}^0\left(\tilde{\boldsymbol{x}}\right)\right)\right) : \tilde{\boldsymbol{H}}^E\right)\right\rangle_{\tilde{Y}} : \tilde{\boldsymbol{K}}^0 + \left\langle\left(\tilde{\boldsymbol{C}} : \tilde{\boldsymbol{H}}^K\left(\tilde{\boldsymbol{y}}\right) \therefore \tilde{\boldsymbol{K}}^0\left(\tilde{\boldsymbol{x}}\right)\right) : \nabla_{\tilde{y}}\tilde{\boldsymbol{H}}^E\right\rangle_{\tilde{Y}} : \tilde{\boldsymbol{E}}^0\right) + o\left(\eta^2\right) \\
&\quad = W_M^0 + \eta W_M^1 + \eta^2 W_M^2, \\
&\left|\begin{aligned}
W_M^0\left(\tilde{\boldsymbol{E}}^0\right) &= \frac{1}{2}\tilde{\boldsymbol{E}}^0 : \tilde{\boldsymbol{C}}^{\hom,0} : \tilde{\boldsymbol{E}}^0 = \frac{1}{2}\boldsymbol{E}^0 . \left(\boldsymbol{A}_M^{-1} \underline{\otimes} \boldsymbol{A}_M^T\right) : \tilde{\boldsymbol{C}}^{\hom,0} : \left(\boldsymbol{A}_M^{-1} \underline{\otimes} \boldsymbol{A}_M^T\right) : \boldsymbol{E}^0, \\
W_M^1\left(\tilde{\boldsymbol{E}}^0, \tilde{\boldsymbol{K}}^0\right) &= \tilde{\boldsymbol{E}}^0 : \tilde{\boldsymbol{C}}^{\hom,0} : \left\langle \boldsymbol{H}^E \right\rangle_{\tilde{Y}} : \tilde{\boldsymbol{K}}^0 \\
&\quad = \frac{1}{2}\boldsymbol{E}^0 . \left(\boldsymbol{A}_M^{-1} \underline{\otimes} \boldsymbol{A}_M^T\right) : \tilde{\boldsymbol{C}}^{\hom,0} : \left\langle \boldsymbol{H}^E \right\rangle_{\tilde{Y}} : \left(-\boldsymbol{A}_M^T . \boldsymbol{A}_M^{-1} . \nabla_x \boldsymbol{A}_M . \left(\boldsymbol{A}_M^{-1} \underline{\otimes} \boldsymbol{A}_M^T\right) : \boldsymbol{E}^0 + \boldsymbol{A}_M^T . \boldsymbol{A}_M^{-1} . \nabla^T{}_x \boldsymbol{A}_M . \boldsymbol{E}^0 + \left(\boldsymbol{A}_M^T \underline{\otimes} \boldsymbol{A}_M^T\right) : \boldsymbol{K}^0\right) \\
W_M^2\left(\tilde{\boldsymbol{E}}^0, \tilde{\boldsymbol{K}}^0\right) &= \frac{1}{2}\tilde{\boldsymbol{K}}^0 : \left\langle \tilde{\boldsymbol{H}}^E : \tilde{\boldsymbol{C}} : \tilde{\boldsymbol{H}}^E + \tilde{\boldsymbol{C}} : \nabla_{\tilde{y}}\tilde{\boldsymbol{H}}^K : \tilde{\boldsymbol{H}}^E \right\rangle_{\tilde{Y}} : \tilde{\boldsymbol{K}}^0 + \tilde{\boldsymbol{K}}^0 \therefore \left\langle \left(\tilde{\boldsymbol{C}} : \tilde{\boldsymbol{H}}^K\right) : \nabla_{\tilde{y}}\tilde{\boldsymbol{H}}^E \right\rangle_{\tilde{Y}} : \tilde{\boldsymbol{E}}^0
\end{aligned}\right.
\end{aligned}
\tag{6.81}
$$

Thereby, the Cauchy, pure strain gradient, and interaction energies between Cauchy and strain gradient behaviors are highlighted as the leading-order (first-order), third-order, and second-order contributions in Eq. 6.81. It seems at first sight surprising that the strain gradient energy $W_M^2\left(\tilde{\boldsymbol{E}}^0, \tilde{\boldsymbol{K}}^0\right)$ includes a coupling term; this results from the specific point mapping Ansatz in Eq.(84), resulting in macroscopic and microscopic tangents sharing the same term $\nabla_{\tilde{x}}\boldsymbol{\varphi}_{\tilde{x}} + \nabla_{\tilde{x}} \otimes \nabla_{\tilde{x}}\boldsymbol{\varphi}_{\tilde{\boldsymbol{x}}} . \tilde{\boldsymbol{y}}$.

Using Eq. 6.76 The resulting macroscopic strain gradient constitutive law is written in the asymptotic form:

$$
\left|\begin{aligned}
&W_M^0\left(\tilde{\boldsymbol{E}}^0\right) = \frac{1}{2}\tilde{\boldsymbol{E}}^0 : \tilde{\boldsymbol{C}}^{\hom,0} : \tilde{\boldsymbol{E}}^0 = \frac{1}{2}\boldsymbol{E}^0 . \left(\boldsymbol{A}_M^{-1} \underline{\otimes} \boldsymbol{A}_M^T\right) : \tilde{\boldsymbol{C}}^{\hom,0} : \left(\boldsymbol{A}_M^{-1} \underline{\otimes} \boldsymbol{A}_M^T\right) : \boldsymbol{E}^0, \\
&W_M^1\left(\tilde{\boldsymbol{E}}^0, \tilde{\boldsymbol{K}}^0\right) = \tilde{\boldsymbol{E}}^0 : \tilde{\boldsymbol{C}}^{\hom,0} : \left\langle \boldsymbol{H}^E \right\rangle_{\tilde{Y}} : \tilde{\boldsymbol{K}}^0 \\
&\qquad = \frac{1}{2}\boldsymbol{E}^0 . \left(\boldsymbol{A}_M^{-1} \underline{\otimes} \boldsymbol{A}_M^T\right) : \tilde{\boldsymbol{C}}^{\hom,0} : \left\langle \boldsymbol{H}^E \right\rangle_{\tilde{Y}} : \left(-\boldsymbol{A}_M^T . \boldsymbol{A}_M^{-1} . \nabla_x \boldsymbol{A}_M . \left(\boldsymbol{A}_M^{-1} \underline{\otimes} \boldsymbol{A}_M^T\right) : \boldsymbol{E}^0 + \boldsymbol{A}_M^T . \boldsymbol{A}_M^{-1} . \nabla^T{}_x \boldsymbol{A}_M . \boldsymbol{E}^0 + \left(\boldsymbol{A}_M^T \underline{\otimes} \boldsymbol{A}_M^T\right) : \boldsymbol{K}^0\right) \\
&W_M^2\left(\tilde{\boldsymbol{E}}^0, \tilde{\boldsymbol{K}}^0\right) = \frac{1}{2}\tilde{\boldsymbol{K}}^0 : \left\langle \tilde{\boldsymbol{H}}^E : \tilde{\boldsymbol{C}} : \tilde{\boldsymbol{H}}^E + \tilde{\boldsymbol{C}} : \nabla_{\tilde{y}}\tilde{\boldsymbol{H}}^K : \tilde{\boldsymbol{H}}^E \right\rangle_{\tilde{Y}} : \tilde{\boldsymbol{K}}^0 + \tilde{\boldsymbol{K}}^0 \therefore \left\langle \left(\tilde{\boldsymbol{C}} : \tilde{\boldsymbol{H}}^K\right) : \nabla_{\tilde{y}}\tilde{\boldsymbol{H}}^E \right\rangle_{\tilde{Y}} : \tilde{\boldsymbol{E}}^0 \\
&\tilde{\boldsymbol{K}}^0\left(\tilde{\boldsymbol{x}}\right) = -\boldsymbol{A}_M^T . \boldsymbol{A}_M^{-1} . \nabla_x \boldsymbol{A}_M . \left(\boldsymbol{A}_M^{-1} \underline{\otimes} \boldsymbol{A}_M^T\right) : \boldsymbol{E}^0 + \boldsymbol{A}_M^T . \boldsymbol{A}_M^{-1} . \nabla^T{}_x \boldsymbol{A}_M . \boldsymbol{E}^0 + \left(\boldsymbol{A}_M^T \underline{\otimes} \boldsymbol{A}_M^T\right) : \boldsymbol{K}^0 \\
&\tilde{\boldsymbol{\Sigma}}^{\eta} := \frac{\partial W_M^{\eta}\left(\tilde{\boldsymbol{E}}^0\right)}{\partial \tilde{\boldsymbol{E}}^0} = \frac{\partial W_M^0\left(\tilde{\boldsymbol{E}}^0\right)}{\partial \tilde{\boldsymbol{E}}^0} + \eta\frac{\partial W_M^1\left(\tilde{\boldsymbol{E}}^0\right)}{\partial \tilde{\boldsymbol{E}}^0} + \eta^2\frac{\partial W_M^2\left(\tilde{\boldsymbol{E}}^0\right)}{\partial \tilde{\boldsymbol{E}}^0} \\
&\qquad = \tilde{\boldsymbol{C}}^{\hom,0} : \tilde{\boldsymbol{E}}^0 + \eta\tilde{\boldsymbol{C}}^{\hom,0} : \left\langle \boldsymbol{H}^E \right\rangle_{\tilde{Y}} : \tilde{\boldsymbol{K}}^0 + \eta^2\left\langle \left(\tilde{\boldsymbol{C}} : \tilde{\boldsymbol{H}}^K\right) : \nabla_{\tilde{y}}\tilde{\boldsymbol{H}}^E \right\rangle_{\tilde{Y}} \therefore \tilde{\boldsymbol{K}}^0, \\
&\tilde{\boldsymbol{S}}^{\eta} := \frac{\partial W_M^{\eta}\left(\tilde{\boldsymbol{E}}^0\right)}{\partial \tilde{\boldsymbol{K}}^0} = \frac{\partial W_M^0\left(\tilde{\boldsymbol{E}}^0\right)}{\partial \tilde{\boldsymbol{K}}^0} + \eta\frac{\partial W_M^1\left(\tilde{\boldsymbol{E}}^0\right)}{\partial \tilde{\boldsymbol{K}}^0} + \eta^2\frac{\partial W_M^2\left(\tilde{\boldsymbol{E}}^0\right)}{\partial \tilde{\boldsymbol{K}}^0} \\
&\qquad = \eta\tilde{\boldsymbol{C}}^{\hom,0} : \left\langle \boldsymbol{H}^E \right\rangle_{\tilde{Y}} : \tilde{\boldsymbol{E}}^0 + \eta\frac{1}{2}\tilde{\boldsymbol{E}}^0 . \left(\boldsymbol{A}_M^{-1} \underline{\otimes} \boldsymbol{A}_M^T\right) : \tilde{\boldsymbol{C}}^{\hom,0} : \left\langle \boldsymbol{H}^E \right\rangle_{\tilde{Y}} : \left(\boldsymbol{A}_M^{-1} \underline{\otimes} \boldsymbol{A}_M^T\right) \\
&\qquad + \eta^2\left(\left\langle \tilde{\boldsymbol{H}}^E : \tilde{\boldsymbol{C}} : \tilde{\boldsymbol{H}}^E + \tilde{\boldsymbol{C}} : \nabla_{\tilde{y}}\tilde{\boldsymbol{H}}^K : \tilde{\boldsymbol{H}}^E \right\rangle_{\tilde{Y}} : \tilde{\boldsymbol{K}}^0 + \left\langle \left(\tilde{\boldsymbol{C}} : \tilde{\boldsymbol{H}}^K\right) : \nabla_{\tilde{y}}\tilde{\boldsymbol{H}}^E \right\rangle_{\tilde{Y}} : \tilde{\boldsymbol{E}}^0\right)
\end{aligned}\right.
\tag{6.82}
$$

In Eq. 6.82, the macroscopic stress tensor $\tilde{\boldsymbol{\Sigma}}^{\eta}$ and hyperstress tensor $\tilde{\boldsymbol{S}}^{\eta}$ have been defined as partial derivatives of the obtained macroscopic energy density W_M^{η} to their conjugated kinematic variables; their (truncated) asymptotic expansion includes higher-order contributions involving couplings between Cauchy and strain gradient mechanics. The importance of higher-order effects in the resulting strain gradient continuum model is quantified by ranking the first and strain gradient contributions versus the small-scale parameter in the resulting homogenized quasi-periodic constitutive law, the set of Eqs. 6.82.

6.6 Conclusion

In this chapter, we have extended the asymptotic homogenization method for quasi-periodic continuous media, assuming that the initial non-periodic geometry can be mapped to a periodic parent domain by a geometrical point mapping of coordinates, thereby allowing to formulate the BVP of quasi-periodic homogenization still from the associated periodic unit cell BVP. Different methodologies for evaluating

the tensors of effective quasi-periodic properties have been proposed, enabling mapping the tensor of quasi-periodic moduli to the tensor of periodic effective moduli. The grading of unit cell geometry has been taken into account at the macro and microscales through elaborating an effective strain gradient model. This enriched model can perform structural computations of FGM composite or architected materials showing significant gradation of their geometry. Smoothness conditions for the existence of geometrical transformations satisfying the design rules have been established.

As a summary, the following main results have been obtained in the present contribution:

- A mathematical framework for quasi-periodic homogenization in linear elasticity has been developed, considering mappings of the quasi-periodic domain into a periodic one, allowing the tensors of effective quasi-periodic moduli to relate to those of the periodic microstructure.
- The choice of non-affine second-order polynomial geometrical transformations leads to the emergence of strain gradient effective models.
- The computation of the tensor of effective quasi-periodic moduli can be done in different manners, so essentially i) by a direct mapping of the periodic homogenized moduli at the leading order of the small-scale parameter, ii) by mapping the solution of the periodic unit cell BVP onto the quasi-periodic domain, or iii) by solving the unit cell BVP onto the transformed unit cell with quasi-periodicity conditions. The most efficient scheme is computing the tensor of homogenized moduli within the parent periodic unit cell and mapping it onto the quasi-periodic domain.

The design of complex shapes in engineering with tunable anisotropic mechanical properties is an important topic nowadays that pair the rapid development of additive manufacturing, allowing the fabrication of complicated designs. Extending the range or reachable properties based on the combination of new design rules and multiscale methods is one of the chief objectives in this field. We plan in future developments to use conformal transformations of initially periodic architectured materials to achieve designs with complex geometries, tunable porosity, and apparent mechanical properties.

Chapter 7

Homogenization of quasi-periodic conformal architectured materials

Summary

In this chapter we extend asymptotic periodic homogenization for non-periodic continuous microstructured media, assuming that the non-periodic geometry (called quasi-periodic) can be designed by a conformal planar transformation of a periodic parent domain architected with periodically disposed unit cells. Conformal transformations are shown to play a privileged role in the design of compatible macroscopic heterogeneous domains tessellated with non-periodic unit cells, obtained from a periodic parent domain architected with these unit cells. The conditions for conformal invariance are established, leading to the general form of conformal transformation in their dependencies upon the periodic coordinates. It is shown that any conformal map can be decomposed into the product of an isotropic dilatation function of the first periodic spatial position of decreasing exponential type and of a rotation characterized by an angular function linear in the second periodic position. A general theory of quasi-periodic homogenization in the framework of conformal transformations is established, leading to an asymptotic expansion of the tensor of quasi-periodic moduli versus those of the periodic unit cell in the parent domain. The influence of microcurvature distortion of individual unit cells on their effective properties is evaluated, and a few illustrative numerical examples are provided.

7.1 Introduction

Conformal transformations find numerous applications in engineering (e.g., electrical engineering, fluid mechanics) to map a physical problem posed over a complex geometry in the plane onto a simpler one for which a solution can more easily be obtained. Another viewpoint is that conformal transformations can serve as a design tool to generate compatible structures with a complicated design from a simple initial design. Mainly, circular heterogeneous architectures have been analyzed in the framework of conformal transformations, resulting in radially graded architectures mimicking the natural structure of sunflowers [238]. While the conformal mapping framework has been used to generate deployable structures [239] and [240], this framework has never been used to generate circular scaffold geometries with the non-uniform spatial distribution of pores.

The selection of a suited scaffold geometry constitutes a milestone in bone regeneration in tissue engineering and regenerative medicine since its morphological and mechanical properties condition cell colonization and bone tissue generation [241] and [242], therefore, its final clinical success. As detailed in [243], the essential requirements to be satisfied for scaffolds in tissue engineering include the biocompatibility of its constitutive material, its 3D morphological properties, and its effective mechanical properties such as apparent stiffness or elastic moduli and fluid mass transport properties. In terms of effective mechanical properties, it is generally admitted that the proposed scaffold must mimic as close as possible the original mechanical, physiological functions of the bone tissue it aims to replace.

For perfectly periodic structures, the effective mechanical properties of porous scaffolds can be obtained by using homogenization techniques from the definition of the unit cell, resulting in the evaluation of permeability [244] or elastic properties [245]. This has led to the emergence of various unit cell geometries issued from topological optimization techniques to find the best structure for a given clinical application [245]. Noteworthy, such homogenization procedures have emphasized the extensive range of effective elastic properties of 2D metamaterials that may be obtained from various unit cells [3] and the crucial role of Poisson's ratio on the metamaterial's bulk and shear response. Effective properties of periodic heterogeneous media may also result from the development of micromechanical models [246,247]. Nevertheless, these techniques are so far limited to perfectly periodic structures, and do not permit to predict the mechanical properties of graded scaffolds.

The main thrust of this chapter is the development of a suitable homogenization framework for quasi-periodic microstructures based on conformal transformations. One objective is to set up a quasi-periodic homogenization theory to relate the tensor of homogenized moduli of the quasi-periodic microstructure to that of a parent periodic microstructure in a parent domain.

This chapter is organized as follows: general properties satisfied by conformal transformations are derived in section 7.2, including aspects related to smoothness, kinematic compatibility. The theory of conformal transformations of microstructures in the planar linear isotropic elasticity framework is exposed in section 7.3, wherein the tensor of quasi-periodic moduli is derived in asymptotic format versus the

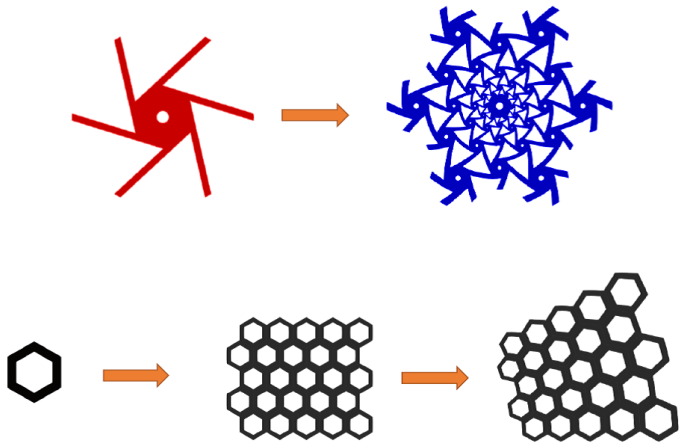

Figure 7.1 (top and bottom left views) Initial periodic domain tessellated with regular hexagonal and hexachiral unit cells, (top and bottom right views) quasi-periodic circular macrodomain resulting from the conformal transformation of the periodic microstructures.

small-scale parameter of a double scale asymptotic method. The effect of unit cell microcurvature on effective properties is devoted to the developments of section 7.4. In section **??**, a surface formulation of Hill's macrohomogeneity condition is implemented to evaluate the apparent macroscopic properties of the quasi-periodic unit cell. Section 7.5 concludes with a summary of the main results and some perspectives for future work.

7.2 Design of quasi-periodic domains by conformal transformations

Design of complex shapes in engineering with tunable anisotropic mechanical properties is an important topic nowadays that pair the rapid development of additive manufacturing, allowing the fabrication of complicated designs. Extending the range or reachable properties based on the combination of new design rules and multiscale methods is one of the chief objectives in this field. We propose to use conformal transformations of initially periodic architectured materials in this contribution to achieving designs with complex geometries and tunable porosity, and apparent mechanical properties. In order to set the stage, we will consider isotropic designs in the framework of linear elasticity. A specific mention will be made in the present contribution to conformal mappings, considered from a design point of view as a convenient and powerful way to generate complex shapes of graded porous micro-architectured materials in 2D. It allows distributing the base unit cell spatially into a macroscopic domain (Fig. 7.1), according to the given requirements of its effective (macroscopic) elastic properties and internal porosity distribution.

Such designs find useful applications in engineering (like electrical machines rotating at high speed) and scaffold-based bone tissue engineering, which require the definition of a scaffold with adapted morphology and properties. This last field has been considerably boosted by the emergence of 3D printing techniques

[248], allowing the fabrication of complex shapes with low dimensions. The definition of the most-suited geometry and material for a given application still constitutes a milestone of the clinical outcome of bone tissue engineering; moreover, the complexity of the inner morphology makes it challenging to compute the apparent macroscopic properties efficiently, possibly, without complete-field heavy simulations.

Conformal transformations have been applied to the initially periodic pattern of unit cell tessellating a rectangular domain with an adjustable number of unit cell in order to generate porous circular geometries with pore size gradients. As future developments will show, one possible form of the tangent map is the following one:

$$\boldsymbol{A}\left(\tilde{y}_1,\tilde{y}_2\right)=K\exp\left(b\tilde{y}_1\right)\begin{pmatrix}\cos b\tilde{y}_2 & -\sin b\tilde{y}_2\\ \sin b\tilde{y}_2 & \cos b\tilde{y}_2\end{pmatrix},\ b<0 \tag{7.1}$$

where $\tilde{y}_1$ and $\tilde{y}_2$ are the two periodic Cartesian coordinates in the periodic domain. Relying on conformal mapping to generate the microstructure design - and thus the spatial distribution of the unit cell within the macro domain - a quasi-periodic microstructure is obtained devoid of translational periodicity but endowed with rotational periodicity instead. In order to be able to relate the tensor of effective moduli in both configurations - the initial periodic and the transformed quasi-periodic ones -, a theoretical framework is needed to underline the nature of admissible conformal transformations together with their smoothness conditions.

7.2.1 General properties of conformal mappings and smoothness conditions

Conformal transformation of material points in 2D with point mapping $y_1\left(\tilde{y}_1,\tilde{y}_2\right), y_2\left(\tilde{y}_1,\tilde{y}_2\right)$ have to satisfy the Cauchy-Riemann conditions [249], leading to simplifications in the Jacobian matrix, which only depends on the two derivatives $\frac{\partial y_1}{\partial\tilde{y}_1},\frac{\partial y_2}{\partial\tilde{y}_2}$ of the tangent map:

$$\begin{aligned}&\boldsymbol{A}:=\nabla_{\tilde{y}}\boldsymbol{y}\rightarrow[A]=\begin{pmatrix}\frac{\partial y_1}{\partial\tilde{y}_1} & \frac{\partial y_1}{\partial\tilde{y}_2}\\ \frac{\partial y_2}{\partial\tilde{y}_1} & \frac{\partial y_2}{\partial\tilde{y}_2}\end{pmatrix},\ \frac{\partial y_1}{\partial\tilde{y}_1}=\frac{\partial y_2}{\partial\tilde{y}_2},\ \frac{\partial y_1}{\partial\tilde{y}_2}+\frac{\partial y_2}{\partial\tilde{y}_1}=0\\ &Det(\boldsymbol{A})=\left(\frac{\partial y_1}{\partial\tilde{y}_1}\right)^2+\left(\frac{\partial y_2}{\partial\tilde{y}_1}\right)^2\geqslant 0\end{aligned} \tag{7.2}$$

Previous relations quickly lead to the general condition for a tangent map to be conformal

$$\boldsymbol{A}^T.\boldsymbol{A}=Det(\boldsymbol{A})\boldsymbol{I}=\boldsymbol{A}.\boldsymbol{A}^T\Leftrightarrow\boldsymbol{B}^T.\boldsymbol{B}=\boldsymbol{I},\ \text{with}\ \boldsymbol{B}:=\boldsymbol{A}/\sqrt{Det(\boldsymbol{A})} \tag{7.3}$$

Identity in Eq. 7.3 shows that the normalized conformal mapping $\boldsymbol{B}$ is an orthogonal transformation. Thus any conformal transformation is the product of an orthogonal transformation and an isotropic dilatation, represented by the (isotropic) tensor $\sqrt{Det(\boldsymbol{A})}\boldsymbol{I}$. More precisely, any conformal tangent map can be decomposed multiplicatively as follows

$$\begin{aligned}&\boldsymbol{A}=\boldsymbol{D}.\boldsymbol{R}\\ &\boldsymbol{R}\left(\boldsymbol{e}_3,\theta\right)=\begin{pmatrix}\cos\theta\left(\tilde{y}_1,\tilde{y}_2\right) & -\sin\theta\left(\tilde{y}_1,\tilde{y}_2\right)\\ \sin\theta\left(\tilde{y}_1,\tilde{y}_2\right) & \cos\left(\tilde{y}_1,\tilde{y}_2\right)\end{pmatrix},\ \boldsymbol{D}=\sqrt{Det(\boldsymbol{A})}\boldsymbol{I}\end{aligned} \tag{7.4}$$

with $\boldsymbol{R}(\boldsymbol{e}_3, \theta)$ the planar rotation with axis $\boldsymbol{e}_3$ and angular variable $\theta(y_1, y_2)$, and $\boldsymbol{D}(\boldsymbol{e}_3, \theta)$ an isotropic dilatation. Note that the allowed orthogonal transformations should be those in the material symmetry group of the microstructure (not to modify the anisotropic class). More generally, conformal transformations preserve the material symmetries since they do not change angles.

Conformal transformations include an isotropic dilatations, rotations, translations, inversions, and special conformal transformations, satisfying the previous general condition.

- Macroscopic fluctuations of the effective moduli should occur with a wavelength much larger than the unit cell size so that the assumption of effective behavior of Cauchy type still holds (otherwise, enriched effective continuum descriptions may be needed). This condition has to be verified a *posteriori* from computational results; this has motivated to limit the transformation mapping to its linearized version, meaning that the variation of the unit cell dimensions has to be 'slow enough' concerning the unit cell size, such that each unit cell witnesses a homogeneous tensor of effective elastic moduli.
- Due to the unit cell's varying dimension(s), the deformation mechanisms should not change drastically from those observed in the periodic reference domain. This criterion could also limit the magnitude of the transformation mapping and has to be verified a *posteriori* from computational results. In case the geometrical design varies too fast, interactions between neighboring unit cells may be generated, triggering higher gradients in the macroscopic response of the quasi-periodic composite.

In mathematical terms, we require the following conditions to be satisfied by the conformal point mapping and its tangent:

(i) Boundedness of the point mapping: $\lim_{\|\tilde{\boldsymbol{x}}\| \to \infty} \|\varphi(\tilde{\boldsymbol{y}})\| \leqslant k$

(ii) Distributing an initially periodic microstructure within a periodic domain (of possibly infinite size) into a quasi-periodic domain having a finite size requires the condition $\lim_{\|\tilde{y}\| \to \infty} \|A(\tilde{\boldsymbol{y}})\| = 0$, so that the quasi-periodic position remains bounded.

(iii) The point mapping $\varphi(\tilde{\boldsymbol{y}})$ should be a monotone growing function of the periodic spatial position variable.

A possible function satisfying these three requirements is the following two parameters exponential function (considered here as a function of a single scalar coordinate $\tilde{y}$):

$$\boldsymbol{\varphi}_{\tilde{\boldsymbol{y}}}(\tilde{y}) = k \exp(-\tilde{y}/c)\,(\cos(-b\tilde{y}), \sin(-b\tilde{y})) \tag{7.5}$$

The parameter k represents the asymptotic limit and c is a. controlling parameter of the function's horizontal asymptote (due to the condition $\lim_{\tilde{y} \to \infty} \frac{d\varphi_{\tilde{y}}(\tilde{y})}{d\tilde{y}} = 0$) at infinity. Note that only its dilatational part intervenes in the conditions mentioned above for the considered conformal transformations since its rotation part is bounded. Since the rotation part of any conformal mapping is bounded in norm (Frobenius matrix norm) by unity, the smoothness conditions hold for the pure dilatational part of it.

For the considered example of Eq. 7.5, it thus holds in a 2D context:

$$D\left(\tilde{y}_1,\tilde{y}_2\right)=-\frac{k}{c}\exp\left(-f\left(\tilde{y}_1,\tilde{y}_2\right)/c\right)\boldsymbol{I} \tag{7.6}$$

with $f\left(\tilde{y}_1,\tilde{y}_2\right)$ a continuous scalar-valued function of $\left(\tilde{y}_1,\tilde{y}_2\right)$ satisfying the smoothness as mentioned above conditions.

In a more general setting, the shape variation can be bounded by an exponential having some 'smooth' variation in space, using Grönwall lemma:

$$\frac{1}{u}\frac{du}{dy}\leqslant\phi\left(y\right)\Rightarrow u(y)\leqslant u\left(y_0\right)\exp\left(\int_{y_0}^{y}\phi\left(s\right)ds\right) \tag{7.7}$$

with $\phi\left(y\right)$ an exponential function of the type $\phi\left(y\right):=e^{-2\pi y/m}$ (up to the multiplication by a trigonometric function, but that is discarded since it is bounded in norm by unity). Thus it holds $u(y)\leqslant u\left(y_0\right)\exp\left(\int_{y_0}^{y}e^{-2\pi y/m}ds\right)\leqslant\frac{m}{2\pi}u\left(y_0\right)e^{-2\pi/m(y-y_0)}$, thereby providing an upper bound of the shape variation of the transformed unit cell.

As an example, an adequate conformal mapping satisfying previous conditions is the product of the exponentially decreasing isotropic planar dilatation and a heterogeneous rotation, obtained from the following single scale point mapping

$$\begin{aligned}&\tilde{\boldsymbol{y}}=\begin{pmatrix}\widetilde{y}_1 & \widetilde{y}_2\end{pmatrix}\Rightarrow\boldsymbol{\varphi}_{\tilde{\boldsymbol{y}}}=\begin{pmatrix}y_1 & y_2\end{pmatrix}=k\exp\left(-b\widetilde{y}_1\right)\left(\cos(-b\widetilde{y}_2),\sin\left(-b\widetilde{y}_2\right)\right)\\&\Rightarrow\mathbf{A}\left(\tilde{\boldsymbol{y}}\right):=\frac{\partial\begin{pmatrix}y_1 & y_2\end{pmatrix}}{\partial\begin{pmatrix}\widetilde{y}_1 & \widetilde{y}_2\end{pmatrix}}=(-bk)\exp\left(-b\widetilde{y}_1\right)\begin{pmatrix}\cos\left(-b\widetilde{y}_2\right) & -\sin\left(-b\widetilde{y}_2\right)\\ \sin\left(-b\widetilde{y}_2\right) & \cos\left(-b\widetilde{y}_2\right)\end{pmatrix},\ \ (b):=\frac{2\pi}{m}\end{aligned} \tag{7.8}$$

The length parameter m therein represents the height of the initial rectangular macroscopic domain that is transformed into a disk-like shape of the macrodomain.

7.2.2 Kinematic compatibility of conformal transformations

The linearized compatibility condition of conformal mappings is shown in the sequel, adopting a perturbative approach consistent with the present framework of linearized elasticity. this means we consider infinitesimal conformal mappings.

For symmetric second-order tensor field, the finite transformations compatibility condition states that the Riemann curvature tensor of the tangent space vanishes (due to its Euclidean structure). Its variation then provides the vanishing of the fourth-order tensor built from the double curl of the small strain tensor, summarizing to a single PDE in a 2D context for a connected domain (the condition is then necessary and sufficient):

$$\varepsilon_{11,22}-2\varepsilon_{12,12}+\varepsilon_{22,11}=0 \tag{7.9}$$

Interpreting the conformal map in terms of an active transformation associated with a displacement gradient, it holds the following writing of the 2D kinematic compatibility in a small perturbations

framework, obtained from the previous linearized conformal mapping condition:

$$\begin{aligned}
&\boldsymbol{A}+\boldsymbol{A}^T = Tr(\boldsymbol{A})\mathbf{I}\\
&\varepsilon_{ij} = \frac{1}{2}\left\{(A_{ij}-\delta_{ij})+(A_{ij}-\delta_{ij})^T\right\} = \frac{1}{2}\left(A_{ij}+A_{ji}\right)-\delta_{ij} = \frac{1}{2}Tr(\boldsymbol{A})\delta_{ij}-\delta_{ij}\\
&\quad = \left(Tr(\boldsymbol{A})/2-1\right)\delta_{ij} \equiv K(y_1,y_2)\delta_{ij}\\
&\varepsilon_{11,22}-2\varepsilon_{12,12}+\varepsilon_{22,11}=0 \Rightarrow \frac{\partial^2 K}{\partial\tilde{y}_1\partial\tilde{y}_2}=0
\end{aligned} \tag{7.10}$$

Eq. 7.10 shows that the conformal mapping trace must be harmonic for the mapping to be compatible. The previously written Cauchy-Riemann conditions entail that this holds as a sufficient condition:

$$\begin{aligned}
&\frac{\partial y_1}{\partial\tilde{y}_1}=\frac{\partial y_2}{\partial\tilde{y}_2},\ \frac{\partial y_1}{\partial\tilde{y}_2}+\frac{\partial y_2}{\partial\tilde{y}_1}=0 \Rightarrow \frac{\partial^2 y_1}{\partial\tilde{y}_1\partial\tilde{y}_1}+\frac{\partial^2 y_1}{\partial\tilde{y}_2\partial\tilde{y}_2}=0\\
&\Rightarrow \frac{\partial^2 Tr(\boldsymbol{A})}{\partial\tilde{y}_1\partial\tilde{y}_1}+\frac{\partial^2 Tr(\boldsymbol{A})}{\partial\tilde{y}_2\partial\tilde{y}_2}=2\frac{\partial}{\partial\tilde{y}_1}\left\{\frac{\partial^2\tilde{y}_1}{\partial\tilde{y}_1\partial\tilde{y}_1}+\frac{\partial^2\tilde{y}_1}{\partial\tilde{y}_2\partial\tilde{y}_2}\right\}=0
\end{aligned} \tag{7.11}$$

A conformal map defines accordingly a sufficient condition for a tangent map to satisfy the local compatibility condition. The fact that this may not be a necessary condition entails the possible existence of other classes of mappings that can be used to generate locally and globally compatible configurations with a quasi-periodic microstructure. Accordingly, conformal mappings play a prominent role in designing locally and globally compatible configurations obtained from an initial domain architectured with a periodic microstructure. It should be noticed that previous conditions may not be necessary, which means that non-conformal transformations may preserve compatibility. Note that the rotation part of conformal transformations is not involved in the (small perturbations) kinematic compatibility.

The employed perturbation approach and viewpoint of conformal transformations as an active transformation (similar to a motion in continuum mechanics) is consistent with the adopted small perturbations framework, which amounts to consider a 'small' perturbation of the initial geometry.

7.2.3 General form of conformal transformations

According to previous considerations, any conformal map can be decomposed into the product of an isotropic dilatation and a planar rotation, viz.

$$\begin{aligned}
&\boldsymbol{A}\left(\tilde{\boldsymbol{y}}\right) = \boldsymbol{D}\left(\tilde{\boldsymbol{y}}\right).\boldsymbol{Q}\left(\theta\left(\tilde{\boldsymbol{y}}\right)\right)\\
&\boldsymbol{A}^T.\boldsymbol{A} = \det(\boldsymbol{A})\mathbf{I}
\end{aligned} \tag{7.12}$$

Previous writing shows that conformal mappings express as a combination of an isotropic dilatation and a rotation,

$$\boldsymbol{A} = \left(\boldsymbol{D} := \sqrt{Det(\boldsymbol{A})}\mathbf{I},\ \boldsymbol{Q}\left(\boldsymbol{e}_3,\theta\right)\right) \tag{7.13}$$

Note that $Det(\boldsymbol{A})$ represents the change of area under conformal transform.

The conformal condition next rewrites:

$$\begin{aligned} &\frac{\boldsymbol{A}^T}{\sqrt{\det(\boldsymbol{A})}}.\frac{\boldsymbol{A}}{\sqrt{\det(\boldsymbol{A})}} = \mathbf{I} \\ &\boldsymbol{A} = \begin{pmatrix} \cos\theta & -\sin\theta \\ \sin\theta & \cos\theta \end{pmatrix}.\begin{pmatrix} D_{,\tilde{y}_1} & D_{,\tilde{y}_2} \\ D\theta_{,\tilde{y}_1} & D\theta_{,\tilde{y}_2} \end{pmatrix} \end{aligned} \tag{7.14}$$

in which the comma denotes the partial derivative concerning the indicated variable in subscript. Since the dilatation part has to be isotropic, it holds consequently the two ordinary differential equations, the integration of which is straightforward:

$$\begin{aligned} &\begin{vmatrix} D_{,\tilde{y}_2} = 0 \Rightarrow D\left(\tilde{\boldsymbol{y}}\right) = D\left(\tilde{y}_1\right) \\ \theta_{,\tilde{y}_1} = 0 \Rightarrow \theta\left(\tilde{\boldsymbol{y}}\right) = \theta\left(\tilde{y}_2\right) \\ \dfrac{D_{,\tilde{y}_1}}{D} = \dfrac{d\theta\left(\tilde{y}_2\right)}{d\tilde{y}_2} \equiv b \end{vmatrix} \\ &\Rightarrow D\left(\tilde{y}_1\right) = k\exp\left(b\tilde{y}_1\right), \theta\left(\tilde{y}_2\right) = b\tilde{y}_2 \end{aligned} \tag{7.15}$$

Previous relations show that the macroscopic part of the conformal tangent map is of the form:

$$\begin{vmatrix} \boldsymbol{A} = k\begin{pmatrix} \exp\left(b\tilde{y}_1\right) & 0 \\ 0 & \exp\left(b\tilde{y}_1\right) \end{pmatrix}\begin{pmatrix} \cos\theta\left(\tilde{y}_2\right) & -\sin\theta\left(\tilde{y}_2\right) \\ \sin\theta\left(\tilde{y}_2\right) & \cos\theta\left(\tilde{y}_2\right) \end{pmatrix} \\ \theta\left(\tilde{y}_2\right) = b\tilde{y}_2 \end{vmatrix} \tag{7.16}$$

The dilatation part of any conformal transformation is a function of the first parameterization variable (note that coefficient b has to be negative or nil according to the above smoothness conditions), while the planar rotation's angular function in the planar rotation is only depending upon the second parameterization variable. Integration of the previous tangent leads after straightforward computations to a point mapping of the following form:

$$\begin{aligned} d\boldsymbol{x} = \boldsymbol{A}.d\tilde{\boldsymbol{y}} &= k\begin{pmatrix} \exp\left(b\tilde{y}_1\right) & 0 \\ 0 & \exp\left(b\tilde{y}_1\right) \end{pmatrix}\begin{pmatrix} \cos\theta\left(\tilde{y}_2\right) & -\sin\theta\left(\tilde{y}_2\right) \\ \sin\theta\left(\tilde{y}_2\right) & \cos\theta\left(\tilde{y}_2\right) \end{pmatrix}.d\tilde{\mathbf{y}} \\ \Rightarrow &\begin{vmatrix} y_1\left(\tilde{y}_1\right) = \left(\dfrac{K}{b}\exp\left(b\tilde{y}_1\right) + C\right)\cos\theta\left(\tilde{y}_2\right) \\ y_2\left(\tilde{y}_2\right) = \left(\dfrac{K}{b}\exp\left(b\tilde{y}_1\right) + C\right)\sin\theta\left(\tilde{y}_2\right) \\ \theta\left(\tilde{y}_2\right) = b\tilde{y}_2 \end{vmatrix} \end{aligned} \tag{7.17}$$

wherein C is a new integration constant.

7.3 Homogenization of quasi-periodic conformal isotropic microstructures

Linearized conformal transformations can map isotropic periodic microstructures to construct suitable designs at the macroscale from a parent domain tessellated with repetitive unit cells. We aim to relate the

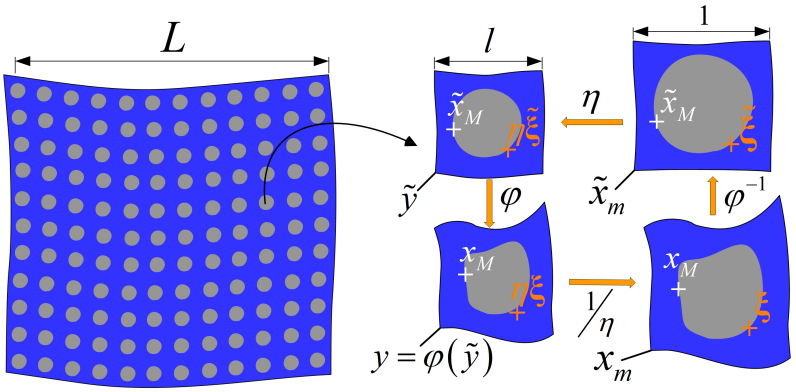

Figure 7.2 (left) Schematic representation of periodic material, (right top row) definition of micropoints within the physical and zoomed non-dimensional unit cells of the periodic, (right bottom row) quasi-periodic domains; The small parameter η is defined as the ratio of a unit cell size to a characteristic macroscopic dimension of the macrodomain.

tensor of effective moduli in both domains mapped by such conformal transformations. The homogenized properties in the periodic domain are classically obtained from double scale asymptotic expansion. In the first step, we write the BVP of linear elasticity in both periodic and quasi-periodic domains.

7.3.1 Microscopic periodic and quasi-periodic boundary value problems

In the present context of periodic homogenization, the microstructure is defined within a representative unit cell, which generates the entire macrodomain by periodic translation.

The double scale asymptotic method used for the evaluation of the effective mechanical properties is based on the existence of a repetitive unit cell; it relies on the conceptual idea of zooming out the unit cell from the physical domain where it lives to pose a problem onto a fixed domain called the zoomed unit cell, being independent of the small-scale parameter. A new spatial variable is introduced, defined as the relative position $\tilde{\boldsymbol{\xi}}$. Any mechanical field defined over the η-dependent unit cell in the physical domain is then defined as a field depending on the two variables $\tilde{\boldsymbol{x}}, \eta\tilde{\boldsymbol{\xi}}$, considered independent since they are representative of two different separated scales. The generic microscopic positions of a micropoint $\tilde{\boldsymbol{x}}_m, \boldsymbol{x}_m$ (respectively in the periodic and quasi-periodic non dimensional domain) are accordingly decomposed into the sum of the macroscopic position of the center of the area and the relative positions $\tilde{\boldsymbol{\xi}}, \boldsymbol{\xi}$ in the physical unit cells, as illustrated in Fig. 7.2:

$$\begin{aligned} \tilde{\boldsymbol{x}}_m = \tilde{\boldsymbol{x}}_M + \tilde{\boldsymbol{\xi}} \Rightarrow & \left| \begin{array}{l} \tilde{\boldsymbol{x}} = \tilde{\boldsymbol{x}}_M \\ \tilde{\boldsymbol{y}} = \tilde{\boldsymbol{x}}_M + \eta\tilde{\boldsymbol{\xi}} \end{array} \right. \\ \tilde{\boldsymbol{y}} = \tilde{\boldsymbol{x}} + \eta\tilde{\boldsymbol{\xi}} \mapsto \boldsymbol{y}\left(\tilde{\boldsymbol{x}}, \tilde{\boldsymbol{\xi}}\right) \equiv \boldsymbol{x} + \eta\boldsymbol{\xi} & \end{aligned} \tag{7.18}$$

The last two relations define the absolute position in the physical periodic and quasi-periodic unit cells. At the microscopic scale of the single unit cell, the material obeys a first gradient linear elasticity

constitutive law given in a static situation by the field equations in the strong format:

$$\left|\begin{array}{l} \underset{\sim}{\sigma} \cdot \nabla_y + \underline{\mathbf{b}} = \underline{\mathbf{0}} \;\; in \;\; Y \\ \underset{\sim}{\sigma} \cdot \underline{\mathbf{n}} = \underline{\mathbf{t}} \quad on \; \partial Y \\ \underset{\sim}{\sigma} = \underset{\approx}{C} : \underset{\sim}{\varepsilon} = \underset{\approx}{C} : \mathbf{u} \otimes \nabla_y \end{array}\right. \tag{7.19}$$

with $\underset{\sim}{\sigma} = \underset{\sim}{\sigma}^T$ the symmetrical Cauchy stress (symmetry being a consequence of the balance of angular momentum), $\underline{\mathbf{b}}$ the body force vector, $\underline{\mathbf{n}}$ the unit-length exterior normal vector, $\underline{\mathbf{t}}$ the traction vector, and $\underset{\approx}{C}$ the fourth-order microscopic rigidity tensor. The center of gravity of the unit cell, point $\mathbf{x}$, defined to the adopted Cartesian basis, is defined implicitly by the integral relation Fig. 7.2

$$\frac{1}{|Y|}\int_Y (\mathbf{y}-\mathbf{x}) dV_y = \mathbf{0} \tag{7.20}$$

Integration is done overall micro points labeled with the position vector within the RVE; Eq. 7.20 means that the relative position of the micro points has zero average over the unit cell. Note that the definition is given in Eq. 7.2 simplifies when the origin of coordinates is selected at the center of gravity of the RVE, and it further guarantees the objectivity of the virtual power of internal forces [126]. The formal evaluation of the homogenized elastic properties resorts to the classical double-scale asymptotic homogenization for periodic media, the developments of which are synthesized in chapter 6.

As detailed in section 6.2.1, for the quasi-periodic homogenization theory to be subsequently developed, we write the transformation laws of the microscopic strain tensor concerning the micro and macro scale variables, considering their covariant and contravariant nature, respectively. When considered as a single scale function, the displacement and its spatial gradient can be decomposed into the local tangent basis in terms of its mixed components (in both the periodic and quasi-periodic domains),

$$\nabla_y \boldsymbol{u}(\boldsymbol{y}) = u^i{}_{,j} \boldsymbol{g}_i \otimes \boldsymbol{g}^j \tag{7.21}$$

The natural basis is denoted $\boldsymbol{g}_k$, $\tilde{\boldsymbol{g}}_k$ on the untransformed and transformed domains, respectively. Each basis vector is defined as the tangent at each point to coordinate lines acting as curvilinear coordinates in both periodic and quasi-periodic domains. The transformation laws of vectors and tensors under a general non-affine change of coordinate are first written as a prerequisite for the homogenization of quasi-periodic structures. It is essential to identify the variance of tensors since contravariant and covariant tensors transform differently [237]. Covariant tensors transform like the basis vectors using the transition matrix, whereas contravariant tensors (contra means 'opposite to') transform in a way opposite to the basis vectors, using the inverse of the transition matrix. Covariant tensors (resp. contravariant) are denoted with their components having lower indices (resp. upper indices). The tangent vectors building the natural basis transform between both configurations as follows:

$$\begin{aligned} \tilde{\boldsymbol{g}}_h &:= \frac{\partial \boldsymbol{y}}{\partial \tilde{y}^h} = \frac{\partial \boldsymbol{y}}{\partial y^j}.\frac{\partial y^j}{\partial \tilde{y}^h} = \frac{\partial y^j}{\partial \tilde{y}^h}\boldsymbol{g}_j \Leftrightarrow \boldsymbol{g}_j = \boldsymbol{g}_k \frac{\partial \tilde{y}^k}{\partial y^j} \equiv \boldsymbol{g}_k \left(A^{-1}\right)^k_{.j} \\ d\boldsymbol{v}_i &= \frac{dv^i}{dy^l} dy^l \boldsymbol{g}_i \Rightarrow \tilde{\boldsymbol{g}}_k d\tilde{y}^k = \frac{\partial y^j}{\partial \tilde{y}^k}\boldsymbol{g}_j \frac{\partial \tilde{y}^k}{\partial y^p} dy^p \equiv \delta_{jp}\boldsymbol{g}_j dy^p = \boldsymbol{g}_q dy^q \end{aligned} \tag{7.22}$$

Remark: the change of components of a vector or tensor from the quasi-periodic to the periodic domain can be expressed equivalently as a passive or an active transformation. For a vector field in the passive viewpoint, it holds the invariance of vectors, $\tilde{\mathbf{v}} = \mathbf{v} = v^j \mathbf{g}_j,\ v^h(y^q) = A^h_{.k} \tilde{v}^k(\tilde{y}^p)$; in the **active viewpoint**, the vector is represented as a covariant vector. Thus it transforms (its components) like the covariant base vectors, which mean the components of the same vector in both domains are the same:

$$\begin{aligned} &\boldsymbol{g}^i = \boldsymbol{A}^{-T}.\tilde{\boldsymbol{g}}^i \\ &\boldsymbol{v} = v_i \boldsymbol{g}^i = \boldsymbol{A}^{-T}.\tilde{\boldsymbol{v}} = \tilde{v}_j \boldsymbol{A}^{-T}.\tilde{\boldsymbol{g}}^j = \tilde{v}_j \boldsymbol{g}^i \Rightarrow v_i = \tilde{v}_j \end{aligned} \tag{7.23}$$

The displacement field is expressed in the tensor format in terms of its covariant representation, leading to the elaboration of the strain as a mixed tensor when considered as a single scale-dependent field from the onset:

$$\begin{aligned} &\nabla_{\tilde{\boldsymbol{y}}} \tilde{\boldsymbol{u}}\left(\tilde{\boldsymbol{y}}\right) = \tilde{u}^i_{,j} \tilde{\boldsymbol{g}}_i \otimes \tilde{\boldsymbol{g}}^j \\ &\nabla_{\boldsymbol{y}} \boldsymbol{u}\left(\boldsymbol{y}\right) = u^i{}_{,j} \boldsymbol{g}_i \otimes \boldsymbol{g}^j \\ &\boldsymbol{g}^i.\boldsymbol{g}_j = \delta^i_{.j} = \tilde{\boldsymbol{g}}^i.\tilde{\boldsymbol{g}}_j \end{aligned} \tag{7.24}$$

We have introduced in previous relations the primal bases in periodic and quasi-periodic domains, the set of tangent vectors $\tilde{\mathbf{g}}_i, \mathbf{g}_i$, with dual (reciprocal) bases satisfying the product relations with the set of primal basis vectors in the last identity of Eq. 7.24. The strain and stress tensors are represented as mixed variant second-order tensors, with the following transformation rules:

$$\begin{aligned} &\tilde{\boldsymbol{\sigma}} = \tilde{\sigma}^{\cdot q}_{p} \tilde{\boldsymbol{g}}^p \otimes \tilde{\boldsymbol{g}}_q,\ \boldsymbol{\sigma} = \sigma^{\cdot q}_{p} \boldsymbol{g}^p \otimes \boldsymbol{g}_q \\ &\left| \begin{aligned} &\nabla_{\boldsymbol{y}} \boldsymbol{u}\left(\boldsymbol{y}\right) = \boldsymbol{A}.\nabla_{\tilde{\boldsymbol{y}}} \tilde{\boldsymbol{u}}\left(\tilde{\boldsymbol{y}}\right).\boldsymbol{A}^{-1} \\ &\boldsymbol{\sigma}\left(\boldsymbol{y}\right) = \boldsymbol{A}^{-T}.\tilde{\boldsymbol{\sigma}}.\boldsymbol{A}^T \end{aligned} \right. \end{aligned} \tag{7.25}$$

Due to the previous transformation relations for the microstrain and stress tensor fields Eq. 7.25 it is straightforward to derive the invariance of the microscopic energy density:

$$w_\mu\left(\boldsymbol{y}\right) := \frac{1}{2}\boldsymbol{\sigma} : \boldsymbol{\varepsilon} = \frac{1}{2} Tr(\boldsymbol{\sigma}^T.\boldsymbol{\varepsilon}) = \frac{1}{2}\sigma_i^{\cdot j}\varepsilon_j^{\cdot i} = \frac{1}{2}\tilde{\sigma}_i^{\cdot j}\tilde{\varepsilon}_j^{\cdot i} = \frac{1}{2}\tilde{\boldsymbol{\sigma}} : \tilde{\boldsymbol{\varepsilon}} = \tilde{w}_\mu\left(\tilde{\boldsymbol{y}}\right) \tag{7.26}$$

In periodic homogenization theory, the period $\tilde{\boldsymbol{Y}}$ is assumed to be very small compared to the dimensions of the overall domain. Thus, the characteristic functions of such heterogeneous media will experience rapid variations within any small neighborhood of a macropoint $\tilde{\boldsymbol{x}}$. On the other hand, mechanical fields at the macroscale can be considered to experience slower variations. These considerations lead to considering all fields in both periodic and quasi-periodic domains as dependent on both the macroscopic and microscopic positions, experiencing respectively slow and fast variations concerning the first and second ones. The existing mapping between the periodic and quasi-periodic domain is assumed to be regular enough that the periodicity conditions that prevail in the periodic domain can be transferred in some sense to the quasi-periodic domain.

7.3.2 Determination of the tensor of quasi-periodic moduli

In a first approach (see Table 6.1), we ignore how the conformal mapping will affect the microstructural information, so by assumption, only the homogenized medium endowed with its tensor of effective properties is considered at the onset. Doing this leads to

$$\mathbf{C}^{\hom}(\mathbf{x}) = \left(\mathbf{A}_M^{-1} \underline{\otimes} \mathbf{A}_M^T\right)(\mathbf{x}) : \tilde{\mathbf{C}}^{\hom} : \left(\mathbf{A}_M^{-1} \underline{\otimes} \mathbf{A}_M^T\right)(\mathbf{x}) = \left(Q_M^{-1} \underline{\otimes} Q_M^T\right)(\mathbf{x}) : \tilde{\mathbf{C}}^{\hom} : \left(Q_M^{-1} \underline{\otimes} Q_M^T\right)(\mathbf{x}) \quad (7.27)$$

The last relation results from the simplification of the dilatation part of the conformal map; since it relies on the view of the unit cell as a homogeneous equivalent material, it ignores the effect of unit cell micrograding of topology on the effective quasi-periodic moduli.
The previous relation entails that the effective moduli are invariant for observers measuring them in the respective local bases attached to the periodic and quasi-periodic (mapped) unit cells.

In a more refined approach, we aim to capture the influence of the micrograding of the unit cell geometry on the macroscopic variation of the quasi-periodic effective moduli. The macroscopic strain energy density is evaluated as the volume average of the microscopic energy over the quasi-periodic unit cell at a given macroscopic position. Use of Hill macrohomogeneity condition and a single change of variable in the corresponding unit cell volume integral then delivers the following relation:

$$W_M = \langle (\varepsilon : \mathbf{C} : \varepsilon) \rangle_Y = \frac{1}{2} \mathbf{E}(\mathbf{x}) : \mathbf{C}^{\hom}(\mathbf{x}) : \mathbf{E}(\mathbf{x}) = \left\langle \det(\mathbf{A}) \left(\tilde{\varepsilon} : \tilde{\mathbf{C}} : \tilde{\varepsilon}\right) \right\rangle_{\tilde{Y}} \quad (7.28)$$

The tensor of effective quasi-periodic moduli is evaluated by first solving the unit cell BVP in the periodic reference domain and mapping the computed periodic microstrain to the quasi-periodic domain reflected in the last volume average in Eq. 7.28 and recalling the following relations from chapter 6:

$$\begin{aligned} &\tilde{\varepsilon} = \tilde{\mathbf{A}}^E(\tilde{\mathbf{y}}) : \tilde{\mathbf{E}}(\tilde{\mathbf{x}}) \\ &\mathbf{E}(\mathbf{x}) = det(\mathbf{A}_M(\tilde{\mathbf{x}})) \mathbf{A}_M(\tilde{\mathbf{x}}) . \tilde{\mathbf{E}}(\tilde{\mathbf{x}}) . \mathbf{A}_M^{-1}(\tilde{\mathbf{x}}) \end{aligned} \quad (7.29)$$

In more detail, we write the previous relation in index format relying on the existence of a strain localization operator mapping the microscopic deformation to the macroscopic deformation applied over the periodic unit cell:

7.3.3 Numerical illustration: case of a conformally mapped tetrachiral microstructure

We compute the spatial distribution of the quasi-periodic moduli for a conformally mapped periodic tetrachiral unit cell pictured in fig. 7.3, using the theoretical prediction from Eq. 7.28. We consider as a starting point the following point transformation of coordinates:

$$\varphi(\tilde{\mathbf{y}}) = k \exp(-b\tilde{y}_1) \begin{pmatrix} \cos(b\tilde{y}_2) \\ \sin(b\tilde{y}_2) \end{pmatrix} \quad (7.30)$$

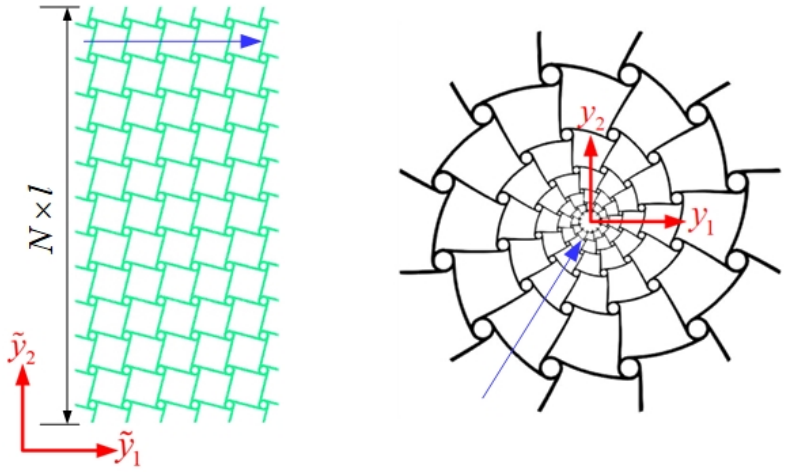

Figure 7.3 Conformal mapping of a (left) tetrachiral periodic unit cell to a (right) quasi-periodic domain.

This point mapping gives rise by taking its spatial gradient to the following conformal tangent map:

$$\mathbf{A}\left(\tilde{\mathbf{y}}\right) = \nabla_{\tilde{\mathbf{y}}}\varphi\left(\tilde{\mathbf{y}}\right) = -kb\exp\left(-b\tilde{y}_1\right)\begin{bmatrix}\cos\left(b\tilde{y}_2\right) & -\sin\left(b\tilde{y}_2\right)\\ \sin\left(b\tilde{y}_2\right) & \cos\left(b\tilde{y}_2\right)\end{bmatrix} \tag{7.31}$$

Using previous Eq. 7.31 then delivers for this specific conformal map the relation:

$$\mathbf{C}^{\text{hom}} = (kb)^2\left\langle \tilde{A}^E : C_\mu : \tilde{A}^E \exp(-2b\tilde{y}_1)\right\rangle_{\tilde{Y}} \tag{7.32}$$

In more detail, we write the previous relation in index format relying on the existence of a strain localization operator $\tilde{\boldsymbol{A}}^{\boldsymbol{E}}$ mapping the microscopic deformation to the macroscopic deformation applied over the periodic unit cell:

$$\begin{aligned}
&\tilde{\varepsilon}_{ij} = \tilde{A}^E_{ijkl}\tilde{E}_{kl}\\
&(c_\mu)_{lmpq} = \lambda\delta_{lm}\delta_{pq} + \mu\delta_{lp}\delta_{mq} + \mu\delta_{lq}\delta_{mp}\\
&C^{\text{hom}}_{abcd} = (kb)^2\left\langle \tilde{A}^{E,T}_{ablm}(c_\mu)_{lmpq}\tilde{A}^E_{pqcd}\exp(-2b\tilde{y}_1)\right\rangle_{\tilde{Y}}\\
&\qquad = (kb)^2\left\langle \lambda[\tilde{A}^{E,T}_{abmm}\tilde{A}^E_{ppcd}] + \mu[\tilde{A}^{E,T}_{abpm}\tilde{A}^E_{pmcd} + \tilde{A}^{E,T}_{ablp}\tilde{A}^E_{plcd}]\exp(-2b\tilde{y}_1)\right\rangle_{\tilde{Y}}
\end{aligned} \tag{7.33}$$

For example for C_{1111}, $\{a,b,c,d\} = \{1\}$ previous relation gives:

$$C^{\text{hom}}_{1111} = (kb)^2\left\langle \lambda[\tilde{A}^E_{mm11}\tilde{A}^E_{pp11}] + \mu[\tilde{A}^E_{pm11}\tilde{A}^E_{pm11} + \tilde{A}^E_{lp11}\tilde{A}^E_{pl11}]\exp(-2b\tilde{y}_1)\right\rangle \tag{7.34}$$

where applying $\tilde{E}_{11} = 1$, gives the following strain localization functions:

$$\tilde{A}^E_{ij11} = \tilde{\varepsilon}_{ij} \Rightarrow \left|\begin{array}{lll}\tilde{A}^E_{1111} = \tilde{\varepsilon}_{11} & ; & \tilde{A}^E_{1211} = \tilde{\varepsilon}_{12}\\ \tilde{A}^E_{2211} = \tilde{\varepsilon}_{22} & ; & \tilde{A}^E_{2111} = \tilde{\varepsilon}_{21}\end{array}\right.$$

The effective quasi-periodic moduli predicted by the previous theoretical relation Eq. 7.32 strongly depend on the number of unit cells, as shown by Fig. 7.4. The effective tensile modulus C_{1111} converges to its asymptotic value when increasing N (up to a large enough value 50); this asymptotic value coincides with the corresponding effective moduli of the periodic unit cell. In the previous figure, we have compared the

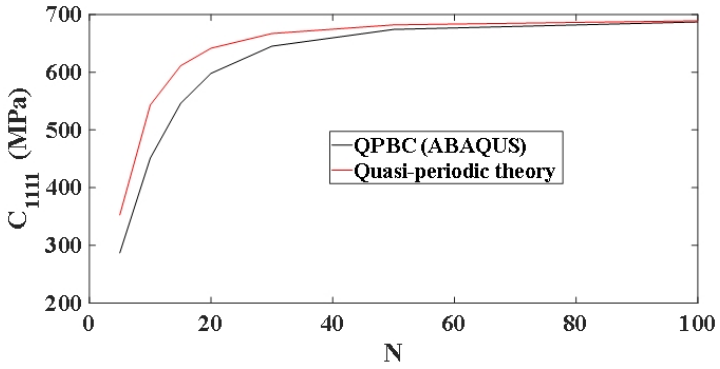

Figure 7.4 Predicted tensile quasi-periodic rigidity versus the number of the unit cells in the circumferential direction.

theoretical predictions with direct FE simulations over the quasi-periodic unit cell (at fixed macroscopic positions) whereby quasi-periodic boundary conditions have been implemented in the local tangent basis attached to the considered unit cell. The difference between both predictions reflects the fact that FE predictions ignore the variation of the local basis on opposite edges within a single unit cell, reflecting microcurvature effects of the unit cell. The quasi-periodic homogenization is more accurate than FE computations since it captures the effect of single unit cell microcurvature, which is not the case for direct FE computations.

The spatial variation of the same quasi-periodic effective tensile rigidity coefficient predicted by the quasi-periodic homogenization theory is plotted versus the radial direction in Fig. 7.5, showing an increase towards the asymptotic limit value corresponding to the periodic moduli. This variation reflects the influence of unit cell microcurvature, the influence of which is decreasing when moving away from the outer edge towards the inner part of the disk; microcurvature effects are indeed of increasing effects for increasing unit cell absolute size, these effects occurring when moving from the center to the external edge of the quasi-periodic domain. Note that FE quasi-periodic direct simulations cannot capture the effect of microcurvature since they do not take into account the variation of the local basis and microcurvature effects. Thus, they predict a constant modulus for all unit cells along the radial coordinate, equal to the periodic effective modulus. The macroscopic spatial variation of the tensile modulus shown in Fig. 7.5 reflects that the conformally mapped disk is a functionally graded material, showing a relatively small variation of about 4.5%. The following subsection aims to provide a theoretical analysis of the microcurvature effects.

7.4 Unit cell microcurvature effect on effective properties

In order to extend previous quasi-periodic homogenization theory to the more accurate setting of curvilinear coordinates, the use of the covariant derivative in place of the classical derivative is involved. The necessary background in differential geometry for handling derivatives in curvilinear coordinates is

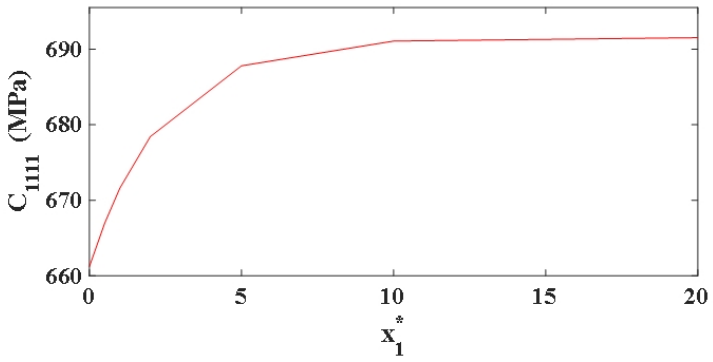

Figure 7.5 Spatial variation of the tensile quasi-periodic modulus along a radius of the quasi-periodic domain for the case of the converged number of unit cells in the circumferential direction (moving from the external edge inwards).

conveniently summarized in Appendix N. Let recall the transformation rule of covariant derivatives (here denoted with an upper case derivative operator D) under a general non-affine change of coordinates:

$$\frac{D\tilde{v}^j}{D\tilde{y}^l} := \left(\partial_l \tilde{v}_j + \Gamma^j_{kl}\tilde{v}^k\right) = \left(\frac{\partial \tilde{y}^j}{\partial y^p}\frac{\partial y^k}{\partial \tilde{y}^l}\right)\frac{Dv^p}{Dy^k} \tag{7.35}$$

Significantly, the quasi-periodic homogenization theory and its unit cell BVP written in section 7.3 remain valid, thereby accounting for the macrocurvature via the covariant derivative that 'absorbs' the macroscopic variation of design in the quasi-periodic domain by accounting for the existing set of curvilinear coordinates over the quasi-periodic domain. On the other hand, conformal transformations introduce a microcurvature in addition to the macrocurvature, not accounted for by the sole covariant derivative, the importance of which we evaluate in this section.

The transformation law of the components of the **gradient of a vector field** $\mathbf{v}(\mathbf{x}) = v^i(x^k)$ now involves second spatial derivatives that have been neglected in the previous section, following the active transformation rule set in Eq. 7.34:

$$\boldsymbol{v}(\boldsymbol{y}) = v^i(y^k)\boldsymbol{g}_k \rightarrow \tilde{\boldsymbol{v}}(\tilde{\boldsymbol{y}}) = \tilde{v}^i(\tilde{y}^k)\tilde{\boldsymbol{g}}_k \rightarrow \tilde{v}^i(\tilde{y}^k) = \frac{\partial \tilde{y}^i}{\partial y^h}v^h(y^q) \tag{7.36}$$

$$\begin{aligned} &\nabla_y \boldsymbol{v}(y) = \frac{dv^i}{dy^k}\boldsymbol{g}_k,\ \nabla_{\tilde{y}}\tilde{\boldsymbol{v}}(\tilde{y}) = \frac{d\tilde{v}^i}{d\tilde{y}^k}\tilde{\boldsymbol{g}}_k \\ &D\tilde{v}^i = \frac{\partial \tilde{y}^i}{\partial y^h}dv^h + \frac{\partial^2 \tilde{y}^i}{\partial y^h \partial y^k}v^h dy^k \equiv \frac{\partial \tilde{y}^i}{\partial y^h}dv^h \Rightarrow \frac{D\tilde{v}^i}{D\tilde{y}^k} = \frac{\partial^2 \tilde{y}^i}{\partial y^l \partial y^h}\frac{\partial y^l}{\partial \tilde{y}^k}v^h + \frac{\partial v^h}{\partial y^l}\frac{\partial \tilde{y}^i}{\partial y^h}\frac{\partial y^l}{\partial \tilde{y}^k} \end{aligned} \tag{7.37}$$

The last relation gives the covariant differential of the coordinates $\tilde{v}^i$ in the transformed coordinates versus the differential elements dv^h, dy^k. The basis vectors transform in a covariant (active) manner, and they are the images of the orthogonal tangent vectors, so it holds adopting here a single spatial scale description

$$
\begin{aligned}
&\tilde{\boldsymbol{g}}_h := \frac{\partial \boldsymbol{y}}{\partial \tilde{y}^h} = \frac{\partial \boldsymbol{y}}{\partial y^j}.\frac{\partial y^j}{\partial \tilde{y}^h} = \frac{\partial y^j}{\partial \tilde{y}^h}\boldsymbol{g}_j \\
&d\boldsymbol{v} = \left(\partial_l v_i + \Gamma^i_{kl} v^k\right) dy^l \boldsymbol{g}_i \equiv \frac{Dv^i}{Dy^l} dy^l \boldsymbol{g}_i,\ \tilde{\boldsymbol{g}}_k d\tilde{y}^k = \frac{\partial y^j}{\partial \tilde{y}^k}\boldsymbol{g}_j \frac{\partial \tilde{y}^k}{\partial y^p} dy^p \equiv \delta_{jp}\boldsymbol{g}_j dy^p = \boldsymbol{g}_q dy^q \\
&\frac{\partial \tilde{v}^j}{\partial \tilde{y}^l} = \left(\frac{\partial^2 \tilde{y}^j}{\partial y^h \partial y^k}\frac{\partial y^k}{\partial \tilde{y}^l}\right) v^h + \frac{\partial \tilde{y}^j}{\partial y^h}\frac{\partial y^k}{\partial \tilde{y}^l}\frac{\partial v^h}{\partial y^k} \Rightarrow \frac{D\tilde{v}^j}{D\tilde{y}^l} := \left(\partial_l \tilde{v}_j + \Gamma^j_{kl}\tilde{v}^k\right) = \left(\frac{\partial \tilde{y}^j}{\partial y^p}\frac{\partial y^k}{\partial \tilde{y}^l}\right)\frac{Dv^p}{Dy^k} \\
&\rightarrow D\tilde{\boldsymbol{v}}(\tilde{\boldsymbol{y}}) = \frac{D\tilde{v}^j}{D\tilde{y}^l}\tilde{\boldsymbol{g}}_j d\tilde{y}^l = \left\{\left(\frac{\partial \tilde{y}^j}{\partial y^p}\frac{\partial y^k}{\partial \tilde{y}^l}\right)\frac{Dv^p}{Dy^k}\right\}\left(\frac{\partial y^r}{\partial \tilde{y}^j}\boldsymbol{g}_r\right)\left(\frac{\partial \tilde{y}^l}{\partial y^r}\right) dy^r = \left(\frac{\partial \tilde{y}^j}{\partial y^p}\frac{\partial y^r}{\partial \tilde{y}^j}\frac{\partial y^k}{\partial \tilde{y}^l}\frac{\partial \tilde{y}^l}{\partial y^r}\right)\frac{Dv^p}{Dy^k}\boldsymbol{g}_r dy^r \\
&\qquad = \left(\delta^r_p \delta^k_r\right)\frac{Dv^p}{Dy^k}\boldsymbol{g}_r dy^r = \frac{Dv^r}{Dy^k}\boldsymbol{g}_r dy^k \equiv D\boldsymbol{v}(\boldsymbol{y})
\end{aligned}
\tag{7.38}
$$

Remark: Eq. 7.38 results show that quantities $D\tilde{v}^i$ constitute the components of a contravariant vector, so they transform like a contravariant vector:

$$
Dv^i = \frac{\partial v^j}{\partial y^k} dy^k + \Gamma^j_{hk} v^h dy^k,\ D\tilde{v}^i = \frac{\partial v^j}{\partial \tilde{y}^k} d\tilde{y}^k + \Gamma^j_{hk} v^h d\tilde{y}^k \Rightarrow D\tilde{v}^i = \frac{\partial \tilde{y}^i}{\partial y^h} Dv^h \tag{7.39}
$$

The virtual power of internal forces due to microcurvature effects receives from previous preliminary steps the following expression:

$$
P^{\eta,curvature} = \left\langle \sigma_{ik} : \frac{\partial^2 y^i}{\partial \tilde{y}^l \partial \tilde{y}^h}\frac{\partial \tilde{y}^l}{\partial y^k} u^h \right\rangle_Y \tag{7.40}
$$

We will not evaluate numerically the effect of microcurvature in this thesis.

7.4.1 Sensitivity of the apparent compressibility modulus to number of unit cells

Recall that the Hill macrohomogeneity condition in the periodic domain writes:

$$
\left\langle \tilde{\boldsymbol{\sigma}} : \tilde{\boldsymbol{\omega}} \otimes^S \nabla_{\tilde{y}} \right\rangle_{\tilde{Y}} = \langle \tilde{\boldsymbol{\sigma}} \rangle_{\tilde{Y}} : \langle \nabla_{\tilde{y}} \tilde{\boldsymbol{\omega}} \rangle_{\tilde{Y}} \tag{7.41}
$$

Summing the previous relation over the entire set of unit cells within the periodic domains lead to the following relation:

$$
\begin{aligned}
&\sum_{k=1}^{N_{UC}} \left\langle \boldsymbol{\sigma}^\eta : \boldsymbol{\omega} \otimes^S \nabla_y \right\rangle_{Y_k} = \sum_{k=1}^{N_{UC}} \left\{ \frac{1}{|\tilde{Y}|} \sum_{i=1,2} \left([\![\tilde{\boldsymbol{u}}]\!]^{\,i} \otimes \tilde{\boldsymbol{N}}^i \right) : \frac{1}{|\tilde{Y}|} \sum_{j=1,2} \left(\int_{\partial Y_k} (\tilde{\boldsymbol{\sigma}}^\eta \cdot \tilde{\boldsymbol{n}})\, ds \otimes \tilde{\boldsymbol{Y}}^j \right) \right\} = \tilde{\boldsymbol{E}}_{\partial \tilde{D}} : \tilde{\boldsymbol{\Sigma}}_{\partial \tilde{D}}, \\
&\tilde{\boldsymbol{\Sigma}}_{\partial D} := \frac{1}{|\tilde{Y}|} \sum_{k=1}^{N_{UC}} \sum_{j=1,2} \left(\int_{\partial Y_k} (\tilde{\boldsymbol{\sigma}}^\eta \cdot \tilde{\boldsymbol{n}})\, ds \otimes \tilde{\boldsymbol{Y}}^j \right),\ \tilde{\boldsymbol{E}}_{\partial D} := \frac{1}{|\tilde{Y}|} \sum_{k=1}^{N_{UC}} \left([\![\tilde{\boldsymbol{u}}]\!]^{\,i} \otimes \tilde{\boldsymbol{N}}^i \right) (\partial \tilde{D})
\end{aligned}
\tag{7.42}
$$

Since the unit cell share common edges with opposite unit normal, all internal unit cell contributions cancel out in the previous summation over the N_{UC} number of the periodic unit cells (Fig. 7.6, left view), leaving the sole contribution of the external boundary contribution, expressed in the last term. It becomes, therefore, possible at the leading order to evaluate the *apparent macroscopic properties* in the periodic domain from the sole knowledge of the surface kinematic and static quantities (applied tractions and induced displacement, or conversely applied kinematic control and induced traction) on the external boundary of the parent (periodic) domain (Fig. 7.6). Note that only the apparent bulk and shear moduli can be computed from the surface macro fields since only the normal projection of the stress and strain fields can be controlled over the macrodomain boundary.

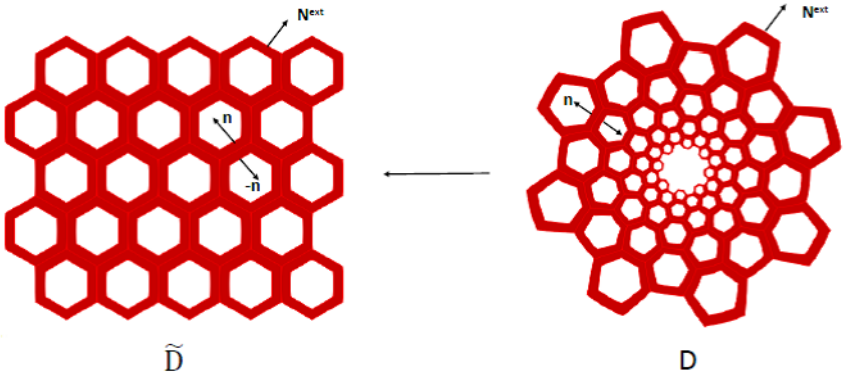

Figure 7.6 Evaluation of the macroscopic and mesoscopic (unit cell based) mechanical properties based on a mapping to a periodic parent domain. The macroscopic moduli express as surface integrals over the external domain boundary due to vanishing internal surface contributions.

The inverse identification of the unit cell moduli can be made based on measurements or virtual tests (numerical) of the apparent properties of such mapped domains. For that purpose, a set of well-chosen kinematic or stating loadings can be applied over the conformally mapped domain boundary to identify the coefficients of the tensor of apparent moduli $\tilde{\boldsymbol{C}}^{App}$, satisfying the following relation written at the leading order of the small-scale parameter:

$$\tilde{\boldsymbol{\Sigma}}_{\partial\tilde{D}} = \tilde{\boldsymbol{C}}^{App} : \tilde{\boldsymbol{E}}_{\partial\tilde{D}} \tag{7.43}$$

A similar relation holds for the quasi-periodic domain, although no relation holds between the unit cell-based properties and the apparent macroscopic properties:

$$\boldsymbol{\Sigma}_{\partial D} = \boldsymbol{C}^{App} : \boldsymbol{E}_{\partial D} \tag{7.44}$$

with $\tilde{\boldsymbol{C}}^{App}$ the tensor of quasi-periodic apparent moduli. The apparent bulk and shear moduli are particularly important in conformal transformations of rectangular domains into circular disks with a quasi-periodic microstructure.

In order to compute the compressibility modulus of the quasi-periodic structure a conformally mapped periodic hexachiral unit cell pictured in fig. 7.7 is considered. The apparent compresibility modulus is obtained by imposing a radial homogeneous macrostrain controlled by a radial displacement onto the edge of the quasi-periodic macrodomain.

The apparent quasi-periodic compressibility moduli predicted by direct finite element simulations using ABAQUS FE code is shown (fig. 7.8) to vary with the number of unit cells along the radius of the disk, with a rapid increase in the first stage, followed by a stabilization for about $N_r = 15$ radially distributed unit cells. We observe that the responses converge for a number $N_\theta = 40$ of distributed unit cells along the circumference of the disk. Under such converged conditions, the apparent quasi-periodic compressibility modulus is shown to converge for $N_r = 25$ number of radially distributed unit cells. The converged value $K^{QP} = 90\ MPa$ slightly differs from the same modulus evaluated over the periodic domain, computed

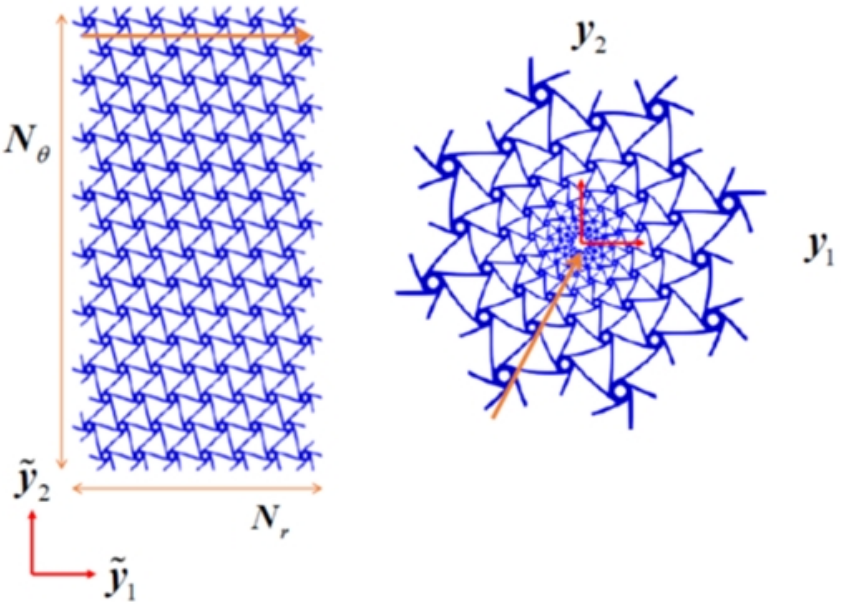

Figure 7.7 Conformal mapping of a (left) hexachiral periodic unit cell to a (right) quasi-periodic domain.

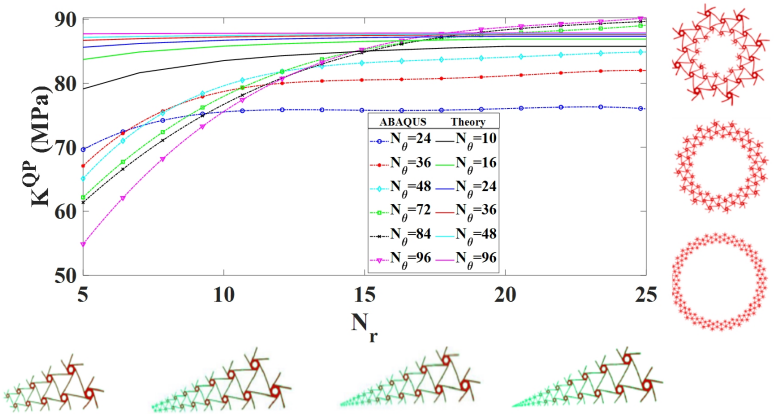

Figure 7.8 Variation of the quasi-periodic compressibility modulus versus the number of radial unit cells of the hexachiral lattice computed by FE simulations and theory, for varying number of angular unit cells. Here, k=50.

to be $K_{app}^{QP} = 87.86\ MPa$.

7.5 Conclusion

Conformal transformations play an important role as both a method of analysis of engineering problems and a way to generate complex 2D shapes from initially simpler ones. In the context of architected media, the initial periodicity of the structure under translation in the periodic domain is transformed into a rotational periodicity in the mapped domain. Conformal transformations of periodic architected media allow geometry to be graded at both macroscale and unit cell levels. The properties of conformal transformations of architected media have been analyzed in the broad sense in this contribution; mainly, the modifications of the effective properties at the level of a periodic unit cell in the initial (periodic)

domain have been analyzed, based on the elaboration of a homogenization theory for quasi-periodic media. The following main results have been obtained in the present contribution:

- Conformal transformations prove convenient for generating complex designs with the gradient of unit cell dimensions and especially porosity gradients, based on mapping a reference isotropic and periodic unit cell. Thereby, we can tune the macroscopic properties by i) selecting a suitable architectured material at the level of an irreducible unit cell, and ii) by distributing this unit cell in a macrodomain based on non-homogeneous (finite) conformal transformations.
- Conformal transformations satisfy the kinematic compatibility condition, thereby proving their adequacy to generate quasi-periodic designs with tunable morphological and mechanical apparent properties.
- A quasi-periodic homogenization theory in the context of conformal mappings has been developed, together with smoothness conditions allowing to design of quasi-periodic architected domains. The effective properties are calculated based on the strain localization over the periodic domain, and they exhibit a dependency upon the macroscopic spatial position underlining the heterogeneous nature of the quasi-periodic properties.
- Macrocurvature resulting from the nonlinear mapping of the initially periodic architectured domain into a quasi-periodic one is incorporated into the BVP posed over the quasi-periodic domain using the covariant derivative. The micro-curvature occurring within the quasi-periodic unit cell has been accounted for theoretically via an asymptotic expansion method.

  We plan in future developments to use conformal transformations of initially periodic architectured materials to achieve designs with complex geometries, tunable porosity, and apparent mechanical properties. Moreover, developments in this chapter have been limited to first gradient homogenization, we may have to recourse to strain effective gradient models in order to account for the existence of a macroscopic or microscopic gradient of geometry (internal porosity, gradation of internal architecture, macroscopic variation of the geometry of the building unit cell, Etc.), following or adapting the developments of chapter 6. The role and properties of conformal transformations will be explored in future contributions, relying on the fact that the unit cell level and apparent macroscopic properties can be tuned by selecting a proper architectured material at the level of an irreducible unit cell and by distributing this unit cell in a macrodomain based on non-homogeneous (finite) conformal transformations.

General conclusion and perspectives

Composites and architectured materials are typical classes of materials widely used in engineering due to their high mechanical performances (like strength, energy absorption capacity, thermal and acoustic insulation properties) at low weight in a wide diversity of applications. Their excellent properties are mainly due to the possibility of adjusting the architecture and microstructural properties of the underlying microstructure to reach targeted properties at the mesoscopic or macroscopic scales. The full exploitation of the potential of these materials requires a clear understanding and prediction of their mechanical response at the level of a unit cell, incorporating the available microstructural information. The development of predictive *micromechanical schemes* to understand the impact of the existing microstructure on the mechanical response at both *mesoscopic and macroscopic levels* is essential to bridge the scales and relate the equivalent properties to both the geometrical properties and mechanical parameters of the structure.

The prediction of the overall mechanical response of microstructured materials like *architected materials* and *cellular materials* cannot be achieved by performing direct numerical simulations, whereby all microstructural details are fully resolved using a sufficiently fine mesh resolution. Indeed, such numerical analyses usually have a substantial computational cost, making them unfeasible for typical engineering problems. Moreover, the experimental determination of such structures' mechanical properties is delicate since the overall anisotropy has to be considered. In addition, the lack of a clear scale separation may require using enriched continuum theories that include many more constitutive parameters than Cauchy elasticity theory. For these reasons, it proves relevant to perform homogenization towards effective microstructure models in a first step that can be used to perform computations at the macrostructural level in a second convenient step.

This thesis aims to revisit *higher-order homogenization schemes* towards *higher-order and higher-gradient continua* - defining the so-called *generalized continua* -, successively for periodic and quasi-periodic architected materials and composites, based on variational principles and an extension of Hill macrohomogeneity condition. All developments have been made in the framework of linearized elasticity. Since architected materials consist of slender structural elements, they can be described in mechanical terms as beam elements. Thus, one may recourse either to discrete homogenization type methods or to *continuous homogenization schemes* that no reduced model is used in this last situation. In **Part**

I, Continuous homogenization methods were exposed for micropolar and *micromorphic media*, followed by an exposition of the alternative discrete homogenization method in **Part II**. While these two first parts deal with periodic materials in which a repetitive unit cell can be identified, we extended in **Part III** these theoretical developments to the situation of quasi-periodic materials, which still have a regular microstructure, which can be continuously mapped to a periodic parent configuration. The common idea to the proposed periodic homogenization methods (of continuous or discrete nature) is to split the microscopic displacement into a homogeneous part representative of the kinematics of the adopted effective continuum and a fluctuation evaluated from a variational principle and characterized by classical and higher-order unit cell boundary value problems. In substance, the theoretical developments allow the elaboration of enriched continua (generalized continua) of micromorphic type and all sub continua obtained from it using suitable degeneration conditions. However, instead of following *a priori* such a top-down approach, we have successfully considered Cosserat (chapter 2) and micromorphic continua (chapter 3) in the present thesis, thereby following order of increased complexity. The theoretical developments have given rise to numerical schemes for computing the classical and non-classical effective properties. Numerical applications have been made for architected materials and inclusion-based composites prone to higher-order effects due to their inner architecture. The justification of a priori choice of a given generalized continuum was provided by the numerical evaluation of the fluctuation energy that quantifies the departure of the selected effective media from the response of the initially (before homogenization) heterogeneous material. The obtained results highlight that the higher-order moduli usually converge very quickly with unit cell size due to considering correction factors based on the higher-order moments of area for the micromorphic continuum. On the theoretical part, the performed developments remedy many existing limitations of existing higher-order homogenization schemes.

In **Part II** of this thesis, the classical and higher-order continuum properties have been enriched either following the path of *phenomenology* or based on *micromechanical schemes*. Consistent couple stress models of enriched beams have been derived in chapter 4, assuming the base material to have an intrinsic length scale parameter. It, however, faces some limitations, since firstly, there is no way to determine the value of the internal length from the outset without any prior knowledge of the microstructure. Secondly, the material is considered a 'black box' at a relatively macroscopic scale of observation, and as a consequence, it does not provide a method for determining the internal length in situations where a microstructure can be identified. In chapter 5, we instead built enriched *Cosserat media* in the spirit of micromechanics, adopting Timoshenko beam models at a microlevel, and applying a *continualization method* towards a Cosserat effective substitution medium. The proposed method combines a reduced number of degrees of freedom at a unit cell level with the continuous set of kinematic variables, representative of a Cosserat continuum at the macroscale. The effective classical and Cosserat moduli are closed-form expressions of the lattice microstructural and mechanical parameters for the specific case of honeycomb lattices. The proposed continualization method proves to be accurate and computationally efficient compared to continuous homogenization schemes and fully resolved finite element simulations.

One key outcome of the performed analyses is the quantification of edge effects in the response of lattice structures, relying on the surface formulation of the extended *Hill macrohomogeneity condition*. The bending moment to curvature relation involves a classical term and a micropolar bending moment, the importance of decreasing asymptotically up to a nil value by increasing the number of unit cells in the height of the macrostructure.

The theoretical background underlying *quasi-periodic asymptotic homogenization* in the framework of linearized anisotropic elasticity deserves the development of **Part III**. Different methodologies for evaluating the tensors of effective quasi-periodic properties are developed in chapter 6. Mainly, one class of homogenization strategies relies on a mapping of the periodic unit cell problem onto the quasi-periodic unit cell problem, whereby the microstructural strain fluctuation within the unit cell was taken into account by solving a localization problem at the unit cell level before evaluating the tensor of quasi-periodic effective moduli. In both strategies, the extended quasi-periodic *Hill macrohomogeneity condition* plays a prominent role. The issues of kinematic compatibility and smoothness of the design transformation are addressed, underlining *conformal transformations* prominent role in designing quasi-periodic compatible architected materials. General properties satisfied by conformal maps were proven in chapter 7.

Numerous **perspectives** can be envisaged, from the performed theoretical and numerical developments, so we here content ourselves to outline the most important ones in our opinion briefly. Selecting the most suitable generalized continuum for a given class of architected materials remains an important issue to be addressed in future developments. While the idea of tuning effective engineering properties by a modification of the topology of architected materials is highly relevant, there is a need to go beyond heuristic to elaborate a rationale for finding architectures giving rise to the emergence of enriched behaviors; topology optimization methods can provide such a systematic strategy. Exploring the possible large strains response of soft lattice materials in the framework of generalized continua is a second central perspective of this thesis. Thirdly, while we have restricted this work to pure mechanical aspects, multiphysical coupled behaviors are a promising research direction to be explored to fully exploit the scientific and technological promises of architected materials and metamaterials. Finally, we would like to mention interesting potential scientific developments and applications of the proposed homogenization methods to the field of bone biomechanics, notwithstanding the additional complexity of accounting for the microstructure evolution when remodeling takes place.

Résumé étendu en français

Contexte général

La recherche des ingénieurs en science des matériaux pour améliorer les propriétés des matériaux afin de répondre aux demandes exigeantes de l'industrie a évolué vers un nouveau paradigme, dans lequel l'architecture interne du matériau apparaît comme un nouveau degré de liberté - au-delà de la composition chimique - dans la conception du matériau pour contrôler et améliorer les propriétés du matériau. L'expression "matériaux architecturés" est apparue dans la littérature dans un article de synthèse [8] afin de relier les méthodes d'optimisation de la topologie utilisées pour concevoir des matériaux légers, très performants et élégants (comme la tour Eiffel), à l'ingénierie structurelle. Tel qu'il est défini, un matériau architecturé (le terme architecturé est également utilisé dans la littérature) combine plusieurs matériaux de base plus simples de manière synergétique - et parfois avec une hiérarchie d'échelles imbriquées, comme la tour Eiffel [10, 11]. Cette organisation de la topologie a pour conséquence l'émergence de nouvelles performances et propriétés non atteignables par aucun des constituants à titre individuel, afin d'atteindre des exigences données par le concepteur. La grande variabilité des géométries possibles des topologies des blocs de construction élémentaires définissant l'architecture interne du matériau offre une énorme richesse de l'espace de conception des matériaux. Les performances des matériaux sont condensées dans les diagrammes visuels d'Ashby, comme celui illustré figure R.1 pour le module de traction, la limite d'élasticité et la densité dans une représentation 3D.

Les matériaux architecturés conçus pour des applications techniques sont le plus souvent caractérisés par une cellule unitaire, définie comme la "brique" élémentaire de matière à partir de laquelle la structure entière est fabriquée en utilisant la notion commode - du point de vue de la fabrication, mais aussi de la modélisation - de périodicité ; quelques exemples de matériaux cellulaires avec une telle architecture régulière sont représentés en figure R.2. Bien que la microstructure réelle ne soit pas exactement périodique, sa représentation comme un milieu périodique en est très souvent une bonne approximation.

L'architecture du matériau peut être réalisée depuis le niveau atomique ou moléculaire jusqu'aux dimensions structurelles (macroscopiques). Il est aujourd'hui courant d'intégrer dès le départ la conception des matériaux dans la mécanique des structures. Malgré sa puissance, cette méthodologie

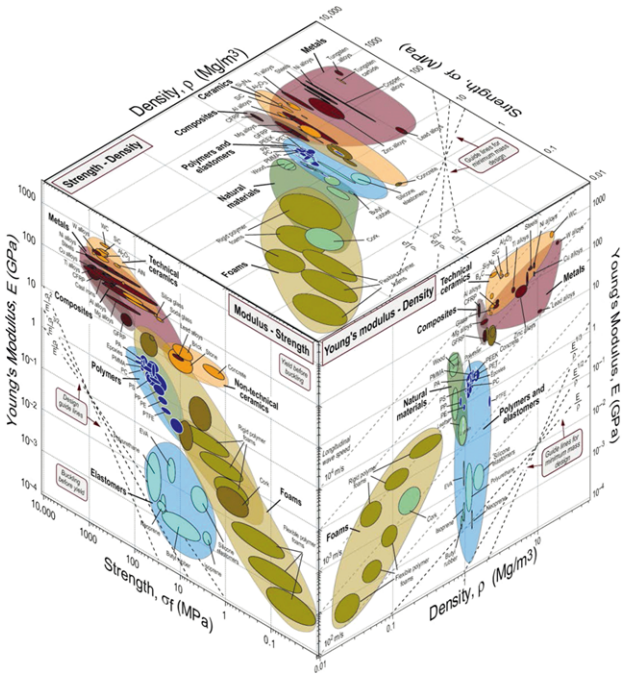

Figure R.1 Diagramme de performance d'Ashby en 3D des matériaux utilisés en ingénierie montrant la relation entre la résistance, le module et la densité pour différentes classes de matériaux [1].

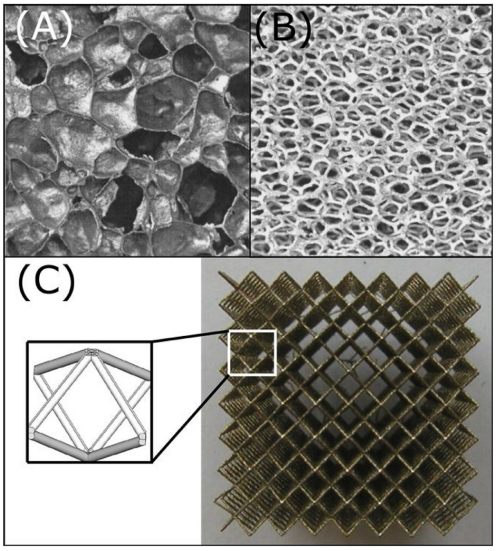

Figure R.2 Exemples de matériaux cellulaires : (A) mousse à cellules fermées, (B) mousse à cellules ouvertes, (C) matériau cellulaire ordinaire (cellule unitaire BCC à corps cubique centré) [2].

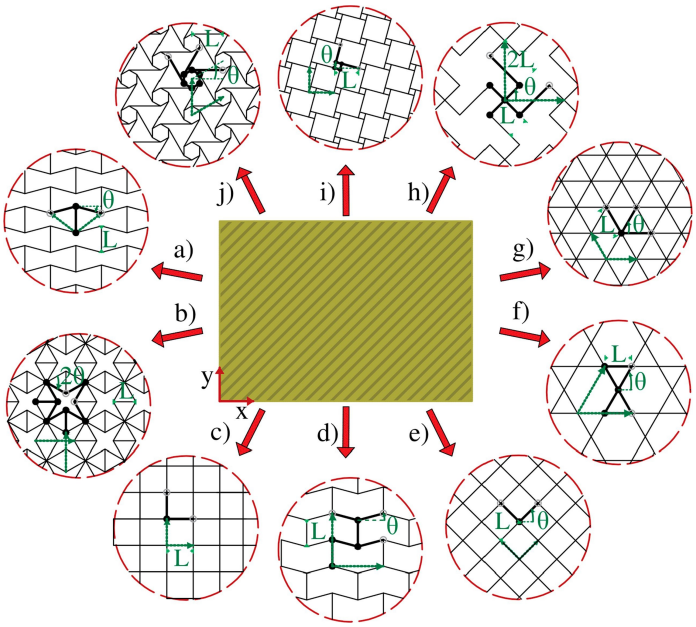

Figure R.3 Architectures 2D avec un coefficient de Poisson contrôlé : (a, b) Hexagonale, étoile rentrante, (c, d) rectangulaire, semi-entrante, (e, f, g) diamant, kagome, triangulaire, treillis chiraux (diamant chiral (h), tétrachiral (i), hexachiral (j)) [3].

emprunte essentiellement à l'heuristique et s'appuie sur l'expérience et l'intuition du concepteur ; il lui manque cependant une méthodologie de raisonnement plus rigoureuse pour définir des topologies appropriées (voire optimales) pour une application donnée ou un ensemble d'exigences mécaniques. Le terme métamatériaux a été créé pour désigner une nouvelle classe de matériaux parmi les matériaux architecturés émergeant au cours des dernières décennies, dotés d'attributs mécaniques statiques ou dynamiques qui ne sont pas couramment rencontrés dans les matériaux naturels et qui ont mérité l'appellation spécifique de métamatériaux [3]. Ce terme désigne la capacité d'ajuster les propriétés effectives du matériau (au niveau de la cellule unitaire d'un continuum de substitution effective) par une modification de sa topologie interne, plutôt que par un changement de la composition chimique pour modifier les propriétés du matériau de base.

Cette avancée technologique est devenue possible en grande partie grâce au développement rapide et aux progrès des techniques de fabrication additive. Parmi les propriétés mécaniques, le coefficient de Poisson joue un rôle privilégié car il est parfois considéré comme une métrique des propriétés des matériaux. Les matériaux auxétiques présentant un coefficient de Poisson négatif ont des propriétés statiques et dynamiques exceptionnelles, telle une résistance élevée aux chocs et aux impacts, ou encore une capacité d'atténuation des vibrations et des ondes sonores importante. La figure R.3 présente un éventail de matériaux à architecturés périodiques au coefficient de Poisson positif ou négatif (auxétiques).

Les composites et les matériaux architecturés sont des classes typiques de matériaux largement utilisés en ingénierie en raison de leurs hautes performances mécaniques (comme la limite d'élasticité ou de rupture, la capacité d'absorption d'énergie, les propriétés d'isolation thermique et acoustique) pour un

faible poids dans une grande diversité d'applications. Leurs excellentes propriétés sont principalement dues à la possibilité d'ajuster l'architecture et les propriétés microstructurales de la microstructure sous-jacente pour atteindre des propriétés ciblées à l'échelle mésoscopique ou macroscopique. L'exploitation complète du potentiel de ces matériaux nécessite une compréhension claire et une prédiction de leur réponse mécanique au niveau d'une cellule unitaire, en incorporant les informations microstructurales disponibles. Le développement de schémas micromécaniques prédictifs pour comprendre l'impact de la microstructure existante sur la réponse mécanique aux niveaux mésoscopique et macroscopique est essentiel pour établir un pont entre les échelles et relier les propriétés équivalentes aux propriétés géométriques et aux paramètres mécaniques de la microstructure. La prédiction de la réponse mécanique globale des matériaux microstructurés, tels que les matériaux architecturés et les matériaux cellulaires, peut difficilement être réalisée en effectuant des simulations numériques directes, dans lesquelles tous les détails microstructuraux sont entièrement résolus à l'aide d'une résolution de maillage suffisamment fine. En effet, de telles analyses numériques ont généralement un coût de calcul prohibitif, ce qui les rend irréalisables pour des problèmes d'ingénierie classiques. De plus, la détermination expérimentale des propriétés mécaniques de telles structures est délicate puisqu'il faut tenir compte de l'anisotropie globale. De plus, l'absence d'une séparation d'échelle claire peut nécessiter l'utilisation de théories de continuum enrichies qui incluent beaucoup plus de paramètres constitutifs que la théorie de l'élasticité de Cauchy. Pour ces raisons, il s'avère pertinent d'effectuer une homogénéisation vers des modèles de microstructure efficaces dans une première étape qui peuvent être utilisés pour effectuer des calculs au niveau macrostructurel dans une seconde étape pratique.

Objectifs de la thèse

Cette thèse vise à revisiter les schémas d'homogénéisation d'ordre supérieur vers des continuums d'ordre et de gradient supérieurs - définissant les continuums dits généralisés -, successivement pour les matériaux et composites architecturés périodiques et quasi-périodiques, en se basant sur des principes variationnels et une extension de la condition de macrohomogénéité de Hill. Tous les développements sont réalisés dans le cadre de l'élasticité linéarisée. Puisque les matériaux architecturés sont constitués d'éléments structurels minces, ils peuvent être décrits en termes mécaniques comme des éléments de poutre, on peut donc avoir recours soit à des méthodes de type homogénéisation discrète, soit à des schémas d'homogénéisation continue, lorsque dans cette dernière situation aucun modèle réduit n'est utilisé. Les méthodes d'homogénéisation continue sont exposées dans la première partie, pour les milieux micropolaires et micromorphes, suivies par une exposition de la méthode alternative d'homogénéisation discrète dans la deuxième partie. Alors que ces deux premières parties traitent des matériaux périodiques dans lesquels une cellule unitaire répétitive peut être identifiée, nous étendons dans la partie III ces développements théoriques à la situation des matériaux quasi-périodiques, qui ont toujours une microstructure régulière, qui peut être continuellement mise en correspondance avec une configuration périodique mère.

Méthodologie d'homogénéisation vers des milieux continus généralisés

L'idée commune aux méthodes d'homogénéisation périodique proposées (de nature continue ou discrète) est de séparer le déplacement microscopique en une partie homogène représentative de la cinématique du continuum effectif adopté, et une fluctuation évaluée à partir d'un principe variationnel et caractérisée par des problèmes de valeurs limites de cellules unitaires classiques et d'ordre supérieur. En substance, les développements théoriques permettent l'élaboration de continuums enrichis (continuums généralisés) de type micromorphique, et de tous les sous-continus qui en découlent en utilisant des conditions de dégénérescence appropriées. Cependant, au lieu de suivre a priori une telle approche appelée 'top down', nous avons considéré avec succès les continuums de Cosserat (chapitre 2) et les continuums micromorphes (chapitre 3) dans la présente thèse, suivant ainsi un ordre de complexité croissante. Les développements théoriques ont donné lieu à des schémas numériques pour le calcul des propriétés effectives classiques et non classiques. Des applications numériques ont été réalisées pour les matériaux architecturés et les composites à base d'inclusion sujets à de tels effets d'ordre supérieur, en raison de leur architecture interne. La justification du choix a priori d'un continuum généralisé donné est fournie par l'évaluation numérique de l'énergie de la fluctuation qui détermine l'écart du milieu effectif sélectionné par rapport à la réponse du matériau initialement hétérogène (avant homogénéisation). Les résultats obtenus mettent en évidence que les modules d'ordre supérieur convergent généralement très rapidement avec la taille de la cellule unitaire, en raison de la prise en compte de facteurs de correction basés sur les moments d'aire d'ordre supérieur pour le continuum micromorphe. Sur le plan théorique, les développements effectués remédient à de nombreuses limitations existantes des schémas d'homogénéisation d'ordre supérieur.

La méthode d'homogénéisation proposée pour les milieux de substitution micromorphes repose sur une formulation variationnelle de l'équilibre combinée à une décomposition du déplacement microscopique en une partie homogène et une fluctuation. Au niveau micro, on suppose une loi constitutive élastique linéaire sans forces de corps. La partie homogène du déplacement microscopique décrit un milieu hétérogène qui se comporterait exactement comme le continuum micromorphe postulé. Ce déplacement homogène est corrigé par une fluctuation supplémentaire au niveau micro, évaluée en raison de la linéarité du problème de la valeur limite utilisant des opérateurs de localisation du déplacement, qui sont caractérisés par un problème aux limites posez sur la cellule unitaire du composite.

L'analyse proposée fournit un champ de déplacement microscopique homogène polynomial d'ordre 4 après recours aux formulations d'énergie potentielle et d'énergie complémentaire, cette dernière formulation fournissant un champ de contrainte microscopique polynomial d'ordre 3. De plus, il a été prouvé que ce déplacement d'ordre 4 est complet dans le sens où aucun autre terme ne doit être ajouté pour capturer le continuum micromorphe effectif. L'approximation quadratique du déplacement homogène est suffisante pour capturer les expressions de contrainte de Cauchy et de contrainte relative

du continuum micromorphe. Ainsi, un champ de déplacement plus complet au niveau micro par rapport à [187] a été obtenu.

Toutes les variables macroscopiques cinématiques et statiques peuvent être converties en intégrales de surface des champs microscopiques sur la cellule unitaire, comme cela est prouvé dans l'annexe H. Cela permet d'appliquer toutes les mesures cinématiques entièrement sur la limite de la cellule unitaire. Les expressions obtenues des variables statiques homogénéisées sont résumées comme suit :

$$\bar{\underline{\boldsymbol{\sigma}}} := \frac{1}{|Y|}\sum_{i=1,2}\left(\int_{\partial Y}\left(\underline{\boldsymbol{\sigma}}\cdot\underline{\boldsymbol{n}}\right)ds\right)\otimes\underline{\boldsymbol{Y}}^{\delta}$$

$$\underset{\approx}{\boldsymbol{\mathfrak{s}}} := \frac{1}{|Y|}\sum_{i=1,2}\left(\left(\int_{\partial Y}\left(\underline{\boldsymbol{\sigma}}\cdot\underline{\boldsymbol{n}}\right)ds_y\right)\otimes\left(\underline{\boldsymbol{Y}}^{\delta}\otimes\underline{\boldsymbol{Y}}^{\delta}\otimes\underline{\boldsymbol{Y}}^{\delta}\right)\right)\therefore\underset{\approx}{\Upsilon}-\frac{1}{|Y|}\sum_{i=1,2}\left(\int_{\partial Y}\left(\underline{\boldsymbol{\sigma}}\cdot\underline{\boldsymbol{n}}\right)ds\right)\otimes\underline{\boldsymbol{Y}}^{\delta}\cdot\underline{\boldsymbol{\Gamma}}$$

$$\underset{\sim}{\mathbf{S}} := \frac{1}{|Y|}\sum_{i=1,2}\left(\left(\int_{\partial Y}\left(\underline{\boldsymbol{\sigma}}\cdot\underline{\boldsymbol{n}}\right)ds_y\right)\otimes\left(\underline{\boldsymbol{Y}}^{\delta}\otimes\underline{\boldsymbol{Y}}^{\delta}\right)\right)$$
$$-\mathrm{P}^{-1}\underset{\sim}{\mathbf{G}}\otimes\underset{\approx}{\boldsymbol{\Lambda}}::\left(\underset{\approx}{\boldsymbol{\Omega}}:\frac{1}{|Y|}\sum_{i=1,2}\left(\left(\int_{\partial Y}\left(\underline{\boldsymbol{\sigma}}\cdot\underline{\boldsymbol{n}}\right)ds_y\right)\otimes\left(\underline{\boldsymbol{Y}}^{\delta}\otimes\underline{\boldsymbol{Y}}^{\delta}\right)\right)+\frac{1}{|Y|}\sum_{i=1,2}\left(\left(\int_{\partial Y}\left(\underline{\boldsymbol{\sigma}}\cdot\underline{\boldsymbol{n}}\right)ds_y\right)\otimes\left(\underline{\boldsymbol{Y}}^{\delta}\otimes\underline{\boldsymbol{Y}}^{\delta}\otimes\underline{\boldsymbol{Y}}^{\delta}\otimes\underline{\boldsymbol{Y}}^{\delta}\right)\right)\right)$$

Cela contraste avec l'approche récente [187], dans laquelle l'auteur ne peut pas convertir complètement toutes les relations micro-macro cinématiques et statiques en intégrales de surface, de sorte qu'elles sont plutôt exprimées comme des contraintes intégrales utilisant des multiplicateurs de Lagrange. La méthode présentée pour la détermination du champ de contrainte microscopique en s'appuyant sur l'énergie complémentaire conduit à des conditions limites de contrainte comme alternative aux conditions limites cinématiques employées ; l'efficacité numérique de ces conditions limites basées sur la contrainte méritera des développements supplémentaires.

De plus, l'énergie associée à la fluctuation montre une très faible contribution relative à l'énergie moyenne totale évaluée sur la cellule unitaire, soit moins de 0,5%. Une question importante de l'homogénéisation vers des continuums généralisés soulevant des controverses dans la littérature pertinente est de savoir si les modules d'ordre supérieur doivent disparaître de manière identique pour un composite homogène ; ce fait a été reconnu dans la littérature, voir par exemple [191]. Les résultats numériques obtenus pour les composites montrent que certains modules d'ordre supérieur disparaissent pour des domaines de cellules unitaires uniformes, alors que d'autres modules supérieurs ne disparaissent pas. Ce comportement est attribué au fait que la présence de cellules unitaires voisines (en raison de l'hypothèse de périodicité) contraint la forme déformée de la cellule unitaire de sorte que la partie de Cauchy de la réponse est également activée lors de l'imposition d'un chargement cinématique supérieur donné (même sans inclure aucune mesure cinématique de type Cauchy). Cela revient à dire que la cellule unitaire ne peut pas se déformer comme le ferait un domaine homogène infini sous le même chargement cinématique, comme le reconnaît [191]. Les résultats numériques mettent en évidence que les modules d'ordre supérieur effectifs convergent très rapidement avec la taille de la cellule unitaire, de sorte que la méthode proposée ne présente pas un effet de taille très faible.

Une convergence rapide est obtenue vers une valeur nulle des modules 'purs' liant la contrainte relative à la déformation relative et de celui des modules de couplage entre contrainte relative et déformations classiques, tenseurs, avec la taille de la cellule unitaire (figure 3.18(b)). D'autre part, les modules ne

disparaissent pas pour une cellule unitaire non centrosymétrique, comme le montre la figure 3.15(b). L'expression sous forme fermée du déplacement et de la contrainte microscopiques montre que la position absolue de l'inclusion dans la cellule unitaire importe (et donc pas seulement la forme de l'inclusion, centrosymétrique ou non). Ainsi, la densité d'énergie intégrée de la cellule unitaire dépend en effet de la position relative de l'origine de la base cartésienne locale attachée à la cellule unitaire, de sorte qu'une translation de celle-ci ne peut être opérée pour annuler les effets centrosymétriques). En revanche, les modules micromorphes purs montrent une convergence après normalisation appropriée du problème d'homogénéisation original par la taille de la cellule unitaire. Cette convergence est attribuée à l'incorporation de la fluctuation du déplacement dans la méthode d'homogénéisation basée sur les variations. Une autre explication est la prise en compte des moments d'inertie supérieurs (Annexe G) dans les coefficients des mesures macro cinématiques qui fournit une correction à la dépendance potentielle de la taille de la cellule unitaire, ce qui élimine le besoin de définir un facteur de correction artificiel défini par les autres auteurs, par exemple [192] pour l'homogénéisation du gradient de déformation. Ces corrections sont capturées dans les expressions de la contrainte relative et de l'hyperstress, ici commodément réécrites :

$$\underset{\sim}{\mathbf{s}} := 3\left\langle \underline{\boldsymbol{\xi}} \otimes \underline{\boldsymbol{\xi}} \otimes \underset{\sim}{\boldsymbol{\sigma}} \right\rangle_Y \therefore \underset{\approx}{\Upsilon} - \langle \underset{\sim}{\boldsymbol{\sigma}} \rangle_Y \cdot \underline{\underline{\boldsymbol{\Gamma}}}$$

$$\underset{\sim}{\mathbf{S}} := 2\left\langle \underline{\boldsymbol{\xi}} \otimes \underset{\sim}{\boldsymbol{\sigma}} \right\rangle_Y - 2\mathrm{P}^{-1}\underset{\sim}{\mathbf{G}} \otimes \underline{\underline{\boldsymbol{\Lambda}}} :: \left(\underset{\approx}{\boldsymbol{\Omega}} : \left\langle \underline{\boldsymbol{\xi}} \otimes \underset{\sim}{\boldsymbol{\sigma}} \right\rangle_Y + 2\left\langle \underline{\boldsymbol{\xi}} \otimes \underline{\boldsymbol{\xi}} \otimes \underline{\boldsymbol{\xi}} \otimes \underset{\sim}{\boldsymbol{\sigma}} \right\rangle_Y \right)$$

Les expressions précédentes montrent que les tenseurs de contrainte et d'hyperstress relatifs impliquent un terme quadratique et cubique supplémentaire dans leur expansion, respectivement.

Comme alternative à l'approche variationnelle proposée de l'homogénéisation micromorphique, certaines idées sur une approche asymptotique de l'homogénéisation micromorphique peuvent être données, voir [193] pour une vue d'ensemble de l'homogénéisation asymptotique. Les modèles de Cosserat ont été dérivés d'une homogénéisation asymptotique de la BVP microscopique de l'élasticité de Cosserat dans [105, 130, 131] et des modèles de substitution micromorphes pour un mélange de continuums micromorphes établis dans [188]. La définition d'une hiérarchie de longueurs caractéristiques permet une classification et un classement du milieu effectif dérivé, qui peut être de type Cauchy, micropolaire, microstrain ou micromorphe complet selon le schéma d'hypothèse considéré. La difficulté de l'émergence d'un continuum effectif micromorphe se pose lorsque le milieu est de type Cauchy au niveau microscopique des constituants individuels puisque la loi constitutive effective au niveau macro implique de nouveaux degrés de liberté micromorphes qui ne sont pas présents à l'échelle microscopique. Il faut donc établir un lien entre le déplacement microscopique et les DOF micromorphes. Une stratégie possible, en accord avec la méthodologie adoptée dans le présent travail, serait d'intégrer la moyenne d'ordre supérieur des lois d'équilibre micro, Eq. 3.6-3.8 dans une famille de lois d'équilibre indexée par le paramètre de petite échelle η, en indiquant $\underline{\boldsymbol{\xi}} = \underline{\mathbf{x}}/\eta$. Ceci implique d'un point de vue cinématique que la partie homogène du déplacement apparaîtra aux premiers ordres du paramètre d'échelle, et sa fluctuation aux ordres supérieurs. Un classement des différents termes composant la partie homogène du micro-déplacement

en fonction du paramètre de petite échelle apparaîtra alors, le continuum effectif de Cauchy devant être retrouvé dans la limite d'un paramètre nul ; la partie fluctuante du déplacement apparaîtra à un ordre supérieur du paramètre de petite échelle. L'expansion asymptotique du déplacement ainsi formulée conduira à une expansion asymptotique correspondante de l'énergie macroscopique effective (en utilisant la condition de macrohomogénéité de Hill étendue) mettant en évidence les tenseurs constitutifs micromorphes effectifs classés aux ordres successifs du paramètre de petite échelle. Au lieu d'une forme locale (forte) du schéma d'homogénéisation asymptotique, on peut recourir à une formulation asymptotique variationnelle, comme cela a été fait dans [194] pour l'homogénéisation du gradient de déformation. L'avantage de la formulation variationnelle par rapport aux modèles asymptotiques standard est de pouvoir tenir compte de la finitude du paramètre d'échelle. De plus, elle a la capacité d'estimer la norme des termes successifs d'ordre supérieur et la convergence de la solution obtenue aux ordres successifs du paramètre de petite échelle par rapport à la solution réelle.

Dans la partie II de cette thèse, les propriétés mécaniques effectives classiques et d'ordre supérieur des matériaux à réseau répétitif ont été évaluées sur la base de schémas d'homogénéisation discrets. En suivant l'idée d'une approche phénoménologique, des modèles cohérents de contraintes de couple de treillis de poutres répétitives ont été élaborés dans le chapitre 4. Dans le chapitre 5, nous construisons plutôt des milieux de Cosserat enrichis dans l'esprit de la micromécanique, en adoptant des modèles de poutre de Timoshenko à un niveau micro, et en appliquant une méthode de continualisation vers un milieu de substitution effectif de Cosserat. La méthode proposée combine un nombre réduit de degrés de liberté au niveau de la cellule unitaire avec l'ensemble continu de variables cinématiques, qui sont représentatives d'un continuum de Cosserat à l'échelle macroscopique. Les modules effectifs classiques et de Cosserat sont à leur tour des expressions à forme fermée des paramètres microstructuraux et mécaniques du réseau pour le cas spécifique des réseaux en nid d'abeille. La méthode de continualisation proposée s'avère précise et efficace en termes de calcul par rapport aux schémas d'homogénéisation continue et aux simulations par éléments finis entièrement résolus. Un résultat clé des analyses effectuées est la quantification des effets de bord dans la réponse des structures en treillis, en s'appuyant sur la formulation de surface de la condition de macrohomogénéité de Hill étendue. La relation entre le moment de flexion et la courbure implique un terme classique et un moment de flexion micropolaire, dont l'importance diminue asymptotiquement jusqu'à une valeur nulle en augmentant le nombre de cellules unitaires dans la hauteur de la macrostructure.

Discussion de la méthode de continualisation et des effets de taille

En résumé, les grandes lignes de la méthode d'homogénéisation discrète et les principaux résultats obtenus sont les suivants :

- La mécanique des poutres développée basée sur la méthode de continualisation vers les milieux de Cosserat s'avère beaucoup plus efficace que les schémas d'homogénéisation continus en raison

du nombre fini de degrés de liberté de la formulation inhérente. La méthode proposée combine la continualisation de la modélisation discrète du réseau avec la description cinématique et statique continue du milieu de Cosserat posé effectif, en s'appuyant sur l'équivalence d'énergie de Hill étendue entre les échelles micro et macro (annexe M). L'homogénéisation discrète présente l'avantage principal, par rapport aux schémas d'homogénéisation continue, de permettre une expression sous forme fermée des modules classique et de Cosserat en fonction des paramètres géométriques et mécaniques de la cellule unitaire. L'expression sous forme fermée des modules de Cosserat a été exploitée pour fournir une analyse de sensibilité des paramètres micro géométriques sur ces modules et les longueurs de flexion internes.

- Nous fournissons une preuve constructive de la condition de macrohomogénéité de Hill pour le continuum effectif de Cosserat, en soulignant les variables statiques continues conjuguées aux variables cinématiques introduites. De plus, les tenseurs de contraintes macroscopiques ont été formulés comme des intégrales de surface sur la frontière de la cellule unitaire.
- Les modules effectifs obtenus par la méthode de continualisation ont été prédits avec une bonne précision, comme le révèle la comparaison avec les calculs EF entièrement résolus mettant en œuvre des CLP sur la cellule unitaire en nid d'abeille pour calculer les propriétés classiques et de Cosserat. Des charges cinématiques polynomiales d'ordre supérieur sont appliquées sur les limites de la cellule unitaire pour capturer les propriétés de Cosserat.
- Les analyses de sensibilité fournies montrent que les effets de Cosserat se sont avérés significatifs au niveau de la cellule unitaire sur toute la gamme des paramètres considérés, suite au fait que le réseau hexagonal est dominé par la flexion. La longueur de flexion interne calculée peut atteindre 8 fois la taille de la cellule unitaire. Ces effets de Cosserat expliquent la réponse prononcée à la flexion de la cellule unitaire hexagonale, qui se reflète dans la cinématique améliorée du continuum effectif (la microrotation apparaît comme une DDL supplémentaire) et l'existence d'une rigidité de flexion contrôlée par la longueur interne (de flexion).
- Des effets de bord apparaissent lorsque l'on change la taille de la fenêtre d'analyse incluant un nombre variable de cellules unitaires, de sorte que l'on montre que les modules de Cosserat effectifs dépendent de la longueur totale des coupes de cellules unitaires traversées par la frontière externe de la fenêtre d'analyse, normalisée par le périmètre de la cellule unitaire. Ce résultat découle de la condition de macrohomogénéité de Hill formulée dans l'annexe M.
- L'importance des effets micropolaires a été analysée à l'échelle supérieure d'une macro-poutre en flexion pure, révélant l'importance des effets de bord micropolaires, en s'appuyant sur la formulation surfacique de la condition de macrohomogénéité de Hill étendue prouvée en annexe M. La relation entre le moment de flexion et la courbure implique un terme classique et un moment de flexion micropolaire (contrôlé par un module micropolaire et certains paramètres géométriques). L'importance de ce dernier diminue asymptotiquement jusqu'à une valeur nulle en augmentant le nombre de cellules unitaires dans le macrodomaine. Le paramètre géométrique déterminant essentiel

pour quantifier les effets Cosserat à l'échelle macroscopique est le nombre de cellules unitaires dans la hauteur du macroréseau.

- Les effets de bord proviennent de la troncature des bords de la cellule unitaire (ces bords coupés sans contrainte ne contribuent pas à la réponse mécanique globale) traversant la frontière externe du domaine. Les effets de bord sont incorporés dans notre formulation en introduisant une hauteur effective représentant la quantité réelle de matériau de treillis dans le macro-domaine, de sorte que le module de flexion de la macro-poutre sera réduit. La rigidité supplémentaire d'ordre supérieur est nécessaire pour capturer de manière adéquate la réponse en flexion de la poutre macro, qui est toujours positive. En revanche, certains auteurs [136, 139] introduisent des effets d'adoucissement associés à une rigidité d'ordre supérieur négative pour tenir compte des effets de bord (une rigidité d'ordre supérieur négative corrige la contribution de Cauchy à la réponse globale de la poutre). Notre analyse montre que cette affirmation est incorrecte en raison de l'absence de prise en compte de la hauteur effective appropriée de la macrostructure architecturée considérée.
- Les résultats expérimentaux des essais de flexion [133] montrent une augmentation significative de la rigidité en flexion lorsque l'épaisseur de la poutre est réduite, l'écart par rapport à la solution de flexion conventionnelle apparaissant en dessous d'une épaisseur de 80 mm. Cet effet est attribué, selon [133], à l'importance décisive des effets de gradient de déformation pour les dimensions de poutre sélectionnées. Ces derniers auteurs invoquent une longueur interne microscopique, mais ils ne considèrent pas l'impact de la topologie du réseau et le nombre de cellules unitaires dans le domaine macro-poutre.

Le contexte théorique qui sous-tend l'homogénéisation asymptotique quasi-périodique dans le cadre de l'élasticité anisotrope linéarisée a pour objet les développements de la troisième partie. Différentes méthodologies pour évaluer les tenseurs des propriétés quasi-périodiques effectives sont développées dans le chapitre 6. En particulier, une classe de stratégies d'homogénéisation repose sur une mise en correspondance du problème de la cellule unitaire périodique avec le problème de la cellule unitaire quasi-périodique, où la fluctuation de la déformation microstructurale dans la cellule unitaire est prise en compte en résolvant un problème de localisation au niveau de la cellule unitaire, avant d'évaluer le tenseur des modules effectifs quasi-périodiques. Dans les deux stratégies, la condition de macrohomogénéité de Hill quasi-périodique étendue joue un rôle prépondérant. Les questions de compatibilité cinématique et de fluidité de la transformation de conception sont abordées, soulignant le rôle prépondérant des transformations conformes pour concevoir des matériaux architecturés compatibles quasi-périodiques. Les propriétés générales satisfaites par les cartes conformes sont prouvées dans le chapitre 7.

Une formulation de surface des tenseurs de contrainte et de déformation mésoscopiques apparaissant dans la construction de la condition de macrohomogénéité de Hill est employée pour calculer la réponse moyenne du macrodomaine. On obtient l'expression suivante de l'énergie moyenne d'une cellule unitaire sur le domaine quasi-périodique à condition que le changement de volume de la transformation puisse

être considéré comme presque uniforme au niveau d'une cellule unitaire :

$$\langle w_\mu \rangle_Y := \frac{1}{2\,|Y|}\int_Y \sigma : (\mathbf{u}\otimes\nabla_y)dV = \frac{1}{2\,|Y|}\sum_{i=1,2}\left(\left[\!\left[\mathbf{u}\right]\!\right]^{\,i}\otimes\mathbf{N}^i\right) : \frac{1}{|Y|}\sum_{j=1,2}\left(\int_{\partial Y}(\sigma\cdot\mathbf{n})\,ds\otimes\mathbf{Y}^j\right)$$

$$= \langle grad_y\mathbf{u}\rangle_Y : \langle\sigma\rangle_Y$$

Dans ces conditions et en supposant une variation régulière du déterminant de la carte tangente (qui peut donc être approximée par sa partie macroscopique), les énergies moyennes de la cellule unitaire dans les domaines périodiques et quasi-périodique sont liées par la relation suivante :

$$\left\langle \sigma : \omega\otimes^S\nabla_y\right\rangle_Y = J^{-1}\left(\tilde{Y}\right)\left\langle\tilde{\sigma} : \tilde{\omega}\otimes^S\nabla_{\tilde{y}}\right\rangle_{\tilde{Y}}$$

Rappelons que la condition de macrohomogénéité de Hill dans le domaine périodique s'écrit :

$$\left\langle\tilde{\sigma} : \tilde{\omega}\otimes^S\nabla_{\tilde{y}}\right\rangle_{\tilde{Y}} = \langle\tilde{\sigma}\rangle_{\tilde{Y}} : \langle grad_{\tilde{y}}\tilde{\omega}\rangle_{\tilde{Y}}$$

L'extensité de l'énergie par rapport au domaine entraîne que l'énergie macroscopique évaluée sur le domaine macro (quasi périodique) est la somme de toutes les énergies quasi périodiques des cellules unitaires. De plus, le travail des contraintes internes peut être ramené au domaine périodique où il a une expression similaire, en supposant dans un premier temps que le déterminant de la mise en correspondance peut être considéré comme homogène sur chaque cellule unitaire individuelle (ses variations se produisant à l'échelle macroscopique) :

$$\sum_{k=1}^{N_{UC}}\left\langle\boldsymbol{\sigma}^\eta : \boldsymbol{\omega}\otimes^S\nabla_y\right\rangle_{Y_k} = \sum_{k=1}^{N_{UC}}\left\{\frac{1}{\left|\tilde{Y}\right|}\sum_{i=1,2}\left(\left[\!\left[\tilde{\boldsymbol{u}}\right]\!\right]^{\,i}\otimes\tilde{\boldsymbol{N}}^i\right) : \frac{1}{\left|\tilde{Y}\right|}\sum_{j=1,2}\left(\int_{\partial Y_k}(\tilde{\boldsymbol{\sigma}}^\eta\cdot\tilde{\boldsymbol{n}})\,ds\otimes\tilde{\boldsymbol{Y}}^j\right)\right\} = \tilde{\boldsymbol{E}}_{\partial\tilde{D}} : \tilde{\boldsymbol{\Sigma}}_{\partial\tilde{D}},$$

$$\tilde{\boldsymbol{\Sigma}}_{\partial D} := \frac{1}{\left|\tilde{Y}\right|}\sum_{k=1}^{N_{UC}}\sum_{j=1,2}\left(\int_{\partial Y_k}(\tilde{\boldsymbol{\sigma}}^\eta\cdot\tilde{\boldsymbol{n}})\,ds\otimes\tilde{\boldsymbol{Y}}^j\right),\ \tilde{\boldsymbol{E}}_{\partial D} := \frac{1}{\left|\tilde{Y}\right|}\sum_{k=1}^{N_{UC}}\left(\left[\!\left[\tilde{\boldsymbol{u}}\right]\!\right]^{\,i}\otimes\tilde{\boldsymbol{N}}^i\right)(\partial\tilde{D})$$

Comme les cellules unitaires partagent des bords communs avec des normales unitaires opposées, toutes les contributions des cellules unitaires internes s'annulent dans la sommation précédente sur le nombre N_{UC} de cellules unitaires périodiques (Fig. reffig:8.4, vue de gauche), laissant la seule contribution de la frontière externe, exprimée dans le dernier terme. Il devient donc possible, à l'ordre principal, d'évaluer le *propriétés macroscopiques apparentes* dans le domaine périodique à partir de la seule connaissance des quantités cinématiques et statiques de surface (tractions appliquées et déplacement induit, ou inversement contrôle cinématique appliqué et traction induite) sur la frontière externe du domaine parent (périodique) (Fig. R.4). Notez que seuls les modules apparents de masse et de cisaillement peuvent être calculés à partir des macrochamps de surface puisque seule la projection normale des champs de contrainte et de déformation peut être contrôlée sur la frontière du macrodomaine.

L'identification inverse des modules unitaires peut être effectuée sur la base de mesures ou de tests virtuels (numériques) des propriétés apparentes de ces domaines cartographiés. À cette fin, un ensemble de charges cinématiques ou statiques bien choisies peut être appliqué sur la limite du domaine cartographié de manière conforme pour identifier les coefficients du tenseur des modules apparents $\tilde{\boldsymbol{C}}^{App}$, satisfaisant la relation suivante écrite à l'ordre principal du paramètre à petite échelle :

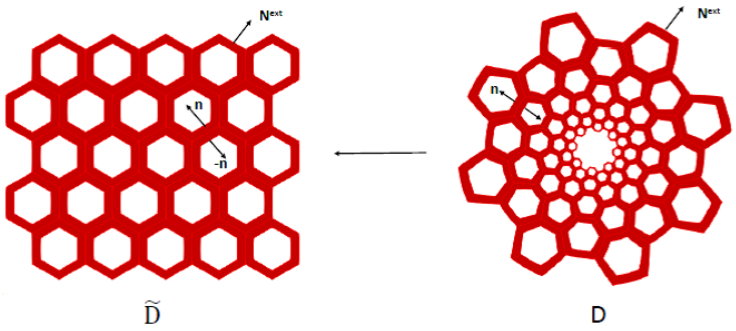

Figure R.4 Evaluation of the macroscopic and mesoscopic (unit cell based) mechanical properties based on a mapping to a periodic parent domain. The macroscopic moduli express as surface integrals over the external domain boundary due to vanishing internal surface contributions.

$$\tilde{\boldsymbol{\Sigma}}_{\partial D} = \tilde{\boldsymbol{C}}^{App} : \tilde{\boldsymbol{E}}_{\partial D}$$

Une relation similaire existe pour le domaine quasi-périodique, bien qu'il n'y ait pas de relation entre les propriétés basées sur les cellules unitaires et les propriétés macroscopiques apparentes :

$$\boldsymbol{\Sigma}_{\partial D} = \boldsymbol{C}^{App} : \boldsymbol{E}_{\partial D}$$

avec $\tilde{\boldsymbol{C}}^{App}$ le tenseur des modules apparents quasi-périodiques. Les modules apparents de masse et de cisaillement sont particulièrement importants dans les transformations conformes de domaines rectangulaires en disques circulaires avec une microstructure quasi-périodique.

Perspectives de la thèse

De nombreuses perspectives de cette thèse peuvent être envisagées, à partir des développements théoriques et numériques réalisés, aussi nous contentons-nous ici d'exposer brièvement les plus importantes à nos yeux. La sélection du continuum généralisé le plus approprié pour une classe donnée de matériaux architecturés reste une question importante à traiter dans les développements futurs. Bien que l'idée d'accorder des propriétés d'ingénierie efficaces par une modification de la topologie des matériaux architecturés soit très pertinente, il est nécessaire d'aller au-delà de l'heuristique et d'élaborer un raisonnement pour trouver des architectures donnant lieu à l'émergence de comportements enrichis ; les méthodes d'optimisation de la topologie peuvent fournir une telle stratégie systématique. Les méthodes d'optimisation topologique peuvent fournir une telle stratégie systématique. L'exploration de la réponse possible aux grandes déformations des matériaux à réseau souple dans le cadre des continuums généralisés est une deuxième perspective principale de cette thèse. Troisièmement, bien que nous nous soyons limités dans ce travail aux aspects mécaniques purs, les comportements couplés multiphysiques sont une direction de recherche prometteuse à explorer pour atteindre une pleine exploitation des promesses scientifiques et technologiques des matériaux architecturés et des métamatériaux.

Enfin, nous souhaitons mentionner des développements scientifiques potentiels intéressants et les applications des méthodes d'homogénéisation proposées au domaine de la biomécanique osseuse, malgré la complexité supplémentaire de la prise en compte de l'évolution de la microstructure lorsque le remodelage a lieu.

References

[1] Julia R. Greer and Vikram S. Deshpande. Three-dimensional architected materials and structures: Design, fabrication, and mechanical behavior. 44(10):750–757, 2019. Publisher: Cambridge University Press.

[2] M. Benedetti, A. du Plessis, R. O. Ritchie, M. Dallago, S. M. J. Razavi, and F. Berto. Architected cellular materials: A review on their mechanical properties towards fatigue-tolerant design and fabrication. 144:100606, 2021.

[3] N. Karathanasopoulos, F. Dos Reis, H. Reda, and J. F. Ganghoffer. Computing the effective bulk and normal to shear properties of common two-dimensional architectured materials. 154:284–294, 2018.

[4] Behrooz Hassani and Ernest Hinton. *Homogenization and Structural Topology Optimization*. Springer London, 1999.

[5] S Forest. Mechanics of generalized continua: construction by homogenization. 8:39–48, 1998.

[6] Armelle Anthoine. Second-order homogenisation of functionally graded materials. 47(11):1477–1489, 2010. Publisher: Elsevier.

[7] William D Callister Jr and David G Rethwisch. *Fundamentals of materials science and engineering: an integrated approach*. John Wiley & Sons, 2020.

[8] Mike F Ashby and Yves JM Bréchet. Designing hybrid materials. *Acta materialia*, 51(19):5801–5821, 2003.

[9] H Loyrette and Gustave Eiffel. Rizolli, 1985.

[10] Joseph Harriss. *The tallest tower*. Unlimited Publishing LLC, 2004.

[11] Benoit B Mandelbrot. The fractal geometry of nature wh freeman and company. *New York*, page 468, 1983.

[12] Enrique Sánchez-Palencia. Non-homogeneous media and vibration theory. 127, 1980. Publisher: Springer-Verlag.

[13] A Bensoussan, J Lions, and G Papanicolau. Homogenization: Averaging processes in periodic media. 1978. Publisher: Amsterdam: North Holland.

[14] Vladimir A Marchenko and Evgueni Ya Khruslov. *Homogenization of partial differential equations*, volume 46. Springer Science & Business Media, 2008.

[15] Grigorii Petrovich Panasenko. *Multi-scale modelling for structures and composites*, volume 615. Springer, 2005.

[16] SM Kozlov. Averaging differential operators with almost periodic, rapidly oscillating coefficients. 35(4):481, 1979. Publisher: IOP Publishing.

[17] Vasilii Vasil'evich Zhikov, Sergei M Kozlov, Olga Arsen'evna Oleinik, and Kha T'en Ngoan. Averaging and g-convergence of differential operators. *Russian Mathematical Surveys*, 34(5):69, 1979.

[18] BE Pobedrya. Principles of computational mechanics of composites. *Mechanics of composite materials*, 32(6):504–515, 1996.

[19] GW Milton. The theory of composites (cambridge monographs on applied and computational mathematics) cambridge university press. 2002.

[20] Nikolaĭ Bogoliubov. *Asymptotic methods in the theory of non-linear oscillations*.

[21] Edward W Larsen and Joseph B Keller. Asymptotic solution of neutron transport problems for small mean free paths. *Journal of Mathematical Physics*, 15(1):75–81, 1974.

[22] Edward W Larsen. Neutron transport and diffusion in inhomogeneous media. i. *Journal of Mathematical Physics*, 16(7):1421–1427, 1975.

[23] Edward W Larsen. Neutron transport and diffusion in inhomogeneous media. ii. *Nuclear science and engineering*, 60(4):357–368, 1976.

[24] Sergio Spagnolo. Sul limite delle soluzioni di problemi di cauchy relativi all'equazione del calore. 21(4):657–699, 1967.

[25] Luc Tartar. Cours peccot au collège de france. 1977.

[26] L Tartar. Cours peccot, collège de france,(1977), partially written in: F. 1978.

[27] François Murat and Luc Tartar. H-convergence. In Andrej V. Cherkaev and Robert Kohn, editors, *Topics in the Mathematical Modelling of Composite Materials*, Modern Birkhäuser Classics, pages 21–43. Springer International Publishing, 2018.

[28] Ennio De Giorgi. G-operators and γ-convergence. volume 1, pages 1175–1191, 1984. Issue: 2.

[29] Gabriel Nguetseng. A general convergence result for a functional related to the theory of homogenization. 20(3):608–623, 1989. Publisher: SIAM.

[30] Grégoire Allaire. Homogenization and two-scale convergence. 23(6):1482–1518, 1992. Publisher: SIAM.

[31] Maria Neuss-Radu. Some extensions of two-scale convergence. 322(9):899–904, 1996.

[32] Gabriel Nguetseng. Asymptotic analysis for a stiff variational problem arising in mechanics. 21(6):1394–1414, 1990. Publisher: SIAM.

[33] Dag Lukkassen, Gabriel Nguetseng, and Peter Wall. Two-scale convergence. 2(1):35–86, 2002.

[34] Martin Heida. An extension of the stochastic two-scale convergence method and application. 72(1):1–30, 2011. Publisher: IOS Press.

[35] Doina Cioranescu, Alain Damlamian, and Georges Griso. Periodic unfolding and homogenization.

335(1):99–104, 2002. Publisher: Elsevier.

[36] Doina Cioranescu, Alain Damlamian, and Georges Griso. The periodic unfolding method in homogenization. 40(4):1585–1620, 2008. Publisher: SIAM.

[37] Jean-François Ganghoffer, Gérard Maurice, and Yosra Rahali. Determination of closed form expressions of the second-gradient elastic moduli of multi-layer composites using the periodic unfolding method. 24(5):1475–1502, 2019. Publisher: SAGE Publications Sage UK: London, England.

[38] Gérard Maurice, Jean-François Ganghoffer, and Yosra Rahali. Second gradient homogenization of multilayered composites based on the method of oscillating functions. 24(7):2197–2230, 2019. Publisher: SAGE Publications Sage UK: London, England.

[39] Aleksandr Andreevich Pankov. *G-convergence and homogenization of nonlinear partial differential operators*, volume 422. Springer Science & Business Media, 1997.

[40] Andrea Braides and Anneliese Defranceschi. *Homogenization of multiple integrals*. Oxford University Press, 1998. Issue: 12.

[41] Grégoire Allaire and François Murat. Homogenization of the neumann problem with nonisolated holes. 7(2):81–95, 1993. Publisher: IOS Press.

[42] Grégoire Allaire. A brief introduction to homogenization and miscellaneous applications. volume 37, pages 1–49. EDP Sciences, 2012.

[43] Yunguang Lu. *Hyperbolic conservation laws and the compensated compactness method*. CRC Press.

[44] François Murat. Compacité par compensation. 1:125–127, 1979.

[45] Gianni Dal Maso. *An introduction to Γ-convergence*, volume 8. Springer Science & Business Media, 2012.

[46] U Hornung. Homogenization and porous media, interdiscipl. *Appl. Math*, 6.

[47] Luc Tartar. H-measures, a new approach for studying homogenisation, oscillations and concentration effects in partial differential equations. *Proceedings of the Royal Society of Edinburgh Section A: Mathematics*, 115(3-4):193–230, 1990.

[48] Doina Cioranescu and Patrizia Donato. *An introduction to homogenization*, volume 17. Oxford University Press Oxford, 1999.

[49] George Papanicolau, Alain Bensoussan, and J-L Lions. *Asymptotic analysis for periodic structures*. Elsevier, 1978.

[50] B Gambin and E Kröner. Higher-order terms in the homogenized stress-strain relation of periodic elastic media. *physica status solidi (b)*, 151(2):513–519, 1989.

[51] C Boutin. Microstructural effects in elastic composites. 33(7):1023–1051, 1996.

[52] Nicolas Triantafyllidis and S Bardenhagen. On higher order gradient continuum theories in 1-d nonlinear elasticity. derivation from and comparison to the corresponding discrete models. 33(3):259–293, 1993.

[53] VP Smyshlyaev and KD Cherednichenko. On rigorous derivation of strain gradient effects in the

overall behaviour of periodic heterogeneous media. 48(6):1325–1357, 2000.

[54] Matthew Mosby and Karel Matouš. Computational homogenization at extreme scales. Complete(6):68–74, 2016.

[55] S. J. Hollister and N. Kikuchi. A comparison of homogenization and standard mechanics analyses for periodic porous composites. 10(2):73–95, 1992.

[56] L Kaczmarczyk, CJ Pearce, and N Bicanic. Studies of microstructural size effect and higher-order deformation in second-order computational homogenization. 88(23):1383–1390, 2010.

[57] F Dos Reis and JF Ganghoffer. Construction of micropolar continua from the asymptotic homogenization of beam lattices. 112:354–363, 2012.

[58] F. Dos Reis and J. F. Ganghoffer. Equivalent mechanical properties of auxetic lattices from discrete homogenization. 1(51):314–321, 2012.

[59] R.G. Hutchinson and Norman Fleck. The structural performance of the periodic truss. 54:756–782, 2006.

[60] I. A. Kunin. *Elastic Media with Microstructure I: One-Dimensional Models*. Springer Science & Business Media, 2012.

[61] Z. P. Bažant and M. Christensen. Analogy between micropolar continuum and grid frameworks under initial stress. 8(3):327–346, 1972.

[62] Andrea Bacigalupo and Luigi Gambarotta. Identification of non-local continua for lattice-like materials. 159:103430, 2021.

[63] A. S. J. Suiker, R. de Borst, and C. S. Chang. Micro-mechanical modelling of granular material. part 1: Derivation of a second-gradient micro-polar constitutive theory. 149(1):161–180, 2001.

[64] Harm Askes and Andrei V. Metrikine. Higher-order continua derived from discrete media: continualisation aspects and boundary conditions. 42(1):187–202, 2005.

[65] Rajesh S. Kumar and David L. McDowell. Generalized continuum modeling of 2-d periodic cellular solids. 41(26):7399–7422, 2004.

[66] Andrei V. Metrikine and Harm Askes. One-dimensional dynamically consistent gradient elasticity models derived from a discrete microstructure: Part 1: Generic formulation. 21(4):555–572, 2002.

[67] Walter Noll and Clifford Ambrose Truesdell. *The non-linear field theories of mechanics*. Springer-Verlag Berlin, 1992.

[68] Clifford Truesdell and Richard Toupin. The classical field theories. In *Principles of classical mechanics and field theory/Prinzipien der Klassischen Mechanik und Feldtheorie*, pages 226–858. Springer, 1960.

[69] Rodney Hill. Generalized constitutive relations for incremental deformation of metal crystals by multislip. *Journal of the Mechanics and Physics of Solids*, 14(2):95–102, 1966.

[70] Rodney Hill. The essential structure of constitutive laws for metal composites and polycrystals. *Journal of the Mechanics and Physics of Solids*, 15(2):79–95, 1967.

[71] Jean Mandel. Contribution théorique à l'étude de l'écrouissage et des lois de l'écoulement plastique.

In *Applied Mechanics*, pages 502–509. Springer, 1966.

[72] Raymond David Mindlin. Microstructure in linear elasticity. Technical report, Columbia Univ New York Dept of Civil Engineering and Engineering Mechanics, 1963.

[73] A Cemal Eringen and ES169423 Suhubi. Nonlinear theory of simple micro-elastic solids—i. 2(2):189–203, 1964. Publisher: Elsevier.

[74] Eugene Cosserat and François Cosserat. *Theorie des corps dédormables*. A. Hermann et fils, 1909.

[75] Paul Germain. La méthode des puissances virtuelles en mécanique des milieux continus, premiere partie: théorie du second gradient. 12(2):235–274, 1973.

[76] WT Koiter. Couple-stresses in the theory of elasticity, i and ii, prec. *Roy. Netherlands Acad. Sci. B*, 67:0964, 1964.

[77] I Goda, M Assidi, and JF Ganghoffer. A 3d elastic micropolar model of vertebral trabecular bone from lattice homogenization of the bone microstructure. 13(1):53–83, 2014.

[78] I Goda, M Assidi, S Belouettar, and JF Ganghoffer. A micropolar anisotropic constitutive model of cancellous bone from discrete homogenization. 16:87–108, 2012.

[79] PH af Segerstad, S Toll, and R Larsson. A micropolar theory for the finite elasticity of open-cell cellular solids. 465(2103):843–865, 2009.

[80] Martin Ostoja-Starzewski and Iwona Jasiuk. Stress invariance in planar cosserat elasticity. *Proceedings of the Royal Society of London. Series A: Mathematical and Physical Sciences*, 451(1942):453–470, 1995.

[81] S Barboura and J Li. Establishment of strain gradient constitutive relations by using asymptotic analysis and the finite element method for complex periodic microstructures. 136:60–76, 2018.

[82] V Monchiet, N Auffray, and J Yvonnet. Strain-gradient homogenization: A bridge between the asymptotic expansion and quadratic boundary condition methods. 143, 2020.

[83] RHJ Peerlings and NA Fleck. Computational evaluation of strain gradient elasticity constants. 2(4), 2004. Publisher: Begel House Inc.

[84] Duy Khanh Trinh, Ralf Janicke, Nicolas Auffray, Stefan Diebels, and Samuel Forest. Evaluation of generalized continuum substitution models for heterogeneous materials. *International Journal for Multiscale Computational Engineering*, 10(6), 2012.

[85] R. D. Mindlin and N. N. Eshel. On first strain-gradient theories in linear elasticity. 4(1):109–124, 1968.

[86] J Yvonnet, Nicolas Auffray, and V Monchiet. Computational second-order homogenization of materials with effective anisotropic strain-gradient behavior. *International Journal of Solids and Structures*, 191:434–448, 2020.

[87] N Auffray, F dell'Isola, VA Eremeyev, A Madeo, and G Rosi. Analytical continuum mechanics a la hamilton-piola least action principle for second gradient continua and capillary fluids. 20(4):375–417, 2015.

[88] A. Bacigalupo and L. Gambarotta. Second-order computational homogenization of

heterogeneous materials with periodic microstructure. 90(10):796–811, 2010. _eprint: https://onlinelibrary.wiley.com/doi/pdf/10.1002/zamm.201000031.

[89] Andrea Bacigalupo. Second-order homogenization of periodic materials based on asymptotic approximation of the strain energy: formulation and validity limits. 49(6):1407–1425, 2014.

[90] Thu-Huong Tran, Vincent Monchiet, and Guy Bonnet. A micromechanics-based approach for the derivation of constitutive elastic coefficients of strain-gradient media. *International Journal of Solids and Structures*, 49(5):783–792, 2012.

[91] M Ben-Amoz. A dynamic theory for composite materials. 27(1):83–99, 1976. Publisher: Springer.

[92] Samuel Forest. Mechanics of generalized continua: construction by homogenizaton. 8:Pr4–39, 1998. Publisher: EDP sciences.

[93] S Forest and K Sab. Cosserat overall modeling of heterogeneous materials. 25(4):449–454, 1998.

[94] S Forest, F Pradel, and K Sab. Asymptotic analysis of heterogeneous cosserat media. 38(26):4585–4608, 2001.

[95] Y Rahali, I Giorgio, JF Ganghoffer, and Francesco dell'Isola. Homogenization à la piola produces second gradient continuum models for linear pantographic lattices. 97:148–172, 2015. Publisher: Elsevier.

[96] M Ayad, N Karathanasopoulos, JF Ganghoffer, and H Lakiss. Higher-gradient and micro-inertia contributions on the mechanical response of composite beam structures. 154, 2020-09.

[97] M Ayad, N Karathanasopoulos, H Reda, JF Ganghoffer, and H Lakiss. On the role of second gradient constitutive parameters in the static and dynamic analysis of heterogeneous media with micro-inertia effects. 190:58–75, 2020.

[98] Mohammad Ayad. Homogenization-based, higher-gradient dynamical response of micro-structured media, 2020.

[99] Ibrahim Goda and Jean-François Ganghoffer. Construction of first and second order grade anisotropic continuum media for 3d porous and textile composite structures. 141:292–327, 2016. Publisher: Elsevier.

[100] Andrea Bacigalupo and Luigi Gambarotta. Homogenization of periodic hexa- and tetrachiral cellular solids. 116:461–476, 2014.

[101] K Berkache, S Deogekar, I Goda, RC Picu, and J-F Ganghoffer. Construction of second gradient continuum models for random fibrous networks and analysis of size effects. 181:347–357, 2017. Publisher: Elsevier.

[102] A Cemal Eringen. Theory of micropolar fluids. *Journal of Mathematics and Mechanics*, pages 1–18, 1966.

[103] CB Kafadar and A Cemal Eringen. Micropolar media—i the classical theory. *International Journal of Engineering Science*, 9(3):271–305, 1971.

[104] S Forest and R Sievert. Elastoviscoplastic constitutive frameworks for generalized continua. 160(1):71–111, 2003.

[105] Samuel Forest and Duy Khanh Trinh. Generalized continua and non-homogeneous boundary conditions in homogenisation methods. 91(2):90–109, 2011. Publisher: Wiley Online Library.

[106] S Forest. Micromorphic approach for gradient elasticity, viscoplasticity, and damage. 135(3):117–131, 2009.

[107] S Forest and R Sievert. Nonlinear microstrain theories. 43(24):7224–7245, 2006.

[108] GA Maugin. Generalized continuum mechanics: What do we mean by that? volume 21, pages 3–13, 2010.

[109] R Biswas and LH Poh. A micromorphic computational homogenization framework for heterogeneous materials. 102:187–208, 2017.

[110] R Biswas, AS Shedbale, and LH Poh. Nonlinear analyses with a micromorphic computational homogenization framework for composite materials. 350:362–395, 2019.

[111] R Biswas, LH Poh, and AS Shedbale. A micromorphic computational homogenization framework for auxetic tetra-chiral structures. 135, 2020.

[112] O Rokos, MM Ameen, RHJ Peerlings, and MGD Geers. Extended micromorphic computational homogenization for mechanical metamaterials exhibiting multiple geometric pattern transformations. 37, 2020-05.

[113] G Hutter, U Muhlich, and M Kuna. Micromorphic homogenization of a porous medium: elastic behavior and quasi-brittle damage. 27(6):1059–1072, 2015.

[114] M Javadi, M Epstein, and M Asghari. Thermomechanics of material growth and remodeling in uniform bodies based on the micromorphic theory. 138, 2020.

[115] K Langenfeld and J Mosler. A micromorphic approach for gradient-enhanced anisotropic ductile damage. 360, 2020.

[116] XZ Ju and R Mahnken. Goal-oriented h-type adaptive finite elements for micromorphic elastoplasticity. 351:297–329, 2019.

[117] M Rys, S Forest, and H Petryk. A micromorphic crystal plasticity model with the gradient-enhanced incremental hardening law. 128, 2020.

[118] M von Hoegen, S Skatulla, and J Schroder. A generalized micromorphic approach accounting for variation and dispersion of preferred material directions. 232, 2020.

[119] G Barbagallo, D Tallarico, MV D'Agostino, A Aivaliotis, P Neff, and A Madeo. Relaxed micromorphic model of transient wave propagation in anisotropic band-gap metastructures. 162:148–163, 2019.

[120] A Misra and N Nejadsadeghi. Longitudinal and transverse elastic waves in 1d granular materials modeled as micromorphic continua. 90:175–195, 2019.

[121] Ondřej Rokoš, Maqsood M Ameen, Ron HJ Peerlings, and Mark GD Geers. Micromorphic computational homogenization for mechanical metamaterials with patterning fluctuation fields. *Journal of the Mechanics and Physics of Solids*, 123:119–137, 2019.

[122] Ondřej Rokoš, Jan Zeman, Martin Doškář, and Petr Krysl. Reduced integration schemes in

micromorphic computational homogenization of elastomeric mechanical metamaterials. *Advanced Modeling and Simulation in Engineering Sciences*, 7(1):1–17, 2020.

[123] Jia Li and Xiao-Bing Zhang. A numerical approach for the establishment of strain gradient constitutive relations in periodic heterogeneous materials. 41:70–85, 2013.

[124] Marc GD Geers, Varvara Kouznetsova, and WAM Brekelmans. Gradient-enhanced computational homogenization for the micro-macro scale transition. 11:Pr5–145, 2001. Publisher: EDP sciences.

[125] V. G. Kouznetsova, M. G. D. Geers, and W. A. M. Brekelmans. Multi-scale second-order computational homogenization of multi-phase materials: a nested finite element solution strategy. 193(48):5525–5550, 2004.

[126] Mihai Gologanu, J-B Leblond, Gilles Perrin, and J Devaux. Recent extensions of gurson's model for porous ductile metals. In *Continuum micromechanics*, pages 61–130. Springer, 1997.

[127] N. Auffray, R. Bouchet, and Y. Bréchet. Strain gradient elastic homogenization of bidimensional cellular media. 47(13):1698–1710, 2010.

[128] C. Huet. Application of variational concepts to size effects in elastic heterogeneous bodies. 38(6):813–841, 1990.

[129] T. Kanit, S. Forest, I. Galliet, V. Mounoury, and D. Jeulin. Determination of the size of the representative volume element for random composites: statistical and numerical approach. 40(13):3647–3679, 2003.

[130] XN Liu and GK Hu. Inclusion problem of microstretch continuum. 42(8):849–860, 2004.

[131] Fei Xun, Gengkai Hu, and Zhuping Huang. Effective in plane moduli of composites with a micropolar matrix and coated fibers. *International Journal of Solids and Structures*, 41(1):247–265, 2004.

[132] E. W Andrews, G Gioux, P Onck, and L. J Gibson. Size effects in ductile cellular solids. part II: experimental results. 43(3):701–713, 2001.

[133] David CC Lam, Fan Yang, ACM Chong, Jianxun Wang, and Pin Tong. Experiments and theory in strain gradient elasticity. 51(8):1477–1508, 2003.

[134] C. Tekoglu, Lorna J. Gibson, and Patrick Onck. Size-effects of metal foams. 2011.

[135] Harm Askes and Elias C. Aifantis. Gradient elasticity in statics and dynamics: An overview of formulations, length scale identification procedures, finite element implementations and new results. 48(13):1962–1990, 2011.

[136] Stefan Liebenstein and Michael Zaiser. Determining cosserat constants of 2d cellular solids from beam models. 2(1):2, 2018.

[137] Shutian Liu and Wenzheng Su. Effective couple-stress continuum model of cellular solids and size effects analysis. 46(14):2787–2799, 2009.

[138] P. R. Onck, E. W. Andrews, and L. J. Gibson. Size effects in ductile cellular solids. part i: modeling. 43(3):681–699, 2001.

[139] Hua Yang and Wolfgang H. Müller. Size effects of mechanical metamaterials: a computational

study based on a second-order asymptotic homogenization method. 91(3):1037–1053, 2021.

[140] C. Tekoglu, L. J. Gibson, T. Pardoen, and P. R. Onck. Size effects in foams: Experiments and modeling. 56(2):109–138, 2011.

[141] Khaled ElNady, Ibrahim Goda, and Jean-François Ganghoffer. Computation of the effective nonlinear mechanical response of lattice materials considering geometrical nonlinearities. 58(6):957–979, 2016.

[142] Hilal Reda, Yosra Rahali, Jean-François Ganghoffer, and Hassan Lakiss. Wave propagation in 3d viscoelastic auxetic and textile materials by homogenized continuum micropolar models. 141:328–345, 2016.

[143] Francesco Dell'Isola, Pierre Seppecher, Jean Jacques Alibert, Tomasz Lekszycki, Roman Grygoruk, Marek Pawlikowski, David Steigmann, Ivan Giorgio, Ugo Andreaus, and Emilio Turco. Pantographic metamaterials: an example of mathematically driven design and of its technological challenges. 31(4):851–884, 2019.

[144] Yosra Rahali, F Dos Reis, and Jean-François Ganghoffer. Multiscale homogenization schemes for the construction of second-order grade anisotropic continuum media of architectured materials. 15(1), 2017.

[145] Stefan Liebenstein, Stefan Sandfeld, and Michael Zaiser. Size and disorder effects in elasticity of cellular structures: From discrete models to continuum representations. 146:97–116, 2018.

[146] S Suresh. Graded materials for resistance to contact deformation and damage. *Science*, 292(5526):2447–2451, 2001.

[147] Thomas Reiter, George J Dvorak, and Viggo Tvergaard. Micromechanical models for graded composite materials. 45(8):1281–1302, 1997. Publisher: Elsevier.

[148] Kumar Vemaganti and Pushkaraj Deshmukh. An adaptive global–local approach to modeling functionally graded materials. *Computer methods in applied mechanics and engineering*, 195(33-36):4230–4243, 2006.

[149] Igor V Andrianov, Jan Awrejcewicz, and Alexander A Diskovsky. Homogenization of quasi-periodic structures. 128(4):532, 2006. Publisher: American Society of Mechanical Engineers.

[150] Laurent Guillot, Yann Capdeville, and Jean-Jacques Marigo. 2-d non-periodic homogenization of the elastic wave equation: SH case. 182(3):1438–1454, 2010. Publisher: Blackwell Publishing Ltd Oxford, UK.

[151] Yann Capdeville, Laurent Guillot, and Jean-Jacques Marigo. 2-d non-periodic homogenization to upscale elastic media for p–sv waves. *Geophysical Journal International*, 182(2):903–922, 2010.

[152] Duc Trung Le and Jean-Jacques Marigo. Second order homogenization of quasi-periodic structures. 40(4):325–348, 2018.

[153] Metamaterials: Theory, design, and applications, 2010. Pages: 367.

[154] YM Liu and X Zhang. Metamaterials: a new frontier of science and technology. 40(5):2494–2507, 2011.

[155] P Wang, F Casadei, SC Shan, JC Weaver, and K Bertoldi. Harnessing buckling to design tunable locally resonant acoustic metamaterials. 113(1), 2014.

[156] F Auricchio, A Bacigalupo, L Gambarotta, M Lepidi, S Morganti, and F Vadala. A novel layered topology of auxetic materials based on the tetrachiral honeycomb microstructure. 179, 2019.

[157] Jae-Hwang Lee, Jonathan P Singer, and Edwin L Thomas. Micro-/nanostructured mechanical metamaterials. *Advanced materials*, 24(36):4782–4810, 2012.

[158] DR Smith and JB Pendry. Homogenization of metamaterials by field averaging (invited paper). 23(3):391–403, 2006.

[159] YP Liu and H Hu. A review on auxetic structures and polymeric materials. 5(10):1052–1063, 2010.

[160] KE Evans and A Alderson. Auxetic materials: Functional materials and structures from lateral thinking! 12(9):617–+, 2000.

[161] JN Grima, L Mizzi, KM Azzopardi, and R Gatt. Auxetic perforated mechanical metamaterials with randomly oriented cuts. 28(2):385–389, 2016.

[162] Yunan Prawoto. Seeing auxetic materials from the mechanics point of view: a structural review on the negative poisson's ratio. *Computational Materials Science*, 58:140–153, 2012.

[163] Y Chen, XN Liu, and GK Hu. Micropolar modeling of planar orthotropic rectangular chiral lattices. 342(5):273–283, 2014.

[164] Alessandro Spadoni and M Ruzzene. Elasto-static micropolar behavior of a chiral auxetic lattice. *Journal of the Mechanics and Physics of Solids*, 60(1):156–171, 2012.

[165] A Bacigalupo and ML De Bellis. Auxetic anti-tetrachiral materials: Equivalent elastic properties and frequency band-gaps. 131:530–544, 2015.

[166] Roderic S. Lakes and Robert L. Benedict. Noncentrosymmetry in micropolar elasticity. 20(10):1161–1167, 1982.

[167] Baron Kelvin Thomson, Baron Kelvin, and William Thomson. *Baltimore lectures on molecular dynamics and the wave theory of light*. Cambridge University Press, 2010.

[168] A Alderson, KL Alderson, D Attard, KE Evans, R Gatt, JN Grima, W Miller, N Ravirala, CW Smith, and K Zied. Elastic constants of 3-, 4-and 6-connected chiral and anti-chiral honeycombs subject to uniaxial in-plane loading. 70(7):1042–1048, 2010.

[169] D Prall and RS Lakes. Properties of a chiral honeycomb with a poisson's ratio of -1. 39(3):305–&, 1997.

[170] D Avnir and D Huylebrouck. On left and right: Chirality in architecture. 15(1):171–182, 2013.

[171] JS Wang, G Wang, XQ Feng, T Kitamura, YL Kang, SW Yu, and QH Qin. Hierarchical chirality transfer in the growth of towel gourd tendrils. 3, 2013.

[172] WW Wu, LC Geng, YH Niu, DX Qi, XG Cui, and DN Fang. Compression twist deformation of novel tetrachiral architected cylindrical tube inspired by towel gourd tendrils. 20:104–111, 2018.

[173] WJ Zhang, R Neville, DY Zhang, F Scarpa, LF Wang, and R Lakes. The two-dimensional elasticity of a chiral hinge lattice metamaterial. 141:254–263, 2018.

[174] A Cemal Eringen. Theory of micropolar elasticity. In *Microcontinuum field theories*, pages 101–248. Springer, 1999.

[175] WW Wu, WX Hu, GA Qian, HT Liao, XY Xu, and F Berto. Mechanical design and multifunctional applications of chiral mechanical metamaterials: A review. 180, 2019.

[176] XN Liu, GL Huang, and GK Hu. Chiral effect in plane isotropic micropolar elasticity and its application to chiral lattices. 60(11):1907–1921, 2012.

[177] Frederick A Howes and Stephen Whitaker. The spatial averaging theorem revisited. *Chemical engineering science*, 40(8):1387–1392, 1985.

[178] B Wood. Technical note: Revisiting the geometric theorems for volume averaging and the meaning of disorder in porous media. 2013.

[179] Rodney Hill. On constitutive macro-variables for heterogeneous solids at finite strain. *Proceedings of the Royal Society of London. A. Mathematical and Physical Sciences*, 326(1565):131–147, 1972.

[180] R Hill. New derivation of some elastic extremum principles. *Progress in applied mechanics, The Prager anniversary volume*, pages 99–106, 1963.

[181] ZH Xia, YF Zhang, and F Ellyin. A unified periodical boundary conditions for representative volume elements of composites and applications. 40(8):1907–1921, 2003.

[182] A Cemal Eringen. Mechanics of micromorphic continua. In *Mechanics of generalized continua*, pages 18–35. Springer, 1968.

[183] R Janicke, S Diebels, HG Sehlhorst, and A Duster. Two-scale modelling of micromorphic continua. 21(4):297–315, 2009.

[184] R Janicke and H Steeb. Minimal loading conditions for higher-order numerical homogenisation schemes cauchy, second gradient and micromorphic substitute media. 82(8):1075–1088, 2012.

[185] Varvara Kouznetsova, Marc GD Geers, and WA Marcel Brekelmans. Multi-scale constitutive modelling of heterogeneous materials with a gradient-enhanced computational homogenization scheme. 54(8):1235–1260, 2002. Publisher: Wiley Online Library.

[186] G Hutter. On the micro-macro relation for the microdeformation in the homogenization towards micromorphic and micropolar continua. 127:62–79, 2019.

[187] G Hutter. An extended coleman-noll procedure for generalized continuum theories. 28(6):1935–1941, 2016.

[188] Samuel Forest. Homogenization methods and mechanics of generalized continua-part 2. *Theoretical and applied mechanics*, (28-29):113–144, 2002.

[189] Maria Laura De Bellis and Daniela Addessi. A cosserat based multi-scale model for masonry structures. *International Journal for Multiscale Computational Engineering*, 9(5), 2011.

[190] A Cemal Eringen. Non-local polar field theory. *Continuum physics*, 4:205–267, 1976.

[191] U Muhlich, L Zybell, and M Kuna. Estimation of material properties for linear elastic strain gradient effective media. 31(1):117–130, 2012.

[192] J Li. A micromechanics-based strain gradient damage model for fracture prediction of brittle

materials - part i: Homogenization methodology and constitutive relations. 48(24):3336–3345, 2011.

[193] Alain Bensoussan, Jacques-Louis Lions, and George Papanicolaou. *Asymptotic analysis for periodic structures*, volume 374. American Mathematical Soc., 2011.

[194] Valery P Smyshlyaev and Kirill D Cherednichenko. On rigorous derivation of strain gradient effects in the overall behaviour of periodic heterogeneous media. *Journal of the Mechanics and Physics of Solids*, 48(6-7):1325–1357, 2000.

[195] AC Pereira, FL Fertonani, GD Neto, LT Kubota, and H Yamanaka. Reagentless biosensor for isocitrate using one step modified pt-ir microelectrode. 53(4):801–806, 2001.

[196] TT Yu, HF Hu, JK Zhang, and TQ Bui. Isogeometric analysis of size-dependent effects for functionally graded microbeams by a non-classical quasi-3d theory. 138:1–14, 2019.

[197] RD Mindlin and HF144513 Tiersten. Effects of couple-stresses in linear elasticity. Technical report, Columbia Univ New York, 1962.

[198] ID Ghiba, P Neff, A Madeo, and I Munch. A variant of the linear isotropic indeterminate couple-stress model with symmetric local force-stress, symmetric nonlocal force-stress, symmetric couple-stresses and orthogonal boundary conditions. 22(6):1221–1266, 2017.

[199] JFC Yang and Roderic S Lakes. Experimental study of micropolar and couple stress elasticity in compact bone in bending. *Journal of biomechanics*, 15(2):91–98, 1982.

[200] M Asghari, MH Kahrobaiyan, M Rahaeifard, and MT Ahmadian. Investigation of the size effects in timoshenko beams based on the couple stress theory. 81(7):863–874, 2011.

[201] G Alotta, G Failla, and M Zingales. Finite element method for a nonlocal timoshenko beam model. 89:77–92, 2014.

[202] AM Dehrouyeh-Semnani and A Bahrami. On size-dependent timoshenko beam element based on modified couple stress theory. 107:134–148, 2016.

[203] SL Kong, SJ Zhou, ZF Nie, and K Wang. The size-dependent natural frequency of bernoulli-euler micro-beams. 46(5):427–437, 2008.

[204] F Yang, ACM Chong, DCC Lam, and P Tong. Couple stress based strain gradient theory for elasticity. 39(10):2731–2743, 2002.

[205] HM Ma, XL Gao, and JN Reddy. A microstructure-dependent timoshenko beam model based on a modified couple stress theory. 56(12):3379–3391, 2008.

[206] MH Kahrobaiyan, M Asghari, and MT Ahmadian. A timoshenko beam element based on the modified couple stress theory. 79:75–83, 2014.

[207] BR Goncalves, A Karttunen, J Romanoff, and JN Reddy. Buckling and free vibration of shear-flexible sandwich beams using a couple-stress-based finite element. 165:233–241, 2017.

[208] AT Karttunen, J Romanoff, and JN Reddy. Exact microstructure-dependent timoshenko beam element. 111:35–42, 2016.

[209] TT Yu, JK Zhang, HF Hu, and TQ Bui. A novel size-dependent quasi-3d isogeometric beam model

for two-directional FG microbeams analysis. 211:76–88, 2019.

[210] BR Goncalves, AT Karttunen, and J Romanoff. A nonlinear couple stress model for periodic sandwich beams. 212:586–597, 2019.

[211] AR Hadjesfandiari and GF Dargush. Couple stress theory for solids. 48(18):2496–2510, 2011.

[212] A Hajesfandiari, GF Dargush, and AR Hadjesfandiari. Size-dependent fluid dynamics with application to lid-driven cavity flow. 223:98–115, 2015.

[213] Ali R Hadjesfandiari, Arezoo Hajesfandiari, Haoyu Zhang, and Gary F Dargush. Size-dependent couple stress timoshenko beam theory. *arXiv preprint arXiv:1712.08527*, 2017.

[214] Z Friedman and John B Kosmatka. An improved two-node timoshenko beam finite element. *Computers & structures*, 47(3):473–481, 1993.

[215] Junuthula Narasimha Reddy. *Energy principles and variational methods in applied mechanics*. John Wiley & Sons, 2017.

[216] I Goda, R Rahouadj, and JF Ganghoffer. Size dependent static and dynamic behavior of trabecular bone based on micromechanical models of the trabecular architecture. 72:53–77, 2013.

[217] SK Park and XL Gao. Bernoulli-euler beam model based on a modified couple stress theory. 16(11):2355–2359, 2006.

[218] R. Hedayati, M. Sadighi, M. Mohammadi-Aghdam, and A. A. Zadpoor. Mechanical properties of additively manufactured octagonal honeycombs. 69:1307–1317, 2016.

[219] H. Yazdani Sarvestani, A. H. Akbarzadeh, A. Mirbolghasemi, and K. Hermenean. 3d printed meta-sandwich structures: Failure mechanism, energy absorption and multi-hit capability. 160:179–193, 2018.

[220] H. Yazdani Sarvestani, A. H. Akbarzadeh, H. Niknam, and K. Hermenean. 3d printed architected polymeric sandwich panels: Energy absorption and structural performance. 200:886–909, 2018.

[221] N Karathanasopoulos, F Dos Reis, M Diamantopoulou, and JF Ganghoffer. Mechanics of beams made from chiral metamaterials: Tuning deflections through normal-shear strain couplings. 189, 2020.

[222] M. Eynbeygui, J. Arghavani, A. H. Akbarzadeh, and R. Naghdabadi. Anisotropic elastic-plastic behavior of architected pyramidal lattice materials. 183:118–136, 2020.

[223] M. Şimşek and H. H. Yurtcu. Analytical solutions for bending and buckling of functionally graded nanobeams based on the nonlocal timoshenko beam theory. 97:378–386, 2013.

[224] Sardar Malek and Lorna Gibson. Effective elastic properties of periodic hexagonal honeycombs. 91:226–240, 2015.

[225] A. Askar and A. S. Cakmak. A structural model of a micropolar continuum. 6(10):583–589, 1968.

[226] Stefano Gonella and Massimo Ruzzene. Multicell homogenization of one-dimensional periodic structures. 132(1), 2010.

[227] Stefano Gonella and Massimo Ruzzene. Homogenization and equivalent in-plane properties of two-dimensional periodic lattices. 45(10):2897–2915, 2008.

[228] Mariateresa Lombardo and Harm Askes. Higher-order gradient continuum modelling of periodic lattice materials. 52(1):204–208, 2012.

[229] JR Brockenbrough, S Suresh, and HA Wienecke. Deformation of fiber-reinforced metal-matrix composites: geometrical effects of fiber shape and distribution. 39:735–52, 1991.

[230] Jacob Aboudi. *Mechanics of composite materials: a unified micromechanical approach*. Elsevier, 2013.

[231] Sadik L. Omairey, Peter D. Dunning, and Srinivas Sriramula. Development of an ABAQUS plugin tool for periodic RVE homogenisation. 35(2):567–577, 2019.

[232] Geng-Dong Cheng, Yuan-Wu Cai, and Liang Xu. Novel implementation of homogenization method to predict effective properties of periodic materials. 29(4):550–556, 2013.

[233] X-Y Zhou, PD Gosling, CJ Pearce, Z Ullah, and L Kaczmarczyk. Perturbation-based stochastic multi-scale computational homogenization method for woven textile composites. 80:368–380, 2016.

[234] D CAILLERIE. Homogénéisation des matériaux à structure périodique, 2012.

[235] Graeme W Milton, Marc Briane, and John R Willis. On cloaking for elasticity and physical equations with a transformation invariant form. *New Journal of Physics*, 8(10):248, 2006.

[236] Andrew N Norris and Alexander L Shuvalov. Elastic cloaking theory. *Wave Motion*, 48(6):525–538, 2011.

[237] David Lovelock and Hanno Rund. *Tensors, differential forms, and variational principles*. Courier Corporation, 1989.

[238] Wiebke Drenckhan, D Weaire, and SJ Cox. The demonstration of conformal maps with two-dimensional foams. *European journal of physics*, 25(3):429, 2004.

[239] Sachiko Ishida, Taketoshi Nojima, and Ichiro Hagiwara. Mathematical approach to model foldable conical structures using conformal mapping. *Journal of mechanical design*, 136(9):091007, 2014.

[240] Sachiko Ishida, Taketoshi Nojima, and Ichiro Hagiwara. Design of deployable membranes using conformal mapping. *Journal of Mechanical Design*, 137(6):061404, 2015.

[241] Amir A Zadpoor. Bone tissue regeneration: the role of scaffold geometry. *Biomaterials science*, 3(2):231–245, 2015.

[242] FSL Bobbert and AA Zadpoor. Effects of bone substitute architecture and surface properties on cell response, angiogenesis, and structure of new bone. *Journal of Materials Chemistry B*, 5(31):6175–6192, 2017.

[243] K Cheikho, C Laurent, and JF Ganghoffer. An advanced method to design graded cylindrical scaffolds with versatile effective cross-sectional mechanical properties. *Journal of the mechanical behavior of biomedical materials*, page 104887, 2021.

[244] MR Dias, PR Fernandes, JM Guedes, and SJ Hollister. Permeability analysis of scaffolds for bone tissue engineering. *Journal of biomechanics*, 45(6):938–944, 2012.

[245] Cheng Yu Lin, Noboru Kikuchi, and Scott J Hollister. A novel method for biomaterial scaffold internal architecture design to match bone elastic properties with desired porosity. *Journal of*

biomechanics, 37(5):623–636, 2004.

[246] Zineeddine Louna, Ibrahim Goda, and Jean-François Ganghoffer. Homogenized strain gradient remodeling model for trabecular bone microstructures. *Continuum Mechanics and Thermodynamics*, 31(5):1339–1367, 2019.

[247] JF Ganghoffer and H Reda. A variational approach of homogenization of heterogeneous materials towards second gradient continua. *Mechanics of Materials*, 158:103743, 2021.

[248] X F Wang, X W Wang, GM Zhou, and CW Zhou. Multi-scale analyses of 3d woven composite based on periodicity boundary conditions. 41(14):1773–1788, 2007. Publisher: Sage Publications Sage UK: London, England.

[249] Peter J Olver. Complex analysis and conformal mapping. *University of Minnesota*, 806, 2017.

[250] Mats Carlin. Computing geometric moments for objects with an exact polygonal representation. 1998.

[251] Mostafa Elsayed. Multiscale mechanics and structural design of periodic cellular materials, 2010.

Appendix A

Evaluation of the effective micropolar moduli

Since the function defined on the right-hand side of Eq. 2.43 is regular in $\mathbf{E}^{sym}(\boldsymbol{x})$, $\boldsymbol{E}^{skew}(\boldsymbol{x})$, and $\mathbf{K}(\boldsymbol{x})$, play the role of parameters in the bounded integrand, partial derivative and integration can be exchanged, so that the stress measures in Eq. 2.23 leads to

$$\begin{aligned}
\Sigma^{sym} &:= \frac{\partial W_M(\mathbf{E}^{sym},\mathrm{E}^{skew},\mathbf{K})}{\partial \mathbf{E}^{sym}} = \underset{\tilde{\mathbf{u}}\in H^1_{per}(Y)}{Min} \frac{\partial}{\partial \mathbf{E}^{sym}} \left\{ \begin{array}{l} \int\limits_Y \frac{1}{2}\mathbf{C}(\mathbf{y}) : \left(\mathrm{A}^{\mathrm{E}^{sym}}(\mathbf{y}) : \mathbf{E}^{sym}(\mathbf{x}) + \mathrm{A}^{\mathrm{E}^{skew}}(\mathbf{y}) \cdot \mathbf{E}^{skew}(\mathbf{x}) + \mathrm{A}^{\mathrm{K}}(\mathbf{y}) : \mathbf{K}(\mathbf{x})\right) : \\ \left(\mathrm{A}^{\mathrm{E}^{sym}}(\mathbf{y}) : \mathbf{E}^{sym}(\mathbf{x}) + \mathrm{A}^{\mathrm{E}^{skew}}(\mathbf{y}) \cdot \mathbf{E}^{skew}(\mathbf{x}) + \mathrm{A}^{\mathrm{K}}(\mathbf{y}) : \mathbf{K}(\mathbf{x})\right) dV_y \end{array} \right\} \\
\Sigma^{skew} &:= \frac{\partial W_M(\mathbf{E}^{sym},\mathrm{E}^{skew},\mathbf{K})}{\partial \mathrm{E}^{skew}} = \underset{\tilde{\mathbf{u}}\in H^1_{per}(Y)}{Min} \frac{\partial}{\partial \mathrm{E}^{skew}} \left\{ \begin{array}{l} \int\limits_Y \frac{1}{2}\mathbf{C}(\mathbf{y}) : \left(\mathrm{A}^{\mathrm{E}^{sym}}(\mathbf{y}) : \mathbf{E}^{sym}(\mathbf{x}) + \mathrm{A}^{\mathrm{E}^{skew}}(\mathbf{y}) \cdot \mathbf{E}^{skew}(\mathbf{x}) + \mathrm{A}^{\mathrm{K}}(\mathbf{y}) : \mathbf{K}(\mathbf{x})\right) : \\ \left(\mathrm{A}^{\mathrm{E}^{sym}}(\mathbf{y}) : \mathbf{E}^{sym}(\mathbf{x}) + \mathrm{A}^{\mathrm{E}^{skew}}(\mathbf{y}) \cdot \mathbf{E}^{skew}(\mathbf{x}) + \mathrm{A}^{\mathrm{K}}(\mathbf{y}) : \mathbf{K}(\mathbf{x})\right) dV_y \end{array} \right\} \\
\mathbf{M} &:= \frac{\partial W_M(\mathbf{E}^{sym},\mathrm{E}^{skew},\mathbf{K})}{\partial \mathbf{K}} = \underset{\tilde{\mathbf{u}}\in H^1_{per}(Y)}{Min} \frac{\partial}{\partial \mathbf{K}} \left\{ \begin{array}{l} \int\limits_Y \frac{1}{2}\mathbf{C}(\mathbf{y}) : \left(\mathrm{A}^{\mathrm{E}^{sym}}(\mathbf{y}) : \mathbf{E}^{sym}(\mathbf{x}) + \mathrm{A}^{\mathrm{E}^{skew}}(\mathbf{y}) \cdot \mathbf{E}^{skew}(\mathbf{x}) + \mathrm{A}^{\mathrm{K}}(\mathbf{y}) : \mathbf{K}(\mathbf{x})\right) : \\ \left(\mathrm{A}^{\mathrm{E}^{sym}}(\mathbf{y}) : \mathbf{E}^{sym}(\mathbf{x}) + \mathrm{A}^{\mathrm{E}^{skew}}(\mathbf{y}) \cdot \mathbf{E}^{skew}(\mathbf{x}) + \mathrm{A}^{\mathrm{K}}(\mathbf{y}) : \mathbf{K}(\mathbf{x})\right) dV_y \end{array} \right\}
\end{aligned} \tag{A.1}$$

Eq. A.1 leads to the expressions of macro stress, antisymmetric macro stress, and micropolar stress tensors after straightforward calculations:

$$\begin{aligned}
\Sigma^{sym} &= \int_Y \mathbf{C}(\mathbf{y}) : \left(\mathrm{A}^{\mathrm{E}^{sym}}(\mathbf{y}) : \mathbf{E}^{sym}(\mathbf{x}) + \mathrm{A}^{\mathrm{E}^{skew}}(\mathbf{y}) \cdot \mathbf{E}^{skew}(\mathbf{x}) + \mathrm{A}^{\mathrm{K}}(\mathbf{y}) : \mathbf{K}(\mathbf{x})\right) : \mathrm{A}^{\mathrm{E}^{sym}}(\mathbf{y})\, dV_y \\
&= \left\{ \int\limits_Y \mathrm{A}^{\mathrm{E}^{sym}}(\mathbf{y}) : \mathbf{C} : \mathrm{A}^{\mathrm{E}^{sym}}(\mathbf{y}) dV_y \right\} : \mathbf{E}^{sym}(\mathbf{x}) + \left\{ \int\limits_Y \mathrm{A}^{\mathrm{E}^{sym}}(\mathbf{y}) : \mathbf{C} : \mathrm{A}^{\mathrm{E}^{skew}}(\mathbf{y}) dV_y \right\} \cdot \mathbf{E}^{skew}(\mathbf{x}) + \left\{ \int\limits_Y \mathrm{A}^{\mathrm{E}^{sym}}(\mathbf{y}) : \mathbf{C} : \mathrm{A}^{\mathrm{K}}(\mathbf{y}) dV_y \right\} : \mathrm{K}(\mathbf{x}) \\
\Sigma^{skew} &= \int_Y \mathbf{C}(\mathbf{y}) : \left(\mathrm{A}^{\mathrm{E}^{sym}}(\mathbf{y}) : \mathbf{E}^{sym}(\mathbf{x}) + \mathrm{A}^{\mathrm{E}^{skew}}(\mathbf{y}) \cdot \mathbf{E}^{skew}(\mathbf{x}) + \mathrm{A}^{\mathrm{K}}(\mathbf{y}) : \mathbf{K}(\mathbf{x})\right) : \mathrm{A}^{\mathrm{E}^{skew}}(\mathbf{y})\, dV_y \\
&= \left\{ \int\limits_Y \mathrm{A}^{\mathrm{E}^{skew}}(\mathbf{y}) : \mathbf{C} : \mathrm{A}^{\mathrm{E}^{sym}}(\mathbf{y}) dV_y \right\} : \mathbf{E}^{sym}(\mathbf{x}) + \left\{ \int\limits_Y \mathrm{A}^{\mathrm{E}^{skew}}(\mathbf{y}) : \mathbf{C} : \mathrm{A}^{\mathrm{E}^{skew}}(\mathbf{y}) dV_y \right\} \cdot \mathrm{E}^{skew}(\mathbf{x}) + \left\{ \int\limits_Y \mathrm{A}^{\mathrm{E}^{skew}}(\mathbf{y}) : \mathbf{C} : \mathrm{A}^{\mathrm{K}}(\mathbf{y}) dV_y \right\} : \mathrm{K}(\mathbf{x}) \\
\mathbf{M} &= \int_Y \mathbf{C}(\mathbf{y}) : \left(\mathrm{A}^{\mathrm{E}^{sym}}(\mathbf{y}) : \mathbf{E}^{sym}(\mathbf{x}) + \mathrm{A}^{\mathrm{E}^{skew}}(\mathbf{y}) \cdot \mathbf{E}^{skew}(\mathbf{x}) + \mathrm{A}^{\mathrm{K}}(\mathbf{y}) : \mathbf{K}(\mathbf{x})\right) : \mathrm{A}^{\mathrm{K}}(\mathbf{y})\, dV_y \\
&= \left\{ \int\limits_Y \mathrm{A}^{\mathrm{K}}(\mathbf{y}) : \mathbf{C} : \mathrm{A}^{\mathrm{E}^{sym}}(\mathbf{y}) dV_y \right\} : \mathbf{E}^{sym}(\mathbf{x}) + \left\{ \int\limits_Y \mathrm{A}^{\mathrm{K}}(\mathbf{y}) : \mathbf{C} : \mathrm{A}^{\mathrm{E}^{skew}}(\mathbf{y}) dV_y \right\} \cdot \mathrm{E}^{skew}(\mathbf{x}) + \left\{ \int\limits_Y \mathrm{A}^{\mathrm{K}}(\mathbf{y}) : \mathbf{C} : \mathrm{A}^{\mathrm{K}}(\mathbf{y}) dV_y \right\} : \mathrm{K}(\mathbf{x})
\end{aligned} \tag{A.2}$$

These writings together with the symmetry of the average quantities therein lead to the following expression of the effective micropolar moduli:

$$\begin{aligned}
&\mathbf{C}^{\mathrm{hom}} = \int\limits_Y \mathrm{A}^{\mathrm{E}^{sym}}(\mathbf{y}) : \mathbf{C} : \mathrm{A}^{\mathrm{E}^{sym}}(\mathbf{y}) dV_y, \mathbf{B}^{\mathrm{hom}} = \int\limits_Y \mathrm{A}^{E^{skew}}(\mathbf{y}) : \mathbf{C} : \mathrm{A}^{\mathrm{E}^{sym}}(\mathbf{y}) dV_y, \mathbf{D}^{\mathrm{hom}} = \int\limits_Y \mathrm{A}^{\mathrm{K}}(\mathbf{y}) : \mathbf{C} : \mathrm{A}^{\mathrm{E}^{sym}}(\mathbf{y}) dV_y, \\
&\mathbf{R}^{\mathrm{hom}} = \int\limits_Y \mathrm{A}^{E^{skew}}(\mathbf{y}) : \mathbf{C} : \mathrm{A}^{E^{skew}}(\mathbf{y}) dV_y, \mathbf{G}^{\mathrm{hom}} = \int\limits_Y \mathrm{A}^{\mathrm{K}}(\mathbf{y}) : \mathbf{C} : \mathrm{A}^{E^{skew}}(\mathbf{y}) dV_y, \mathbf{S}^{\mathrm{hom}} = \int\limits_Y \mathrm{A}^{\mathrm{K}}(\mathbf{y}) : \mathbf{C} : \mathrm{A}^{\mathrm{K}}(\mathbf{y}) dV_y
\end{aligned} \tag{A.3}$$

From previous expressions, one can quickly check the transpose property of the coupling tensors leading to the overall symmetry of the effective stiffness rigidity tensor.

The strain energy of the effective micropolar continuum writes as the following bilinear form of the kinematic measures, as the result of the obtained homogenized constitutive law Eq. A.3 and Euler's theorem for quadratic functions in their tensor arguments (a linear theory at both microscopic and macroscopic levels is formulated):

$$\begin{aligned} W_M\left(\boldsymbol{E}^{sym},\, \mathbf{E}^{skew},\, \boldsymbol{K}\right) &= \frac{1}{2}\boldsymbol{E}^{sym} : \boldsymbol{C}^{\hom} : \boldsymbol{E}^{sym} + \frac{1}{2}\mathbf{E}^{skew} \cdot \boldsymbol{R}^{\hom} \cdot \mathbf{E}^{skew} + \frac{1}{2}\boldsymbol{K} : \boldsymbol{S}^{\hom} : \boldsymbol{K} + \boldsymbol{E}^{sym} : \left(\boldsymbol{B}^{\hom} + \boldsymbol{B}^{\hom,T}\right) \cdot \mathbf{E}^{skew} \\ &+ \boldsymbol{E}^{sym} : \left(\boldsymbol{D}^{\hom} + \boldsymbol{D}^{\hom,T}\right) : \boldsymbol{K} + \mathbf{E}^{skew} \cdot \left(\boldsymbol{G}^{\hom} + \boldsymbol{G}^{\hom,T}\right) : \boldsymbol{K} = \langle w_\mu(\boldsymbol{\varepsilon})\rangle_Y = \left\langle \frac{1}{2}\boldsymbol{\varepsilon}(\boldsymbol{y}) : \boldsymbol{C}(\boldsymbol{y}) : \boldsymbol{\varepsilon}(\boldsymbol{y}) \right\rangle_Y \end{aligned} \tag{A.4}$$

with $\boldsymbol{S}^{\hom}$, $\boldsymbol{R}^{\hom}$, and $\boldsymbol{C}^{\hom}$ therein the fourth-order tensor of couple stress moduli, the second-order tensor of antisymmetric moduli, and the fourth-order tensor of micropolar moduli. $\boldsymbol{B}^{\hom}$ is a third-order tensor of coupling moduli for micropolar strain and rotation, $\boldsymbol{D}^{\hom}$ and $\boldsymbol{G}^{\hom}$ are fourth and third-order tensors of coupling moduli of micropolar strain and rotation with curvature, respectively. The presence of the sums $\left(\boldsymbol{B}^{\hom} + \boldsymbol{B}^{\hom,T}\right)$, $\left(\boldsymbol{D}^{\hom} + \boldsymbol{D}^{\hom,T}\right)$ and $\left(\boldsymbol{G}^{\hom} + \boldsymbol{G}^{\hom,T}\right)$ in Eq.A.4 follow from the existence of a strain energy potential which guarantees the symmetry of the effective overall stiffness matrix, by Schwarz relation. The macroscopic micropolar energy density entails the following micropolar constitutive law at the macroscopic level, relating stress tensors $\boldsymbol{\Sigma}^{sym}$, $\boldsymbol{\Sigma}^{skew}$ and $\boldsymbol{M}$ to the micropolar strain, rotation and curvature kinematic measures, respectively:

$$\begin{aligned} \boldsymbol{\Sigma}^{sym} &:= \frac{\partial W_M(\boldsymbol{E}^{sym},\, \mathbf{E}^{skew},\, \boldsymbol{K})}{\partial \boldsymbol{E}^{sym}} \equiv \boldsymbol{C}^{\hom} : \boldsymbol{E}^{sym} + \boldsymbol{B}^{\hom} \cdot \mathbf{E}^{skew} + \boldsymbol{D}^{\hom} : \boldsymbol{K} \\ \boldsymbol{\Sigma}^{skew} &:= \frac{\partial W_M(\boldsymbol{E}^{sym},\, \mathbf{E}^{skew},\, \boldsymbol{K})}{\partial \mathbf{E}^{skew}} \equiv \boldsymbol{B}^{\hom,T} : \boldsymbol{E}^{sym} + \boldsymbol{R}^{\hom} \cdot \mathbf{E}^{skew} + \boldsymbol{G}^{\hom} : \boldsymbol{K} \\ \boldsymbol{M} &:= \frac{\partial W_M(\boldsymbol{E}^{sym},\, \mathbf{E}^{skew},\, \boldsymbol{K})}{\partial \boldsymbol{K}} \equiv \boldsymbol{D}^{\hom,T} : \boldsymbol{E}^{sym} + \boldsymbol{G}^{\hom,T} \cdot \mathbf{E}^{skew} + \boldsymbol{S}^{\hom} : \boldsymbol{K} \end{aligned} \tag{A.5}$$

Appendix B

Effective engineering material parameters

B.1 Tetrachiral lattice

Considering the plane strain condition, and according to the 2D Cauchy stiffness matrix, $\boldsymbol{C}^{\mathrm{hom}}$, the effective behavior of the tetrachiral lattice can be considered as a monoclinic elastic solid with five independent coefficients in 2D. The compliance matrix for the case where the normal of the symmetry plate is along e_3 can be written:

$$\begin{pmatrix} E_{11}^{sym} \\ E_{22}^{sym} \\ E_{12}^{sym} \\ E_{21}^{sym} \end{pmatrix} = \begin{pmatrix} \frac{1}{\mathrm{E}_1} & -\frac{\nu_{21}}{\mathrm{E}_2} & \frac{\eta_{61}}{\mathrm{G}_6} & \frac{\eta_{61}}{\mathrm{G}_6} \\ -\frac{\nu_{12}}{\mathrm{E}_1} & \frac{1}{\mathrm{E}_2} & \frac{\eta_{62}}{\mathrm{G}_6} & \frac{\eta_{62}}{\mathrm{G}_6} \\ \frac{\eta_{16}}{\mathrm{E}_1} & \frac{\eta_{26}}{\mathrm{E}_2} & \frac{1}{\mathrm{G}_6} & \frac{1}{\mathrm{G}_6} \\ \frac{\eta_{16}}{\mathrm{E}_1} & \frac{\eta_{26}}{\mathrm{E}_2} & \frac{1}{\mathrm{G}_6} & \frac{1}{\mathrm{G}_6} \end{pmatrix} \begin{pmatrix} \Sigma_{11}^{sym} \\ \Sigma_{22}^{sym} \\ \Sigma_{12}^{sym} \\ \Sigma_{21}^{sym} \end{pmatrix}$$

The symmetry of the compliance matrix requires that:

$$\frac{\nu_{21}}{\mathrm{E}_2}=\frac{\nu_{12}}{\mathrm{E}_1};\quad \frac{\eta_{61}}{\mathrm{G}_6}=\frac{\eta_{16}}{\mathrm{E}_1};\quad \frac{\eta_{62}}{\mathrm{G}_6}=\frac{\eta_{26}}{\mathrm{E}_2}$$

So, the effective engineering material parameters are evaluated as:

$$\mathrm{E}_1=\frac{2\mathrm{C}_4^2\left(\mathrm{C}_1+\mathrm{C}_2\right)+\mathrm{C}_3\left(\mathrm{C}_2^2-\mathrm{C}_1^2\right)}{\mathrm{C}_4^2-\mathrm{C}_1\mathrm{C}_3};\qquad \mathrm{E}_1=\mathrm{E}_2$$

$$\nu_{12}=\frac{\left(\mathrm{C}_4^2+\mathrm{C}_2\mathrm{C}_3\right)\left(\mathrm{C}_1\mathrm{C}_3-\mathrm{C}_4^2\right)}{\left(\mathrm{C}_1+\mathrm{C}_2\right)^2\left(2\mathrm{C}_4^2-\mathrm{C}_1\mathrm{C}_3+\mathrm{C}_2\mathrm{C}_3\right)^2};\qquad \nu_{12}=\nu_{21}$$

$$\mathrm{G}_6=\frac{2\mathrm{C}_4^2-\mathrm{C}_1\mathrm{C}_3+\mathrm{C}_2\mathrm{C}_3}{\mathrm{C}_2-\mathrm{C}_1}$$

$$\eta_{16}=\frac{\mathrm{C}_4\left(\mathrm{C}_1\mathrm{C}_3-\mathrm{C}_4^2\right)}{\left(\mathrm{C}_1+\mathrm{C}_2\right)\left(2\mathrm{C}_4^2-\mathrm{C}_1\mathrm{C}_3+\mathrm{C}_2\mathrm{C}_3\right)^2};\qquad \eta_{16}=-\eta_{26}$$

$$\eta_{61}=\frac{\mathrm{C}_4\left(\mathrm{C}_1-\mathrm{C}_2\right)}{\left(2\mathrm{C}_4^2-\mathrm{C}_1\mathrm{C}_3+\mathrm{C}_2\mathrm{C}_3\right)^2};\qquad \eta_{61}=-\eta_{62}$$

B.2 Anti-tetrachiral lattice

Considering the plane strain condition, and according to the 2D Cauchy stiffness matrix $\boldsymbol{C}^{\hom}$ the effective behavior of the anti-tetrachiral lattice can be considered as a orthotropic elastic solid with three independent coefficients in 2D. The compliance matrix for the case where normal of the symmetry plate is along e_3 can be written:

$$\begin{pmatrix} E_{11}^{sym} \\ E_{22}^{sym} \\ E_{12}^{sym} \\ E_{21}^{sym} \end{pmatrix} = \begin{pmatrix} \frac{1}{\mathrm{E}_1} & -\frac{\nu_{21}}{\mathrm{E}_2} & 0 & 0 \\ -\frac{\nu_{12}}{\mathrm{E}_1} & \frac{1}{\mathrm{E}_2} & 0 & 0 \\ 0 & 0 & \frac{1}{\mathrm{G}_6} & \frac{1}{\mathrm{G}_6} \\ 0 & 0 & \frac{1}{\mathrm{G}_6} & \frac{1}{\mathrm{G}_6} \end{pmatrix} \begin{pmatrix} \Sigma_{11}^{sym} \\ \Sigma_{22}^{sym} \\ \Sigma_{12}^{sym} \\ \Sigma_{21}^{sym} \end{pmatrix}$$

The symmetry of the compliance matrix requires that:

$$\frac{\nu_{21}}{\mathrm{E}_2}=\frac{\nu_{12}}{\mathrm{E}_1};$$

So, the effective engineering material parameters are evaluated as:

$$\mathrm{E}_1=\frac{\left(\mathrm{C}_1^2-\mathrm{C}_2^2\right)}{\mathrm{C}_1}; \qquad \mathrm{E}_1=\mathrm{E}_2$$

$$\nu_{12}=\frac{\mathrm{C}_1\mathrm{C}_2}{\left(\mathrm{C}_1^2-\mathrm{C}_2^2\right)^2}; \qquad \nu_{12}=\nu_{21}$$

$$\mathrm{G}_6=\mathrm{C}_3$$

Appendix C

Boundary constraint equations and corresponding classical rigidity components

Rigidity Components	Periodic Boundary Conditions ($E_{ij}=1;\ \ i,j=x,\,y,\,z$)
$C_{11}=\frac{2U^{cell}}{V^{cell}}$	$u_x^{F2}-u_x^{F1}-l_x\epsilon_{xx}=0,\quad u_y^{F4}-u_y^{F3}=0,\quad u_z^{F6}-u_z^{F5}=0$
$C_{22}=\frac{2U^{cell}}{V^{cell}}$	$u_x^{F2}-u_x^{F1}=0,\quad u_y^{F4}-u_y^{F3}-l_y\epsilon_{yy}=0,\quad u_z^{F6}-u_z^{F5}=0$
$C_{33}=\frac{2U^{cell}}{V^{cell}}$	$u_x^{F2}-u_x^{F1}=0,\quad u_y^{F4}-u_y^{F3}=0,\quad u_z^{F6}-u_z^{F5}-l_z\epsilon_{zz}=0$
$C_{44}=\frac{U^{cell}}{2V^{cell}}$	$u_x^{F2}-u_x^{F1}-l_x\epsilon_{xz}=0,\quad u_y^{F4}-u_y^{F3}=0,\quad u_z^{F6}-u_z^{F5}-l_z\epsilon_{xz}=0$
$C_{55}=\frac{U^{cell}}{2V^{cell}}$	$u_x^{F2}-u_x^{F1}=0,\quad u_y^{F4}-u_y^{F3}-l_y\epsilon_{yz}=0,\quad u_z^{F6}-u_z^{F5}-l_z\epsilon_{yz}=0$
$C_{66}=\frac{U^{cell}}{2V^{cell}}$	$u_x^{F2}-u_x^{F1}-l_x\epsilon_{xy}=0,\quad u_y^{F4}-u_y^{F3}-l_y\epsilon_{xy}=0,\quad u_z^{F6}-u_z^{F5}=0$
$C_{12}=\frac{U^{cell}}{V^{cell}}-\frac{C_{11}+C_{22}}{2}$	$u_x^{F2}-u_x^{F1}-l_x\epsilon_{xx}=0,\quad u_y^{F4}-u_y^{F3}-l_y\epsilon_{yy}=0,\quad u_z^{F6}-u_z^{F5}=0$
$C_{13}=\frac{U^{cell}}{V^{cell}}-\frac{C_{11}+C_{33}}{2}$	$u_x^{F2}-u_x^{F1}-l_x\epsilon_{xx}=0,\quad u_y^{F4}-u_y^{F3}=0,\quad u_z^{F6}-u_z^{F5}-l_z\epsilon_{zz}=0$
$C_{14}=\frac{U^{cell}}{2V^{cell}}-\frac{C_{11}}{4}-C_{44}$	$u_x^{F2}-u_x^{F1}-l_x\epsilon_{xx}=0,\ \ u_z^{F2}-u_z^{F1}-l_x\epsilon_{xz}=0,\ u_y^{F4}-u_y^{F3}=0,\ \ u_z^{F6}-u_z^{F5}=0,\ \ u_x^{F6}-u_x^{F5}-l_z\epsilon_{xz}=0$
$C_{15}=\frac{U^{cell}}{2V^{cell}}-\frac{C_{11}}{4}-C_{55}$	$u_x^{F2}-u_x^{F1}-l_x\epsilon_{xx}=0,\ u_y^{F4}-u_y^{F3}=0\,,\ u_y^{F4}-u_y^{F3}-l_y\epsilon_{yz}=0,\ \ u_z^{F6}-u_z^{F5}=0,\ \ u_x^{F6}-u_x^{F5}-l_y\epsilon_{yz}=0$
$C_{16}=\frac{U^{cell}}{2V^{cell}}-\frac{C_{11}}{4}-C_{66}$	$u_x^{F2}-u_x^{F1}-l_x\epsilon_{xx}=0,\ \ u_y^{F2}-u_y^{F1}-l_x\epsilon_{xy}=0,\ u_y^{F4}-u_y^{F3}=0,\ \ u_x^{F4}-u_x^{F3}-l_y\epsilon_{xy}=0,\ \ u_z^{F6}-u_z^{F5}=0$
$C_{23}=\frac{U^{cell}}{V^{cell}}-\frac{C_{22}+C_{33}}{2}$	$u_x^{F2}-u_x^{F1}=0,\quad u_y^{F2}-u_y^{F1}-l_y\epsilon_{yy}=0,\quad u_z^{F6}-u_z^{F5}-l_z\epsilon_{zz}=0$
$C_{24}=\frac{U^{cell}}{2V^{cell}}-\frac{C_{22}}{4}-C_{44}$	$u_x^{F2}-u_x^{F1}=0,\ \ u_z^{F2}-u_z^{F1}-l_x\epsilon_{xz}=0,\ u_y^{F4}-u_y^{F3}-l_y\epsilon_{yy}=0,\ \ u_z^{F6}-u_z^{F5}=0,\ \ u_x^{F6}-u_x^{F5}-l_z\epsilon_{xz}=0$
$C_{25}=\frac{U^{cell}}{2V^{cell}}-\frac{C_{22}}{4}-C_{55}$	$u_x^{F2}-u_x^{F1}=0,\ u_y^{F4}-u_y^{F3}-l_y\epsilon_{yy}=0\,,\ u_y^{F4}-u_y^{F3}-l_y\epsilon_{yz}=0,\ \ u_z^{F6}-u_z^{F5}=0,\ \ u_x^{F6}-u_x^{F5}-l_y\epsilon_{yz}=0$
$C_{26}=\frac{U^{cell}}{2V^{cell}}-\frac{C_{22}}{4}-C_{66}$	$u_x^{F2}-u_x^{F1}=0,\ \ u_y^{F2}-u_y^{F1}-l_x\epsilon_{xy}=0,\ u_y^{F4}-u_y^{F3}-l_y\epsilon_{yy}=0,\ \ u_x^{F4}-u_x^{F3}-l_y\epsilon_{xy}=0,\ \ u_z^{F6}-u_z^{F5}=0$
$C_{34}=\frac{U^{cell}}{2V^{cell}}-\frac{C_{33}}{4}-C_{44}$	$u_x^{F2}-u_x^{F1}=0,\ \ u_z^{F2}-u_z^{F1}-l_x\epsilon_{xz}=0,\ \ u_y^{F4}-u_y^{F3}=0,\ u_z^{F6}-u_z^{F5}-l_z\epsilon_{zz}=0,\ \ u_x^{F6}-u_x^{F5}-l_z\epsilon_{xz}=0$
$C_{35}=\frac{U^{cell}}{2V^{cell}}-\frac{C_{33}}{4}-C_{55}$	$u_x^{F2}-u_x^{F1}=0,\ u_y^{F4}-u_y^{F3}=0\,,\ u_y^{F4}-u_y^{F3}-l_y\epsilon_{yz}=0,\ u_z^{F6}-u_z^{F5}-l_z\epsilon_{zz}=0,\ \ u_x^{F6}-u_x^{F5}-l_y\epsilon_{yz}=0$
$C_{36}=\frac{U^{cell}}{2V^{cell}}-\frac{C_{33}}{4}-C_{66}$	$u_x^{F2}-u_x^{F1}=0,\ \ u_y^{F2}-u_y^{F1}-l_x\epsilon_{xy}=0,\ \ u_y^{F4}-u_y^{F3}=0,\ u_x^{F4}-u_x^{F3}-l_y\epsilon_{xy}=0,\ \ u_z^{F6}-u_z^{F5}-l_z\epsilon_{zz}=0$
$C_{45}=\frac{U^{cell}}{4V^{cell}}-\frac{C_{44}+C_{55}}{2}$	$u_x^{F2}-u_x^{F1}=0,\ \ u_z^{F2}-u_z^{F1}-l_x\epsilon_{xz}=0,\ \ u_y^{F4}-u_y^{F3}=0,\ u_z^{F4}-u_z^{F3}-l_y\epsilon_{yz}=0,$ $u_z^{F6}-u_z^{F5}=0,\ \ u_x^{F6}-u_x^{F5}-l_z\epsilon_{xz}=0,\ \ u_y^{F6}-u_y^{F5}-l_z\epsilon_{yz}=0$
$C_{46}=\frac{U^{cell}}{4V^{cell}}-\frac{C_{44}+C_{66}}{2}$	$u_x^{F2}-u_x^{F1}=0,\ \ u_y^{F2}-u_y^{F1}-l_x\epsilon_{xy}=0,\ \ u_z^{F2}-u_z^{F1}-l_x\epsilon_{xz}=0,$ $u_y^{F4}-u_y^{F3}=0,\ \ u_x^{F4}-u_x^{F3}-l_y\epsilon_{xy}=0,\ \ u_z^{F6}-u_z^{F5}=0,\ \ u_x^{F6}-u_x^{F5}-l_z\epsilon_{xz}=0$
$C_{56}=\frac{U^{cell}}{4V^{cell}}-\frac{C_{55}+C_{66}}{2}$	$u_x^{F2}-u_x^{F1}=0,\ \ u_y^{F2}-u_y^{F1}-l_{xxy}=0,\ \ u_y^{F4}-u_y^{F3}=0,\ \ u_x^{F4}-u_x^{F3}-l_{yxy}=0,\ \ u_z^{F4}-u_z^{F3}-l_{yyz}=0,$ $u_z^{F6}-u_z^{F5}=0,\ \ u_y^{F6}-u_y^{F5}-l_{zyz}=0$

Appendix D

Proof of Whitaker averaging theorem

In order to relate volume averages of microscopic gradients in terms of macroscopic gradients of their averages to be able to write the micro-macro kinematic and static relations, Withaker averaging theorem is needed, a proof of which is conveniently recalled. Consider a general static balance equation at the microscale of the form

$$\int_Y \psi_m dV + \oint_{\partial Y} \underline{\boldsymbol{n}} \cdot \underline{\psi}_a ds = 0 \tag{D.1}$$

with $\psi_m$and $\underline{\psi}_a$being the sources and flux, respectively. The global balance Eq. D.1 can be localized to deliver the following strong form

$$\psi_m + \underline{\psi}_a \cdot \nabla_x = 0 \quad in\, Y \tag{D.2}$$

Here the traditional form of the averaging theorem [177]; [178] is applied on a two-phase heterogeneous material, with an assumed continuity of displacement and traction at the interface between constituents. According to this theorem and for a two-phase material depicted in Fig. 3.3, it holds

$$< \nabla_y \psi_a >_y = \nabla_x < \psi_a >_y + \frac{1}{|Y|} \int_{\partial_y} n_{12} \psi_1 ds_y \tag{D.3}$$

$< \psi_a >_y$ is generally known as the phase average and is defined explicitly as

$$< \psi_a >_y = \frac{1}{|Y|} \int_Y \psi_a dV_y \tag{D.4}$$

It will be proved that for the above problem (Fig. 3.3), the second interfacial term in Eq. D.3 vanishes. To this end, let consider the general balance Eq. D.1 is considered, from which the following consequences can be drawn:

- If Y_1 and Y_2 are sub regions of Y with disjoint interiors and if y_0 belongs to the boundary of both, then:

$$\underline{\boldsymbol{n}} \cdot \psi_a \left(y_0,\ \partial y_1\right) = -\underline{\boldsymbol{n}} \cdot \psi_a \left(y_0,\ \partial y_2\right) \tag{D.5}$$

- The surface term $\underline{\boldsymbol{n}} \cdot \psi_a \left(y_0,\ \partial y_1\right)$ depends on ∂y only through the exterior unit normal $\underline{\boldsymbol{n}}$ to ∂y at y_0:

$$\underline{\boldsymbol{n}} \cdot \psi_a \left(y_0,\ \partial y_1\right) = \underline{\boldsymbol{n}} \cdot \psi_a \left(y_0,\ n\right) \tag{D.6}$$

So it holds

$$\underline{\boldsymbol{n}} \cdot \psi_a \left(y_0,\ n\right) = -\underline{\boldsymbol{n}} \cdot \psi_a \left(y_0, -n\right) \tag{D.7}$$

Using the above statement and Eq. D.3, it results:

$$< \nabla_y \psi_a >_y = \nabla_x < \psi_a >_y + \frac{1}{|Y|} \int_{\partial y} \underline{\boldsymbol{n}} \cdot \psi_a \left(y, n_{12}\right) ds_y \tag{D.8}$$

For the two-phase material depicted in Fig. 3.3, where y_0 belongs to the boundary of Y_1 and Y_2, reads

$$\left.\begin{array}{c} \underline{\boldsymbol{n}} \cdot \psi_a \left(y_0, n_1\right) + \underline{\boldsymbol{n}} \cdot \psi_a \left(y_0,\ n_2\right) = 0 \\ n_1 = -n_2 \end{array}\right\} \rightarrow \underline{\boldsymbol{n}} \cdot \psi_a \left(y_0, n_1\right) - \underline{\boldsymbol{n}} \cdot \psi_a \left(y_0,\ n_1\right) = 0 \tag{D.9}$$

The second part of the above integral accordingly vanishes and it results in the equality

$$< \nabla_y \psi_a >_y = \nabla_x < \psi_a >_y \tag{D.10}$$

The derived averaging theorem, Eq. D.10, will subsequently be used to express the volume averages of microscopic gradients in terms of macroscopic gradients of their averages.

Appendix E

Derivation of the two balance laws of the effective micromorphic medium

Application of the divergence theorem $< \underset{\sim}{\boldsymbol{\sigma}} >_Y$ leads to the expression of the volume average of Cauchy stress:

$$\bar{\underset{\sim}{\boldsymbol{\sigma}}} = \langle \underset{\sim}{\boldsymbol{\sigma}} \rangle_Y = \left\langle \underline{\boldsymbol{\xi}} \otimes \underset{\sim}{\boldsymbol{\sigma}} \right\rangle_{\partial Y} - \left\langle \underline{\boldsymbol{\xi}} \otimes (\underset{\sim}{\boldsymbol{\sigma}} \cdot \nabla_y) \right\rangle_Y \tag{E.1}$$

The first equilibrium equation is obtained by taking the average of Eq. 3.2 and considering the averaging theorem, Eq. D.10, as follows:

$$\left\langle \underline{\boldsymbol{\xi}} \otimes \underset{\sim}{\boldsymbol{\sigma}} \right\rangle_{\partial Y} \cdot \nabla_x - \left\langle \underline{\boldsymbol{\xi}} \otimes (\underset{\sim}{\boldsymbol{\sigma}} \cdot \nabla_y) \right\rangle_Y \cdot \nabla_x + \left\langle \underline{\boldsymbol{b}} \right\rangle_Y = 0 \tag{E.2}$$

The tensor product of the balance of linear momentum, Eq. 3.2 by the macroscopic position $\underline{\boldsymbol{x}}$ is taken, leading to higher-order balance law

$$\underset{\sim}{\boldsymbol{\sigma}}(y) \cdot \nabla_y + \underline{\boldsymbol{b}}(y) = 0 \overset{\mathbf{x}\otimes}{\rightarrow} \left(\underline{\boldsymbol{x}} \otimes \underset{\sim}{\boldsymbol{\sigma}} \right) \cdot \nabla_y + \left(\underline{\boldsymbol{x}} \otimes \underline{\boldsymbol{b}} \right) = 0 \tag{E.3}$$

Taking the average of Eq. E.3 over the volume Y delivers the higher-order balance equation

$$\left\langle \left(\underline{\boldsymbol{x}} \otimes \underset{\sim}{\boldsymbol{\sigma}} \right) \cdot \nabla_y \right\rangle_Y + \left\langle \underline{\boldsymbol{x}} \otimes \underline{\boldsymbol{b}} \right\rangle_Y = 0 \tag{E.4}$$

Using the averaging theorem Eq. D.10, Eq. E.4 rewrites in the following form:

$$\left\langle \underline{\boldsymbol{x}} \otimes \underset{\sim}{\boldsymbol{\sigma}} \right\rangle_Y \cdot \nabla_x + \left\langle \underline{\boldsymbol{x}} \otimes \underline{\boldsymbol{b}} \right\rangle_Y = 0 \tag{E.5}$$

Applying the divergence theorem to the first term of Eq. E.5 yields

$$\begin{aligned} \left\langle \underline{\boldsymbol{x}} \otimes \underset{\sim}{\boldsymbol{\sigma}} \right\rangle_Y &= \frac{1}{|Y|} \int_Y \underline{\boldsymbol{x}} \otimes \underset{\sim}{\boldsymbol{\sigma}} dV_y = \frac{1}{|Y|} \int_{\partial Y} \underline{\boldsymbol{n}} \cdot \underline{\boldsymbol{\xi}} \otimes \underline{\boldsymbol{x}} \otimes \underset{\sim}{\boldsymbol{\sigma}} ds_y - \left\langle \underline{\boldsymbol{\xi}} \otimes \underline{\boldsymbol{x}} \otimes (\underset{\sim}{\boldsymbol{\sigma}} \cdot \nabla_y) \right\rangle_Y \\ &= \frac{1}{|Y|} \int_{\partial Y} \underline{\boldsymbol{\xi}} \otimes \underline{\boldsymbol{x}} \otimes \underset{\sim}{\boldsymbol{\sigma}} \cdot \left(\underline{\boldsymbol{n}} ds_y \right) - \left\langle \underline{\boldsymbol{\xi}} \otimes \underline{\boldsymbol{x}} \otimes (\underset{\sim}{\boldsymbol{\sigma}} \cdot \nabla_y) \right\rangle_Y \end{aligned} \tag{E.6}$$

Proof: $A_{ijk} := \frac{1}{|Y|} \int_Y (\xi_i x_j \sigma_{pk})_{,p} dV_y = \frac{1}{|Y|} \int_Y x_j \sigma_{ik} dV_y + \frac{1}{|Y|} \int_Y \xi_i x_j \sigma_{pk,p} dV_y$ Substituting Eq. E.6 into Eq. E.5 leads to the relation

$$\left\langle \underline{\boldsymbol{\xi}} \otimes \underline{\boldsymbol{x}} \otimes \underset{\sim}{\boldsymbol{\sigma}} \right\rangle_{\partial Y} \cdot \nabla_x - \left\langle \underline{\boldsymbol{\xi}} \otimes \underline{\boldsymbol{x}} \otimes (\nabla_y \cdot \underset{\sim}{\boldsymbol{\sigma}}) \right\rangle_Y \cdot \nabla_x + \left\langle \underline{\boldsymbol{x}} \otimes \underline{\boldsymbol{b}} \right\rangle_Y = 0 \tag{E.7}$$

Multiplying the equilibrium Eq. 3.2 by $\underline{\mathbf{y}}$ and integrating it over the unit cell domain Ydelivers

$$\left\langle \left(\underline{\mathbf{y}} \otimes \underline{\boldsymbol{\sigma}} \right) \cdot \nabla_y \right\rangle_Y - \langle \underline{\boldsymbol{\sigma}} \rangle_Y + \left\langle \underline{\mathbf{y}} \otimes \underline{\boldsymbol{b}} \right\rangle_Y = 0 \tag{E.8}$$

Applying Eq. D.10 to Eq. E.8 results in the following relation

$$\left\langle \underline{\mathbf{y}} \otimes \underline{\boldsymbol{\sigma}} \right\rangle_Y \cdot \nabla_x - \langle \underline{\boldsymbol{\sigma}} \rangle_Y + \left\langle \underline{\mathbf{y}} \otimes \underline{\boldsymbol{b}} \right\rangle_Y = 0 \tag{E.9}$$

Application of the divergence theorem to the first term of Eq. E.9 leads to:

$$\left\langle \underline{\mathbf{y}} \otimes \underline{\boldsymbol{\sigma}} \right\rangle_Y = \frac{1}{|Y|} \int_Y \underline{\mathbf{y}} \otimes \underline{\boldsymbol{\sigma}} \, dV_y = \frac{1}{|Y|} \int_{\partial Y} \underline{\boldsymbol{\xi}} \otimes \underline{\mathbf{y}} \otimes \underline{\boldsymbol{\sigma}} \cdot (\boldsymbol{n} \, ds_y) - \left\langle \underline{\boldsymbol{\xi}} \otimes \underline{\mathbf{y}} \otimes (\underline{\boldsymbol{\sigma}} \cdot \nabla_y) \right\rangle_Y - \left\langle \underline{\boldsymbol{\xi}} \otimes \underline{\boldsymbol{\sigma}} \right\rangle_Y \tag{E.10}$$

Proof: $B_{ijk} := \frac{1}{|Y|} \int_Y \left(\xi_i y_j \sigma_{pk} \right)_{,p} dV_y = \frac{1}{|Y|} \int_Y \left(y_j \sigma_{ik} + \xi_i \sigma_{jk} + \xi_i y_j \sigma_{pk,p} \right) dV_y$ By substituting Eq. E.10 into Eq. E.9, the following equation is obtained

$$\left\langle \underline{\boldsymbol{\xi}} \otimes \underline{\mathbf{y}} \otimes \underline{\boldsymbol{\sigma}} \right\rangle_{\partial Y} \cdot \nabla_x - \left\langle \underline{\boldsymbol{\xi}} \otimes \underline{\mathbf{y}} \otimes (\underline{\boldsymbol{\sigma}} \cdot \nabla_y) \right\rangle_Y \cdot \nabla_x - \left\langle \underline{\boldsymbol{\xi}} \otimes \underline{\boldsymbol{\sigma}} \right\rangle_Y \cdot \nabla_x - \langle \underline{\boldsymbol{\sigma}} \rangle_Y + \left\langle \underline{\boldsymbol{x}} \otimes \underline{\boldsymbol{b}} \right\rangle_Y = 0 \tag{E.11}$$

Subtracting then Eq. E.7 from Eq. E.11 and considering Eq. E.1, denoting the relative position $\underline{\mathbf{y}} - \underline{\boldsymbol{x}}$ by $\underline{\boldsymbol{\xi}}$ leads to the following equilibrium equation

$$\left\langle \underline{\boldsymbol{\xi}} \otimes \underline{\boldsymbol{\xi}} \otimes \underline{\boldsymbol{\sigma}} \right\rangle_{\partial Y} \cdot \nabla_x - \left\langle \underline{\boldsymbol{\xi}} \otimes \underline{\boldsymbol{\xi}} \otimes (\underline{\boldsymbol{\sigma}} \cdot \nabla_y) \right\rangle_Y \cdot \nabla_x - \left\langle \underline{\boldsymbol{\xi}} \otimes \underline{\boldsymbol{\sigma}} \right\rangle_Y \cdot \nabla_x - \left\langle \underline{\boldsymbol{\xi}} \otimes \underline{\boldsymbol{\sigma}} \right\rangle_{\partial Y} + \left\langle \underline{\boldsymbol{\xi}} \otimes (\underline{\boldsymbol{\sigma}} \cdot \nabla_y) \right\rangle_Y + \left\langle \underline{\boldsymbol{\xi}} \otimes \underline{\boldsymbol{b}} \right\rangle_Y = 0 \tag{E.12}$$

Eq. E.12 can be formulated in more compact form as

$$\left\langle \underline{\boldsymbol{\xi}} \otimes \underline{\boldsymbol{\xi}} \otimes \underline{\boldsymbol{\sigma}} \right\rangle_{\partial Y} \cdot \nabla_x - \left\langle \underline{\boldsymbol{\xi}} \otimes \underline{\boldsymbol{\xi}} \otimes (\underline{\boldsymbol{\sigma}} \cdot \nabla_y) \right\rangle_Y \cdot \nabla_x - \left\langle \underline{\boldsymbol{\xi}} \otimes \underline{\boldsymbol{\sigma}} \right\rangle_Y \cdot \nabla_x = \left\langle \underline{\boldsymbol{\xi}} \otimes \underline{\boldsymbol{\sigma}} \right\rangle_Y \cdot \nabla_x$$

Inserting the last relation into Eq. E.12 leads to the first equilibrium equation of the micromorphic continuum

$$\left\langle \underline{\boldsymbol{\xi}} \otimes \underline{\boldsymbol{\sigma}} \right\rangle_Y \cdot \nabla_x - \left\langle \underline{\boldsymbol{\xi}} \otimes \underline{\boldsymbol{\sigma}} \right\rangle_{\partial Y} + \left\langle \underline{\boldsymbol{\xi}} \otimes (\underline{\boldsymbol{\sigma}} \cdot \nabla_y) \right\rangle_Y + \left\langle \underline{\boldsymbol{\xi}} \otimes \underline{\boldsymbol{b}} \right\rangle_Y = 0 \tag{E.13}$$

Appendix F

Determination of the microscopic displacement field for the effective micromorphic continuum

The micro displacement field Eq. 3.68 contains five unknown coefficients that can be determined from the definitions 3.43-3.45, 3.13, and 3.14, and by recoursing to the averaging theorem together with the symmetry properties of the tensors (for centrosymmetric unit cells, $\left\langle \underset{\sim}{\boldsymbol{\xi}}^{n} \right\rangle_{Y}$ is equal to zero for odd values of n:

$$\mathrm{E}_{ij} = \langle u_{i,j} \rangle_{Y} = B_{ij}\left(\mathbf{x}\right) + \frac{1}{3} D_{imkl}\left(\mathbf{x}\right) \left[G_{kl} (\mathrm{I}_2)_{mj} + G_{km} (\mathrm{I}_2)_{lj} + G_{lm} (\mathrm{I}_2)_{kj} \right] \tag{F.1}$$

$$\mathrm{E}_{ij} = \langle u_{i,j} \rangle_{Y} = B_{ij}\left(\mathbf{x}\right) + \frac{1}{3} D_{imkl}\left(\mathbf{x}\right) \left[G_{kl} (\mathrm{I}_2)_{mj} + G_{km} (\mathrm{I}_2)_{lj} + G_{lm} (\mathrm{I}_2)_{kj} \right] \tag{F.2}$$

$$\chi_{ij} = \langle u_i \xi_p \rangle_{Y} G^{-1}_{pj} = B_{ij}\left(\mathbf{x}\right) + \frac{1}{3} D_{inkl}\left(\mathbf{x}\right) \left(G_4\right)_{nklp} G^{-1}_{pj} \tag{F.3}$$

$$\begin{aligned} \mathrm{K}_{ijk} &= 2 \left[\langle u_i \xi_p \xi_q \rangle_{Y} - \langle u_i \rangle_{Y} G_{pq} \right] \left(\left(G_4\right)_{pqjk} - G_{pq} G_{jk} \right)^{-1} \\ &= C_{ijk}\left(\mathbf{x}\right) + \frac{1}{2} E_{irlmn}\left(\mathbf{x}\right) \left[\left(G_6\right)_{rlmnpq} - \left(G_4\right)_{rlmn} G_{pq} \right] \left(\left(G_4\right)_{pqjk} - G_{pq} G_{jk} \right)^{-1} \end{aligned} \tag{F.4}$$

$$\begin{aligned} \mathrm{K}_{ijk} = \chi_{ij,k} &= \left\langle \left(u_i \xi_p\right)_{,k} \right\rangle_{Y} G^{-1}_{pj} = \langle u_{i,k} \xi_p + u_i \delta_{pk} \rangle_{Y} G^{-1}_{pj} \\ &= C_{ijk}\left(\mathbf{x}\right) + U_i G^{-1}_{jk} + \frac{1}{4} E_{irlmn}\left(\mathbf{x}\right) \left[\left(G_4\right)_{rlmp} (\mathrm{I}_2)_{nk} + \left(G_4\right)_{rnlp} (\mathrm{I}_2)_{mk} + \left(G_4\right)_{rmnp} (\mathrm{I}_2)_{lk} + \left(G_4\right)_{lmnp} (\mathrm{I}_2)_{rk} \right] G^{-1}_{pj} \end{aligned} \tag{F.5}$$

It should be noted that the second moment of area tensor $\underset{\sim}{\mathbf{G}}$ is a diagonal matrix which can be written as

$$G_{pj} = G^{0}_{2} (\mathrm{I}_2)_{pj} \tag{F.6}$$

where G^{0}_{2} is a constant depending to the unit cell shape. Subtracting Eq. F.2 from Eq. F.3, and using the definition of the relative strain, Eq. 3.18, leads to the evaluation of the coefficient $\underset{\sim}{\mathbf{e}}$ (a fourth-order tensor) as

$$e_{ij}\left(\mathbf{x}\right) = \frac{1}{3} D_{iklm}\left(\underline{\boldsymbol{x}}\right) \left[G_{kl} (\mathrm{I}_2)_{mj} + G_{km} (\mathrm{I}_2)_{lj} + G_{lm} (\mathrm{I}_2)_{kj} - \left(G_4\right)_{klmp} G^{-1}_{pj} \right] \tag{F.7}$$

Implementing the expression in Eq. F.6, the coefficient D_{inkl} can be written as

$$D_{iklm}(\mathbf{x}) = 3e_{iq}(\mathbf{x})\left[G_{kl}(\mathrm{I}_2)_{mq} + G_{km}(\mathrm{I}_2)_{lq} + G_{lm}(\mathrm{I}_2)_{kq} - \left(G_2^0\right)^{-1}(G_4)_{klmq}\right]^{-1} \tag{F.8}$$

Previous relation has the following tensor format

$$\underset{\approx}{\mathbf{D}}(\mathbf{x}) = 3\underset{\sim}{\mathbf{e}}(\mathbf{x}) \cdot \underset{\approx}{\Upsilon} \tag{F.9}$$

In Eq. F.9, $\underset{\approx}{\Upsilon}$ is the fourth-order tensor of the higher-order moments of unit cell area which is defined as

$$\Upsilon_{klmq} := \left[G_{kl}(\mathrm{I}_2)_{mq} + G_{km}(\mathrm{I}_2)_{lq} + G_{lm}(\mathrm{I}_2)_{kq} - \left(G^0\right)^{-1}(G_4)_{klmq}\right]^{-1}$$

By substituting Eq. F.9 into Eq. F.2 the coefficient $\underset{\sim}{\mathbf{B}}$ expresses as

$$B_{ij}(\mathbf{x}) = \mathrm{E}_{ij}(\mathbf{x}) - e_{iq}(\mathbf{x})\left[G_{kl}(\mathrm{I}_2)_{mq} + G_{km}(\mathrm{I}_2)_{lq} + G_{lm}(\mathrm{I}_2)_{kq} - \left(G^0\right)^{-1}(G_4)_{klmq}\right]^{-1} \times \left[G_{kl}(\mathrm{I}_2)_{mj} + G_{km}(\mathrm{I}_2)_{lj} + G_{lm}(\mathrm{I}_2)_{kj}\right] \tag{F.10}$$

which receives the following tensor format

$$\underset{\sim}{\mathbf{B}}(\mathbf{x}) = \underset{\sim}{\mathbf{E}} - \underset{\sim}{\mathbf{e}}(\mathbf{x}) \cdot \underset{\sim}{\boldsymbol{\Gamma}} \tag{F.11}$$

with the second-order tensor $\underset{\sim}{\boldsymbol{\Gamma}}$ defined in index format as

$$\Gamma_{qj} := \left[G_{kl}(\mathrm{I}_2)_{mq} + G_{km}(\mathrm{I}_2)_{lq} + G_{lm}(\mathrm{I}_2)_{kq} - \left(G^0\right)^{-1}(G_4)_{klmq}\right]^{-1}\left[G_{kl}(\mathrm{I}_2)_{mj} + G_{km}(\mathrm{I}_2)_{lj} + G_{lm}(\mathrm{I}_2)_{kj}\right]$$

To facilitate the calculation of the remaining coefficients, further simplification can be done as follow:

$$\left((G_4)_{pqjk} - G_{pq}G_{jk}\right)^{-1} G_{jk} = G_4^0(\mathrm{I}_2)_{pq} \tag{F.12}$$

where G_4^0 is a constant related to the fourth and second moment of areas. Subtracting Eq. F.5 from Eq. F.4 results in the relation

$$\begin{aligned} E_{irlmn}(\mathbf{x}) = U_i \Bigg\{ & \frac{1}{2}\left[(G_6)_{rlmnpq} - (G_4)_{rlmn}G_{pq}\right]\left((G_4)_{pqjk} - G_{pq}G_{jk}\right)^{-1} G_{jk} \\ & -\frac{1}{4}\left[(G_4)_{rlmp}(\mathrm{I}_2)_{nk} + (G_4)_{rnlp}(\mathrm{I}_2)_{mk} + (G_4)_{rmnp}(\mathrm{I}_2)_{lk} + (G_4)_{lmnp}(\mathrm{I}_2)_{rk}\right] G_{pj}^{-1}G_{jk}\Bigg\}^{-1} \end{aligned} \tag{F.13}$$

Using Eqs. F.13 and F.12, tensor $\underset{\approx}{\mathbf{E}}(\mathbf{x})$ can be written as

$$E_{irlmn}(\mathbf{x}) = U_i(\mathbf{x})\left[\frac{1}{2}G_4^0\left[(G_6)_{rlmnpp} - (G_4)_{rlmn}G_{pp}\right] - (G_4)_{rlmn}\right]^{-1} \tag{F.14}$$

Defining the fourth-order tensor $\underset{\approx}{\boldsymbol{\Lambda}}$ as

$$\Lambda_{rlmn} := \left[\frac{1}{2}G_4^0\left[(G_6)_{rlmnpp} - (G_4)_{rlmn}G_{pp}\right] - (G_4)_{rlmn}\right]^{-1} \tag{F.15}$$

results in the following tensor expression of tensor $\underset{\approx}{\mathbf{E}}$

$$\underset{\approx}{\mathbf{E}}(\mathbf{x}) = \underline{\mathbf{U}}(\mathbf{x}) \otimes \underset{\approx}{\boldsymbol{\Lambda}} \tag{F.16}$$

By substituting the expression F.14 into F.4, the tensor $\underset{\sim}{\boldsymbol{C}}(\mathbf{x})$ involved in Eq. D.1 is determined as

$$C_{ijk}(\mathbf{x}) = \mathrm{K}_{ijk}(\mathbf{x}) - \tfrac{1}{2}U_i(\mathbf{x})\left\{\tfrac{1}{2}G_4^0\left[(G_6)_{rlmnpp} - (G_4)_{rlmn}G_{pp}\right] - (G_4)_{rlmn}\right\}^{-1} \times \left[(G_6)_{rlmnpq} - (G_4)_{rlmn}G_{pq}\right]\left((G_4)_{pqjk} - G_{pq}G_{jk}\right)^{-1} \tag{F.17}$$

Defining the six-order tensor $\underset{\approx}{\boldsymbol{\Omega}}$ as

$$\Omega_{rlmnjk} := \left[(G_6)_{rlmnpq} - (G_4)_{rlmn}G_{pq}\right]\left((G_4)_{pqjk} - G_{pq}G_{jk}\right)^{-1} \tag{F.18}$$

resulting in the following expression of $\underset{\sim}{\boldsymbol{C}}$

$$\underset{\sim}{\mathbf{C}}(\mathbf{x}) = \underset{\sim}{\mathbf{K}} - \frac{1}{2}\underline{\mathbf{U}}(\mathbf{x}) \otimes \underset{\approx}{\boldsymbol{\Lambda}} :: \underset{\approx}{\boldsymbol{\Omega}} \tag{F.19}$$

Assuming no zero rigid body motion ($\underline{\boldsymbol{A}} = 0$), and substituting Eq. F.14 and Eq. F.17 into Eq. F.1 gives the vector $\underline{\mathbf{U}}$ versus the macroscopic tensor $\underset{\sim}{\mathbf{K}}$ as

$$U_i(\mathbf{x}) = \mathrm{P}^{-1}\mathbf{K}_{ijk}(\mathbf{x})\, G_{jk} \tag{F.20}$$

wherein P is the scalar defined by the relation

$$\mathrm{P} = 2 + \frac{1}{2}\left[\frac{1}{2}G_4^0\left[(G_6)_{rlmnpp} - (G_4)_{rlmn}G_{pp}\right] - (G_4)_{rlmn}\right]^{-1}\left\{\left[G_4^0(G_6)_{rlmnqq} - G_{qq}\right] - (G_4)_{rlmn}\right\}$$

Substituting the coefficients $\underset{\sim}{\mathbf{B}}$, $\underset{\sim}{\boldsymbol{C}}$, $\underset{\approx}{\mathbf{D}}$, and $\underset{=}{\underset{\approx}{\mathbf{E}}}$ along with the expression F.20 into Eq. 3.68 gives the total homogenous microscopic displacement as the following fourth-order polynomial expression of the relative microscopic position:

$$\begin{aligned}\underline{\mathbf{u}}^{\mathrm{hom}}(\boldsymbol{\xi}, \mathbf{x}) = {} & \underset{\sim}{\mathbf{E}}(\mathbf{x}) \cdot \underline{\boldsymbol{\xi}} - \underset{\sim}{\mathbf{e}}(\mathbf{x}) \cdot \underset{\sim}{\boldsymbol{\Gamma}} \cdot \underline{\boldsymbol{\xi}} + \underset{\sim}{\mathbf{e}}(\mathbf{x}) \cdot \underset{\approx}{\boldsymbol{\Upsilon}} \therefore \left(\underline{\boldsymbol{\xi}} \otimes \underline{\boldsymbol{\xi}} \otimes \underline{\boldsymbol{\xi}}\right) + \frac{1}{2}\underset{\sim}{\mathbf{K}} : \left(\underline{\boldsymbol{\xi}} \otimes \underline{\boldsymbol{\xi}}\right) \\ & - \frac{1}{4}\left(\mathrm{P}^{-1}\underset{\sim}{\mathbf{K}} : \underset{\sim}{\mathbf{G}}\right) \otimes \underset{\approx}{\boldsymbol{\Lambda}} :: \underset{\approx}{\boldsymbol{\Omega}} : \left(\underline{\boldsymbol{\xi}} \otimes \underline{\boldsymbol{\xi}}\right) + \frac{1}{4}\left(\mathrm{P}^{-1}\underset{\sim}{\mathbf{K}} : \underset{\sim}{\mathbf{G}}\right) \otimes \underset{\approx}{\boldsymbol{\Lambda}} :: \left(\underline{\boldsymbol{\xi}} \otimes \underline{\boldsymbol{\xi}} \otimes \underline{\boldsymbol{\xi}} \otimes \underline{\boldsymbol{\xi}}\right)\end{aligned} \tag{F.21}$$

The full kinematics of the micromorphic continuum and its two degenerated media (micropolar and strain gradient) is expressed in the set of equations F.22.

Micromorphic:

$$\underset{\sim}{\boldsymbol{U}}(\boldsymbol{x}) = \left\langle \underset{\sim}{\boldsymbol{u}}(\boldsymbol{\xi}) \right\rangle_Y, \qquad \underset{\approx}{\mathrm{E}}(\boldsymbol{x}) = \nabla_x \underset{\sim}{\boldsymbol{U}}$$

$$\underset{\approx}{\boldsymbol{\chi}}(\boldsymbol{x}) = \frac{1}{|\mathrm{Y}|}\left(\int_Y \underset{\sim}{\boldsymbol{u}} \otimes \underset{\sim}{\boldsymbol{\xi}}\, dV_y\right) \cdot \underset{\approx}{\boldsymbol{G}}^{-1}, \qquad \underset{\sim}{\mathbf{K}}(\boldsymbol{x}) = \nabla_x \underset{\approx}{\boldsymbol{\chi}}$$

$$\underset{\sim}{\mathbf{K}}(\boldsymbol{x}) = \frac{2}{|\mathrm{Y}|}\left[\int_Y \underset{\sim}{\boldsymbol{u}} \otimes \underset{\sim}{\boldsymbol{\xi}} \otimes \underset{\sim}{\boldsymbol{\xi}}\, dV_y - \int_Y \underset{\sim}{\boldsymbol{u}}\, dV_y \otimes \underset{\approx}{\boldsymbol{G}}\right] : \left[\underset{\approx}{\boldsymbol{G}}_4 - \underset{\approx}{\boldsymbol{G}} \otimes \underset{\approx}{\boldsymbol{G}}\right]^{-1}$$

$$\begin{aligned}\underset{\sim}{\boldsymbol{u}}^{\mathrm{hom}}(\boldsymbol{\xi},\boldsymbol{x}) = {} & \underset{\sim}{\boldsymbol{E}}(\boldsymbol{x}) \cdot \underset{\sim}{\boldsymbol{\xi}} - \underset{\sim}{\boldsymbol{e}}(\boldsymbol{x}) \cdot \underset{\sim}{\boldsymbol{\Gamma}} \cdot \underset{\sim}{\boldsymbol{\xi}} + \underset{\sim}{\boldsymbol{e}}(\boldsymbol{x}) \cdot \underset{\approx}{\boldsymbol{\Upsilon}} \therefore \left(\underset{\sim}{\boldsymbol{\xi}} \otimes \underset{\sim}{\boldsymbol{\xi}} \otimes \underset{\sim}{\boldsymbol{\xi}}\right) + \frac{1}{2}\underset{\sim}{\mathbf{K}} : \left(\underset{\sim}{\boldsymbol{\xi}} \otimes \underset{\sim}{\boldsymbol{\xi}}\right) \\ & - \frac{1}{4}\left(\mathrm{P}^{-1}\underset{\sim}{\mathbf{K}} : \underset{\approx}{\boldsymbol{G}}\right) \otimes \underset{\approx}{\boldsymbol{A}} :: \underset{\approx}{\boldsymbol{\Omega}} : \left(\underset{\sim}{\boldsymbol{\xi}} \otimes \underset{\sim}{\boldsymbol{\xi}}\right) + \frac{1}{4}\left(\mathrm{P}^{-1}\underset{\sim}{\mathbf{K}} : \underset{\approx}{\boldsymbol{G}}\right) \otimes \underset{\approx}{\boldsymbol{A}} :: \left(\underset{\sim}{\boldsymbol{\xi}} \otimes \underset{\sim}{\boldsymbol{\xi}} \otimes \underset{\sim}{\boldsymbol{\xi}} \otimes \underset{\sim}{\boldsymbol{\xi}}\right)\end{aligned}$$

Micropolar:

$$\underset{\sim}{\boldsymbol{U}}(\boldsymbol{x}) = \left\langle \underset{\sim}{\boldsymbol{u}}(\boldsymbol{\xi}) \right\rangle_Y, \qquad \underset{\approx}{\mathrm{E}}(\boldsymbol{x}) = \nabla_x \underset{\sim}{\boldsymbol{U}} - \underset{\sim}{\boldsymbol{\epsilon}} \cdot \underset{\sim}{\Phi}(\boldsymbol{x})$$

$$\boldsymbol{\epsilon} \cdot \underset{\sim}{\Phi}(\boldsymbol{x}) = \frac{1}{|\mathrm{Y}|}\left(\int_Y \underset{\sim}{\boldsymbol{u}} \otimes \underset{\sim}{\boldsymbol{\xi}}\, dV_y\right) \cdot \underset{\approx}{\boldsymbol{G}}^{-1}, \qquad \underset{\sim}{\mathbf{K}}(\boldsymbol{x}) = \nabla_x \Phi$$

$$\boldsymbol{\epsilon} \cdot \underset{\sim}{\mathbf{K}}(\boldsymbol{x}) = \frac{2}{|\mathrm{Y}|}\left[\int_Y \underset{\sim}{\boldsymbol{u}} \otimes \underset{\sim}{\boldsymbol{\xi}} \otimes \underset{\sim}{\boldsymbol{\xi}}\, dV_y - \int_Y \underset{\sim}{\boldsymbol{u}}\, dV_y \otimes \underset{\approx}{\boldsymbol{G}}\right] : \left[\underset{\approx}{\boldsymbol{G}}_4 - \underset{\approx}{\boldsymbol{G}} \otimes \underset{\approx}{\boldsymbol{G}}\right]^{-1}$$

$$\begin{aligned}\underset{\sim}{\boldsymbol{u}}^{\mathrm{hom}}(\boldsymbol{\xi},\boldsymbol{x}) = {} & \underset{\sim}{\boldsymbol{E}}(\boldsymbol{x}) \cdot \underset{\sim}{\boldsymbol{\xi}} - \underset{\sim}{\boldsymbol{E}}(\boldsymbol{x}) \cdot \underset{\sim}{\boldsymbol{\Gamma}} \cdot \underset{\sim}{\boldsymbol{\xi}} + \underset{\sim}{\boldsymbol{\epsilon}} \cdot \underset{\sim}{\Phi}(\boldsymbol{x}) \cdot \underset{\sim}{\boldsymbol{\xi}} + \underset{\sim}{\boldsymbol{E}}(\boldsymbol{x}) \cdot \underset{\approx}{\boldsymbol{\Upsilon}} \therefore \left(\underset{\sim}{\boldsymbol{\xi}} \otimes \underset{\sim}{\boldsymbol{\xi}} \otimes \underset{\sim}{\boldsymbol{\xi}}\right) + \frac{1}{2}\underset{\sim}{\boldsymbol{\epsilon}} \cdot \underset{\sim}{\mathbf{K}} : \left(\underset{\sim}{\boldsymbol{\xi}} \otimes \underset{\sim}{\boldsymbol{\xi}}\right) \\ & - \frac{1}{4}\left(\mathrm{P}^{-1}\underset{\sim}{\boldsymbol{\epsilon}} \cdot \underset{\sim}{\mathbf{K}} : \underset{\approx}{\boldsymbol{G}}\right) \otimes \underset{\approx}{\boldsymbol{A}} :: \underset{\approx}{\boldsymbol{\Omega}} : \left(\underset{\sim}{\boldsymbol{\xi}} \otimes \underset{\sim}{\boldsymbol{\xi}}\right) + \frac{1}{4}\left(\mathrm{P}^{-1}\underset{\sim}{\boldsymbol{\epsilon}} \cdot \underset{\sim}{\mathbf{K}} : \underset{\approx}{\boldsymbol{G}}\right) \otimes \underset{\approx}{\boldsymbol{A}} :: \left(\underset{\sim}{\boldsymbol{\xi}} \otimes \underset{\sim}{\boldsymbol{\xi}} \otimes \underset{\sim}{\boldsymbol{\xi}} \otimes \underset{\sim}{\boldsymbol{\xi}}\right)\end{aligned}$$

Second gradient :

$$\underset{\sim}{\boldsymbol{U}}(\boldsymbol{x}) = \left\langle \underset{\sim}{\boldsymbol{u}}(\boldsymbol{\xi}) \right\rangle_Y, \qquad \underset{\approx}{\mathrm{E}}(\boldsymbol{x}) = \nabla_x \underset{\sim}{\boldsymbol{U}}$$

$$\underset{\approx}{\mathrm{E}}(\boldsymbol{x}) = \frac{1}{|\mathrm{Y}|}\left(\int_Y \underset{\sim}{\boldsymbol{u}} \otimes \underset{\sim}{\boldsymbol{\xi}}\, dV_y\right) \cdot \underset{\approx}{\boldsymbol{G}}^{-1}, \qquad \underset{\sim}{\mathbf{K}}(\boldsymbol{x}) = \nabla_x \underset{\approx}{\mathrm{E}}$$

$$\underset{\sim}{\mathbf{K}}(\boldsymbol{x}) = \frac{2}{|\mathrm{Y}|}\left[\int_Y \underset{\sim}{\boldsymbol{u}} \otimes \underset{\sim}{\boldsymbol{\xi}} \otimes \underset{\sim}{\boldsymbol{\xi}}\, dV_y - \int_Y \underset{\sim}{\boldsymbol{u}}\, dV_y \otimes \underset{\approx}{\boldsymbol{G}}\right] : \left[\underset{\approx}{\boldsymbol{G}}_4 - \underset{\approx}{\boldsymbol{G}} \otimes \underset{\approx}{\boldsymbol{G}}\right]^{-1}$$

$$\underset{\sim}{\boldsymbol{u}}^{\mathrm{hom}}(\boldsymbol{\xi},\boldsymbol{x}) = \underset{\sim}{\boldsymbol{E}}(\boldsymbol{x}) \cdot \underset{\sim}{\boldsymbol{\xi}} + \frac{1}{2}\underset{\sim}{\mathbf{K}} : \left(\underset{\sim}{\boldsymbol{\xi}} \otimes \underset{\sim}{\boldsymbol{\xi}}\right) \tag{F.22}$$

Appendix G

Computation of the higher-order moments of area and expression of strain components in 2D

The regular expression for the geometric moments is [250]:

$$m_{pq} = \int_{-\infty}^{\infty} \int_{-\infty}^{\infty} y_1^p y_2^q dy_1 dy_2 \tag{G.1}$$

Suppose there exists an exact parametric contour of the unit cell domain, so it is possible to use Green's theorem to reduce the double integral to a simpler line integral:

$$m_{pq} = \frac{1}{p+1} \oint_C y_1^{p+1} y_2^q dy_2 = -\frac{1}{q+1} \oint_C y_1^p y_2^{q+1} dy_1 \tag{G.2}$$

where $\oint_C$ is the line integral along the considered contour.

For the square unit cell with side length of 'a' the nonzero components of the second, fourth, and sixth

order moment of area - after normalizing by unit cell area - are represented using Eq. G.2 as follows

$$
\begin{aligned}
&G_{11} = G_{22} = \frac{a^2}{12},\\
&(G_4)_{1111} = (G_4)_{2222} = \frac{a^4}{80},\\
&(G_4)_{1122} = (G_4)_{2211} = (G_4)_{1212} = (G_4)_{1221} = (G_4)_{2112} = (G_4)_{2121} = \frac{a^4}{144},\\
&(G_6)_{111111} = (G_6)_{222222} = \frac{a^6}{448},\\
&(G_6)_{111122} = (G_6)_{112211} = (G_6)_{221111} = (G_6)_{121211} = (G_6)_{122111} = (G_6)_{212111} = \frac{a^6}{960},\\
&(G_6)_{211211} = (G_6)_{112112} = (G_6)_{112121} = (G_6)_{111221} = (G_6)_{111212} = (G_6)_{211112} = \frac{a^6}{960},\\
&(G_6)_{211121} = (G_6)_{121121} = (G_6)_{121112} = (G_6)_{222211} = (G_6)_{221122} = (G_6)_{112222} = \frac{a^6}{960},\\
&(G_6)_{212122} = (G_6)_{211222} = (G_6)_{121222} = (G_6)_{122122} = (G_6)_{221221} = (G_6)_{221212} = \frac{a^6}{960},\\
&(G_6)_{222112} = (G_6)_{222121} = (G_6)_{122221} = (G_6)_{122212} = (G_6)_{212212} = (G_6)_{212221} = \frac{a^6}{960}.
\end{aligned}
\tag{G.3}
$$

According to the definition of the higher–order moments of area, relation G.3, one can conclude that the values of coefficients of the displacement field Eq. 3.69 are function of the unit cell side length 'a'. In the sequel, the displacement field and related strain measures are presented. The displacement field in Eq. 3.69 can be expressed as,

$$
\begin{aligned}
u_1 = {} & \mathrm{E}_{11}y_1 + \mathrm{E}_{12}y_2 - \frac{5}{2}e_{11}y_1 - \frac{5}{2}e_{12}y_2 + 3\mathrm{K}_{111}y_1^2 - \frac{35}{3a^2}\mathrm{K}_{111}y_1^4 + \frac{5}{2}\mathrm{K}_{122}y_1^2 - \frac{35}{3a^2}\mathrm{K}_{122}y_1^4\\
& + \frac{5}{2}\mathrm{K}_{111}y_2^2 - \frac{35}{3a^2}\mathrm{K}_{111}y_2^4 + 3\mathrm{K}_{122}y_2^2 - \frac{35}{3a^2}\mathrm{K}_{122}y_2^4 + \frac{10}{a^2}e_{11}y_1^3 + \frac{10}{a^2}e_{12}y_2^3 + \frac{1}{2}\mathrm{K}_{112}y_1y_2 + \frac{1}{2}\mathrm{K}_{121}y_1y_2
\end{aligned}
\tag{G.4}
$$

$$
\begin{aligned}
u_2 = {} & \mathrm{E}_{22}y_2 + \mathrm{E}_{21}y_1 - \frac{5}{2}e_{22}y_2 - \frac{5}{2}e_{21}y_1 + 3\mathrm{K}_{222}y_2^2 - \frac{35}{3a^2}\mathrm{K}_{222}y_2^4 + \frac{5}{2}\mathrm{K}_{211}y_2^2 - \frac{35}{3a^2}\mathrm{K}_{211}y_2^4\\
& + \frac{5}{2}\mathrm{K}_{222}y_1^2 - \frac{35}{3a^2}\mathrm{K}_{222}y_1^4 + 3\mathrm{K}_{211}y_1^2 - \frac{35}{3a^2}\mathrm{K}_{211}y_1^4 + \frac{10}{a^2}e_{22}y_2^3 + \frac{10}{a^2}e_{21}y_1^3 + \frac{1}{2}\mathrm{K}_{221}y_1y_2 + \frac{1}{2}\mathrm{K}_{212}y_1y_2
\end{aligned}
\tag{G.5}
$$

Using the above displacement fields, the homogenous part of the micro strain expresses versus the macro strain measures as

$$
\varepsilon_{11} = \mathrm{E}_{11} - \frac{5}{2}e_{11} + 6\mathrm{K}_{111}y_1 - \frac{140}{3a^2}\mathrm{K}_{111}y_1^3 + 5\mathrm{K}_{122}y_1 - \frac{140}{3a^2}\mathrm{K}_{122}y_1^3 + \frac{30}{a^2}e_{11}y_1^2 + \frac{1}{2}\mathrm{K}_{112}y_1 + \frac{1}{2}\mathrm{K}_{121}y_1 \tag{G.6}
$$

$$
\varepsilon_{22} = \mathrm{E}_{22} - \frac{5}{2}e_{22} + 6\mathrm{K}_{222}y_2 - \frac{140}{3a^2}\mathrm{K}_{222}y_2^3 + 5\mathrm{K}_{211}y_2 - \frac{140}{3a^2}\mathrm{K}_{211}y_2^3 + \frac{30}{a^2}e_{22}y_2^2 + \frac{1}{2}\mathrm{K}_{221}y_2 + \frac{1}{2}\mathrm{K}_{212}y_2 \tag{G.7}
$$

$$
\begin{aligned}
\varepsilon_{12} = {} & \frac{1}{2}\left(\mathrm{E}_{12} + \mathrm{E}_{21}\right) - \frac{5}{4}\left(e_{12} + e_{21}\right) + \frac{1}{4}y_1\left(\mathrm{K}_{112} + \mathrm{K}_{121}\right) + 3\mathrm{K}_{211}y_1 + \frac{5}{2}\mathrm{K}_{222}y_1 + \frac{5}{2}\mathrm{K}_{111}y_2 + 3\mathrm{K}_{122}y_2\\
& + \frac{1}{4}y_2\left(\mathrm{K}_{221} + \mathrm{K}_{212}\right) - \frac{70}{3a^3}y_1^3\left(\mathrm{K}_{211} + \mathrm{K}_{222}\right) - \frac{70}{3a^3}y_2^3\left(\mathrm{K}_{111} + \mathrm{K}_{122}\right) + \frac{15}{a^2}e_{21}x^2 + \frac{15}{a^2}e_{12}y^2
\end{aligned}
\tag{G.8}
$$

Appendix H

extended macrohomogeneity lemma for the micromorphic continuum

Let consider a symmetrical stress tensor field $\underset{\sim}{\boldsymbol{\sigma}}$ defined in the unit cell Y assumed to have a rectangular shape (Fig. H.1) and verifying the following BVP over the unit cell in the absence of body forces and with anti-periodic traction:

$$\left| \begin{array}{l} \underset{\sim}{\boldsymbol{\sigma}} \cdot \nabla_y = \mathbf{0} \\ \underset{\sim}{\boldsymbol{\sigma}}.\underline{\boldsymbol{n}} \quad \textit{opposite on the opposite edges of } \partial Y \end{array} \right. \tag{H.1}$$

The weak formulation of previous equations is obtained in a conventional way, multiplying the BVP Eq. H.1 with an arbitrary differentiable vector field $\underline{\boldsymbol{\omega}}$ and integrating over the unit cell domain Y, so that it holds

$$\int_Y (\nabla_y \cdot \underset{\sim}{\boldsymbol{\sigma}}) \cdot \underline{\boldsymbol{\omega}} \, dV_y = 0; \forall \underline{\boldsymbol{\omega}} \tag{H.2}$$

Integrating by parts Eq. H.2 and using the divergence theorem delivers the relation

$$-\int_Y \underset{\sim}{\boldsymbol{\sigma}} : (\underline{\boldsymbol{\omega}} \otimes \nabla_y) dV_y + \int_{\partial Y} \left(\underset{\sim}{\boldsymbol{\sigma}} \cdot \underline{\boldsymbol{n}} \right) \cdot \underline{\boldsymbol{\omega}} \, ds_y = 0 \tag{H.3}$$

Taking into account the boundary condition Eq. H.1 provides the weak formulation of the balance Eq. H.1 as

$$-\int_Y \underset{\sim}{\boldsymbol{\sigma}} : (\underline{\boldsymbol{\omega}} \otimes \nabla_y) dV_y + \sum_{i=1,2} \int_{\partial Y} \left(\underset{\sim}{\boldsymbol{\sigma}} \cdot \underline{\boldsymbol{n}} \right) \cdot \left[\!\left[\underline{\boldsymbol{\omega}} \right]\!\right]^{\delta} ds_y = 0; \forall \underline{\boldsymbol{\omega}} \tag{H.4}$$

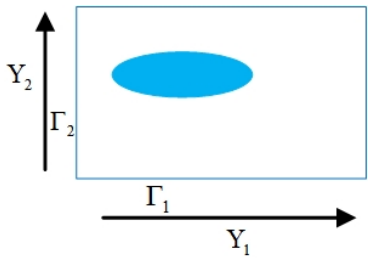

Figure H.1 Composite unit cell and the associated periodicity vectors Y_1,Y_2 in a 2D situation.

with the difference of the vector field $\underline{\boldsymbol{\omega}}$ taken over opposite edges of the unit cell:

$$\left[\left[\underline{\boldsymbol{\omega}}\right]\right]^{\delta} := \underline{\boldsymbol{\omega}}\left(\mathbf{y}+\boldsymbol{Y}^{\delta}\right) - \underline{\boldsymbol{\omega}}\left(\boldsymbol{Y}^{\delta}\right),\ \delta = 1{,}2 \tag{H.5}$$

By imposing $\left[\left[\underline{\boldsymbol{\omega}}\right]\right]^{\delta} = \text{cst}$ on the unit cell boundary $\partial\Omega^{\delta}, \delta = 1,2$ it holds

$$-\int_{Y} \underset{\sim}{\boldsymbol{\varrho}} : (\underline{\boldsymbol{\omega}} \otimes \nabla_y) dV_y + \sum_{i=1,2} \left[\left[\underline{\boldsymbol{\omega}}\right]\right]^{i} \cdot \int_{\partial Y} \left(\underset{\sim}{\boldsymbol{\varrho}}.\underline{\boldsymbol{n}}\right) ds_y = 0 \tag{H.6}$$

Assuming $\underline{\boldsymbol{\omega}}$ of the form of the homogenous displacement 3.69 with $\underline{\boldsymbol{\xi}} := \underline{\mathbf{y}} - \underline{\boldsymbol{x}}$ therein the relative position of the micropoints within the unit cell Y, it holds due to Eq. H.5 and Eq. H.6 the two following relations

$$\begin{aligned}
\omega_{i,j} &= \mathrm{E}_{ij} - e_{iq}\Gamma_{qj} + e_{iq}\Upsilon_{qklm}\left(\xi_k\xi_l(\mathrm{I}_2)_{mj} + \xi_k\xi_m(\mathrm{I}_2)_{lj} + \xi_l\xi_m(\mathrm{I}_2)_{kj}\right) \\
&+ \frac{1}{2}\mathrm{K}_{ikl}\left(\xi_k(\mathrm{I}_2)_{lj} + \xi_l(\mathrm{I}_2)_{kj}\right) - \frac{1}{4}\left(\mathrm{P}^{-1}\mathrm{K}_{ist}G_{st}\right)\Lambda_{rlmn}\Omega_{rlmnpq}\left(\xi_p(\mathrm{I}_2)_{qj} + \xi_q(\mathrm{I}_2)_{pj}\right) \\
&+ \frac{1}{4}\left(\mathrm{P}^{-1}\mathrm{K}_{ist}G_{st}\right)\Lambda_{rlmn}\left(\xi_r\xi_l\xi_m(\mathrm{I}_2)_{nj} + \xi_r\xi_l\xi_n(\mathrm{I}_2)_{mj} + \xi_r\xi_m\xi_n(\mathrm{I}_2)_{lj} + \xi_l\xi_m\xi_n(\mathrm{I}_2)_{rj}\right) \\
[\![\omega_i]\!]^{\delta} &= \mathrm{E}_{ij}Y_j^{\delta} + e_{iq}\left(\Upsilon_{qklm}Y_k^{\delta}Y_l^{\delta}Y_m^{\delta} - \Gamma_{qk}Y_k^{\delta}\right) + \frac{1}{2}\mathrm{K}_{ikl}Y_k^{\delta}Y_l^{\delta} + \frac{1}{4}\mathrm{P}^{-1}\mathrm{K}_{ist}G_{st}\Lambda_{rlmn}\left(Y_r^{\delta}Y_l^{\delta}Y_m^{\delta}Y_n^{\delta} - \Omega_{rlmnpq}Y_p^{\delta}Y_q^{\delta}\right)
\end{aligned} \tag{H.7}$$

Substituting Eq. 3.69 and Eq. H.7 into Eq. H.6 results after straightforward calculations in:

$$\forall \underset{\sim}{\mathbf{E}}(\mathbf{x}),\ \underset{\sim}{\mathbf{e}}(\mathbf{x}),\ \underset{\sim}{\mathbf{K}}(\mathbf{x}):\qquad \left\{-\int_{Y}\sigma_{ij}dV_y + \sum_{i=1,2}\left(\int_{\partial Y}(\sigma_{ik}n_k)\,ds_y\right)Y_j^{\delta}\right\}\mathrm{E}_{ij} = 0 \tag{H.8}$$

$$\left\{-\int_Y \sigma_{iq}\left(\Upsilon_{qklm}\left(\xi_k\xi_l(\mathrm{I}_2)_{mj} + \xi_k\xi_m(\mathrm{I}_2)_{lj} + \xi_l\xi_m(\mathrm{I}_2)_{kj}\right) - \Gamma_{qj}\right)dV_y + \sum_{i=1,2}\left(\left(\int_{\partial Y}(\sigma_{is}n_s)\,ds_y\right)\left(\Upsilon_{jklm}Y_k^{\delta}Y_l^{\delta}Y_m^{\delta} - \Gamma_{qj}Y_q^{\delta}\right)\right)\right\}e_{ij} = 0 \tag{H.9}$$

$$\begin{aligned}
&\left\{-\frac{1}{2}\int_Y \sigma_{il}\left(\xi_k(\mathrm{I}_2)_{lj} + \xi_l(\mathrm{I}_2)_{kj}\right)dV_y + \frac{1}{4}\mathrm{P}^{-1}\int_Y \sigma_{is}\left(G_{jk}\Lambda_{rlmn}\Omega_{rlmnpq}\left(\xi_p(\mathrm{I}_2)_{qs} + \xi_q(\mathrm{I}_2)_{ps}\right)\right)dV_y\right. \\
&-\frac{1}{4}\mathrm{P}^{-1}\int_Y \sigma_{is}\left(G_{jk}\Lambda_{rlmn}\left(\xi_r\xi_l\xi_m(\mathrm{I}_2)_{ns} + \xi_r\xi_l\xi_n(\mathrm{I}_2)_{ms} + \xi_r\xi_m\xi_n(\mathrm{I}_2)_{ls} + \xi_l\xi_m\xi_n(\mathrm{I}_2)_{rs}\right)\right)dV_y + \frac{1}{2}\sum_{i=1,2}\left(\left(\int_{\partial Y}(\sigma_{il}n_l)\,ds_y\right)Y_j^{\delta}Y_k^{\delta}\right) \\
&\left.-\frac{1}{4}\mathrm{P}^{-1}\sum_{i=1,2}\left(\left(\int_{\partial Y}(\sigma_{is}n_s)\,ds_y\right)G_{jk}\Lambda_{rlmn}\Omega_{rlmnpq}Y_p^{\delta}Y_q^{\delta}\right) + \frac{1}{4}\mathrm{P}^{-1}\sum_{i=1,2}\left(\left(\int_{\partial Y}(\sigma_{is}n_s)\,ds_y\right)G_{jk}\Lambda_{rlmn}Y_r^{\delta}Y_l^{\delta}Y_m^{\delta}Y_n^{\delta}\right)\right\}\mathrm{K}_{ijk} = 0
\end{aligned} \tag{H.10}$$

Eq. H.8 results in the elaboration of the static measures of the strain gradient effective continuum as the following sums over the unit cell boundaries:

$$\langle \underset{\sim}{\boldsymbol{\varrho}} \rangle_Y = \frac{1}{|Y|}\sum_{i=1,2}\left(\int_{\partial Y}\left(\underset{\sim}{\boldsymbol{\varrho}}\cdot\underline{\boldsymbol{n}}\right)ds\right)\otimes\underline{\boldsymbol{Y}}^{\delta} \tag{H.11}$$

Eq. H.9 can be written as

$$\left\{\int_Y \sigma_{iq}dV_y - \sum_{i=1,2}\left(\int_{\partial Y}(\sigma_{is}n_s)\,ds_y\right)Y_q^{\delta}\right\}\Gamma_{qj} + 3\left\{\int_Y \sigma_{ik}\left(\xi_l\xi_m\right)dV_y + \frac{1}{3}\sum_{i=1,2}\left(\int_{\partial Y}(\sigma_{is}n_s)\,ds_y\right)Y_k^{\delta}Y_l^{\delta}Y_m^{\delta}\right\}\Upsilon_{klmj} = 0 \tag{H.12}$$

Using relation H.11, the first part of Eq. H.12 is equal to zero, and the second part it rewrites

$$\left\langle\left(\underline{\boldsymbol{\xi}}\otimes\underline{\boldsymbol{\xi}}\right)\otimes\underset{\sim}{\boldsymbol{\varrho}}\right\rangle_Y = \frac{1}{|Y|}\sum_{i=1,2}\frac{1}{3}\left(\left(\int_{\partial Y}\left(\underset{\sim}{\boldsymbol{\varrho}}\cdot\underline{\boldsymbol{n}}\right)ds_y\right)\otimes\left(\underline{\boldsymbol{Y}}^{\delta}\otimes\underline{\boldsymbol{Y}}^{\delta}\otimes\underline{\boldsymbol{Y}}^{\delta}\right)\right) \tag{H.13}$$

Eq. H.10 can be decomposed into three parts as follows

$$
\begin{aligned}
&-\frac{2}{2}\left\{\int_Y \sigma_{ij}\left(\xi_k\right) dV_y - \frac{1}{2}\sum_{i=1,2}\left(\left(\int_{\partial Y}\left(\sigma_{il}n_l\right) ds_y\right) Y_j^\delta Y_k^\delta\right)\right\} \\
&+\frac{2}{2}\mathrm{P}^{-1}\left[G_{jk}\Lambda_{rlmn}\Omega_{rlmnpq}\right]\left\{\int_Y \sigma_{ip}\left(\xi_q\right) dV_y - \frac{1}{2}\sum_{i=1,2}\left(\left(\int_{\partial Y}\left(\sigma_{is}n_s\right) ds_y\right) Y_p^\delta Y_q^\delta\right)\right\} \\
&+\frac{4}{4}\mathrm{P}^{-1}\left[G_{jk}\Lambda_{rlmn}\right]\left\{\int_Y \sigma_{ir}\left(\xi_l\xi_m\xi_n\right) dV_y - \frac{1}{4}\sum_{i=1,2}\left(\left(\int_{\partial Y}\left(\sigma_{is}n_s\right) ds_y\right) Y_r^\delta Y_l^\delta Y_m^\delta Y_n^\delta\right)\right\} = 0
\end{aligned}
\tag{H.14}
$$

Setting each part of relation H.14 separately equal to zero leads to the following relations:

$$
\left\langle \underline{\underline{\boldsymbol{\xi}}} \otimes \underline{\underline{\boldsymbol{\varrho}}} \right\rangle_Y = \frac{1}{|Y|}\sum_{i=1,2}\frac{1}{2}\left(\left(\int_{\partial Y}\left(\underline{\underline{\boldsymbol{\varrho}}}\cdot\underline{\boldsymbol{n}}\right) ds_y\right)\otimes\left(\underline{\boldsymbol{Y}}^\delta\otimes\underline{\boldsymbol{Y}}^\delta\right)\right) \tag{H.15}
$$

$$
\left\langle \left(\underline{\underline{\boldsymbol{\xi}}}\otimes\underline{\underline{\boldsymbol{\xi}}}\otimes\underline{\underline{\boldsymbol{\xi}}}\right)\otimes\underline{\underline{\boldsymbol{\varrho}}} \right\rangle_Y = \frac{1}{|Y|}\sum_{i=1,2}\frac{1}{4}\left(\left(\int_{\partial Y}\left(\underline{\underline{\boldsymbol{\varrho}}}\cdot\underline{\boldsymbol{n}}\right) ds_y\right)\otimes\left(\underline{\boldsymbol{Y}}^\delta\otimes\underline{\boldsymbol{Y}}^\delta\otimes\underline{\boldsymbol{Y}}^\delta\otimes\underline{\boldsymbol{Y}}^\delta\right)\right) \tag{H.16}
$$

Using further the following relation [234]

$$
\sum_{i=1,2}\underline{\boldsymbol{N}}^i\otimes\underline{\boldsymbol{Y}}^j = |Y|\,\underline{\underline{\boldsymbol{I}}}_2 \tag{H.17}
$$

with $\underline{\underline{\boldsymbol{I}}}_2$ the second-order identity tensor, Eq. H.6 rewrites selecting a constant difference $\left[\!\left[\underline{\boldsymbol{\omega}}\right]\!\right]^{\delta}$ as

$$
\forall\underline{\boldsymbol{\omega}},\quad \left[\!\left[\underline{\boldsymbol{\omega}}\right]\!\right]^{\delta} = cst \rightarrow \int_Y \underline{\underline{\boldsymbol{\varrho}}} : \left(\underline{\boldsymbol{\omega}}\otimes\nabla_y\right) dV_y = \sum_{\delta,\beta=1,2}\delta_{\delta\beta}\left[\!\left[\underline{\boldsymbol{\omega}}\right]\!\right]^{\delta}\cdot\int_{\partial Y}\left(\underline{\underline{\boldsymbol{\varrho}}}\cdot\underline{\boldsymbol{n}}\right) ds_y \tag{H.18}
$$

Using the relation $\sum_{i=1,2}\underline{\boldsymbol{N}}^i.\underline{\boldsymbol{Y}}^j = |Y|\,\delta_{ij}$ arising as a consequence of Eq. H.17, see [234], relation H.18 rewrites:

$$
\int_Y \underline{\underline{\boldsymbol{\varrho}}} : \left(\underline{\boldsymbol{\omega}}\otimes\nabla_y\right) dV_y = \frac{1}{|Y|}\sum_{i,j=1,2}\underline{\boldsymbol{N}}^i\cdot\underline{\boldsymbol{Y}}^j\left[\!\left[\underline{\boldsymbol{\omega}}\right]\!\right]^{i}\cdot\int_{\partial Y}\left(\underline{\underline{\boldsymbol{\varrho}}}\cdot\underline{\boldsymbol{n}}\right) ds_y \tag{H.19}
$$

Eq. H.19 can be rewritten as

$$
\int_Y \underline{\underline{\boldsymbol{\varrho}}} : \left(\underline{\boldsymbol{\omega}}\otimes\nabla_y\right) dV_y = \frac{1}{|Y|}\sum_{i=1,2}\left(\left[\!\left[\underline{\boldsymbol{\omega}}\right]\!\right]^{i}\otimes\underline{\boldsymbol{N}}^i\right) : \sum_{j=1,2}\left(\int_{\partial Y}\left(\underline{\underline{\boldsymbol{\varrho}}}\cdot\underline{\boldsymbol{n}}\right) ds_y\otimes\underline{\boldsymbol{Y}}^j\right) \tag{H.20}
$$

Inserting relations Eq. H.7 into relation H.20 delivers the equality

$$
\begin{aligned}
\int_Y \underline{\underline{\boldsymbol{\varrho}}} : \left(\underline{\boldsymbol{\omega}}\otimes\nabla_y\right) dV_y = {}& \frac{1}{|Y|}\sum_{i=1,2}\left(\left(\underline{\underline{\mathbf{E}}}(\mathbf{x})\cdot\underline{\boldsymbol{Y}}^i\right)\otimes\underline{\boldsymbol{N}}^i\right) : \sum_{j=1,2}\left(\int_{\partial Y}\left(\underline{\underline{\boldsymbol{\varrho}}}\cdot\underline{\boldsymbol{n}}\right) ds_y\otimes\underline{\boldsymbol{Y}}^j\right) \\
&+\frac{3}{|Y|}\sum_{i=1,2}\left(\left(\underline{\underline{\mathbf{e}}}(\mathbf{x})\cdot\underline{\underline{\boldsymbol{\Gamma}}}\cdot\underline{\boldsymbol{Y}}^i\cdot\underline{\boldsymbol{Y}}^i\cdot\underline{\boldsymbol{Y}}^i\right)\otimes\underline{\boldsymbol{N}}^i\right) : \sum_{j=1,2}\frac{1}{3}\left(\int_{\partial Y}\left(\underline{\underline{\boldsymbol{\varrho}}}\cdot\underline{\boldsymbol{n}}\right) ds_y\otimes\underline{\boldsymbol{Y}}^j\right) - \frac{1}{|Y|}\sum_{i=1,2}\left(\left(\underline{\underline{\mathbf{e}}}(\mathbf{x})\cdot\underline{\underline{\boldsymbol{\Gamma}}}\cdot\underline{\boldsymbol{Y}}^i\right)\otimes\underline{\boldsymbol{N}}^i\right) : \sum_{j=1,2}\left(\int_{\partial Y}\left(\underline{\underline{\boldsymbol{\varrho}}}\cdot\underline{\boldsymbol{n}}\right) ds_y\otimes\underline{\boldsymbol{Y}}^j\right) \\
&+\frac{2}{|Y|}\sum_{i=1,2}\left(\left(\underline{\underline{\mathbf{K}}}(\mathbf{x})\cdot\underline{\boldsymbol{Y}}^i\cdot\underline{\boldsymbol{Y}}^i\right)\otimes\underline{\boldsymbol{N}}^i\right) : \sum_{j=1,2}\frac{1}{2}\left(\int_{\partial Y}\left(\underline{\underline{\boldsymbol{\varrho}}}\cdot\underline{\boldsymbol{n}}\right) ds_y\otimes\underline{\boldsymbol{Y}}^j\right) - \mathrm{P}^{-1}\frac{2}{|Y|}\sum_{i=1,2}\left(\left(\underline{\underline{\mathbf{K}}}(\mathbf{x}) : \underline{\underline{\mathbf{G}}}\otimes\underline{\underline{\underline{\underline{\boldsymbol{\Lambda}}}}} :: \underline{\underline{\underline{\underline{\boldsymbol{\Omega}}}}}\cdot\underline{\boldsymbol{Y}}^i\cdot\underline{\boldsymbol{Y}}^i\right)\otimes\underline{\boldsymbol{N}}^i\right) : \sum_{j=1,2}\frac{1}{2}\left(\int_{\partial Y}\left(\underline{\underline{\boldsymbol{\varrho}}}\cdot\underline{\boldsymbol{n}}\right) ds_y\otimes\underline{\boldsymbol{Y}}^j\right) \\
&+\mathrm{P}^{-1}\frac{4}{|Y|}\sum_{i=1,2}\left(\left(\underline{\underline{\mathbf{K}}}(\mathbf{x}) : \underline{\underline{\mathbf{G}}}\otimes\underline{\underline{\underline{\underline{\boldsymbol{\Lambda}}}}}\cdot\underline{\boldsymbol{Y}}^i\cdot\underline{\boldsymbol{Y}}^i\cdot\underline{\boldsymbol{Y}}^i\cdot\underline{\boldsymbol{Y}}^i\right)\otimes\underline{\boldsymbol{N}}^i\right) : \sum_{j=1,2}\frac{1}{4}\left(\int_{\partial Y}\left(\underline{\underline{\boldsymbol{\varrho}}}\cdot\underline{\boldsymbol{n}}\right) ds_y\otimes\underline{\boldsymbol{Y}}^j\right)
\end{aligned}
\tag{H.21}
$$

Using the relation $\underline{\boldsymbol{N}}^i \cdot \underline{\boldsymbol{Y}}^j = |Y|\,\delta_{ij}$, Eq. H.21 can be rewritten after straightforward calculations as

$$
\begin{aligned}
\int_Y \underline{\underline{\boldsymbol{\sigma}}} : (\underline{\boldsymbol{\omega}} \otimes \nabla_y) dV_y = & \frac{1}{|Y|} \sum_{i=1,2} \left(\left(\underline{\underline{\mathbf{E}}}(\mathbf{x}) \cdot \underline{\boldsymbol{Y}}^i \right) \otimes \underline{\boldsymbol{N}}^i \right) : \sum_{j=1,2} \left(\int_{\partial Y} \left(\underline{\underline{\boldsymbol{\sigma}}} \cdot \underline{\boldsymbol{n}} \right) ds_y \otimes \underline{\boldsymbol{Y}}^j \right) \\
& + \frac{3}{|Y|} \sum_{i=1,2} \left(\left(\underline{\underline{\mathbf{e}}}(\mathbf{x}) \cdot \underline{\underline{\underline{\Upsilon}}} \cdot \underline{\boldsymbol{Y}}^i \right) \otimes \underline{\boldsymbol{N}}^i \right) :: \sum_{j=1,2} \frac{1}{3} \left(\int_{\partial Y} \left(\underline{\underline{\boldsymbol{\sigma}}} \cdot \underline{\boldsymbol{n}} \right) ds_y \otimes \underline{\boldsymbol{Y}}^j \otimes \underline{\boldsymbol{Y}}^j \otimes \underline{\boldsymbol{Y}}^j \right) \\
& - \frac{1}{|Y|} \sum_{i=1,2} \left(\left(\underline{\underline{\mathbf{e}}}(\mathbf{x}) \cdot \underline{\underline{\boldsymbol{\Gamma}}} \cdot \underline{\boldsymbol{Y}}^i \right) \otimes \underline{\boldsymbol{N}}^i \right) : \sum_{j=1,2} \left(\int_{\partial Y} \left(\underline{\underline{\boldsymbol{\sigma}}} \cdot \underline{\boldsymbol{n}} \right) ds_y \otimes \underline{\boldsymbol{Y}}^j \right) \\
& + \frac{2}{|Y|} \sum_{i=1,2} \left(\left(\underline{\underline{\underline{\mathrm{K}}}}(\mathbf{x}) \cdot \underline{\boldsymbol{Y}}^i \right) \otimes \underline{\boldsymbol{N}}^i \right) \therefore \sum_{j=1,2} \frac{1}{2} \left(\int_{\partial Y} \left(\underline{\underline{\boldsymbol{\sigma}}} \cdot \underline{\boldsymbol{n}} \right) ds_y \otimes \underline{\boldsymbol{Y}}^j \otimes \underline{\boldsymbol{Y}}^j \right) \\
& - \mathrm{P}^{-1} \frac{2}{|Y|} \sum_{i=1,2} \left(\left(\underline{\underline{\underline{\mathrm{K}}}}(\mathbf{x}) : \underline{\underline{\underline{\underline{\mathbf{G}}}}} \otimes \underline{\underline{\underline{\underline{\boldsymbol{A}}}}} :: \underline{\underline{\underline{\underline{\boldsymbol{\Omega}}}}} \cdot \underline{\boldsymbol{Y}}^i \right) \otimes \underline{\boldsymbol{N}}^i \right) \therefore \sum_{j=1,2} \frac{1}{2} \left(\int_{\partial Y} \left(\underline{\underline{\boldsymbol{\sigma}}} \cdot \underline{\boldsymbol{n}} \right) ds_y \otimes \underline{\boldsymbol{Y}}^j \right) \\
& + \mathrm{P}^{-1} \frac{4}{|Y|} \sum_{i=1,2} \left(\left(\underline{\underline{\underline{\mathrm{K}}}}(\mathbf{x}) : \underline{\underline{\underline{\underline{\mathbf{G}}}}} \otimes \underline{\underline{\underline{\underline{\boldsymbol{A}}}}} \cdot \underline{\boldsymbol{Y}}^i \right) \otimes \underline{\boldsymbol{N}}^i \right) :: \cdot \sum_{j=1,2} \frac{1}{4} \left(\int_{\partial Y} \left(\underline{\underline{\boldsymbol{\sigma}}} \cdot \underline{\boldsymbol{n}} \right) ds_y \otimes \underline{\boldsymbol{Y}}^j \otimes \underline{\boldsymbol{Y}}^j \otimes \underline{\boldsymbol{Y}}^j \otimes \underline{\boldsymbol{Y}}^j \right) \\
& = \langle \underline{\underline{\boldsymbol{\sigma}}} \rangle_Y : \underline{\underline{\mathbf{E}}}(\mathbf{x}) + \left[3 \left\langle \underline{\boldsymbol{\xi}} \otimes \underline{\boldsymbol{\xi}} \otimes \underline{\underline{\boldsymbol{\sigma}}} \right\rangle_Y \therefore \underline{\underline{\underline{\Upsilon}}} - \langle \underline{\underline{\boldsymbol{\sigma}}} \rangle_Y \cdot \underline{\underline{\boldsymbol{\Gamma}}} \right] : \underline{\underline{\mathbf{e}}}(\mathbf{x}) \\
& + \left[2 \left\langle \underline{\boldsymbol{\xi}} \otimes \underline{\underline{\boldsymbol{\sigma}}} \right\rangle_Y - 2\mathrm{P}^{-1} \underline{\underline{\underline{\underline{\mathbf{G}}}}} \otimes \underline{\underline{\underline{\underline{\boldsymbol{A}}}}} :: \left(\underline{\underline{\underline{\underline{\boldsymbol{\Omega}}}}} : \left\langle \underline{\boldsymbol{\xi}} \otimes \underline{\underline{\boldsymbol{\sigma}}} \right\rangle_Y + 2 \left\langle \underline{\boldsymbol{\xi}} \otimes \underline{\boldsymbol{\xi}} \otimes \underline{\boldsymbol{\xi}} \otimes \underline{\underline{\boldsymbol{\sigma}}} \right\rangle_Y \right) \right] \therefore \underline{\underline{\underline{\mathrm{K}}}}(\mathbf{x})
\end{aligned}
\tag{H.22}
$$

The previous relation constitutes Hill lemma for the strain gradient effective continuum. From this relation, one can define the new stress measures conjugated to the macroscopic kinematic variables, tensors $\underline{\underline{\mathbf{e}}}(\mathbf{x})$, $\underline{\underline{\underline{\mathrm{K}}}}(\mathbf{x})$ as the relative stress and hyperstress tensors

$$
\underline{\underline{\underline{\boldsymbol{s}}}} := 3 \left\langle \underline{\boldsymbol{\xi}} \otimes \underline{\boldsymbol{\xi}} \otimes \underline{\underline{\boldsymbol{\sigma}}} \right\rangle_Y \therefore \underline{\underline{\underline{\Upsilon}}} - \langle \underline{\underline{\boldsymbol{\sigma}}} \rangle_Y \cdot \underline{\underline{\boldsymbol{\Gamma}}} \tag{H.23}
$$

$$
\underline{\underline{\underline{\underline{\boldsymbol{S}}}}} := 2 \left\langle \underline{\boldsymbol{\xi}} \otimes \underline{\underline{\boldsymbol{\sigma}}} \right\rangle_Y - 2\mathrm{P}^{-1} \underline{\underline{\underline{\underline{\boldsymbol{G}}}}} \otimes \underline{\underline{\underline{\underline{\boldsymbol{A}}}}} :: \left(\underline{\underline{\underline{\underline{\boldsymbol{\Omega}}}}} : \left\langle \underline{\boldsymbol{\xi}} \otimes \underline{\underline{\boldsymbol{\sigma}}} \right\rangle_Y + 2 \left\langle \underline{\boldsymbol{\xi}} \otimes \underline{\boldsymbol{\xi}} \otimes \underline{\boldsymbol{\xi}} \otimes \underline{\underline{\boldsymbol{\sigma}}} \right\rangle_Y \right) \tag{H.24}
$$

Appendix I

Index computations to the effective micromorphic moduli

The energy functional in Eq. 3.80 writes in index format as

$$\begin{aligned} F\left[\tilde{\boldsymbol{u}}\right] &:= \frac{1}{2}\int\limits_{Y} C_{\alpha\delta qp}\left(a_{\alpha\beta\gamma,\delta}E_{\beta\gamma}+b_{\alpha\beta\gamma,\delta}e_{\beta\gamma}+c_{\alpha\beta\gamma\lambda,\delta}K_{\beta\gamma\lambda}+\tilde{u}_{\alpha,\delta}\right)\left(a_{qij,p}E_{ij}+b_{qij,p}e_{ij}+c_{qijk,p}K_{ijk}+\tilde{u}_{q,p}\right)dV_y \\ &= \frac{1}{2}\int\limits_{Y} C_{\alpha\delta qp}\left(a_{qij,p}E_{ij}+b_{qij,p}e_{ij}+c_{qijk,p}K_{ijk}+\tilde{u}_{q,p}\right)\left(a_{\alpha\beta\gamma,\delta}E_{\beta\gamma}+b_{\alpha\beta\gamma,\delta}e_{\beta\gamma}+c_{\alpha\beta\gamma\lambda,\delta}K_{\beta\gamma\lambda}+\tilde{u}_{\alpha,\delta}\right)dV_y \end{aligned} \tag{I.1}$$

The fluctuating part of the strain can be expressed as

$$\tilde{u}_{q,p} = H^{E}_{qij,p}E_{ij} + H^{e}_{qij,p}e_{ij} + H^{K}_{qijk,p}K_{ijk} \tag{I.2}$$

Defining the microstrain as the symmetric part of the displacement gradient leads to the following definition,

$$\varepsilon_{q,p} = u^{s}_{q,p} = u^{\mathrm{hom}}_{q,p} + \tilde{u}^{s}_{q,p} \equiv \mathrm{A}^{\mathrm{E}}_{qij,p}\mathrm{E}_{ij} + \mathrm{A}^{e}_{qij,p}e_{ij} + \mathrm{A}^{\mathrm{K}}_{qijk,p}\mathrm{K}_{ijk} \tag{I.3}$$

where $\mathrm{A}^{\mathrm{E}}_{qij,p}$, $\mathrm{A}^{e}_{qij,p}$ and $\mathrm{A}^{\mathrm{K}}_{qijk,p}$ represent the localization tensors relating the microstrains to the macroscopic kinematic variables, viz.

$$\begin{aligned} \mathrm{A}^{\mathrm{E}}_{qij,p} &= a_{qij,p} + H^{E}_{qij,p} \\ \mathrm{A}^{e}_{qij,p} &= b_{qij,p} + H^{e}_{qij,p} \\ \mathrm{A}^{\mathrm{K}}_{qijk,p} &= c_{qijk,p} + H^{K}_{qijk,p} \end{aligned} \tag{I.4}$$

This writing entails the following expression of the stress, relative stress, and hyperstress in index format, successively:

$$\begin{aligned}\bar{\sigma}_{ij} &= \frac{\partial}{\partial E_{ij}}\left\{\frac{1}{2}\int\limits_Y C_{\alpha\delta qp}\left(\mathrm{A}^{\mathrm{E}}_{qij,p}E_{ij}+\mathrm{A}^{e}_{qij,p}e_{ij}+\mathrm{A}^{\mathrm{K}}_{qijk,p}K_{ijk}\right)\left(\mathrm{A}^{\mathrm{E}}_{\alpha\beta\gamma,\delta}E_{\beta\gamma}+\mathrm{A}^{e}_{\alpha\beta\gamma,\delta}e_{\beta\gamma}+\mathrm{A}^{\mathrm{K}}_{\alpha\beta\gamma\lambda,\delta}K_{\beta\gamma\lambda}\right)dV_y\right\}\\ &= \int\limits_Y C_{\alpha\delta qp}\left(\mathrm{A}^{\mathrm{E}}_{\alpha\beta\gamma,\delta}E_{\beta\gamma}+\mathrm{A}^{e}_{\alpha\beta\gamma,\delta}e_{\beta\gamma}+\mathrm{A}^{\mathrm{K}}_{\alpha\beta\gamma\lambda,\delta}K_{\beta\gamma\lambda}\right)\mathrm{A}^{\mathrm{E}}_{qij,p}dV_y\\ &= \left\{\int\limits_Y C_{\alpha\delta qp}\mathrm{A}^{\mathrm{E}}_{\alpha\beta\gamma,\delta}\mathrm{A}^{\mathrm{E}}_{qij,p}dV_y\right\}E_{\beta\gamma}+\left\{\int\limits_Y C_{\alpha\delta qp}\mathrm{A}^{e}_{\alpha\beta\gamma,\delta}\mathrm{A}^{\mathrm{E}}_{qij,p}dV_y\right\}e_{\beta\gamma}+\left\{\int\limits_Y C_{\alpha\delta qp}\mathrm{A}^{\mathrm{K}}_{\alpha\beta\gamma\lambda,\delta}\mathrm{A}^{\mathrm{E}}_{qij,p}dV_y\right\}K_{\beta\gamma\lambda}\end{aligned} \tag{I.5}$$

$$\begin{aligned}s_{ij} &= \frac{\partial}{\partial e_{ij}}\left\{\frac{1}{2}\int\limits_Y C_{\alpha\delta qp}\left(\mathrm{A}^{\mathrm{E}}_{qij,p}E_{ij}+\mathrm{A}^{e}_{qij,p}e_{ij}+\mathrm{A}^{\mathrm{K}}_{qijk,p}K_{ijk}\right)\left(\mathrm{A}^{\mathrm{E}}_{\alpha\beta\gamma,\delta}E_{\beta\gamma}+\mathrm{A}^{e}_{\alpha\beta\gamma,\delta}e_{\beta\gamma}+\mathrm{A}^{\mathrm{K}}_{\alpha\beta\gamma\lambda,\delta}K_{\beta\gamma\lambda}\right)dV_y\right\}\\ &= \int\limits_Y C_{\alpha\delta qp}\left(\mathrm{A}^{\mathrm{E}}_{\alpha\beta\gamma,\delta}E_{\beta\gamma}+\mathrm{A}^{e}_{\alpha\beta\gamma,\delta}e_{\beta\gamma}+\mathrm{A}^{\mathrm{K}}_{\alpha\beta\gamma\lambda,\delta}K_{\beta\gamma\lambda}\right)\mathrm{A}^{e}_{qij,p}dV_y\\ &= \left\{\int\limits_Y C_{\alpha\delta qp}\mathrm{A}^{\mathrm{E}}_{\alpha\beta\gamma,\delta}\mathrm{A}^{e}_{qij,p}dV_y\right\}E_{\beta\gamma}+\left\{\int\limits_Y C_{\alpha\delta qp}\mathrm{A}^{e}_{\alpha\beta\gamma,\delta}\mathrm{A}^{e}_{qij,p}dV_y\right\}e_{\beta\gamma}+\left\{\int\limits_Y C_{\alpha\delta qp}\mathrm{A}^{\mathrm{K}}_{\alpha\beta\gamma\lambda,\delta}\mathrm{A}^{e}_{qij,p}dV_y\right\}K_{\beta\gamma\lambda}\end{aligned} \tag{I.6}$$

$$\begin{aligned}S_{ijk} &= \frac{\partial}{\partial \mathrm{K}_{ijk}}\left\{\frac{1}{2}\int\limits_Y C_{\alpha\delta qp}\left(\mathrm{A}^{\mathrm{E}}_{qij,p}E_{ij}+\mathrm{A}^{e}_{qij,p}e_{ij}+\mathrm{A}^{\mathrm{K}}_{qijk,p}K_{ijk}\right)\left(\mathrm{A}^{\mathrm{E}}_{\alpha\beta\gamma,\delta}E_{\beta\gamma}+\mathrm{A}^{e}_{\alpha\beta\gamma,\delta}e_{\beta\gamma}+\mathrm{A}^{\mathrm{K}}_{\alpha\beta\gamma\lambda,\delta}K_{\beta\gamma\lambda}\right)dV_y\right\}\\ &= \int\limits_Y C_{\alpha\delta qp}\left(\mathrm{A}^{\mathrm{E}}_{\alpha\beta\gamma,\delta}E_{\beta\gamma}+\mathrm{A}^{e}_{\alpha\beta\gamma,\delta}e_{\beta\gamma}+\mathrm{A}^{\mathrm{K}}_{\alpha\beta\gamma\lambda,\delta}K_{\beta\gamma\lambda}\right)\mathrm{A}^{\mathrm{K}}_{qijk,p}dV_y\\ &= \left\{\int\limits_Y C_{\alpha\delta qp}\mathrm{A}^{\mathrm{E}}_{\alpha\beta\gamma,\delta}\mathrm{A}^{\mathrm{K}}_{qijk,p}dV_y\right\}E_{\beta\gamma}+\left\{\int\limits_Y C_{\alpha\delta qp}\mathrm{A}^{e}_{\alpha\beta\gamma,\delta}\mathrm{A}^{\mathrm{K}}_{qijk,p}dV_y\right\}e_{\beta\gamma}+\left\{\int\limits_Y C_{\alpha\delta qp}\mathrm{A}^{\mathrm{K}}_{\alpha\beta\gamma\lambda,\delta}\mathrm{A}^{\mathrm{K}}_{qijk,p}dV_y\right\}K_{\beta\gamma\lambda}\end{aligned} \tag{I.7}$$

Expressions I.5- I.7 together with the symmetry in the average quantities therein lead to the constitutive homogenized tensors written in index format:

$$\begin{aligned}C^{\mathrm{hom}}_{ij\beta\gamma} &= \int\limits_Y \mathrm{A}^{\mathrm{E}}_{\alpha\beta\gamma,\delta}C_{\alpha\delta qp}\mathrm{A}^{\mathrm{E}}_{qij,p}dV_y,\\ B^{\mathrm{hom}}_{ij\beta\gamma} &= \int\limits_Y \mathrm{A}^{e}_{\alpha\beta\gamma,\delta}C_{\alpha\delta qp}\mathrm{A}^{\mathrm{E}}_{qij,p}dV_y,\\ D^{\mathrm{hom}}_{ij\beta\gamma\lambda} &= \int\limits_Y \mathrm{A}^{\mathrm{K}}_{\alpha\beta\gamma\lambda,\delta}C_{\alpha\delta qp}\mathrm{A}^{\mathrm{E}}_{qij,p}dV_y,\\ H^{\mathrm{hom}}_{ij\beta\gamma} &= \int\limits_Y \mathrm{A}^{e}_{\alpha\beta\gamma,\delta}C_{\alpha\delta qp}\mathrm{A}^{e}_{qij,p}dV_y,\\ G^{\mathrm{hom}}_{ij\beta\gamma\lambda} &= \int\limits_Y \mathrm{A}^{\mathrm{K}}_{\alpha\beta\gamma\lambda,\delta}C_{\alpha\delta qp}\mathrm{A}^{e}_{\alpha\beta\gamma,\delta}dV_y,\\ K^{\mathrm{hom}}_{ijk\beta\gamma\lambda} &= \int\limits_Y \mathrm{A}^{\mathrm{K}}_{\alpha\beta\gamma\lambda,\delta}C_{\alpha\delta qp}\mathrm{A}^{\mathrm{K}}_{qijk,p}dV_y\end{aligned} \tag{I.8}$$

Appendix J

Exact C-CST shape functions

The elements of the shape functions corresponding to the exact solution of consistent couple stress Timoshenko beam are as follows:

$\boldsymbol{N}_{u_z} = [U_1\ U_2\ U_3\ U_4\ U_5\ U_6]$

$\boldsymbol{N}_{\phi} = [U_7\ U_8\ U_9\ U_{10}\ U_{11}\ U_{12}]$

$$U_1 = \frac{\lambda\left(L-x\right)\left(L^2a_1a_3+2L^2a_3^2+Lxa_1a_3+2Lxa_3^2-2x^2a_1a_3-4x^2a_3^2-24a_1^2a_2-48a_1a_2a_3-24a_2a_3^2\right)\sinh\left(\lambda L\right)}{\Phi_1}$$
$$+\frac{24a_2(a_1+a_3)^2\left(\cosh\left(\lambda L\right)-\cosh\left(\lambda x\right)+cosh\left(\lambda\left(L-x\right)\right)-1\right)}{\Phi_1}$$

$$U_2 = \frac{\lambda(a_1+a_3)}{\Phi_1 L\sinh(\lambda L)(a_1+2a_3)^2}\left\{\left[\lambda a_1a_2(2La_3)\Phi_2\sinh\left(\lambda L\right)+L^2a_3\left(\cosh(\lambda L)-1\right)\Phi_3\right]x^3\right.$$
$$+\left[\lambda a_1a_2\left((-3L^2a_3)\Phi_2+24a_2\Phi_4\right)\sinh\left(\lambda L\right)+L\left(\cosh(\lambda L)-1\right)\left(-2L^2a_3\Phi_3+12a_2\Phi_5\right)\right]x^2$$
$$+\left[\lambda a_1a_2(-24La_2)\Phi_4\sinh\left(\lambda L\right)+L\left(\cosh(\lambda L)-1\right)\left(L^3a_3\Phi_3-12La_2\Phi_5\right)\right]x$$
$$+\lambda a_1a_2\left(\left(\cosh(\lambda(L-x))-\cosh(\lambda L)\right)\Phi_6+12L^2a_2\Phi_4\right)\sinh\left(\lambda L\right)$$
$$\left.-\ 24La_1{a_2}^2\left(\cosh(\lambda(L-x))+\cosh(\lambda x)-\cosh(\lambda L)-1\right)\Phi_4\right\}$$

$$U_3 = \frac{\lambda(a_1+a_3)}{\Phi_1 L\sinh(\lambda L)(a_1+2a_3)^2}\left\{\left[\lambda a_1a_2(2La_3)\Phi_2\sinh\left(\lambda L\right)+L^2a_3\left(\cosh(\lambda L)-1\right)\Phi_3\right]x^3\right.$$
$$+\left[\lambda a_1a_2\left((-3L^2a_3)\Phi_2-24a_2\Phi_4\right)\sinh\left(\lambda L\right)-L\left(\cosh(\lambda L)-1\right)\left(L^2a_3\Phi_3+12a_2\Phi_5\right)\right]x^2$$
$$+\left[\lambda a_1a_2(4La_2)\Phi_4\sinh\left(\lambda L\right)+L\left(\cosh(\lambda L)-1\right)(12La_2\Phi_5)\right]x$$
$$+\lambda a_1a_2\left(\left(\cosh(\lambda(L-x))-\cosh(\lambda L)\right)\Phi_6+12L^2a_2\Phi_4\right)\sinh\left(\lambda L\right)$$
$$\left.+\ 24La_1{a_2}^2\left(\cosh(\lambda(L-x))+\cosh(\lambda x)-\cosh(\lambda L)-1\right)\Phi_4\right\}$$

$U_4 = 1 - U_1$

$$U_5 = \frac{\lambda(a_1+a_3)}{\Phi_1 L\sinh(\lambda L)(a_1+2a_3)^2}\left\{\left[\lambda a_1 a_2(2La_3)\Phi_2\sinh(\lambda L)+L^2a_3\left(\cosh(\lambda L)-1\right)\Phi_3\right]x^3\right.$$
$$+\left[\lambda a_1a_2\left((-3L^2a_3)\Phi_2-24a_2\Phi_4\right)\sinh(\lambda L)-L\left(\cosh(\lambda L)-1\right)\left(L^2a_3\Phi_3+12a_2\Phi_5\right)\right]x^2$$
$$+\left[\lambda a_1a_2(24La_2)\Phi_4\sinh(\lambda L)+L\left(\cosh(\lambda L)-1\right)(12La_2\Phi_5)\right]x$$
$$+\lambda a_1a_2\left(\left(\cosh(\lambda(L-x))-\cosh(\lambda L)\right)(-12L^2a_2)(a_1+a_3)^2-\left(\cosh(\lambda L)-1\right)\Phi_6\right)\sinh(\lambda L)$$
$$\left.+\,24La_1{a_2}^2\left(\cosh(\lambda(L-x))+\cosh(\lambda x)-\cosh(\lambda L)-1\right)\Phi_4\right\}$$

$$U_6 = \frac{-\lambda}{\Phi_1 L\sinh(\lambda L)(a_1+2a_3)^2}\left\{\left[\lambda a_1a_2(2La_3)(a_1+a_3)\Phi_2\sinh(\lambda L)-L^2{a_3}^2\left(\cosh(\lambda L)-1\right)\Phi_3\right]x^3\right.$$
$$+\left[\lambda a_1a_2\left((-3L^2a_3)(a_1+a_3)\Phi_2+24a_2a_3\Phi_4\right)\sinh(\lambda L)-L\left(\cosh(\lambda L)-1\right)\left(L^2{a_3}^2\Phi_3+12a_2a_3\Phi_5\right)\right]x^2$$
$$+\left[\lambda a_1a_2(24La_2)(a_1+a_3)\Phi_4\sinh(\lambda L)-L\left(\cosh(\lambda L)-1\right)(12La_2a_3\Phi_5)\right]x$$
$$+\lambda a_1a_2\left(\left(-\cosh(\lambda(L-x))+\cosh(\lambda L)\right)(-12L^2a_2a_3)(a_1+a_3)^2+L^4a_3(a_1+a_3)\Phi_2-(12L^2a_2)(2a_1+3a_3)\Phi_4\right)\sinh(\lambda L)$$
$$\left.+\,24La_1{a_2}^2(a_1+a_3)\left(\cosh(\lambda(L-x))+\cosh(\lambda x)-\cosh(\lambda L)-1\right)\Phi_4\right\}$$

$$U_7 = -\frac{6\lambda a_3}{\Phi_1}\left[-\left(a_1+2a_3\right)\sinh(\lambda L)\,x^2+L\left(a_1+2a_3\right)\sinh(\lambda L)\,x+4a_2\left(a_1+a_3\right)\left(\sinh(\lambda L)-\sinh(\lambda x)-\sinh\left(\lambda\left(L-x\right)\right)\right)\right]$$

$$U_8 = \frac{1}{\Phi_1 L\sinh(\lambda L)(a_1+2a_3)^2}\left\{3La_3(a_1+a_3)\Phi_2\left[-2\sinh(\lambda L)+L\lambda\right]x^2\right.$$
$$+\left[\left((6L^2a_3)\Phi_2-48a_2\Phi_4\right)\left(a_1+a_3\right)\sinh(\lambda L)-4\lambda L\left(\cosh(\lambda L)+1\right)\left(a_1+a_3\right)\left(6a_2\Phi_4-L^2a_3\Phi_2\right)\right]x$$
$$+\left((24a_2)(2a_1+3a_3)\Phi_4-\sinh(\lambda(L-x))(a_3\lambda)\Phi_6+\sinh(\lambda x)\left(12L^2a_2a_3\right)\left(a_1+a_3\right)^2\right)\sinh(\lambda L)$$
$$\left.+\left(\sinh(\lambda(L-x))-\sinh(\lambda x)\right)(24La_2a_3)\Phi_4+L^2a_3\lambda\left(\cosh(\lambda L)+1\right)\left(L^2(a_1+a_3)\Phi_2-12(2a_1+3a_3)\Phi_4\right)\right\}$$

$$U_9 = \frac{a_3}{\Phi_1 L\sinh(\lambda L)(a_1+2a_3)^2}\left\{3L\Phi_2\left[2(a_1+a_3)\sinh(\lambda L)+La_3\lambda\left(\cosh(\lambda L)+1\right)\right]x^2\right.$$
$$+\left[\left((-6L^2)(a_1+a_3)\Phi_2-48a_2\Phi_4\right)\sinh(\lambda L)+4\lambda L\left(\cosh(\lambda L)+1\right)\left(6a_2\Phi_4-L^2a_3\Phi_2\right)\right]x$$
$$+\left((24La_2)\Phi_4+\sinh(\lambda(L-x))\left(\Phi_6+12L^2a_2(a_1+a_3)(a_1+2a_3)\right)+\sinh(\lambda x)\left(12L^2a_2a_3\lambda\right)(a_1+a_3)\right)\sinh(\lambda L)$$
$$\left.+\left(-\sinh(\lambda(L-x))+\sinh(\lambda x)\right)(12La_2)\Phi_4-12L^2a_2\left(\cosh(\lambda L)+1\right)\left(a_1+a_3\right)\Phi_2-\lambda\left(\cosh^2(\lambda L)-1\right)\Phi_6\right\}$$

$$U_{10} = -U_7$$

$$U_{11} = \frac{1}{\Phi_1 L\sinh(\lambda L)(a_1+2a_3)^2}\left\{3La_3(a_1+a_3)\Phi_2\left[-2\sinh(\lambda L)+L\lambda\right]x^2\right.$$
$$+\left[\left((6L^2a_3)\Phi_2+48a_2\Phi_4\right)\left(a_1+a_3\right)\sinh(\lambda L)-2\lambda L\left(\cosh(\lambda L)+1\right)\left(a_1+a_3\right)\left(12a_2\Phi_4+L^2a_3\Phi_2\right)\right]x$$
$$+\left((24La_2a_3)\Phi_4-\sinh(\lambda x)(a_3\lambda)\Phi_6+\sinh\left(\lambda(L-x)\right)\left(12L^2a_2a_3\lambda\right)(a_1+a_3)^2\right)\sinh(\lambda L)$$
$$\left.+\left(-\sinh(\lambda(L-x))+\sinh(\lambda x)\right)(24La_2a_3)\Phi_4-12L^2a_2\lambda\left(\cosh(\lambda L)+1\right)\Phi_4\right\}$$

$$U_{12} = \frac{-a_3}{\Phi_1 L\sinh(\lambda L)(a_1+2a_3)^2}\left\{-3L\Phi_2\left[2(a_1+a_3)\sinh(\lambda L)+La_3\lambda\left(\cosh(\lambda L)+1\right)\right]x^2\right.$$
$$+\left[\left((6L^2)(a_1+a_3)\Phi_2-48a_2\Phi_4\right)\sinh(\lambda L)+2\lambda L\left(\cosh(\lambda L)+1\right)\left(12a_2\Phi_4+L^2a_3\Phi_2\right)\right]x$$
$$+\left((24La_2)\Phi_4-\lambda\sinh(\lambda x)\left(\Phi_6+12L^2a_2(a_1+a_3)(a_1+2a_3)\right)-\sinh\left(\lambda(L-x)\right)\left(12L^2a_2a_3\lambda\right)(a_1+a_3)\right)\sinh(\lambda L)$$
$$\left.+\left(-\sinh(\lambda(L-x))+\sinh(\lambda x)\right)(24La_2)\Phi_4+12L^2a_2a_3\lambda\left(\cosh^2(\lambda L)-1\right)\left(a_1+a_3\right)\right\}$$

$$\Phi_1 = \lambda L \left(L^2 a_1 a_3 + 2L^2 a_3^2 - 24 a_2 (a_1 + a_3)^2 \right) sinh\left(\lambda L\right) + 48 a_2 \Phi_4$$

$$\Phi_2 = (a_1 + 2a_3)\left(\cosh\left(\lambda L\right) - 1\right)$$

$$\Phi_3 = (a_1 + 2a_3)^2 \left(\cosh(\lambda L) + 1\right)$$

$$\Phi_4 = (a_1 + a_3)^2 \left(\cosh(\lambda L) - 1\right)$$

$$\Phi_5 = (a_1 + a_3)^2 (a_1 + 2a_3)\left(\cosh(\lambda L) + 1\right)$$

$$\Phi_6 = -L^2 \left(L^2 a_1 a_3 + 2L^2 {a_3}^2 - 12 a_2 (a_1 + a_3)^2 \right)$$

Appendix K

Stiffness matrix of the C-CST Ritz approximate solution

The coefficients of the stiffness matrix, Eq. 4.88, related to the Ritz approximate solution are

$$K'_{11} = \frac{5k_sAG\left[21\alpha^2\beta^2 + 56\alpha\beta\left(\alpha+2\beta\right) + 12(\alpha+2\beta)^2\right]}{L\left[56(\alpha+\beta)^2 + 35\alpha\beta\left(6\alpha+3\beta+8\right) + 60\left(\alpha+2\beta\right)\right]}$$

$$K'_{12} = \frac{7\left(\alpha+\beta\right)\left(8\beta+4\alpha+15\alpha\beta\right)}{k_\mu k_sAGL^4l^2\left[56(\alpha+\beta)^2 + 35\alpha\beta\left(6\alpha+3\beta+8\right) + 60\left(\alpha+2\beta\right)\right]}$$

$$K'_{13} = \frac{k_sAG\left[105\alpha^2\beta^2 + 70\alpha\beta\left(\alpha+5\beta\right) + 4\left(\alpha^2+32\beta^2+18\alpha\beta\right)\right]}{2\left[56(\alpha+\beta)^2 + 35\alpha\beta\left(6\alpha+3\beta+8\right) + 60\left(\alpha+2\beta\right)\right]}$$

$$K'_{14} = -K'_{11}, \quad K'_{15} = K'_{12}, \quad K'_{16} = K'_{13}, \quad K'_{24} = -K'_{12}, \quad K'_{34} = -K'_{13}, \quad K'_{44} = K'_{11}$$

$$K'_{45} = -K'_{12}, \quad K'_{46} = -K'_{13}, \quad K'_{55} = K'_{22}, \quad K'_{56} = K'_{23}, \quad K'_{66} = K'_{33}, \quad K'_{35} = K'_{26}$$

$$K'_{22} = \frac{k_sAGL\begin{bmatrix}\left(161700\beta^3+160720\beta^2+43120\beta+3136\right)\alpha^4+\left(161700\beta^4+1272600\beta^3+944160\beta^2+208544\beta+13216\right)\alpha^3+\\ \left(40425\beta^5+731640\beta^4+2187640\beta^3+912960\beta^2+90384\beta+1152\right)\alpha^2+\left(67760\beta^5+766920\beta^4+1035392\beta^3+\\ 167520\beta^2+4608\beta\right)\alpha+24640\beta^5+218560\beta^4+79232\beta^3+4608\beta^2\end{bmatrix}}{24(56\beta+440\beta^2+28\alpha+280\alpha\beta+35\alpha\beta^2)(120\beta+56\beta^2+60\alpha+392\alpha\beta+105\alpha\beta^2+56\alpha^2+210\alpha^2\beta)}$$

$$K'_{23} = \frac{-k_sAGL\begin{bmatrix}\left(-80850\beta^4+81340\beta^3+74480\beta^2+14224\beta+448\right)\alpha^3+\left(-40425\beta^5-434420\beta^4+67480\beta^3+148176\beta^2+26544\beta+1152\right)\alpha^2+\\ \left(-67760\beta^5-575960\beta^4+54240\beta^3+65376\beta^2+4608\beta\right)\alpha-24640\beta^5-188992\beta^4+28160\beta^3+4608\beta^2\end{bmatrix}}{24(56\beta+440\beta^2+28\alpha+280\alpha\beta+35\alpha\beta^2)(120\beta+56\beta^2+60\alpha+392\alpha\beta+105\alpha\beta^2+56\alpha^2+210\alpha^2\beta)}$$

$$K'_{25} = \frac{\left[\begin{array}{l}\left(-323400\beta^3 - 321440\beta^2 - 86240\beta - 6272\right)\alpha^4 + \left(-323400\beta^4 - 604800\beta^3 + 40320\beta^2 + 100352\beta + 11200\right)\alpha^3 + \\ \left(-80850\beta^5 - 493080\beta^4 + 229600\beta^3 + 378240\beta^2 + 43680\beta + 384\right)\alpha^2 + \left(-135520\beta^5 + 92400\beta^4 + 442496\beta^3 + \\ 43200\beta^2 + 1536\beta\right)\alpha - 49280\beta^5 + 154240\beta^4 + 1280\beta^3 + 1536\beta^2\end{array}\right]}{24(56\beta + 440\beta^2 + 28\alpha + 280\alpha\beta + 35\alpha\beta^2)(120\beta + 56\beta^2 + 60\alpha + 392\alpha\beta + 105\alpha\beta^2 + 56\alpha^2 + 210\alpha^2\beta)}$$

$$K'_{26} = \frac{-k_s AGL\left[\begin{array}{l}\left(161700\beta^4 - 162680\beta^3 - 148960\beta^2 - 28448\beta - 896\right)\alpha^3 + \left(80850\beta^5 - 101360\beta^4 - 711200\beta^3 - 235872\beta^2 - 16800\beta + 384\right)\alpha^2 + \\ \left(135520\beta^5 - 474320\beta^4 - 404160\beta^3 - 53568\beta^2 + 1536\beta\right)\alpha + 49280\beta^5 - 213376\beta^4 - 47104\beta^3 + 1536\beta\end{array}\right]}{24(56\beta + 440\beta^2 + 28\alpha + 280\alpha\beta + 35\alpha\beta^2)(120\beta + 56\beta^2 + 60\alpha + 392\alpha\beta + 105\alpha\beta^2 + 56\alpha^2 + 210\alpha^2\beta)}$$

$$K'_{33} = \frac{k_s AGL\left[\begin{array}{l}\left(323400\beta^4 + 580160\beta^3 + 262080\beta^2 + 35840\beta + 1120\right)\alpha^3 + \left(40425\beta^5 + 1196720\beta^4 + 1386280\beta^3 + 423840\beta^2 + 43344\beta + 1152\right)\alpha^2 + \\ \left(67760\beta^5 + 1124200\beta^4 + 744000\beta^3 + 124512\beta^2 + 4608\beta\right)\alpha + 24640\beta^5 + 260800\beta^4 + 84608\beta^3 + 4608\beta^2\end{array}\right]}{24(56\beta + 440\beta^2 + 28\alpha + 280\alpha\beta + 35\alpha\beta^2)(120\beta + 56\beta^2 + 60\alpha + 392\alpha\beta + 105\alpha\beta^2 + 56\alpha^2 + 210\alpha^2\beta)}$$

$$K'_{36} = \frac{k_s AGL\left[\begin{array}{l}\left(323400\beta^4 + 192080\beta^3 + 53760\beta^2 + 2240\beta + 448\right)\alpha^3 + \left(-80850\beta^5 + 979160\beta^4 + 548800\beta^3 + 68160\beta^2 + 3360\beta + 384\right)\alpha^2 + \\ \left(-135520\beta^5 + 1004080\beta^4 + 307200\beta^3 + 10944\beta^2 + 1536\beta\right)\alpha - 49280\beta^5 + 238720\beta^4 + 12032\beta^3 + 1536\beta^2\end{array}\right]}{24(56\beta + 440\beta^2 + 28\alpha + 280\alpha\beta + 35\alpha\beta^2)(120\beta + 56\beta^2 + 60\alpha + 392\alpha\beta + 105\alpha\beta^2 + 56\alpha^2 + 210\alpha^2\beta)}$$

Appendix L

Continualization Method for repetitive periodic lattices

The continualization technique follows the method introduced in [251], however restricted to Cauchy homogenization. It includes replacing the vector of discrete microscopic displacements $\boldsymbol{u}_i = \left((u_i)_{y_1}, (u_i)_{y_2}, \phi_i\right)$ with the vector of continuous macroscopic components $\mathbf{u}(\boldsymbol{x},\boldsymbol{y}) = (u_{x_1}(\boldsymbol{x},\boldsymbol{y}), u_{x_2}(\boldsymbol{x},\boldsymbol{y}), \phi(\boldsymbol{x},\mathbf{y}))$. The Taylor series expansion can be written as follows [228]

$$\boldsymbol{u}_i = \boldsymbol{u}((y_1)_i,(y_2)_i) = \sum_{m=0}^{N}\sum_{n=0}^{N} \frac{(y_1)_i{}^m}{m!}\frac{(y_2)_i{}^n}{n!}\frac{\partial^{m+n}\boldsymbol{u}(\boldsymbol{x},\boldsymbol{y})}{\partial {y_1}^m \partial {y_2}^n} \tag{L.1}$$

where $(y_1)_i$ and $(y_2)_i$ are the coordinates of the node number 'i'. As an example, the following truncation of the Taylor series expansion Eq. L.1 leads to the construction of the macroscopic continua as,

$$u_{x_i} = u_{x_0} + x_i\frac{\partial u_{x_0}}{\partial x} + y_i\frac{\partial u_{x_0}}{\partial y} + \frac{x_i^2}{2}\frac{\partial^2 u_{x_0}}{\partial x^2} + \frac{y_i^2}{2}\frac{\partial^2 u_{x_0}}{\partial y^2} + x_i y_i\frac{\partial^2 u_{x_0}}{\partial x\partial y} \tag{L.2}$$

$$u_{y_i} = u_{y_0} + x_i\frac{\partial u_{y_0}}{\partial x} + y_i\frac{\partial u_{y_0}}{\partial y} + \frac{x_i^2}{2}\frac{\partial^2 u_{y_0}}{\partial x^2} + \frac{y_i^2}{2}\frac{\partial^2 u_{y_0}}{\partial y^2} + x_i y_i\frac{\partial^2 u_{y_0}}{\partial x\partial y} \tag{L.3}$$

$$\phi_i = \phi_0 + x_i\frac{\partial \phi_0}{\partial x} + y_i\frac{\partial \phi_0}{\partial y} \tag{L.4}$$

Before calculating the effective mechanical properties of a periodic structure, one needs to apply periodic boundary conditions on it. For this purpose, a series of definitions are needed, which are introduced below.

L.1 Direct translational bases

The lattice translational symmetry primitive bases, $\vec{a}_k$, are referred to as the direct translational bases. These translational bases are used to tessellate the unit cell that fills the space under translational symmetry. The direct translational bases are feature of the unit cell envelope, which demonstrates the axes through which the unit cell is tessellated to fill the space.

L.1.1 Direct translational vector

A direct translational vector, expressed as a linear combination of the direct translational bases, is used to translate the reference unit cell to any other cell in the lattice space. This is represented by the primitive lattice vector spanned over a set of cells in the lattice space, defined as:

$$\mathcal{R} = \sum_{k}^{n} m_k \vec{a}_k \tag{L.5}$$

where m_k is any set of integers and n is the dimensional space of the lattice ($n = 2$ in 2D and $n = 3$ in 3D).

L.1.2 Position vector

The position vector of nodes of the whole lattice material can be expressed as a function of the node bases, defined with reference to the unit cell envelope in addition to the direct translational vector as:

$$p_l = j_l + \mathcal{R} = j_l + \sum_{k}^{n} m_k \vec{a}_k \qquad \forall l \in \{1, ..., J\} \tag{L.6}$$

where p_l is the node position vector, and $J$is the number of independent nodes within the reference unit cell.

L.1.3 Direct lattice

The direct lattice is the set of independent node bases, over the reference unit cell envelope, spanned over the infinite periodic lattice material by their position vectors. To determine this independent set of node vectors over the reference unit cell, we verify whether a vector j_{l-1} is dependent on a vector j_l over one unit cell period through the relation:

$$j_{l-1} = j_l + \sum_{k}^{n} \hat{x}_k \vec{a}_k \tag{L.7}$$

The dependency information is used later on to modify the strain energy over the reference unit cell to generate the periodic strain energy over the entire lattice material.

L.1.4 Periodic transformation matrices

Applying periodic displacement boundary conditions over the generic unit cell of Fig. L.1 leads to the following conditions:

$$q_R = q_L; \;\; q_T = q_B; \;\; q_{RB} = q_{LB}; \;\; q_{LT} = q_{LB}; \;\; q_{RT} = q_{LB}; \tag{L.8}$$

where q is a generic nodal or element function, such as force and deformation, and T, B, L and R denote top, bottom, left and right edges, respectively. Eq. L.8 can be arranged in matrix format as:

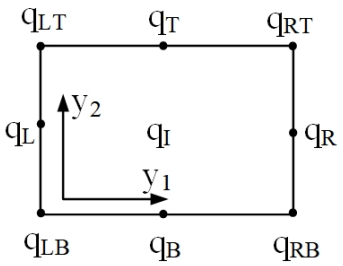

Figure L.1 A generic unit cell with its periodic displacement boundary conditions.

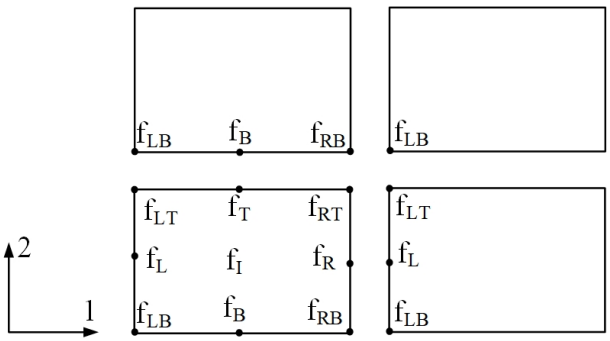

Figure L.2 Generic unit cell with its periodic equilibrium boundary conditions.

$$\begin{bmatrix} q_I \\ q_B \\ q_T \\ q_L \\ q_R \\ q_{LB} \\ q_{RB} \\ q_{LT} \\ q_{RT} \end{bmatrix} = \begin{bmatrix} 1 & 0 & 0 & 0 \\ 0 & 1 & 0 & 0 \\ 0 & 1 & 0 & 0 \\ 0 & 0 & 1 & 0 \\ 0 & 0 & 1 & 0 \\ 0 & 0 & 0 & 1 \\ 0 & 0 & 0 & 1 \\ 0 & 0 & 0 & 1 \\ 0 & 0 & 0 & 1 \end{bmatrix} \begin{bmatrix} q_I \\ q_B \\ q_L \\ q_{LB} \end{bmatrix}, \quad or\ q = \mathbf{T}\tilde{q} \tag{L.9}$$

where T is the transformation matrix from the primitive cell degrees of freedom, 'q' to the reduced cell degrees of freedom, '$\tilde{q}$'.

The same concept used to derive the kinematic transformation matrix can be applied to generate the equilibrium transformation matrix that considers the anti-periodic constraints necessary for the static equilibrium of the lattice. For the cluster of four generic unit cells shown in Fig. L.2, the following static equilibrium relations can be written:

$$f_R + f_L = 0; \;\; f_T + f_B = 0; \;\; f_{RT} + f_{LT} + f_{RB} + f_{LB} = 0; \tag{L.10}$$

Eq. L.10 can be arranged in matrix form as:

$$\begin{bmatrix} f_I \\ f_B \\ f_L \\ f_{LB} \end{bmatrix} = \begin{bmatrix} 1 & 0 & 0 & 0 & 0 & 0 & 0 & 0 & 0 \\ 0 & 1 & 1 & 0 & 0 & 0 & 0 & 0 & 0 \\ 0 & 0 & 0 & 1 & 1 & 0 & 0 & 0 & 0 \\ 0 & 0 & 0 & 0 & 0 & 1 & 1 & 1 & 1 \end{bmatrix} \begin{bmatrix} f_I \\ f_B \\ f_T \\ f_L \\ f_R \\ f_{LB} \\ f_{RB} \\ f_{LT} \\ f_{RT} \end{bmatrix}, \quad or\ \tilde{f} = \mathbf{T}^T f = 0 \tag{L.11}$$

where $\boldsymbol{T}^T$ is the transpose of the transformation matrix $\boldsymbol{T}$.

L.2 Stiffness system of the unit cell

The stiffness system of a unit cell that has b elements connected between j nodes is expressed as:

$$\boldsymbol{K}d = f \tag{L.12}$$

where $\boldsymbol{K} \in R^{j \times j}$ is the stiffness matrix of the structure that relates the applied force vector, $f \in R^j$ into the nodal deformation vector, $d \in R^j$. Eqs. L.9 and L.11 are substituted into the stiffness system of the unit cell, Eq. L.12, to derive its periodic reduced form as

$$\tilde{\boldsymbol{K}}\tilde{d} = \tilde{f} \tag{L.13}$$

where $\tilde{\boldsymbol{K}}$ is the reduced stiffness matrix of the unit cell, expressed as:

$$\tilde{\boldsymbol{K}} = \boldsymbol{T}^T \boldsymbol{K} \boldsymbol{T} \tag{L.14}$$

L.3 Homogenization process to derive the macroscopic stiffness of periodic lattice materials

The stiffness properties of the microscopic lattice material are homogenized to generate its effective macroscopic properties, using a continualization method.

From the definition of Eqs. L.2- L.4, the infinitesimal displacement field of a periodic node in a lattice material can be formulated as:

$$d_i = d_j + \boldsymbol{A}\bar{\varepsilon} \tag{L.15}$$

where d_i is the continuous displacement field of the dependent node 'i', while 'j' is the continuous displacement of the independent node 'j'. The vector $\bar{\varepsilon}$ depends on the continuum model implemented

for homogenization contains different gradients of deformation and rotation fields. $\boldsymbol{A}$ is a matrix that implements Eqs. L.2- L.4 to create the continues nodal displacements within the domain of the lattice material. Substituting Eq. L.9 into Eq. L.15 results in

$$d = \boldsymbol{T}\tilde{d} + \boldsymbol{A}\bar{\varepsilon} \tag{L.16}$$

For the generic unit cell of Fig. L.1, Eq. L.16 can be formulated in matrix format as

$$\begin{bmatrix} d_I \\ d_B \\ d_L \\ d_{LB} \\ d_R \\ d_T \\ d_{RB} \\ d_{LT} \\ d_{RT} \end{bmatrix} = \begin{bmatrix} 1 & 0 & 0 & 0 \\ 0 & 1 & 0 & 0 \\ 0 & 0 & 1 & 0 \\ 0 & 0 & 0 & 1 \\ 0 & 0 & 1 & 0 \\ 0 & 1 & 0 & 0 \\ 0 & 0 & 0 & 1 \\ 0 & 0 & 0 & 1 \\ 0 & 0 & 0 & 1 \end{bmatrix} \begin{bmatrix} d_I \\ d_B \\ d_L \\ d_{LB} \end{bmatrix} + \begin{bmatrix} 0 & 0 & 0 & 0 & 0 \\ 0 & 0 & 0 & 0 & 0 \\ 0 & 0 & 0 & 0 & 0 \\ 0 & 0 & 0 & 0 & 0 \\ \Delta y_1^{RL} & \Delta y_2^{RL} & \left(\Delta y_1^{RL}\right)^2/2 & \left(\Delta y_2^{RL}\right)^2/2 & \Delta y_1^{RL}\Delta y_2^{RL} \\ \Delta y_1^{TB} & \Delta y_2^{TB} & \left(\Delta y_1^{TB}\right)^2/2 & \left(\Delta y_2^{TB}\right)^2/2 & \Delta y_1^{TB}\Delta y_2^{TB} \\ \Delta y_1^{LTLB} & \Delta y_2^{LTLB} & \left(\Delta y_1^{LTLB}\right)^2/2 & \left(\Delta y_2^{LTLB}\right)^2/2 & \Delta y_1^{LTLB}\Delta y_2^{LTLB} \\ \Delta y_1^{LTLB} & \Delta y_2^{LTLB} & \left(\Delta y_1^{LTLB}\right)^2/2 & \left(\Delta y_2^{LTLB}\right)^2/2 & \Delta y_1^{LTLB}\Delta y_2^{LTLB} \\ \Delta y_1^{LTLB} & \Delta y_2^{LTLB} & \left(\Delta y_1^{LTLB}\right)^2/2 & \left(\Delta y_2^{LTLB}\right)^2/2 & \Delta y_1^{LTLB}\Delta y_2^{LTLB} \end{bmatrix} \begin{bmatrix} \mathbf{u}_{,x_1} \\ \mathbf{u}_{,x_2} \\ \mathbf{u}_{,x_1x_1} \\ \mathbf{u}_{,x_2x_2} \\ \mathbf{u}_{,x_1x_2} \end{bmatrix} \tag{L.17}$$

L.3.1 Microscopic nodal deformations in terms of the macroscopic strain field

The independent microscopic nodal deformations in terms of the macroscopic gradient field can be computed by substituting Eq. L.17 and L.11 into Eq. L.12, resulting in:

$$\tilde{\boldsymbol{K}}\tilde{d} + \boldsymbol{T}^T\boldsymbol{K}\boldsymbol{A}\bar{\varepsilon} = \tilde{f} \tag{L.18}$$

Writing the balance equation of independent nodes in all directions results in a set of algebraic equations, which can be solved for the microscopic nodal deformations. But to have a unique solution, translational rigid-body motion should be eliminated; to this end, one of the independent nodes should be set as a reference node and the translational degree of freedom related to this node should be eliminated.

L.3.2 Homogenized macroscopic stiffness of lattice materials

The nodal forces and deformations formulated in the previous section are used to derive the effective mechanical properties using the principle of the virtual work and Hill-Mandel macrohomogeneity condition, as:

$$W_M = \frac{1}{2}d^T\mathbf{K}d = \frac{1}{2}\left[\mathbf{T}\tilde{d} + \mathbf{A}\bar{\varepsilon}\right]^T\mathbf{K}\left[\mathbf{T}\tilde{d} + \mathbf{A}\bar{\varepsilon}\right] \tag{L.19}$$

The nodal DOF's are here substituted by the continuous kinematic variables from the localization step.

Appendix M

Extended macrohomogeneity lemma for the micropolar continuum

Let consider a symmetrical stress tensor field $\boldsymbol{\sigma}$ defined in the unit cell Y assumed to have a rectangular shape (Fig. M.1) and verifying the following BVP over the unit cell in the absence of body forces and with anti-periodic traction:

$$\left| \begin{array}{l} \boldsymbol{\sigma} \cdot \nabla_y = \mathbf{0} \\ \boldsymbol{\sigma}.\boldsymbol{n} \quad \textit{opposite on the opposite edges of } \partial Y \end{array} \right. \tag{M.1}$$

The weak formulation of previous equations is obtained in a conventional way, multiplying the BVP Eq. M.1 with an arbitrary differentiable vector field $\boldsymbol{\omega}$ and integrating over the unit cell domain Y, so that it holds

$$\int_Y (\nabla_y \cdot \boldsymbol{\sigma}) \cdot \boldsymbol{\omega} \, dV_y = 0; \forall \boldsymbol{\omega} \tag{M.2}$$

Integrating by parts Eq. M.2 and using the divergence theorem delivers the relation

$$-\int_Y \boldsymbol{\sigma} : (\boldsymbol{\omega} \otimes \nabla_y) dV_y + \int_{\partial Y} (\boldsymbol{\sigma} \cdot \boldsymbol{n}) \cdot \boldsymbol{\omega} \, ds_y = 0 \tag{M.3}$$

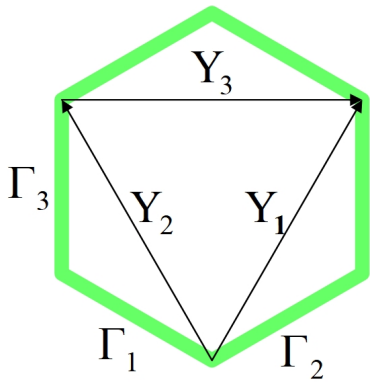

Figure M.1 Hexagon unit cell and the associated periodicity vectors Y_1,Y_2,Y_3 in a 2D situation.

Taking into account the boundary condition Eq. M.1 provides the weak formulation of the balance equation as

$$\forall \boldsymbol{\omega}; \quad -\int_Y \boldsymbol{\sigma} : (\boldsymbol{\omega} \otimes \nabla_y) dV_y + \sum_{i=1,2,3} \int_{\partial Y} (\boldsymbol{\sigma} \cdot \boldsymbol{n}) \cdot [\![\boldsymbol{\omega}]\!]^{\delta} ds_y = 0 \tag{M.4}$$

with the difference of the vector field $\boldsymbol{\omega}$ taken over opposite edges of the unit cell:

$$[\![\boldsymbol{\omega}]\!]^{\delta} := \boldsymbol{\omega}\left(\boldsymbol{y} + \boldsymbol{Y}^{\delta}\right) - \boldsymbol{\omega}\left(\boldsymbol{Y}^{\delta}\right), \delta = 1,2,3 \tag{M.5}$$

By imposing $[\![\boldsymbol{\omega}]\!]^{\delta} = \text{cst}$ on the unit cell boundary $\partial\Omega^{\delta}, \delta = 1,2,3$ it holds

$$-\int_Y \boldsymbol{\sigma} : (\boldsymbol{\omega} \otimes \nabla_y) dV_y + \sum_{i=1,2,3} [\![\boldsymbol{\omega}]\!]^{i} \cdot \int_{\partial Y} (\boldsymbol{\sigma} \cdot \boldsymbol{n}) \, ds_y = 0 \tag{M.6}$$

Assuming $\boldsymbol{\omega}$ of the form of the homogenous displacement 5.15 with $\boldsymbol{\xi} := \boldsymbol{y} - \boldsymbol{x}$ therein the relative position of the micropoints within the unit cell Y, it holds due to Eq. M.5 and Eq. M.6 the two following relations

$$\begin{aligned} \omega_{i,j} &= \mathrm{E}_{ij} - \epsilon_{ijk}\Phi_k - \epsilon_{ijk}\mathrm{K}_{kl}\xi_l + \epsilon_{imk}\mathrm{K}_{mj}\xi_k \\ [\omega_i]^{\delta} &= \mathrm{E}_{ij}Y_j^{\delta} + \epsilon_{ijk}\Phi_j Y_k^{\delta} + \epsilon_{ijk}\mathrm{K}_{jl}Y_l^{\delta}Y_k^{\delta} \end{aligned} \tag{M.7}$$

Substituting Eq. 5.15 and Eq. M.7 into Eq. M.6 results after straightforward calculations $\forall \mathbf{E}(\boldsymbol{x})$, $\boldsymbol{\Phi}(\boldsymbol{x})$, $\mathbf{K}(\boldsymbol{x})$:

$$\left\{ -\int_Y \sigma_{ij} dV_y + \sum_{i=1,2,3} \left(\int_{\partial Y} (\sigma_{ik} n_k) \, ds_y \right) Y_j^{\delta} \right\} \mathrm{E}_{ij} = 0 \tag{M.8}$$

$$\left\{ \int_Y \epsilon_{ijk}\sigma_{ij} dV_y - \sum_{i=1,2,3} \left(\int_{\partial Y} (\epsilon_{ijk}\sigma_{il} n_l) \, ds_y \right) Y_j^{\delta} \right\} \Phi_k = 0 \tag{M.9}$$

$$\left\{ \int_Y (\epsilon_{ijk}\sigma_{ij}\xi_l + \epsilon_{ijk}\sigma_{il}\xi_j) \, dV_y - \sum_{i=1,2,3} \left(\int_{\partial Y} (\epsilon_{ijk}\sigma_{im} n_m) \, ds_y \right) Y_j^{\delta} Y_l^{\delta} \right\} \mathrm{K}_{kl} = 0 \tag{M.10}$$

Eq. M.8 results in the elaboration of the static measure of the strain in the effective continuum as the following sums over the unit cell boundaries:

$$\boldsymbol{\Sigma} = \langle \boldsymbol{\sigma} \rangle_Y = \frac{1}{|Y|} \sum_{i=1,2,3} \left(\int_{\partial Y} (\boldsymbol{\sigma} \cdot \boldsymbol{n}) \, ds \right) \otimes \boldsymbol{Y}^{\delta} \tag{M.11}$$

Eq. M.9, show the static measure of the skew-symmetric part of the strain and can be written as

$$\boldsymbol{\Sigma}^{skew} = \langle \boldsymbol{\epsilon} : \boldsymbol{\sigma} \rangle_Y = \frac{1}{|Y|} \sum_{i=1,2,3} \left(\int_{\partial Y} (\boldsymbol{\epsilon} \cdot \boldsymbol{\sigma} \cdot \boldsymbol{n}) \, ds \right) \cdot \boldsymbol{Y}^{\delta} \tag{M.12}$$

Finally, Eq. M.10 is the static measure of the curvature in the effective micropolar continuum which can be written as follows

$$\boldsymbol{M} = \langle \boldsymbol{\epsilon} : \boldsymbol{\sigma} \otimes \boldsymbol{\xi} + \boldsymbol{\xi} \times \boldsymbol{\sigma} \rangle_Y = \sum_{i=1,2,3} \left(\int_{\partial Y} (\boldsymbol{\epsilon} \cdot \boldsymbol{\sigma} \cdot \boldsymbol{n}) \, ds_y \right) \cdot \boldsymbol{Y} \otimes \boldsymbol{Y} \tag{M.13}$$

Using further the relation [234]

$$\sum_{i=1,2,3} \boldsymbol{N} \otimes \boldsymbol{Y} = |Y| \, \boldsymbol{I}_2 \tag{M.14}$$

with $\boldsymbol{I}_2$ the second-order identity tensor, Eq. M.6 rewrites selecting a constant difference $[\![\boldsymbol{\omega}]\!]^{\delta}$ as

$$[\![\boldsymbol{\omega}]\!]^{\delta} = cst \rightarrow \int_Y \boldsymbol{\sigma} : (\boldsymbol{\omega} \otimes \nabla_y) dV_y = \sum_{\delta,\beta=1,2,3} \delta_{\delta\beta} [\![\boldsymbol{\omega}]\!]^{\delta} \cdot \int_{\partial Y} (\boldsymbol{\sigma} \cdot \boldsymbol{n}) \, ds_y ; \forall \boldsymbol{\omega} \tag{M.15}$$

Using the relation $\sum_{i=1,2,3} \boldsymbol{N}^i . \boldsymbol{Y}^j = |Y| \, \delta_{ij}$ arising as a consequence of Eq. M.14, see [234], relation rewrites:

$$\int_Y \boldsymbol{\sigma} : (\boldsymbol{\omega} \otimes \nabla_y) dV_y = \frac{1}{|Y|} \sum_{i,j=1,2,3} \boldsymbol{N}^i \cdot \boldsymbol{Y}^j [\![\boldsymbol{\omega}]\!]^{i} \cdot \int_{\partial Y} (\boldsymbol{\sigma} \cdot \boldsymbol{n}) \, ds_y \tag{M.16}$$

Eq. M.16 can be rewritten as

$$\int_Y \boldsymbol{\sigma} : (\boldsymbol{\omega} \otimes \nabla_y) dV_y = \frac{1}{|Y|} \sum_{i=1,2,3} \left([\![\boldsymbol{\omega}]\!]^{i} \otimes \boldsymbol{N}^i \right) : \sum_{j=1,2,3} \left(\int_{\partial Y} (\boldsymbol{\sigma} \cdot \boldsymbol{n}) \, ds_y \otimes \boldsymbol{Y}^j \right) \tag{M.17}$$

Inserting relations Eq. M.7 into relation M.17 delivers the equality

$$\begin{aligned}
\int_Y \boldsymbol{\sigma} : (\boldsymbol{\omega} \otimes \nabla_y) dV_y = & \frac{1}{|Y|} \sum_{i=1,2,3} \left(\left(\boldsymbol{E} \cdot \boldsymbol{Y}^i \right) \otimes \boldsymbol{N}^i \right) : \sum_{j=1,2,3} \left(\int_{\partial Y} (\boldsymbol{\sigma} \cdot \boldsymbol{n}) \, ds_y \otimes \boldsymbol{Y}^j \right) \\
& - \frac{1}{|Y|} \sum_{i=1,2,3} \left(\left((\epsilon \cdot \Phi) \cdot \boldsymbol{Y}^i \right) \otimes \boldsymbol{N}^i \right) : \sum_{j=1,2,3} \left(\int_{\partial Y} (\boldsymbol{\sigma} \cdot \boldsymbol{n}) \, ds_y \otimes \boldsymbol{Y}^j \right) \\
& + \frac{1}{|Y|} \sum_{i=1,2,3} \left(\left((\epsilon \cdot \mathrm{K}) \cdot \boldsymbol{Y}^i \cdot \boldsymbol{Y}^i \right) \otimes \boldsymbol{N}^i \right) : \sum_{j=1,2,3} \left(\int_{\partial Y} (\boldsymbol{\sigma} \cdot \boldsymbol{n}) \, ds_y \otimes \boldsymbol{Y}^j \right)
\end{aligned} \tag{M.18}$$

Using again the relation $\underline{\boldsymbol{N}}^i \cdot \underline{\boldsymbol{Y}}^j = |Y| \, \delta_{ij}$ along with Eqs. 5.8- 5.18, Eq. M.18 can be rewritten after straightforward calculations as

$$\begin{aligned}
\int_Y \boldsymbol{\sigma} : (\boldsymbol{\omega} \otimes \nabla_y) dV_y = & \frac{1}{|Y|} \sum_{i=1,2,3} \left(\left((\nabla_x \boldsymbol{U} - \boldsymbol{\epsilon} \cdot \boldsymbol{\Phi}) \cdot \boldsymbol{Y}^i \right) \otimes \boldsymbol{N}^i \right) : \sum_{j=1,2,3} \left(\int_{\partial Y} (\boldsymbol{\sigma} \cdot \boldsymbol{n}) \, ds_y \otimes \boldsymbol{Y}^j \right) \\
& - \frac{1}{|Y|} \sum_{i=1,2,3} \left(\left((\boldsymbol{\epsilon} \cdot \boldsymbol{\Phi}) \cdot \boldsymbol{Y}^i \right) \otimes \boldsymbol{N}^i \right) : \sum_{j=1,2,3} \left(\int_{\partial Y} (\boldsymbol{\sigma} \cdot \boldsymbol{n}) \, ds_y \otimes \boldsymbol{Y}^j \right) \\
& + \frac{1}{|Y|} \sum_{i=1,2,3} \left(\left((\mathbf{K}) \cdot \boldsymbol{Y}^i \right) \otimes \boldsymbol{N}^i \right) \therefore \sum_{j=1,2,3} \left(\int_{\partial Y} (\boldsymbol{\sigma} \cdot \boldsymbol{n}) \, ds_y \otimes \boldsymbol{Y}^j \otimes \boldsymbol{Y}^j \right) \\
= & \frac{1}{|Y|} \sum_{i=1,2,3} \left(\left(\nabla_x^{sym} \boldsymbol{U} \cdot \boldsymbol{Y}^i \right) \otimes \boldsymbol{N}^i \right) : \sum_{j=1,2,3} \left(\int_{\partial Y} (\boldsymbol{\sigma} \cdot \boldsymbol{n}) \, ds_y \otimes \boldsymbol{Y}^j \right) \\
& + \frac{1}{|Y|} \sum_{i=1,2,3} \left(\left((\nabla_x^{skew} \boldsymbol{U} - 2\boldsymbol{\epsilon} \cdot \Phi) \cdot \boldsymbol{Y}^i \right) \otimes \boldsymbol{N}^i \right) : \sum_{j=1,2,3} \left(\int_{\partial Y} (\boldsymbol{\sigma} \cdot \boldsymbol{n}) \, ds_y \otimes \boldsymbol{Y}^j \right) \\
& + \frac{1}{|Y|} \sum_{i=1,2,3} \left(\left((\mathbf{K}) \cdot \boldsymbol{Y}^i \right) \otimes \boldsymbol{N}^i \right) : \sum_{j=1,2,3} \left(\int_{\partial Y} (\boldsymbol{\epsilon} \cdot \boldsymbol{\sigma} \cdot \boldsymbol{n}) \, ds_y \cdot \boldsymbol{Y}^j \otimes \boldsymbol{Y}^j \right) \\
= & \frac{1}{|Y|} \sum_{i=1,2,3} \left(\left(\nabla_x^{sym} \boldsymbol{U} \cdot \boldsymbol{Y}^i \right) \otimes \boldsymbol{N}^i \right) : \sum_{j=1,2,3} \left(\int_{\partial Y} (\boldsymbol{\sigma} \cdot \boldsymbol{n}) \, ds_y \otimes \boldsymbol{Y}^j \right)^{sym} \\
& + \frac{1}{|Y|} \sum_{i=1,2,3} \left(\left(\mathbf{E}^{Tskew} \cdot \boldsymbol{Y}^i \right) \otimes \boldsymbol{N}^i \right) : \sum_{j=1,2,3} \left(\int_{\partial Y} (\boldsymbol{\sigma} \cdot \boldsymbol{n}) \, ds_y \otimes \boldsymbol{Y}^j \right)^{skew} \\
& + \frac{1}{|Y|} \sum_{i=1,2,3} \left(\left((\mathbf{K}) \cdot \boldsymbol{Y}^i \right) \otimes \boldsymbol{N}^i \right) : \sum_{j=1,2,3} \left(\int_{\partial Y} (\boldsymbol{\epsilon} \cdot \boldsymbol{\sigma} \cdot \boldsymbol{n}) \, ds_y \cdot \boldsymbol{Y}^j \otimes \boldsymbol{Y}^j \right) \\
= & \boldsymbol{\Sigma}^{sym} : \boldsymbol{E}^{sym}(\boldsymbol{x}) + \boldsymbol{\Sigma}^{skew} : \boldsymbol{E}^{skew}(\boldsymbol{x}) + \mathbf{M}(\boldsymbol{x}) : \mathbf{K}(\boldsymbol{x})
\end{aligned} \tag{M.19}$$

Previous relation constitutes Hill lemma for the Cosserat effective continuum that can measure all of the macro kinematic and static variables as a surface integral over the unit cell boundaries.

Appendix N

A reminder of differential geometry in curvilinear coordinates

The differential or covariant derivative of a contravariant vector field $\boldsymbol{X} = X^j g_j$ writes using the Christoffel symbols Γ^j_{hk} [237]

$$\begin{aligned} &X^j = X^j(x^q) \rightarrow DX^j = dX^j + \Gamma^j_{hk} X^h dx^k \\ &\Rightarrow \frac{DX^j}{Dx^k} = \frac{\partial X^j}{\partial x^k} + \Gamma^j_{hk} X^h \end{aligned} \tag{N.1}$$

The last relation defines the covariant derivative of the contravariant vector field; the first term on the right-hand side is the classical partial derivative $\frac{\partial X^j}{\partial x^k}$, whereas the second term is due to the change of the structure of the vector field as the local basis changes with position.

Similarly, for a covariant vector field $\boldsymbol{Y} = Y_h g^h$ with components $Y_h = Y_h(x^k)$, its covariant derivative is evaluated as

$$DY_h = dY_h - \Gamma^l_{hk} Y_l dx^k \rightarrow \frac{DY_h}{dx^k} = \frac{\partial Y_h}{\partial x^k} - \Gamma^l_{hk} Y_l \tag{N.2}$$

These covariant derivatives extend to tensor fields. The volume element transform as

$$d\boldsymbol{x} = \nabla_{\tilde{x}} \boldsymbol{\varphi} . d\tilde{\boldsymbol{x}} \rightarrow dV_x = \det\left(\nabla_{\tilde{x}} \boldsymbol{\varphi}\right) dV_{\tilde{x}} \tag{N.3}$$

A vector field $\boldsymbol{v}(\boldsymbol{x}) = v^i(x^k)$ transforms as follows:

$$\boldsymbol{v}(\boldsymbol{x}) = v^i(x^k) g_k \ \wedge \ \tilde{\boldsymbol{v}}(\tilde{\boldsymbol{x}}) = \tilde{v}^i(\tilde{x}^k)\tilde{g}_k, \ \tilde{v}^i(\tilde{x}^k) = \frac{\partial \tilde{x}^i}{\partial x^h} v^h(x^q) \tag{N.4}$$

Moreover, its differential and gradient transform as:

$$\nabla_x \boldsymbol{v}(x) = \frac{Dv^i}{Dx^k} g_k, \ \nabla_{\tilde{x}} \tilde{\boldsymbol{v}}(\tilde{x}) = \frac{D\tilde{v}^i}{D\tilde{x}^k} \tilde{g}_k \tag{N.5}$$

with

$$\frac{D\tilde{v}^i}{D\tilde{x}^k} = \frac{\partial^2 \tilde{x}^i}{\partial x^l \partial x^h} \frac{\partial x^l}{\partial \tilde{x}^k} v^h + \frac{\partial v^h}{\partial x^l} \frac{\partial \tilde{x}^i}{\partial x^h} \frac{\partial x^l}{\partial \tilde{x}^k} \Rightarrow D\tilde{v}^i = \frac{\partial \tilde{x}^i}{\partial x^h} dv^h + \frac{\partial^2 \tilde{x}^i}{\partial x^h \partial x^k} v^h dx^k$$

The last relation gives the covariant differential of the vector coordinates $\tilde{v}^i$ versus the differential elements dv^h, dx^k. The basis vectors transform in a covariant manner, so it holds

$$\tilde{g}_h := \frac{\partial \boldsymbol{x}}{\partial \tilde{x}^h} = \frac{\partial \boldsymbol{x}}{\partial x^j}.\frac{\partial x^j}{\partial \tilde{x}^h} = \frac{\partial x^j}{\partial \tilde{x}^h} g_j \tag{N.6}$$

Note that it holds the following relations:

$$\begin{aligned}
&\sum_h \frac{\partial \tilde{x}^j}{\partial x^h}\frac{\partial x^h}{\partial \tilde{x}^l} = \delta_{jl},\ \frac{\partial x^h}{\partial \tilde{x}^j}\frac{\partial \tilde{x}^j}{\partial x^k} = \delta_{hk} \\
&\tilde{A}_j\tilde{B}_l = \sum_h\sum_k \frac{\partial \tilde{x}^j}{\partial x^h}\frac{\partial \tilde{x}^l}{\partial x^k}A_hB_k \to \sum_{j=1}^{n}\tilde{A}_j\tilde{B}_j = \sum_j\sum_h\sum_k \frac{\partial \tilde{x}^j}{\partial x^h}\frac{\partial \tilde{x}^j}{\partial x^k}A_hB_k \\
&Let\ g_{hk} := \sum_j \frac{\partial \tilde{x}^j}{\partial x^h}\frac{\partial \tilde{x}^j}{\partial x^k} \to \sum_{j=1}^{n}\tilde{A}_j\tilde{B}_j = g_{hk}A_hB_k \equiv \langle \boldsymbol{A}, \boldsymbol{B}\rangle
\end{aligned} \tag{N.7}$$

The last relation introduces the **metric tensor** as the symmetric tensor with matrix (g_{hk}) and inverse denoted $\left(g^{hk}\right)$, such that $\sum_l g^{jl}g_{hl} = \delta_h^j$. Thus the covariant derivatives (as vectors) transform like a contravariant vector and opposite to the transformation rule of the covariant basis vectors g_j. The Christoffel symbols can be expressed from the derivatives of the tangent vector's basis as (the dot therein indicates the position of indices)

$$dg_i = \Gamma_{ki}^j g_j du^k \Rightarrow \Gamma_{ki}^j = \frac{\partial g_i}{\partial u^k}.g^j \Rightarrow Dv^j = dv^j + \Gamma_{hk}^j v^h dx^k \tag{N.8}$$

The last expression represents the covariant differential of the component v^j; the Christoffel symbols accordingly represent the projections of the partial derivatives of the basis vectors concerning the curvilinear coordinates. One can further define the Christoffel symbols of the first kind by contracting with the metric to lower all indices,

$$g_{ij} := g_i.g_j \Rightarrow \Gamma_{ijk} = g_{jl}\Gamma_{i.k}^l \tag{N.9}$$

Accordingly, the quantities $D\tilde{v}^i$ constitute the components of a contravariant vector, so they transform like a contravariant vector:

$$Dv^i = \frac{\partial v^j}{\partial x^k}dx^k + \Gamma_{hk}^j v^h dx^k,\ D\tilde{v}^i = \frac{\partial v^j}{\partial \tilde{x}^k}d\tilde{x}^k + \Gamma_{hk}^j v^h d\tilde{x}^k \Rightarrow D\tilde{v}^i = \frac{\partial \tilde{x}^i}{\partial x^h}Dv^h \tag{N.10}$$

Abstract: Homogenization of periodic and quasi-periodic architected media towards generalized continua

This thesis aims to revisit higher-order homogenization schemes towards higher-order or higher gradient continua, successively for periodic and quasi-periodic architected materials and composites, based on variational principles and an extension of Hill macrohomogeneity condition. Continuous homogenization methods are exposed in Part I for micropolar and micromorphic media, followed by an exposition of the alternative discrete homogenization method.

We have extended these theoretical developments to the situation of quasi-periodic materials, which still have a regular microstructure. The common idea to the proposed periodic homogenization methods of continuous or discrete nature is to split the microscopic displacement into a homogeneous part representative of the kinematics of the adopted effective continuum and a fluctuation evaluated from a variational principle. In substance, the theoretical developments allow the elaboration of enriched continua (generalized continua) of micromorphic type and all sub continua obtained using suitable degeneration conditions. Numerical applications have been made for architected materials and inclusion-based composites prone to higher-order effects due to their inner architecture. On the theoretical framework, the performed developments remedy many existing limitations of existing higher-order homogenization schemes.

In Part II, the classical and higher-order continuum properties have been evaluated either following the path of phenomenology or based on micromechanical schemes. Consistent couple stress models of repetitive beam lattices have been elaborated in a phenomenological manner. Enriched Cosserat media have been derived in the spirit of micromechanics, adopting Timoshenko beam models at a microlevel, and applying a continualization method towards a Cosserat effective substitution medium. The proposed discrete homogenization method proves to be accurate and computationally efficient compared to continuous homogenization schemes and fully resolved finite element simulations. One key outcome of the performed analyses is the quantification of edge effects in the response of lattice structures, relying on the surface formulation of the extended Hill macrohomogeneity condition.

The theoretical background underlying quasi-periodic asymptotic homogenization in the framework of linearized anisotropic elasticity deserves the development of Part III. Different methodologies for evaluating the effective quasi-periodic properties have been elaborated, leading to the emergence of strain gradient effective media. Conformal transformations define a specific class of geometrical mappings, allowing for designing compatible architected materials with inner porosity gradient, making them suitable bone biomechanics candidates.

Key words: Architectural materials, Homogenization methods, Numerical methods, Periodic and quasi-periodic media, Continuous or discrete homogenization, Generalized continua, Periodic boundary condition.

Résumé: Homogénéisation de milieux architecturés périodiques et quasi-périodiques vers des milieux continus généralisés

Cette thèse vise à revisiter les schémas d'homogénéisation d'ordre supérieur vers des continuums d'ordre ou de gradient supérieurs, successivement pour les matériaux et composites architecturés périodiques et quasi-périodiques, en se basant sur des principes variationnels et une extension de la condition de macrohomogénéité de Hill. Les méthodes d'homogénéisation continues sont exposées dans la première partie pour les milieux micropolaires et micromorphes, suivies par une présentation d'une théorie de l'homogénéisation discrète, alternative de l'homogénéisation continue.

Nous avons étendu ces développements théoriques à la situation des matériaux quasi-périodiques, de microstructure régulière, qui peut être transformée en une configuration périodique de référence. L'idée commune aux méthodes d'homogénéisation périodique proposées (de nature continue ou discrète) est de décomposer le déplacement microscopique en une partie homogène représentative de la cinématique du milieu continu effectif adopté, et une fluctuation évaluée à partir d'un principe variationnel. En substance, les développements théoriques permettent l'élaboration de continuums enrichis (milieux continus généralisés) de type micromorphe, et des variantes qui en découlent en utilisant des conditions de dégénérescence appropriées. Des applications numériques ont été réalisées pour des matériaux architecturés et des composites à renforts de type inclusion. Sur le plan théorique, les développements réalisés remédient à de nombreuses limitations des schémas d'homogénéisation d'ordre supérieur existants.

Dans la partie II, les propriétés mécaniques du continuum ont été enrichies par une voie phénoménologique ou en suivant des approches micromécaniques. Des modèles à couple de contraintes de poutres enrichies sont construits, en supposant le matériau doté d'un paramètre additionnel de longueur interne. En guise d'alternative, des milieux de Cosserat enrichis ont été élaborés dans l'esprit de la micromécanique, en adoptant des modèles de poutre de Timoshenko à un niveau microscopique, et en appliquant une méthode de continualisation vers un milieu de substitution effectif de Cosserat. La méthode d'homogénéisation discrète s'avère précise et efficace en termes de calcul par rapport aux schémas d'homogénéisation continus et aux simulations par éléments finis réalisés sur la microstructure initiale. Un résultat essentiel des analyses effectuées est la quantification des effets de bord.

Le contexte théorique qui sous-tend l'homogénéisation asymptotique quasi-périodique dans le cadre de l'élasticité anisotrope linéarisée est abordé dans la troisième partie. Différentes méthodologies d'évaluation des propriétés effectives quasi-périodiques ont été élaborées, conduisant à l'émergence de milieux effectifs à gradient de déformation. Les transformations conformes définissent une classe de transformations géométriques permettant de concevoir des matériaux architecturés générant un gradient de porosité interne, ce qui en fait de bons candidats pour des biosubstituts en biomécanique osseuse.

Mots clés: Matériaux architecturés, Méthodes d'homogénéisation, Méthodes numériques, Milieux périodiques et quasi-périodiques, Homogénéisation continue ou discrète, Milieux continus généralisés.